UNIVERSITY OF CALIFORNIA, SAN DIEGO

RELIABILITY-BASED FRAMEWORK FOR FATIGUE DAMAGE PROGNOSIS OF BONDED STRUCTURAL ELEMENTS IN AEROSPACE COMPOSITE STRUCTURES

A dissertation submitted in partial satisfaction of the requirements for the degree

Doctor of Philosophy

in

Structural Engineering

by

Maurizio Gobbato

Committee in charge:

Professor Joel P. Conte, Chair
Professor John B. Kosmatka, Co-Chair
Professor David J. Benson
Professor Charles R. Farrar
Professor François M. Hemez
Professor Dimitris N. Politis

2011

The dissertation of Maurizio Gobbato is approved, and it is acceptable in quality and form for publication on microfilm and electronically:

_____

_____

_____

_____

_____
Co-Chair

_____
Chair

University of California, San Diego

2011

To my Family

TABLE OF CONTENTS

LIST OF SYMBOLS

$\alpha_0^{(i,j)}$ = coefficient of the model proposed by Berens (1989) for the probability of detection (*POD*) curve associated with the detectability of the j^{th} damage mechanism evolving/developing at the i^{th} damage location

$\hat{\alpha}_0^{(i,j)}$ = estimate of the *POD* curve parameter $\alpha_0^{(i,j)}$ through logistic regression analysis

$\alpha_1^{(i,j)}$ = coefficient of the model proposed by Berens (1989) for the *POD* curve associated with the detectability of the j^{th} damage mechanism evolving/developing at the i^{th} damage location

$\hat{\alpha}_1^{(i,j)}$ = estimate of the *POD* curve parameter $\alpha_1^{(i,j)}$ through logistic regression analysis

$\alpha_2^{(i,j)}$ = coefficient of the model proposed by Staat (1993) for the *POD* curve associated with the detectability of the j^{th} damage mechanism evolving/developing at the i^{th} damage location

$\hat{\alpha}_2^{(i,j)}$ = estimate of the *POD* curve parameter $\alpha_2^{(i,j)}$ through logistic regression analysis

$\beta_0^{(i,j)}$ = coefficient of the linear damage sizing model associated with the j^{th} damage mechanism evolving/developing at the i^{th} damage location

$\hat{\beta}_0^{(i,j)}$ = estimate of the linear damage sizing model $\beta_0^{(i,j)}$ through linear regression analysis

$\beta_1^{(i,j)}$ = coefficient of the linear damage sizing model associated with the j^{th} damage mechanism evolving/developing at the i^{th} damage location

$\hat{\beta}_1^{(i,j)}$ = estimate of the linear damage sizing model $\beta_1^{(i,j)}$ through linear regression analysis

$\Delta\sigma$ = stress range within a given load cycle

ΔK = stress intensity factor

$\Delta S_T^{(k)}$ = random variable describing the extent of the atmospheric turbulence patches encountered by the aircraft during the k^{th} flight segment

ΔT_a = random variable describing the duration of the load fluctuation pulses (having their intensity probabilistically characterized by the random variable Σ_a)

ΔT_m = random variable describing the mean-load pulse duration

$\Delta T_M^{(k)}$ = random variable describing the maneuver duration (i.e., the duration of a given maneuver performed by the pilot) during the k^{th} flight segment

$\Delta\tau$ = interval of time (expressed in hours of flight) between two subsequent damage prognosis predictions.

ΔN = number of cycles between two subsequent damage prognosis predictions.

ε_{ij} = random measurement error (Gaussian distributed with zero mean and standard deviation equal to $\sigma_{\varepsilon_{ij}}$) associated with the j^{th} damage mechanism evolving at the i^{th} damage location

$\eta_0^{(i,j)}$ = coefficient of the logit damage sizing model associated with the j^{th} damage mechanism evolving/developing at the i^{th} damage location

$\eta_1^{(i,j)}$ = coefficient of the logit damage sizing model associated with the j^{th} damage mechanism evolving/developing at the i^{th} damage location

$\boldsymbol{\Theta}_{\mathrm{a}}$ = random vector collecting the distribution parameters used to characterized the stochastic load fluctuations about the average load intensity (probabilistically characterized by $\mathbf{IM}_{\mathrm{m}}$)

$\boldsymbol{\Theta}_{\mathrm{dam}}$ = random vector collecting the damage evolution model parameters (notation used when the PDF of $\boldsymbol{\Theta}_{\mathrm{dam}}$ is not recursively updated after each NDE inspection)

$\boldsymbol{\Theta}_{\mathrm{dam}}^{p}$ = random vector collecting the damage evolution model parameters at time t_p (notation used when the PDF of $\boldsymbol{\Theta}_{\mathrm{dam}}^{p}$ is recursively updated after each NDE inspection)

$\boldsymbol{\Theta}_{\mathrm{dam}}^{(i,p)}$ = random vector collecting the damage evolution model parameters at the i^{th} damage location at time t_p ($i = 1, \ldots, n_{\mathrm{L}}^{[0,p]}$)

$\boldsymbol{\Theta}_{\mathrm{dam}}^{(i,j,p)}$ = random vector collecting the damage evolution model parameters associated with the j^{th} damage mechanism evolving/developing at the i^{th} damage location at time t_p ($j = 1, \ldots, n_{\mathrm{DM}}^{(i,[0,p])}$)

$\boldsymbol{\Theta}_{\mathrm{F}}^{(k)}$ = random vector collecting the flight profile parameters during the k^{th} flight segment

$\boldsymbol{\Theta}_{\mathrm{F}}$ = random vector collecting the flight profile parameters for all the n_S flight segments in $\left[t_p, t_p^{\bar{q}}\right]$ as $\boldsymbol{\Theta}_{\mathrm{F}} = \left\{\boldsymbol{\Theta}_{\mathrm{F}}^{(k)}, k = 1, ..., n_s\right\}$

$\boldsymbol{\Theta}_{\mathrm{M}}^{(k)}$ = random vector collecting the maneuver parameters during the k^{th} flight segment

$\boldsymbol{\Theta}_{\mathrm{M}}$ = random vector collecting the maneuver parameters for all the n_S flight segments in $\left[t_p, t_p^{\bar{q}}\right]$ as $\boldsymbol{\Theta}_{\mathrm{M}} = \left\{\boldsymbol{\Theta}_{\mathrm{M}}^{(k)}, k = 1, ..., n_s\right\}$

$\boldsymbol{\Theta}_{\mathrm{m}}$ = random vector collecting the distribution parameters used to characterized the average load (mean-load) acting on a structure

$\boldsymbol{\Theta}_{\mathrm{mat}}$ = random vector collecting the material model(s) parameters

$\boldsymbol{\Theta}_{\mathrm{T}}^{(k)}$ = random vector collecting the turbulence model parameters during the k^{th} flight segment

$\boldsymbol{\Theta}_{\mathrm{T}}$ = random vector collecting the turbulence model parameters for all the n_S flight segments in $\left[t_p, t_p^{\bar{q}}\right]$ as $\boldsymbol{\Theta}_{\mathrm{T}} = \left\{\boldsymbol{\Theta}_{\mathrm{T}}^{(k)}, k = 1, ..., n_s\right\}$

λ_{a} = mean rate of occurrence of the rectangular pulses characterizing intensity and duration of the random load fluctuations about the average (mean) load acting on a structure

$\lambda_{\mathrm{M}}^{(k)}$ = mean rate of occurrence of maneuvers during the k^{th} flight segment

$\lambda_{\mathrm{M},c}^{(k)}$ = mean rate of occurrence of the censored Poisson point process defined as $\lambda_{\mathrm{M},c}^{(k)} = \lambda_{\mathrm{M},u}^{(k)} \cdot p_{Z_{\mathrm{M}}}^{(k)} = \lambda_{\mathrm{M}}^{(k)}$

$\lambda_{\mathrm{M},u}^{(k)}$ = mean rate of occurrence of the (underlying) uncensored Poisson point process defined as $\lambda_{\mathrm{M},u}^{(k)} = 1/\mu_{T_{\mathrm{M}}^{(k)}}$

λ_{m} = mean rate of occurrence of the *mean-load* rectangular pulses — i.e., the rectangular pulses characterizing intensity and duration of the mean-load acting on a structure

$\hat{\mu}_{A_m|A_a}^{(i,j,p)}$ = estimate for the mean measurement outcome conditional on $A_a^{(i,j,p)} = a_a^{(i,j,p)}$

$\mu_{T_{\mathrm{M}}^{(k)}}$ = mean value (derived from flight test data) of the maneuvers duration during the k^{th} flight segment

Σ_{a} = root mean square value of the stochastic load fluctuations about the average/mean load acting on a structure

$\Sigma_{\mathrm{T}}^{(k)}$ = root mean square value of the turbulence velocity fluctuations during the k^{th} flight segment (viewed as a random variable)

$\sigma_{\varepsilon_{ij}}$ = standard deviation of the random measurement error (assumed to be Gaussian distributed with zero mean)

$\hat{\sigma}_{\varepsilon_{ij}}$ = estimate of $\sigma_{\varepsilon_{ij}}$ through linear regression analysis

$\Phi(x)$ = Standard Normal cumulative distribution function (CDF)

$\varphi(x;\mu,\sigma)$ = Gaussian PDF of the random variable X with mean μ and standard deviation σ

$\tilde{\varphi}(x;\mu,\sigma)$ = Gaussian PDF of the random variable X, with mean μ and standard deviation σ, normalized such that $\int_0^{+\infty} \tilde{\varphi}(x;\mu,\sigma) = 1$

$\boldsymbol{\Psi}_{\mathrm{g}}^{[p,q]}$ = vector of global performance measures at time t_p^q

$Z_M^{(k)}$ = maneuver-induced load factor during the k^{th} flight segment

$A_a^{(i,j,N)}$ = actual damage size, at load cycle $N \geq 0$, associated with the j^{th} damage mechanism evolving at the i^{th} damage location

$A_a^{(i,j,p)}$ = actual damage size, at time t_p, associated with the j^{th} damage mechanism evolving at the i^{th} damage location

$A_a^{(i,j,t)}$ = actual damage size, at time $t \geq 0$, associated with the j^{th} damage mechanism evolving at the i^{th} damage location

$A_a^{(i,j,[p,N])}$ = actual damage size at load cycle $N \geq N_p$ (i.e., as predicted from load cycle N_p) associated with the j^{th} damage mechanism evolving at the i^{th} damage location

$A_a^{(i,j,[p,q])}$ = actual damage size at time t_p^q (i.e., as predicted from time t_p) associated with the j^{th} damage mechanism evolving at the i^{th} damage location

$A_a^{(i,j,[p,t])}$ = actual damage size at time $t \geq t_p$ (i.e., as predicted from time t_p) associated with the j^{th} damage mechanism evolving at the i^{th} damage location

$\mathbf{A}_a^p$ = random vector collecting the actual damage sizes/extents, at time t_p, at all the monitored (up to time t_p) damage locations

$\mathbf{A}_a^{(i,p)}$ = random vector collecting the actual damage sizes/extents at the i^{th} damage location at time t_p ($i = 1, \ldots, n_L^{[0,p]}$)

$\mathbf{A}_a^{[p,q]}$ = random vector collecting the predicted (from time t_p) actual damage sizes/extents at time t_p^q

$a_{a,\text{true}}^{(i,j,N)}$ = true damage size, at load cycle $N \geq 0$, associated with the j^{th} damage mechanism evolving at the i^{th} damage location

$a_{a,\text{true}}^{(i,j,p)}$ = true damage size, at time t_p, associated with the j^{th} damage mechanism evolving at the i^{th} damage location

$a_{a,\text{true}}^{(i,j,t)}$ = true damage size, at time $t \geq 0$, associated with the j^{th} damage mechanism evolving at the i^{th} damage location

a_c^{ij} = critical damage size (i.e., critical threshold) associated with the j^{th} damage mechanism evolving at the i^{th} damage location

$A_m^{(i,j,p)}$ = measured damage size (viewed as random variable) associated with the j^{th} damage mechanism evolving at the i^{th} damage location at time t_p

$A_m^{(i,j,[p,q])}$ = random NDE measurement outcome/result, associated with the j^{th} damage mechanism evolving at the i^{th} damage location, from the assumed single inspection opportunity at future time t_p^q

$\mathbf{A}_{\text{m}}^{(i,j,[p,q])}$ = random vector collecting the NDE measurement outcomes, associated with the j^{th} damage mechanism evolving at the i^{th} damage location, from the assumed multiple (i.e., a total of $n_{\text{MS}}^{(i,j,[p,q])}$) inspection opportunities performed at future time t_p^q. $\mathbf{A}_{\text{m}}^{(i,j,[p,q])} = \left\{ A_{m_k}^{(i,j,[p,q])},\, k = 1,\ldots,n_{\text{MS}}^{(i,j,[p,q])} \right\} = \left\{ \widehat{\mathbf{A}}_{\text{m}}^{(i,j,[p,q])},\, \breve{\mathbf{A}}_{\text{m}}^{(i,j,[p,q])} \right\}$

$\widehat{\mathbf{A}}_{\text{m}}^{(i,j,[p,q])}$ = random sub-vector collecting the NDE measurement outcomes, associated with the j^{th} damage mechanism evolving at the i^{th} damage location at time t_p^q, satisfying the condition $A_{m_k}^{(i,j,[p,q])} < a_c^{ij}$ $(k = 1,\ldots,n_{\text{MS}}^{(i,j,[p,q])})$

$\breve{\mathbf{A}}_{\mathrm{m}}^{(i,j,[p,q])}$ = random sub-vector collecting the NDE measurement outcomes, associated with the j^{th} damage mechanism evolving at the i^{th} damage location at time t_p^q, satisfying the condition $A_{m_k}^{(i,j,[p,q])} \geq a_c^{ij}$ $(k=1,\ldots,n_{\mathrm{MS}}^{(i,j,[p,q])})$

$\mathbf{A}_{\mathrm{m}}^{p}$ = random vector collecting the measured damage sizes, at time t_p, at the monitored (at time t_p) damage locations

$\mathbf{A}_{\mathrm{m}}^{[0,p]}$ = random vector collecting the measured damage sizes, up to time t_p, at the monitored (up to time t_p) damage locations

$\mathbf{a}_{\mathrm{m}}^{p}$ = vector collecting the measured damage sizes at time t_p (i.e., a realization of the random vector $\mathbf{A}_{\mathrm{m}}^{p}$)

$\mathbf{a}_{\mathrm{m}}^{[0,p]}$ = vector collecting all the p+1 NDE measurement outcomes obtained up to time t_p (i.e., a realization of $\mathbf{A}_{\mathrm{m}}^{[0,p]}$)

$a_{m_k}^{(i,j,p)}$ = k^{th} NDE measurement result obtained from the NDE inspection performed at time t_p on the j^{th} damage mechanism evolving at the i^{th} damage location

AMP = random amplitude of the harmonic load fluctuations superimposed to the applied average/mean load.

$b_1\left(h^{(k)}\right)$ = altitude-dependent distribution parameter used to characterized the PDF of the turbulence intensity in the non-storm range

$b_2\left(h^{(k)}\right)$ = altitude-dependent distribution parameter used to characterized the PDF of the turbulence intensity in the storm range

$\mathbf{D}_{\mathrm{L,G}}^{[p,q]}$ = random vector characterizing the overall state of damage of the monitored structure (or structural element/component) at time t_p^q and defined as $\mathbf{D}_{\mathrm{L,G}}^{[p,q]} = \left\{\mathbf{A}_{\mathrm{a}}^{[p,q]}, \mathbf{V}_{\mathrm{F,LCO}}^{[p,q]}\right\}$

$\mathrm{F}_{\mathrm{G},r}^{[p,q]}$ = global failure event, at time t_p^q, associated with the r^{th} global failure mode (i.e., the r^{th} global reliability component); $r = 1,...,n_{\mathrm{G}}$

$\tilde{\mathrm{F}}_{\mathrm{G},r}^{[p,q]}$ = alternative global failure event, at time t_p^q, associated with the r^{th} global failure mode (i.e., the r^{th} global reliability component); $r = 1,...,n_{\mathrm{G}}$

$\mathrm{F}_{\mathrm{L},ij}^{[p,q]}$ = local failure event, at time t_p^q, associated with the j^{th} damage mechanism evolving at the i^{th} damage location; $i = 1,\ldots,n_{\mathrm{L}}^{[0,p]}$ and $j = 1,\ldots,n_{\mathrm{DM}}^{(i,[0,p])}$

$\tilde{\mathrm{F}}_{\mathrm{L},ij}^{[p,q]}$ = alternative local failure event based on the level-of safety formulation with single NDE inspection opportunity at time t_p^q, associated with the j^{th} damage mechanism evolving at the i^{th} damage location; $i = 1,\ldots,n_{\mathrm{L}}^{[0,p]}$ and $j = 1,\ldots,n_{\mathrm{DM}}^{(i,[0,p])}$

$\hat{\mathrm{F}}_{\mathrm{L},ij}^{[p,q]}$ = alternative local failure event based on the level-of safety formulation with multiple NDE inspection opportunities at time t_p^q, associated with the j^{th} damage mechanism evolving at the i^{th} damage location; $i = 1,\ldots,n_{\mathrm{L}}^{[0,p]}$ and $j = 1,\ldots,n_{\mathrm{DM}}^{(i,[0,p])}$

$\tilde{\mathscr{F}}_{\mathrm{L},ij}^{[p,q]}$ = local false-call event based on the level-of safety formulation with single NDE inspection opportunity at time t_p^q, associated with the j^{th} damage mechanism evolving at the i^{th} damage location; $i = 1,\ldots,n_{\mathrm{L}}^{[0,p]}$ and $j = 1,\ldots,n_{\mathrm{DM}}^{(i,[0,p])}$

$\hat{\mathscr{F}}_{\mathrm{L},ij}^{[p,q]}$ = local false-call event based on the level-of safety formulation with multiple NDE inspection opportunities at time t_p^q, associated with the j^{th} damage mechanism evolving at the i^{th} damage location; $i = 1,\ldots,n_{\mathrm{L}}^{[0,p]}$ and $j = 1,\ldots,n_{\mathrm{DM}}^{(i,[0,p])}$

$\mathrm{F}_{\mathrm{sys}}^{[p,q]}$ = failure event associated with the failure of the system (abstracted to a series system) at time t_p^q

$\breve{\mathrm{F}}_{\mathrm{sys}}^{[p,q]}$ = alternative failure event associated with the failure of the system at time t_p^q and based on the level-of safety formulation with single NDE inspection opportunity at time t_p^q

$\widehat{\mathrm{F}}_{\mathrm{sys}}^{[p,q]}$ = alternative failure event associated with the failure of the system at time t_p^q and based on the level-of safety formulation with multiple NDE inspection opportunities at time t_p^q

$\breve{\mathcal{F}}_{\mathrm{sys}}^{[p,q]}$ = false-call event (at the system level) at time t_p^q and based on the level-of safety formulation with single NDE inspection opportunity at time t_p^q

$\widehat{\mathcal{F}}_{\mathrm{sys}}^{[p,q]}$ = false-call event (at the system level) at time t_p^q and based on the level-of safety formulation with multiple NDE inspection opportunities at time t_p^q

$f'_{X|Y}\left(x\middle|y\right)$ = prior probability distribution function of the random variable X given $Y = y$

$f''_{X|Y}\left(x\middle|y\right)$ = posterior probability distribution function of the random variable X given $Y = y$

$f'_{\boldsymbol{\Theta}_{\mathrm{dam}}^0}\left(\boldsymbol{\theta}_{\mathrm{dam}}^0\right)$ = initial (i.e., before the first NDE inspection at time t_0) PDF model for the damage evolution model parameters $\boldsymbol{\Theta}_{\mathrm{dam}}^0$

$f'_{\mathbf{A}_{\mathrm{a}}^0}\left(\mathbf{a}_{\mathrm{a}}^0\right)$ = initial (i.e., before the first NDE inspection at time t_0) PDF model for the actual damage size vector $\mathbf{A}_{\mathrm{a}}^0$

$\tilde{f}_{A_a^{(i,j,0)}}\left(a_a^{(i,j,0)}\right)$ = probability distribution function of the damage size $a_a^{(i,j,0)}$ in the range $a_a^{(i,j,0)} > 0$ normalized such that $\int_{0^+}^{+\infty} \tilde{f}_{A_a^{(i,j,0)}}\left(a_a^{(i,j,0)}\right) = 1 - p_0^{(i,j,0)}$

$f_{Z_{\mathrm{M}}^{(k)}}\left(\zeta_{\mathrm{M}}^{(k)}\right)$ = probability distribution function characterizing the maneuver intensity during the k^{th} flight segment

$\tilde{f}_{Z_{\mathrm{M}}^{(k)}}\left(\zeta_{\mathrm{M}}^{(k)}\right)$ = mixed probability distribution function describing the maneuver intensity during the k^{th} flight segment and accounting for the fact that (within this segment) $\left(1 - p_{Z_{\mathrm{M}}}^{(k)}\right) \times 100\%$ of the time the aircraft is not maneuvering (i.e., $Z_{\mathrm{M}}^{(k)} = 1$)

FCP = false call probability

$H^{(k)}$ = random altitude of flight during the k^{th} flight segment

$I_{(0)}$ = cross-section moment of inertia for a composite beam, made out of two composite adherends bonded together, with its adhesive interface completely damaged (i.e., with total loss of slip stiffness and strength)

$I_{(\infty)}$ = cross-section moment of inertia for a composite beam, made out of two composite adherends bonded together, with its adhesive interface completely undamaged (i.e., with infinite slip stiffness and pristine ultimate strength)

$\mathbf{IM}_{\mathrm{a}}$ = intensity measure vector characterizing the stochastic load fluctuations about the average load intensity (probabilistic characterized by the intensity measure vector $\mathbf{IM}_{\mathrm{m}}$)

$\mathbf{IM}_{\mathrm{m}}$ = intensity measure vector characterizing the random average/mean load acting on a structure, defined as $\mathbf{IM}_{\mathrm{m}} = \left\{P_{\mathrm{m}}, \Delta T_{\mathrm{m}}\right\}$

$\mathbf{IM}_{\mathrm{M}}^{(k)}$ = random vector collecting the maneuver-induced intensity measures during the k^{th} flight segment

$\mathbf{IM}_{\mathrm{M}}$ = random vector collecting the maneuver-induced intensity measures for all the n_S flight segments in $\left[t_p, t_p^{\bar{q}}\right]$ as $\mathbf{IM}_{\mathrm{M}} = \left\{\mathbf{IM}_{\mathrm{M}}^{(k)},\, k = 1, ..., n_s\right\}$

$\mathbf{IM}_{\mathrm{T}}^{(k)}$ = random vector collecting the turbulence-induced intensity measures during the k^{th} flight segment

$\mathbf{IM}_{\mathrm{T}}$ = random vector collecting the turbulence-induced intensity measures for all the n_S flight segments in $\left[t_p, t_p^{\bar{q}}\right]$ as $\mathbf{IM}_{\mathrm{T}} = \left\{\mathbf{IM}_{\mathrm{T}}^{(k)},\, k = 1, ..., n_s\right\}$

$\left(i, j, p\right)$ = triplet identifying damage location (i), damage mechanism (j) and time of inspection (t_p)

$\left(i, j, [p,q]\right)$ = triplet identifying damage location (i), damage mechanism (j) and future time (t_p^q)

$L\left(x \middle| D\right)$ = likelihood function of x for a given set of data (D) collected

N_0 = number of cycles at the time of the first NDE inspection (in the application examples presented in this thesis $N_0 = 0$ cycles)

N_p = number of cycles at current time, i.e., at the time of most recent NDE inspection

N_p^q = $N_p^q = N_p + q\Delta N$ with $q \in \left\{1, 2, ..., \bar{q}\right\}$

$N_p^{\bar{q}}$ = $N_p^{\bar{q}} = N_p + \bar{q}\Delta N$

$N_p^{\tilde{q}}$ = $N_p^q = N_p + \tilde{q}\Delta N$ with $i - 1 < \tilde{q} < i$ and $i \in \left\{1, 2, ..., \bar{q}\right\}$

n_{A}^{p} = dimension of the random vector $\mathbf{A}_{\mathrm{a}}^{p}$ at time t_p; with n_{A}^{p} defined as $n_{\mathrm{A}}^{p}=\sum_{i=1}^{n_{\mathrm{L}}^{[0,p]}} n_{\mathrm{DM}}^{(i,[0,p])}$

$n_{\mathrm{DM}}^{(i,p)}$ = number of monitored (at time t_p) damage mechanisms evolving at the i^{th} location (i.e., number of damage mechanisms at the i^{th} location for which new NDE data at time t_p are available)

$n_{\mathrm{DM}}^{(i,[0,p])}$ = number of detected (up to time t_p) damage mechanisms evolving at the i^{th} damage location

n_{L}^{p} = number of inspected damage locations at time t_p

$n_{\mathrm{L}}^{[0,p]}$ = number of inspected damage locations up to time t_p

$n_{\mathrm{L,G}}^{[0,p]}$ = number of reliability components used in the prognosis analysis performed at time t_p

n_{G} = number of global (aeroelastic) failure modes; $n_{\mathrm{G}}=1+n_{\mathrm{LCO}}$

n_{LCO} = number of limit cycle oscillation (LCO) velocities

$n_{\mathrm{M}}^{(k)}$ = number of maneuvers (within the k^{th} flight segment) randomly generated during the stochastic realization of the random vector $\mathbf{IM}_{\mathrm{M}}^{(k)}$ using a censored Poisson rectangular pulse process

$n_{\mathrm{MS}}^{(i,j,p)}$ = number of NDE measurements collected at time t_p, associated with the j^{th} damage mechanism evolving at the i^{th} damage location

$n_{\mathrm{MS}}^{(i,j,[p,q])}$ = number of NDE measurements that will be performed/collected at time t_p^q, associated with the j^{th} damage mechanism evolving at the i^{th} damage location

$\overline{n}_{\mathrm{MS}}^{(i,j,[p,q])}$ = number of NDE measurements that will be performed/collected at time t_p^q, associated with the j^{th} damage mechanism evolving at the i^{th} damage location and satisfying the condition $A_{m_k}^{(i,j,[p,q])} < a_c^{ij}$ ($k = 1, \ldots, n_{\mathrm{MS}}^{(i,j,[p,q])}$)

n_S = number of flight segments in $\left[t_p, t_p^{\bar{q}}\right]$

$n_{\mathrm{T}}^{(k)}$ = number of turbulence patches (within the k^{th} flight segment) randomly generated during the stochastic realization of the random vector $\mathbf{IM}_{\mathrm{T}}^{(k)}$ using a censored Poisson rectangular pulse process.

P_{m} = random intensity of the average/mean load applied on a structure

$P\left[\mathrm{F}_{\mathrm{G},r}^{[p,q]}\right]$ = probability of failure at time t_p^q associated with the r^{th} global failure mode, $\mathrm{F}_{\mathrm{G},r}^{[p,q]}$ ($r = 1, \ldots, n_{\mathrm{G}}$)

$P\left[\tilde{\mathrm{F}}_{\mathrm{G},r}^{[p,q]}\right]$ = probability of failure at time t_p^q associated with the r^{th} global failure mode, $\tilde{\mathrm{F}}_{\mathrm{G},r}^{[p,q]}$ ($r = 1, \ldots, n_{\mathrm{G}}$)

$P\left[\mathrm{F}_{\mathrm{L},ij}^{[p,q]}\right]$ = probability of local component failure at time t_p^q according to the local failure event $\mathrm{F}_{\mathrm{L},ij}^{[p,q]}$ associated with the j^{th} damage mechanism evolving at the i^{th} damage location; $j = 1, \ldots, n_{\mathrm{DM}}^{(i,[0,p])}$ and $i = 1, \ldots, n_{\mathrm{L}}^{[0,p]}$

$P\left[\tilde{\mathrm{F}}_{\mathrm{L},ij}^{[p,q]}\right]$ = probability of local component failure at time t_p^q according to the local failure event $\tilde{\mathrm{F}}_{\mathrm{L},ij}^{[p,q]}$ associated with the j^{th} damage mechanism evolving at the i^{th} damage location; $j = 1, \ldots, n_{\mathrm{DM}}^{(i,[0,p])}$ and $i = 1, \ldots, n_{\mathrm{L}}^{[0,p]}$

$P\left[\hat{\mathrm{F}}_{\mathrm{L},ij}^{[p,q]}\right]$ = probability of local component failure at time t_p^q according to the local failure event $\hat{\mathrm{F}}_{\mathrm{L},ij}^{[p,q]}$ associated with the j^{th} damage mechanism evolving at the i^{th} damage location; $j=1,\ldots,n_{\mathrm{DM}}^{(i,[0,p])}$ and $i=1,...,n_{\mathrm{L}}^{[0,p]}$

$P\left[\tilde{\mathscr{F}}_{\mathrm{L},ij}^{[p,q]}\right]$ = probability of local component false-call at time t_p^q according to the local false-call event $\tilde{\mathscr{F}}_{\mathrm{L},ij}^{[p,q]}$ associated with the j^{th} damage mechanism evolving at the i^{th} damage location; $j=1,\ldots,n_{\mathrm{DM}}^{(i,[0,p])}$ and $i=1,...,n_{\mathrm{L}}^{[0,p]}$

$P\left[\hat{\mathscr{F}}_{\mathrm{L},ij}^{[p,q]}\right]$ = probability of local component false-call at time t_p^q according to the local false-call event $\hat{\mathscr{F}}_{\mathrm{L},ij}^{[p,q]}$ associated with the j^{th} damage mechanism evolving at the i^{th} damage location; $j=1,\ldots,n_{\mathrm{DM}}^{(i,[0,p])}$ and $i=1,...,n_{\mathrm{L}}^{[0,p]}$

$P\left[\mathrm{F}_{\mathrm{sys}}^{[p,q]}\right]$ = probability of system failure at time t_p^q according to the system failure event $\mathrm{F}_{\mathrm{sys}}^{[p,q]}$

$P\left[\breve{\mathrm{F}}_{\mathrm{sys}}^{[p,q]}\right]$ = probability of system failure at time t_p^q according to the system failure event $\breve{\mathrm{F}}_{\mathrm{sys}}^{[p,q]}$

$P\left[\widehat{\mathrm{F}}_{\mathrm{sys}}^{[p,q]}\right]$ = probability of system failure at time t_p^q according to the system failure event $\widehat{\mathrm{F}}_{\mathrm{sys}}^{[p,q]}$

$P\left[\breve{\mathscr{F}}_{\mathrm{sys}}^{[p,q]}\right]$ = probability of false-call at the global system level at time t_p^q according to the false-call event $\breve{\mathscr{F}}_{\mathrm{sys}}^{[p,q]}$

$P\left[\widehat{\mathscr{F}}_{\mathrm{sys}}^{[p,q]}\right]$ = probability of false-call at the global system level at time t_p^q according to the false-call event $\widehat{\mathscr{F}}_{\mathrm{sys}}^{[p,q]}$

$P_0\left(h^{(k)}\right)$ = probability of encountering no turbulence (i.e., quiet air) at a given instant of time during the k^{th} flight segment at altitude $h^{(k)}$; $P_0\left(h^{(k)}\right) = 1 - P_1\left(h^{(k)}\right) - P_2\left(h^{(k)}\right)$

$P_1\left(h^{(k)}\right)$ = probability of encountering non-storm turbulence at a given instant of time during the k^{th} flight segment at altitude $h^{(k)}$

$P_2\left(h^{(k)}\right)$ = probability of encountering storm turbulence at a given instant of time during the k^{th} flight segment at altitude $h^{(k)}$

POD = probability of detection

PND = probability of non-detection

$p_0^{(i,j,0)}$ = probability of having no damage (i.e., $a_a^{(i,j,0)} = 0$) for a given damage location and damage mechanism

$p_\infty^{(i,j)}$ = probability of missing the detection of a very large damage according to the *POD* curve model proposed by Staat (1993). This value is associated with the detectability of the j^{th} damage mechanism evolving at the i^{th} damage location

$\overline{p}_{\mathrm{F}}$ = maximum allowable probability of failure (safety threshold) for the monitored structural system

$p_{Z_{\mathrm{M}}}^{(k)}$ = fraction of time (within the k^{th} flight segment) during which the aircraft is maneuvering (i.e., $Z_{\mathrm{M}}^{(k)} \neq 1$)

q = q^{th} (out of a total of $\overline{q}$) damage prognosis prediction/evaluation performed at time t_p

$\overline{q}$ = total number of damage prognosis predictions/evaluations

$\overline{q}$ = total number of damage prognosis predictions/evaluations

R_σ = stress ratio within a given loading cycle, defined as the ratio between minimum ($\sigma_{\min}$) and maximum ($\sigma_{\max}$) stresses, i.e., $R_\sigma = \sigma_{\min}/\sigma_{\max}$

t_0 = time of the first NDE inspection

t_p = current time, time of most recent NDE inspection performed

t_p^q = $t_p^q = t_p + q\Delta\tau$ with $q \in \{1, 2, ..., \bar{q}\}$

$t_p^{\bar{q}}$ = $t_p^{\bar{q}} = t_p + \bar{q}\Delta\tau$

$t_p^{\tilde{q}}$ = $t_p^q = t_p + \tilde{q}\Delta\tau$ with $i-1 < \tilde{q} < i$ and $i \in \{1, 2, ..., \bar{q}\}$

$\mathbf{V}^{(k)}$ = random vector describing the mean air stream velocity w.r.t. a reference system attached to the aircraft

$V_{\mathrm{F}}^{[p,q]}$ = flutter instability boundary at time t_p^q (viewed as a random variable)

$\mathbf{V}_{\mathrm{LCO}}^{[p,q]}$ = random vector of LCO velocities at time t_p^q

$\mathbf{V}_{\mathrm{F,LCO}}^{[p,q]}$ = random vector of flutter and LCO velocities at time t_p^q defined as $\mathbf{V}_{\mathrm{F,LCO}}^{[p,q]} = \left\{V_{\mathrm{F}}^{[p,q]}, \mathbf{V}_{\mathrm{LCO}}^{[p,q]}\right\}$

$\overline{\mathbf{v}}_{\mathrm{F,LCO}}^{[p,q]}$ = vector of flutter and LCO velocities (for a given/fixed realization of $\mathbf{A}_{\mathrm{a}}^{[p,q]}$, $\boldsymbol{\Theta}_{\mathrm{mat}}$, and $\boldsymbol{\Theta}_{\mathrm{dam}}$) obtained as output of the metamodel used in the flutter & LCO analyses step

$Z_{\mathrm{M}}^{(k)}$ = random variable characterizing the maneuver-induced load factor during the k^{th} flight segment

LIST OF FIGURES

ACKNOWLEDGEMENTS

The research for this dissertation was performed at the University of California at San Diego (UCSD) under the supervision of Professor Joel P. Conte and Professor John B. Kosmatka. I would like to express my deepest and most sincere gratitude to them. They have been for me rigorous and insightful teachers, reliable guides in the research, and an inspiration in my decision to continue pursuing a career in academia. Their guidance and support have been the key to my academic and personal growth over the past seven years.

Special thanks and gratitude are given to all the members of my doctoral committee, Professors David J. Benson, Charles R. Farrar, Dimitris N. Politis, and Dr. François M. Hemez who have always been willing to dedicate their time to help me with all the technical issues related to my research.

Very important were also the collaborations with Professor Petr Krysl, Professor Vlado Lubarda, and Professors David J. Benson; I served in fact as teaching assistant for some of their undergraduate classes during the time spent at UCSD. They contributed significantly to my academic growth with their guidance and I want to sincerely thank them for all they did for me.

I would like also to thank Professor Claudio Modena from the University of Padova (Italy), Dr. Gianmario Benzoni (UCSD), and Professor Francesco Lanza di Scalea (UCSD) without whom I would not have had the opportunity to perform academic research in the USA and then pursue my Ph.D. Degree at UCSD.

I am thankful to all the people who helped me with the experimental parts of other research projects I worked on. Among them, a special thank to Dr. Christopher Latham, Professor Hyonny Kim, and Mr. Zhi Chen.

I wish to thank my fellow students, researchers, and co-workers who shared with me highs and lows of the academic life at UCSD: Professors Michele Barbato, Ivan Bartoli, Quan Gu, Geert Lombaert, Fabio Matta, Babak Moaveni, Ozgur Ozcelik, Piervincenzo Rizzo, Salvatore Salamone, Andreas Stavridis, and Alessandro Zona; Drs. Carmen Amaddeo, Andrea Belleri, Giuseppe Canducci, Chiara Casarotti, Giovanni Castellazzi, Pietro Ciccotti, Stefano Coccia, Marco Faggella, Xianfei He, Robb kulin, Alessandro Marzani, David Mascarenas, Flavio Mosele, and Yuyi Zhang; Mr./Ms. Gabriel Acero, Rodrigo Astrosa, Andre Barbosa, Chad Foerster, Gabriele Guerrini, Hamed Hebrahim, Armando Lanzi, Katharine LaZansky, Yong Li, Yujia Liu, Juan Murcia, Claudio Nucera, Joseph Oliver, Robert Phillips, Ronnie Sokotoff, Trevor Tippetts, Eduardo Velazquez, and Federica Venturi.

I am also particularly grateful to all my friends in Italy and here in San Diego who shared with me joy and hard work during all my life. In particular, a sincere thank to all the *Ragazzi di Villa Lamont*! Without them, all these years spent in San Diego would not have been that great!

The most sincere and deepest gratitude to Elisabeth, for all the time she has dedicated to me and for her enormous help in editing and proofreading my dissertation. Last but not least, I am most grateful to my family for their help, encouragement, and support in all these years. I dedicate my work to them.

Partial supports of this research by (i) the Educational Collaboration between the Los Alamos National Laboratory (LANL) and the University of California, San Diego, (UCSD) on “A Damage Prognosis System for Unmanned Aerial Vehicles” and (ii) the UCSD Academic Senate Research Grant RJ086G-CONTE are gratefully acknowledged.

VITA

2004	Bachelor Degree (Laurea, Magna cum Laude) in Civil Engineering, University of Padova, Italy.
2004-2011	Research Assistant, Department of Structural Engineering, University of California, San Diego.
2006	Master of Science, University of California, San Diego.
2008	Candidate in Philosophy, University of California, San Diego.
2011	Doctor of Philosophy, University of California, San Diego.

ABSTRACT OF THE DISSERTATION

RELIABILITY-BASED FRAMEWORK FOR FATIGUE DAMAGE PROGNOSIS OF BONDED STRUCTURAL ELEMENTS IN AEROSPACE COMPOSITE STRUCTURES

by

Maurizio Gobbato

Doctor of Philosophy in Structural Engineering

University of California, San Diego, 2011

Professor Joel P. Conte, Chair

Professor John B. Kosmatka, Co-Chair

Fatigue-induced damage is one of the most uncertain and extremely unpredictable failure mechanisms for a large variety of structural systems (e.g., aerospace, automotive, offshore, and civil structures) subjected to stochastic and cyclic loading during service life. Among these systems, composite lightweight aerospace structures — such as fighter aircrafts and unmanned aerial vehicles (UAVs) — are particularly sensitive to both fatigue-induced and impact-induced damage. Within this scenario, an integrated hardware & software system capable of (i) monitoring the critical components of these systems, (ii) periodically assessing their structural

integrity, (iii) predicting their remaining fatigue life (damage prognosis), and (iv) accomplishing a cost-efficient condition-based maintenance (CBM) is ultimately needed. This research contributes to the aforementioned objectives by providing a novel and comprehensive probabilistic methodology for predicting the remaining fatigue life of adhesively-bonded joints in composite structures. According to this methodology, non-destructive evaluation (NDE) techniques and recursive Bayesian inference are repeatedly employed to update the probability distributions of damage extents and damage evolution model parameters at various damage locations after each NDE inspection. The propagation of damage is then stochastically simulated using a probabilistic model for future operational loads and a surrogate model (calibrated and validated at various damage levels using a mechanics-based model) capable of predicting the structural response quantities of interest. Finally, local and global failure criteria are considered simultaneously to compute the probabilities of failure and false-alarm at future times by abstracting the structure (or structural component) into a combination of series and parallel sub-systems. Three benchmark applications are provided in this work to exercise, verify, and validate the proposed framework. The first two benchmark applications analyze the fatigue-driven debonding propagation along a pre-defined adhesive interface in a simply supported laminated composite beam. They demonstrate the efficiency of the proposed recursive Bayesian inference scheme, show the use of the proposed component and system reliability analyses to recursively predict and update the evolution in time of the probabilities of failure and false-alarm of the structure, and illustrate the robustness of

the framework. Finally, the third benchmark application validates the proposed damage prognosis methodology by using experimental fatigue test data obtained from the literature.

CHAPTER 1

INTRODUCTION

1.1. Background and motivation

Probabilistic design and risk assessment methodologies for commercial, transport, and fighter aircrafts have been under development by the research community for a considerable time (Yang and Trapp, 1974; Deodatis *et al*., 1996; Lin and Styuart, 2007) and, more recently, the increasing use of high-performance lightweight composite materials is rendering rigorous probabilistic approaches essential. Fiber-reinforced polymer (FRP) composites are characterized by a large statistical variability in their mechanical properties, and are extremely sensitive to both fatigue-induced and impact-induced damage, as well as to aging caused by operational hydrothermal cycling — phenomena that cannot be treated in a deterministic fashion, and require periodic monitoring of the structure. Unmanned aerial vehicles (UAVs) are a typical example of how extensively composite materials can be used in aircraft

structures; additionally, the absence of a pilot on this type of vehicles leads to higher levels of damage tolerance in the airframe. Various damage mechanisms — e.g., debonding, inter-ply delamination, fiber breakage, and matrix cracking — can initiate and invisibly propagate to catastrophic levels in the most damage-sensitive UAV primary structural components, such as the wings, the tail stabilizers, and the fuselage. In particular, the adhesive joints that bond the aircraft skin to the primary airframe components (i.e., wing-spars, bulkheads, stringers, frames, and longerons) are recognized as the most fatigue-sensitive subcomponents of a lightweight composite UAV, with the skin-to-spar adhesive joints being the most critical. Most importantly, the progressive debonding — evolving from the wing-root along these joints (Oliver *et al.*, 2007) — can compromise both local component/subcomponent strength and global aeroelastic performance of the vehicle, as demonstrated by Bauchau and Loewy (1997), and Wang *et al.* (2005). There is therefore the need for a field-deployable Integrated Vehicle Health Management System (IVHMS), as described by Gorinevsky *et al*. (2005), capable of monitoring the composite UAV airframe, assessing its structural integrity, identifying a cost-efficient condition/risk-based maintenance program, and predicting in probabilistic terms the remaining useful life of its critical structural components (damage prognosis) as detailed by Inman *et al*. (2005).

Two examples of modern UAVs, manufactured with advanced light-weight and damage-sensitive composite materials, are provided in Figures 1.1 and 1.2. The Altair Predator B, shown in Figure 1.1, is a UAV designed for civil applications that have been developed under the Environmental Research Aircraft and Sensor

Technology (ERAST) program at NASA's Dryden Flight Research Center at Edwards, California. The Altair is a modified civil version of the MQ-9 Predator B, a military UAV developed through a partnership with General Atomics Aeronautical Systems, Inc. (GA-ASI, http://www.ga-asi.com, web page accessed on September 27, 2010). Researchers, who developed this type of UAV for civil purposes, believe that the Altair has significant disaster-management potential, and have proposed using the Altair to provide firefighters and rescue workers "bird's-eye images" of wild/forest fires and other natural disasters, such as floods and earthquakes, in real time. (source: http://www.nasa.gov/centers/dryden/news/ResearchUpdate/PredatorB/index.html, web page accessed on September 27, 2010).

Figure 1.1: Altair Predator B, a UAV used by NASA for environmental research, http://www.dfrc.nasa.gov/Gallery/Photo/Altair_PredatorB/Medium/ED06-0208-1.jpg (webpage accessed on September 27, 2010).

The second example of a UAV, shown in Figure 1.2, is represented by the General Atomics MQ-1 Predator, a military UAV used primarily by the United States Air Force (USAF) and Central Intelligence Agency (CIA). Initially conceived in the

early 1990s for reconnaissance and forward observation roles, the MQ-1 Predator carries cameras and other sensors but has been modified and upgraded to carry and fire two AGM-114 Hellfire missiles or other munitions. The aircraft, in use since 1995, has seen combats over Afghanistan, Pakistan, Bosnia, Serbia, Iraq, and Yemen (source: http://en.wikipedia.org/wiki/General_Atomics_MQ-1_Predator, web- page accessed on September 27, 2010). The increase of its operational payloads, especially in terms of ammunitions, drastically increased the stress range on the composite wings and, as a direct consequence, also the concern for their structural integrity and damage tolerance.

Figure 1.2: General Atomics MQ-1 Predator,
http://img244.imageshack.us/img244/5470/59983012nd8.jpg
(webpage accessed on September 27, 2010).

UAVs, such as those presented above, are nowadays widely used by several research agencies (e.g., to monitor the environment) as well as by the military in many different geographical areas. To further confirm the truth of this fact, a statement found on the US Army website is reported herein: “WASHINGTON (Army News

Service, May 27, 2010) — The Army recognized a milestone of 1 million hours of flight for unmanned aerial systems, May 25 at the Pentagon […]. According to the Army Unmanned Aircraft Systems Project Office, Army UAS actually surpassed one million flight hours April 14. Of those hours, 88 percent were flown in Iraq and Afghanistan. According to the project office, the RQ-7B Shadow flew nearly half of those hours, with 478,350 hours to its credit." (web-source: http://www.army.mil/news/2010/05/27/39902-army-hits-1-million-flight-hours-with-unmanned-aircraft, web page accessed on September 27, 2010). It is therefore evident that the whole structural health monitoring (SHM) and damage prognosis process for this type of aerial vehicles is crucial and can lead to a substantial operational cost reduction.

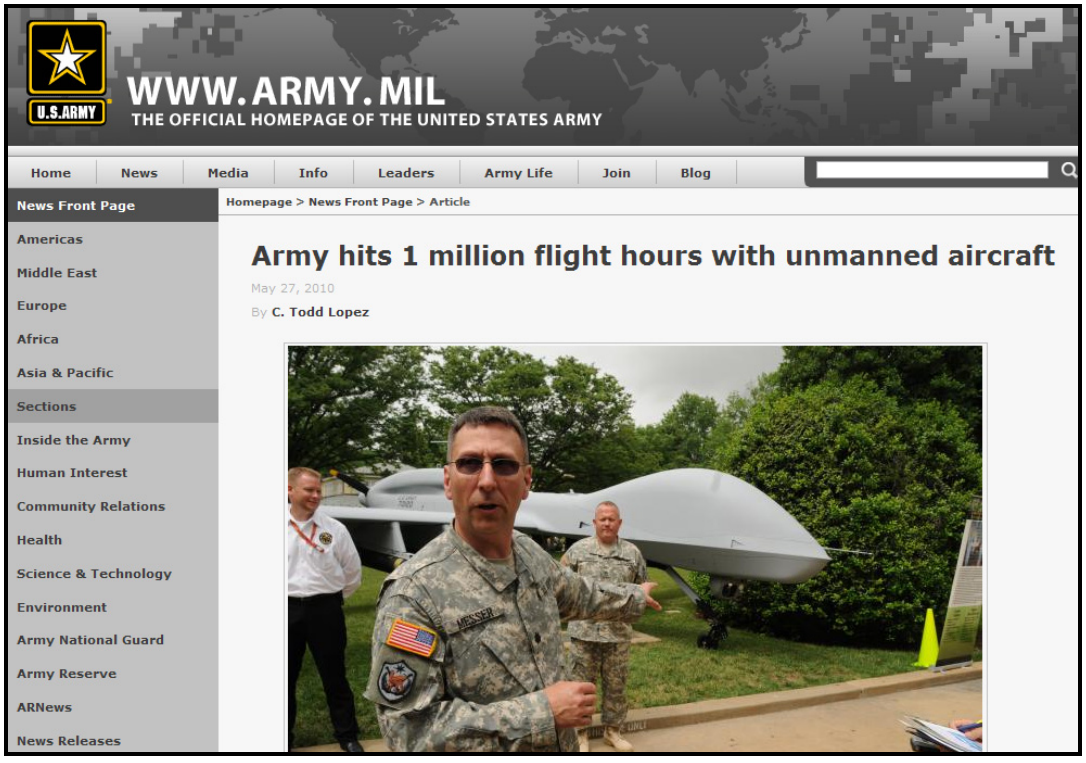

Figure 1.3: One million flight-hours milestone achieved by the US army, http://www.army.mil/-news/2010/05/27/39902-army-hits-1-million-flight-hours with-unmanned-aircraft (website accessed on September 27, 2010).

The probabilistic framework for remaining service life prediction presented in this thesis was inspired by a performance-based analysis framework developed in the area of earthquake engineering (Moehle, 2004) and constitutes the most complete version of the methodology presented by the author in previous technical publications (Gobbato *et al*., 2008, 2009, 2010). According to this approach, data collected during pre- and/or in-flight non-destructive evaluation (NDE) inspections (Lanza *et al*., 2007) are used to assess probabilistically the current state of damage of the monitored structural components (i.e., damage location, damage mechanism, and damage size/extent) considering multiple potential damage mechanisms and locations. The uncertainty characterizing the results obtained from the imperfect NDE inspection technique is efficiently assimilated by a recursive Bayesian inference scheme that intermittently updates the joint probability distribution function (PDF) of the damage extent at the inspected locations. A load hazard model for future aerodynamic loads (both atmospheric-induced and maneuver-induced) and a damage evolution model — either mechanics-based, purely phenomenological (i.e., based on experimental observations), or a combination of the two — are then used to stochastically propagate the damage in time. Combined local (e.g., exceedance of a critical damage size at a damage location) and global (e.g., exceedance of the flutter or divergence instability boundary, or initiation of limit cycle oscillation (LCO) behavior) failure criteria, similar to those used by Lin *et al*. (2000) and Styuart *et al*. (2007), are finally used to compute the evolution in time of the probability of system failure (i.e., occurrence of one or more failure limit-states) using well-established system reliability analysis

methods (Ditlevsen and Madsen, 1996). This information is required to develop a cost-efficient condition-based maintenance and repair plan.

Due to the complexity of solving the full-system problem, this study focuses on the simplified case of a composite UAV wing with the skin-to-spar adhesive joints as the only possible damageable subcomponents (see Figure 1.4). Additionally, the debonding along the joints is assumed to progressively evolve from the wing root (i.e., the potential damage locations are known a priori), and to be purely fatigue-driven, thus not considering randomly distributed (in time and space) impact-induced damage as another possible source of damage initiation. However, the whole formulation can be easily extended to the broader scenario in which both sources of damage initiation can simultaneously be considered. The propagation of damage along the adhesive interfaces can be simulated by using either a purely phenomenological model such as Paris-Erdogan Law (Paris and Erdogan, 1963) or other similar phenomenological models as reviewed by Degrieck and Paepegem (2001) and Blanco *et al*. (2004), or a cohesive zone model (CZM) with cyclic degradation behavior (Nguyen *et al*., 2001), fully embedded in the finite element (FE) model of the wing. The proposed methodology can accommodate both damage propagation modeling approaches. However, in both cases, validation and calibration of the damage propagation model with experimental static and fatigue test data is essential in order to achieve accurate predictions. This important aspect will be discussed and properly addressed — together with all the other main building blocks of the proposed damage prognosis methodology — in the following chapters of the dissertation.

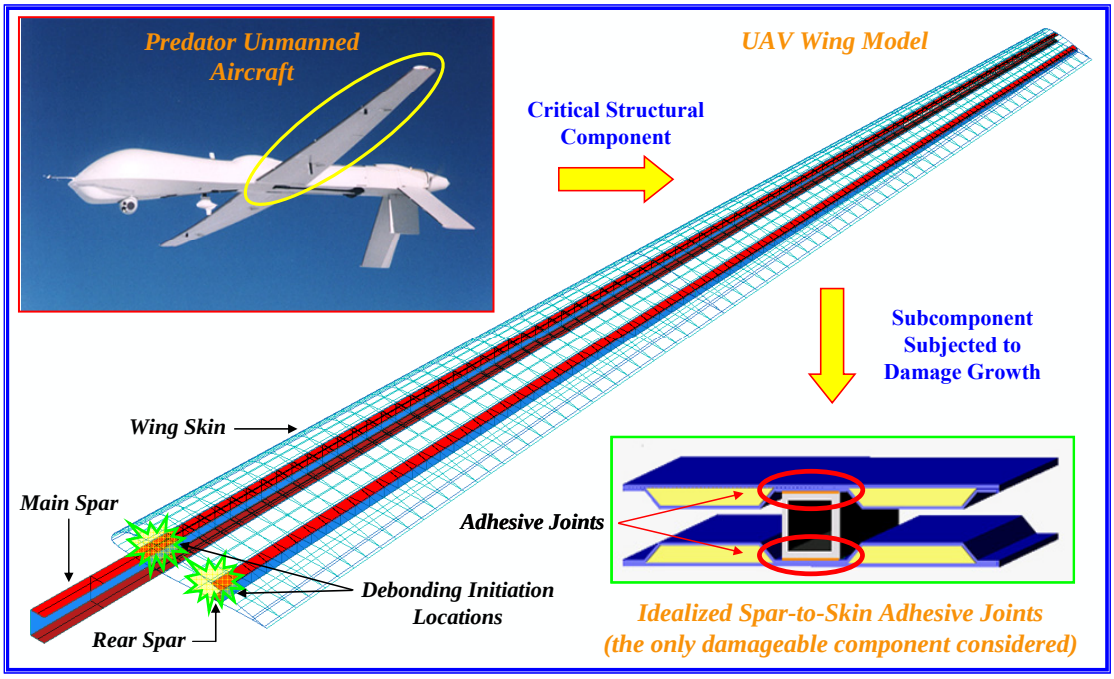

Figure 1.4: Idealized composite UAV wing with the skin-to-spar adhesive joints (highlighted in red in the figure) considered as one of the most damage-sensitive structural sub-components (Oliver *et al.*, 2007).

1.2. From structural health monitoring to damage prognosis

As pointed out by Sohn *et al.* (2003), *structural health monitoring* (SHM) is the process of damage detection for aerospace, civil, and mechanical engineering infrastructure. Damage, in a structural or mechanical system, is herein defined as intentional or unintentional changes to its material and/or geometric properties, including variations of its boundary conditions and connectivities, which adversely affect its current and future performance. As an example, a crack that forms in a given structural component produces a change that alters the stress distribution and stiffness characteristics of the given component. Depending on the size and location of the

crack and the loads applied to the system, the adverse effects of this damage can be either immediate or may take some time to alter the system's performance. In terms of length scales, all damage begins at the material level and then, under appropriate loading conditions, progresses to component-level and system-level damage at various rates. In terms of time scales, damage can accumulate incrementally over long periods of time, such as damage associated with fatigue or corrosion, or can occur on much shorter time scales as a result of scheduled discrete events, such as aircraft landings, and from unscheduled discrete events, such as rapid maneuvers or random impacts. Implicit in this definition of damage is the concept that damage is not meaningful without a comparison between two different system states.

SHM involves the observation of a system over time, using periodically sampled dynamic response measurements from an array of sensors; the extraction of damage-sensitive features from these measurements; and the statistical analysis of these features to determine the current state of the system. For long-term SHM, the output of this process is providing periodically updated information regarding the ability of the structure to perform its intended function as the inevitable aging and degradation, resulting from operational environments, advance. After extreme events, such as earthquakes or blast loading, SHM can be used for remote and rapid condition assessment with the aim to provide, in nearly real time, reliable information regarding the integrity of the structure. This process is also referred to as condition monitoring, particularly when it is applied to rotating machinery, or simply diagnosis. One of the most essential parts of an SHM system is therefore given by the embedment of an

NDE system (or a set of NDE systems) into a structure to allow continuous remote monitoring for damage. There are several advantages in using an SHM system over traditional inspection cycles. The primary goal of SHM is to replace current inspection cycles with a continuous monitoring system. This would reduce the downtime of the vehicle, and increase the probability of damage detection prior to catastrophic failure. More importantly, a continuous monitoring system would allow for shifting towards a cost-efficient conditioned-based maintenance (CBM) — i.e., a set of maintenance processes based on continuous real-time assessment of the structural health from data provided by embedded sensors and/or external tests and measurements (Fitzwater, 2011). The final objective of CBM is to be able to perform maintenance only upon evidence of need. Several parts of SHM systems have been developed and tested successfully, however much work remains to be done before these systems can be reliably implemented and deployed in an operational vehicle.

According to Farrar *et al.* (2003) and Inman *et al.* (2005), *damage prognosis* is instead the estimate of a system's remaining useful life. This estimate is based on the output of predictive models, which develop such estimates by coupling information from (i) usage monitoring; (ii) structural health monitoring; (iii) past, current, and predicted future environmental and operational conditions; (iv) original design assumptions regarding loading and operational environments; and (v) previous component-level and system-level testing. In other words, damage prognosis attempts to forecast the performance of a system by assessing its current state of damage through NDE measurements, by estimating the future loading environments for that

system, and by predicting through simulation and past experience its remaining useful life. The damage prognosis problem presents three main critical areas: (i) sensing and processing hardware, (ii) modeling and simulation, and (iii) data interrogation. In the area of measurement and instrumentation, key challenges include increasing the sensor density (i.e., the NDE sensor network embedded in the system) and moving to an active sensing approach (Lanza *et al.*, 2007). Modeling and simulation challenges include (i) predicting the evolution of component-level damage and its effects on system-level failures at future times; (ii) developing reduced-order predictive models (i.e., response surface models) for embedment in microprocessors; and (iii) quantifying the level of uncertainty and/or confidence in these predictive models. Data interrogation challenges include data management and data mining on large databases resulting from the increased number of sensors used in the NDE monitoring.

1.3. Review of NDE techniques for composite materials

Since NDE techniques represent a crucial part of the damage prognosis methodology proposed in this thesis, a brief overview of some of these techniques — commonly used to detect, locate, and quantify damage in composite materials and structures — is presented in this section. As discussed by Kessler (2002), there are several difficulties in detecting damage in composite materials as opposed to more traditional engineering materials such as metals and plastics. One reason is due to their inherent inhomogeneity and anisotropy: while most metals and plastics are formed by one type of uniformly isotropic material with very well known mechanical properties, laminated composite materials can exhibit a large variability of their material

properties based on the chosen fibers, matrix, layup, and manufacturing process. This fact, besides rendering the mathematical modeling of composite materials a very complex task, it also considerably complicates the analysis and processing of NDE sensor data (Salamone *et al.*, 2009). Other challenges come from the fact that typical damage mechanisms in composite materials frequently initiate and propagate below the surface (e.g., impact-induced inter-ply delamination, fatigue-induced debonding, etc.), a scenario which further prevents the implementation of several, and more traditional, detection methods. Furthermore, the importance of damage detection in composite structures is accentuated over its counterpart in metallic and unreinforced plastic structures because of their (extremely demanding) load bearing requirements which could cause an unexpected sudden failure of a composite component and lead to the catastrophic failure of the entire system. Therefore, the development of reliable damage detection methods is essential to maintain the integrity of structural systems employing these materials. The following represent some of the various nondestructive techniques that have been developed for the detection of damage in composite materials:

(i) Visual inspection methods

(ii) X-ray and C-scan methods

(iii) Strain-gauge and fiber-optic methods

(iv) Vibration-based methods

(v) Ultrasonic methods

(vi) Eddy current methods

1.3.1. Review of NDE techniques used for bond inspection

As already pointed out earlier in this chapter, for aircrafts mainly constructed with lightweight carbon fiber composites, such as unmanned aerial vehicles (UAVs), the skin-to-spar adhesive joints are among the most critical sub-components. Structural defects that initiate (and then invisibly propagate) in these joints can lead to a consistent deterioration of the flight performance and even to catastrophic failures. Typical bond defects include disbonds, porosity, poor adhesion between adhesive and adherend, and poor cohesive strength. Several NDE techniques are currently used by the industry as well as the academic world: eddy currents, acoustic emission (Velasquez and Kosmatka, 2011), ultrasonic inspections (Blitz and Simpson, 1996), radiography, thermography, or just basic visual inspection. Among them, ultrasonic inspection (Bartoli, 2007) is considered the only low-cost technique able to achieve high level of accuracy in damage detection or materials characterization, and has been under development for decades for bond inspection applications.

In ultrasonic inspection, normal-incidence testing (through-transmission and pulse-echo) has been widely used in the past and has been proven to be useful for defects detection and mechanical material properties characterization. These techniques, which essentially analyze the transmission and reflection of the energy carried by the bulk ultrasonic waves, may help calculate stiffness and thickness of the bond layer in adhesive joints that, in turn, can be related to the bond cohesive strength. Using the same principles, NDE techniques can also be used to evaluate the presence and extent of a disbond (i.e., locating the disbond and quantifying its extent).

An alternative new ultrasonic approach, for the inspection of the bond state, makes use of guided waves. These waves propagate along the structure (i.e., the wave guide) with a particular behavior driven by the geometry and material properties of the system. The main advantage of this approach is the possibility to inspect a long segment of the test piece at once. Larger areas, compared to those normally being monitored by localized point-by-point standard bulk wave ultrasonic testing, can in fact be inspected using guided waves and single pulse excitation. While the potential for long-range propagation of ultrasonic guided waves through layered metal-to-metal adhesive interfaces has been investigated and validated by experiments, fewer references can be found regarding composite joints. However, the use of ultrasonic guided waves presents itself as one of the most realistic methods due to its capability of long-range inspection and the ability to work on various types of structural components.

1.4. Damage prognosis applications beyond composite aerospace structures

The work presented in this thesis can be extended, with some modifications and additions, to other engineering fields in which damage prognosis is becoming more and more important for a cost-effective life-cycle management of a particular structure or system. In Civil Engineering, for instance, the driver for prognosis is largely governed by large-scale discrete events rather than more continuous degradation (Farrar *et al.*, 2003). Typical examples are aerodynamic gust loads on long span bridges and earthquake loading on all types of civil infrastructure. Although cyclic loads caused by traffic are also a consideration (Nakasa *et al.*, 1983; Li *et al.*,

2010; Morcous *et al.*, 2010), the discrete events are the ones that require immediate prognosis for future use. Damage prognosis applications in the civil engineering field requires a much denser array of sensors to identify local structural degradation than is typical for most current instrumentation systems, designed for seismic monitoring. Current wired technology in the seismic field has a cost of about $10,000 per node (Farrar *et al.*, 2003), including installation, which limits the sensor density. In California, for example, the most densely instrumented structures have on the order of 10–30 sensors to measure seismic response. For damage prognosis, a one to two orders of magnitude increase in sensor density is required. It is the opinion of the entire research community that this increase can only be achieved economically by the use of new sensing technologies such as wireless, self-assembling, and embedded devices based on integrated circuit fabrication technologies.

Another possible outlet for the damage prognosis methodology proposed herein is given by wind turbines and, in particular, composite wind turbine blades (Ciang *et al.*, 2008). Renewable energy sources have in fact gained much attention due to the recent energy crisis and the urge for clean energy. Among the main options being studied, wind energy is a strong contender because of its reliability due to the maturity of the technology, good infrastructure and relative cost competitiveness. In order to harvest wind energy more efficiently, the size of wind turbines has become physically larger, making maintenance and repair work difficult. In order to (i) improve safety standards, (ii) minimize downtime, (iii) lower the frequency of sudden breakdowns and associated huge maintenance and logistic costs, and (iv) provide

reliable power generation, wind turbines must be periodically or continuously monitored to ensure that they are in safe operational conditions. Among all possible monitoring systems, a continuous structural health monitoring (SHM) solution, leveraging on sensor-based non-destructive inspections and evaluation methods, can represent the cardinal point to then efficiently perform damage prognosis on this type of structures.

Finally, the proposed damage prognosis framework can also be extended and appropriately adapted to study the reliability of aging offshore platforms (Moan, 2005, 2007, 2008), develop a reliability-based management and maintenance program for these critical systems, and to monitor their structural integrity in order to prevent environmental disasters such as the one recently occurred in the Gulf of Mexico on April 20th, 2010 (http://en.wikipedia.org/wiki/Deepwater_Horizon_oil_spill, webpage accessed on May 16th, 2011). Adequate performance of offshore structures is ensured by designing for a service life of twenty years or more (Moan, 2005) and safety requirements are imposed to avoid ultimate consequences such as fatalities, environmental damage (as mentioned earlier) or property damage. However, periodic monitoring of these types of structures represents an essential ingredient for maintaining an adequate safety level, especially with respect to fatigue, corrosion and other degradation phenomena developing during service life. Periodic monitoring is also essential to avoid local failures that could be very expensive to repair (particularly for underwater sub-structures) and may result in pollution of the surrounding environment. It is also worth noting that operational and environmental loads, acting

on offshore structures and thus driving the fatigue damage growth, are highly stochastic in nature (Moan *et al.*, 2005) and must be treated in a rigorous probabilistic sense. Moreover, for many practical reliability assessment applications, combined wave and wind loads must also be simultaneously considered during the analyses (Ditlevsen, 2002). A comprehensive framework capable of handling multiple loading scenarios and superimposing their effects on the structure is therefore needed also within this field of application.

1.5. Research needs, objectives, and scope

As pointed out earlier in this chapter, damage prognosis is a multidisciplinary field with several challenges. It involves the use of NDE techniques to monitor and assess the current state of damage of the structural system under consideration. Measurement errors are part of every NDE technique and they need to be rigorously taken into account in the damage prognosis process. The uncertainty associated with these measurements must be quantified and then propagated through all the subsequent prognosis stages up to the final decision making process. These stages involve the probabilistic characterization of future operational loads, the propagation of the current state of damage through predictive modeling techniques, and the computation of the overall system reliability at future times. The outcomes from this last stage constitute the basis for the decision making process mentioned above; these outcomes are inherently affected by (i) the initial NDE measurement uncertainty, (ii) the error in the prediction of future loading conditions, and (iii) all the predictive modeling errors.

One of the main objectives of this research work is to provide a rigorous and robust mathematical integration and connection (within a unique and exhaustive probabilistic framework) of all the analysis steps involved in the damage prognosis process. Additionally, the proposed research provides the fundamental basis to systematically quantify the uncertainty in each of these prognosis steps, and to propagate all these sources of uncertainty from the initial NDE inspection up to the final decision making step. Furthermore, it also outlines how advanced analysis techniques for Bayesian updating, such as Markov Chain Monte Carlo methods, and computationally efficient modeling approaches, such as mechanics-based damage evolution modeling and response surface methodologies (also known as metamodeling or surrogate modeling techniques), can be synergically integrated within the proposed damage prognosis framework.

This framework is verified and validated through three benchmark applications with increasing levels of complexity. This strategy allowed for (i) rigorous verification and validation of each of the main steps of the methodology, (ii) execution of extensive parametric and sensitivity studies, and (iii) comparison of the results obtained from the numerical simulations with analytical (closed-form) solutions.

1.6. Organization of the thesis

The presentation of this research work has been divided into ten chapters, the contents of which are outlined below:

Chapter 1 serves as an introduction to the topic of structural health monitoring and damage prognosis (SHM-DP) of composite aerospace structures and composite

UAVs in particular. It provides an overview of the damage mechanisms typical of composite structures, with emphasis on fatigue-induced damage evolution along the adhesive joints part of this type of structural systems. It also stresses the need for an integrated SHM-DP approach for composite aerospace structures, emphasizing its interdisciplinarity and complexity. The research needs and objectives of this work are also outlined.

Chapter 2 offers an overview of the proposed reliability-based damage prognosis framework for remaining fatigue life prediction of a composite UAV wing. Each of the five main analysis steps of the methodology is concisely described in this chapter; furthermore, its specific contribution, primarily objective, and inherent uncertainty added to the damage prognosis process are clearly highlighted. Finally, an overview of a possible extension of the proposed framework to other structural and/or mechanical systems is also presented.

Chapter 3 analyzes in detail the first analytical step of the methodology, namely *Bayesian inference*. This step aims at providing the probabilistic assessment of the current state of damage of the monitored structural component and/or sub-component (e.g., the entire UAV wing or the skin-to-spar adhesive joints of a UAV wing). Emphasis is placed on (i) the probabilistic treatment of the NDE inspection outcomes and (ii) the proposed recursive Bayesian updating scheme used to update the probability distribution functions of both damage sizes and fatigue damage evolution parameters.

Chapter 4 unveils (after the brief overview provided in Chapter 2) the details of the second step of the proposed damage prognosis framework, namely *probabilistic load hazard analysis*. Turbulence- and maneuver-induced load models are presented and validated through flight test data found in the literature. Furthermore, the extension of the proposed load modeling approaches to other types of loads (acting on structural systems different from a composite UAV wing) is also discussed.

Chapter 5 thoroughly examines the third step of the methodology, namely *probabilistic structural response analysis*. It represents the most complex and computationally challenging step of the overall framework, involving fatigue-induced damage propagation predictions and multiple applications of the total probability theorem in a nested fashion. Both mechanics-based damage models (e.g., cohesive zone models) and damage evolution models based on linear elastic fracture mechanics (LEFM) and experimental observations are discussed and linked to the proposed prognosis framework.

Chapter 6 uses the damage evolution results, discussed in the previous Chapter, to assess probabilistically the global performance level of the structural system through the computation of a series of global damage variables (or indicators). For the specific case of a composite UAV wing, focus is on its global aeroelastic performance. These tasks are part of the fourth step of the proposed framework, namely *probabilistic flutter & LCO analyses*.

Chapter 7 completes the theoretical illustration of the proposed damage prognosis methodology by analyzing its fifth step, namely *damage prognosis analysis*.

In this chapter, the structural system is abstracted to a series system and expressions for the computations of uni-modal bounds to the probability of *system failure* and *false-alarm* at future times are derived and discussed. Both local and global failure modes are considered in the analyses.

Chapter 8 represents the first partial verification and validation of the proposed methodology through its application to a simple testbed structure: a simply-supported composite laminated beam made out of two unidirectional composite adherends bonded together through an (imperfect) adhesive interface and subjected to an external concentrated load applied at midspan. The adhesive interface is considered as the unique damageable sub-component of the beam and the fatigue-driven damage evolution along this joint is modeled through a postulated (exponential) damage propagation/evolution process; an approach essentially dictated by mathematical and computational convenience, and already used in previous research work (Deodatis *et al.*, 1992; Ito *et al.*, 1992; Mohanty *et al.*, 2009).

Chapter 9 verifies and validates the methodology in its entirety by using the same benchmark structure introduced in Chapter 8. However, the fatigue damage evolution process along the adhesive interface is herein simulated via a damage propagation law based on linear elastic fracture mechanics (LEFM) principles and experimental observations: the Forman's model (Forman, 1972; Chow, 1990). Additionally, this chapter validates the proposed recursive Bayesian inference and probabilistic damage evolution analysis steps by using a set of fatigue test data found in the literature (Virkler *et al.*, 1979). These test data are represented by 68 crack

propagation trajectories that were obtained from center-cracked aluminum plates made out of 2024-T3 aluminum alloy and fatigued under constant amplitude harmonic load. Two of these trajectories are selected and used as underlying true damage propagation paths within the application of the proposed damage prognosis framework. Given the characteristics of the applied load during the experimental tests (i.e., harmonic load with fixed load ratio and constant amplitude and frequency), Paris law (Paris and Erdogan, 1963) is used as damage propagation model for this specific experimental validation of the proposed prognosis methodology.

Chapter 10 summarizes the research work performed, emphasizes the important original contributions and findings of this dissertation, and discusses future research directions and recommendations.

References

I. Bartoli, *Structural health monitoring by ultrasonic guided waves*, Ph.D. Thesis, Department of Structural Engineering, University of California, San Diego, CA, 2007.

O.A. Bauchau, and R.G. Loewy, *Nonlinear aeroelastic effects in damaged composite aerospace structures*, Technical Report, School of Aerospace Engineering, Georgia Institute of Technology, Atlanta, GA, 1997.

N. Blanco, E.K. Gamstedt, L.E. Asp, and J. Costa, Mixed-mode delamination growth in carbon-fiber composite laminates under cyclic loading, *International Journal of Solids and Structures*, 41(15), 4219-4235, 2004.

J. Blitz and G Simpson, *Ultrasonic Methods of Non-destructive Testing*, Chapman & Hall, 1996.

C.C. Ciang, J.-R. Lee, and H.-J. Bang, Structural health monitoring for a wind turbine system: a review of damage detection methods, *Measurement Science and Technologies*, 19(12), 2008.

C.L. Chow and T.J. Lu, A unified approach to fatigue crack propagation in metals and polymers, *Journal of Material Science Letters*, 9(12), 1427-1430, 1990.

J. Degrieck, and W.V. Paepegem, Fatigue damage modeling of fibre-reinforced composite materials: Review, *Applied Mechanics Reviews*, 54(4), 279-299, 2001.

G. Deodatis, H. Asada, and S. Ito, Reliability of aircraft structures under non-periodic inspection: a Bayesian approach, *Engineering Fracture Mechanics*, 53(5), 789-805 1996.

G. Deodatis, Y. Fujimoto, S. Ito, J. Spencer, and H. Itagaki, Non-periodic inspection by Bayesian method I, *Probabilistic Engineering Mechanics*, 7(4), 191-204, 1992.

O. Ditlevsen, Stochastic model for joint wave and wind loads on offshore structures, *Structural Safety*, 24(2-4), 139-163, 2002.

O. Ditlevsen and H.O. Madsen, *Structural reliability methods*, Wiley, West Sussex, England, 1996.

C.R. Farrar, H. Sohn, F.M. Hemez, M.C. Anderson, M.T. Bement, P.J. Cornwell, S.W. Doebling, J.F. Schultze, N. Lieven, and A.N. Robertson, *Damage prognosis: current status and future needs*, Los Alamos National Laboratory Report, LA-14051-MS, 2003.

L. Fitzwater, C. Davis, T. Torng, and J. Poblete, Non-Deterministic approaches to structural health management- diagnosis and prognosis: cost/benefit analysis for integration of non-deterministic analysis and in-situ monitoring for structural integrity, *Proc. 52nd AIAA/ASME/ASCE/AHS/ASC Structures, Structural Dynamics, and Materials Conference*, Denver, CO, USA, April 4-7, 2011.

R.G. Forman, Study of fatigue crack initiation from flaws using fracture mechanics theory. *Engineering Fracture Mechanics*, 4(2), 333-345, 1972.

V. Giurgiutiu, K. Harries, M. Petrou, J. Bost, and J.B. Quattlebaum, Disbond detection with piezoelectric wafer active sensors in RC structures strengthened with FRP composite overlays, *Earthquake engineering and Engineering Vibration*, 2(2), 213-223, 2003.

M. Gobbato, J.P. Conte, J.B. Kosmatka, J.A. Oliver, and C.R. Farrar, Reliability-based framework for damage prognosis of composite unmanned aerial vehicles structural

components, *Proc. The Inaugural International Conference of the Engineering Mechanics Institute (EM08)*, Minneapolis, MN, USA, May 18-21, 2008.

M. Gobbato, J.P. Conte, J.B. Kosmatka, J.A. Oliver, and C.R. Farrar, Damage prognosis of adhesively-bonded joints in laminated composite structural components of unmanned aerial vehicles, *Proc. COMPDYN 2009 – ECCOMAS Thematic Conference on Computational Methods in Structural Dynamics and Earthquake Engineering*, Rhodes, Greece, June 22-24, 2009.

M. Gobbato, J.P. Conte, J.B. Kosmatka, and C.R. Farrar, Reliability-based framework for damage prognosis of adhesively-bonded joints in composite UAV wings, *Proc. 51st AIAA/ASME/ASCE/AHS/ASC Structures, Structural Dynamics, and Materials Conference*, Orlando, FL, USA, April 12-15, 2010.

D. Gorinevsky, G.A. Gordon, S. Beard, A. Kumar, and F.-K. Chang, Design of integrated SHM system for commercial aircraft applications, *Proc. 5th International Workshop on Structural Health Monitoring*, Stanford, CA, USA, September 2005.

D.J. Inman, C.R. Farrar, V. Lopez Jr., V. Steffen Jr., *Damage prognosis for aerospace, civil and mechanical systems*. Wiley, 2005.

S. Ito, G. Deodatis, Y. Fujimoto, H. Asada, and M. Shinozuka, Non-periodic inspection by Bayesian method II: Structures with elements subjected to different stress levels, Probabilistic Engineering Mechanics, 7(4), 205-215, 1992.

S.S. Kessler, *Piezoelectric-based in-situ damage detection of composite materials for structural health monitoring systems*, Ph.D. Thesis, Department of Aeronautics and Astronautics, Massachusetts Institute of Technology, Cambridge, MA, 2002.

F. Lanza di Scalea, H.M. Matt, I. Bartoli, S. Coccia, G. Park, and C.R. Farrar, Health monitoring of UAV skin-to-spar joints using guided waves and macro fiber composite transducers, *Journal of Intelligent Material Systems and Structures*, 18(4), 373-388, 2007.

S. Li, S. Zhu, Y.-L. Xu, Z.-W. Chen, and H. Li, Long-term condition assessment of suspenders under traffic loads based on structural monitoring system: Application to the Tsing Ma Bridge, *Structural Control and Health Monitoring*, n/a. doi: 10.1002/stc.427, 2010.

K.Y. Lin, J. Du, and D. Rusk, *Structural design methodology based on concepts of uncertainty*, Report NASA/CR-2000-209847, NASA Langley Research Center, Hampton, VA, 2000.

K.Y. Lin, and A.V. Styuart, Probabilistic approach to damage tolerance design of aircraft composite structures, *Journal of Aircraft*, 44(4), 1309-1317, 2007.

A. Marzani, *Guided wave modeling for bond inspection in aerospace structures*, Ph.D. Thesis, Department of Structural Engineering, University of California, San Diego, CA, 2004.

T. Moan, Reliability-based management of inspection, maintenance and repair of offshore structures, *Structure and Infrastructure Engineering*, 1(1), 33-62, 2005.

T. Moan, Design of offshore structures and ships for damage tolerance, Systems & Ocean Technology, *Journal of SOBENA*, 3(1), 51-65, 2007.

T. Moan, Reliability of aged offshore structures Chapter 11, In Paik, J.K. & Melchers, R.E. Condition Assessment of Aged Structures, CRC Press, Boca Raton, 2008.

T. Moan, Z. Gao, and E. Ayala-Uraga, Uncertainty of wave-induced response of marine structures due to long-term variation of extratropical wave conditions, *Journal of Marine Structures*, 18(4), 359-382, 2005.

J. Moehle, and G.G. Deierlein, A framework methodology for performance-based earthquake engineering, *Proc. 13th Conference on Earthquake Engineering*, Vancouver, Canada, August 1-6, 2004.

J.R. Mohanty, B.B. Verma, and P.K. Ray, Prediction of fatigue crack growth and residual life using an exponential model: Part I (constant amplitude loading), International Journal of Fatigue, 31(3), 418-424, 2009.

J.R. Mohanty, B.B. Verma, and P.K. Ray, Prediction of fatigue crack growth and residual life using an exponential model: Part II (mode-I overload induced retardation), International Journal of Fatigue, 31(3), 425-432, 2009.

G. Morcous, Z. Lounis, and Y. Cho, An Integrated System for Bridge Management Using Probabilistic and Mechanistic Deterioration Models: Application to Bridge Decks, *KSCE Journal of Civil Engineering*, 14(4), 527-537, 2010.

K. Nakasa, H. Takei, and H. Itoh, Mechanism of corrosion fatigue crack propagation in high strength steel, *Engineering Fracture Mechanics*, 17(5), 449-459, 1983.

O. Nguyen, E.A. Repetto, M. Ortiz, and R.A. Radovitzky, A cohesive model of fatigue crack growth, *International Journal of Fracture*, 110(4), 351-369, 2001.

J.A. Oliver, J.B. Kosmatka, C.R. Farrar, and Gyuhae Park, Development of a composite UAV wing test-bed for structural health monitoring research, *Proc.*

SPIE Smart Structures and Materials & Nondestructive Evaluation and Health Monitoring, San Diego, CA, USA, March 18-22, 2007.

P.C. Paris and F.A. Erdogan, Critical analysis of crack propagation laws, *Journal of Basic Engineering*, TRANS ASME, 85(Series D), 528-534, 1963.

S. Salamone, I. Bartoli, F. Lanza di Scalea, and S. Coccia, Guided-wave health monitoring of aircraft composite panels under changing temperature, *Journal of Intelligent Material Systems and Structures*, 20(9), 1079-1090, (2009).

H. Sohn, C.R. Farrar, F.M. Hemez, D.D. Shunk, D.W. Stinemates, and B.R. Nadler, *A review of structural health monitoring literature: 1996-2001*, Los Alamos National Laboratory, Report LA-13976-MS, 2003.

A.V. Styuart, M. Mor, E. Livne, and K.Y. Lin., Aeroelastic failure risk assessment in damage tolerant composite airframe structures, *Proc. 48th AIAA/ASME/ASCE/ AHS/ASC Structures, Structural Dynamics, and Materials Conference*, Honolulu, Hi, April 23-26,2007.

E. Velazquez and J.B. Kosmatka, Detecting shear and tension bond failures in composite aircraft structures, *Proc. 52nd AIAA/ASME/ASCE/AHS/ASC Structures, Structural Dynamics, and Materials Conference*, Denver, CO, USA, April 4-7, 2011.

D.A. Virkler, B.M. Hillberry, and P.K. Goel, The statistical nature of fatigue crack propagation, Transactions of ASME – *Journal of Engineering Materials and Technology*, 101, 148-153, 1979.

K. Wang, D.J. Inman, and C.R. Farrar, Crack-induced changes in divergence and flutter of cantilevered composite panels, *Structural Health Monitoring*, 4(4), 377-392, 2005.

Z. Wu, X.P. Qing, K. Ghosh, Vistasp Karbhari, and Fu-Kuo Chang, Health monitoring of bonded composite repair in bridge rehabilitation, *Smart Materials and Structures*, 17(4), 045014.1-045014.9, 2008.

J.N. Yang, and W.J. Trapp, Reliability analysis of aircraft structures under random loading and periodic inspection, *AIAA Journal*, 12(12), 1623-1630, 1974.

CHAPTER 2

OVERVIEW OF PROPOSED DAMAGE PROGNOSIS METHODOLOGY

2.1. Introduction

This chapter presents an overview of a newly developed reliability-based damage prognosis methodology for remaining fatigue life prediction of composite UAV wings, monitored through (local) non destructive evaluation (NDE) inspections. As illustrated in Figure 2.1, this methodology aims at providing recursive predictions of the future performance level and the corresponding reliability index of the monitored structure by taking advantage of NDE measurements results that become available every time new NDE data are collected and processed. From Figure 2.1, it can also be deduced that the proposed framework involves three main fundamental blocks, namely, *Bayesian inference*, *predictive modeling*, and *damage prognosis*.

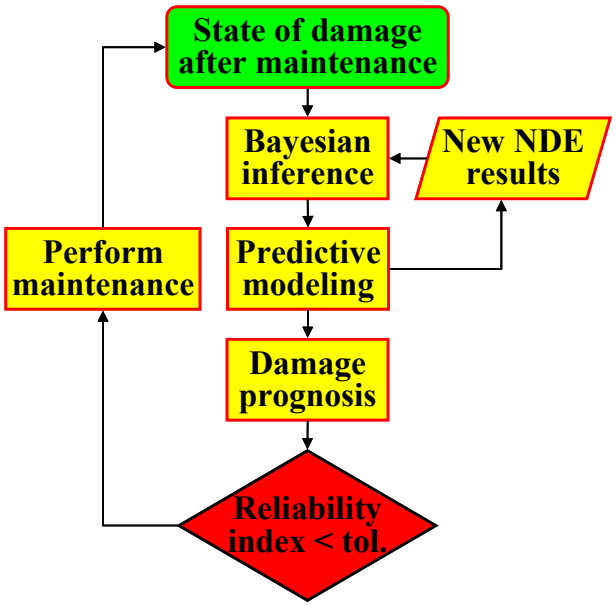

Figure 2.1: Flowchart illustrating the proposed recursive damage prognosis scheme driven by continuous and/or periodic NDE (sensor-based) monitoring results.

In the first fundamental step, the proposed Bayesian inference scheme is used to update the joint probability distribution function (PDF) of the damage extents at the inspected damage locations. In other words, it provides an updated/posterior information on the current state of damage by combining a prior information on the current state of damage and the processed NDE results. The outcome from this first fundamental step (i.e. the posterior knowledge about the current state of damage of the monitored system) is then used as input for the predictive modeling part. This second fundamental step of the proposed framework provides recursive predictions of the future (and more severe) states of damage of the structure. Furthermore, when new NDE results become available, a subset of the results obtained from this second block is used as new prior knowledge to repeat the Bayesian inference step. Finally, the damage prognosis step uses the predictive modeling results to compute the reliability

index of the structure (or, in an equivalent fashion, the probability of failure of the overall system) at future times.

The predictive modeling part of the proposed methodology can be further decomposed into three steps, thereby leading to a total of five analytical steps as clearly shown in Figure 2.2. In this Chapter, a brief description of each of these five analytical steps is provided in order to introduce the reader to the rigorous in-depth analysis presented in Chapters 3 through 7. These five steps are: (1) Bayesian inference, (2) probabilistic load hazard analysis, (3) probabilistic structural response analysis (sometimes denoted also as probabilistic damage evolution analysis in Chapters 8 and 9), (4) probabilistic flutter & limit cycle oscillation (LCO) analyses, and (5) damage prognosis analysis. All these steps, linked together, lead to the final decision making process aimed at providing a conditioned-based cost-efficient maintenance plan.

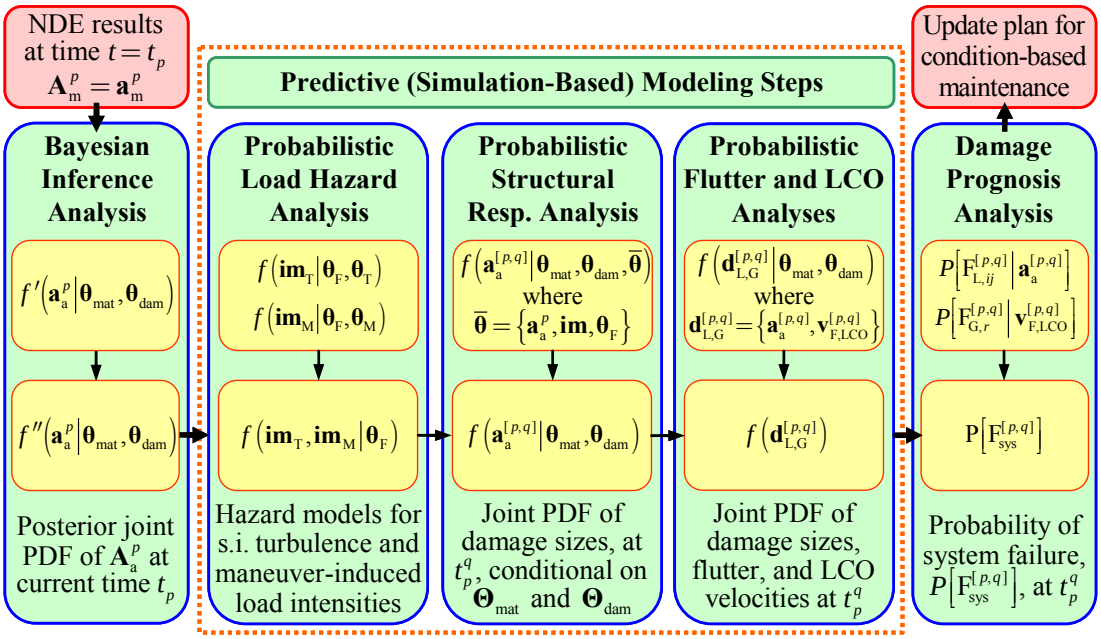

Figure 2.2: Overview of the proposed reliability-based damage prognosis methodology for remaining service life prediction of a composite UAV wing.

More specifically, the flowchart shown in Figure 2.2 conceptually illustrates the main analytical steps of the proposed damage prognosis methodology, as well as the process of uncertainty quantification (within each step) and propagation (between subsequent steps) necessary to estimate the remaining service life of a UAV structural component (with special focus on a composite UAV wing) once a new NDE inspection outcome, at current time t_p (i.e., from the most recent NDE inspection), becomes available. Additionally, the flowchart clearly shows how the five steps, previously mentioned, are all linked together (in a probabilistic sense) and it also displays the main random variables considered in each analytical step.

2.2. Bayesian inference

This first step aims at providing the posterior joint PDF of the damage sizes at the monitored locations by repeatedly using/incorporating the NDE inspection outcome obtained after each NDE inspection. The inspection outcome is represented by the measured (through NDE sensor data processing) damage size/extent vector, $\mathbf{a}_{\mathrm{m}}^{p}$, at the inspected locations at time t_p, and is viewed herein as a particular realization of the random vector $\mathbf{A}_{\mathrm{m}}^{p}$. It is worth noting that for the case of a composite UAV wing, whose skin-to-spar adhesive joints are periodically monitored through NDE inspections, the vector $\mathbf{a}_{\mathrm{m}}^{p}$ would represent the collection of the measured disbond lengths (from the wing-root) at time t_p. This new information, $\mathbf{a}_{\mathrm{m}}^{p}$, is used (in the first step of the methodology, *Bayesian inference*) to compute, through a Bayesian updating procedure, the posterior joint PDF of the actual/true damage size vector, $\mathbf{A}_{\mathrm{a}}^{p}$,

at time t_p, conditional on the material ($\boldsymbol{\Theta}_{\text{mat}}$) and damage model ($\boldsymbol{\Theta}_{\text{dam}}$) parameters, and all the previous $p+1$ NDE measurement outcomes obtained up to time t_p, denoted as $\mathbf{a}_{\text{m}}^{[0,p]} = \left\{\mathbf{a}_{\text{m}}^{0}, \mathbf{a}_{\text{m}}^{1}, ..., \mathbf{a}_{\text{m}}^{p}\right\}$. For the sake of simplicity, this posterior joint conditional PDF, given in full form as $f''_{\mathbf{A}_{\text{a}}^{p}\left|\boldsymbol{\Theta}_{\text{mat}},\boldsymbol{\Theta}_{\text{dam}},\mathbf{A}_{\text{m}}^{[0,p]}\right.}\left(\mathbf{a}_{\text{a}}^{p}\left|\boldsymbol{\theta}_{\text{mat}},\boldsymbol{\theta}_{\text{dam}},\mathbf{a}_{\text{m}}^{[0,p]}\right.\right)$, is hereafter denoted $f''_{\mathbf{A}_{\text{a}}^{p}\left|\boldsymbol{\Theta}_{\text{mat}},\boldsymbol{\Theta}_{\text{dam}}\right.}\left(\mathbf{a}_{\text{a}}^{p}\left|\boldsymbol{\theta}_{\text{mat}},\boldsymbol{\theta}_{\text{dam}}\right.\right)$, without explicitly including the dependency on $\mathbf{A}_{\text{m}}^{[0,p]}$. Similarly, the prior knowledge about $\mathbf{A}_{\text{a}}^{p}$ is given by $f'_{\mathbf{A}_{\text{a}}^{p}\left|\boldsymbol{\Theta}_{\text{mat}},\boldsymbol{\Theta}_{\text{dam}},\mathbf{A}_{\text{m}}^{[0,p-1]}\right.}\left(\mathbf{a}_{\text{a}}^{p}\left|\boldsymbol{\theta}_{\text{mat}},\boldsymbol{\theta}_{\text{dam}},\mathbf{a}_{\text{m}}^{[0,p-1]}\right.\right)$, or $f'_{\mathbf{A}_{\text{a}}^{p}\left|\boldsymbol{\Theta}_{\text{mat}},\boldsymbol{\Theta}_{\text{dam}}\right.}\left(\mathbf{a}_{\text{a}}^{p}\left|\boldsymbol{\theta}_{\text{mat}},\boldsymbol{\theta}_{\text{dam}}\right.\right)$ in the simplified manner. The computed (at time t_p) posterior joint conditional PDF, $f''_{\mathbf{A}_{\text{a}}^{p}\left|\boldsymbol{\Theta}_{\text{mat}},\boldsymbol{\Theta}_{\text{dam}}\right.}\left(\mathbf{a}_{\text{a}}^{p}\left|\boldsymbol{\theta}_{\text{mat}},\boldsymbol{\theta}_{\text{dam}}\right.\right)$, is unconditional on the damage size vectors $\mathbf{A}_{\text{a}}^{0}, \mathbf{A}_{\text{a}}^{1}, ..., \mathbf{A}_{\text{a}}^{p-1}$ and the entire dynamic loading history (from t_0 to t_p), because during each of the p runs of the prognosis methodology, between t_0 and t_p, the uncertainty associated with $\mathbf{A}_{\text{a}}^{0}, \mathbf{A}_{\text{a}}^{1}, ..., \mathbf{A}_{\text{a}}^{p-1}$ and the loading characteristics is integrated out (in the application of the total probability theorem, TPT); this point is shown later in Equation (2.7). As a further remark, multiple damage locations and multiple damage mechanisms (evolving simultaneously at a given location) can potentially be considered by the recursive Bayesian updating procedure used herein, with the actual size of the j^{th} detected damage mechanism evolving at the i^{th} monitored damage location at time t_p, denoted as $A_a^{(i,j,p)}$. Damage locations and damage mechanisms are uncertain, due to the inherent imperfections of NDE techniques;

however, as a simplifying assumption, they are considered deterministic and known throughout this study.

The random parameter vector $\boldsymbol{\Theta}_{\text{mat}}$ (of length n_{mat}) exclusively describes the uncertainty in the (potentially time-dependent due to aging) material properties used to model the parts of the airframe — such as wing-spars, bulkheads, and stringers — which are herein assumed to be non-damageable (within the range of damage mechanisms typical of laminated composites mentioned earlier in Chapter 1), while the random vector $\boldsymbol{\Theta}_{\text{dam}}$ (of length n_{dam}) quantifies the uncertainty of those parameters that control the mechanical properties (and especially the fatigue-induced material degradation) in the pre-identified damageable subcomponents. For the specific case being studied herein — a composite UAV wing whose skin-to-spar adhesive joints are considered the only damageable subcomponents — $\boldsymbol{\Theta}_{\text{mat}}$ defines density, damping, stiffness and strength parameters of (i) the composite laminated spars, and (ii) the honeycomb-core composite panels of the wing-skin. On the other hand, $\boldsymbol{\Theta}_{\text{dam}}$ characterizes the mechanical properties of the adhesive joints where debonding can occur — e.g., mode I & II critical fracture energies, peak shear strength, ultimate opening or sliding displacements before complete debonding, and rate of fatigue degradation (through a series of fatigue degradation parameters). Therefore, $\boldsymbol{\Theta}_{\text{dam}}$ does not characterize the bulk material properties of the adhesive/epoxy but it rather describes the uncertainty of the adhesive interface, which implicitly accounts for the statistical variability induced by other factors such as surface preparation of the adherends, bond geometry, etc. In this study, in order to simplify the problem, $\boldsymbol{\Theta}_{\text{mat}}$ and $\boldsymbol{\Theta}_{\text{dam}}$ are

assumed to be statistically independent (s.i.) ; additionally, they are also considered to be time-invariant (i.e., they do not renew in time; Der Kiureghian, 2005).

As a final remark for this section, it is also worth noting that the joint PDF of the damage evolution parameter vector, $\boldsymbol{\Theta}_{\text{dam}}$, can be recursively updated using the NDE inspection outcome after each NDE inspection. In light of this consideration, whenever this second update is performed, the damage evolution parameter vector at time t_p will be denoted by $\boldsymbol{\Theta}_{\text{dam}}^{p}$ and its corresponding posterior joint PDF will be identified as $f''_{\boldsymbol{\Theta}_{\text{dam}}^{p}\left|\mathbf{A}_{\text{m}}^{[0,p]}\right.}\left(\boldsymbol{\theta}_{\text{dam}}^{p}\left|\mathbf{a}_{\text{m}}^{[0,p]}\right.\right)$ or, in condensed notation, as $f''_{\boldsymbol{\Theta}_{\text{dam}}^{p}}\left(\boldsymbol{\theta}_{\text{dam}}^{p}\right)$. The procedure to achieve this second update will be later described in detail in Chapters 3, 8, and 9.

2.3. Probabilistic load hazard analysis

The second step of the damage prognosis methodology, *probabilistic load hazard analysis*, defines the joint PDF of the turbulence ($\mathbf{IM}_{\text{T}}$) and maneuver ($\mathbf{IM}_{\text{M}}$) intensity measures, conditional on the flight profile ($\boldsymbol{\Theta}_{\text{F}}$) and the assumed statistically independent turbulence ($\boldsymbol{\Theta}_{\text{T}}$) and maneuver ($\boldsymbol{\Theta}_{\text{M}}$) random parameter vectors. This joint conditional PDF is denoted as $f_{\mathbf{IM}_{\text{T}},\mathbf{IM}_{\text{M}}|\boldsymbol{\Theta}_{\text{F}}}\left(\mathbf{im}_{\text{T}},\mathbf{im}_{\text{M}}\left|\boldsymbol{\theta}_{\text{F}}\right.\right)$ and is numerically computed by unconditioning the joint conditional PDF $f_{\mathbf{IM}_{\text{T}},\mathbf{IM}_{\text{M}}|\boldsymbol{\Theta}_{\text{T}},\boldsymbol{\Theta}_{\text{M}},\boldsymbol{\Theta}_{\text{F}}}\left(\mathbf{im}_{\text{T}},\mathbf{im}_{\text{M}}\left|\boldsymbol{\theta}_{\text{T}},\boldsymbol{\theta}_{\text{M}},\boldsymbol{\theta}_{\text{F}}\right.\right)$ with respect to (w.r.t.) $\boldsymbol{\Theta}_{\text{T}}$ and $\boldsymbol{\Theta}_{\text{M}}$, as shown later in Equation (2.8). The random vector $\mathbf{IM}_{\text{T}}$ is considered to be statistically independent of $\boldsymbol{\Theta}_{\text{M}}$; similarly, the random vector $\mathbf{IM}_{\text{M}}$ is assumed to be statistically independent of $\boldsymbol{\Theta}_{\text{T}}$; however, both $\boldsymbol{\Theta}_{\text{T}}$ and $\boldsymbol{\Theta}_{\text{M}}$ are generally not statistically

independent of $\boldsymbol{\Theta}_{\mathrm{F}}$ (as shown in Chapter 4). Additionally, by defining the intensity measure random vector as $\mathbf{IM}=\left\{\mathbf{IM}_{\mathrm{T}},\mathbf{IM}_{\mathrm{M}}\right\}$, it is possible to write, in a more compact form, the joint conditional PDF $f_{\mathbf{IM}_{\mathrm{T}},\mathbf{IM}_{\mathrm{M}}|\boldsymbol{\Theta}_{\mathrm{F}}}\left(\mathbf{im}_{\mathrm{T}},\mathbf{im}_{\mathrm{M}}\middle|\boldsymbol{\theta}_{\mathrm{F}}\right)$ as $f_{\mathbf{IM}|\boldsymbol{\Theta}_{\mathrm{F}}}\left(\mathbf{im}\middle|\boldsymbol{\theta}_{\mathrm{F}}\right)$. The probabilistic load hazard analysis step described above provides the information on the aerodynamic loads necessary to stochastically compute the structural response of the UAV wing at a future time $t>t_p$. In the proposed methodology, this task is achieved in a discrete fashion by defining $\bar{q}$ equally spaced future times $\left\{t_p^q=t_p+q\Delta\tau,\ q=1,2,...,\bar{q}\right\}$, at which the response of the system (in terms of damage propagation results) is evaluated in probabilistic terms.

Within the time window (or *duty cycle*) $\left[t_p,t_p^{\bar{q}}\right]$, an unknown — a priori — number of flight segments (n_s), can occur and each of them is characterized herein by a unique altitude of flight. Therefore, the vector $\boldsymbol{\Theta}_{\mathrm{F}}$ collects the flight profile parameters for each of these n_s flight segments in $\left[t_p,t_p^{\bar{q}}\right]$ as $\boldsymbol{\Theta}_{\mathrm{F}}=\left\{\boldsymbol{\Theta}_{\mathrm{F}}^{(k)},\ k=1,...,n_s\right\}$. Similarly, it is possible to rewrite the turbulence and maneuver parameter vectors (introduced in the previous paragraph) as $\boldsymbol{\Theta}_{\mathrm{T}}=\left\{\boldsymbol{\Theta}_{\mathrm{T}}^{(k)},\ k=1,...,n_s\right\}$ and $\boldsymbol{\Theta}_{\mathrm{M}}=\left\{\boldsymbol{\Theta}_{\mathrm{M}}^{(k)},\ k=1,...,n_s\right\}$, respectively. Examples of parameters collected in $\boldsymbol{\Theta}_{\mathrm{F}}^{(k)}$ (Guo *et al.*, 2011) include the altitude of flight, $H^{(k)}$; the mean airstream velocity w.r.t. a reference system fixed to the aircraft, $\mathbf{V}^{(k)}$; and the time of flight during the k^{th} flight segment, $T^{(k)}$; all of them viewed as random quantities, with their own PDFs and potential statistical correlations. As a direct consequence of these considerations, the vector $\mathbf{IM}_{\mathrm{T}}$ must

define (probabilistically) the intensity of the turbulence velocity field for each flight segment in $\left[t_p, t_p^{\bar{q}}\right]$ as $\mathbf{IM}_{\mathrm{T}} = \left\{\mathbf{IM}_{\mathrm{T}}^{(k)},\, k = 1, ..., n_{\mathrm{s}}\right\}$, where the sub-vectors $\mathbf{IM}_{\mathrm{T}}^{(k)}$ are assumed to be mutually s.i. and independent of $\boldsymbol{\Theta}_{\mathrm{M}}$; however, each of them depends on $\boldsymbol{\Theta}_{\mathrm{T}}^{(k)}$ as well as on $\boldsymbol{\Theta}_{\mathrm{F}}^{(k)}$ through the altitude $H^{(k)}$ only, as clarified later in Chapter 4. The two random components of $\mathbf{IM}_{\mathrm{T}}^{(k)}$ are chosen to be the root-mean-square (RMS) value ($\Sigma_{\mathrm{T}}^{(k)}$) of the atmospheric turbulence velocity field and the extent along the flight path of the turbulent patches ($\Delta S_{\mathrm{T}}^{(k)}$) during the k^{th} flight segment.

On the other hand, $\mathbf{IM}_{\mathrm{M}}$ provides the probabilistic characterization of the intensity and duration of the maneuver-induced loads (acting on the UAV wing) during the time window $\left[t_p, t_p^{\bar{q}}\right]$ — e.g., the increment (w.r.t. the straight-and-level unaccelerated flight conditions) of the aerodynamic lift generated by the aircraft wings during a steady-level banked turn. In this work, since the main focus is on the load-induced stresses at the wing-root and large angles of attack as well as rapid acrobatic maneuvers are not considered, the intensity of a maneuver-induced load is treated, as an increment (positive or negative) of the aerodynamic lift acting on the UAV wing during straight-and-level unaccelerated flight conditions, and it is quantified through a non-dimensional (multiplicative) maneuver-induced load factor, herein denoted as Z_{M}. It is worth noting that (i) the condition $Z_{\mathrm{M}} = 1$ corresponds to a straight-and-level unaccelerated flight and (ii) the load factor Z_{M} is also applied/multiplied to each mass particle of the wing; consequently, the intensity of the total maneuver-induced load is

the sum of the scaled aerodynamic lift and the scaled self-weight of the wing. Furthermore, the maneuver intensity Z_{M}, treated as a random quantity in the proposed framework, is assumed to be constant during the entire maneuver (i.e., micro-scale fluctuations of the maneuver-induced load within a certain maneuver are not considered herein) and its PDF is assumed to be statistically dependent on $\boldsymbol{\Theta}_{\mathrm{F}}$. Therefore, in the most general case, also $\mathbf{IM}_{\mathrm{M}}$ must be specified for each flight segment in $\left[t_p, t_p^{\bar{q}}\right]$ as $\mathbf{IM}_{\mathrm{M}} = \left\{\mathbf{IM}_{\mathrm{M}}^{(k)},\, k = 1, ..., n_s\right\}$ where the sub-vectors $\mathbf{IM}_{\mathrm{M}}^{(k)}$ are assumed to be mutually s.i. and independent of $\boldsymbol{\Theta}_{\mathrm{T}}$. The components of $\mathbf{IM}_{\mathrm{M}}^{(k)}$ completely characterize the intensity and duration of maneuvers during the k^{th} flight segment and are: the maneuver-induced load factor ($Z_{\mathrm{M}}^{(k)}$) and the maneuver duration ($\Delta T_{\mathrm{M}}^{(k)}$). In general, $\mathbf{IM}_{\mathrm{M}}$ is strongly dependent on the type of aircraft, and its probabilistic characterization should thus be based on flight test data (Rustenburg *et al.*, 1998, 1999, 2008) from similar aircrafts during similar mission profiles. Furthermore, especially for fighter aircrafts and UAVs, the characteristics of a maneuver can be reasonably considered independent of the atmospheric turbulence level (i.e., $\mathbf{IM}_{\mathrm{T}}$ and $\mathbf{IM}_{\mathrm{M}}$ are s.i.) and therefore the joint conditional PDF $f_{\mathbf{IM}_{\mathrm{T}},\mathbf{IM}_{\mathrm{M}}|\boldsymbol{\Theta}_{\mathrm{F}}}\left(\mathbf{im}_{\mathrm{T}}, \mathbf{im}_{\mathrm{M}} \middle| \boldsymbol{\theta}_{\mathrm{F}}\right)$ can be written as the product of the two s.i. terms $f_{\mathbf{IM}_{\mathrm{T}}|\boldsymbol{\Theta}_{\mathrm{F}}}\left(\mathbf{im}_{\mathrm{T}} \middle| \boldsymbol{\theta}_{\mathrm{F}}\right)$ and $f_{\mathbf{IM}_{\mathrm{M}}|\boldsymbol{\Theta}_{\mathrm{F}}}\left(\mathbf{im}_{\mathrm{M}} \middle| \boldsymbol{\theta}_{\mathrm{F}}\right)$. These two intensity measures, combined together, are then used as driving sources of uncertainty for the stochastic realization of the aerodynamic load input as discussed in Chapter 4.

2.4. Probabilistic structural response analysis

In the third step of the proposed methodology, namely *probabilistic structural response analysis*, the joint conditional PDF of the structural response of the system — expressed in terms of the predicted (from time t_p) damage size vector ($\mathbf{A}_{\mathrm{a}}^{[p,q]}$) at the generic future time $t_p^q = t_p + q\Delta\tau$ with $q \in \{1, 2, ..., \bar{q}\}$ — is computed through extensive Monte Carlo (MC) simulations or more advanced semi-analytical methods using either the detailed FE model of the structure or a computationally more efficient surrogate model (e.g., metamodel or response surface model; Myers and Montgomery, 1995; McFarland, 2008) derived from the FE model. This joint PDF, conditional on $\boldsymbol{\Theta}_{\mathrm{mat}}$, $\boldsymbol{\Theta}_{\mathrm{dam}}$, and all the previous NDE outcomes $\mathbf{a}_{\mathrm{m}}^{[0,p]}$ (not explicitly included in the notation), is denoted $f_{\mathbf{A}_{\mathrm{a}}^{[p,q]}|\boldsymbol{\Theta}_{\mathrm{mat}},\boldsymbol{\Theta}_{\mathrm{dam}}}\left(\mathbf{a}_{\mathrm{a}}^{[p,q]}\middle|\boldsymbol{\theta}_{\mathrm{mat}},\boldsymbol{\theta}_{\mathrm{dam}}\right)$ and is computed by unconditioning the joint conditional PDF $f_{\mathbf{A}_{\mathrm{a}}^{[p,q]}|\boldsymbol{\Theta}_{\mathrm{mat}},\boldsymbol{\Theta}_{\mathrm{dam}},\mathbf{A}_{\mathrm{a}}^{p},\mathbf{IM},\boldsymbol{\Theta}_{\mathrm{F}}}\left(\mathbf{a}_{\mathrm{a}}^{[p,q]}\middle|\boldsymbol{\theta}_{\mathrm{mat}},\boldsymbol{\theta}_{\mathrm{dam}},\mathbf{a}_{\mathrm{a}}^{p},\mathbf{im},\boldsymbol{\theta}_{\mathrm{F}}\right)$ w.r.t. $\mathbf{A}_{\mathrm{a}}^{p}$, $\mathbf{IM}$, and $\boldsymbol{\Theta}_{\mathrm{F}}$. It is worth noting that the conditional joint PDF $f_{\mathbf{A}_{\mathrm{a}}^{[p,q]}|\boldsymbol{\Theta}_{\mathrm{mat}},\boldsymbol{\Theta}_{\mathrm{dam}}}\left(\mathbf{a}_{\mathrm{a}}^{[p,q]}\middle|\boldsymbol{\theta}_{\mathrm{mat}},\boldsymbol{\theta}_{\mathrm{dam}}\right)$ is not unconditioned w.r.t. $\boldsymbol{\Theta}_{\mathrm{mat}}$ and $\boldsymbol{\Theta}_{\mathrm{dam}}$, at this stage of the uncertainty propagation process, since these conditioning variables are used explicitly in the next analytical step of the methodology as outlined in the next section. Furthermore, the interpolated (or extrapolated) joint conditional PDF of the system response at time t_{p+1}, $f_{\mathbf{A}_{\mathrm{a}}^{[p,p+1]}|\boldsymbol{\Theta}_{\mathrm{mat}},\boldsymbol{\Theta}_{\mathrm{dam}}}\left(\mathbf{a}_{\mathrm{a}}^{[p,p+1]}\middle|\boldsymbol{\theta}_{\mathrm{mat}},\boldsymbol{\theta}_{\mathrm{dam}}\right)$, is also used as prior information for the next Bayesian updating aimed at computing the posterior joint conditional PDF

$f''_{\mathbf{A}_{\mathrm{a}}^{p+1}|\boldsymbol{\Theta}_{\mathrm{mat}},\boldsymbol{\Theta}_{\mathrm{dam}}}\left(\mathbf{a}_{\mathrm{a}}^{p+1}\middle|\boldsymbol{\theta}_{\mathrm{mat}},\boldsymbol{\theta}_{\mathrm{dam}}\right)$ as the next NDE inspection outcome ($\mathbf{a}_{\mathrm{m}}^{p+1}$), at time t_{p+1}, becomes available.

2.5. Probabilistic flutter and limit cycle oscillation (LCO) analyses

The fourth step, namely *probabilistic flutter and limit cycle oscillation (LCO) analyses*, estimates the joint PDF of the predicted damage size vector $\mathbf{A}_{\mathrm{a}}^{[p,q]}$, flutter velocity $V_{\mathrm{F}}^{[p,q]}$, and the (n_{LCO}-dimensional) vector of LCO velocities ($\mathbf{V}_{\mathrm{LCO}}^{[p,q]}$) at the generic future time $t_p^q = t_p + q\Delta\tau$ — i.e., the joint PDF $f_{\mathbf{A}_{\mathrm{a}}^{[p,q]},V_{\mathrm{F}}^{[p,q]},\mathbf{V}_{\mathrm{LCO}}^{[p,q]}}\left(\mathbf{a}_{\mathrm{a}}^{[p,q]},v_{\mathrm{F}}^{[p,q]},\mathbf{v}_{\mathrm{LCO}}^{[p,q]}\right)$, or $f_{\mathbf{A}_{\mathrm{a}}^{[p,q]},\mathbf{V}_{\mathrm{F,LCO}}^{[p,q]}}\left(\mathbf{a}_{\mathrm{a}}^{[p,q]},\mathbf{v}_{\mathrm{F,LCO}}^{[p,q]}\right)$ in a more condensed notation, where the n_{G}-dimensional (with $n_{\mathrm{G}} = 1 + n_{\mathrm{LCO}}$) vector $\mathbf{V}_{\mathrm{F,LCO}}^{[p,q]}$ is defined as $\mathbf{V}_{\mathrm{F,LCO}}^{[p,q]} = \left\{V_{\mathrm{F}}^{[p,q]},\mathbf{V}_{\mathrm{LCO}}^{[p,q]}\right\}$. The flutter velocity (altitude-dependent in the most general case) represents the lowest velocity at which flutter occurs whereas each of the n_{LCO} LCO velocities, collected in the random vector $\mathbf{V}_{\mathrm{LCO}}^{[p,q]}$, indicates the velocity at which the corresponding LCO amplitude (e.g., maximum wing tip displacement or twist amplitude) reaches a predefined limit threshold. The joint PDF $f_{\mathbf{A}_{\mathrm{a}}^{[p,q]},\mathbf{V}_{\mathrm{F,LCO}}^{[p,q]}}\left(\mathbf{a}_{\mathrm{a}}^{[p,q]},\mathbf{v}_{\mathrm{F,LCO}}^{[p,q]}\right)$ is based on the posterior information on the level of damage at time t_p and the damage propagation results from time t_p to t_p^q; both contributions are combined into the joint conditional PDF $f_{\mathbf{A}_{\mathrm{a}}^{[p,q]}|\boldsymbol{\Theta}_{\mathrm{mat}},\boldsymbol{\Theta}_{\mathrm{dam}}}\left(\mathbf{a}_{\mathrm{a}}^{[p,q]}\middle|\boldsymbol{\theta}_{\mathrm{mat}},\boldsymbol{\theta}_{\mathrm{dam}}\right)$ computed in the third step of the methodology. Additionally, it contains both local (through $\mathbf{A}_{\mathrm{a}}^{[p,q]}$) and global (through

$\mathbf{V}_{\mathrm{F,LCO}}^{[p,q]}$) damage-related information and can be theoretically derived by using the definition of conditional probability as

$$f_{\mathbf{A}_{\mathrm{a}}^{[p,q]},\mathbf{V}_{\mathrm{F,LCO}}^{[p,q]}}\left(\mathbf{a}_{\mathrm{a}}^{[p,q]},\mathbf{v}_{\mathrm{F,LCO}}^{[p,q]}\right)=f_{\mathbf{V}_{\mathrm{F,LCO}}^{[p,q]}\left|\mathbf{A}_{\mathrm{a}}^{[p,q]}\right.}\left(\mathbf{v}_{\mathrm{F,LCO}}^{[p,q]}\left|\mathbf{a}_{\mathrm{a}}^{[p,q]}\right.\right)\cdot f_{\mathbf{A}_{\mathrm{a}}^{[p,q]}}\left(\mathbf{a}_{\mathrm{a}}^{[p,q]}\right) \tag{2.1}$$

where both PDFs, $f_{\mathbf{V}_{\mathrm{F,LCO}}^{[p,q]}\left|\mathbf{A}_{\mathrm{a}}^{[p,q]}\right.}\left(\mathbf{v}_{\mathrm{F,LCO}}^{[p,q]}\left|\mathbf{a}_{\mathrm{a}}^{[p,q]}\right.\right)$ and $f_{\mathbf{A}_{\mathrm{a}}^{[p,q]}}\left(\mathbf{a}_{\mathrm{a}}^{[p,q]}\right)$, are determined by unconditioning the joint conditional PDFs $f_{\mathbf{V}_{\mathrm{F,LCO}}^{[p,q]}\left|\mathbf{A}_{\mathrm{a}}^{[p,q]},\boldsymbol{\Theta}_{\mathrm{mat}},\boldsymbol{\Theta}_{\mathrm{dam}}\right.}\left(\mathbf{v}_{\mathrm{F,LCO}}^{[p,q]}\left|\mathbf{a}_{\mathrm{a}}^{[p,q]},\boldsymbol{\theta}_{\mathrm{mat}},\boldsymbol{\theta}_{\mathrm{dam}}\right.\right)$ and $f_{\mathbf{A}_{\mathrm{a}}^{[p,q]}\left|\boldsymbol{\Theta}_{\mathrm{mat}},\boldsymbol{\Theta}_{\mathrm{dam}}\right.}\left(\mathbf{a}_{\mathrm{a}}^{[p,q]}\left|\boldsymbol{\theta}_{\mathrm{mat}},\boldsymbol{\theta}_{\mathrm{dam}}\right.\right)$ w.r.t. $\boldsymbol{\Theta}_{\mathrm{mat}}$ and $\boldsymbol{\Theta}_{\mathrm{dam}}$. Since the vector $\left\{\mathbf{A}_{\mathrm{a}}^{[p,q]},\mathbf{V}_{\mathrm{F,LCO}}^{[p,q]}\right\}$ provides information on the overall (i.e., local and global) state of damage of the system at time t_p^q, it is denoted $\mathbf{D}_{\mathrm{L,G}}^{[p,q]}$ hereafter, i.e., $\mathbf{D}_{\mathrm{L,G}}^{[p,q]}=\left\{\mathbf{A}_{\mathrm{a}}^{[p,q]},\mathbf{V}_{\mathrm{F,LCO}}^{[p,q]}\right\}$, and all its components are clearly mutually statistically correlated.

2.6. Damage prognosis analysis

Once the joint PDF $f_{\mathbf{D}_{\mathrm{L,G}}^{[p,q]}}\left(\mathbf{d}_{\mathrm{L,G}}^{[p,q]}\right)=f_{\mathbf{A}_{\mathrm{a}}^{[p,q]},\mathbf{V}_{\mathrm{F,LCO}}^{[p,q]}}\left(\mathbf{a}_{\mathrm{a}}^{[p,q]},\mathbf{v}_{\mathrm{F,LCO}}^{[p,q]}\right)$ is determined, the probability of *system failure* at time t_p^q, $P\left[\mathrm{F}_{\mathrm{sys}}^{[p,q]}\right]$, can be estimated by performing component and system reliability analyses using well established methods (Ditlevsen and Madsen, 1996). As detailed in Chapter 7, these analyses are part of the fifth and final analytical step of the proposed framework, namely *damage prognosis analysis*, through three sub-steps: (i) computation of the component (or modal) conditional failure probabilities, $P\left[\mathrm{F}_{\mathrm{L},ij}^{[p,q]}\left|\mathbf{a}_{\mathrm{a}}^{[p,q]}\right.\right]$ and $P\left[\mathrm{F}_{\mathrm{G},r}^{[p,q]}\left|\mathbf{v}_{\mathrm{F,LCO}}^{[p,q]}\right.\right]$, associated with each of the n_{A}^p Local

and n_{G} Global (aeroelastic) failure modes, respectively; (ii) computation of the unconditional modal failure probabilities, $P\left[\mathrm{F}_{\mathrm{L},ij}^{[p,q]}\right]$ and $P\left[\mathrm{F}_{\mathrm{G},r}^{[p,q]}\right]$ by unconditioning the terms $P\left[\mathrm{F}_{\mathrm{L},ij}^{[p,q]}\middle|\mathbf{a}_{\mathrm{a}}^{[p,q]}\right]$ and $P\left[\mathrm{F}_{\mathrm{G},r}^{[p,q]}\middle|\mathbf{v}_{\mathrm{F,LCO}}^{[p,q]}\right]$ w.r.t. $\mathbf{A}_{\mathrm{a}}^{[p,q]}$ and $\mathbf{V}_{\mathrm{F,LCO}}^{[p,q]}$, respectively; and (iii) computation of lower and upper bounds for $P\left[\mathrm{F}_{\mathrm{sys}}^{[p,q]}\right]$ by abstracting the UAV wing as a series system (i.e., a system that fails if any of its reliability components fails) or a combination of series and parallel systems. It is worth noting that the failure event $\mathrm{F}_{\mathrm{sys}}^{[p,q]}$ does not necessarily reflect a physical failure of the UAV wing at time t_p^q. Finally, as a further remark, by considering different values of q, it is possible to predict the evolution in time of the reliability of the system. This step of the proposed methodology is described in more detail in Chapter 7.

2.7. Decision making

The final and most important outcome of the proposed methodology consists of the *decision making* process. It essentially uses the damage prognosis results obtained in the previous step — i.e., the predicted evolution in time of $P\left[\mathrm{F}_{\mathrm{sys}}^{[p,q]}\right]$ — to optimize maintenance, ground inspection and repair programs, and consequently reduce their cost over the service life of the structure. The decisions made at current time t_p can be revised later (at times t_{p+1}, t_{p+2}, etc.) as new NDE data (from both on-ground and in-flight monitoring) are collected; a concept illustrated in Figure 2.3. Scheduling of the next on-ground inspection, maintenance or repair is obtained by

interpolating (or possibly extrapolating) the predictions for $P\left[\mathrm{F}_{\mathrm{sys}}^{[p,q]}\right]$ (with $q=1,2,...,\bar{q}$) in order to estimate the time at which this probability will exceed a specified safety threshold (or decision value) $\bar{p}_{\mathrm{F}}$. The accepted range for $\bar{p}_{\mathrm{F}}$ strongly depends on the modal failure criteria adopted in the component reliability analyses (discussed in Chapter 7) and on the type of aircraft being monitored. Larger values of $\bar{p}_{\mathrm{F}}$ are generally tolerated for fighter aircrafts and UAVs, which normally operate over military zones, whereas a more strict threshold is assigned to commercial carriers.

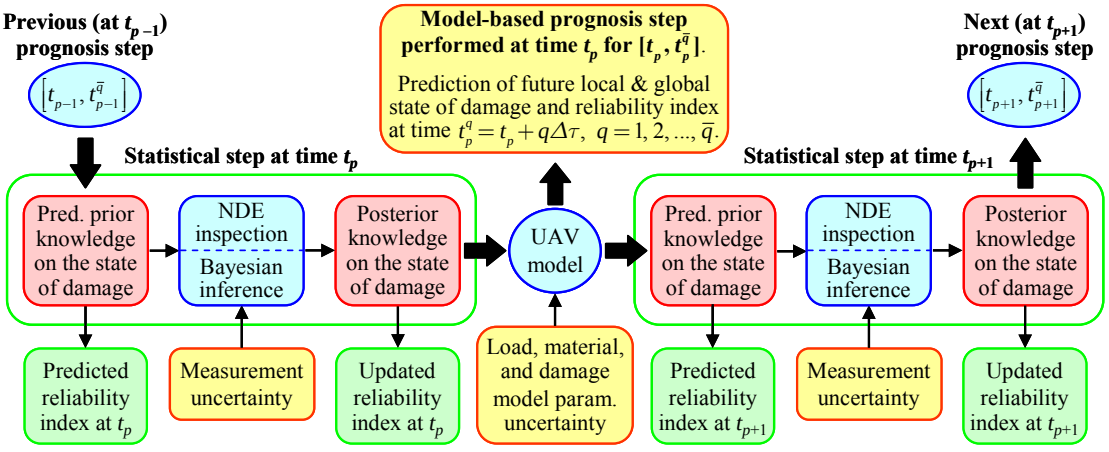

Figure 2.3: Conceptual representation of proposed damage prognosis algorithm for two successive NDE inspections (at time t_p and t_{p+1}) emphasizing the alternative and recursive use of statistical (i.e., data driven) and predictive modeling/analysis steps.

2.8. Proposed damage prognosis framework viewed as an application of the total probability theorem

The proposed reliability-based damage prognosis framework overviewed in this chapter can be interpreted (especially under the uncertainty propagation

perspective) as a conceptual application of the total probability theorem (TPT). Using the assumptions stated thus far in the current chapter together with the notation

$$dP\left[X\right]=P\left[x<X\le x+dx\right]=f_X\left(x\right)dx \tag{2.2}$$

$$dP\left[X,Y\right]=P\left[x<X\le x+dx\cap y<Y\le y+dy\right]=f_{X,Y}\left(x,y\right)dx\,dy \tag{2.3}$$

$$dP\left[X\left|z\right.\right]=dP\left[X\left|Z=z\right.\right]=P\left[x<X\le x+dx\middle|Z=z\right]=f_{X|Z}\left(x\middle|z\right)dx \tag{2.4}$$

the probability of *system failure* at time t_p^q can be obtained by using the TPT multiple times in a nested fashion as

$$\begin{aligned}P\left[\mathrm{F}_{\mathrm{sys}}^{[p,q]}\right]&=\int_{\mathbf{D}_{\mathrm{L,G}}^{[p,q]}}P\left[\mathrm{F}_{\mathrm{sys}}^{[p,q]}\middle|\mathbf{D}_{\mathrm{L,G}}^{[p,q]}\right]dP\left[\mathbf{D}_{\mathrm{L,G}}^{[p,q]}\right]\\&=\int_{\mathbf{A}_{\mathrm{a}}^{[p,q]}}\int_{\mathbf{V}_{\mathrm{F,LCO}}^{[p,q]}}P\left[\mathrm{F}_{\mathrm{sys}}^{[p,q]}\middle|\mathbf{A}_{\mathrm{a}}^{[p,q]},\mathbf{V}_{\mathrm{F,LCO}}^{[p,q]}\right]dP\left[\mathbf{A}_{\mathrm{a}}^{[p,q]},\mathbf{V}_{\mathrm{F,LCO}}^{[p,q]}\right]\end{aligned} \tag{2.5}$$

where the term $dP\left[\mathbf{D}_{\mathrm{L,G}}^{[p,q]}\right]=dP\left[\mathbf{A}_{\mathrm{a}}^{[p,q]},\mathbf{V}_{\mathrm{F,LCO}}^{[p,q]}\right]$ can be expressed as

$$\begin{aligned}&dP\left[\mathbf{A}_{\mathrm{a}}^{[p,q]},\mathbf{V}_{\mathrm{F,LCO}}^{[p,q]}\right]=\\&\int_{\boldsymbol{\Theta}_{\mathrm{mat}}}\int_{\boldsymbol{\Theta}_{\mathrm{dam}}}dP\left[\mathbf{V}_{\mathrm{F,LCO}}^{[p,q]}\middle|\mathbf{A}_{\mathrm{a}}^{[p,q]},\boldsymbol{\Theta}_{\mathrm{mat}},\boldsymbol{\Theta}_{\mathrm{dam}}\right]dP\left[\mathbf{A}_{\mathrm{a}}^{[p,q]}\middle|\boldsymbol{\Theta}_{\mathrm{mat}},\boldsymbol{\Theta}_{\mathrm{dam}}\right]dP\left[\boldsymbol{\Theta}_{\mathrm{mat}}\right]dP\left[\boldsymbol{\Theta}_{\mathrm{dam}}\right]\end{aligned} \tag{2.6}$$

and the quantity $dP\left[\mathbf{A}_{\mathrm{a}}^{[p,q]}\middle|\boldsymbol{\Theta}_{\mathrm{mat}},\boldsymbol{\Theta}_{\mathrm{dam}}\right]$ can be obtained by unconditioning the conditional joint probability $dP\left[\mathbf{A}_{\mathrm{a}}^{[p,q]}\middle|\boldsymbol{\Theta}_{\mathrm{mat}},\boldsymbol{\Theta}_{\mathrm{dam}},\mathbf{A}_{\mathrm{a}}^{p},\mathbf{IM},\boldsymbol{\Theta}_{\mathrm{F}}\right]$ w.r.t. $\mathbf{A}_{\mathrm{a}}^{p},\mathbf{IM},\boldsymbol{\Theta}_{\mathrm{F}}$, and accounting for the fact that $\mathbf{A}_{\mathrm{a}}^{p}$ is s.i. of both $\mathbf{IM}$ and $\boldsymbol{\Theta}_{\mathrm{F}}$ (between time t_p and $t_p^{\bar{q}}=t_p+\bar{q}\Delta\tau$), as

$$dP\left[\mathbf{A}_{\mathrm{a}}^{[p,q]}\middle|\boldsymbol{\Theta}_{\mathrm{mat}},\boldsymbol{\Theta}_{\mathrm{dam}}\right]=\int_{\mathbf{A}_{\mathrm{a}}^{p}}\int_{\mathbf{IM}}\int_{\boldsymbol{\Theta}_{\mathrm{F}}} dP\left[\mathbf{A}_{\mathrm{a}}^{[p,q]}\middle|\boldsymbol{\Theta}_{\mathrm{mat}},\boldsymbol{\Theta}_{\mathrm{dam}},\mathbf{A}_{\mathrm{a}}^{p},\mathbf{IM},\boldsymbol{\Theta}_{\mathrm{F}}\right] \cdot dP''\left[\mathbf{A}_{\mathrm{a}}^{p}\middle|\boldsymbol{\Theta}_{\mathrm{mat}},\boldsymbol{\Theta}_{\mathrm{dam}}\right]\cdot dP\left[\mathbf{IM}\middle|\boldsymbol{\Theta}_{\mathrm{F}}\right]\cdot dP\left[\boldsymbol{\Theta}_{\mathrm{F}}\right] \tag{2.7}$$

where $dP''\left[\mathbf{A}_{\mathrm{a}}^{p}\middle|\boldsymbol{\Theta}_{\mathrm{mat}},\boldsymbol{\Theta}_{\mathrm{dam}}\right]$ denotes the posterior conditional knowledge of $\mathbf{A}_{\mathrm{a}}^{p}$. Finally, the term $dP\left[\mathbf{IM}\middle|\boldsymbol{\Theta}_{\mathrm{F}}\right]$, which characterizes — in probabilistic terms — the turbulence- and maneuver-induced aerodynamic loads within the time window $\left[t_p, t_p^{\bar{q}}\right]$, can conceptually be written as the product of two s.i. sub-terms as

$$dP\left[\mathbf{IM}\middle|\boldsymbol{\Theta}_{\mathrm{F}}\right]=dP\left[\mathbf{IM}_{\mathrm{T}},\mathbf{IM}_{\mathrm{M}}\middle|\boldsymbol{\Theta}_{\mathrm{F}}\right]=\int_{\boldsymbol{\Theta}_{\mathrm{T}}} dP\left[\mathbf{IM}_{\mathrm{T}}\middle|\boldsymbol{\Theta}_{\mathrm{T}},\boldsymbol{\Theta}_{\mathrm{F}}\right]\cdot dP\left[\boldsymbol{\Theta}_{\mathrm{T}}\middle|\boldsymbol{\Theta}_{\mathrm{F}}\right] \cdot\int_{\boldsymbol{\Theta}_{\mathrm{M}}} dP\left[\mathbf{IM}_{\mathrm{M}}\middle|\boldsymbol{\Theta}_{\mathrm{M}},\boldsymbol{\Theta}_{\mathrm{F}}\right]\cdot dP\left[\boldsymbol{\Theta}_{\mathrm{M}}\middle|\boldsymbol{\Theta}_{\mathrm{F}}\right] \tag{2.8}$$

If the joint PDF of $\boldsymbol{\Theta}_{\mathrm{dam}}$ is also recursively updated after each NDE inspection (i.e., at time t_p, t_{p+1}, t_{p+2}, etc.) then the damage parameter vector is denoted as $\boldsymbol{\Theta}_{\mathrm{dam}}^{p}$ and Equations (2.6) and (2.7) must be rewritten as

$$dP\left[\mathbf{A}_{\mathrm{a}}^{[p,q]},\mathbf{V}_{\mathrm{F,LCO}}^{[p,q]}\right]= \int_{\boldsymbol{\Theta}_{\mathrm{mat}}}\int_{\boldsymbol{\Theta}_{\mathrm{dam}}^{p}} dP\left[\mathbf{V}_{\mathrm{F,LCO}}^{[p,q]}\middle|\mathbf{A}_{\mathrm{a}}^{[p,q]},\boldsymbol{\Theta}_{\mathrm{mat}},\boldsymbol{\Theta}_{\mathrm{dam}}^{p}\right]dP\left[\mathbf{A}_{\mathrm{a}}^{[p,q]}\middle|\boldsymbol{\Theta}_{\mathrm{mat}},\boldsymbol{\Theta}_{\mathrm{dam}}^{p}\right]dP\left[\boldsymbol{\Theta}_{\mathrm{mat}}\right]dP''\left[\boldsymbol{\Theta}_{\mathrm{dam}}^{p}\right] \tag{2.9}$$

$$dP\left[\mathbf{A}_{\mathrm{a}}^{[p,q]}\middle|\boldsymbol{\Theta}_{\mathrm{mat}},\boldsymbol{\Theta}_{\mathrm{dam}}^{p}\right]=\int_{\mathbf{A}_{\mathrm{a}}^{p}}\int_{\mathbf{IM}}\int_{\boldsymbol{\Theta}_{\mathrm{F}}} dP\left[\mathbf{A}_{\mathrm{a}}^{[p,q]}\middle|\boldsymbol{\Theta}_{\mathrm{mat}},\boldsymbol{\Theta}_{\mathrm{dam}}^{p},\mathbf{A}_{\mathrm{a}}^{p},\mathbf{IM},\boldsymbol{\Theta}_{\mathrm{F}}\right] \cdot dP''\left[\mathbf{A}_{\mathrm{a}}^{p}\middle|\boldsymbol{\Theta}_{\mathrm{mat}},\boldsymbol{\Theta}_{\mathrm{dam}}^{p}\right]\cdot dP\left[\mathbf{IM}\middle|\boldsymbol{\Theta}_{\mathrm{F}}\right]\cdot dP\left[\boldsymbol{\Theta}_{\mathrm{F}}\right] \tag{2.10}$$

where $dP''\left[\boldsymbol{\Theta}_{\mathrm{dam}}^{p}\right]= f''_{\boldsymbol{\Theta}_{\mathrm{dam}}^{p}}\left(\boldsymbol{\theta}_{\mathrm{dam}}^{p}\right)d\boldsymbol{\theta}_{\mathrm{dam}}^{p}$ and $f''_{\boldsymbol{\Theta}_{\mathrm{dam}}^{p}}\left(\boldsymbol{\theta}_{\mathrm{dam}}^{p}\right)$ represents the posterior joint PDF of $\boldsymbol{\Theta}_{\mathrm{dam}}^{p}$ (at time t_p).

2.9. Rapid assessment of the UAV wing reliability after each NDE inspection

In the formulation presented above, the damage prognosis analysis step consists of component and system reliability analyses performed at current time t_p and based on the joint probabilistic characterization of the local and global states of damage at time t_p^q. These states of damage, at future time t_p^q, are predicted during the probabilistic damage evolution step, from time t_p to time t_p^q, and the probabilistic flutter and LCO analyses step. The joint probabilistic characterization of local and global states of damage is provided by the joint PDF $f_{\mathbf{D}_{\mathrm{L,G}}^{[p,q]}}\left(\mathbf{d}_{\mathrm{L,G}}^{[p,q]}\right)$, computed through Equation (2.6) and used to then provide an estimate for $P\left[\mathrm{F}_{\mathrm{sys}}^{[p,q]}\right]$ at time t_p^q, $q=1,2,...,\overline{q}$. Additionally, as illustrated in Figure 2.4, the proposed prognosis framework can provide lower and upper bounds for the probability of *system failure* not only at an arbitrary time t_p^q in the future but also (in nearly real time) at the time just after the last NDE inspection (performed at t_p). This goal is achieved by (i) using the posterior joint conditional PDF, $f''_{\mathbf{A}_{\mathrm{a}}^p\left|\boldsymbol{\Theta}_{\mathrm{mat}},\boldsymbol{\Theta}_{\mathrm{dam}}\right.}\left(\mathbf{a}_{\mathrm{a}}^p\left|\boldsymbol{\theta}_{\mathrm{mat}},\boldsymbol{\theta}_{\mathrm{dam}}\right.\right)$ — which characterizes the local state of damage just after the last NDE inspection at time t_p — in the flutter & LCO analyses step (i.e., without carrying out the probabilistic load hazard analysis and damage evolution steps), (ii) computing the joint PDF $f_{\mathbf{D}_{\mathrm{L,G}}^p}\left(\mathbf{d}_{\mathrm{L,G}}^p\right)$ at time t_p, and (iii) performing, with this piece of information, the component and system reliability analyses necessary to estimate the probability $P\left[\mathrm{F}_{\mathrm{sys}}^p\right]$.

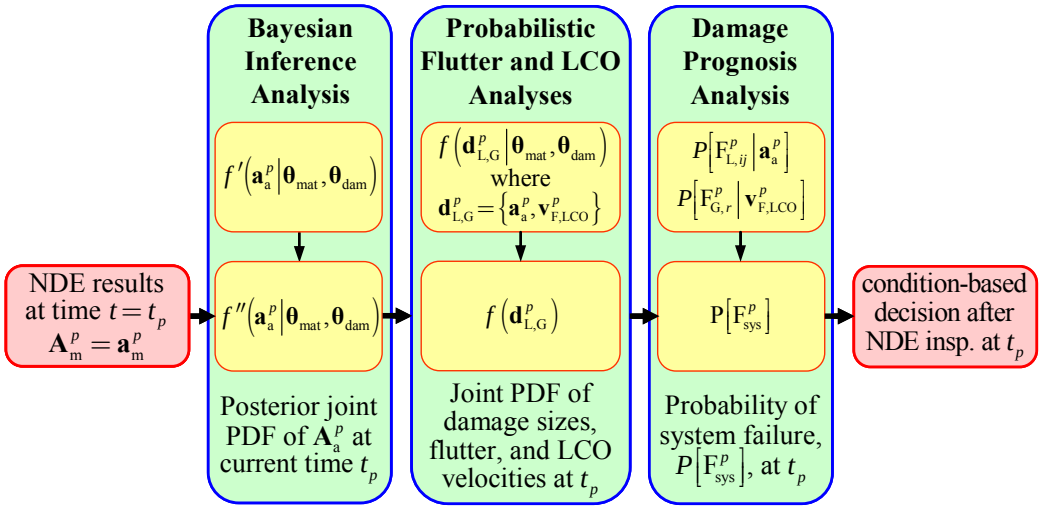

Figure 2.4: Adaptation of proposed damage prognosis methodology for the reliability assessment just after the last NDE inspection at current time t_p.

2.10. Summary of novel contributions provided by the proposed methodology

In summary, the proposed methodology represents an advanced tool integrating NDE inspection results, Bayesian updating, mechanics-based damage prediction, uncertainty quantification & propagation, and decision making related to the damage prognosis of a UAV wing. However, this methodology could be extended to the entire UAV structure (airframe), as well as to other mechanical and structural systems, such as wind turbines, critical components in offshore structures, etc. These extensions were already briefly discussed in Chapter 1 and will be further analyzed later on, with specific application examples, in Chapters 8 and 9. This methodology alternates between mechanics-based damage evolution prediction and Bayesian statistical inference to march forward in time — through successive duty cycles — and provide an estimate for the trend of the residual useful life of the structure (damage

prognosis). The proposed framework uses the new NDE inspection outcome at time t_p to update the joint PDF of the damage size vector ($\mathbf{A}_{\mathrm{a}}^{p}$) — numerically predicted from time $t_{p\text{-}1}$ — through Bayesian updating. Simultaneously, using the same NDE outcome, the proposed Bayesian inference scheme can also provide an update for the joint PDF of the damage evolution parameter vector $\boldsymbol{\Theta}_{\mathrm{dam}}$. Notice that the prior information (i.e., the prior joint PDF) on the state of damage at time t_p is based on all the available NDE inspection data up to time $t_{p\text{-}1}$ and the numerical prediction from time $t_{p\text{-}1}$ to time t_p. It is therefore based on a combination of mechanics-based prediction — inherently affected by the modeling assumptions behind the mathematical idealization of the real world structural system — and statistical inference from NDE results accounting for the uncertainty characterizing the latter. This uncertainty stems from the facts that the NDE technique itself is not fully reliable and the sensor data used in NDE may be contaminated by systematic errors and measurement noise (see Chapter 3). Once the Bayesian updating step (at t_p) is completed, the trend in time — in $\left[t_p, t_p^{\bar{q}}\right]$ — of the system reliability is predicted and the state of damage at the time of the next NDE inspection (at t_{p+1}) can be estimated by interpolating or extrapolating the damage evolution prediction results obtained from the *probabilistic structural response analysis* step performed at time t_p. The overall damage prognosis procedure can then be applied again (i.e., recursively) over the next duty cycle (from time t_{p+1} to time t_{p+2}) in the same manner. All these concepts are also illustrated in Figure 2.3 (which was introduced earlier in this Chapter in Section 2.7).

2.11. Extension of the proposed damage prognosis framework to other structural and mechanical systems monitored through NDE inspections

The applicability of the proposed damage prognosis framework is definitely not limited to a composite UAV-wing or an entire UAV airframe. For instance, with minor changes, it can be used to estimate the remaining fatigue life of composite wind turbine blades (as briefly outlined in Chapter 1) periodically and/or continuously monitored through NDE inspections. Some changes to the probabilistic load hazard models (especially the turbulence model) must be considered and appropriately embedded in the framework but, on the other hand, the same local and global failure criteria, outlined previously in Section 2.5 (and discussed in depth later in Chapter 7) would still be utterly applicable.

The same general approach can also be extended to civil structures such as cable-stayed bridges, suspension bridges, and FRP-retrofitted concrete bridges, as well as to other monitored structural and mechanical components fabricated with advanced composite materials prone to experience fatigue-induced damage along their adhesive joints/interfaces such as the simple composite laminated beam shown in Figure 2.5.

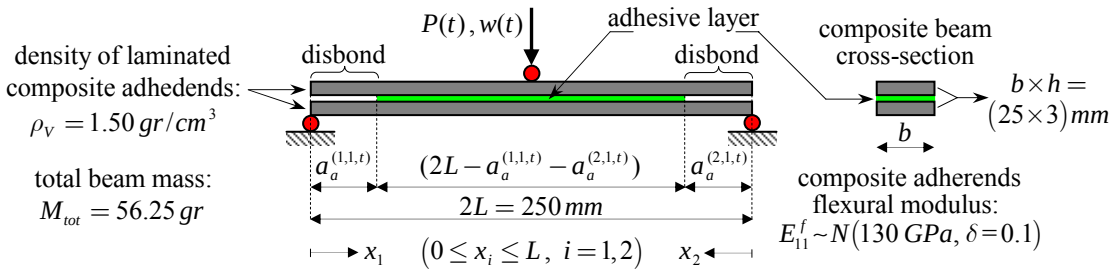

Figure 2.5: Simply-supported composite beam with two debonding fronts (evolving from the beam ends) subjected to a concentrated load, $P(t)$, applied at its midspan. A case study extensively analyzed and thoroughly discussed in Chapter 8.

Figure 2.6 shows an adaptation and generalization of the original flowchart presented earlier in Figure 2.2 that can be used for estimating the remaining fatigue life of mechanical and structural systems with multi-site fatigue-driven damage growth. First of all, conversely to what is shown in Figure 2.2, this new flowchart considers the case in which both posterior joint PDFs, $f''\left(\mathbf{a}_{\mathrm{a}}^{p}\middle|\boldsymbol{\theta}_{\mathrm{mat}},\boldsymbol{\theta}_{\mathrm{dam}}^{p}\right)$ and $f''_{\boldsymbol{\Theta}_{\mathrm{dam}}^{p}}\left(\boldsymbol{\theta}_{\mathrm{dam}}^{p}\right)$, are simultaneously computed after each NDE inspection outcome. This represents a more general scenario, within the proposed Bayesian inference step, which will be thoroughly discussed in Chapter 3 and successfully verified and validated through the two application examples presented in Chapter 8 and Chapter 9.

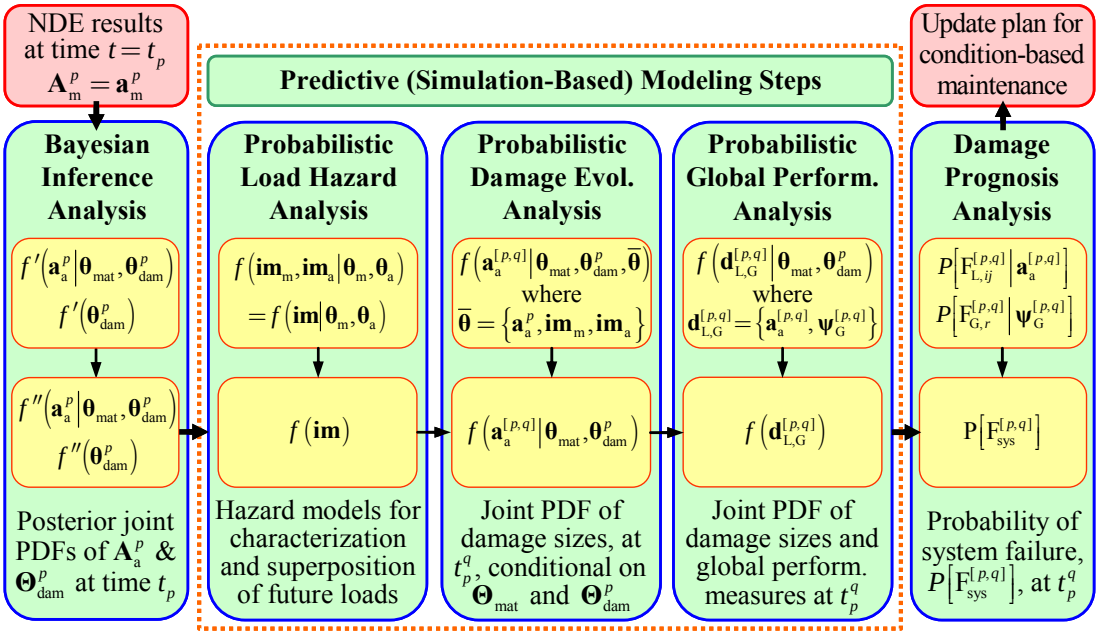

Figure 2.6: Extension of the proposed damage prognosis methodology to other monitored structural systems with multi-site fatigue-driven damage growth.

As a second change, within the probabilistic load hazard analysis step (i.e., the second analysis step of the proposed methodology), maneuver- and turbulence-induced loads

are now (respectively) substituted by (i) the mean/average intensity of the applied external load, probabilistically characterized by the intensity measure vector $\mathbf{IM}_{\mathrm{m}}$, and (ii) the superimposed random stochastic load (or load fluctuations) about the mean-load intensity, probabilistically described by the intensity measure vector $\mathbf{IM}_{\mathrm{a}}$. For instance, the random intensity measure vector $\mathbf{IM}_{\mathrm{m}}$ can characterize the intensity/magnitude and duration of the random mean-load, whereas $\mathbf{IM}_{\mathrm{a}}$ can collect all those random variables defining the power spectral density (PSD) function of the random load oscillations/fluctuations about the mean-load intensity. The joint PDF of $\mathbf{IM}_{\mathrm{m}}$ and $\mathbf{IM}_{\mathrm{a}}$ is herein denoted as $f_{\mathbf{IM}_{\mathrm{m}},\mathbf{IM}_{\mathrm{a}}}\left(\mathbf{im}_{\mathrm{m}},\mathbf{im}_{\mathrm{a}}\right)$ and is computed by unconditioning the conditional joint PDF $f_{\mathbf{IM}_{\mathrm{m}},\mathbf{IM}_{\mathrm{a}}|\boldsymbol{\Theta}_{\mathrm{m}},\boldsymbol{\Theta}_{\mathrm{a}}}\left(\mathbf{im}_{\mathrm{m}},\mathbf{im}_{\mathrm{a}}\left|\boldsymbol{\theta}_{\mathrm{m}},\boldsymbol{\theta}_{\mathrm{a}}\right.\right)$ w.r.t. $\boldsymbol{\Theta}_{\mathrm{m}}$ (i.e., the random parameter vector associated to the mean-load) and $\boldsymbol{\Theta}_{\mathrm{a}}$ (i.e., the random parameter vector associated with the stochastic load fluctuations about the mean-load intensity), respectively. Some Illustrations of this concept for load effects generation and superposition are provided in Figure 2.7, Figure 2.8, and Figure 2.9. More specifically, Figure 2.7 and Figure 2.8 consider the case in which the load fluctuations (red lines in the plots) about the mean-load intensity (dashed blue lines in the plots) are assumed to be a stochastic process. Additionally, in Figure 2.7 the root mean square (RMS) value of the load fluctuations is considered to be statistically independent of the mean-load intensity. On the other hand, in Figure 2.8, these two quantities are instead considered to be statistically dependent (i.e., the two intensity measure vectors $\mathbf{IM}_{\mathrm{m}}$ and $\mathbf{IM}_{\mathrm{a}}$ are statistically dependent).

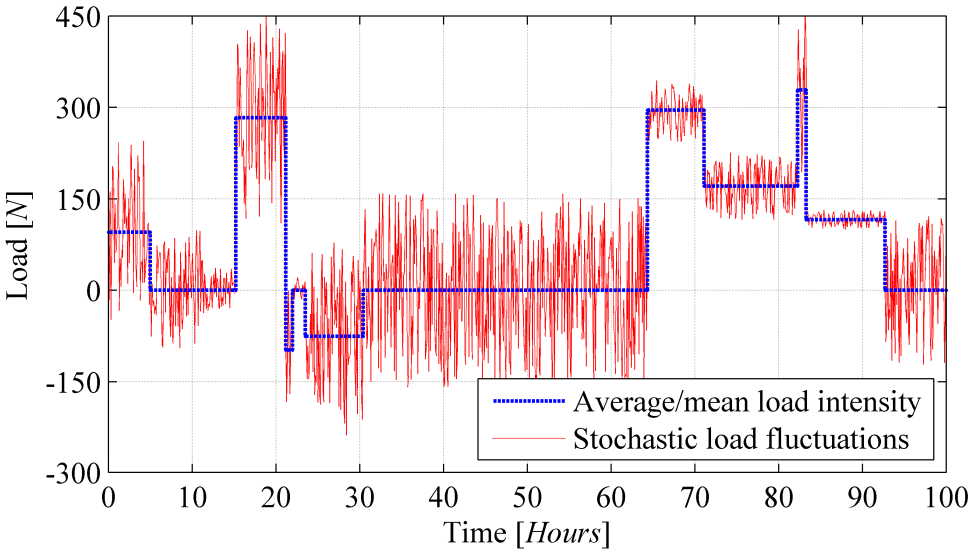

Figure 2.7: Illustrative example of load superposition for the case in which mean-load intensity and RMS value of the load fluctuations are considered to be statistically independent. The RMS value of the load fluctuations is renewed at each mean-load pulse occurrence and remains constant for the entire duration of each mean-load pulse.

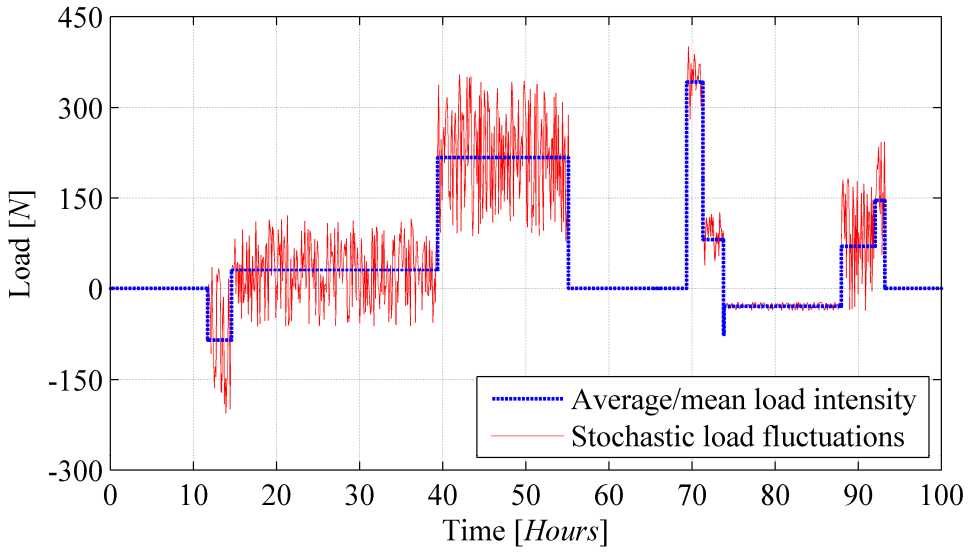

Figure 2.8: Illustrative example of load superposition for the case in which mean-load intensity and RMS value of the load fluctuations are considered to be statistically dependent. The RMS value of the load fluctuations is renewed at each mean-load pulse occurrence, it remains constant for the entire duration of each mean-load pulse, and is equal to zero when the mean-load pulse intensity is equal to zero.

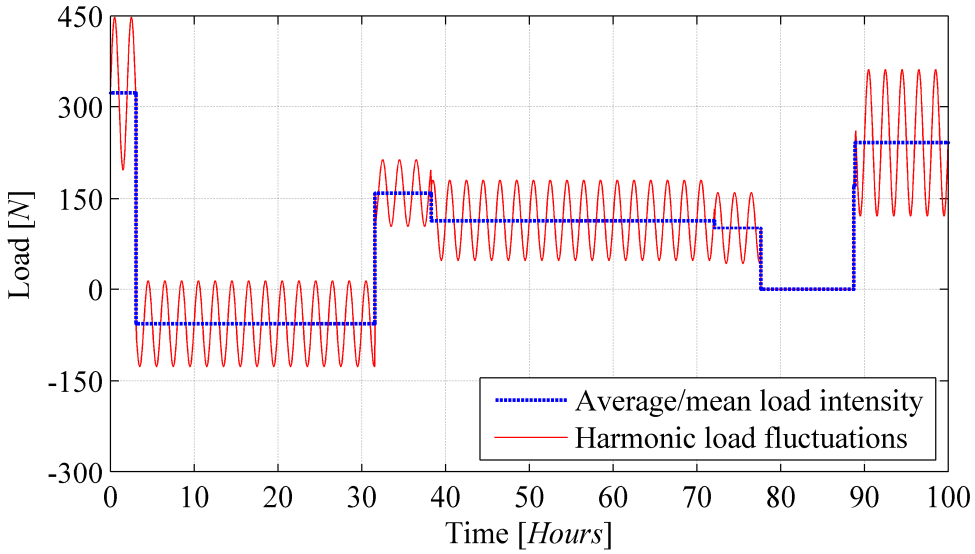

Figure 2.9: Illustrative example of load superposition for the case in which mean-load intensity and the amplitude of the harmonic load fluctuations are considered to be statistically dependent. The amplitude value of the load fluctuations is renewed at each mean-load pulse occurrence, it remains constant for the entire duration of each mean-load pulse, and is equal to zero when the mean-load pulse intensity is equal to zero.

The third important difference, w.r.t. the framework originally presented in Sections 1.2 through 1.7, is represented by the introduction of the random vector $\boldsymbol{\Psi}_{\mathrm{G}}^{[p,q]}$ (hereafter referred to as vector of global performance metrics/measures) in the probabilistic global performance analysis step. This step constitutes a generalization of the probabilistic flutter & LCO analyses step discussed in Section 1.5. The damage-sensitive random quantities, collected in $\boldsymbol{\Psi}_{\mathrm{G}}^{[p,q]}$, can be represented by selected subsets of (i) natural frequencies, (ii) mode shapes, (iii) mode shapes curvatures, (iv) modal strain energies, as well as by generalized displacements under given maximum operational loads at the most critical points of the structure — e.g., midspan deflection of a single-span bridge under maximum design load, the reduced (due to damage)

initial stiffness and/or peak resistance of a structure under a push-over load of a given/fixed spatial distribution, etc.). Nevertheless, the random vector $\boldsymbol{\Psi}_{\mathrm{G}}^{[p,q]}$ can still contain global aeroelastic damage indicators, such as flutter velocity and LCO velocities. A thorough and exhaustive description of all the five analytical steps of this generalized/extended damage prognosis framework, together with specific numerical applications involving the simple testbed/benchmark structure shown in Figure 2.5, is carried out in Chapters 8 and 9.

Finally, in a very similar fashion to what was already presented in Section 2.9, also in this case it is possible to provide a rapid (i.e., in nearly real-time) assessment of the system reliability immediately after the last NDE inspection (at current time t_p). As illustrated in Figure 2.10, this result is obtained by (i) using the posterior joint conditional PDFs — $f''_{\mathbf{A}_{\mathrm{a}}^{p}\left|\boldsymbol{\Theta}_{\mathrm{mat}},\boldsymbol{\Theta}_{\mathrm{dam}}^{p}\right.}\left(\mathbf{a}_{\mathrm{a}}^{p}\left|\boldsymbol{\theta}_{\mathrm{mat}},\boldsymbol{\theta}_{\mathrm{dam}}^{p}\right.\right)$ and $f''_{\boldsymbol{\Theta}_{\mathrm{dam}}^{p}}\left(\boldsymbol{\theta}_{\mathrm{dam}}^{p}\right)$ — in the probabilistic

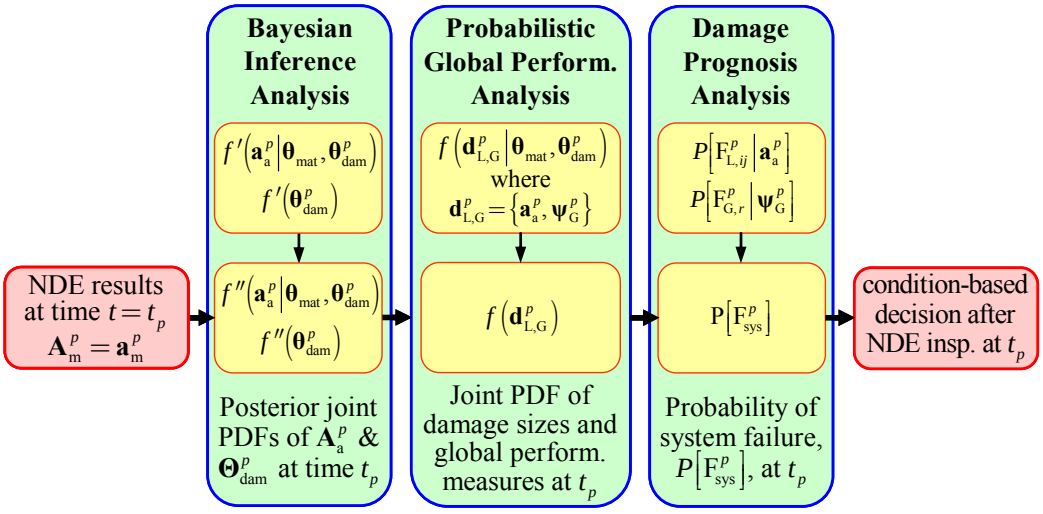

Figure 2.10: Adaptation of the proposed damage prognosis methodology for the rapid reliability assessment (in nearly real time) immediately after the last NDE inspection at current time t_p.

global performance analysis step, (ii) computing the joint PDF $f_{\mathbf{D}^p_{\mathrm{L,G}}}\left(\mathbf{d}^p_{\mathrm{L,G}}\right)$ at time t_p, and (iii) performing, with this piece of information, the component and system reliability analyses necessary to estimate upper and lower uni-modal bounds of the probability of failure, $P\left[\mathrm{F}^p_{\mathrm{sys}}\right]$.

References

A. Der Kiureghian, Non-ergodicity and PEER's framework formula, *Earthquake Engineering & Structural Dynamics*, 34(13), 1643-1652, 2005.

O. Ditlevsen and H.O. Madsen, *Structural reliability methods*, Wiley, West Sussex, England, 1996.

J. Guo, B. Smarslok, R. Penmetsa, and E. Tuegel, Determining most likely flight parameters from aircraft usage for damage prognosis, *Proc. 52nd AIAA/ASME/ASCE/AHS/ASC Structures, Structural Dynamics, and Materials Conference*, Denver, CO, USA, April 4-7, 2011.

J.M. McFarland, *Uncertainty analysis for computer simulations through validation and calibration*, Ph.D. Thesis, Department of Mechanical Engineering, Vanderbilt University, Nashville, TN, 2008.

R.H. Myers, and D.C. Montgomery, *Response surface methodology*, John Wiley and Sons, Inc., New York, NY, 1995.

J.W. Rustenburg, D. Skinn, and D.O. Tipps, *Statistical Loads Data for Boeing 737-400 Aircraft in Commercial Operations*, U.S. Department of Transportation, Federal Aviation Administration, 1998.

J.W. Rustenburg, D. Skinn, and D.O. Tipps, *An evaluation of methods to separate maneuver and gust load factors from measured acceleration time histories*, U.S. Department of Transportation, Federal Aviation Administration, Report n. DOT/ FAA/AR-99/14, 1999.

J.W. Rustenburg, D. Skinn, and D.O. Tipps, *Development of an improved maneuver-gust separation criterion*, University of Dayton Research Institute (UDRI), Structural Integrity Division, 2008.

CHAPTER 3

RECURSIVE PROBABILISTIC ASSESSMENT OF THE CURRENT STATE OF DAMAGE OF THE COMPOSITE UAV WING

3.1. Introduction

In this chapter non destructive evaluation (NDE) inspection results (i.e., the measured damage sizes obtained at each NDE inspection opportunity after sensor-based data processing) are used to (i) probabilistically assess the current state of damage (at the local level, through $\mathbf{A}_{a}^{p}$) of the structural system or sub-component being monitored, and (ii) recursively update the probabilistic information associated with the damage evolution model parameter vector ($\mathbf{\Theta}_{dam}$), which was already introduced in the previous chapter.

Information on the current structural integrity of the UAV wing is assumed to be provided by continuous in-flight monitoring (through a built-in sensor network), as well as by more sophisticated and accurate (but less frequent) on-ground inspections. Both of these NDE approaches must be characterized probabilistically in order to assess their reliability and fidelity, and within this objective, the following three points are the main assumptions made regarding an NDE inspection:

(i) An NDE inspection can detect and locate damage, identify the (potentially multiple) damage mechanisms simultaneously evolving at a certain damage location, and (in the best case scenario) quantify the extents of damage — by using, for instance, an equivalent damage size/extent — for each damage mechanism detected and identified at the monitored damage locations;

(ii) The overall uncertainty (including systematic and random errors) in the measured extent of damage, for a given NDE technique, is dependent on damage location, damage mechanism, and extent of damage (Silk *et al.*, 1987), where the first dependency, in the case of sensor-based in-flight monitoring (Lanza di Scalea *et al.*, 2007), may arise from the non-uniform sensor distribution and/or from the temporary dysfunctional behavior of some network nodes;

(iii) To simplify the problem formulation, it is assumed that detection and measurement of the extent of a certain damage mechanism evolving at a certain damage location only depend on the true (and

unknown) damage size of that particular damage mechanism at the time of inspection (Heasler, 1990; Berens, 1989; Staat, 1993; Zhang and Mahadevan, 2001).

3.2. Probability of detection curves

The detection capability of a particular NDE technique — for a given damage mechanism (j) evolving at a given damage location (I) at time t_p — is provided by the so-called *probability of detection* (*POD*). The *POD*, for a particular (i, j, p) combination, is defined as the probability of detecting damage of any size (i.e., $A_m^{(i,j,p)} > 0$) given that the actual/true damage size, at time t_p, is $A_a^{(i,j,p)} = a_a^{(i,j,p)}$ (with $a_a^{(i,j,p)} > 0$), i.e.,

$$POD\left(a_a^{(i,j,p)}\right) = P\left[A_m^{(i,j,p)} > 0 \,\middle|\, A_a^{(i,j,p)} = a_a^{(i,j,p)}\right] \tag{3.1}$$

On the other hand, the probability that the NDE outcome/result constitutes a false alarm — i.e., damage detected ($A_m^{(i,j,p)} > 0$) when in reality there is no actual damage ($a_a^{(i,j,p)} = 0$) associated with that particular (i, j, p) combination — is referred to as *false-call probability (FCP)*; it is defined as

$$FCP_{(i,j,p)} = P\left[A_m^{(i,j,p)} > 0 \,\middle|\, A_a^{(i,j,p)} = 0\right] = POD\left(a_a^{(i,j,p)} = 0\right) \tag{3.2}$$

and it can be obtained by performing multiple NDE measurements (in a controlled environment) on unflawed components for each (i, j) combination of interest. The two pieces of information provided by Equations (3.1) and (3.2), with the former

viewed as a continuous function of $a_a^{(i,j,p)}$, are combined together in the so-called *POD curve*. Furthermore, for a given (i, j, p) combination, the conditional event $D \triangleq \left(A_m^{(i,j,p)} > 0 \,\middle|\, A_a^{(i,j,p)} = a_a^{(i,j,p)} \right)$ (i.e., damage detected given that the actual damage size is equal to $a_a^{(i,j,p)}$) has for complement the conditional event $ND \triangleq \left(A_m^{(i,j,p)} = 0 \,\middle|\, A_a^{(i,j,p)} = a_a^{(i,j,p)} \right)$ (i.e., no damage detected given that the actual/true damage size is equal to $a_a^{(i,j,p)}$), with $a_a^{(i,j,p)} \geq 0$. The probability associated with this latter conditional event is referred to as *probability of non detection* (*PND*), it is defined as

$$PND\left(a_a^{(i,j,p)}\right) = P\left[A_m^{(i,j,p)} = 0 \,|\, A_a^{(i,j,p)} = a_a^{(i,j,p)}\right] = 1 - POD\left(a_a^{(i,j,p)}\right) \tag{3.3}$$

and, if viewed as a continuous function of $a_a^{(i,j,p)}$, Equation (3.3) is referred to as *PND curve*. Lastly, from Equations (3.2) and (3.3), the value of the *PND* curve evaluated at $a_a^{(i,j,p)} = 0$ (i.e., the probability of correctly classifying as unflawed a component that, at location *I* and at time t_p, does not have any damage mechanism of type *j*) is equal to $1 - FCP_{(i,j,p)}$. Several parametric models, for defining a *POD* curve from the curve-fit (e.g. using logistic regression; Kutner *et al.*, 2004) of experimental binary data (i.e., $POD = 1$ if $A_m^{(i,j,p)} > 0 \,|\, A_a^{(i,j,p)} = a_a^{(i,j,p)}$ and $POD = 0$ if $A_m^{(i,j,p)} = 0 \,|\, A_a^{(i,j,p)} = a_a^{(i,j,p)}$), can be found in the literature (Berens, 1989; Heasler, 1990, Staat, 1993). Among these models, those proposed by Berens (1989) and Staat (1993) are shown in Equations (3.4) and (3.5), respectively.

$$POD\left(a_a^{(i,j,p)}\right)=\frac{e^{-\alpha_0^{(i,j)}+\alpha_1^{(i,j)}\ln\left[a_a^{(i,j,p)}\right]}}{1+e^{-\alpha_0^{(i,j)}+\alpha_1^{(i,j)}\ln\left[a_a^{(i,j,p)}\right]}} \tag{3.4}$$

$$POD\left(a_a^{(i,j,p)}\right)=\left(1-p_\infty^{(i,j)}\right)\left(1-e^{-\alpha_2^{(i,j)}a_a^{(i,j,p)}}\right) \tag{3.5}$$

where $\alpha_0^{(i,j)}$, $\alpha_1^{(i,j)}$, and $\alpha_2^{(i,j)}$ are regression coefficients and $p_\infty^{(i,j)}$ accounts for the fact that the *POD* for a very large damage size, $a_a^{(i,j,p)}$, is not necessarily equal to 1 (i.e., there could be a very small probability, $1-p_\infty^{(i,j)}$, of miss-detecting large crack sizes). For illustration purposes, the *POD* curves that can be obtained from Equations (3.4) and (3.5), for some particular values of the regression coefficients mentioned above, are depicted in Figure 3.1.

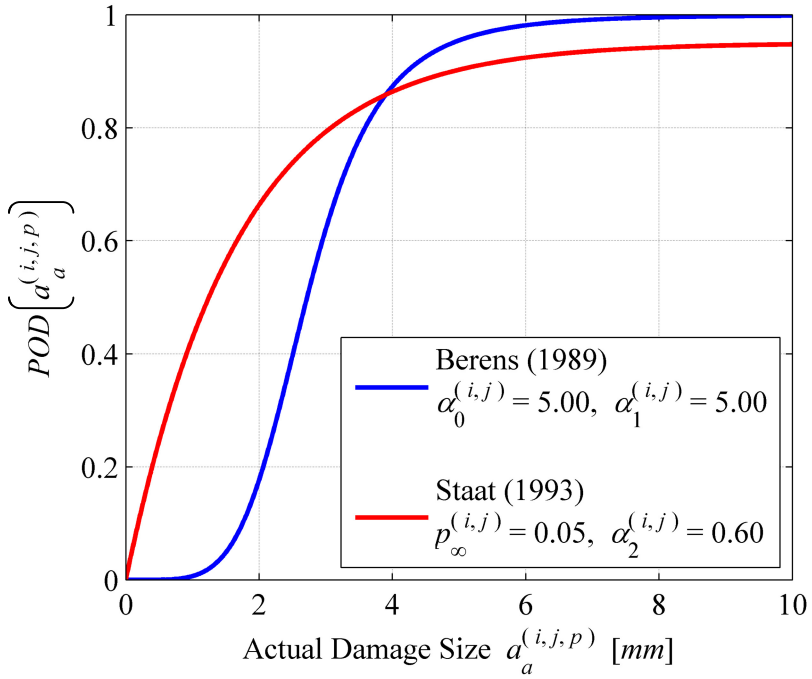

Figure 3.1: Examples of two *POD* curve models found in the literature and evaluated for given sets of arbitrarily chosen model parameters.

3.2.1. Linear damage-size measurement model

Once, for a particular (i, j, p) combination, damage is detected (*D*) and its extent measured, it is natural to question the fidelity/precision of that NDE measurement conditional on the actual damage size. To this end, the NDE measurement accuracy is herein accounted for by the following (linear) damage-size measurement model, used by Zhang and Mahadevan (2001):

$$A_m^{(i,j,p)}\left(A_a^{(i,j,p)} = a_a^{(i,j,p)}, D\right) = \beta_0^{(i,j)} + \beta_1^{(i,j)}\, a_a^{(i,j,p)} + \varepsilon_{ij} \tag{3.6}$$

where $A_a^{(i,j,p)}$ and $A_m^{(i,j,p)}$ (both considered as random variables within the proposed Bayesian inference scheme) are respectively the actual and the measured (i.e., inferred from NDE data processing) damage size for damage location *I*, damage mechanism *j*, and inspection time t_p. The quantity $a_a^{(i,j,p)}$ denotes the value of the actual (but unknown) damage size for the particular (i, j, p) combination considered. The two terms $\beta_0^{(i,j)}$ and $\beta_1^{(i,j)}$ are the coefficients of the (assumed) linear model in Equation (3.6) accounting for the systematic measurement errors, intrinsic of the NDE technique employed, and generally dependent on both damage location and damage mechanism. Finally, $\varepsilon_{ij} \sim N\left(0, \sigma_{\varepsilon_{ij}}\right)$ represents the random measurement error/noise assumed to be Gaussian distributed with zero-mean and standard deviation $\sigma_{\varepsilon_{ij}}$ (considered herein, for the sake of simplicity, to be independent of the true damage size $A_a^{(i,j,p)} = a_a^{(i,j,p)}$; Zhang and Mahadevan, 2001). The quantities $\beta_0^{(i,j)}$, $\beta_1^{(i,j)}$, and $\sigma_{\varepsilon_{ij}}$ are unknown and have to be estimated for the particular model shown in Equation (3.6), and for each

(i, j) combination, through a linear regression analysis (Seber and Lee, 2003) on a given set of known damage sizes, on which several measurements are performed in a controlled environment. The estimated linear regression coefficients and standard deviation of the random measurement error are respectively denoted as $\hat{\beta}_0^{(i,j)}$, $\hat{\beta}_1^{(i,j)}$, and $\hat{\sigma}_{\varepsilon_{ij}}$ (See Section 3.2.2 for a detailed discussion of this topic). Once $\hat{\beta}_0^{(i,j)}$ and $\hat{\beta}_1^{(i,j)}$ are determined, for each (i, j) combination, the estimated mean measurement outcome, $\hat{\mu}_{A_m|A_a}^{(i,j,p)}$, conditional on the true damage size $A_a^{(i,j,p)} = a_a^{(i,j,p)}$, can then be derived from Equation (3.6) and expressed as

$$\hat{\mu}_{A_m|A_a}^{(i,j,p)} = \hat{\mu}_{A_m^{(i,j,p)}|A_a^{(i,j,p)}=a_a^{(i,j,p)}} = \hat{\beta}_0^{(i,j)} + \hat{\beta}_1^{(i,j)} a_a^{(i,j,p)} \tag{3.7}$$

From Equations (3.6) and (3.7), it is now possible to provide the best estimate for the PDF of the measured damage size $A_m^{(i,j,p)}$, conditional on the true damage size $A_a^{(i,j,p)} = a_a^{(i,j,p)}$ and the estimated linear regression parameters, as

$$\begin{aligned} f_{A_m|A_a}^{(i,j,p)}\left(a_m \middle| a_a\right) &= f_{A_m^{(i,j,p)}|A_a^{(i,j,p)}}\left(a_m^{(i,j,p)} \middle| a_a^{(i,j,p)}\right) = \frac{1}{\sqrt{2\pi}\hat{\sigma}_{\varepsilon_{ij}}} e^{-\frac{1}{2}\left[\frac{a_m^{(i,j,p)} - \hat{\mu}_{A_m|A_a}^{(i,j,p)}}{\hat{\sigma}_{\varepsilon_{ij}}}\right]^2} \\ &= \varphi\left(a_m^{(i,j,p)}; \hat{\mu}_{A_m|A_a}^{(i,j,p)}, \hat{\sigma}_{\varepsilon_{ij}}\right) \end{aligned} \tag{3.8}$$

where $\varphi\left(a_m^{(i,j,p)}; \hat{\mu}_{A_m|A_a}^{(i,j,p)}, \hat{\sigma}_{\varepsilon_{ij}}\right)$ is the conditional Normal PDF of $A_m^{(i,j,p)}$ with mean $\hat{\mu}_{A_m|A_a}^{(i,j,p)}$ and standard deviation $\sigma_{A_m|A_a}^{(i,j,p)} = \hat{\sigma}_{\varepsilon_{ij}}$. However, this conditional PDF is meaningful only in the range $A_m^{(i,j,p)} > 0$ and it is therefore renormalized as

$$\tilde{\varphi}\left(a_m^{(i,j,p)};\hat{\mu}_{A_m|A_a}^{(i,j,p)},\hat{\sigma}_{\varepsilon_{ij}}\right)=\varphi\left(a_m^{(i,j,p)};\hat{\mu}_{A_m|A_a}^{(i,j,p)},\hat{\sigma}_{\varepsilon_{ij}}\right)\left[\Phi\left(\frac{\hat{\beta}_0^{(i,j)}+\hat{\beta}_1^{(i,j)}a_a^{(i,j,p)}}{\hat{\sigma}_{\varepsilon_{ij}}}\right)\right]^{-1} \quad (3.9)$$

where $\Phi(\cdot)$ represents the Standard Normal cumulative distribution function (CDF). All these concepts described above are illustrated in Figure 3.2.

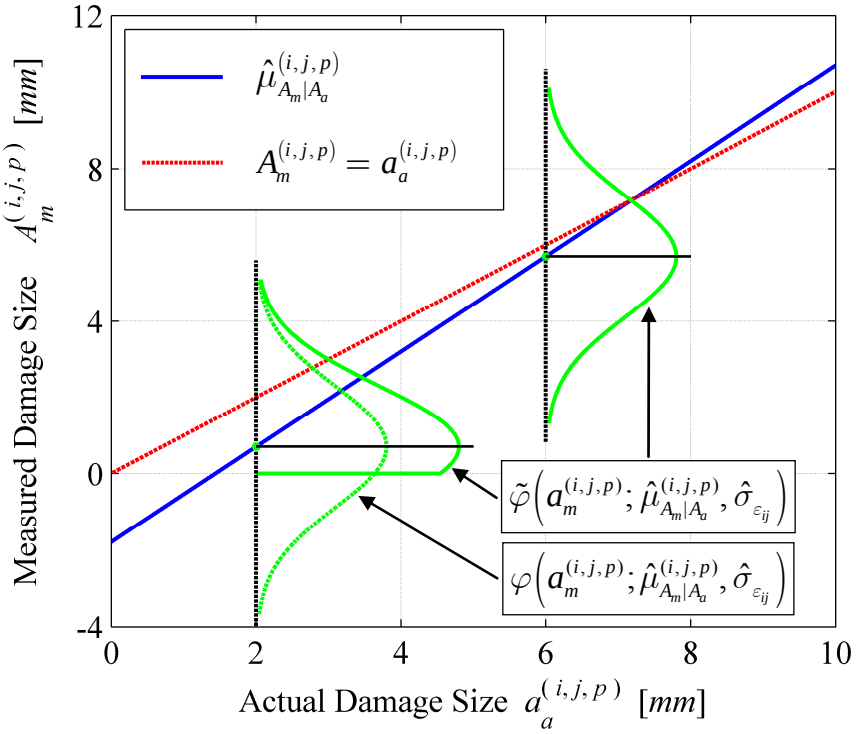

Figure 3.2: Damage-size measurement model adopted in this study (Zhang and Mahadevan, 2001) and plotted for the following set of model parameters: $\hat{\beta}_0^{(i,j)}=-1.8\,mm$, $\hat{\beta}_1^{(i,j)}=1.25$, and $\hat{\sigma}_{\varepsilon_{ij}}=1.5\,mm$.

3.2.2. Regression analysis for the estimation of the sizing model parameters

As anticipated above, linear regression analysis is used to provide an estimate for the quantities $\beta_0^{(i,j)}$, $\beta_1^{(i,j)}$, and $\sigma_{\varepsilon_{ij}}$ for each (i,j) combination. In a controlled

environment (e.g., in a laboratory test setup) several measurements ($\overline{n}$) on a given set of $n_{\bar{\mathrm{A}}}$ known damage sizes artificially created for each (i,j) combination — herein denoted as $\overline{\mathbf{a}}_{\mathrm{a}}^{(i,j)} = \left\{ \overline{a}_a^{(i,j,1)}, \overline{a}_a^{(i,j,2)}, \ldots, \overline{a}_a^{(i,j,n_{\bar{\mathrm{A}}})} \right\}^{\mathrm{T}}$ — are performed using the NDE technique that will be later deployed on the field (to monitor the real structure) and whose measurement uncertainty must therefore be quantified. These measurements are collected in the vector $\overline{\mathbf{a}}_{\mathrm{m}}^{(i,j)} = \left\{ \left\{ \overline{\mathbf{a}}_{\mathrm{m}}^{(i,j,1)} \right\}^{\mathrm{T}}, \left\{ \overline{\mathbf{a}}_{\mathrm{m}}^{(i,j,2)} \right\}^{\mathrm{T}}, \ldots, \left\{ \overline{\mathbf{a}}_{\mathrm{m}}^{(i,j,n_{\bar{\mathrm{A}}})} \right\}^{\mathrm{T}} \right\}^{\mathrm{T}}$ whose generic sub-vector, $\overline{\mathbf{a}}_{\mathrm{m}}^{(i,j,k)}$, is defined as $\overline{\mathbf{a}}_{\mathrm{m}}^{(i,j,k)} = \left\{ \overline{a}_{m,1}^{(i,j,k)}, \overline{a}_{m,2}^{(i,j,k)}, \ldots, \overline{a}_{m,\overline{n}_k}^{(i,j,k)} \right\}^{\mathrm{T}}$ and represents the series of $\overline{n}_k$ measurements performed on the known damage size equal to $\overline{a}_a^{(i,j,k)}$. The total number of measurements performed is therefore equal to $\overline{n} = \sum_{k=1}^{n_{\bar{\mathrm{A}}}} \overline{n}_k$ and each of these measurements collected in $\overline{\mathbf{a}}_{\mathrm{m}}^{(i,j)}$ satisfies the condition $\overline{a}_{m,1}^{(i,j,k)} > 0$ — i.e., the non-detection results are not used to fit the linear measurement model of Equation (3.6). Assuming that the $\overline{n}$ random measurement errors (i.e., the measurement errors occurred in each of the $\overline{n}$ measurements performed) are independent and identically distributed (i.i.d.), an unbiased estimate for the two linear regression coefficients of the proposed damage size measurement model can be computed as (Seber and lee, 2003)

$$\hat{\boldsymbol{\beta}}^{(i,j)} = \begin{Bmatrix} \hat{\beta}_0^{(i,j)} \\ \hat{\beta}_1^{(i,j)} \end{Bmatrix} = \left(\mathbf{X}^{\mathrm{T}} \mathbf{X} \right)^{-1} \mathbf{X}^{\mathrm{T}} \, \overline{\mathbf{a}}_{\mathrm{m}}^{(i,j)} \tag{3.10}$$

where the full-rank regression (or design) matrix $\mathbf{X}$ is given by (Seber and Lee, 2003)

$$\mathbf{X}=\begin{bmatrix}\mathbf{1}_1 & \overline{\mathbf{a}}_{\mathrm{a}}^{(i,j,1)}\\ \mathbf{1}_2 & \overline{\mathbf{a}}_{\mathrm{a}}^{(i,j,2)}\\ \vdots & \vdots\\ \mathbf{1}_{n_{\overline{\mathrm{A}}}} & \overline{\mathbf{a}}_{\mathrm{a}}^{(i,j,n_{\overline{\mathrm{A}}})}\end{bmatrix}_{(\overline{n}\times 2)} \tag{3.11}$$

in which the generic vector $\mathbf{1}_k$ (with $k=1,\ldots,n_{\overline{\mathrm{A}}}$) is an $(\overline{n}_k\times 1)$ vector of ones and $\overline{\mathbf{a}}_{\mathrm{a}}^{(i,j,k)}$ is defined as $\overline{\mathbf{a}}_{\mathrm{a}}^{(i,j,k)}=\overline{a}_a^{(i,j,k)}\mathbf{1}_k$. On the other hand, an unbiased estimate for the variance ($\sigma^2_{\varepsilon_{ij}}$) of the random measurement error (ε_{ij}) is given by (Seber and Lee, 2003)

$$\hat{\sigma}^2_{\varepsilon_{ij}}=\frac{\left[\overline{\mathbf{a}}_{\mathrm{m}}^{(i,j)}-\mathbf{X}\hat{\boldsymbol{\beta}}^{(i,j)}\right]^{\mathrm{T}}\left[\overline{\mathbf{a}}_{\mathrm{m}}^{(i,j)}-\mathbf{X}\hat{\boldsymbol{\beta}}^{(i,j)}\right]}{\overline{n}-2}=\frac{RSS}{\overline{n}-2} \tag{3.12}$$

where the numerator of equation (3.12) represents the residual sum of squares (RSS) between the measured and the predicted (through the regressed linear model) damage sizes. Using the results obtained thus far, it is also possible to provide confidence bounds for both $\mu^{(i,j,p)}_{A_m|A_a}=\beta_0^{(i,j)}+\beta_1^{(i,j)}a_a^{(i,j,p)}$ and $\sigma^2_{\varepsilon_{ij}}$ based on their underline PDFs, from which $\hat{\mu}^{(i,j,p)}_{A_m|A_a}$ and $\hat{\sigma}^2_{\varepsilon_{ij}}$ are particular realizations (once the measurement vector $\overline{\mathbf{a}}_{\mathrm{m}}^{(i,j)}$ is available). 100(1−α)% confidence bounds for $\hat{\mu}^{(i,j,p)}_{A_m|A_a}$ and $\hat{\sigma}^2_{\varepsilon_{ij}}$ are functions of the true damage size $a_a^{(i,j,p)}$ and can respectively be expressed as

$$\hat{\mu}^{(i,j,p)}_{A_m|A_a}-\hat{\sigma}_{\varepsilon_{ij}}\nu\left(a_a^{(i,j,p)}\right)t^{(1-\alpha/2)}_{\overline{n}-2}\le\mu^{(i,j,p)}_{A_m|A_a}\le\hat{\mu}^{(i,j,p)}_{A_m|A_a}+\hat{\sigma}_{\varepsilon_{ij}}\nu\left(a_a^{(i,j,p)}\right)t^{(1-\alpha/2)}_{\overline{n}-2} \tag{3.13}$$

$$\hat{\sigma}^2_{\varepsilon_{ij}}\frac{\overline{n}-2}{\chi^2_{\overline{n}-2}\left(1-\alpha/2\right)}\le\sigma^2_{\varepsilon_{ij}}\le\hat{\sigma}^2_{\varepsilon_{ij}}\frac{\overline{n}-2}{\chi^2_{\overline{n}-2}\left(\alpha/2\right)} \tag{3.14}$$

where $t_{\bar{n}-2}^{(\cdot)}$ and $\chi_{\bar{n}-2}^{2}(\bullet)$ are the $(\bullet)\%$ percentile of the *Student-T* and the *Chi-Square* distributions with $\bar{n}-2$ degrees of freedom, respectively; and the function $\nu\left(a_a^{(i,j,p)}\right)$ is expressed as

$$\nu\left(a_a^{(i,j,p)}\right)=\sqrt{\frac{1}{\bar{n}}+\frac{\left(a_a^{(i,j,p)}-\overline{\bar{a}}_a^{(i,j)}\right)^2}{\sum_{l=1}^{n_{\bar{A}}}\left(\bar{a}_a^{(i,j,l)}-\overline{\bar{a}}_a^{(i,j)}\right)^2}} \tag{3.15}$$

in which $\overline{\bar{a}}_a^{(i,j)}$ represents the mean value of the components of the vector $\bar{\mathbf{a}}_{\mathrm{a}}^{(i,j)}$, i.e.,

$$\overline{\bar{a}}_a^{(i,j)}=\frac{1}{n_{\bar{A}}}\sum_{l=1}^{n_{\bar{A}}}\bar{a}_a^{(i,j,l)} \tag{3.16}$$

It is therefore easily recognizable how the uncertainty associated with $\hat{\mu}_{A_m|A_a}^{(i,j,p)}$ and $\hat{\sigma}_{\varepsilon_{ij}}^2$ can be controlled and reduced by increasing the number of measurements ($\bar{n}$) and choosing an appropriate vector $\bar{\mathbf{a}}_{\mathrm{a}}^{(i,j)}$. The $n_{\bar{A}}$ known damage sizes in $\bar{\mathbf{a}}_{\mathrm{a}}^{(i,j)}$ must, in fact, cover as widely as possible all the damage sizes that can be encountered during the NDE monitoring of the real structure. For these reasons outlined above the two additional layers of uncertainty associated with $\hat{\mu}_{A_m|A_a}^{(i,j,p)}$ and $\hat{\sigma}_{\varepsilon_{ij}}^2$ — and quantified in Equations (3.13) and (3.14) — are not included in the damage prognosis framework proposed in this thesis.

3.2.3. An alternative damage size measurement model

The linear damage size measurement model introduced in Equation (3.6) can be substituted with other sizing models proposed and/or used by other researchers.

These models can be easily found in the literature; for example, Simola and Pulkkinen (1998) proposed the following *logit model*:

$$\ln\left[Z_m^{(i,j,p)}\left(Z_a^{(i,j,p)}=z_a^{(i,j,p)},D\right)\right]=\eta_0^{(i,j)}+\eta_1^{(i,j)}\ln\left[z_a^{(i,j,p)}\right]+\varepsilon_{ij} \tag{3.17}$$

where $\eta_0^{(i,j)}$ and $\eta_1^{(i,j)}$ are the model coefficients to be determined through a linear regression analysis in the logarithmic space defined by $\ln\left[z_a^{(i,j,p)}\right]-\ln\left[z_m^{(i,j,p)}\right]$, ε_{ij} represents the random measurement error assumed to be Gaussian distributed with zero-mean and standard deviation $\sigma_{\varepsilon_{ij}}$, and the quantities $Z_m^{(i,j,p)}$ and $Z_a^{(i,j,p)}$ are respectively the normalized measured and actual damage sizes defined as

$$Z_m^{(i,j,p)}=\frac{A_m^{(i,j,p)}}{A_{\max}^{(i,j)}-A_m^{(i,j,p)}} \tag{3.18}$$

$$Z_a^{(i,j,p)}=\frac{A_a^{(i,j,p)}}{A_{\max}^{(i,j)}-A_a^{(i,j,p)}} \tag{3.19}$$

Finally, the term $A_{\max}^{(i,j)}$ in Equations (3.18) and (3.19) denotes the maximum observable damage size for a given (i,j) combination.

3.3. Recursive Bayesian updating scheme for the damage size vector $\mathbf{A}_{\mathrm{a}}^{p}$

Equation (3.3), one of the models shown in Equations (3.4) and (3.5), and Equation (3.9) are then combined to build the likelihood function needed to update — within the proposed recursive Bayesian updating scheme — the prior joint conditional PDF, $f'_{\mathbf{A}_{\mathrm{a}}^{p}\left|\boldsymbol{\Theta}_{\mathrm{mat}},\boldsymbol{\Theta}_{\mathrm{dam}}\right.}\left(\mathbf{a}_{\mathrm{a}}^{p}\left|\boldsymbol{\theta}_{\mathrm{mat}},\boldsymbol{\theta}_{\mathrm{dam}}\right.\right)$, into the posterior joint conditional PDF,

$f''_{\mathbf{A}_{\mathrm{a}}^{p}\left|\boldsymbol{\Theta}_{\mathrm{mat}},\boldsymbol{\Theta}_{\mathrm{dam}}\right.}\left(\mathbf{a}_{\mathrm{a}}^{p}\left|\boldsymbol{\theta}_{\mathrm{mat}},\boldsymbol{\theta}_{\mathrm{dam}}\right.\right)$, as the new measurement result, $\mathbf{a}_{\mathrm{m}}^{p}$, becomes available at time t_p. This recursive Bayesian updating scheme, based on previous work by Zheng and Ellingwood (1998), Lin *et al.*(2000), Zhang and Mahadevan (2001), and Kulkarni and Achenbach (2008), can be written as

$$\underbrace{f_{\mathbf{A}_{\mathrm{a}}^{p}\left|\boldsymbol{\Theta}_{\mathrm{mat}},\boldsymbol{\Theta}_{\mathrm{dam}},\mathbf{A}_{\mathrm{m}}^{[0,p]}\right.}\left(\mathbf{a}_{\mathrm{a}}^{p}\left|\boldsymbol{\theta}_{\mathrm{mat}},\boldsymbol{\theta}_{\mathrm{dam}},\mathbf{a}_{\mathrm{m}}^{[0,p]}\right.\right)}_{=f''_{\boldsymbol{\Lambda}_{\mathrm{a}}^{p}\left|\boldsymbol{\Theta}_{\mathrm{mat}},\boldsymbol{\Theta}_{\mathrm{dam}}\right.}\left(\boldsymbol{\lambda}_{\mathrm{a}}^{p}\left|\boldsymbol{\theta}_{\mathrm{mat}},\boldsymbol{\theta}_{\mathrm{dam}}\right.\right)} \propto L\left(\mathbf{a}_{\mathrm{a}}^{p}\left|\mathbf{a}_{\mathrm{m}}^{p}\right.\right) \underbrace{f_{\mathbf{A}_{\mathrm{a}}^{p}\left|\boldsymbol{\Theta}_{\mathrm{mat}},\boldsymbol{\Theta}_{\mathrm{dam}},\mathbf{A}_{\mathrm{m}}^{[0,p-1]}\right.}\left(\mathbf{a}_{\mathrm{a}}^{p}\left|\boldsymbol{\theta}_{\mathrm{mat}},\boldsymbol{\theta}_{\mathrm{dam}},\mathbf{a}_{\mathrm{m}}^{[0,p-1]}\right.\right)}_{=f'_{\boldsymbol{\Lambda}_{\mathrm{a}}^{p}\left|\boldsymbol{\Theta}_{\mathrm{mat}},\boldsymbol{\Theta}_{\mathrm{dam}}\right.}\left(\boldsymbol{\lambda}_{\mathrm{a}}^{p}\left|\boldsymbol{\theta}_{\mathrm{mat}},\boldsymbol{\theta}_{\mathrm{dam}}\right.\right)} \tag{3.20}$$

where $L\left(\mathbf{a}_{\mathrm{a}}^{p}\left|\mathbf{a}_{\mathrm{m}}^{p}\right.\right)$ represents the likelihood function of the true damage size vector at time t_p once the new NDE results (i.e., the processed NDE measurements) are available. Furthermore, by assuming that the conditional NDE measurement outcomes $\left\{a_{m_k}^{(i,j,p)}\left|a_a^{(i,j,p)},\, k=1,...,n_{\mathrm{MS}}^{(i,j,p)}\right.\right\}$, (where $n_{\mathrm{MS}}^{(i,j,p)}$ is the number of NDE measurements performed at time t_p, at location i, for damage mechanism j) are realizations from statistically independent random variables for every (i,j) combination, Equation (3.20) can be rewritten as

$$f''_{\mathbf{A}_{\mathrm{a}}^{p}\left|\boldsymbol{\Theta}_{\mathrm{mat}},\boldsymbol{\Theta}_{\mathrm{dam}}\right.}\left(\mathbf{a}_{\mathrm{a}}^{p}\left|\boldsymbol{\theta}_{\mathrm{mat}},\boldsymbol{\theta}_{\mathrm{dam}}\right.\right) \propto \left[\prod_{i=1}^{n_{\mathrm{L}}^{p}}\prod_{j=1}^{n_{\mathrm{DM}}^{(i,p)}}\prod_{k=1}^{n_{\mathrm{MS}}^{(i,j,p)}} L\left(a_a^{(i,j,p)}\left|a_{m_k}^{(i,j,p)}\right.\right)\right] f'_{\mathbf{A}_{\mathrm{a}}^{p}\left|\boldsymbol{\Theta}_{\mathrm{mat}},\boldsymbol{\Theta}_{\mathrm{dam}}\right.}\left(\mathbf{a}_{\mathrm{a}}^{p}\left|\boldsymbol{\theta}_{\mathrm{mat}},\boldsymbol{\theta}_{\mathrm{dam}}\right.\right) \tag{3.21}$$

where n_{L}^{p} denotes the number of inspected locations at time t_p (with $n_{\mathrm{L}}^{p} \le n_{\mathrm{L}}^{[0,p]}$ and $n_{\mathrm{L}}^{[0,p]}$ representing the total number of inspected locations up to time t_p), and $n_{\mathrm{DM}}^{(i,p)}$

represents the number of detected damage mechanisms at location i at time t_p (with $n_{\mathrm{DM}}^{(i,p)} \le n_{\mathrm{DM}}^{(i,[0,p])}$ and $n_{\mathrm{DM}}^{(i,[0,p])}$ representing the total number of detected damage mechanisms at location i up to time t_p). Furthermore, the vector $\mathbf{A}_{\mathrm{a}}^{p} = \left\{ \mathbf{A}_{\mathrm{a}}^{(i,p)},\, i = 1,\ldots,n_{\mathrm{L}}^{[0,p]} \right\}$, with $\mathbf{A}_{\mathrm{a}}^{(i,p)} = \left\{ A_a^{(i,j,p)},\, j = 1,\ldots,n_{\mathrm{DM}}^{(i,[0,p])} \right\}$, represents the collection of the actual damage sizes at all inspected locations and all detected damage mechanisms up to time t_p. The size (at time t_p) of the damage size vector $\mathbf{A}_{\mathrm{a}}^{p}$ is thus equal to $n_{\mathrm{A}}^{p} = \sum_{i=1}^{n_{\mathrm{L}}^{[0,p]}} n_{\mathrm{DM}}^{(i,[0,p])}$. On the other hand, the vector $\mathbf{a}_{\mathrm{m}}^{p} = \left\{ \mathbf{a}_{\mathrm{m}}^{(i,p)},\, i = 1,\ldots,n_{\mathrm{L}}^{p} \right\}$ — with its sub-vectors defined as $\mathbf{a}_{\mathrm{m}}^{(i,p)} = \left\{ \mathbf{a}_{\mathrm{m}}^{(i,j,p)},\, j = 1,\ldots,n_{\mathrm{DM}}^{(i,p)} \right\}$ and $\mathbf{a}_{\mathrm{m}}^{(i,j,p)} = \left\{ a_{m_k}^{(i,j,p)},\, k = 1,\ldots,n_{\mathrm{MS}}^{(i,j,p)} \right\}$ — collects all the $n_{\mathrm{MS}}^{p} = \sum_{i=1}^{n_{\mathrm{L}}^{p}} \sum_{j=1}^{n_{\mathrm{DM}}^{(i,p)}} n_{\mathrm{MS}}^{(i,j,p)}$ NDE measurement results obtained at time t_p. Finally, $L\left(a_a^{(i,j,p)} \middle| a_{m_k}^{(i,j,p)} \right)$ represents the likelihood function of $a_a^{(i,j,p)}$ once the k^{th} NDE measurement result, $a_{m_k}^{(i,j,p)}$, becomes available. It should be noted that: (i) the equality $L\left(\mathbf{a}_{\mathrm{a}}^{p} \middle| a_{m_k}^{(i,j,p)} \right) = L\left(a_a^{(i,j,p)} \middle| a_{m_k}^{(i,j,p)} \right)$ is a direct consequence of the measurement model introduced in Equation (3.6), and (ii) the mathematical form of the likelihood function depends on the NDE measurement outcome, $a_{m_k}^{(i,j,p)}$, as

$$L\left(a_a^{(i,j,p)} \middle| a_{m_k}^{(i,j,p)} \right) = \begin{cases} \tilde{\varphi}\left(a_{m_k}^{(i,j,p)}; \hat{\mu}_{A_m \mid A_a}^{(i,j,p)}, \hat{\sigma}_{\varepsilon_{ij}} \right) \cdot POD\left(a_a^{(i,j,p)} \right) & \text{if } a_{m_k}^{(i,j,p)} > 0 \\ PND\left(a_a^{(i,j,p)} \right) & \text{if } a_{m_k}^{(i,j,p)} = 0 \end{cases} \tag{3.22}$$

Equation (3.22) combines the binary source of information provided by $POD\left(a_a^{(i,j,p)} \right)$

and $PND\left(a_a^{(i,j,p)}\right)$ with the continuous resolution of the NDE measurement uncertainty, through $\tilde{\varphi}\left(a_{m_k}^{(i,j,p)};\hat{\mu}_{A_m|A_a}^{(i,j,p)},\hat{\sigma}_{\varepsilon_{ij}}\right)$, and thus constitutes an improvement of previous research work carried out by Chen (2011) and An *et al*. (2011). Furthermore, for the case in which the NDE technique can only provide either detection (i.e., $a_{m_k}^{(i,j,p)}>0$) or non-detection (i.e., $a_{m_k}^{(i,j,p)}=0$) results, Equation (3.22) reduces to

$$L\left(a_a^{(i,j,p)}\middle|a_{m_k}^{(i,j,p)}\right)=\begin{cases}POD\left(a_a^{(i,j,p)}\right) & \text{if } a_{m_k}^{(i,j,p)}>0\\ PND\left(a_a^{(i,j,p)}\right) & \text{if } a_{m_k}^{(i,j,p)}=0\end{cases} \tag{3.23}$$

It must also be mentioned that: (i) the initial (i.e., before the first NDE inspection at time t_0) damage-size PDF model, $f'_{\mathbf{A}_{\mathrm{a}}^0}\left(\mathbf{a}_{\mathrm{a}}^0\right)$, and its parameters are chosen on the basis of engineering judgment, as pointed out — among others — by Lin *et al*. (2000), and (ii) the components of the random vector $\mathbf{A}_{\mathrm{a}}^0$, at time t_0, can be reasonably considered mutually statistically independent as well as statistically independent of $\boldsymbol{\Theta}_{\mathrm{mat}}$ and $\boldsymbol{\Theta}_{\mathrm{dam}}$. These assumptions are translated into the following equation:

$$f'_{\mathbf{A}_{\mathrm{a}}^0|\boldsymbol{\Theta}_{\mathrm{mat}},\boldsymbol{\Theta}_{\mathrm{dam}}}\left(\mathbf{a}_{\mathrm{a}}^0\middle|\boldsymbol{\theta}_{\mathrm{mat}},\boldsymbol{\theta}_{\mathrm{dam}}\right)=f'_{\boldsymbol{\Lambda}_{\mathrm{a}}^0}\left(\mathbf{a}_{\mathrm{a}}^0\right)=\prod_{i=1}^{n_{\mathrm{L}}^0}\prod_{j=1}^{n_{\mathrm{DM}}^{(i,0)}}f'_{A_a^{(i,j,0)}}\left(a_a^{(i,j,0)}\right) \tag{3.24}$$

For instance, both Lognormal and Exponential PDF models are possible and reasonable choices for $f'_{\mathbf{A}_{\mathrm{a}}^0}\left(\mathbf{a}_{\mathrm{a}}^0\right)$. However, the choice of the PDF model, $f'_{\mathbf{A}_{\mathrm{a}}^0}\left(\mathbf{a}_{\mathrm{a}}^0\right)$, has a negligible influence on the posterior joint conditional PDF, $f''_{\mathbf{A}_{\mathrm{a}}^p|\boldsymbol{\Theta}_{\mathrm{mat}},\boldsymbol{\Theta}_{\mathrm{dam}}}\left(\mathbf{a}_{\mathrm{a}}^p\middle|\boldsymbol{\theta}_{\mathrm{mat}},\boldsymbol{\theta}_{\mathrm{dam}}\right)$, when a large amount of NDE measurement data is available in the Bayesian updating

procedure. Therefore, this initial choice of the PDF model for $f'_{\mathbf{A}_{\mathrm{a}}^0}\left(\mathbf{a}_{\mathrm{a}}^0\right)$ does not represent a crucial decision in the damage prognosis framework presented herein. As a final remark, mixed PDF models for $f'_{\mathbf{A}_{\mathrm{a}}^0}\left(\mathbf{a}_{\mathrm{a}}^0\right)$ can also be used and efficiently incorporated into the proposed Bayesian inference scheme. It is possible, for instance, to define each of the $n_{\mathrm{A}}^0 = \sum_{i=1}^{n_{\mathrm{L}}^0} n_{\mathrm{DM}}^0$ marginal PDFs of the random vector $\mathbf{A}_{\mathrm{a}}^0$ as

$$f'_{A_a^{(i,j,0)}}\left(a_a^{(i,j,0)}\right) = p_0^{(i,j,0)} \cdot \delta\left(a_a^{(i,j,0)}\right) + \left(1 - p_0^{(i,j,0)}\right) \cdot \tilde{f}_{A_a^{(i,j,0)}}\left(a_a^{(i,j,0)}\right) \tag{3.25}$$

where the quantity $p_0^{(i,j,0)}$ represents — for the particular (i,j) combination — the probability of having no damage (i.e., $a_a^{(i,j,0)} = 0$), $\delta\left(a_a^{(i,j,0)}\right)$ denotes the *Dirac delta*, and $\tilde{f}_{A_a^{(i,j,0)}}\left(a_a^{(i,j,0)}\right)$ constitutes the PDF of the damage size $a_a^{(i,j,0)}$ in the range $a_a^{(i,j,0)} > 0$; Lognormal and Exponential PDF models are possible and reasonable choices for $\tilde{f}_{A_a^{(i,j,0)}}\left(a_a^{(i,j,0)}\right)$ as well.

3.4. Bayesian inference scheme for the recursive updating of the joint PDF of the damage evolution parameter vector $\boldsymbol{\Theta}_{\mathrm{dam}}^p$

Processed NDE inspection results (at time t_p) can be used not only to compute the posterior conditional joint PDF $f''_{\mathbf{A}_{\mathrm{a}}^p|\boldsymbol{\Theta}_{\mathrm{mat}},\boldsymbol{\Theta}_{\mathrm{dam}}}\left(\mathbf{a}_{\mathrm{a}}^p \,\middle|\, \boldsymbol{\theta}_{\mathrm{mat}}, \boldsymbol{\theta}_{\mathrm{dam}}\right)$ (as shown in Section 3.3) but also to provide a recursive update of the joint PDF of the damage evolution parameter vector $\boldsymbol{\Theta}_{\mathrm{dam}}^p$. The proposed recursive Bayesian updating scheme used to achieve this result can be expressed as

$$\underbrace{f_{\boldsymbol{\Theta}_{\text{dam}}^{p}\left|\mathbf{A}_{\text{m}}^{[0,p]}\right.}\left(\boldsymbol{\theta}_{\text{dam}}^{p}\left|\mathbf{a}_{\text{m}}^{[0,p]}\right.\right)}_{=f''_{\boldsymbol{\Theta}_{\text{dam}}^{p}}\left(\boldsymbol{\theta}_{\text{dam}}^{p}\right)} \propto f_{\mathbf{A}_{\text{m}}^{p}\left|\boldsymbol{\Theta}_{\text{dam}}^{p},\mathbf{A}_{\text{m}}^{[0,p-1]}\right.}\left(\mathbf{a}_{\text{m}}^{p}\left|\boldsymbol{\theta}_{\text{dam}}^{p},\mathbf{a}_{\text{m}}^{[0,p-1]}\right.\right) \underbrace{f_{\boldsymbol{\Theta}_{\text{dam}}^{p}\left|\mathbf{A}_{\text{m}}^{[0,p-1]}\right.}\left(\boldsymbol{\theta}_{\text{dam}}^{p}\left|\mathbf{a}_{\text{m}}^{[0,p-1]}\right.\right)}_{=f'_{\boldsymbol{\Theta}_{\text{dam}}^{p}}\left(\boldsymbol{\theta}_{\text{dam}}^{p}\right)} \tag{3.26}$$

or, in a more compact form, as

$$f''_{\boldsymbol{\Theta}_{\text{dam}}^{p}}\left(\boldsymbol{\theta}_{\text{dam}}^{p}\right) \propto f_{\mathbf{A}_{\text{m}}^{p}\left|\boldsymbol{\Theta}_{\text{dam}}^{p},\mathbf{A}_{\text{m}}^{[0,p-1]}\right.}\left(\mathbf{a}_{\text{m}}^{p}\left|\boldsymbol{\theta}_{\text{dam}}^{p},\mathbf{a}_{\text{m}}^{[0,p-1]}\right.\right) f'_{\boldsymbol{\Theta}_{\text{dam}}^{p}}\left(\boldsymbol{\theta}_{\text{dam}}^{p}\right) \tag{3.27}$$

where the conditional joint PDF $f_{\mathbf{A}_{\text{m}}^{p}\left|\boldsymbol{\Theta}_{\text{dam}}^{p},\mathbf{A}_{\text{m}}^{[0,p-1]}\right.}\left(\mathbf{a}_{\text{m}}^{p}\left|\boldsymbol{\theta}_{\text{dam}}^{p},\mathbf{a}_{\text{m}}^{[0,p-1]}\right.\right)$ (i.e., the likelihood function of the proposed recursive Bayesian updating scheme) can be computed by taking advantage of the total probability theorem as follows:

$$\begin{aligned} &f_{\mathbf{A}_{\text{m}}^{p}\left|\boldsymbol{\Theta}_{\text{dam}}^{p},\mathbf{A}_{\text{m}}^{[0,p-1]}\right.}\left(\mathbf{a}_{\text{m}}^{p}\left|\boldsymbol{\theta}_{\text{dam}}^{p},\mathbf{a}_{\text{m}}^{[0,p-1]}\right.\right)= \\ &\int_{\mathbf{A}_{\text{a}}^{p}}\int_{\boldsymbol{\Theta}_{\text{mat}}} f_{\mathbf{A}_{\text{m}}^{p}\left|\mathbf{A}_{\text{a}}^{p},\boldsymbol{\Theta}_{\text{mat}},\boldsymbol{\Theta}_{\text{dam}}^{p},\mathbf{A}_{\text{m}}^{[0,p-1]}\right.}\left(\mathbf{a}_{\text{m}}^{p}\left|\mathbf{a}_{\text{a}}^{p},\boldsymbol{\theta}_{\text{mat}},\boldsymbol{\theta}_{\text{dam}}^{p},\mathbf{a}_{\text{m}}^{[0,p-1]}\right.\right) \\ &\qquad f_{\mathbf{A}_{\text{a}}^{p}\left|\boldsymbol{\Theta}_{\text{mat}},\boldsymbol{\Theta}_{\text{dam}}^{p},\mathbf{A}_{\text{m}}^{[0,p-1]}\right.}\left(\mathbf{a}_{\text{a}}^{p}\left|\boldsymbol{\theta}_{\text{mat}},\boldsymbol{\theta}_{\text{dam}}^{p},\mathbf{a}_{\text{m}}^{[0,p-1]}\right.\right) f_{\boldsymbol{\Theta}_{\text{mat}}}\left(\boldsymbol{\theta}_{\text{mat}}\right) d\boldsymbol{\theta}_{\text{mat}}\, d\mathbf{a}_{\text{a}}^{p} \end{aligned} \tag{3.28}$$

and by noting that $f_{\mathbf{A}_{\text{a}}^{p}\left|\boldsymbol{\Theta}_{\text{mat}},\boldsymbol{\Theta}_{\text{dam}}^{p},\mathbf{A}_{\text{m}}^{[0,p-1]}\right.}\left(\mathbf{a}_{\text{a}}^{p}\left|\boldsymbol{\theta}_{\text{mat}},\boldsymbol{\theta}_{\text{dam}}^{p},\mathbf{a}_{\text{m}}^{[0,p-1]}\right.\right)= f'_{\mathbf{A}_{\text{a}}^{p}\left|\boldsymbol{\Theta}_{\text{mat}},\boldsymbol{\Theta}_{\text{dam}}^{p}\right.}\left(\mathbf{a}_{\text{a}}^{p}\left|\boldsymbol{\theta}_{\text{mat}},\boldsymbol{\theta}_{\text{dam}}^{p}\right.\right)$ and $f_{\mathbf{A}_{\text{m}}^{p}\left|\mathbf{A}_{\text{a}}^{p},\boldsymbol{\Theta}_{\text{mat}},\boldsymbol{\Theta}_{\text{dam}}^{p},\mathbf{A}_{\text{m}}^{[0,p-1]}\right.}\left(\mathbf{a}_{\text{m}}^{p}\left|\mathbf{a}_{\text{a}}^{p},\boldsymbol{\theta}_{\text{mat}},\boldsymbol{\theta}_{\text{dam}}^{p},\mathbf{a}_{\text{m}}^{[0,p-1]}\right.\right)= f_{\mathbf{A}_{\text{m}}^{p}\left|\mathbf{A}_{\text{a}}^{p}\right.}\left(\mathbf{a}_{\text{m}}^{p}\left|\mathbf{a}_{\text{a}}^{p}\right.\right)$, Equation (3.28) can be simplified and rewritten as

$$\begin{aligned} &f_{\mathbf{A}_{\text{m}}^{p}\left|\boldsymbol{\Theta}_{\text{dam}}^{p},\mathbf{A}_{\text{m}}^{[0,p-1]}\right.}\left(\mathbf{a}_{\text{m}}^{p}\left|\boldsymbol{\theta}_{\text{dam}}^{p},\mathbf{a}_{\text{m}}^{[0,p-1]}\right.\right)= \\ &\int_{\mathbf{A}_{\text{a}}^{p}} f_{\mathbf{A}_{\text{m}}^{p}\left|\mathbf{A}_{\text{a}}^{p}\right.}\left(\mathbf{a}_{\text{m}}^{p}\left|\mathbf{a}_{\text{a}}^{p}\right.\right)\left[\int_{\boldsymbol{\Theta}_{\text{mat}}} f'_{\mathbf{A}_{\text{a}}^{p}\left|\boldsymbol{\Theta}_{\text{mat}},\boldsymbol{\Theta}_{\text{dam}}^{p}\right.}\left(\mathbf{a}_{\text{a}}^{p}\left|\boldsymbol{\theta}_{\text{mat}},\boldsymbol{\theta}_{\text{dam}}^{p}\right.\right) f_{\boldsymbol{\Theta}_{\text{mat}}}\left(\boldsymbol{\theta}_{\text{mat}}\right) d\boldsymbol{\theta}_{\text{mat}}\right] d\mathbf{a}_{\text{a}}^{p} \end{aligned} \tag{3.29}$$

thereby leading to recast Equation (3.26) as

$$f''_{\boldsymbol{\Theta}^p_{\text{dam}}}\left(\boldsymbol{\theta}^p_{\text{dam}}\right) \propto$$

$$\left\{\int_{\mathbf{A}^p_{\text{a}}} f_{\mathbf{A}^p_{\text{m}}\left|\mathbf{A}^p_{\text{a}}\right.}\left(\mathbf{a}^p_{\text{m}}\left|\mathbf{a}^p_{\text{a}}\right.\right)\left[\int_{\boldsymbol{\Theta}_{\text{mat}}} f'_{\mathbf{A}^p_{\text{a}}\left|\boldsymbol{\Theta}_{\text{mat}},\boldsymbol{\Theta}^p_{\text{dam}}\right.}\left(\mathbf{a}^p_{\text{a}}\left|\boldsymbol{\theta}_{\text{mat}},\boldsymbol{\theta}^p_{\text{dam}}\right.\right) f_{\boldsymbol{\Theta}_{\text{mat}}}\left(\boldsymbol{\theta}_{\text{mat}}\right) d\boldsymbol{\theta}_{\text{mat}}\right] d\mathbf{a}^p_{\text{a}}\right\}\times \qquad (3.30)$$

$$f'_{\boldsymbol{\Theta}^p_{\text{dam}}}\left(\boldsymbol{\theta}^p_{\text{dam}}\right)$$

or, in a more compact way, as

$$f''_{\boldsymbol{\Theta}^p_{\text{dam}}}\left(\boldsymbol{\theta}^p_{\text{dam}}\right) \propto \left[\int_{\mathbf{A}^p_{\text{a}}} f_{\mathbf{A}^p_{\text{m}}\left|\mathbf{A}^p_{\text{a}}\right.}\left(\mathbf{a}^p_{\text{m}}\left|\mathbf{a}^p_{\text{a}}\right.\right) f'_{\mathbf{A}^p_{\text{a}}\left|\boldsymbol{\Theta}^p_{\text{dam}}\right.}\left(\mathbf{a}^p_{\text{a}}\left|\boldsymbol{\theta}^p_{\text{dam}}\right.\right) d\mathbf{a}^p_{\text{a}}\right] f'_{\boldsymbol{\Theta}^p_{\text{dam}}}\left(\boldsymbol{\theta}^p_{\text{dam}}\right) \qquad (3.31)$$

Furthermore, as already shown in Equation (3.21), the term $f_{\mathbf{A}^p_{\text{m}}\left|\mathbf{A}^p_{\text{a}}\right.}\left(\mathbf{a}^p_{\text{m}}\left|\mathbf{a}^p_{\text{a}}\right.\right)$ can be expressed in the following way:

$$f_{\mathbf{A}^p_{\text{m}}\left|\mathbf{A}^p_{\text{a}}\right.}\left(\mathbf{a}^p_{\text{m}}\left|\mathbf{a}^p_{\text{a}}\right.\right) = \prod_{i=1}^{n^p_{\text{L}}} \prod_{j=1}^{n^{(i,p)}_{\text{DM}}} \prod_{k=1}^{n^{(i,j,p)}_{\text{MS}}} L\left(a^{(i,j,p)}_a \left| a^{(i,j,p)}_{m_k}\right.\right) \qquad (3.32)$$

with the likelihood function $L\left(a^{(i,j,p)}_a \left| a^{(i,j,p)}_{m_k}\right.\right)$ taking the same exact mathematical form shown previously in Equation (3.22) and repeated below for the sake of convenience

$$L\left(a^{(i,j,p)}_a \left| a^{(i,j,p)}_{m_k}\right.\right) = \begin{cases} \tilde{\varphi}\left(a^{(i,j,p)}_{m_k}; \hat{\mu}^{(i,j,p)}_{A_m\left|A_a\right.}, \hat{\sigma}_{\varepsilon_{ij}}\right) \cdot POD\left(a^{(i,j,p)}_a\right) & \text{if } a^{(i,j,p)}_{m_k} > 0 \\ PND\left(a^{(i,j,p)}_a\right) & \text{if } a^{(i,j,p)}_{m_k} = 0 \end{cases} \qquad (3.33)$$

The damage evolution parameter vector $\boldsymbol{\Theta}^p_{\text{dam}}$ (at time t_p) can be written as $\boldsymbol{\Theta}^p_{\text{dam}} = \left\{\boldsymbol{\Theta}^{(i,p)}_{\text{dam}},\, i = 1,\ldots,n^{[0,p]}_{\text{L}}\right\}$, where $\boldsymbol{\Theta}^{(i,p)}_{\text{dam}} = \left\{\boldsymbol{\Theta}^{(i,j,p)}_{\text{dam}},\ j = 1,\ldots,n^{(i,[0,p])}_{\text{DM}}\right\}$ represents the sub-vector collecting the damage evolution parameters used to propagate damage

at the i^{th} damage location. It is assumed in this study that these $n_{\mathrm{L}}^{[0,p]}$ sub-vectors are mutually statistically independent; a reasonable and realistic assumption when the mechanical proprieties of the damageable structural sub-components are primarily governed by imperfections that can randomly occur during the manufacturing process. To provide a practical example related to the research topic of this study, it is well known that the mechanical properties of an adhesive interface are strongly affected by the presence of voids, normally introduced during the manufacturing process, and these voids can randomly occur at any location along the adhesive interface without any particular (or known a priori) degree of statistical dependence. This assumption allows for rewriting Equation (3.26) in the following (mathematically and computationally more convenient) way:

$$\underbrace{f_{\boldsymbol{\Theta}_{\mathrm{dam}}^{(i,p)}\left|\mathbf{A}_{\mathrm{m}}^{(i,[0,p])}\right.}\left(\boldsymbol{\theta}_{\mathrm{dam}}^{(i,p)}\left|\mathbf{a}_{\mathrm{m}}^{(i,[0,p])}\right.\right)}_{=f''_{\boldsymbol{\Theta}_{\mathrm{dam}}^{(i,p)}}\left(\boldsymbol{\theta}_{\mathrm{dam}}^{(i,p)}\right)} \propto f_{\mathbf{A}_{\mathrm{m}}^{(i,p)}\left|\boldsymbol{\Theta}_{\mathrm{dam}}^{(i,p)},\mathbf{A}_{\mathrm{m}}^{[0,p-1]}\right.}\left(\mathbf{a}_{\mathrm{m}}^{(i,p)}\left|\boldsymbol{\theta}_{\mathrm{dam}}^{(i,p)},\mathbf{a}_{\mathrm{m}}^{(i,[0,p-1])}\right.\right) \underbrace{f_{\boldsymbol{\Theta}_{\mathrm{dam}}^{(i,p)}\left|\mathbf{A}_{\mathrm{m}}^{[0,p-1]}\right.}\left(\boldsymbol{\theta}_{\mathrm{dam}}^{(i,p)}\left|\mathbf{a}_{\mathrm{m}}^{[0,p-1]}\right.\right)}_{=f'_{\boldsymbol{\Theta}_{\mathrm{dam}}^{(i,p)}}\left(\boldsymbol{\theta}_{\mathrm{dam}}^{(i,p)}\right)} \tag{3.34}$$

with $i=1,\ldots,n_{\mathrm{L}}^{[0,p]}$. Furthermore, by taking advantage of the total probability theorem as already done previously in Equation (3.28), the conditional joint PDF $f_{\mathbf{A}_{\mathrm{m}}^{(i,p)}\left|\boldsymbol{\Theta}_{\mathrm{dam}}^{(i,p)},\mathbf{A}_{\mathrm{m}}^{[0,p-1]}\right.}\left(\mathbf{a}_{\mathrm{m}}^{(i,p)}\left|\boldsymbol{\theta}_{\mathrm{dam}}^{(i,p)},\mathbf{a}_{\mathrm{m}}^{(i,[0,p-1])}\right.\right)$ — i.e., the likelihood function of the proposed Bayesian updating scheme in Equation (3.34) — can be expressed as

$$f_{\mathbf{A}_{\mathrm{m}}^{(i,p)}\left|\boldsymbol{\Theta}_{\mathrm{dam}}^{(i,p)},\mathbf{A}_{\mathrm{m}}^{[0,p-1]}\right.}\left(\mathbf{a}_{\mathrm{m}}^{(i,p)}\left|\boldsymbol{\theta}_{\mathrm{dam}}^{(i,p)},\mathbf{a}_{\mathrm{m}}^{(i,[0,p-1])}\right.\right)=$$
$$\int_{\mathbf{A}_{\mathrm{a}}^{(i,p)}} f_{\mathbf{A}_{\mathrm{m}}^{p}\left|\mathbf{A}_{\mathrm{a}}^{(i,p)}\right.}\left(\mathbf{a}_{\mathrm{m}}^{p}\left|\mathbf{a}_{\mathrm{a}}^{(i,p)}\right.\right)\left[\int_{\boldsymbol{\Theta}_{\mathrm{mat}}} f'_{\mathbf{A}_{\mathrm{a}}^{(i,p)}\left|\boldsymbol{\Theta}_{\mathrm{mat}},\boldsymbol{\Theta}_{\mathrm{dam}}^{(i,p)}\right.}\left(\mathbf{a}_{\mathrm{a}}^{(i,p)}\left|\boldsymbol{\theta}_{\mathrm{mat}},\boldsymbol{\theta}_{\mathrm{dam}}^{(i,p)}\right.\right) f_{\boldsymbol{\Theta}_{\mathrm{mat}}}\left(\boldsymbol{\theta}_{\mathrm{mat}}\right) d\boldsymbol{\theta}_{\mathrm{mat}}\right] d\mathbf{a}_{\mathrm{a}}^{(i,p)} \tag{3.35}$$

thereby leading to recast Equation (3.34) as follows:

$$f''_{\boldsymbol{\Theta}_{\text{dam}}^{(i,p)}}\left(\boldsymbol{\theta}_{\text{dam}}^{(i,p)}\right) \propto \left\{\int_{\mathbf{A}_{\text{a}}^{(i,p)}} f_{\mathbf{A}_{\text{m}}^{p}\left|\mathbf{A}_{\text{a}}^{(i,p)}\right.}\left(\mathbf{a}_{\text{m}}^{p}\left|\mathbf{a}_{\text{a}}^{(i,p)}\right.\right)\left[\int_{\boldsymbol{\Theta}_{\text{mat}}} f'_{\mathbf{A}_{\text{a}}^{(i,p)}\left|\boldsymbol{\Theta}_{\text{mat}},\boldsymbol{\Theta}_{\text{dam}}^{(i,p)}\right.}\left(\mathbf{a}_{\text{a}}^{(i,p)}\left|\boldsymbol{\theta}_{\text{mat}},\boldsymbol{\theta}_{\text{dam}}^{(i,p)}\right.\right) f_{\boldsymbol{\Theta}_{\text{mat}}}\left(\boldsymbol{\theta}_{\text{mat}}\right) d\boldsymbol{\theta}_{\text{mat}}\right] d\mathbf{a}_{\text{a}}^{(i,p)}\right\} \times f'_{\boldsymbol{\Theta}_{\text{dam}}^{(i,p)}}\left(\boldsymbol{\theta}_{\text{dam}}^{(i,p)}\right) \tag{3.36}$$

Or, in a more compact way (after carrying out the integration w.r.t. the material model parameter vector, $\boldsymbol{\Theta}_{\text{mat}}$) as

$$f''_{\boldsymbol{\Theta}_{\text{dam}}^{(i,p)}}\left(\boldsymbol{\theta}_{\text{dam}}^{(i,p)}\right) \propto \left[\int_{\mathbf{A}_{\text{a}}^{(i,p)}} f_{\mathbf{A}_{\text{m}}^{p}\left|\mathbf{A}_{\text{a}}^{(i,p)}\right.}\left(\mathbf{a}_{\text{m}}^{p}\left|\mathbf{a}_{\text{a}}^{(i,p)}\right.\right) f'_{\mathbf{A}_{\text{a}}^{(i,p)}\left|\boldsymbol{\Theta}_{\text{dam}}^{(i,p)}\right.}\left(\mathbf{a}_{\text{a}}^{(i,p)}\left|\boldsymbol{\theta}_{\text{dam}}^{(i,p)}\right.\right) d\mathbf{a}_{\text{a}}^{(i,p)}\right] f'_{\boldsymbol{\Theta}_{\text{dam}}^{(i,p)}}\left(\boldsymbol{\theta}_{\text{dam}}^{(i,p)}\right) \tag{3.37}$$

Once the posterior marginal joint PDFs, $f''_{\boldsymbol{\Theta}_{\text{dam}}^{(i,p)}}\left(\boldsymbol{\theta}_{\text{dam}}^{(i,p)}\right)$ (with $i=1,\ldots,n_{\text{L}}^{[0,p]}$), are computed according to the above equation, the full joint PDF of the damage evolution parameter vector can be ideally reconstructed as

$$f''_{\boldsymbol{\Theta}_{\text{dam}}^{p}}\left(\boldsymbol{\theta}_{\text{dam}}^{p}\right) = \prod_{i=1}^{n_{\text{L}}^{[0,p]}} f''_{\boldsymbol{\Theta}_{\text{dam}}^{(i,p)}}\left(\boldsymbol{\theta}_{\text{dam}}^{(i,p)}\right) \tag{3.38}$$

A simple case is hereafter considered in order to prove that Equation (3.31) — i.e., the most general form of the proposed recursive Bayesian updating scheme for repeatedly computing $f''_{\boldsymbol{\Theta}_{\text{dam}}^{p}}\left(\boldsymbol{\theta}_{\text{dam}}^{p}\right)$ every time new NDE results become available — can be reduced to Equation (3.37) when the prior joint PDF of $\boldsymbol{\Theta}_{\text{dam}}^{p}$ can be expressed as

$$f'_{\boldsymbol{\Theta}^{p}_{\text{dam}}}\left(\boldsymbol{\theta}^{p}_{\text{dam}}\right)=\prod_{i=1}^{n_{\text{L}}^{[0,p]}} f'_{\boldsymbol{\Theta}^{(i,p)}_{\text{dam}}}\left(\boldsymbol{\theta}^{(i,p)}_{\text{dam}}\right) \tag{3.39}$$

Suppose, in fact, that in a given structure two damage locations (i.e., $i=1,2$) have been identified and are being monitored through periodic NDE inspections at time $t_0, t_1, t_p, ..., t_{p+1}, ...$. Additionally, assume that the particular NDE technique employed to monitor the structure is capable of providing only a single measurement outcome, at inspection time t_p, at each of the two damage locations, i.e., $\mathbf{a}^{p}_{\text{m}}=\left\{a_m^{(1,1,p)}, a_m^{(2,1,p)}\right\}$, with $p=0,1,2,...$. Furthermore, suppose also that, at each damage location, the same type of damage mechanism (e.g., debonding between to laminated composite adherends) is evolving/developing in time, i.e., $j=1$ at both damage locations. Under these assumptions, the actual damage size/extent vector, $\mathbf{A}^{p}_{\text{a}}$, is expressed as $\mathbf{A}^{p}_{\text{a}}=\left\{A^{(1,1,p)}_{\text{a}}, A^{(2,1,p)}_{\text{a}}\right\}$ and Equation (3.31) can be rewritten as

$$\begin{aligned}
&f''_{\boldsymbol{\Theta}^{(1,1,p)}_{\text{dam}},\boldsymbol{\Theta}^{(2,1,p)}_{\text{dam}}}\left(\boldsymbol{\theta}^{(1,1,p)}_{\text{dam}},\boldsymbol{\theta}^{(2,1,p)}_{\text{dam}}\right)\propto \\
&\left[\int_{A^{(1,1,p)}_{\text{a}}}\int_{A^{(2,1,p)}_{\text{a}}} L\left(a_a^{(1,1,p)}\middle|a_m^{(1,1,p)}\right)L\left(a_a^{(2,1,p)}\middle|a_m^{(2,1,p)}\right)\right. \\
&\left.f'_{A^{(1,1,p)}_{\text{a}},A^{(2,1,p)}_{\text{a}}\left|\boldsymbol{\Theta}^{(1,1,p)}_{\text{dam}},\boldsymbol{\Theta}^{(2,1,p)}_{\text{dam}}\right.}\left(a^{(1,1,p)}_{\text{a}},a^{(2,1,p)}_{\text{a}}\middle|\boldsymbol{\theta}^{(1,1,p)}_{\text{dam}},\boldsymbol{\theta}^{(2,1,p)}_{\text{dam}}\right)da^{(1,1,p)}_{\text{a}}da^{(2,1,p)}_{\text{a}}\right]\times \\
&f'_{\boldsymbol{\Theta}^{(1,1,p)}_{\text{dam}}}\left(\boldsymbol{\theta}^{(1,1,p)}_{\text{dam}}\right)f'_{\boldsymbol{\Theta}^{(2,1,p)}_{\text{dam}}}\left(\boldsymbol{\theta}^{(2,1,p)}_{\text{dam}}\right)
\end{aligned} \tag{3.40}$$

and, by integrating both left and right hand sides of the above equation with respect to $\boldsymbol{\Theta}^{(2,1,p)}_{\text{dam}}$, the following result is obtained:

$$f''_{\boldsymbol{\Theta}_{\text{dam}}^{(1,1,p)}}\left(\boldsymbol{\theta}_{\text{dam}}^{(1,1,p)}\right) \propto$$

$$\left\{\int_{A_{\text{a}}^{(1,1,p)}} L\left(a_a^{(1,1,p)}\middle|a_m^{(1,1,p)}\right)\left[\int_{A_{\text{a}}^{(2,1,p)}} L\left(a_a^{(2,1,p)}\middle|a_m^{(2,1,p)}\right)\right.\right. \tag{3.41}$$

$$\left.\left. f'_{A_{\text{a}}^{(1,1,p)},A_{\text{a}}^{(2,1,p)}\middle|\boldsymbol{\Theta}_{\text{dam}}^{(1,1,p)}}\left(a_{\text{a}}^{(1,1,p)},a_{\text{a}}^{(2,1,p)}\middle|\boldsymbol{\theta}_{\text{dam}}^{(1,1,p)}\right)da_{\text{a}}^{(2,1,p)}\right]da_{\text{a}}^{(1,1,p)}\right\}\times f'_{\boldsymbol{\Theta}_{\text{dam}}^{(1,1,p)}}\left(\boldsymbol{\theta}_{\text{dam}}^{(1,1,p)}\right)$$

Furthermore, the conditional joint PDF $f'_{A_{\text{a}}^{(1,1,p)},A_{\text{a}}^{(2,1,p)}\middle|\boldsymbol{\Theta}_{\text{dam}}^{(1,1,p)}}\left(a_{\text{a}}^{(1,1,p)},a_{\text{a}}^{(2,1,p)}\middle|\boldsymbol{\theta}_{\text{dam}}^{(1,1,p)}\right)$, inside the integral in Equation (3.41) can be expressed as

$$\begin{aligned}&f'_{A_{\text{a}}^{(1,1,p)},A_{\text{a}}^{(2,1,p)}\middle|\boldsymbol{\Theta}_{\text{dam}}^{(1,1,p)}}\left(a_{\text{a}}^{(1,1,p)},a_{\text{a}}^{(2,1,p)}\middle|\boldsymbol{\theta}_{\text{dam}}^{(1,1,p)}\right)=\\&f'_{A_{\text{a}}^{(2,1,p)}\middle|A_{\text{a}}^{(1,1,p)},\boldsymbol{\Theta}_{\text{dam}}^{(1,1,p)}}\left(a_{\text{a}}^{(2,1,p)}\middle|a_{\text{a}}^{(1,1,p)},\boldsymbol{\theta}_{\text{dam}}^{(1,1,p)}\right)\cdot f'_{A_{\text{a}}^{(1,1,p)}\middle|\boldsymbol{\Theta}_{\text{dam}}^{(1,1,p)}}\left(a_{\text{a}}^{(1,1,p)}\middle|\boldsymbol{\theta}_{\text{dam}}^{(1,1,p)}\right)\end{aligned} \tag{3.42}$$

and, by substituting Equation (3.42) into Equation (3.41), the following result is easily obtained:

$$f''_{\boldsymbol{\Theta}_{\text{dam}}^{(1,1,p)}}\left(\boldsymbol{\theta}_{\text{dam}}^{(1,1,p)}\right) \propto$$

$$\left\{\int_{A_{\text{a}}^{(1,1,p)}} L\left(a_a^{(1,1,p)}\middle|a_m^{(1,1,p)}\right) f'_{A_{\text{a}}^{(1,1,p)}\middle|\boldsymbol{\Theta}_{\text{dam}}^{(1,1,p)}}\left(a_{\text{a}}^{(1,1,p)}\middle|\boldsymbol{\theta}_{\text{dam}}^{(1,1,p)}\right)\left[\int_{A_{\text{a}}^{(2,1,p)}} L\left(a_a^{(2,1,p)}\middle|a_m^{(2,1,p)}\right)\right.\right. \tag{3.43}$$

$$\left.\left. f'_{A_{\text{a}}^{(2,1,p)}\middle|A_{\text{a}}^{(1,1,p)},\boldsymbol{\Theta}_{\text{dam}}^{(1,1,p)}}\left(a_{\text{a}}^{(2,1,p)}\middle|a_{\text{a}}^{(1,1,p)},\boldsymbol{\theta}_{\text{dam}}^{(1,1,p)}\right)da_{\text{a}}^{(2,1,p)}\right]da_{\text{a}}^{(1,1,p)}\right\}\times f'_{\boldsymbol{\Theta}_{\text{dam}}^{(1,1,p)}}\left(\boldsymbol{\theta}_{\text{dam}}^{(1,1,p)}\right)$$

It should now be recognized that

$$\begin{aligned}&f''_{A_{\text{a}}^{(2,1,p)}\middle|A_{\text{a}}^{(1,1,p)},\boldsymbol{\Theta}_{\text{dam}}^{(1,1,p)}}\left(a_{\text{a}}^{(2,1,p)}\middle|a_{\text{a}}^{(1,1,p)},\boldsymbol{\theta}_{\text{dam}}^{(1,1,p)}\right)\propto\\&L\left(a_a^{(2,1,p)}\middle|a_m^{(2,1,p)}\right) f'_{A_{\text{a}}^{(2,1,p)}\middle|A_{\text{a}}^{(1,1,p)},\boldsymbol{\Theta}_{\text{dam}}^{(1,1,p)}}\left(a_{\text{a}}^{(2,1,p)}\middle|a_{\text{a}}^{(1,1,p)},\boldsymbol{\theta}_{\text{dam}}^{(1,1,p)}\right)\end{aligned} \tag{3.44}$$

and therefore, Equation (3.43) can be rewritten as

$$f''_{\boldsymbol{\Theta}_{\text{dam}}^{(1,1,p)}}\left(\boldsymbol{\theta}_{\text{dam}}^{(1,1,p)}\right) \propto$$

$$\left\{\int_{A_{\text{a}}^{(1,1,p)}} L\left(a_a^{(1,1,p)}\middle|a_m^{(1,1,p)}\right) f'_{A_{\text{a}}^{(1,1,p)}\middle|\boldsymbol{\Theta}_{\text{dam}}^{(1,1,p)}}\left(a_{\text{a}}^{(1,1,p)}\middle|\boldsymbol{\theta}_{\text{dam}}^{(1,1,p)}\right)\times\right. \tag{3.45}$$

$$\left.\left[\int_{A_{\text{a}}^{(2,1,p)}} f''_{A_{\text{a}}^{(2,1,p)}\middle|A_{\text{a}}^{(1,1,p)},\boldsymbol{\Theta}_{\text{dam}}^{(1,1,p)}}\left(a_{\text{a}}^{(2,1,p)}\middle|a_{\text{a}}^{(1,1,p)},\boldsymbol{\theta}_{\text{dam}}^{(1,1,p)}\right)da_{\text{a}}^{(2,1,p)}\right]da_{\text{a}}^{(1,1,p)}\right\}\times f'_{\boldsymbol{\Theta}_{\text{dam}}^{(1,1,p)}}\left(\boldsymbol{\theta}_{\text{dam}}^{(1,1,p)}\right)$$

Finally, by making use of the fact that (i.e., normality axiom)

$$\int_{A_{\text{a}}^{(2,1,p)}} f''_{A_{\text{a}}^{(2,1,p)}\middle|A_{\text{a}}^{(1,1,p)},\boldsymbol{\Theta}_{\text{dam}}^{(1,1,p)}}\left(a_{\text{a}}^{(2,1,p)}\middle|a_{\text{a}}^{(1,1,p)},\boldsymbol{\theta}_{\text{dam}}^{(1,1,p)}\right)da_{\text{a}}^{(2,1,p)} = 1 \tag{3.46}$$

the following important result is obtained

$$f''_{\boldsymbol{\Theta}_{\text{dam}}^{(1,1,p)}}\left(\boldsymbol{\theta}_{\text{dam}}^{(1,1,p)}\right) \propto$$

$$\left\{\int_{A_{\text{a}}^{(1,1,p)}} L\left(a_a^{(1,1,p)}\middle|a_m^{(1,1,p)}\right) f'_{A_{\text{a}}^{(1,1,p)}\middle|\boldsymbol{\Theta}_{\text{dam}}^{(1,1,p)}}\left(a_{\text{a}}^{(1,1,p)}\middle|\boldsymbol{\theta}_{\text{dam}}^{(1,1,p)}\right)\right\}\times f'_{\boldsymbol{\Theta}_{\text{dam}}^{(1,1,p)}}\left(\boldsymbol{\theta}_{\text{dam}}^{(1,1,p)}\right) \tag{3.47}$$

The same exact procedure can be initiated by integrating both left and right hand sides of Equation (3.40) with respect to $\boldsymbol{\Theta}_{\text{dam}}^{(1,1,p)}$. This alternative process would lead to:

$$f''_{\boldsymbol{\Theta}_{\text{dam}}^{(2,1,p)}}\left(\boldsymbol{\theta}_{\text{dam}}^{(2,1,p)}\right) \propto$$

$$\left\{\int_{A_{\text{a}}^{(2,1,p)}} L\left(a_a^{(2,1,p)}\middle|a_m^{(2,1,p)}\right) f'_{A_{\text{a}}^{(2,1,p)}\middle|\boldsymbol{\Theta}_{\text{dam}}^{(2,1,p)}}\left(a_{\text{a}}^{(2,1,p)}\middle|\boldsymbol{\theta}_{\text{dam}}^{(2,1,p)}\right)\right\}\times f'_{\boldsymbol{\Theta}_{\text{dam}}^{(2,1,p)}}\left(\boldsymbol{\theta}_{\text{dam}}^{(2,1,p)}\right) \tag{3.48}$$

Taking the product of Equations (3.47) and (3.48), and making use of Equation (3.39), allows retrieving the desired final result:

$$
\begin{aligned}
f''_{\boldsymbol{\Theta}_{\text{dam}}^{(1,1,p)},\boldsymbol{\Theta}_{\text{dam}}^{(2,1,p)}}\left(\boldsymbol{\theta}_{\text{dam}}^{(1,1,p)},\boldsymbol{\theta}_{\text{dam}}^{(2,1,p)}\right) &\overset{s.i.}{=} f''_{\boldsymbol{\Theta}_{\text{dam}}^{(1,1,p)}}\left(\boldsymbol{\theta}_{\text{dam}}^{(1,1,p)}\right)\cdot f''_{\boldsymbol{\Theta}_{\text{dam}}^{(2,1,p)}}\left(\boldsymbol{\theta}_{\text{dam}}^{(2,1,p)}\right)\propto \\
&\left\{\int_{A_{\text{a}}^{(1,1,p)}} L\left(a_a^{(1,1,p)}\middle|a_m^{(1,1,p)}\right) f'_{A_{\text{a}}^{(1,1,p)}\middle|\boldsymbol{\Theta}_{\text{dam}}^{(1,1,p)}}\left(a_{\text{a}}^{(1,1,p)}\middle|\boldsymbol{\theta}_{\text{dam}}^{(1,1,p)}\right)\right\}\times \\
&\left\{\int_{A_{\text{a}}^{(2,1,p)}} L\left(a_a^{(2,1,p)}\middle|a_m^{(2,1,p)}\right) f'_{A_{\text{a}}^{(2,1,p)}\middle|\boldsymbol{\Theta}_{\text{dam}}^{(2,1,p)}}\left(a_{\text{a}}^{(2,1,p)}\middle|\boldsymbol{\theta}_{\text{dam}}^{(2,1,p)}\right)\right\}\times \\
&f'_{\boldsymbol{\Theta}_{\text{dam}}^{(1,1,p)},\boldsymbol{\Theta}_{\text{dam}}^{(2,1,p)}}\left(\boldsymbol{\theta}_{\text{dam}}^{(1,1,p)},\boldsymbol{\theta}_{\text{dam}}^{(2,1,p)}\right)
\end{aligned}
\tag{3.49}
$$

Equation (3.49) essentially states that when the prior joint PDF of $\boldsymbol{\Theta}_{\text{dam}}^{(1,1,p)}$ and $\boldsymbol{\Theta}_{\text{dam}}^{(2,1,p)}$ can be written as the product of the marginal PDFs $f'_{\boldsymbol{\Theta}_{\text{dam}}^{(1,1,p)}}\left(\boldsymbol{\theta}_{\text{dam}}^{(1,1,p)}\right)$ and $f'_{\boldsymbol{\Theta}_{\text{dam}}^{(2,1,p)}}\left(\boldsymbol{\theta}_{\text{dam}}^{(2,1,p)}\right)$, then the posterior joint PDF, $f''_{\boldsymbol{\Theta}_{\text{dam}}^{(1,1,p)},\boldsymbol{\Theta}_{\text{dam}}^{(2,1,p)}}\left(\boldsymbol{\theta}_{\text{dam}}^{(1,1,p)},\boldsymbol{\theta}_{\text{dam}}^{(2,1,p)}\right)$, can also be expressed as the product of the two corresponding posterior marginal distributions $f''_{\boldsymbol{\Theta}_{\text{dam}}^{(1,1,p)}}\left(\boldsymbol{\theta}_{\text{dam}}^{(1,1,p)}\right)$ and $f''_{\boldsymbol{\Theta}_{\text{dam}}^{(2,1,p)}}\left(\boldsymbol{\theta}_{\text{dam}}^{(2,1,p)}\right)$. This result can be easily generalized to multiple damage locations and multiple NDE measurements as shown in Equation (3.37).

References

J. An, R. Haftka, and N. Kim, Improving diagnosis from past prognosis in structural health monitoring, *Proc. 52nd AIAA/ASME/ASCE/AHS/ASC Structures, Structural Dynamics, and Materials Conference*, Denver, CO, USA, April 4-7, 2011.

A.P. Berens, NDE reliability analysis, *Metals Handbook*, Vol. 17. 9th ed. ASM International, 689-701, 1989.

T. Chen, An integrated prognostic and diagnostic model for airframes, *Proc. 52nd AIAA/ASME/ASCE/AHS/ASC Structures, Structural Dynamics, and Materials Conference*, Denver, CO, USA, April 4-7, 2011.

J. Ching and Y.-C. Chen, Transitional markov chain monte carlo method for Bayesian model updating, model class selection, and model averaging, *Journal of Engineering Mechanics*, 133(7), 816-832, 2007.

P.G. Heasler, T.T. Taylor, and S.R. Doctor, *Statistically based reevaluation of PISC-II round robin test data*, Report NUREG/CR-5410, U.S. Nuclear Regulatory Commission, Washington, D.C., 1990.

S.S. Kulkarni, and J.D. Achenbach, Structural health monitoring and damage prognosis in fatigue, *Structural Health Monitoring*, 7(1), 37-49, 2008.

M. Kutner, C. Nachtsheim, J. Neter, and W. Li, *Applied linear statistical models*, 5th edition, McGraw-Hill, 2004.

F. Lanza di Scalea, H.M. Matt, I. Bartoli, S. Coccia, G. Park, and C.R. Farrar, Health monitoring of UAV skin-to-spar joints using guided waves and macro fiber composite transducers, *Journal of Intelligent Material Systems and Structures*, 18(4), 373-388, 2007.

K.Y. Lin, J. Du, and D. Rusk, *Structural design methodology based on concepts of uncertainty*, Report NASA/CR-2000-209847, NASA Langley Research Center, Hampton, VA, 2000.

G.A.F. Seber, and A.J. Lee, Linear regression analysis, second edition, Wiley Series in Probability and Statistics, John Wiley & Sons Inc., NJ, 2003.

M.G. Silk, A.M. Stonehamm, and J.A.G. Temple, *The reliability of nondestructive inspection*, Institute of Physics Publishing, 1987.

K. Simola and U. Pulkkinen, Models for non-destructive inspection data, *Reliability Engineering and System Safety*, 60(1), 1-12, 1998.

M. Staat, Sensitivity of and influences on the reliability of an HTR-module primary circuit pressure boundary, *Proc. 12th International Conference on Structural Mechanics in Reactor Technology (SMiRT)*, Amsterdam, The Netherlands, August 1993.

R. Zhang, and S. Mahadevan, Fatigue reliability analysis using non-destructive inspection, *Journal of Structural Engineering*, 127(8), 957-965, 2001.

R. Zheng, and B.R. Ellingwood, Role of non-destructive evaluation in time-dependent reliability analysis, *Structural Safety*, 20(4), 325-339, 1998.

CHAPTER 4

PROBABILISTIC LOAD HAZARD ANALYSIS

4.1. Introduction

The first part of this study (i.e., from Chapter 2 through Chapter 7) focuses on the development of a comprehensive damage prognosis framework for estimating the remaining fatigue life of a lightweight composite unmanned aerial vehicle (UAV) wing. Two types of external actions are considered to contribute significantly to the fatigue-driven damage accumulation in the skin-to-spar adhesive joints of the wing, namely turbulence- and maneuver-induced loads (Wright and Cooper, 2007). The probabilistic characterization of these two loading actions constitutes the objective of the second analytical step of the proposed framework, *namely probabilistic load hazard analysis* (PLHA), and is essential to then performing the damage evolution analysis and assessing the structural integrity of the UAV wing at future time. PLHA is thoroughly described in the subsequent sections of this chapter: Section 4.2 analyzes

the modeling and simulation of turbulence-induced loads, while Section 4.3 discusses the proposed simplified approach to model and simulate maneuver-induced loads acting on an aircraft wing (e.g., a UAV wing). Later, in Chapter 8, the main concepts of PLHA presented in the subsequent sections of this chapter will be generalized and applied to other types of structural systems subjected to different loading scenarios.

4.2. Turbulence-induced aerodynamic loads

Turbulence-induced aerodynamic loads are modeled by directly characterizing the stochasticity of the atmospheric turbulence velocity patches that can be encountered by an aircraft during flight rather than focusing on the pressure load distribution induced by these velocity fields. This approach is dictated by the fact that pressure load distribution (or any other aerodynamic load distribution acting on an aircraft wing) is inherently a response dependent quantity and cannot be modeled as an independent variable. Conversely, the atmospheric turbulence velocity field surrounding the aircraft is reasonably considered as an independent random field. In other words, it is herein assumed that the atmospheric turbulent field is not affected (or modified) by the presence of the aircraft flying through it at high speed. However, this assumption can no longer be used in the PLHA if, in a given study, *aircraft wake turbulence* (http://en.wikipedia.org/wiki/Wake_turbulence) is an important factor and has to be included in the analyses.

Atmospheric turbulence is modeled as a zero-mean, isotropic, stationary (in time), and homogeneous (in space) stochastic Gaussian random velocity field, as discussed in detail by Hoblit (1988), and Van Staveren (2003). Its intensity, associated

with the k^{th} flight segment in the time window $\left[t_p, t_p^{\bar{q}}\right]$ characterized by the parameter vector $\boldsymbol{\Theta}_{\mathrm{F}}^{(k)}$, is a scalar random variable taken as the root mean square (RMS) value of the wind velocity fluctuations. This random quantity, denoted as $\Sigma_{\mathrm{T}}^{(k)}$ in this study, is probabilistically characterized by the conditional PDF

$$f_{\Sigma_{\mathrm{T}}^{(k)}|\boldsymbol{\Theta}_{\mathrm{T}}^{(k)},\boldsymbol{\Theta}_{\mathrm{F}}^{(k)}}\left(\sigma_{\mathrm{T}}^{(k)} \mid \boldsymbol{\theta}_{\mathrm{T}}^{(k)}, \boldsymbol{\theta}_{\mathrm{F}}^{(k)}\right) =$$

$$P_0\left(h^{(k)}\right)\delta\left(\sigma_{\mathrm{T}}^{(k)}\right) + \frac{P_1\left(h^{(k)}\right)}{b_1\left(h^{(k)}\right)}\sqrt{\frac{2}{\pi}}\, e^{-\frac{1}{2}\left(\frac{\sigma_{\mathrm{T}}^{(k)}}{b_1\left(h^{(k)}\right)}\right)^2} + \frac{P_2\left(h^{(k)}\right)}{b_2\left(h^{(k)}\right)}\sqrt{\frac{2}{\pi}}\, e^{-\frac{1}{2}\left(\frac{\sigma_{\mathrm{T}}^{(k)}}{b_2\left(h^{(k)}\right)}\right)^2} \tag{4.1}$$

where $\delta\left(\sigma_{\mathrm{T}}^{(k)}\right)$ denotes the *Dirac delta*, $P_0\left(h^{(k)}\right)$, $P_1\left(h^{(k)}\right)$, $P_2\left(h^{(k)}\right)$, $b_1\left(h^{(k)}\right)$, $b_2\left(h^{(k)}\right)$ are altitude-dependent distribution parameters collected (for each flight segment) in the vector $\boldsymbol{\Theta}_{\mathrm{T}}^{(k)}$ and the additional constraint, $P_0\left(h^{(k)}\right) = 1 - P_1\left(h^{(k)}\right) - P_2\left(h^{(k)}\right)$, is essentially used to guarantee that $f_{\Sigma_{\mathrm{T}}^{(k)}|\boldsymbol{\Theta}_{\mathrm{T}}^{(k)},\boldsymbol{\Theta}_{\mathrm{F}}^{(k)}}\left(\sigma_{\mathrm{T}}^{(k)} \mid \boldsymbol{\theta}_{\mathrm{T}}^{(k)}, \boldsymbol{\theta}_{\mathrm{F}}^{(k)}\right)$ is a proper PDF. Additionally, by simple inspection of Equation (4.1), it is worth noting that $\Sigma_{\mathrm{T}}^{(k)}$ is statistically dependent on $\boldsymbol{\Theta}_{\mathrm{F}}^{(k)}$ exclusively through $h^{(k)}$ (i.e., the altitude of flight during the k^{th} flight segment). The first term on the right-hand-side (RHS) of Equation (4.1), $P_0\left(h^{(k)}\right)\delta\left(\sigma_{\mathrm{T}}^{(k)}\right)$, is normally referred to as *quiet air*, the second one as *non-storm turbulence*, and the third one as *storm turbulence* (Hoblit, 1988). Finally, for illustration purposes, a simple comparison between the turbulence distribution parameters suggested by the Federal Aviation Regulations (FAR) and those derived from flight test data on a Boeing 737 (found in the literature; Rustenburg *et al.*, 1999) is shown in Figure 4.1.

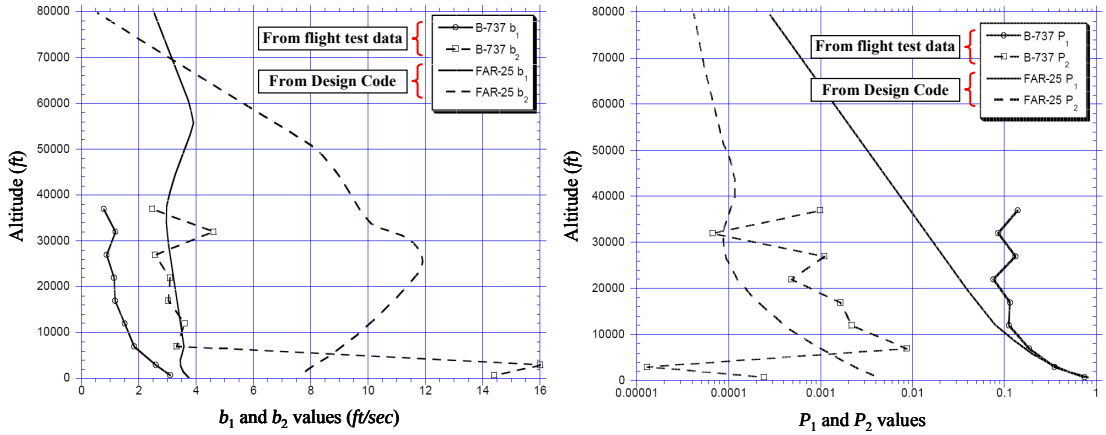

Figure 4.1: Comparison between the turbulence distribution parameters suggested by the Federal Aviation Regulations (FAR) for design purposes and those experimentally derived from flight test data on a Boeing 737 aircraft as found in the literature.

Another essential piece of information for characterizing the intensity measure vector, $\mathbf{IM}_{\mathrm{T}}$, associated with the turbulence-induced loads is provided by the spatial extent, $\Delta S_{\mathrm{T}}^{(k)}$, of the turbulent patches during the k^{th} flight segment. In this study the quantity $\Delta S_{\mathrm{T}}^{(k)}$ is considered as a random variable distributed according to an exponential distribution with mean value (collected in $\mathbf{\Theta}_{\mathrm{T}}^{(k)}$ and possibly dependent on $h^{(k)}$) denoted as $\mu_{\Delta S_{\mathrm{T}}^{(k)}}$. This assumption is well validated through the analysis of some recorded flight data found in the literature (Coleman and Steiner, 1960; Kordes and Love, 1967) as shown in Figure 4.2. For each flight segment in $\left[t_p, t_p^{\bar{q}}\right]$, turbulence intensity ($\Sigma_{\mathrm{T}}^{(k)}$) and the extent of the turbulent patches ($\Delta S_{\mathrm{T}}^{(k)}$) are collected in the turbulence intensity measure vector $\mathbf{IM}_{\mathrm{T}}^{(k)} = \left\{\Sigma_{\mathrm{T}}^{(k)}, \Delta S_{\mathrm{T}}^{(k)}\right\}$. Furthermore, for all the flight segments in the time window $\left[t_p, t_p^{\bar{q}}\right]$, the random quantities $\mathbf{IM}_{\mathrm{T}}^{(k)}$ and $\mathbf{\Theta}_{\mathrm{F}}^{(k)}$ are collected

in the random vectors $\mathbf{IM}_{\mathrm{T}} = \left\{ \mathbf{IM}_{\mathrm{T}}^{(k)},\, k = 1, ..., n_s \right\}$ and $\mathbf{\Theta}_{\mathrm{F}} = \left\{ \mathbf{\Theta}_{\mathrm{F}}^{(k)},\, k = 1, ..., n_s \right\}$, respectively.

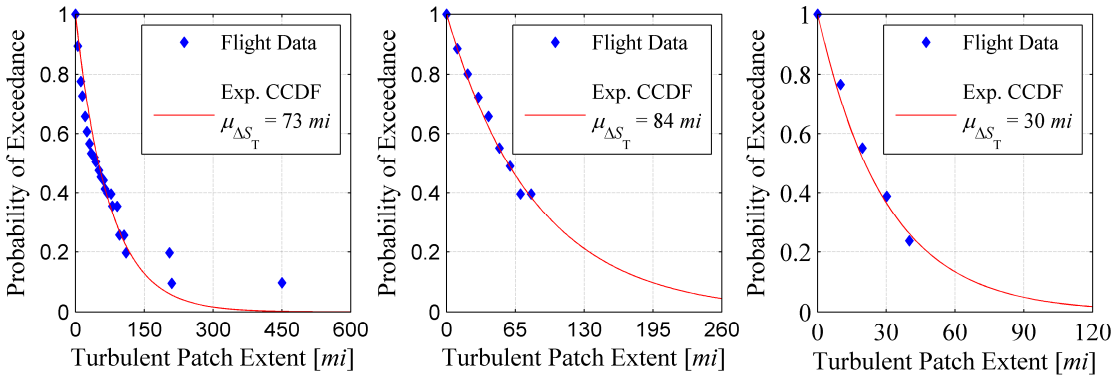

(a) (b) (c)

Figure 4.2: Probability of turbulent patches exceeding a specified extent in different geographical areas (from refs.): (a) From XB-70 flight test data collected in Western USA and altitudes above 40,000 ft, (b) From flight data collected in Southern USA and altitudes above 40,000 ft, (c) From flight data collected in Western Europe and altitudes between 20,000 ft and 40,000 ft. The red lines represent the fitted Exponential complementary cumulative distribution function (CDF).

4.2.1. Proposed approach for the stochastic realization of turbulence intensity sequences along the flight-path

The random sequence of the intensity of the turbulent patches encountered by the aircraft during each of the n_s flight segments in $\left[t_p, t_p^{\bar{q}}\right]$ can be modeled and simulated using homogeneous Poisson rectangular pulse processes with mean rate of occurrence $\lambda_{\mathrm{T}}^{(k)} = 1/\mu_{\Delta S_{\mathrm{T}}^{(k)}}$. Each arrival (in space) of a Poisson event raises a rectangular pulse of random intensity $\Sigma_{\mathrm{T}}^{(k)}$ — according to the conditional PDF $f_{\Sigma_{\mathrm{T}}^{(k)} | \mathbf{\Theta}_{\mathrm{T}}^{(k)}, \mathbf{\Theta}_{\mathrm{F}}^{(k)}} \left(\sigma_{\mathrm{T}}^{(k)} \,|\, \boldsymbol{\theta}_{\mathrm{T}}^{(k)}, \boldsymbol{\theta}_{\mathrm{F}}^{(k)} \right)$ in Equation (4.1) — until the next arrival. An illustrative

example, for a given set of values for $P_1\left(h^{(k)}\right)$, $P_2\left(h^{(k)}\right)$, $b_1\left(h^{(k)}\right)$, $b_2\left(h^{(k)}\right)$, and $\mu_{\Delta s_T^{(k)}}$, is shown in Figure 4.3.

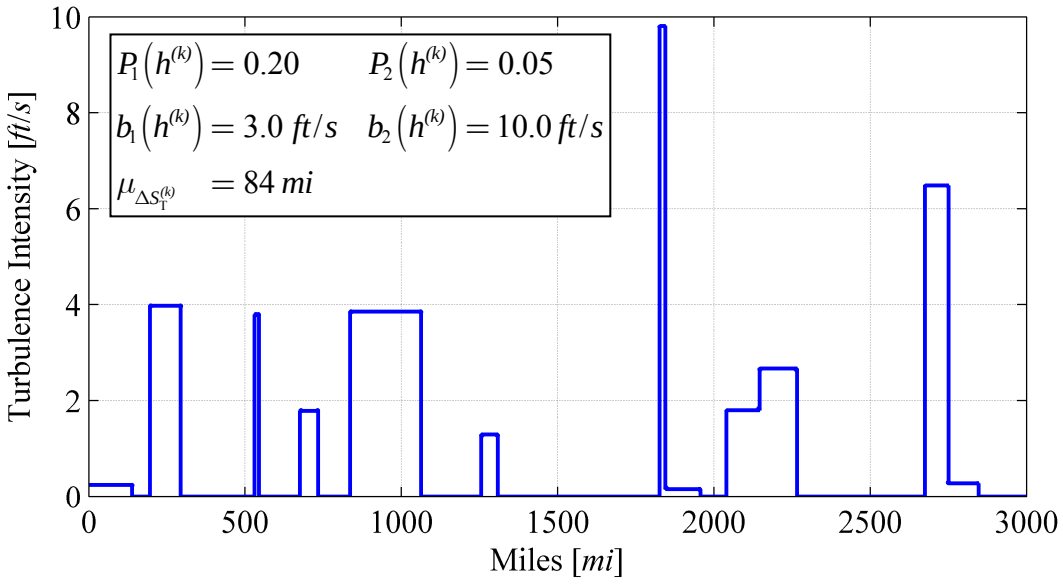

Figure 4.3: Illustrative example of homogeneous Poisson rectangular pulse process used as stochastic model to simulate the sequence of turbulence-induced intensities (within the k^{th} flight segment) for a given set of turbulence distribution parameters and an average turbulence patch extent of 84 miles (i.e., the average extent from flight data collected in Southern USA as shown in Figure 4.2).

Additionally, a generic realization of the random vector $\mathbf{IM}_T$ in $\left[t_p, t_p^{\bar{q}}\right]$ is herein denoted $\mathbf{im}_T = \left\{\mathbf{im}_T^{(k)}, k = 1, ..., n_s\right\}$ where the sub-vector $\mathbf{im}_T^{(k)}$ is defined as $\mathbf{im}_T^{(k)} \triangleq \left\{\mathbf{im}_T^{(k,m)}, m = 1, ..., n_T^{(k)}\right\}$ with (i) $\mathbf{im}_T^{(k,m)} = \left\{\sigma_T^{(k,m)}, \Delta s_T^{(k,m)}\right\}$ denoting the intensity and extent of the m^{th} turbulent patch and (ii) $n_T^{(k)}$ representing the total number of turbulence patches (within the k^{th} flight segment) randomly generated during a generic realization of $\mathbf{IM}_T^{(k)}$. The turbulence intensity, $\sigma_T^{(k,m)}$, is sampled according to the conditional PDF shown in Equation (4.1) while the m^{th} turbulent patch extent, $\Delta s_T^{(k,m)}$, is

drawn from the exponential distribution of $\Delta S_{\mathrm{T}}^{(k)}$ characterized (as mentioned earlier) by the mean value $\mu_{\Delta S_{\mathrm{T}}^{(k)}}$. Finally, for each turbulence velocity intensity, $\sigma_{\mathrm{T}}^{(k,m)}$, randomly sampled as described above, it is then possible to stochastically realize an ensemble of turbulence velocity fields by making use of turbulence velocity spectra. This process is outlined in the next section.

4.2.2. Turbulence velocity spectra

Once an ensemble of turbulence intensity time histories in $\left[t_p, t_p^{\bar{q}}\right]$ is generated, Von Karman or Dryden turbulence velocity spectra (Kim and Hwang, 2004;Van Staveren, 2003) are then used — for each sequence of turbulence intensities characterized by the vector $\mathbf{im}_{\mathrm{T}}$ — to stochastically realize an ensemble of 1-, 2-, or 3-D (spatially correlated) turbulence velocity fields/paths for each turbulence intensity $\sigma_{\mathrm{T}}^{(k,m)}$ (i.e., for each Poisson rectangular pulse) realized in the previous step. These paths are subsequently employed, together with the remaining flight profile information stored in $\mathbf{\Theta}_{\mathrm{F}}$ — e.g., $\left\{\mathbf{V}^{(k)}, k=1,...,n_s\right\}$ and $\left\{T^{(k)}, k=1,...,n_s\right\}$ — to generate the ensemble of time histories of the turbulence-induced loads for each flight segment in $\left[t_p, t_p^{\bar{q}}\right]$. A detailed discussion on this topic is provided by Van Staveren (2003).

4.3. Maneuver-induced aerodynamic loads

As already introduced in Chapter 2, maneuver-induced loads experienced by the UAV wing during the k^{th} flight segment are probabilistically characterized by the vector $\mathbf{IM}_{\mathrm{M}}$. This vector provides the probabilistic characterization of the intensity

and duration of the maneuver-induced loads (acting on the UAV wing) during the time window $\left[t_p, t_p^{\bar{q}}\right]$ — e.g., the increment (w.r.t. the straight-and-level unaccelerated flight conditions) of the aerodynamic lift generated by the aircraft wings during a steady-level banked turn. In this work, since the main focus is on the load-induced stresses at the wing-root and since large angles of attack as well as rapid acrobatic maneuvers are not considered, the intensity of a maneuver-induced load is thus treated, as a perturbation/change (positive or negative) of the aerodynamic lift acting on the UAV wing during straight-and-level unaccelerated flight conditions. The following points describe the random variables used in this study to model and simulate maneuver intensity time histories:

(i) The mean rate of occurrence of maneuvers during the k^{th} flight segment, $\lambda_{\mathrm{M}}^{(k)}$ (collected in $\mathbf{\Theta}_{\mathrm{M}}^{(k)}$ and assumed herein to be a deterministic function of $\mathbf{\Theta}_{\mathrm{F}}^{(k)}$);

(ii) The non-dimensional maneuver load factor (multiplicative of the straight-and-level aerodynamic lift as well as of each mass particle of the wing), $Z_{\mathrm{M}}^{(k)}$, modeled as a random variable and renewed at each occurrence of a maneuver. The condition $Z_{\mathrm{M}} = 1$ thus corresponds to a straight-and-level unaccelerated flight. It is worth noting that the load factor Z_{M} is also applied/multiplied to each mass particle of the wing; consequently, the intensity of the total maneuver-induced load is the sum of the scaled aerodynamic lift

and the scaled self-weight of the wing.

(iii) The maneuver duration, $\Delta T_{\mathrm{M}}^{(k)}$, represented by a random variable (renewed at each occurrence of a maneuver) following an exponential distribution with mean value $\mu_{\Delta T_{\mathrm{M}}^{(k)}}$. As discussed in Chapter 2, all these maneuver-related measures are typically characterized (in probabilistic terms) on the basis of flight data previously collected which make it possible to (i) derive $\lambda_{\mathrm{M}}^{(k)}$ as a function of the altitude of flight, (ii) assign a certain PDF, $f_{Z_{\mathrm{M}}^{(k)}}\left(\zeta_{\mathrm{M}}^{(k)}\right)$, to the maneuver intensity, $Z_{\mathrm{M}}^{(k)}$, and (iii) estimate the mean value, $\mu_{\Delta T_{\mathrm{M}}^{(k)}}$, of the maneuver duration within a given flight segment.

4.3.1. Proposed approach for the stochastic realization of ensembles of maneuver intensity time histories

In this study, the time histories of the maneuver-induced loads are modeled and simulated as censored homogeneous Poisson rectangular pulse processes with mean rate of occurrence $\lambda_{\mathrm{M}}^{(k)}$ for the random arrival in time of the rectangular pulses (Wen, 1990). The sequence of these random processes, covering all n_s flight segments in $\left[t_p, t_p^{\bar{q}}\right]$, is completely characterized by the vector intensity measure $\mathbf{IM}_{\mathrm{M}} = \left\{\mathbf{IM}_{\mathrm{M}}^{(k)}, k = 1, ..., n_s\right\}$ in which the sub-vector $\mathbf{IM}_{\mathrm{M}}^{(k)}$ is defined as $\mathbf{IM}_{\mathrm{M}}^{(k)} = \left\{Z_{\mathrm{M}}^{(k)}, \Delta T_{\mathrm{M}}^{(k)}\right\}$. The random components $Z_{\mathrm{M}}^{(k)}$ and $\Delta T_{\mathrm{M}}^{(k)}$ can be in general

statistically correlated (Wen, 1990) and their statistical parameters — such as the mean value of the maneuver duration, $\mu_{\Delta T_{\mathrm{M}}^{(k)}}$, and the distribution parameters of the PDF $f_{Z_{\mathrm{M}}^{(k)}}\left(\zeta_{\mathrm{M}}^{(k)}\right)$ — are collected (for each flight segment) in the vector $\boldsymbol{\Theta}_{\mathrm{M}} = \left\{\boldsymbol{\Theta}_{\mathrm{M}}^{(k)},\, k = 1, ..., n_s\right\}$. This notation is introduced because the vector $\boldsymbol{\Theta}_{\mathrm{M}}$ is generally dependent on $\boldsymbol{\Theta}_{\mathrm{F}} = \left\{\boldsymbol{\Theta}_{\mathrm{F}}^{(k)},\, k = 1, ..., n_s\right\}$ since (for instance) the intensity and duration of a maneuver can depend on the altitude of flight, $H^{(k)}$, and/or the aircraft velocity, $\mathbf{V}^{(k)}$, as defined in Chapter 2; and both variables are collected in $\boldsymbol{\Theta}_{\mathrm{F}}^{(k)}$. Furthermore, the values of $\lambda_{\mathrm{M}}^{(k)}$ and $\mu_{\Delta T_{\mathrm{M}}^{(k)}}$ estimated from fight data satisfy the condition $p_{Z_{\mathrm{M}}}^{(k)} = \lambda_{\mathrm{M}}^{(k)} \cdot \mu_{\Delta T_{\mathrm{M}}^{(k)}} \leq 1$, where the quantity $p_{Z_{\mathrm{M}}}^{(k)}$ (normally referred to as *probability of selection*) represents the fraction of time (within the k^{th} flight segment) during which the aircraft is maneuvering (i.e., $Z_{\mathrm{M}}^{(k)} \neq 1$). It is worth noting that the limiting case $p_{Z_{\mathrm{M}}}^{(k)} = 1$ — i.e., when $\lambda_{\mathrm{M}}^{(k)} = 1 \big/ \mu_{\Delta T_{\mathrm{M}}^{(k)}}$ — represents a flight segment entirely covered by a continuous sequence of maneuvers.

In light of these considerations, the stochastic modeling and simulation of the maneuver-induced loads, for each of the n_s flight segments in $\left[t_p, t_p^{\bar{q}}\right]$, are performed in two steps. In the first step, an underlying (uncensored) Poisson point process with mean rate of occurrence ($\lambda_{\mathrm{M},u}^{(k)}$) equal to $\lambda_{\mathrm{M},u}^{(k)} = 1 \big/ \mu_{\Delta T_{\mathrm{M}}^{(k)}}$ is defined and each arrival in time of a Poisson event raises a rectangular pulse of intensity $Z_{\mathrm{M}}^{(k)}$, lasting/enduring until the next Poisson arrival. In the second step, only a fraction $p_{Z_{\mathrm{M}}}^{(k)}$ of these

rectangular pulses is randomly selected thereby leading to a censored Poisson process with mean rate of occurrence $\lambda_{\mathrm{M},c}^{(k)} = \lambda_{\mathrm{M},u}^{(k)} \cdot p_{Z_{\mathrm{M}}}^{(k)} = \lambda_{\mathrm{M}}^{(k)}$. Following this approach, the rectangular load pulses do not overlap as illustrated in Figure 4.4.

The two steps described above are automatically realized by using the following mixed PDF for the load intensity $Z_{\mathrm{M}}^{(k)}$ at each Poisson arrival of the underlying (uncensored) Poisson process,

$$\tilde{f}_{Z_{\mathrm{M}}^{(k)}}\left(\zeta_{\mathrm{M}}^{(k)}\right) = \left(1 - p_{Z_{\mathrm{M}}}^{(k)}\right) \cdot \delta\left(\zeta_{\mathrm{M}}^{(k)} - 1\right) + p_{Z_{\mathrm{M}}}^{(k)} \cdot f_{Z_{\mathrm{M}}^{(k)}}\left(\zeta_{\mathrm{M}}^{(k)}\right) \tag{4.2}$$

which expresses that during $\left(1 - p_{Z_{\mathrm{M}}}^{(k)}\right) \times 100\%$ of the time, the load intensity is equal to $Z_{\mathrm{M}}^{(k)} = 1$, corresponding to an aerodynamic lift (for straight-and-level flight) balancing the aircraft's own weight.

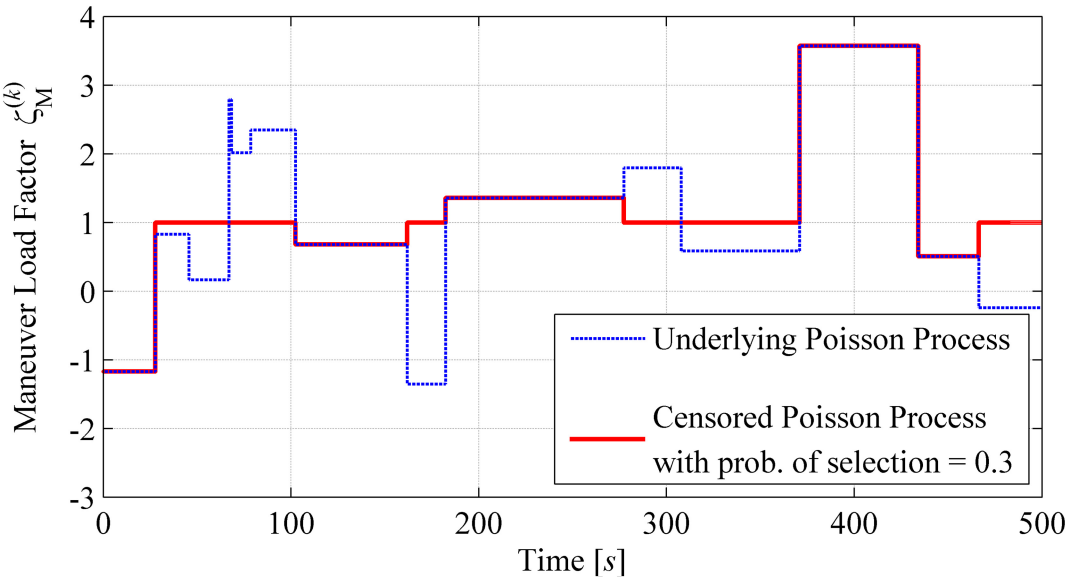

Figure 4.4: Illustration of censored Poisson rectangular pulse process (with mean maneuver duration of 30 s) used to define the intensity of maneuver-induced loads (through a maneuver-induced load factor) within the k^{th} flight segment.

Thus, it is evident that $p_{Z_M}^{(k)}$ controls the sparseness of the pulses in the censored Poisson process. When $p_{Z_M}^{(k)} \ll 1$, the occurrence of a maneuver during the k^{th} flight segment is very unlikely and therefore $Z_M^{(k)} = 1$ for a large fraction $(1 - p_{Z_M}^{(k)})$ of

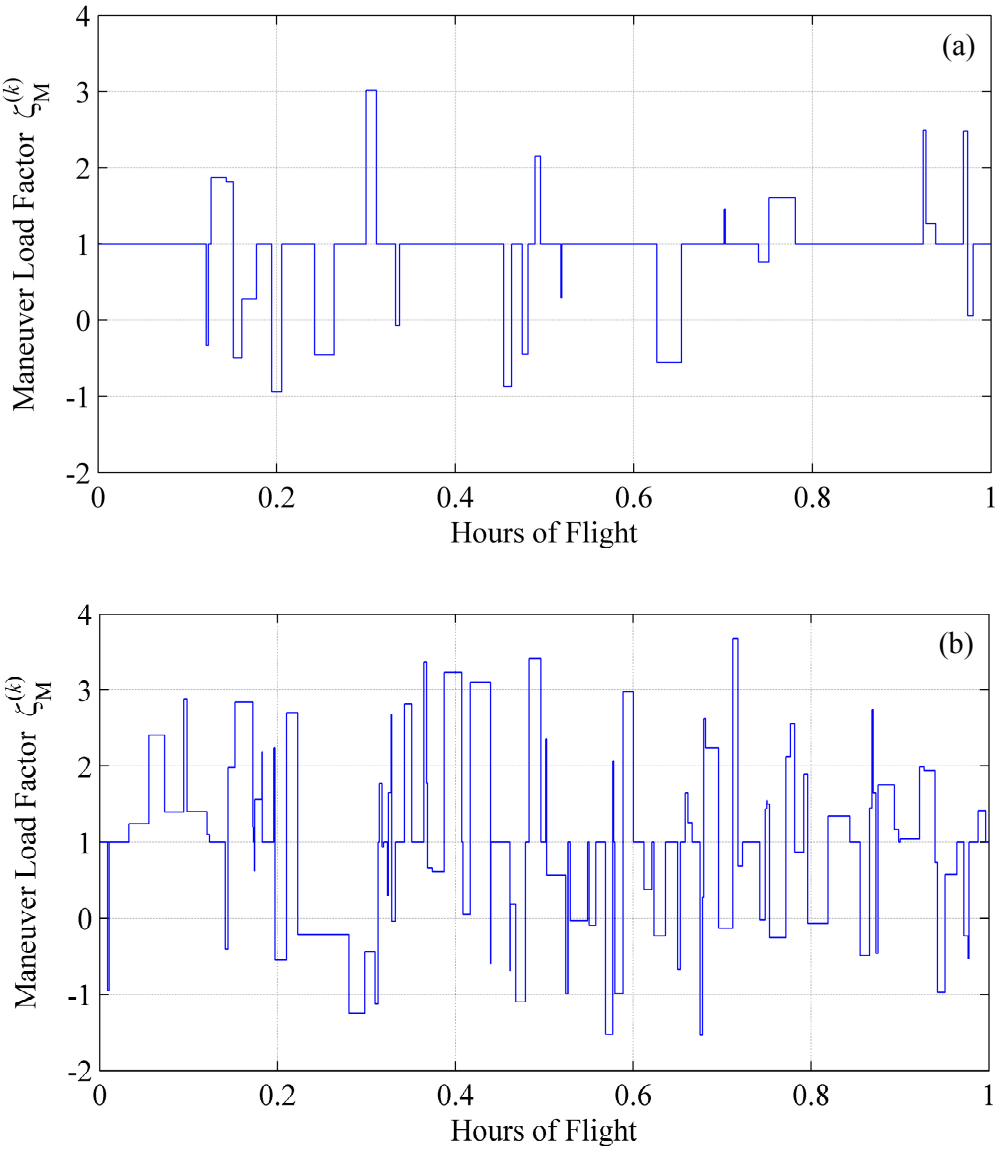

Figure 4.5: Examples of stochastic realizations of maneuver-induced loads (during the k^{th} flight segment) with mean maneuver duration of 30 s and with two different mean rate of occurrence: (a) 20 maneuvers per flight-hour, (b) 80 maneuvers per flight-hour.

the time; this is generally the case for surveillance UAVs. On the other hand, when $p_{Z_M}^{(k)} \gg 0$, the k^{th} flight segment is covered by a dense sequence of maneuvers; and this resembles the typical condition of a fighter aircraft. All these concepts are conceptually illustrated in Figure 4.5 where the maneuver intensity, described by $Z_M^{(k)}$, is assumed (for the sake of simplicity) to be statistically independent of the maneuver duration, and its PDF, $f_{Z_M}^{(k)}\left(\zeta_M^{(k)}\right)$, is modeled using a scaled and shifted Beta distribution, $B(\alpha,\beta)$ (bounded between 0 and 1), as $f_{Z_M}^{(k)}(\zeta) = 6B(2,2) - 2$, where the term $B(2,2)$ is defined as a random variable following a symmetric Beta distribution of parameters $\alpha = 2$ and $\beta = 2$. The maneuver induced load factor $Z_M^{(k)}$ thus lies in the interval $-2.0 \le \zeta_M^{(k)} \le 4.0$ and its mean value is equal to one. This range of the maneuver load factor is consistent with measurements reported in the literature (Allen and Dibley, 2003) and aircraft design provisions (FAR, part 23 and part 25; Air Force MIL-A-8860B) aimed at preventing maneuver-induced structural damage.

Finally, with a notation very similar to the one used previously in this chapter, a generic realization of the random vector $\mathbf{IM}_M$ is denoted $\mathbf{im}_M = \left\{\mathbf{im}_M^{(k)},\, k = 1, ..., n_s\right\}$ where the sub-vector $\mathbf{im}_M^{(k)}$ is defined as $\mathbf{im}_M^{(k)} \triangleq \left\{\mathbf{im}_M^{(k,m)},\, m = 1, ..., n_M^{(k)}\right\}$ with (i) $\mathbf{im}_M^{(k,m)} = \left\{\zeta_M^{(k,m)}, \Delta t_M^{(k)}\right\}$ denoting the intensity and duration of the m^{th} maneuver and (ii) $n_M^{(k)}$ representing the total number of maneuvers (within the k^{th} flight segment) randomly generated in a generic realization of $\mathbf{IM}_M^{(k)}$. The maneuver intensity, $\zeta_M^{(k,m)}$, is sampled according to the PDF shown in Equation (4.2) while the maneuver duration, $\Delta t_M^{(k)}$, is

drawn from the exponential distribution of $\Delta T_{\mathrm{M}}^{(k)}$ characterized by the mean value $\mu_{\Delta T_{\mathrm{M}}^{(k)}}$. Recalling the notation $\mathbf{IM} = \{\mathbf{IM}_{\mathrm{T}}, \mathbf{IM}_{\mathrm{M}}\}$ introduced in Chapter 2, it is easy to realize that $\mathbf{IM} = \mathbf{im}$ essentially fixes a particular realization of the combined turbulence and maneuver-induced load intensities in $\left[t_p, t_p^{\bar{q}}\right]$.

References

Air Force MIL-A-8860B: General specifications for airplane strength and rigidity.

M.J. Allen and R.P. Dibley, *Modeling aircraft wing loads from flight data using neural networks*, NASA/TM-2003-212032, NASA Dryden Flight Research Center, Edwards, California, September 2003.

T.L. Coleman, and R. Steiner, *Atmospheric turbulence measurements obtained from airplanes operations at altitudes between 20,000 and 75,000 feet for several areas in the northern hemisphere*, NASA Langley Research Center, Hampton, Virginia, NASA TN D-548, 1960.

O. Ditlevsen and H.O. Madsen, Stochastic vehicle-queue-load model for large bridges, *Journal of Engineering Mechanics*, 120(9), 1829-1847, 1994.

Federal Aviation Regulations (FAR). Part 23: Airworthiness standards: normal, utility, acrobatic, and commuter category airplanes. Part 25: Airworthiness standards, transport category airplanes.

F.M. Hoblit, *Gust loads on aircraft: concepts and applications*, AIAA Ed. Series, Washington, D.C., 1988.

T.-U. Kim and I.H. Hwang, Reliability analysis of composite wing subjected to gust loads, *Composite Structures*, 66(1-4), 537-531, 2004

E.E. Kordes, and B.J. Love, *Preliminary evaluation of XB-70 airplane encounters with high-altitude turbulence*, NASA Flight Research Center, Edwards, California, NASA TN D-4209, 1967.

C. Lan, H. Li, and J.Ou, Traffic load modeling based on structural health monitoring data, Proc. *International Symposium on Life-Cycle Civil Engineering, IALCCE '08*, Varenna, Lake Como, Italy, June 11-14, 2008.

J. Rustenburg, D. Skinn, D.O. Tipps, *An evaluation of atmospheric continuous turbulence field parameters based on commercial aircraft measurements*, University of Dayton Research Institute, Structural Integrity Division, 1999.

W.H Van Staveren, *Analyses of aircraft responses to atmospheric turbulence*, Ph.D. Dissertation, Department of Aerospace Design, Integration & Operations, Delft University of Technology, The Netherlands, 2003.

Y.-K. Wen, *Structural load modeling and combination for performance and safety evaluation*, Elsevier, 1990.

J Wright and J. Cooper, Introduction *to aircraft aeroelasticity and loads*, John Wiley & Sons Inc., 2007.

CHAPTER 5

PROBABILISTIC STRUCTURAL RESPONSE AND DAMAGE EVOLUTION ANALYSES

5.1. Introduction

This chapter analyzes in detail the third step of the proposed damage prognosis framework, namely *probabilistic structural response analysis* (or, following the notation used later in Chapter 8, *probabilistic damage evolution analysis*), and discusses the use of surrogate modeling techniques to gain computational feasibility. It is worth noting that the theory presented in this chapter refers to the case in which only the joint PDF of the damage sizes is recursively updated after each NDE inspection. However, all derivations can easily be extended to the more general case in which the joint PDF of the damage evolution model parameters is also repeatedly updated. A detailed discussion of the latter, and more general case, is provided in Chapter 8.

5.2. Proposed stochastic damage evolution analysis approach

Once the two types of aerodynamic loads are characterized probabilistically, the joint conditional PDF of the damage extents (at multiple locations) at time $t_p^q = t_p + q\Delta\tau$ (with $q = 1, 2, ..., \overline{q}$), $f_{\mathbf{A}_{\mathrm{a}}^{[p,q]}|\boldsymbol{\Theta}_{\mathrm{mat}},\boldsymbol{\Theta}_{\mathrm{dam}}}\left(\mathbf{a}_{\mathrm{a}}^{[p,q]}\middle|\boldsymbol{\theta}_{\mathrm{mat}},\boldsymbol{\theta}_{\mathrm{dam}}\right)$, is computed through extensive Monte Carlo (MC) simulations during which the random vectors $\mathbf{A}_{\mathrm{a}}^{p}$, $\mathbf{IM}$, and $\boldsymbol{\Theta}_{\mathrm{F}}$ are sampled according to their PDFs — i.e., $f''_{\mathbf{A}_{\mathrm{a}}^{p}|\boldsymbol{\Theta}_{\mathrm{mat}},\boldsymbol{\Theta}_{\mathrm{dam}}}\left(\mathbf{a}_{\mathrm{a}}^{p}\middle|\boldsymbol{\theta}_{\mathrm{mat}},\boldsymbol{\theta}_{\mathrm{dam}}\right)$, $f_{\mathbf{IM}|\boldsymbol{\Theta}_{\mathrm{F}}}\left(\mathbf{im}\middle|\boldsymbol{\theta}_{\mathrm{F}}\right)$, and $f_{\boldsymbol{\Theta}_{\mathrm{F}}}\left(\boldsymbol{\theta}_{\mathrm{F}}\right)$ — in the application of the total probability theorem (TPT) as shown below:

$$\begin{aligned} dP\left[\mathbf{A}_{\mathrm{a}}^{[p,q]}\middle|\boldsymbol{\Theta}_{\mathrm{mat}},\boldsymbol{\Theta}_{\mathrm{dam}}\right] = \int_{\mathbf{A}_{\mathrm{a}}^{p}}\int_{\mathbf{IM}}\int_{\boldsymbol{\Theta}_{\mathrm{F}}} & dP\left[\mathbf{A}_{\mathrm{a}}^{[p,q]}\middle|\boldsymbol{\Theta}_{\mathrm{mat}},\boldsymbol{\Theta}_{\mathrm{dam}},\mathbf{A}_{\mathrm{a}}^{p},\mathbf{IM},\boldsymbol{\Theta}_{\mathrm{F}}\right] \\ & \cdot dP''\left[\mathbf{A}_{\mathrm{a}}^{p}\middle|\boldsymbol{\Theta}_{\mathrm{mat}},\boldsymbol{\Theta}_{\mathrm{dam}}\right]\cdot dP\left[\mathbf{IM}\middle|\boldsymbol{\Theta}_{\mathrm{F}}\right]\cdot dP\left[\boldsymbol{\Theta}_{\mathrm{F}}\right] \end{aligned} \tag{5.1}$$

Equation (5.1) was already introduced and discussed in Chapter 2 and it makes use of the following notation:

$$dP\left[X\right] = P\left[x < X \le x + dx\right] = f_X\left(x\right)dx \tag{5.2}$$

$$dP\left[X,Y\right] = P\left[x < X \le x + dx \cap y < Y \le y + dy\right] = f_{X,Y}\left(x,y\right)dx\,dy \tag{5.3}$$

$$dP\left[X\middle|z\right] = dP\left[X\middle|Z=z\right] = P\left[x < X \le x + dx\middle|Z=z\right] = f_{X|Z}\left(x\middle|z\right)dx \tag{5.4}$$

It is worth noting that the uncertainty of $\mathbf{A}_{\mathrm{a}}^{[p,q]}$ for given/fixed values of $\boldsymbol{\Theta}_{\mathrm{mat}} = \boldsymbol{\theta}_{\mathrm{mat}}$, $\boldsymbol{\Theta}_{\mathrm{dam}} = \boldsymbol{\theta}_{\mathrm{dam}}$, $\mathbf{A}_{\mathrm{a}}^{p} = \mathbf{a}_{\mathrm{a}}^{p}$, $\mathbf{IM} = \mathbf{im}$, and $\boldsymbol{\Theta}_{\mathrm{F}} = \boldsymbol{\theta}_{\mathrm{F}}$ — i.e., the uncertainty quantified by the joint conditional PDF $f_{\mathbf{A}_{\mathrm{a}}^{[p,q]}|\boldsymbol{\Theta}_{\mathrm{mat}},\boldsymbol{\Theta}_{\mathrm{dam}},\mathbf{A}_{\mathrm{a}}^{p},\mathbf{IM},\boldsymbol{\Theta}_{\mathrm{F}}}\left(\mathbf{a}_{\mathrm{a}}^{[p,q]}\middle|\boldsymbol{\theta}_{\mathrm{mat}},\boldsymbol{\theta}_{\mathrm{dam}},\mathbf{a}_{\mathrm{a}}^{p},\mathbf{im},\boldsymbol{\theta}_{\mathrm{F}}\right)$ inside the

integral in Equation (5.1) — rises from the record-to-record variability of the structural response across the ensemble of turbulence paths that can be stochastically realized for a given value of the turbulence intensity $\mathbf{IM}_{\mathrm{T}} = \mathbf{im}_{\mathrm{T}}$ (i.e., for a given/fixed power spectral density representation of the turbulence velocity field for each flight segment; Van Staveren, 2003). The variability of the structural response across the ensemble of the turbulence paths realized adds an additional (nested) layer of uncertainty within this third step of the proposed methodology. Therefore, especially when dealing with a nonlinear structural system, providing the complete probabilistic characterization of the joint conditional PDF, $f_{\mathbf{A}_{\mathrm{a}}^{[p,q]}\left|\boldsymbol{\Theta}_{\mathrm{mat}},\boldsymbol{\Theta}_{\mathrm{dam}},\mathbf{A}_{\mathrm{a}}^{p},\mathbf{IM},\boldsymbol{\Theta}_{\mathrm{F}}\right.}\left(\mathbf{a}_{\mathrm{a}}^{[p,q]}\left|\boldsymbol{\theta}_{\mathrm{mat}},\boldsymbol{\theta}_{\mathrm{dam}},\mathbf{a}_{\mathrm{a}}^{p},\mathbf{im},\boldsymbol{\theta}_{\mathrm{F}}\right.\right)$, becomes a formidable task. Estimating the conditional mean $E_{\mathrm{ens}}\left[\mathbf{a}_{\mathrm{a}}^{[p,q]}\left|\boldsymbol{\theta}_{\mathrm{mat}},\boldsymbol{\theta}_{\mathrm{dam}},\mathbf{a}_{\mathrm{a}}^{p},\mathbf{im},\boldsymbol{\theta}_{\mathrm{F}}\right.\right]$ and the conditional variance $Var_{\mathrm{ens}}\left[\mathbf{a}_{\mathrm{a}}^{[p,q]}\left|\boldsymbol{\theta}_{\mathrm{mat}},\boldsymbol{\theta}_{\mathrm{dam}},\mathbf{a}_{\mathrm{a}}^{p},\mathbf{im},\boldsymbol{\theta}_{\mathrm{F}}\right.\right]$, across the ensemble of turbulence patches stochastically realized, is thus a more realistic and computationally achievable goal. Furthermore, for the case in which only the conditional mean $\overline{\mathbf{a}}_{\mathrm{a}}^{[p,q]} = \overline{\mathbf{a}}_{\mathrm{a}}^{[p,q]}\left(\boldsymbol{\theta}_{\mathrm{mat}},\boldsymbol{\theta}_{\mathrm{dam}},\mathbf{a}_{\mathrm{a}}^{p},\mathbf{im},\boldsymbol{\theta}_{\mathrm{F}}\right) = E_{\mathrm{ens}}\left[\mathbf{a}_{\mathrm{a}}^{[p,q]}\left|\boldsymbol{\theta}_{\mathrm{mat}},\boldsymbol{\theta}_{\mathrm{dam}},\mathbf{a}_{\mathrm{a}}^{p},\mathbf{im},\boldsymbol{\theta}_{\mathrm{F}}\right.\right]$ is estimated and used in the analyses — i.e., when the record-to-record variability of the quantity $\left(\mathbf{a}_{\mathrm{a}}^{[p,q]}\left|\boldsymbol{\theta}_{\mathrm{mat}},\boldsymbol{\theta}_{\mathrm{dam}},\mathbf{a}_{\mathrm{a}}^{p},\mathbf{im},\boldsymbol{\theta}_{\mathrm{F}}\right.\right)$, across the ensemble of turbulence patches stochastically realized, is neglected — the conditional joint PDF inside the integral in Equation (5.1) can be rewritten as

$$f_{\mathbf{A}_{\mathrm{a}}^{[p,q]}\left|\boldsymbol{\Theta}_{\mathrm{mat}},\boldsymbol{\Theta}_{\mathrm{dam}},\mathbf{A}_{\mathrm{a}}^{p},\mathbf{IM},\boldsymbol{\Theta}_{\mathrm{F}}\right.}\left(\mathbf{a}_{\mathrm{a}}^{[p,q]}\left|\boldsymbol{\theta}_{\mathrm{mat}},\boldsymbol{\theta}_{\mathrm{dam}},\mathbf{a}_{\mathrm{a}}^{p},\mathbf{im},\boldsymbol{\theta}_{\mathrm{F}}\right.\right) = \delta\left(\mathbf{a}_{\mathrm{a}}^{[p,q]} - \overline{\mathbf{a}}_{\mathrm{a}}^{[p,q]}\right) \tag{5.5}$$

and Equation (5.1), which represents an application of the TPT within the third analytical step of the proposed damage prognosis methodology, can be simplified as follows:

$$f_{\mathbf{A}_{\mathrm{a}}^{[p,q]}|\boldsymbol{\Theta}_{\mathrm{mat}},\boldsymbol{\Theta}_{\mathrm{dam}}}\left(\mathbf{a}_{\mathrm{a}}^{[p,q]}\middle|\boldsymbol{\theta}_{\mathrm{mat}},\boldsymbol{\theta}_{\mathrm{dam}}\right)= \int_{\mathbf{A}_{\mathrm{a}}^{p}}\int_{\mathbf{IM}}\int_{\boldsymbol{\Theta}_{\mathrm{F}}}\delta\left(\mathbf{a}_{\mathrm{a}}^{[p,q]}-\overline{\mathbf{a}}_{\mathrm{a}}^{[p,q]}\right) f''_{\mathbf{A}_{\mathrm{a}}^{p}|\boldsymbol{\Theta}_{\mathrm{mat}},\boldsymbol{\Theta}_{\mathrm{dam}}}\left(\mathbf{a}_{\mathrm{a}}^{p}\middle|\boldsymbol{\theta}_{\mathrm{mat}},\boldsymbol{\theta}_{\mathrm{dam}}\right) f_{\mathbf{IM}|\boldsymbol{\Theta}_{\mathrm{F}}}\left(\mathbf{im}\middle|\boldsymbol{\theta}_{\mathrm{F}}\right) f_{\boldsymbol{\Theta}_{\mathrm{F}}}\left(\boldsymbol{\theta}_{\mathrm{F}}\right) d\mathbf{a}_{\mathrm{a}}^{p}\, d\mathbf{im}\, d\boldsymbol{\theta}_{\mathrm{F}} \tag{5.6}$$

The quantity $\Delta\tau$, introduced above, is a suitable fixed time interval related to the time-scale of the damage propagation process of interest. For example, 100 to 500 flight-hours for UAVs whose most critical structural components are approaching their expected fatigue life, which is generally of the order of tens of thousands of flight-hours, as reported by the Department of Defense in "*Unmanned aerial vehicles reliability study*, 2003". However, $\Delta\tau$ needs to be sufficiently short and lead to a satisfactory grid of response evaluations in $\left[t_p, t_p^{\bar{q}}\right]$, in order to facilitate the interpolation (i.e., at $t = t_p^{\tilde{q}}$ with $i-1<\tilde{q}<i$ and $i \in \left\{1, 2, ..., \bar{q}\right\}$) and/or the extrapolation (i.e., at $t > t_p^{\bar{q}}$) of the response of the system at different times in the future. This approach aims at providing an accurate and reliable prediction for the trend of the structural response of interest (i.e., the trend of damage evolution) as well as for the trend of the reliability index of the structure. Furthermore, the value of $\bar{q}$ needs to guarantee a sufficiently wide prediction window $\left[t_p, t_p^{\bar{q}}\right]$ thereby making the prognosis results meaningful for the decision making process. To this end, the fatigue-induced debonding evolution process taking place along the skin-to-spar adhesive joints can be simulated

— within the proposed damage prognosis framework — through a mechanics-based damage evolution model (as described by Gobbato *et al.*, 2009) or an empirical damage-growth model — such as the Paris-Erdogan law (Paris and Erdogan,1963) or other similar models (Degrieck and Paepegem,2001; Blanco *et al.*, 2004) — based on linear elastic fracture mechanics (LEFM) principles and experimental observations. In the former case, the use of a cohesive zone model (CZM) was already proposed in several studies analyzing the pseudo-static, and dynamic (i.e., impact-induced and fatigue-induced) delamination and debonding propagation process in laminated composite structures (Nguyen *et al.*, 2001; Alfano and Crisfield, 2001; Tippetts and Hemez, 2005). This modeling approach leads to a damage evolution model fully embedded into the FE model (through special cohesive elements) subjected to the aerodynamic loads described in Chapter 4. The mechanical/material model parameters of the CZM (e.g., mode I and mode II critical fracture energies, maximum normal and tangential cohesive stresses, fatigue degradation parameters) are viewed as random variables and collected in the vector $\boldsymbol{\Theta}_{\text{dam}}$ with joint PDF denoted as $f_{\boldsymbol{\Theta}_{\text{dam}}}\left(\boldsymbol{\theta}_{\text{dam}}\right)$. On the other hand, if an empirical damage-growth model is used, $\boldsymbol{\Theta}_{\text{dam}}$ collects the parameters of that particular model.

5.3. Surrogate modeling of the fatigue-induced damage evolution process

The time domain simulations using the mechanics-based approach, which employs a CZM for discretizing the skin-to-spar adhesive layer, are computationally expensive because of:

(i) The highly nonlinear response of the adhesive joint,

(ii) The highly refined FE mesh needed in proximity of the debonding propagation fronts,

(iii) The much larger — compared to the characteristic time of the dynamics of the UAV wing — timescale of the debonding propagation process along the skin-to-spar adhesive joints.

For this reason, the use of metamodels — such as polynomial response surface models (Myers and Montgomery, 1995), Gaussian Process (GP) models (McFarland, 2008), and Kriging interpolation (Stein, 1999) — has to be considered in order to efficiently compute the joint conditional PDF of the damage extent at time t_p^q, $f_{\mathbf{A}_{\mathrm{a}}^{[p,q]}|\boldsymbol{\Theta}_{\mathrm{mat}},\boldsymbol{\Theta}_{\mathrm{dam}}}\left(\mathbf{a}_{\mathrm{a}}^{[p,q]}\middle|\boldsymbol{\theta}_{\mathrm{mat}},\boldsymbol{\theta}_{\mathrm{dam}}\right)$, i.e., the final outcome of the third step of the proposed methodology. This joint conditional PDF is obtained by computing the quantity $\mathbf{a}_{\mathrm{a}}^{[p,q]}$, through a series of MC simulations (performed using the metamodel) during which the input parameters $\mathbf{a}_{\mathrm{a}}^{p}, \mathbf{im}$, and $\boldsymbol{\theta}_{\mathrm{F}}$ are sampled from their joint PDFs, while the samples from the random parameter vectors $\boldsymbol{\theta}_{\mathrm{mat}}$ and $\boldsymbol{\theta}_{\mathrm{dam}}$ are kept constant from the first damage inspection until the time at which the UAV wing failure probability has exceeded an acceptable threshold (as presented in Chapter 7). The mathematical reason behind this type of approach (within the proposed process of uncertainty propagation) is dictated by the intrinsic non-ergodicity nature of the random variables collected in $\boldsymbol{\theta}_{\mathrm{mat}}$ and $\boldsymbol{\theta}_{\mathrm{dam}}$; an important aspect thoroughly discussed by Der Kiureghian (2005).

Based on previous considerations and following a dimensional analysis approach (Navarro and De Los Rios, 1987; Sanford, 2003) applied to the specific case

studied herein, a possible mathematical form for the metamodel, capable of providing (as output) the average rate of fatigue-induced damage propagation (across the ensemble of the turbulence paths realized) for a given set of the input parameters, is given by

$$E_{\text{ens}}\left[\frac{d}{dt}\left(\mathbf{A}_{\text{a}}^{[p,t]}\middle|\boldsymbol{\theta}_{\text{mat}},\boldsymbol{\theta}_{\text{dam}}^{p},\mathbf{a}_{\text{a}}^{p},\mathbf{im},\boldsymbol{\theta}_{\text{F}}\right)\right]=\mathbf{G}\left(\overline{\mathbf{a}}_{\text{a}}^{[p,t]},\mathbf{v},\zeta_{\text{M}},\sigma_{\text{T}};\boldsymbol{\theta}_{\text{mat}},\boldsymbol{\theta}_{\text{dam}}\right) \tag{5.7}$$

where: (i) $E_{\text{ens}}\left[d\left(\mathbf{A}_{\text{a}}^{[p,t]}\middle|\boldsymbol{\theta}_{\text{mat}},\boldsymbol{\theta}_{\text{dam}}^{p},\mathbf{a}_{\text{a}}^{p},\mathbf{im},\boldsymbol{\theta}_{\text{F}}\right)/dt\right]$ — with dt being a "macro" increment of time expressed in flight-hours — represents the expected rate of damage propagation at time t for fixed values; the vector term $\overline{\mathbf{a}}_{\text{a}}^{[p,t]}$ (of length n_{A}^{p}) represents the conditional expectation of the damage-size vector (at future time $t\geq t_p$) defined as $\overline{\mathbf{a}}_{\text{a}}^{[p,t]}=\ \overline{\mathbf{a}}_{\text{a}}^{[p,t]}\left(\boldsymbol{\theta}_{\text{mat}},\boldsymbol{\theta}_{\text{dam}},\mathbf{a}_{\text{a}}^{p},\mathbf{im},\boldsymbol{\theta}_{\text{F}}\right)=E_{\text{ens}}\left[\mathbf{A}_{\text{a}}^{[p,t]}\middle|\boldsymbol{\theta}_{\text{mat}},\boldsymbol{\theta}_{\text{dam}},\mathbf{a}_{\text{a}}^{p},\mathbf{im},\boldsymbol{\theta}_{\text{F}}\right]$; (ii) the three-component vector $\mathbf{v}$ quantifies the velocity of the mean airstream w.r.t. a reference system fixed to the aircraft; (iii) ζ_{M} defines a particular realization of the maneuver-induced load factor; and (iv) σ_{T} characterizes the intensity of the turbulence field. The general nonlinear mapping $\mathbf{G}\left(\cdot\right):\mathbb{R}^{n_{\text{inp}}}\rightarrow\mathbb{R}_{+}^{n_{\text{A}}^{p}}$ (with $n_{\text{inp}}=n_{\text{A}}^{p}+5+n_{\text{mat}}+n_{\text{dam}}$), between the input and (positive) output real vector spaces, represents the metamodel fitted (through an appropriate and computationally feasible *design of experiments*) over the desired design space for the input parameters using the simulation results from the (physics-based) nonlinear FE model of the UAV wing. Thus, Equation (5.7) states that the average rate of damage propagation, at a given time $t\geq t_p$, is a function

of the current damage extent $\overline{\mathbf{a}}_{\mathrm{a}}^{[p,t]}$, the intensity of the applied external loads (i.e., straight-and-level flight loads, turbulence- and maneuver- induced loads, quantified through the variables $\mathbf{v}$, σ_{T}, and ζ_{M}, respectively), and the material and damage model parameters ($\boldsymbol{\theta}_{\mathrm{mat}}$ and $\boldsymbol{\theta}_{\mathrm{dam}}$). Furthermore, if the condition for mean square differentiability of the random process $\left(\mathbf{A}_{\mathrm{a}}^{[p,t]}\middle|\boldsymbol{\theta}_{\mathrm{mat}},\boldsymbol{\theta}_{\mathrm{dam}}^{p},\mathbf{a}_{\mathrm{a}}^{p},\mathbf{im}\right)$ is satisfied, expectation and differentiation operators can permute, i.e.,

$$\begin{aligned} E_{\mathrm{ens}}\left[\frac{d}{dt}\left(\mathbf{A}_{\mathrm{a}}^{[p,t]}\middle|\boldsymbol{\theta}_{\mathrm{mat}},\boldsymbol{\theta}_{\mathrm{dam}}^{p},\mathbf{a}_{\mathrm{a}}^{p},\mathbf{im},\boldsymbol{\theta}_{\mathrm{F}}\right)\right] &= \frac{d}{dt}E_{\mathrm{ens}}\left[\mathbf{A}_{\mathrm{a}}^{[p,t]}\middle|\boldsymbol{\theta}_{\mathrm{mat}},\boldsymbol{\theta}_{\mathrm{dam}}^{p},\mathbf{a}_{\mathrm{a}}^{p},\mathbf{im},\boldsymbol{\theta}_{\mathrm{F}}\right] \\ &= \frac{d}{dt}\overline{\mathbf{a}}_{\mathrm{a}}^{[p,t]} \end{aligned} \tag{5.8}$$

and Equation (5.7) can now be rewritten as

$$\begin{cases} \dfrac{d}{dt}\overline{\mathbf{a}}_{\mathrm{a}}^{[p,t]} = \mathbf{G}\left(\overline{\mathbf{a}}_{\mathrm{a}}^{[p,t]},\mathbf{v},\zeta_{\mathrm{M}},\sigma_{\mathrm{T}};\boldsymbol{\theta}_{\mathrm{mat}},\boldsymbol{\theta}_{\mathrm{dam}}\right) \\ \overline{\mathbf{a}}_{\mathrm{a}}^{p} = \mathbf{a}_{\mathrm{a}}^{p} \end{cases} \tag{5.9}$$

where $\overline{\mathbf{a}}_{\mathrm{a}}^{p}$ represents the value of the vector $\overline{\mathbf{a}}_{\mathrm{a}}^{[p,t]}$ at time $t=t_p$ and $\mathbf{a}_{\mathrm{a}}^{p}$ is a particular realization of $\mathbf{A}_{\mathrm{a}}^{p}$ according to the posterior joint PDF $f''_{\mathbf{A}_{\mathrm{a}}^{p}|\boldsymbol{\Theta}_{\mathrm{mat}},\boldsymbol{\Theta}_{\mathrm{dam}}}\left(\mathbf{a}_{\mathrm{a}}^{p}\middle|\boldsymbol{\theta}_{\mathrm{mat}},\boldsymbol{\theta}_{\mathrm{dam}}\right)$. Equation (5.9) represents a system of first-order ordinary differential equations that can now be numerically integrated (e.g., by using the 4$^{\mathrm{th}}$ order Runge-Kutta time marching scheme) between current time, t_p, and t_p^q to compute $\overline{\mathbf{a}}_{\mathrm{a}}^{[p,q]}$.

Following this approach, the practical computation of the conditional joint PDF $f_{\mathbf{A}_{\mathrm{a}}^{[p,q]}|\boldsymbol{\Theta}_{\mathrm{mat}},\boldsymbol{\Theta}_{\mathrm{dam}}}\left(\mathbf{a}_{\mathrm{a}}^{[p,q]}\middle|\boldsymbol{\theta}_{\mathrm{mat}},\boldsymbol{\theta}_{\mathrm{dam}}\right)$ (with $q=1,2,...,\overline{q}$) consists of four stages:

(i) In the first stage, a random sample ($\mathbf{a}_{\mathrm{a},1}^{p}, \mathbf{a}_{\mathrm{a},2}^{p}, \ldots, \mathbf{a}_{\mathrm{a},n_{\mathrm{sp}}}^{p}$) from the posterior (i.e., after Bayesian updating) joint conditional PDF, $f''_{\mathbf{A}_{\mathrm{a}}^{p}|\boldsymbol{\Theta}_{\mathrm{mat}},\boldsymbol{\Theta}_{\mathrm{dam}}}\left(\mathbf{a}_{\mathrm{a}}^{p}\middle|\boldsymbol{\theta}_{\mathrm{mat}},\boldsymbol{\theta}_{\mathrm{dam}}\right)$, is generated using, for instance, Markov Chain Monte Carlo (MCMC) simulation techniques (Robert and Casella, 2004) in a computationally efficient sampling-resampling fashion (Smith and Gelfand, 1992; Berzuini *et al.*, 1997; Ching and Chen, 2007);

(ii) In the second stage, a random ensemble of loading time histories, combining both turbulence- and maneuver-induced loads, and covering the entire time window $\left[t_p, t_p^{\bar{q}}\right]$, is realized according to the procedures presented in Chapter 4;

(iii) In the third stage, the evolution in time of the damage extent is computed by integrating (sequentially, segment by segment) Equation (5.9) for each of the n_{sp} realizations of the actual damage size vector generated in the first stage (i.e., $\mathbf{a}_{\mathrm{a},1}^{p}, \mathbf{a}_{\mathrm{a},2}^{p}, \ldots, \mathbf{a}_{\mathrm{a},n_{\mathrm{sp}}}^{p}$) and now combined with the ensemble of loading inputs generated in the second stage; finally,

(iv) In the fourth and final stage, the joint conditional PDF, $f_{\mathbf{A}_{\mathrm{a}}^{[p,q]}|\boldsymbol{\Theta}_{\mathrm{mat}},\boldsymbol{\Theta}_{\mathrm{dam}}}\left(\mathbf{a}_{\mathrm{a}}^{[p,q]}\middle|\boldsymbol{\theta}_{\mathrm{mat}},\boldsymbol{\theta}_{\mathrm{dam}}\right)$, is estimated $\bar{q}$ times (at $t_p^q = t_p + q\Delta\tau$, with $q = 1, 2, ..., \bar{q}$) by evaluating the distribution of $\mathbf{a}_{\mathrm{a}}^{[p,q]}$ on the basis of the ensemble of the predicted paths of the damage evolution in time.

Kernel density estimation (Li and Racine, 2006) can represent a useful tool to perform this fourth and last stage of the proposed probabilistic analysis of damage propagation in time.

These four stages for the computation of $f_{\mathbf{A}_a^{[p,q]}|\boldsymbol{\Theta}_{mat},\boldsymbol{\Theta}_{dam}}\left(\mathbf{a}_a^{[p,q]}\middle|\boldsymbol{\theta}_{mat},\boldsymbol{\theta}_{dam}\right)$ are conceptually illustrated in Figure 5.1 and Figure 5.2 below, for a given and unique combination of damage location (i), damage mechanism (j), and two subsequent NDE inspection times (t_p and t_{p+1}).

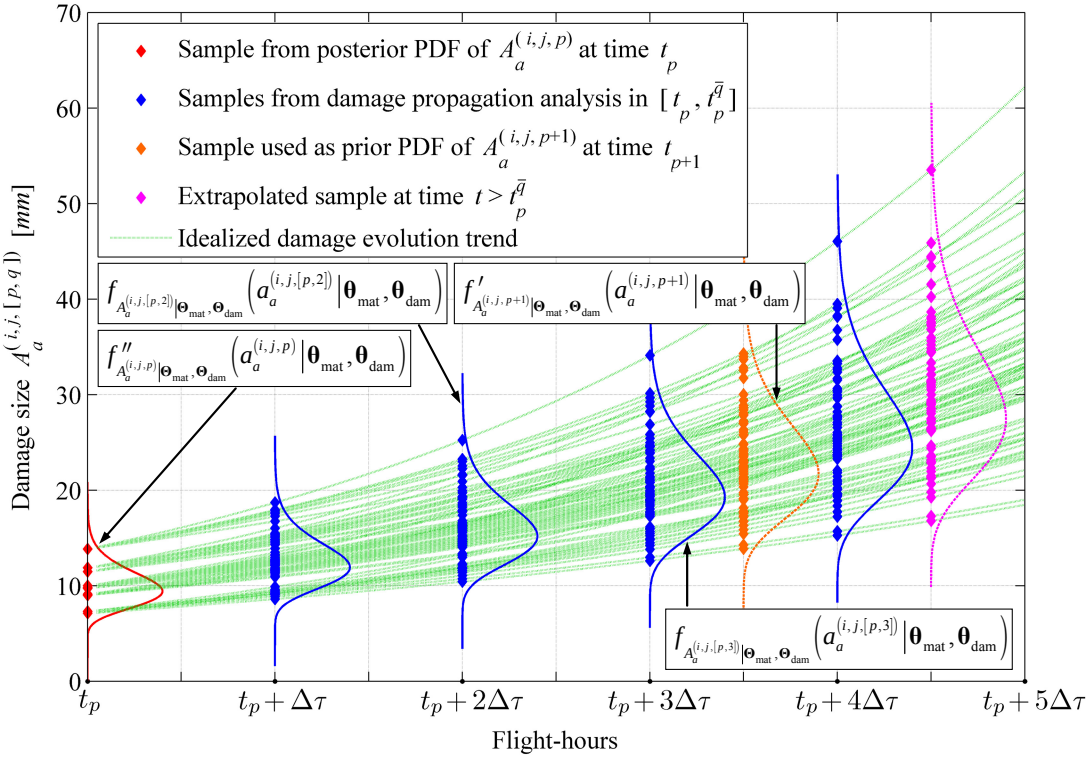

Figure 5.1: Illustrative example of the proposed damage evolution prediction approach for a particular combination of damage location (i), damage mechanism (j) and four evaluations (i.e., $\bar{q}=4$) of the damage-size PDF across the predicted (at time t_p) ensemble of damage sizes.

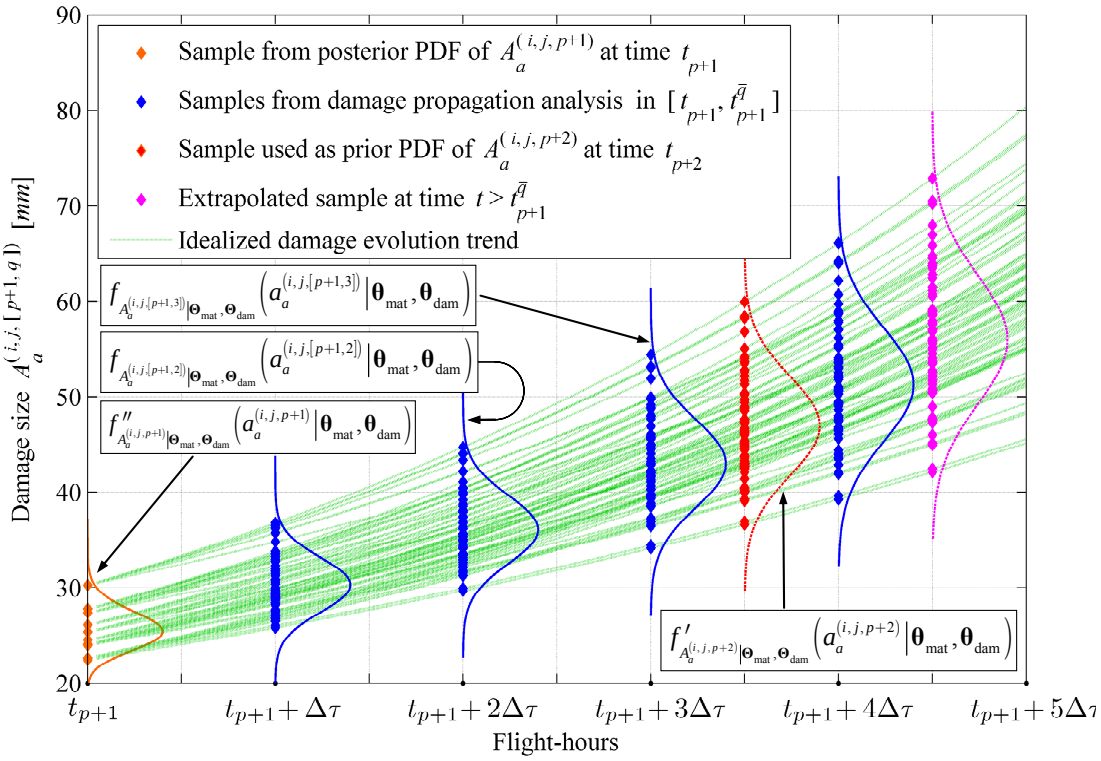

Figure 5.2: Illustrative example of the proposed damage evolution prediction approach for a particular combination of damage location (i), damage mechanism (j) and four evaluations (i.e., $\bar{q}=4$) of the damage-size PDF across the predicted (at time t_{p+1}) ensemble of damage sizes.

Figure 5.1 illustrates how the sample for the damage size $A_a^{(i,j,p)}$, distributed according to the posterior marginal PDF $f''_{A_a^{(i,j,p)}|\boldsymbol{\Theta}_{mat},\boldsymbol{\Theta}_{dam}}\left(a_a^{(i,j,p)}|\boldsymbol{\theta}_{mat},\boldsymbol{\theta}_{dam}\right)$, is propagated in time in order to evaluate, across the ensemble of damage propagation paths generated, the marginal PDF of $A_a^{(i,j,[p,q])}$, herein denoted as $f_{A_a^{(i,j,[p,q])}|\boldsymbol{\Theta}_{mat},\boldsymbol{\Theta}_{dam}}\left(a_a^{(i,j,[p,q])}|\boldsymbol{\theta}_{mat},\boldsymbol{\theta}_{dam}\right)$. Within the proposed framework, this task is performed in a discrete fashion by evaluating the damage size distribution at $t_p^q = t_p + q\Delta\tau$ (for $q=1,2,...,\bar{q}$); the propagated samples and the corresponding PDFs,

evaluated at these (future) instants of time for the particular case in which $\bar{q} = 4$, are represented by the blue diamonds and the blue PDF curves shown in Figures 5.1 and 5.2. These damage propagation results can be extrapolated at instants of time beyond $t_p^{\bar{q}} = t_p + \bar{q}\Delta\tau$ (magenta sample and PDF curve shown in Figures 5.1) or interpolate at any given time between t_p and $t_p^{\bar{q}}$ (orange sample and PDF curve shown in Figure 5.1). The interpolated sample and PDF at time t_{p+1}, shown by the orange diamonds and curve in Figure 5.1, provide the prior probabilistic information — $f'_{A_a^{(i,j,p+1)}|\boldsymbol{\Theta}_{\text{mat}},\boldsymbol{\Theta}_{\text{dam}}}\left(a_a^{(i,j,p+1)}\middle|\boldsymbol{\theta}_{\text{mat}},\boldsymbol{\theta}_{\text{dam}}\right)$ — for the Bayesian inference step to be performed at time t_{p+1} when new NDE measurement results are available. The output of this analysis step, at time t_{p+1}, is given by the posterior sample and PDF of $A_a^{(i,j,p+1)}$, $f''_{A_a^{(i,j,p+1)}|\boldsymbol{\Theta}_{\text{mat}},\boldsymbol{\Theta}_{\text{dam}}}\left(a_a^{(i,j,p+1)}\middle|\boldsymbol{\theta}_{\text{mat}},\boldsymbol{\theta}_{\text{dam}}\right)$, depicted in Figure 5.2. At this point the damage propagation analysis can be repeated in order to provide the PDF of $A_a^{(i,j,[p+1,q])}$ at the instants of time identified as $t_{p+1}^q = t_{p+1} + q\Delta\tau$ (for $q = 1, 2, ..., \bar{q}$). This family of PDFs is herein denoted as $f_{A_a^{(i,j,[p+1,q])}|\boldsymbol{\Theta}_{\text{mat}},\boldsymbol{\Theta}_{\text{dam}}}\left(a_a^{(i,j,[p+1,q])}\middle|\boldsymbol{\theta}_{\text{mat}},\boldsymbol{\theta}_{\text{dam}}\right)$ (with $q = 1, 2, ..., \bar{q}$) and they are shown in Figure 5.2 for the particular case in which $\bar{q} = 4$. These new damage propagation results can be extrapolated at instants of time beyond $t_{p+1}^{\bar{q}} = t_{p+1} + \bar{q}\Delta\tau$ (magenta sample and PDF curve shown in Figure 5.2) or interpolated at any given time between t_{p+1} and $t_{p+1}^{\bar{q}}$ (red sample and PDF curve shown in Figure 5.2). The interpolated sample and its associated PDF at time t_{p+2}, shown by the red

diamonds and curve in Figure 5.2, provide the prior probabilistic information — $f'_{A_a^{(i,j,p+2)}|\boldsymbol{\Theta}_{\text{mat}},\boldsymbol{\Theta}_{\text{dam}}}\left(a_a^{(i,j,p+2)}\middle|\boldsymbol{\theta}_{\text{mat}},\boldsymbol{\theta}_{\text{dam}}\right)$ — for the Bayesian inference step to be performed at time t_{p+2} when another series of new NDE measurement results are available.

References

G. Alfano, and M.A. Crisfield, Finite element interface models for the delamination analysis of laminated composites: mechanical and computational issues, *International Journal for Numerical Methods in Engineering*, 50(7), 1701-1736, 2001.

C. Berzuini, N.G. Best, W.R. Gilks, and C. Larizza, Dynamic conditional independence models and Markov Chain Monte Carlo Methods, *Journal of the American Statistical Association*, 92(440), 1403-1412, 1997.

N. Blanco, E.K. Gamstedt, L.E. Asp, and J. Costa, Mixed-mode delamination growth in carbon-fiber composite laminates under cyclic loading, *International Journal of Solids and Structures*, 41(15), 4219-4235, 2004.

J. Ching and Y.-C. Chen, Transitional markov chain monte carlo method for Bayesian model updating, model class selection, and model averaging, *Journal of Engineering Mechanics*, 133(7), 816-832, 2007.

J. Degrieck, and W.V. Paepegem, Fatigue damage modeling of fibre-reinforced composite materials: Review, *Applied Mechanics Reviews*, 54(4), 279-299, 2001.

A. Der Kiureghian, Non-ergodicity and PEER's framework formula, *Earthquake Engineering & Structural Dynamics*, 34(13), 1643-1652, 2005.

Department of Defense, Office of the Secretary of Defense, *Unmanned aerial vehicles reliability study*, Washington, DC, February 2003.

M. Gobbato, J.P. Conte, J.B. Kosmatka, J.A. Oliver, and C.R. Farrar, Damage prognosis of adhesively-bonded joints in laminated composite structural components of unmanned aerial vehicle, *Proc. COMPDYN 2009 - ECCOMAS*

Thematic Conference on Computational Methods in Structural Dynamics and Earthquake Engineering, Rhodes, Greece, June 22-24, 2009.

Q. Li and J.S. Racine, *Nonparametric econometrics: theory and practice*, Princeton University Press, 2006.

J.M. McFarland, *Uncertainty analysis for computer simulations through validation and calibration*, Ph.D. Thesis, Department of Mechanical Engineering, Vanderbilt University, Nashville, TN, 2008.

R.H. Myers, and D.C. Montgomery, *Response surface methodology*, John Wiley and Sons, Inc., New York, NY, 1995.

A. Navarro and E.R De Los Rios, On dimensional analysis of fatigue crack growth rate and geometrical similitude of cracks, *Fatigue & Fracture of Engineering Materials and Structures*, 9(5), 373-378, 1987.

O. Nguyen, E.A. Repetto, M. Ortiz, and R.A. Radovitzky, A cohesive model of fatigue crack growth, *International Journal of Fracture*, 110(4), 351-369, 2001.

P.C. Paris and F.A. Erdogan, Critical analysis of crack propagation laws, *Journal of Basic Engineering*, TRANS ASME, 85(Series D), 528-534, 1963.

C.P. Robert and G. Casella, *Monte Carlo statistical methods*, Springer, New York, 2004.

R.J. Sanford, *Principles of fracture mechanics*, Prentice Hall, 2003.

A.F.M. Smith and A.E. Gelfand, Bayesian statistics without tears: a sampling-resampling perspective, *The American Statistician*, 46(2), 84-88, 1992.

M.L. Stein, *Statistical interpolation of spatial data: some theory for kriging*, Springer, New York, 1999.

T.B. Tippetts, and F.M. Hemez, Non-linear models of composite laminates, *Proc. 23rd SEM International Modal Analysis Conference (IMAC-XXIII)*, Orlando, FL, USA, January 31 - February 3, 2005.

W.H Van Staveren, *Analyses of aircraft responses to atmospheric turbulence*, Ph.D. Dissertation, Department of Aerospace Design, Integration & Operations, Delft University of Technology, The Netherlands, 2003.

CHAPTER 6

PROBABILISTIC FLUTTER AND LIMIT CYCLE OSCILLATION (LCO) ANALYSES

6.1. Introduction

This chapter describes in detail the fourth analytical step of the damage prognosis framework, namely probabilistic flutter and limit cycle oscillation (LCO) analyses. This step represents the last computational effort — before the subsequent component and system reliability analyses part of the sixth and last step of the methodology — and aims at providing the joint probabilistic information of both, local and global, states of damage at future times. Practically, this fourth step aims at assessing, in probabilistic terms, the overall (global) performance level of the monitored structural systems as damage progresses throughout the most critical damageable sub-components (e.g., the skin-to-spar adhesive joints of a composite

UAV wing). This goal is achieved by probabilistically characterizing a series of global performance measures capable of assessing the structural integrity and the performance level of the structure of interest. As an example, if an aircraft wing represents the structural system of interest, focus can be addressed on its overall aeroelastic behavior/performance as damage progresses in time (Bauchau and Loewy, 1997; Lin and Styuart, 2007; Styuart *et al*., 2008). In the first part of this thesis (i.e., in Chapters 2 through 7), which focuses on the development and applicability of the proposed damage prognosis framework to a composite UAV wing, these global performance measures are selected to be (i) the flutter velocity, and (ii) a set of limit cycle oscillation (LCO) velocities (Safi *et al*., 2002). The evolution in time of all these quantities is probabilistically characterized at discrete (future) times after each NDE inspection — i.e., at $t_p^q = t_p + q\Delta\tau$ with $q = 1, 2, ..., \overline{q}$ — accounting for all the material and damage model parameter uncertainties carried out up to the fourth analytical step of the damage prognosis framework (Pettit, 2006).

As pointed out by Le Meitour *et al*. (2010), the prediction of the flutter onset speed — sometimes referred to as flutter instability boundary (Librescu, 2003) — is fundamental in the aerospace field. The loss of dynamic stability results in unbounded vibrations of the structure and may lead to the failure of the aircraft's primary structural components. When structural and/or aerodynamic nonlinearities are present, the growth in the amplitude of the structural response quantities of interest (e.g., wing-tip vertical displacement) is stabilized to limit cycle oscillations (Lee *et al*., 1999; Librescu *et al*., 2003). These types of phenomena can lead to an excessive fatigue of

the airframe as well as to unacceptable workloads for pilots thereby increasing the risk of incorrectly performing critical tasks (Bunton and Denegri, 1999; Thompson and Strganac, 2000).

Another important nonlinear phenomenon which can affect the global performance of an aeroelastic system is the so-called internal resonance (Thompson and Strganac, 2000). This phenomenon is caused by the nonlinear coupling between different vibration modes and cannot be captured through linear analysis. More precisely, when the frequencies of vibration are nearly proportional to each other (e.g., $\omega_2 \approx 2\omega_1$, $\omega_2 \approx 3\omega_1$, etc.) strong interactions between different modes and a transfer of energy from one mode to the other may occur (Nayfeh and Mook, 1979). These considerations suggest that these modal frequencies are worth monitoring, as damage evolves throughout the structure, in order to prevent any nonlinear coupling phenomena within the range of airspeeds of interest. However, for the sake of simplicity, they are not included in the theoretical treatment presented in this chapter.

To conclude this introduction, it is worth mentioning (as already stated at the beginning of Chapter 5) that the theory and derivations presented in this chapter refer to the case in which only the joint PDF of the damage sizes is recursively updated after each NDE inspection. However, all the derivations discussed in the following sections can easily be extended to the more general case in which the joint PDF of the damage evolution model parameters is also repeatedly updated after each NDE inspection. A detailed discussion of the latter, and more general case, is provided in Section 8.3 in Chapter 8.

6.2. Proposed predictive modeling approach for the derivation of the Joint PDF of local and global states of damage at future times

The fourth step of the proposed damage prognosis methodology uses the results obtained from the damage evolution prediction analysis from time t_p to time t_p^q (with $q = 1, 2, ..., \overline{q}$), for estimating (at future time t_p^q) the joint PDF of (i) the damage size vector $\mathbf{A}_{\mathrm{a}}^{[p,q]}$, (ii) the flutter velocity $V_{\mathrm{F}}^{[p,q]}$ — i.e., the velocity at which the flutter instability boundary is reached — and (iii) the vector of LCO velocities $\mathbf{V}_{\mathrm{LCO}}^{[p,q]}$ — i.e., the velocities at which the considered LCOs reach their respective pre-defined amplitude threshold, beyond which the structural integrity of the UAV wing is compromised. The LCO velocities are computed via aerodynamic analyses performed in the time domain and can potentially be lower — in the case of a damaged wing — than the (linear) flutter velocity (Safi *et al*., 2002). In the proposed framework, these LCO velocities are collected in the random vector $\mathbf{V}_{\mathrm{LCO}}^{[p,q]} = \left\{ V_{\mathrm{LCO}}^{(r,[p,q])},\ r = 1, \ldots, n_{\mathrm{LCO}} \right\}$ and their joint PDF at time t_p^q is denoted by $f_{\mathbf{V}_{\mathrm{LCO}}^{[p,q]}}\left(\mathbf{v}_{\mathrm{LCO}}^{[p,q]}\right)$. The total number of global aeroelastic failure modes considered in this fourth step is therefore equal to $n_{\mathrm{G}} = 1 + n_{\mathrm{LCO}}$ and also represents the dimension of the random vector $\mathbf{V}_{\mathrm{F,LCO}}^{[p,q]} = \left\{ V_{\mathrm{F,LCO}}^{(r,[p,q])},\ r = 1, \ldots, n_{\mathrm{G}} \right\}$ probabilistically characterized by the joint PDF $f_{\mathbf{V}_{\mathrm{F,LCO}}^{[p,q]}}\left(\mathbf{v}_{\mathrm{F,LCO}}^{[p,q]}\right)$. The random flutter velocity $V_{\mathrm{F}}^{[p,q]}$ and the random vector $\mathbf{V}_{\mathrm{LCO}}^{[p,q]}$ are clearly statistically dependent and also dependent on the (numerically predicted) damage size vector $\mathbf{A}_{\mathrm{a}}^{[p,q]}$.

The (ideal) final outcome of this step is represented by the joint PDF, $f_{\mathbf{D}_{\mathrm{L,G}}^{[p,q]}}\left(\mathbf{d}_{\mathrm{L,G}}^{[p,q]}\right) = f_{\mathbf{A}_{\mathrm{a}}^{[p,q]},\mathbf{V}_{\mathrm{F,LCO}}^{[p,q]}}\left(\mathbf{a}_{\mathrm{a}}^{[p,q]}, \mathbf{v}_{\mathrm{F,LCO}}^{[p,q]}\right)$, of the random vector $\mathbf{D}_{\mathrm{L,G}}^{[p,q]} = \left\{\mathbf{A}_{\mathrm{a}}^{[p,q]}, \mathbf{V}_{\mathrm{F,LCO}}^{[p,q]}\right\}$. This joint PDF can be obtained through two sub-steps. In the first sub-step, the joint conditional PDF $f_{\mathbf{V}_{\mathrm{F,LCO}}^{[p,q]}\left|\mathbf{A}_{\mathrm{a}}^{[p,q]},\boldsymbol{\Theta}_{\mathrm{mat}},\boldsymbol{\Theta}_{\mathrm{dam}}\right.}\left(\mathbf{v}_{\mathrm{F,LCO}}^{[p,q]}\left|\mathbf{a}_{\mathrm{a}}^{[p,q]}, \boldsymbol{\theta}_{\mathrm{mat}}, \boldsymbol{\theta}_{\mathrm{dam}}\right.\right)$ is numerically estimated by performing multiple flutter and LCO analyses — each of them for a fixed realization of (i) the predicted (during the probabilistic structural response and damage evolution analysis) damage size vector $\mathbf{a}_{\mathrm{a}}^{[p,q]}$, and (ii) the vectors $\boldsymbol{\theta}_{\mathrm{mat}}$ and $\boldsymbol{\theta}_{\mathrm{dam}}$ sampled from their PDFs $f_{\boldsymbol{\Theta}_{\mathrm{mat}}}\left(\boldsymbol{\theta}_{\mathrm{mat}}\right)$ and $f_{\boldsymbol{\Theta}_{\mathrm{dam}}}\left(\boldsymbol{\theta}_{\mathrm{dam}}\right)$ at the time of the first NDE inspection as mentioned earlier in Chapter 5 (Der Kiureghian, 2005). In the second sub-step, the unconditional joint PDF of $\mathbf{D}_{\mathrm{L,G}}^{[p,q]}$ is computed as

$$f_{\mathbf{D}_{\mathrm{L,G}}^{[p,q]}}\left(\mathbf{d}_{\mathrm{L,G}}^{[p,q]}\right) = f_{\mathbf{A}_{\mathrm{a}}^{[p,q]},\mathbf{V}_{\mathrm{F,LCO}}^{[p,q]}}\left(\mathbf{a}_{\mathrm{a}}^{[p,q]}, \mathbf{v}_{\mathrm{F,LCO}}^{[p,q]}\right) = f_{\mathbf{V}_{\mathrm{F,LCO}}^{[p,q]}\left|\mathbf{A}_{\mathrm{a}}^{[p,q]}\right.}\left(\mathbf{v}_{\mathrm{F,LCO}}^{[p,q]}\left|\mathbf{a}_{\mathrm{a}}^{[p,q]}\right.\right) \cdot f_{\mathbf{A}_{\mathrm{a}}^{[p,q]}}\left(\mathbf{a}_{\mathrm{a}}^{[p,q]}\right) \quad (6.1)$$

where the term $f_{\mathbf{V}_{\mathrm{F,LCO}}^{[p,q]}\left|\mathbf{A}_{\mathrm{a}}^{[p,q]}\right.}\left(\mathbf{v}_{\mathrm{F,LCO}}^{[p,q]}\left|\mathbf{a}_{\mathrm{a}}^{[p,q]}\right.\right)$ is derived as

$$f_{\mathbf{V}_{\mathrm{F,LCO}}^{[p,q]}\left|\mathbf{A}_{\mathrm{a}}^{[p,q]}\right.}\left(\mathbf{v}_{\mathrm{F,LCO}}^{[p,q]}\left|\mathbf{a}_{\mathrm{a}}^{[p,q]}\right.\right) = \int_{\boldsymbol{\Theta}_{\mathrm{mat}}}\int_{\boldsymbol{\Theta}_{\mathrm{dam}}} f_{\mathbf{V}_{\mathrm{F,LCO}}^{[p,q]}\left|\mathbf{A}_{\mathrm{a}}^{[p,q]},\boldsymbol{\Theta}_{\mathrm{mat}},\boldsymbol{\Theta}_{\mathrm{dam}}\right.}\left(\mathbf{v}_{\mathrm{F,LCO}}^{[p,q]}\left|\mathbf{a}_{\mathrm{a}}^{[p,q]}, \boldsymbol{\theta}_{\mathrm{mat}}, \boldsymbol{\theta}_{\mathrm{dam}}\right.\right) f_{\boldsymbol{\Theta}_{\mathrm{mat}}}\left(\boldsymbol{\theta}_{\mathrm{mat}}\right) f_{\boldsymbol{\Theta}_{\mathrm{dam}}}\left(\boldsymbol{\theta}_{\mathrm{dam}}\right) d\boldsymbol{\theta}_{\mathrm{mat}}\, d\boldsymbol{\theta}_{\mathrm{dam}} \quad (6.2)$$

and the term $f_{\mathbf{A}_{\mathrm{a}}^{[p,q]}}\left(\mathbf{a}_{\mathrm{a}}^{[p,q]}\right)$ can be expressed as

$$f_{\mathbf{A}_{\mathrm{a}}^{[p,q]}}\left(\mathbf{a}_{\mathrm{a}}^{[p,q]}\right) = \int_{\boldsymbol{\Theta}_{\mathrm{mat}}}\int_{\boldsymbol{\Theta}_{\mathrm{dam}}} f_{\mathbf{A}_{\mathrm{a}}^{[p,q]}\left|\boldsymbol{\Theta}_{\mathrm{mat}},\boldsymbol{\Theta}_{\mathrm{dam}}\right.}\left(\mathbf{a}_{\mathrm{a}}^{[p,q]}\left|\boldsymbol{\theta}_{\mathrm{mat}}, \boldsymbol{\theta}_{\mathrm{dam}}\right.\right) f_{\boldsymbol{\Theta}_{\mathrm{mat}}}\left(\boldsymbol{\theta}_{\mathrm{mat}}\right) f_{\boldsymbol{\Theta}_{\mathrm{dam}}}\left(\boldsymbol{\theta}_{\mathrm{dam}}\right) d\boldsymbol{\theta}_{\mathrm{mat}}\, d\boldsymbol{\theta}_{\mathrm{dam}} \quad (6.3)$$

Similarly, the joint marginal PDF of the vector $\mathbf{V}_{\mathrm{F,LCO}}^{[p,q]}$, denoted as $f_{\mathbf{V}_{\mathrm{F,LCO}}^{[p,q]}}\left(\mathbf{v}_{\mathrm{F,LCO}}^{[p,q]}\right)$, can be expressed as

$$f_{\mathbf{V}_{\mathrm{F,LCO}}^{[p,q]}}\left(\mathbf{v}_{\mathrm{F,LCO}}^{[p,q]}\right)=\int_{\mathbf{A}_{\mathrm{a}}^{[p,q]}} f_{\mathbf{V}_{\mathrm{F,LCO}}^{[p,q]}\left|\mathbf{A}_{\mathrm{a}}^{[p,q]}\right.}\left(\mathbf{v}_{\mathrm{F,LCO}}^{[p,q]}\left|\mathbf{a}_{\mathrm{a}}^{[p,q]}\right.\right) f_{\mathbf{A}_{\mathrm{a}}^{[p,q]}}\left(\mathbf{a}_{\mathrm{a}}^{[p,q]}\right) d\mathbf{a}_{\mathrm{a}}^{[p,q]} \tag{6.4}$$

For many practical applications, the joint PDF $f_{\mathbf{D}_{\mathrm{L,G}}^{[p,q]}}\left(\mathbf{d}_{\mathrm{L,G}}^{[p,q]}\right)$ is never fully computed during this fourth step of the damage prognosis methodology. More precisely, if only uni-modal bounds (Ditlevsen, 1996) of the probability of system failure, $P\left[\mathrm{F}_{\mathrm{sys}}^{[p,q]}\right]$ at time t_p^q, have to be determined in the subsequent analytical step of damage prognosis, then: (i) the n_{A}^p marginal PDFs of the individual components of the damage size vector $f_{A_a^{(i,j,[p,q])}}\left(a_a^{(i,j,[p,q])}\right)$, $\forall\ i=1,\ldots,n_{\mathrm{L}}^{[0,p]}$ and $j=1,\ldots,n_{\mathrm{DM}}^{(i,[0,p])}$, (ii) the marginal PDF of the flutter velocity $f_{V_{\mathrm{F}}^{[p,q]}}\left(v_{\mathrm{F}}^{[p,q]}\right)$, and (iii) the n_{LCO} marginal PDFs of the individual LCO velocities, $f_{V_{\mathrm{LCO}}^{(r,[p,q])}}\left(v_{\mathrm{LCO}}^{(r,[p,q])}\right)$, (with $r=1,\ldots,n_{\mathrm{LCO}}$) are sufficient. Conversely, if a better estimation of the reliability index of the UAV wing is needed and bi-modal bounds of $P\left[\mathrm{F}_{\mathrm{sys}}^{[p,q]}\right]$ have to be computed, then in addition to the marginal PDFs mentioned above, the bivariate joint PDFs of all possible pairs of failure modes are needed. These bivariate joint PDFs can characterize two local random quantities (e.g., $A_a^{(i_1,j,[p,q])}$ and $A_a^{(i_2,j,[p,q])}$), a local and a global random quantity (e.g., $A_a^{(i_1,j,[p,q])}$ and $V_{\mathrm{F}}^{[p,q]}$), or two global random quantities (e.g., $V_{\mathrm{F,LCO}}^{(r_1,[p,q])}$ and $V_{\mathrm{F,LCO}}^{(r_2,[p,q])}$ with $r_1, r_2 \in \{1,\ldots,n_{\mathrm{LCO}}\}$ and $r_1 \neq r_2$).

6.3. Surrogate modeling for the efficient computation of flutter and LCO velocities at future times

The use of metamodels is also extremely useful in this step in order to reduce the computational cost of the probabilistic flutter and LCO analyses aimed at determining the joint conditional PDF $f_{\mathbf{V}_{\mathrm{F,LCO}}^{[p,q]}\left|\mathbf{A}_{\mathrm{a}}^{[p,q]},\boldsymbol{\Theta}_{\mathrm{mat}},\boldsymbol{\Theta}_{\mathrm{dam}}\right.}\left(\mathbf{v}_{\mathrm{F,LCO}}^{[p,q]}\left|\mathbf{a}_{\mathrm{a}}^{[p,q]},\boldsymbol{\theta}_{\mathrm{mat}},\boldsymbol{\theta}_{\mathrm{dam}}\right.\right)$. It is well known that flutter and LCO velocities are primarily governed by the stiffness, strength and level of damage of the wing. Additionally, if the air density — which renders the flutter and LCO velocities dependent on $\boldsymbol{\Theta}_{\mathrm{F}}$ through the altitude of flight $H^{(k)}, k=1,...,n_{\mathrm{s}}$ — is considered as a deterministic quantity and assumed (as a simplification) to be independent of $H^{(k)}$ (Wilts, 1957), then a possible mathematical form for the metamodel is given by

$$\overline{\mathbf{v}}_{\mathrm{F,LCO}}^{[p,q]}=\mathbf{Q}\left(\mathbf{a}_{\mathrm{a}}^{[p,q]};\boldsymbol{\theta}_{\mathrm{mat}},\boldsymbol{\theta}_{\mathrm{dam}}\right) \tag{6.5}$$

where the vector $\overline{\mathbf{v}}_{\mathrm{F,LCO}}^{[p,q]}$, defined as $\overline{\mathbf{v}}_{\mathrm{F,LCO}}^{[p,q]}=\left(\mathbf{V}_{\mathrm{F,LCO}}^{[p,q]}\left|\mathbf{A}_{\mathrm{a}}^{[p,q]},\boldsymbol{\Theta}_{\mathrm{mat}},\boldsymbol{\Theta}_{\mathrm{dam}}\right.\right)$, represents the output of the metamodel for a given set of the input parameters ($\mathbf{A}_{\mathrm{a}}^{[p,q]}=\mathbf{a}_{\mathrm{a}}^{[p,q]}$, $\boldsymbol{\Theta}_{\mathrm{mat}}=\boldsymbol{\theta}_{\mathrm{mat}}$, and $\boldsymbol{\Theta}_{\mathrm{dam}}=\boldsymbol{\theta}_{\mathrm{dam}}$), and $\mathbf{Q}(\cdot):\mathbb{R}^{n_{\mathrm{inp}}}\rightarrow\mathbb{R}_{+}^{n_{\mathrm{G}}}$ — with $n_{\mathrm{inp}}=n_{\mathrm{A}}^{p}+n_{\mathrm{mat}}+n_{\mathrm{dam}}$ and $n_{\mathrm{A}}^{p}=\sum_{i=1}^{n_{\mathrm{L}}^{[0,p]}}n_{\mathrm{DM}}^{(i,[0,p])}$ — is a general nonlinear mapping, between the input and (positive) output real vector spaces, representing the metamodel fitted — over the desired design space for the input parameters — by making use of the simulation results from the coupled physics-based finite element (FE) and aerodynamic models of the UAV wing. Furthermore, as a direct consequence of Equation (6.5), the joint

conditional PDF of the vector $\mathbf{V}_{\mathrm{F,LCO}}^{[p,q]}$, $f_{\mathbf{V}_{\mathrm{F,LCO}}^{[p,q]}\left|\mathbf{A}_{\mathrm{a}}^{[p,q]},\boldsymbol{\Theta}_{\mathrm{mat}},\boldsymbol{\Theta}_{\mathrm{dam}}\right.}\left(\mathbf{v}_{\mathrm{F,LCO}}^{[p,q]}\left|\mathbf{a}_{\mathrm{a}}^{[p,q]},\boldsymbol{\theta}_{\mathrm{mat}},\boldsymbol{\theta}_{\mathrm{dam}}\right.\right)$, can be rewritten as

$$f_{\mathbf{V}_{\mathrm{F,LCO}}^{[p,q]}\left|\mathbf{A}_{\mathrm{a}}^{[p,q]},\boldsymbol{\Theta}_{\mathrm{mat}},\boldsymbol{\Theta}_{\mathrm{dam}}\right.}\left(\mathbf{v}_{\mathrm{F,LCO}}^{[p,q]}\left|\mathbf{a}_{\mathrm{a}}^{[p,q]},\boldsymbol{\theta}_{\mathrm{mat}},\boldsymbol{\theta}_{\mathrm{dam}}\right.\right)=\delta\left(\mathbf{v}_{\mathrm{F,LCO}}^{[p,q]}-\overline{\mathbf{v}}_{\mathrm{F,LCO}}^{[p,q]}\right) \tag{6.6}$$

and Equation (6.2) can then be simplified as

$$\begin{aligned} &f_{\mathbf{V}_{\mathrm{F,LCO}}^{[p,q]}\left|\mathbf{A}_{\mathrm{a}}^{[p,q]}\right.}\left(\mathbf{v}_{\mathrm{F,LCO}}^{[p,q]}\left|\mathbf{a}_{\mathrm{a}}^{[p,q]}\right.\right)= \\ &\int_{\boldsymbol{\Theta}_{\mathrm{mat}}}\int_{\boldsymbol{\Theta}_{\mathrm{dam}}}\delta\left(\mathbf{v}_{\mathrm{F,LCO}}^{[p,q]}-\overline{\mathbf{v}}_{\mathrm{F,LCO}}^{[p,q]}\right)f_{\boldsymbol{\Theta}_{\mathrm{mat}}}\left(\boldsymbol{\theta}_{\mathrm{mat}}\right)f_{\boldsymbol{\Theta}_{\mathrm{dam}}}\left(\boldsymbol{\theta}_{\mathrm{dam}}\right)d\boldsymbol{\theta}_{\mathrm{mat}}\,d\boldsymbol{\theta}_{\mathrm{dam}} \end{aligned} \tag{6.7}$$

References

O. A. Bauchau, and R. G. Loewy, *Nonlinear aeroelastic effects in damaged composite aerospace structures*, Technical Report, School of Aerospace Engineering, Georgia Institute of Technology, Atlanta, GA, 1997.

R.W. Bunton and C.M. Denegri, Limit Cycle Oscillation Characteristics of Fighter Aircraft, *Journal of Aircraft*, 37, 916-918 2000.

A. Der Kiureghian, Non-ergodicity and PEER's framework formula, *Earthquake Engineering & Structural Dynamics*, 34(13), 1643-1652, 2005.

O. Ditlevsen and H.O. Madsen, *Structural reliability methods*, Wiley, West Sussex, England, 1996.

J. Le Meitour, D. Lucor, and J.-C. Chassain, Prediction of stochastic limit cycle oscillations using an adaptive Polynomial Chaos method, Journal of Aeroelasticity and Structural Dynamics, 2(1), 3-22, 2010.

B.H.K. Lee, S.J. Prince, and Y.S. Wong, Nonlinear aeroelastic analysis of airfoils: bifurcation and chaos, *Progress in aerospace sciences*, 35, 205-334, 1999.

L. Librescu, G. Chiocchia, and P. Marzocca, Implications of cubic physical aerodynamic non-linearities on the character of the flutter instability boundary, *International journal of Non-Linear Mechanics*, 38, 173-199, 2003.

K. Y. Lin, and A. V. Styuart, Probabilistic approach to damage tolerance design of aircraft composite structures, *Journal of Aircraft*, 44(4), 1309-1317, 2007.

A.H. Nayfeh and D.T. Mook, *Nonlinear oscillations*, John Wiley and Sons, New York, 1979.

C.L. Pettit, Uncertainty and risk in aircraft structures: current status and recommended directions, *International Journal of Materials and Product Technology*, 25(1-3), 211-230, 2006.

S.A. Safi, D.W. Kelly, and R.D. Archer, Interaction between wear processes and limit cycle oscillations of a control surface with free-play nonlinearity, *Proceedings of the Institution of Mechanical Engineers, Part G: Journal of Aerospace Engineering*, 216(3), 143-153, 2002.

A.V Styuart, L. Demasi, E. Liven, and K.Y. Lin, Probabilistic model of the aeroelastic life cycle for risk evaluation of composite structures, *Proc. 49th AIAA/ASME/ASCE/AHS/ASC Structures, Structural Dynamics, and Materials Conference*, Schaumburg, IL, IL, USA, April 7-10, 2008.

D.E. Thompson, Jr. and T.W. Strganac, Store-induced limit cycle oscillations and internal resonances in aeroelastic systems, *Proc. 41st AIAA/ASME/ASCE/AHS/ ASC Structures, Structural Dynamics, and Materials Conference*, Atlanta, GA, USA, April 3-6, 2000.

C.H. Wilts, *Incompressible flutter characteristics of representative aircraft wings*, National advisory committee for aeronautics, NACA TN3780, 1957.

CHAPTER 7

DAMAGE PROGNOSIS ANALYSIS

7.1. Introduction

This chapter concludes the theoretical description and discussion of all five analytical steps of the proposed reliability-based damage prognosis methodology. The Bayesian inference step was covered in Chapter 3; the three steps part of the predictive modeling block (i.e., probabilistic load hazard analysis, probabilistic structural response and damage evolution analysis, and probabilistic flutter and LCO analyses) were analyzed in Chapters 4, 5, and 6, respectively; finally, in this Chapter, the fifth and last analysis step of the methodology, namely *damage prognosis analysis*, is thoroughly examined. A general overview of the proposed reliability assessment procedure, part of this fifth step, is presented in Section 7.2; the component reliability analyses involving local and global failure modes are then illustrated in Sections 7.3 and 7.4, respectively; and finally, the suggested system reliability analyses, used for

the computation/estimation of the probability of failure and false-call at the overall (global) system level, are discussed in Section 7.5.

7.2. Overview of proposed reliability assessment approach

The fifth and final step of the proposed reliability-based SHM framework — namely *damage prognosis analysis* — can be carried out in three sub-steps by (i) using the joint probabilistic information (computed in the previous steps of the methodology as described in Chapters 2 through 6) of the local and global states of damage at time t_p^q, and (ii) defining appropriate limit-state functions for both local and global (aeroelastic) potential failure modes. In this step, the real structural system (i.e., the UAV wing in this first part of the thesis) is abstracted to a collection of reliability components linked together as a combination of series and parallel sub-systems. Each reliability component is associated with a single limit-state (defined by a single mathematical function referred to as limit-state function) and is considered failed when the associated limit-state is reached or exceeded. Thus, component failure does not necessarily represent a physical failure of the UAV wing.

For the case in which uni-modal bounds of the probability of *system failure* are to be determined, the three sub-steps can be described as follows. The first sub-step consists of computing the modal failure probability — for each (local and global) reliability component (or failure mode) considered in the damage prognosis analysis — conditional on the true damage size (for local failure modes) and the flutter or LCO velocities (for global failure modes); i.e., $P\left[\mathrm{F}_{\mathrm{L},ij}^{[p,q]} \middle| \mathbf{a}_{\mathrm{a}}^{[p,q]}\right]$ (with $i = 1, \ldots, n_{\mathrm{L}}^{[0,p]}$ and

$j = 1, \ldots, n_{\mathrm{DM}}^{(i,[0,p])}$) and $P\left[\mathrm{F}_{\mathrm{G},r}^{[p,q]} \middle| \mathbf{v}_{\mathrm{F,LCO}}^{[p,q]}\right]$ (with $r = 1, \ldots, n_{\mathrm{G}}$), respectively. The definition of the local failure event $\mathrm{F}_{\mathrm{L},ij}^{[p,q]}$ involves the marginal PDF of $A_a^{(i,j,[p,q])}$ and, potentially, the fidelity of the NDE technique. Conversely, the definition of the global failure event $\mathrm{F}_{\mathrm{G},r}^{[p,q]}$ considers the uncertainty of the random velocity $V_{\mathrm{F,LCO}}^{(r,[p,q])}$ and, potentially, the variability of the maximum aircraft velocity V_{MAX} (e.g., the maximum diving speed of the aircraft). Hence, the total number of local failure modes is equal to the dimension of the damage size vector $\mathbf{A}_{\mathrm{a}}^{[p,q]}$ (n_{A}^{p}), whereas the total number of global failure modes is equal to the size of the random vector $\mathbf{V}_{\mathrm{F,LCO}}^{[p,q]}$ (denoted earlier as n_{G}). In the second sub-step, the local and global conditional modal failure probabilities computed in the first sub-step are unconditioned w.r.t. $\mathbf{A}_{\mathrm{a}}^{[p,q]}$ and $\mathbf{V}_{\mathrm{F,LCO}}^{[p,q]}$, respectively; and the two outcomes are denoted by $P\left[\mathrm{F}_{\mathrm{L},ij}^{[p,q]}\right]$ (with $i = 1, \ldots, n_{\mathrm{L}}^{[0,p]}$ and $j = 1, \ldots, n_{\mathrm{DM}}^{(i,[0,p])}$) and $P\left[\mathrm{F}_{\mathrm{G},r}^{[p,q]}\right]$ (with $r = 1, \ldots, n_{\mathrm{G}}$). In general, as described in Chapter 3, multiple damage mechanisms can evolve simultaneously at the same damage location, and therefore n_{A}^{p} can be larger than the number of inspected locations up to time t_p, $n_{\mathrm{L}}^{[0,p]}$. Thus, the final number of reliability components (considered in the reliability analysis performed at time t_p) is equal to $n_{\mathrm{L,G}}^{[0,p]} = n_{\mathrm{A}}^{p} + n_{\mathrm{G}}$. Finally, in the third and last sub-step, lower and upper bounds for the probability of *system failure*, denoted $P\left[\mathrm{F}_{\mathrm{sys}}^{[p,q]}\right]$, are computed by considering the UAV wing as a combination of series and parallel sub-systems.

7.3. Local failure modes

The following sub-sections present all the different failure criteria proposed herein and derive the analytical expressions necessary to compute the associated modal probabilities of failure and false-call at the local component level (i.e., for each combination of damage location and damage mechanism). Section 7.3.1 discusses the simplest failure criterion based on the exceedance of a pre-defined critical crack/damage size; Section 7.3.2 introduces an alternative local failure event based on the level-of-safety (LOS) formulation (Lin *et al.*, 2000; Huang and Lin, 2005; Backman, 2005); Section 7.3.3 extends the LOS formulation to the case of multiple NDE measurements; Section 7.3.4 defines and examines the false-call event with a single NDE measurement; finally, Section 7.3.5 extends the derivations of Section 7.3.4 to the case of multiple NDE measurements.

7.3.1. Probability of local component failure, $P\left[\mathbf{F}_{\mathbf{L},ij}^{[p,q]}\right]$, based on the actual damage extent exceeding a pre-defined critical threshold

The simplest (and most logical) local failure event $\mathrm{F}_{\mathrm{L},ij}^{[p,q]}$ — i.e., the failure event (at time t_p^q) associated with the j^{th} detected damage mechanism, evolving at the i^{th} monitored damage location — can be defined as

$$\mathrm{F}_{\mathrm{L},ij}^{[p,q]} \triangleq \left\{ A_a^{(i,j,[p,q])} \geq a_c^{ij} \right\} \tag{7.1}$$

where a_c^{ij} represents a pre-defined critical damage size. It is worth noting that a_c^{ij} generally depends on both damage location and damage mechanism, and its magnitude

is governed by residual strength and damage propagation stability considerations, generally based on coupon test data. Strictly speaking, a_c^{ij} should also be treated as a random variable, but in this study, it is considered deterministic. According to the above definition for $\mathrm{F}_{\mathrm{L},ij}^{[p,q]}$, the conditional modal failure probability $P\left[\mathrm{F}_{\mathrm{L},ij}^{[p,q]}\middle|\mathbf{a}_{\mathrm{a}}^{[p,q]}\right]$ is given by

$$P\left[\mathrm{F}_{\mathrm{L},ij}^{[p,q]}\middle|\mathbf{a}_{\mathrm{a}}^{[p,q]}\right]=P\left[\mathrm{F}_{\mathrm{L},ij}^{[p,q]}\middle|a_a^{(i,j,[p,q])}\right]=\begin{cases}0 & \text{if } a_a^{(i,j,[p,q])}<a_c^{ij}\\ 1 & \text{if } a_a^{(i,j,[p,q])}\geq a_c^{ij}\end{cases} \tag{7.2}$$

and the unconditional modal failure probability is then computed as

$$\begin{aligned}P\left[\mathrm{F}_{\mathrm{L},ij}^{[p,q]}\right]&=\int_0^{+\infty}P\left[\mathrm{F}_{\mathrm{L},ij}^{[p,q]}\middle|a_a^{(i,j,[p,q])}\right]f_{A_a^{(i,j,[p,q])}}\left(a_a^{(i,j,[p,q])}\right)da_a^{(i,j,[p,q])}\\&=\int_{a_c^{ij}}^{+\infty}f_{A_a^{(i,j,[p,q])}}\left(a_a^{(i,j,[p,q])}\right)da_a^{(i,j,[p,q])}=1-F_{A_a^{(i,j,[p,q])}}\left(a_c^{ij}\right)\end{aligned} \tag{7.3}$$

where the term $F_{A_a^{(i,j,[p,q])}}(\cdot)$ represents the cumulative distribution function (CDF) of the random variable $A_a^{(i,j,[p,q])}$.

7.3.2. Probability of local component failure, $P\left[\tilde{\mathbf{F}}_{\mathbf{L},ij}^{[p,q]}\right]$, based on the level-of-safety (LOS) formulation with single NDE inspection opportunity at time $t_p^q=t_p+q\Delta\tau$

Alternative definitions for the local failure event (i.e., local component failure) can be adopted in the proposed framework. For instance, in previous research by Lin *et al.*(2000), Huang and Lin (2005), and Backman (2005), the local failure event $\tilde{\mathrm{F}}_{\mathrm{L},ij}^{[p,q]}$ is defined as

$$\tilde{\mathrm{F}}_{\mathrm{L},ij}^{[p,q]} \triangleq \left\{\left(A_a^{(i,j,[p,q])} \geq a_c^{ij}\right) \cap \left(A_m^{(i,j,[p,q])} < a_c^{ij}\right)\right\} = \left\{\mathrm{F}_{\mathrm{L},ij}^{[p,q]} \cap \left(A_m^{(i,j,[p,q])} < a_c^{ij}\right)\right\} \qquad (7.4)$$

This definition is herein referred to as level-of-safety (LOS) formulation and represents the event that the actual damage size, $A_a^{(i,j,[p,q])}$, is greater than the pre-defined critical damage size (a_c^{ij}), and that the outcome, $A_m^{(i,j,[p,q])}$, of the (assumed) single NDE inspection opportunity at future time t_p^q is lower than a_c^{ij}. This definition of the failure event is illustrated graphically in Figures 7.1, 7.2, and 7.3.

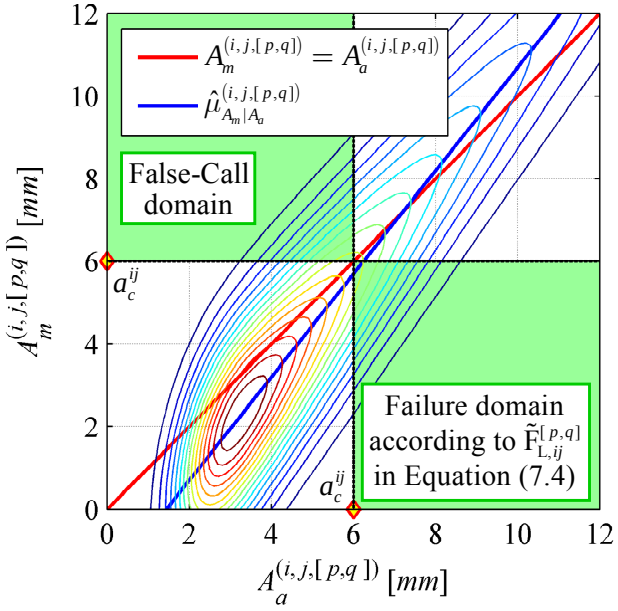

Figure 7.1: Conceptual illustration of the failure and false-call domains according to the (local component) failure and false-call events $\tilde{\mathrm{F}}_{\mathrm{L},ij}^{[p,q]}$ and $\tilde{\mathcal{F}}_{\mathrm{L},ij}^{[p,q]}$, respectively.

According to this alternative failure criterion (at the local component level), the probability of the failure event $\tilde{\mathrm{F}}_{\mathrm{L},ij}^{[p,q]}$, conditional on the true damage size $\mathbf{A}_{\mathrm{a}}^{[p,q]} = \mathbf{a}_{\mathrm{a}}^{[p,q]}$, is given by

$$P\left[\tilde{\mathrm{F}}_{\mathrm{L},ij}^{[p,q]}\middle|\mathbf{a}_{\mathrm{a}}^{[p,q]}\right]=P\left[\tilde{\mathrm{F}}_{\mathrm{L},ij}^{[p,q]}\middle|a_a^{(i,j,[p,q])}\right]=\begin{cases}0 & \text{if } a_a^{(i,j,[p,q])}<a_c^{ij}\\ \overline{\psi}\left(a_a^{(i,j,[p,q])}\right) & \text{if } a_a^{(i,j,[p,q])}\geq a_c^{ij}\end{cases} \tag{7.5}$$

where the function $\overline{\psi}\left(a_a^{(i,j,[p,q])}\right)$ is defined as

$$\overline{\psi}\left(a_a^{(i,j,[p,q])}\right)=1-\hat{\psi}\left(a_a^{(i,j,[p,q])}\right)\cdot POD\left(a_a^{(i,j,[p,q])}\right) \tag{7.6}$$

and the non-negative function $\hat{\psi}\left(a_a^{(i,j,[p,q])}\right)=\hat{\psi}\left(a_a^{(i,j,[p,q])};\hat{\beta}_0^{(i,j)},\hat{\beta}_1^{(i,j)},\hat{\sigma}_{\varepsilon_{ij}}\right)$ — the derivation of which is provided in Appendix A — is expressed as

$$\hat{\psi}\left(a_a^{(i,j,[p,q])}\right)=\Phi\left(\frac{\hat{\beta}_0^{(i,j)}+\hat{\beta}_1^{(i,j)}a_a^{(i,j,[p,q])}-a_c^{ij}}{\hat{\sigma}_{\varepsilon_{ij}}}\right)\cdot\left[\Phi\left(\frac{\hat{\beta}_0^{(i,j)}+\hat{\beta}_1^{(i,j)}a_a^{(i,j,[p,q])}}{\hat{\sigma}_{\varepsilon_{ij}}}\right)\right]^{-1} \tag{7.7}$$

Finally, using the total probability theorem (TPT) and recalling Equation (7.3), the unconditional modal failure probability, $P\left[\tilde{\mathrm{F}}_{\mathrm{L},ij}^{[p,q]}\right]$, is then computed as

$$\begin{aligned}
&P\left[\tilde{\mathrm{F}}_{\mathrm{L},ij}^{[p,q]}\right]=\\
&\int_0^{+\infty}P\left[\tilde{\mathrm{F}}_{\mathrm{L},ij}^{[p,q]}\middle|a_a^{(i,j,[p,q])}\right]f_{A_a^{(i,j,[p,q])}}\left(a_a^{(i,j,[p,q])}\right)da_a^{(i,j,[p,q])}=\\
&\left[1-F_{A_a^{(i,j,[p,q])}}\left(a_c^{ij}\right)\right]-\int_{a_c^{ij}}^{+\infty}\hat{\psi}\left(a_a^{(i,j,[p,q])}\right)POD\left(a_a^{(i,j,[p,q])}\right)f_{A_a^{(i,j,[p,q])}}\left(a_a^{(i,j,[p,q])}\right)da_a^{(i,j,[p,q])}=\\
&P\left[\mathrm{F}_{\mathrm{L},ij}^{[p,q]}\right]-\int_{a_c^{ij}}^{+\infty}\hat{\psi}\left(a_a^{(i,j,[p,q])}\right)POD\left(a_a^{(i,j,[p,q])}\right)f_{A_a^{(i,j,[p,q])}}\left(a_a^{(i,j,[p,q])}\right)da_a^{(i,j,[p,q])}
\end{aligned} \tag{7.8}$$

Figures 7.2 and 7.3 provide three-dimensional views (from two different view point) of the joint PDF of $A_a^{(i,j,[p,q])}$ and $A_m^{(i,j,[p,q])}$ at time t_p^q together with the failure domain defined by the failure event $\tilde{\mathrm{F}}_{\mathrm{L},ij}^{[p,q]}$, introduced in Equation (7.4). The solid

magenta line in Figures 7.2 and 7.3 represents the *POD* curve (scaled by a factor of 1/100) used to generate the plots; the dashed green line identifies the (predicted) marginal PDF of $A_a^{(i,j,[p,q])}$ (scaled by a factor of 1/10); while the solid red line denotes the joint PDF (scaled by a factor of 1/10) of $A_a^{(i,j,[p,q])}$ and the non-detection result ($a_m^{(i,j,[p,q])} = 0$) from the assumed single NDE inspection opportunity at time t_p^q. This joint PDF is denoted by $f_{A_a^{(i,j,[p,q])},\, A_m^{(i,j,[p,q])}=0}\left(a_a^{(i,j,[p,q])}, a_m^{(i,j,[p,q])}=0\right)$ and is computed as

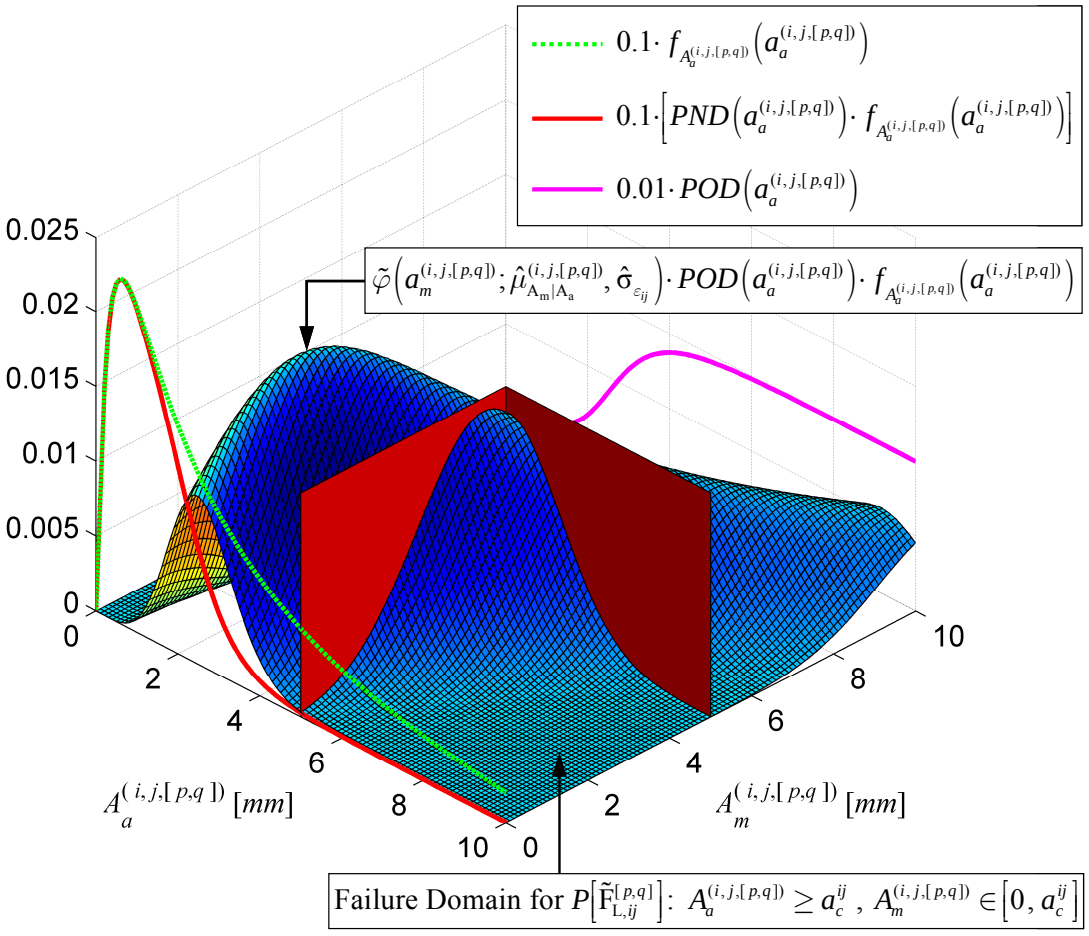

Figure 7.2: Conceptual illustration of (i) the joint PDF of $A_a^{(i,j,[p,q])}$ and $A_m^{(i,j,[p,q])}$ at time t_p^q and (ii) the failure domain according to the failure event $\tilde{F}_{L,ij}^{[p,q]}$. View point #1.

$$
\begin{aligned}
&f_{A_a^{(i,j,[p,q])},\,A_m^{(i,j,[p,q])}=0}\left(a_a^{(i,j,[p,q])},\,a_m^{(i,j,[p,q])}=0\right)=\\
&f_{A_a^{(i,j,[p,q])}\left|A_m^{(i,j,[p,q])}=0\right.}\left(a_a^{(i,j,[p,q])}\left|a_m^{(i,j,[p,q])}=0\right.\right)\cdot f_{A_a^{(i,j,[p,q])}}\left(a_a^{(i,j,[p,q])}\right)=\\
&\left[1-f_{A_a^{(i,j,[p,q])}\left|A_m^{(i,j,[p,q])}>0\right.}\left(a_a^{(i,j,[p,q])}\left|a_m^{(i,j,[p,q])}>0\right.\right)\right]\cdot f_{A_a^{(i,j,[p,q])}}\left(a_a^{(i,j,[p,q])}\right)= \qquad (7.9)\\
&\left[1-POD\left(a_a^{(i,j,[p,q])}\right)\right]\cdot f_{A_a^{(i,j,[p,q])}}\left(a_a^{(i,j,[p,q])}\right)=\\
&PND\left(a_a^{(i,j,[p,q])}\right)\cdot f_{A_a^{(i,j,[p,q])}}\left(a_a^{(i,j,[p,q])}\right)
\end{aligned}
$$

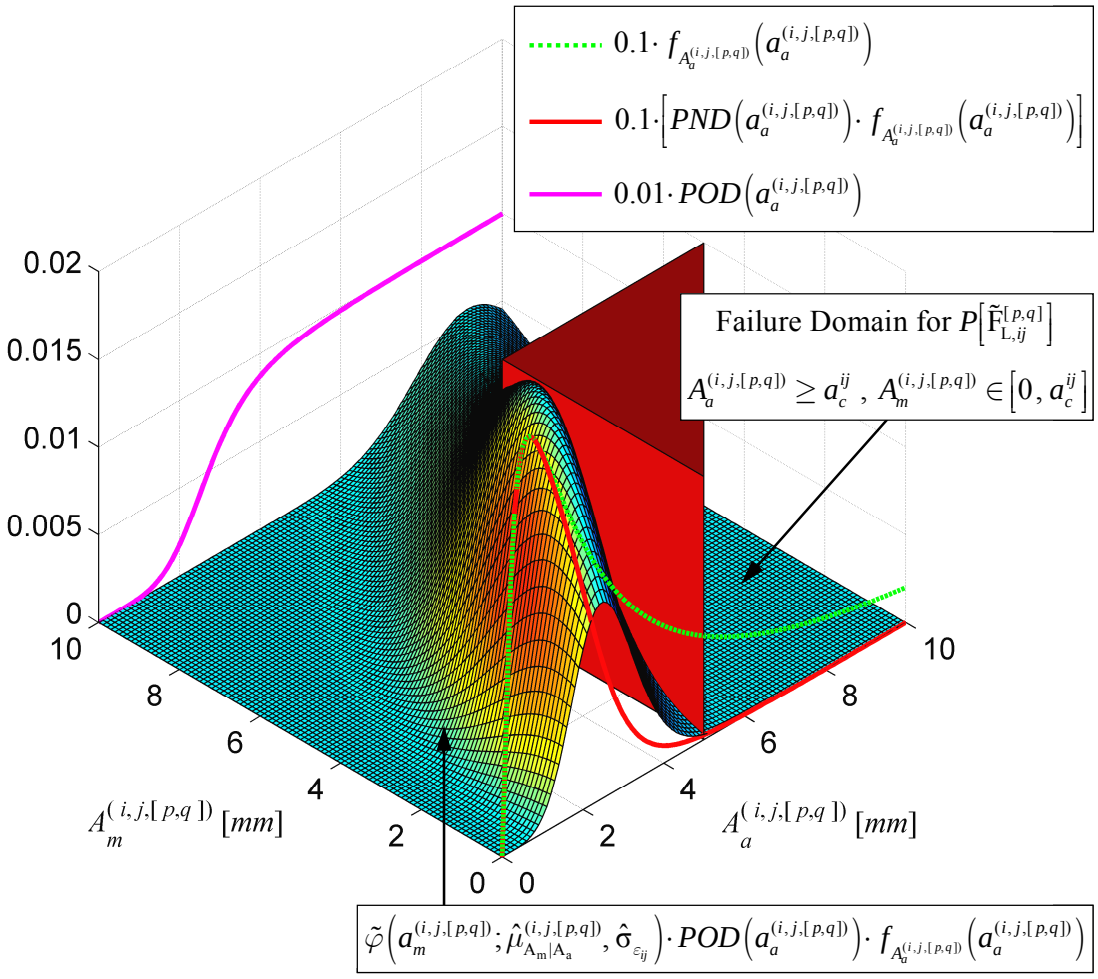

Figure 7.3: Conceptual illustration of (i) the joint PDF of $A_a^{(i,j,[p,q])}$ and $A_m^{(i,j,[p,q])}$ at time t_p^q and (ii) the failure domain according to the failure event $\tilde{F}_{L,ij}^{[p,q]}$. View point #2.

On the other hand, the marginal PDF of $A_a^{(i,j,[p,q])}$ conditional on a particular measured outcome from the assumed single NDE inspection opportunity at time t_p^q — i.e., damage detected and measured $A_m^{(i,j,[p,q])} = a_m^{(i,j,[p,q])}$ with $a_m^{(i,j,[p,q])} > 0$ — can be expressed as

$$f_{A_a^{(i,j,[p,q])}\left| A_m^{(i,j,[p,q])}\right.}\left(a_a^{(i,j,[p,q])}\left| a_m^{(i,j,[p,q])}\right.\right) = \tilde{\varphi}\left(a_m^{(i,j,[p,q])}; \hat{\mu}_{A_m|A_a}^{(i,j,[p,q])}, \hat{\sigma}_{\varepsilon_{ij}}\right) POD\left(a_a^{(i,j,[p,q])}\right) \quad (7.10)$$

Leading to rewrite the joint PDF of $A_a^{(i,j,[p,q])}$ and $A_m^{(i,j,[p,q])}$ (under the condition $a_m^{(i,j,[p,q])} > 0$) as

$$\begin{aligned} & f_{A_a^{(i,j,[p,q])}, A_m^{(i,j,[p,q])}}\left(a_a^{(i,j,[p,q])}, a_m^{(i,j,[p,q])}\right) = \\ & f_{A_a^{(i,j,[p,q])}\left| A_m^{(i,j,[p,q])}=0\right.}\left(a_a^{(i,j,[p,q])}\left| a_m^{(i,j,[p,q])}=0\right.\right) \cdot f_{A_a^{(i,j,[p,q])}}\left(a_a^{(i,j,[p,q])}\right) = \\ & \tilde{\varphi}\left(a_m^{(i,j,[p,q])}; \hat{\mu}_{A_m|A_a}^{(i,j,[p,q])}, \hat{\sigma}_{\varepsilon_{ij}}\right) \cdot POD\left(a_a^{(i,j,[p,q])}\right) \cdot f_{A_a^{(i,j,[p,q])}}\left(a_a^{(i,j,[p,q])}\right) \end{aligned} \quad (7.11)$$

As a final verification, the total probability content (P_{tot}) under the joint PDF of $A_a^{(i,j,[p,q])}$ and $A_m^{(i,j,[p,q])}$ over the domain $\left(A_a^{(i,j,[p,q])} \geq 0\right) \times \left(A_m^{(i,j,[p,q])} \geq 0\right)$ satisfies the normality axiom. P_{tot} can in fact be expressed as

$$\begin{aligned} P_{tot} &= \int_0^{+\infty}\int_0^{+\infty} f_{A_m^{(i,j,[p,q])}, A_a^{(i,j,[p,q])}}\left(a_m^{(i,j,[p,q])}, a_a^{(i,j,[p,q])}\right) da_m^{(i,j,[p,q])} da_a^{(i,j,[p,q])} \\ &= \int_0^{+\infty} \left\{ \left[\int_{0^+}^{+\infty} \tilde{\varphi}\left(a_m^{(i,j,[p,q])}; \hat{\mu}_{A_m|A_a}^{(i,j,[p,q])}, \hat{\sigma}_{\varepsilon_{ij}}\right) POD\left(a_a^{(i,j,[p,q])}\right) da_m^{(i,j,[p,q])} \right] + \right. \\ &\qquad \left. \left[1 - POD\left(a_a^{(i,j,[p,q])}\right)\right] \right\} f_{A_a^{(i,j,[p,q])}}\left(a_a^{(i,j,[p,q])}\right) da_a^{(i,j,[p,q])} \end{aligned} \quad (7.12)$$

and, by noticing that (see Section 3.2.1 in Chapter 3)

$$\begin{aligned}
&\int_{0^+}^{+\infty} \tilde{\varphi}\left(a_m^{(i,j,[p,q])}; \hat{\mu}_{A_m|A_a}^{(i,j,[p,q])}, \hat{\sigma}_{\varepsilon_{ij}}\right) POD\left(a_a^{(i,j,[p,q])}\right) da_m^{(i,j,[p,q])} = \\
&POD\left(a_a^{(i,j,[p,q])}\right)\left[\int_{0^+}^{+\infty} \tilde{\varphi}\left(a_m^{(i,j,[p,q])}; \hat{\mu}_{A_m|A_a}^{(i,j,[p,q])}, \hat{\sigma}_{\varepsilon_{ij}}\right) da_m^{(i,j,[p,q])}\right] = \\
&POD\left(a_a^{(i,j,[p,q])}\right)\cdot 1 = POD\left(a_a^{(i,j,[p,q])}\right)
\end{aligned} \tag{7.13}$$

Equation (7.12) can be reduced as follows:

$$\begin{aligned}
P_{tot} &= \int_0^{+\infty} \left\{POD\left(a_a^{(i,j,[p,q])}\right) + \left[1 - POD\left(a_a^{(i,j,[p,q])}\right)\right]\right\} f_{A_a^{(i,j,[p,q])}}\left(a_a^{(i,j,[p,q])}\right) da_a^{(i,j,[p,q])} \\
&= \int_0^{+\infty} f_{A_a^{(i,j,[p,q])}}\left(a_a^{(i,j,[p,q])}\right) da_a^{(i,j,[p,q])} = 1
\end{aligned} \tag{7.14}$$

7.3.3. Probability of local component failure, $P\left[\hat{\mathbf{F}}_{\mathbf{L},ij}^{[p,q]}\right]$, based on the level-of-safety (LOS) formulation with multiple NDE inspection opportunities at time $t_p^q = t_p + q\Delta\tau$

The level-of-safety formulation used in Section 7.3.2 can be generalized to multiple NDE measurements at time t_p^q. The total number of (processed) NDE measurements, for each (i, j) combination, is hereafter denoted as $n_{\mathrm{MS}}^{(i,j,[p,q])}$ and the measurement results are collected in the vector $\mathbf{A}_{\mathrm{m}}^{(i,j,[p,q])}$, defined as

$$\mathbf{A}_{\mathrm{m}}^{(i,j,[p,q])} = \left\{A_{m_k}^{(i,j,[p,q])},\ k = 1, \ldots, n_{\mathrm{MS}}^{(i,j,[p,q])}\right\} \tag{7.15}$$

This can be rearranged as follows:

$$\mathbf{A}_{\mathrm{m}}^{(i,j,[p,q])} = \left\{ \widehat{\mathbf{A}}_{\mathrm{m}}^{(i,j,[p,q])}, \breve{\mathbf{A}}_{\mathrm{m}}^{(i,j,[p,q])} \right\} \tag{7.16}$$

where the sub-vector $\widehat{\mathbf{A}}_{\mathrm{m}}^{(i,j,[p,q])} = \left\{ A_{m_k}^{(i,j,[p,q])},\ k = 1,\ldots,\overline{n}_{\mathrm{MS}}^{(i,j,[p,q])} \right\}$ collects the $\overline{n}_{\mathrm{MS}}^{(i,j,[p,q])}$ NDE measurement results lower than the critical threshold a_c^{ij} while the other sub-vector, $\breve{\mathbf{A}}_{\mathrm{m}}^{(i,j,[p,q])} = \left\{ A_{m_k}^{(i,j,[p,q])},\ k = \left(\overline{n}_{\mathrm{MS}}^{(i,j,[p,q])} + 1\right),\ldots,n_{\mathrm{MS}}^{(i,j,[p,q])} \right\}$, collects the remaining $\left(n_{\mathrm{MS}}^{(i,j,[p,q])} - \overline{n}_{\mathrm{MS}}^{(i,j,[p,q])} \right)$ NDE measurements which are greater or equal than the pre-defined critical threshold a_c^{ij}. Under these considerations, the local failure event $\hat{\mathrm{F}}_{\mathrm{L},ij}^{[p,q]}$ can be defined as

$$\hat{\mathrm{F}}_{\mathrm{L},ij}^{[p,q]} \triangleq \left\{ \left(A_a^{(i,j,[p,q])} \geq a_c^{ij} \right) \cap \left(\overline{n}_{\mathrm{MS}}^{(i,j,[p,q])} \geq \overline{\overline{n}}_{\mathrm{MS}}^{(i,j,[p,q])} \right) \right\} \tag{7.17}$$

where the notation $\overline{n}_{\mathrm{MS}}^{(i,j,[p,q])} \geq \overline{\overline{n}}_{\mathrm{MS}}^{(i,j,[p,q])}$ can be read as follows: at least $\overline{\overline{n}}_{\mathrm{MS}}^{(i,j,[p,q])}$ out of the assumed $n_{\mathrm{MS}}^{(i,j,[p,q])}$ NDE measurements (performed at time t_p^q) are lower than the critical crack damage size (a_c^{ij}). If $\overline{n}_{\mathrm{MS}}^{(i,j,[p,q])} \geq \overline{\overline{n}}_{\mathrm{MS}}^{(i,j,[p,q])}$, then the monitored component is not considered to have failed and therefore is not stopped from operating; while, on the other hand, if $\overline{n}_{\mathrm{MS}}^{(i,j,[p,q])} < \overline{\overline{n}}_{\mathrm{MS}}^{(i,j,[p,q])}$ the system is stopped and maintenance (at the i^{th} damage location) is performed. The value to be assigned to $\overline{\overline{n}}_{\mathrm{MS}}^{(i,j,[p,q])}$ can be chosen as a reasonably large fraction of the total number of NDE measurements assumed to be performed at time t_p^q, i.e., $n_{\mathrm{MS}}^{(i,j,[p,q])}$. For example, if at least 90% of the $n_{\mathrm{MS}}^{(i,j,[p,q])}$ NDE measurements are below the critical threshold a_c^{ij} — i.e., $\overline{n}_{\mathrm{MS}}^{(i,j,[p,q])} \geq \overline{\overline{n}}_{\mathrm{MS}}^{(i,j,[p,q])}$ with $\overline{\overline{n}}_{\mathrm{MS}}^{(i,j,[p,q])} = 0.9 \cdot n_{\mathrm{MS}}^{(i,j,[p,q])}$ — that particular local reliability component (or local failure

mode) is not classified, by the NDE inspection outcome, as "failed" and it would not be stopped from operating.

According to the failure criterion (at the local component level) introduced in Equation (7.17), the probability of the failure event $\hat{\mathrm{F}}_{\mathrm{L},ij}^{[p,q]}$, conditional on the true damage size $\mathbf{A}_{\mathrm{a}}^{[p,q]} = \mathbf{a}_{\mathrm{a}}^{[p,q]}$, is given by

$$P\left[\hat{\mathrm{F}}_{\mathrm{L},ij}^{[p,q]} \middle| \mathbf{a}_{\mathrm{a}}^{[p,q]}\right] = P\left[\hat{\mathrm{F}}_{\mathrm{L},ij}^{[p,q]} \middle| a_a^{(i,j,[p,q])}\right] = \begin{cases} 0 & \text{if } a_a^{(i,j,[p,q])} < a_c^{ij} \\ \overline{\overline{\psi}}\left(a_a^{(i,j,[p,q])}\right) & \text{if } a_a^{(i,j,[p,q])} \geq a_c^{ij} \end{cases} \tag{7.18}$$

in which the term $\overline{\overline{\psi}}\left(a_a^{(i,j,[p,q])}\right)$ is the Binomial complementary CDF expressed as

$$\overline{\overline{\psi}}\left(a_a^{(i,j,[p,q])}\right) = \sum_{l=\overline{n}_{\mathrm{MS}}^{(i,j,[p,q])}}^{n_{\mathrm{MS}}^{(i,j,[p,q])}} \binom{n_{\mathrm{MS}}^{(i,j,[p,q])}}{l} \left[\overline{\psi}\left(a_a^{(i,j,[p,q])}\right)\right]^l \left[1-\overline{\psi}\left(a_a^{(i,j,[p,q])}\right)\right]^{\left(n_{\mathrm{MS}}^{(i,j,[p,q])}-l\right)} \tag{7.19}$$

The function $\overline{\psi}\left(a_a^{(i,j,[p,q])}\right)$ in Equation (7.19) was derived in Section 7.3.2 and is shown in Equation (7.6), whereas the binomial coefficient is explicitly written as

$$\binom{n_{\mathrm{MS}}^{(i,j,[p,q])}}{l} = \frac{\left[n_{\mathrm{MS}}^{(i,j,[p,q])}\right]!}{l!\left[n_{\mathrm{MS}}^{(i,j,[p,q])}-l\right]!} \tag{7.20}$$

Finally, by using the total probability theorem (TPT), the unconditional modal failure probability, $P\left[\hat{\mathrm{F}}_{\mathrm{L},ij}^{[p,q]}\right]$, is then computed as

$$\begin{aligned} P\left[\hat{\mathrm{F}}_{\mathrm{L},ij}^{[p,q]}\right] &= \int_0^{+\infty} P\left[\hat{\mathrm{F}}_{\mathrm{L},ij}^{[p,q]} \middle| a_a^{(i,j,[p,q])}\right] f_{A_a^{(i,j,[p,q])}}\left(a_a^{(i,j,[p,q])}\right) da_a^{(i,j,[p,q])} \\ &= \int_{a_c^{ij}}^{+\infty} \overline{\overline{\psi}}\left(a_a^{(i,j,[p,q])}\right) f_{A_a^{(i,j,[p,q])}}\left(a_a^{(i,j,[p,q])}\right) da_a^{(i,j,[p,q])} \end{aligned} \tag{7.21}$$

For the special case in which $\overline{n}_{\mathrm{MS}}^{(i,j,[p,q])} = \overline{\overline{n}}_{\mathrm{MS}}^{(i,j,[p,q])} = n_{\mathrm{MS}}^{(i,j,[p,q])} = 1$ (i.e., a single inspection opportunity at time t_p^q) the function $\overline{\overline{\psi}}\left(a_a^{(i,j,[p,q])}\right)$ reduces to $\overline{\psi}\left(a_a^{(i,j,[p,q])}\right)$ and therefore the results derived in Equations (7.5) and (7.7) can be retrieved. In other words, the LOS formulation with multiple NDE inspection opportunities at time t_p^q yields to the same result as the LOS formulation derived for a single NDE inspection opportunity at time t_p^q.

7.3.4. Probability of local component false-call based on the level-of-safety formulation (LOS) with single NDE inspection opportunity with single NDE inspection opportunity at time $t_p^q = t_p + q\Delta\tau$

Besides the modal probability of failure, computed according to the alternative definition of the local failure event $\tilde{\mathrm{F}}_{\mathrm{L},ij}^{[p,q]}$ introduced in Section 7.3.2, it is also of interest to compute the modal probability of false-call (or false-alarm) for each of the n_{A}^p local reliability components identified up to time t_p.

The false-call event $\tilde{\mathcal{F}}_{\mathrm{L},ij}^{[p,q]}$, at the local component level, is defined as

$$\tilde{\mathcal{F}}_{\mathrm{L},ij}^{[p,q]} \triangleq \left\{\left(A_a^{(i,j,[p,q])} < a_c^{ij}\right) \cap \left(A_m^{(i,j,[p,q])} \geq a_c^{ij}\right)\right\} \tag{7.22}$$

and its graphical interpretation is shown in Figure 7.1. Hence, from the above equation, a false-call represents the joint event that the actual damage size, $A_a^{(i,j,[p,q])}$, is lower than the pre-defined critical damage size (a_c^{ij}), and the measured damage size, $A_m^{(i,j,[p,q])}$, from the (assumed) single NDE inspection opportunity at time t_p^q is larger

than or equal to a_c^{ij}. The probability of the false-call event $\tilde{\mathcal{F}}_{\mathrm{L},ij}^{[p,q]}$ conditional on the true damage size $\mathbf{A}_{\mathrm{a}}^{[p,q]} = \mathbf{a}_{\mathrm{a}}^{[p,q]}$ (referred herein as conditional modal false-call probability) is given by

$$P\left[\tilde{\mathcal{F}}_{\mathrm{L},ij}^{[p,q]} \middle| \mathbf{a}_{\mathrm{a}}^{[p,q]}\right] = P\left[\tilde{\mathcal{F}}_{\mathrm{L},ij}^{[p,q]} \middle| a_a^{(i,j,[p,q])}\right] = \begin{cases} 1-\overline{\psi}\left(a_a^{(i,j,[p,q])}\right) & \text{if } a_a^{(i,j,[p,q])} < a_c^{ij} \\ 0 & \text{if } a_a^{(i,j,[p,q])} \geq a_c^{ij} \end{cases} \tag{7.23}$$

Using the TPT, the unconditional modal false-call probability, $P\left[\tilde{\mathcal{F}}_{\mathrm{L},ij}^{[p,q]}\right]$, is then computed as

$$\begin{aligned} P\left[\tilde{\mathcal{F}}_{\mathrm{L},ij}^{[p,q]}\right] &= \int_0^{+\infty} P\left[\tilde{\mathcal{F}}_{\mathrm{L},ij}^{[p,q]} \middle| a_a^{(i,j,[p,q])}\right] f_{A_a^{(i,j,[p,q])}}\left(a_a^{(i,j,[p,q])}\right) da_a^{(i,j,[p,q])} \\ &= \int_0^{a_c^{ij}} \left[1-\overline{\psi}\left(a_a^{(i,j,[p,q])}\right)\right] f_{A_a^{(i,j,[p,q])}}\left(a_a^{(i,j,[p,q])}\right) da_a^{(i,j,[p,q])} \\ &= \int_0^{a_c^{ij}} \hat{\psi}\left(a_a^{(i,j,[p,q])}\right) POD\left(a_a^{(i,j,[p,q])}\right) f_{A_a^{(i,j,[p,q])}}\left(a_a^{(i,j,[p,q])}\right) da_a^{(i,j,[p,q])} \end{aligned} \tag{7.24}$$

where the functions $\overline{\psi}\left(a_a^{(i,j,[p,q])}\right)$ and $\hat{\psi}\left(a_a^{(i,j,[p,q])}\right)$ were defined previously in Equations (7.6) and (7.7).

7.3.5. Probability of local component false-call based on the level-of-safety (LOS) formulation with multiple NDE inspection opportunities at time $t_p^q = t_p + q\Delta\tau$

The false-call event introduced in Section 7.3.4 can also be generalized to the case in which multiple NDE measurements are collected at time t_p^q. Following the

same definitions introduced and used in Section 7.3.3, the false-call event at the local component level, $\hat{\mathcal{F}}_{\mathrm{L},ij}^{[p,q]}$, can be defined as

$$\hat{\mathcal{F}}_{\mathrm{L},ij}^{[p,q]} \triangleq \left\{ \left(A_a^{(i,j,[p,q])} < a_c^{ij} \right) \cap \left(\overline{n}_{\mathrm{MS}}^{(i,j,[p,q])} < \overline{\overline{n}}_{\mathrm{MS}}^{(i,j,[p,q])} \right) \right\} \tag{7.25}$$

where the event represented by the inequality $\overline{n}_{\mathrm{MS}}^{(i,j,[p,q])} < \overline{\overline{n}}_{\mathrm{MS}}^{(i,j,[p,q])}$ can be read as follows: at most $\left(\overline{\overline{n}}_{\mathrm{MS}}^{(i,j,[p,q])} - 1 \right)$ out of the $n_{\mathrm{MS}}^{(i,j,[p,q])}$ NDE measurements (assumed to be performed at time t_p^q) are lower than the critical damage size for that particular (i, j) combination. According to the above definition, the conditional modal probability of false-call can be expressed as

$$P\left[\hat{\mathcal{F}}_{\mathrm{L},ij}^{[p,q]} \middle| \mathbf{a}_{\mathrm{a}}^{[p,q]} \right] = P\left[\hat{\mathcal{F}}_{\mathrm{L},ij}^{[p,q]} \middle| a_a^{(i,j,[p,q])} \right] = \begin{cases} 1 - \overline{\overline{\psi}}\left(a_a^{(i,j,[p,q])} \right) & \text{if } a_a^{(i,j,[p,q])} < a_c^{ij} \\ 0 & \text{if } a_a^{(i,j,[p,q])} \geq a_c^{ij} \end{cases} \tag{7.26}$$

and the unconditional modal probability of false-call, $P\left[\hat{\mathcal{F}}_{\mathrm{L},ij}^{[p,q]} \right]$, can then be derived by taking advantage of the TPT as shown below:

$$\begin{aligned} P\left[\hat{\mathcal{F}}_{\mathrm{L},ij}^{[p,q]} \right] &= \int_0^{+\infty} P\left[\hat{\mathcal{F}}_{\mathrm{L},ij}^{[p,q]} \middle| a_a^{(i,j,[p,q])} \right] f_{A_a^{(i,j,[p,q])}}\left(a_a^{(i,j,[p,q])} \right) da_a^{(i,j,[p,q])} \\ &= \int_0^{a_c^{ij}} \left[1 - \overline{\overline{\psi}}\left(a_a^{(i,j,[p,q])} \right) \right] f_{A_a^{(i,j,[p,q])}}\left(a_a^{(i,j,[p,q])} \right) da_a^{(i,j,[p,q])} \end{aligned} \tag{7.27}$$

It is worth noting that for the special case in which $\overline{n}_{\mathrm{MS}}^{(i,j,[p,q])} = \overline{\overline{n}}_{\mathrm{MS}}^{(i,j,[p,q])} = n_{\mathrm{MS}}^{(i,j,[p,q])} = 1$ (i.e., a single NDE inspection opportunity at time t_p^q) the function $\overline{\overline{\psi}}\left(a_a^{(i,j,[p,q])} \right)$ simplifies to $\overline{\psi}\left(a_a^{(i,j,[p,q])} \right)$ and therefore Equation (7.27) reduces to Equation (7.24).

7.4. Proposed global component failure criteria and derivation of the corresponding probabilities of global component failure

The global failure event $\mathrm{F}_{\mathrm{G},r}^{[p,q]}$ — i.e., the failure event (at time t_p^q) associated with the r^{th} global reliability component or modal failure mode — can be defined as $\mathrm{F}_{\mathrm{G},r}^{[p,q]} \triangleq \left\{ V_{\mathrm{F,LCO}}^{(r,[p,q])} \le v_c^r \right\}$, where v_c^r represents the pre-defined critical velocity associated with the r^{th} global failure mode. According to this definition for the failure event $\mathrm{F}_{\mathrm{G},r}^{[p,q]}$, the conditional modal failure probabilities $P\left[\mathrm{F}_{\mathrm{G},r}^{[p,q]} \middle| \mathbf{v}_{\mathrm{F,LCO}}^{[p,q]}\right]$ (with $r = 1, \ldots, n_{\mathrm{G}}$) are now given by

$$P\left[\mathrm{F}_{\mathrm{G},r}^{[p,q]} \middle| \mathbf{v}_{\mathrm{F,LCO}}^{[p,q]}\right] = P\left[\mathrm{F}_{\mathrm{G},r}^{[p,q]} \middle| v_{\mathrm{F,LCO}}^{(r,[p,q])}\right] = \begin{cases} 0 & \text{if } v_{\mathrm{F,LCO}}^{(r,[p,q])} > v_c^r \\ 1 & \text{if } v_{\mathrm{F,LCO}}^{(r,[p,q])} \le v_c^r \end{cases} \tag{7.28}$$

and, by using the TPT, the unconditional modal failure probabilities $P\left[\mathrm{F}_{\mathrm{G},r}^{[p,q]}\right]$ (with $r = 1, \ldots, n_{\mathrm{G}}$) can then be written as

$$\begin{aligned} P\left[\mathrm{F}_{\mathrm{G},r}^{[p,q]}\right] &= \int_0^{+\infty} P\left[\mathrm{F}_{\mathrm{G},r}^{[p,q]} \middle| v_{\mathrm{F,LCO}}^{(r,[p,q])}\right] f_{V_{\mathrm{F,LCO}}^{(r,[p,q])}}\left(v_{\mathrm{F,LCO}}^{(r,[p,q])}\right) dv_{\mathrm{F,LCO}}^{(r,[p,q])} \\ &= \int_0^{v_c^r} f_{V_{\mathrm{F,LCO}}^{(r,[p,q])}}\left(v_{\mathrm{F,LCO}}^{(r,[p,q])}\right) dv_{\mathrm{F,LCO}}^{(r,[p,q])} = F_{V_{\mathrm{F,LCO}}^{(r,[p,q])}}\left(v_c^r\right) \end{aligned} \qquad r = 1, \ldots, n_{\mathrm{G}} \tag{7.29}$$

where the term $F_{V_{\mathrm{F,LCO}}^{(r,[p,q])}}(\cdot)$ represents the cumulative distribution function (CDF) of the random variable $V_{\mathrm{F,LCO}}^{(r,[p,q])}$.

Similarly to what was shown before in Section 7.3.4, alternative definitions for $\mathrm{F}_{\mathrm{G},r}^{[p,q]}$ can also be used within the proposed framework. For example, a possible

alternative global failure criterion (Lin *et al.*, 2000; Styuart *et al.*, 2007) considers the structural system to have failed when the maximum operational aircraft velocity (V_{MAX}) exceeds either the reduced (due to damage) flutter velocity ($V_{\mathrm{F}}^{[p,q]}$), or any of the n_{LCO} components of the LCO velocity vector ($\mathbf{V}_{\mathrm{LCO}}^{[p,q]}$), at time t_p^q. Each of the $n_{\mathrm{G}} = 1 + n_{\mathrm{LCO}}$ global failure events, with graphical interpretation provided in Figure 7.4, is defined as

$$\tilde{\mathrm{F}}_{\mathrm{G},r}^{[p,q]} \triangleq \left\{ V_{\mathrm{MAX}} \geq V_{\mathrm{F,LCO}}^{(r,[p,q])} \right\}, \qquad r = 1, \ldots, n_{\mathrm{G}} \tag{7.30}$$

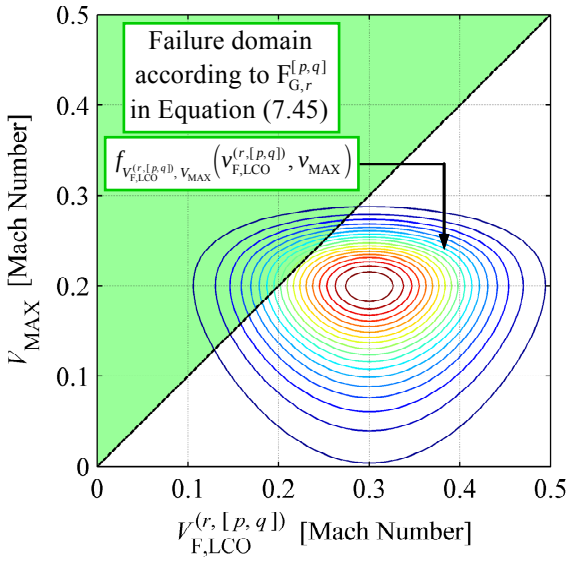

Figure 7.4: Failure domain according to the global failure criterion in Equation (7.30): V_{MAX} exceeding the r^{th} component of the velocity vector $\mathbf{V}_{\mathrm{F,LCO}}^{[p,q]}$, at future time t_p^q, after damage propagation from time t_p to time t_p^q.

where the variable V_{MAX} can be characterized probabilistically by the extreme value type I (Gumbel) distribution (Styuart *et al.*, 2007). Furthermore, in this part of the

study, V_{MAX} is considered to be statistically independent of $\mathbf{V}_{\mathrm{F,LCO}}^{[p,q]}$ — a reasonable assumption for UAVs which do not have an onboard pilot. According to the alternative definition for the global component failure event, provided in Equation (7.30), the conditional modal failure probabilities can be expressed as

$$P\left[\tilde{\mathrm{F}}_{\mathrm{G},r}^{[p,q]}\,\middle|\,\mathbf{v}_{\mathrm{F,LCO}}^{[p,q]}\right]=P\left[\tilde{\mathrm{F}}_{\mathrm{G},r}^{[p,q]}\,\middle|\,v_{\mathrm{F,LCO}}^{(r,[p,q])}\right]=1-F_{V_{\mathrm{MAX}}}\left(v_{\mathrm{F,LCO}}^{(r,[p,q])}\right),\qquad r=1,\ldots,n_{\mathrm{G}}\qquad(7.31)$$

and, using the TPT, the corresponding unconditional global component failure probabilities, $P\left[\tilde{\mathrm{F}}_{\mathrm{G},r}^{[p,q]}\right]$ (with $r=1,\ldots,n_{\mathrm{G}}$), are then computed as

$$\begin{aligned}P\left[\tilde{\mathrm{F}}_{\mathrm{G},r}^{[p,q]}\right]&=\int_{0}^{+\infty}P\left[\tilde{\mathrm{F}}_{\mathrm{G},r}^{[p,q]}\,\middle|\,v_{\mathrm{F,LCO}}^{(r,[p,q])}\right]f_{V_{\mathrm{F,LCO}}^{(r,[p,q])}}\left(v_{\mathrm{F,LCO}}^{(r,[p,q])}\right)dv_{\mathrm{F,LCO}}^{(r,[p,q])}\\&=1-\int_{0}^{+\infty}F_{V_{\mathrm{MAX}}}\left(v_{\mathrm{F,LCO}}^{(r,[p,q])}\right)f_{V_{\mathrm{F,LCO}}^{(r,[p,q])}}\left(v_{\mathrm{F,LCO}}^{(r,[p,q])}\right)dv_{\mathrm{F,LCO}}^{(r,[p,q])}\end{aligned}\qquad r=1,\ldots,n_{\mathrm{G}}\qquad(7.32)$$

The final result obtained from Equation (7.32) represents the probability content of the triangular failure domain shown in Figure 7.4.

7.5. System reliability analysis for the computation of lower and upper uni-modal bounds of the probabilities of system failure and false-call

Once component reliability analysis has been performed for all n_{A}^{p} local and n_{G} global failure modes (identified up to time t_p) and all the corresponding modal failure probabilities have been computed, it is possible to compute lower and upper bounds for the probabilities of *system failure* and *false-call*, by abstracting the UAV wing into a combination of series and parallel systems involving the local and global component failure and false-call probabilities derived in the previous sections. Several

failure and false-call criteria (at the system level) can be formulated and used within the proposed framework; these criteria are presented and discussed in the following sub-sections as follows:

(i) Section 7.5.1 uses $P\left[\mathrm{F}_{\mathrm{L},ij}^{[p,q]}\right]$ together with either $P\left[\mathrm{F}_{\mathrm{G},r}^{[p,q]}\right]$ or $P\left[\tilde{\mathrm{F}}_{\mathrm{G},r}^{[p,q]}\right]$ to provide lower and upper uni-modal bounds for the probability of system failure denoted as $P\left[\mathrm{F}_{\mathrm{sys}}^{[p,q]}\right]$;

(ii) Section 7.5.2 combines the local component failure probabilities $P\left[\tilde{\mathrm{F}}_{\mathrm{L},ij}^{[p,q]}\right]$ with either $P\left[\mathrm{F}_{\mathrm{G},r}^{[p,q]}\right]$ or $P\left[\tilde{\mathrm{F}}_{\mathrm{G},r}^{[p,q]}\right]$ to derive lower and upper uni-modal bounds for the probability of system failure denoted as $P\left[\breve{\mathrm{F}}_{\mathrm{sys}}^{[p,q]}\right]$;

(iii) Section 7.5.3 provides a logical expression, using set theory language, for the failure event, $\widehat{\mathrm{F}}_{\mathrm{sys}}^{[p,q]}$, by combining $P\left[\mathrm{F}_{\mathrm{L},ij}^{[p,q]}\right]$, with either $P\left[\mathrm{F}_{\mathrm{G},r}^{[p,q]}\right]$ or $P\left[\tilde{\mathrm{F}}_{\mathrm{G},r}^{[p,q]}\right]$, and with the reliability/fidelity of the NDE technique used to monitor the structure;

(iv) Section 7.5.4 makes use of $P\left[\mathrm{F}_{\mathrm{L},ij}^{[p,q]}\right]$ and $P\left[\tilde{\mathscr{F}}_{\mathrm{L},ij}^{[p,q]}\right]$ together with either $P\left[\mathrm{F}_{\mathrm{G},r}^{[p,q]}\right]$ or $P\left[\tilde{\mathrm{F}}_{\mathrm{G},r}^{[p,q]}\right]$ to obtain a mathematical expression for the lower and upper uni-modal bounds for the probability of false-call (at the overall system level) denoted as $P\left[\breve{\mathscr{F}}_{\mathrm{sys}}^{[p,q]}\right]$;

(v) Finally, Section 7.5.5 presents a logical expression, using set theory language, for the false-call event, $\widehat{\mathscr{F}}_{\mathrm{sys}}^{[p,q]}$, by combining $P\left[\mathrm{F}_{\mathrm{L},ij}^{[p,q]}\right]$, with

either $P\left[\mathrm{F}_{\mathrm{G},r}^{[p,q]}\right]$ or $P\left[\tilde{\mathrm{F}}_{\mathrm{G},r}^{[p,q]}\right]$, and with the reliability/fidelity of the NDE technique used to monitor the structure.

Analytical expressions for the probabilities $P\left[\widehat{\mathrm{F}}_{\mathrm{sys}}^{[p,q]}\right]$ and $P\left[\widehat{\mathscr{F}}_{\mathrm{sys}}^{[p,q]}\right]$ — associated with the failure and false-call events $\widehat{\mathrm{F}}_{\mathrm{sys}}^{[p,q]}$ and $\widehat{\mathscr{F}}_{\mathrm{sys}}^{[p,q]}$ — are not provided in this thesis; however, $P\left[\widehat{\mathrm{F}}_{\mathrm{sys}}^{[p,q]}\right]$ can be derived by generalizing the approach discussed in Section 7.5.2 and Appendix C, whereas $P\left[\widehat{\mathscr{F}}_{\mathrm{sys}}^{[p,q]}\right]$ could be obtained by extending and adapting in Section 7.5.4 and Appendix D.

7.5.1. Derivation of lower and upper uni-modal bounds for the probability of system failure $P\left[\mathbf{F}_{\mathbf{sys}}^{[p,q]}\right]$

As conceptually shown in Figure 7.5, the event of system failure, $\mathrm{F}_{\mathrm{sys}}^{[p,q]}$, can be defined as the union of all the n_{A}^{p} local and n_{G} global component failure events, $\mathrm{F}_{\mathrm{L},ij}^{[p,q]}$ (with $i=1,\ldots,n_{\mathrm{L}}^{[0,p]}$ and $j=1,\ldots,n_{\mathrm{DM}}^{(i,[0,p])}$) and $\mathrm{F}_{\mathrm{G},r}^{[p,q]}$ (with $r=1,\ldots,n_{\mathrm{G}}$), described earlier; i.e.,

$$\mathrm{F}_{\mathrm{sys}}^{[p,q]} \triangleq \left\{\left[\bigcup_{i=1}^{n_{\mathrm{L}}^{[0,p]}}\left(\bigcup_{j=1}^{n_{\mathrm{DM}}^{(i,[0,p])}}\mathrm{F}_{\mathrm{L},ij}^{[p,q]}\right)\right]\cup\left(\bigcup_{r=1}^{n_{\mathrm{G}}}\mathrm{F}_{\mathrm{G},r}^{[p,q]}\right)\right\} \tag{7.33}$$

Equation (7.33) indicates that the whole system is considered to have failed when at least one of its $n_{\mathrm{A}}^{p}+n_{\mathrm{G}}$ reliability components ($\mathrm{F}_{\mathrm{L},ij}^{[p,q]}$ and $\mathrm{F}_{\mathrm{G},r}^{[p,q]}$) has failed. n_{A}^{p} represents the number of local reliability components at time t_p, defined as

$n_{\mathrm{A}}^{p}=\sum_{i=1}^{n_{\mathrm{L}}^{[0,p]}} n_{\mathrm{DM}}^{(i,[0,p])}$, whereas, $n_{\mathrm{G}}=1+n_{\mathrm{LCO}}$ denotes the number of global failure modes considered. Lower and upper uni-modal bounds (also referred to as *Boole's Bounds*; Boole, 1854) for the probability of this failure event, $\mathrm{F}_{\mathrm{sys}}^{[p,q]}$, are given by

$$\max_{i,j,r}\left(P\left[\mathrm{F}_{\mathrm{L},ij}^{[p,q]}\right], P\left[\mathrm{F}_{\mathrm{G},r}^{[p,q]}\right]\right) \leq P\left[\mathrm{F}_{\mathrm{sys}}^{[p,q]}\right] \leq \min\left(1, \left[\sum_{i=1}^{n_{\mathrm{L}}^{[0,p]}} \sum_{j=1}^{n_{\mathrm{DM}}^{(i,[0,p])}} P\left[\mathrm{F}_{\mathrm{L},ij}^{[p,q]}\right] + \sum_{r=1}^{n_{\mathrm{G}}} P\left[\mathrm{F}_{\mathrm{G},r}^{[p,q]}\right]\right]\right) \quad (7.34)$$

where the lower bound corresponds to the exact solution in the case of fully correlated failure modes. Furthermore, as pointed out by Christensen and Sorensen (1982), in the case of positively correlated failure modes, an improved uni-modal upper bound for the probability of system failure is given by

$$P\left[\mathrm{F}_{\mathrm{sys}}^{[p,q]}\right] \leq 1-\left[\prod_{i=1}^{n_{\mathrm{L}}^{[0,p]}} \prod_{j=1}^{n_{\mathrm{DM}}^{(i,[0,p])}} \left(1-P\left[\mathrm{F}_{\mathrm{L},ij}^{[p,q]}\right]\right)\right] \times \prod_{r=1}^{n_{\mathrm{G}}}\left(1-P\left[\mathrm{F}_{\mathrm{G},r}^{[p,q]}\right]\right) \quad (7.35)$$

and it corresponds to the exact solution for the case of statistically independent failure modes. Additionally, Equations (7.34) and (7.35) remain valid when the global component failure probabilities $P\left[\mathrm{F}_{\mathrm{G},r}^{[p,q]}\right]$ are replaced by $P\left[\tilde{\mathrm{F}}_{\mathrm{G},r}^{[p,q]}\right]$.

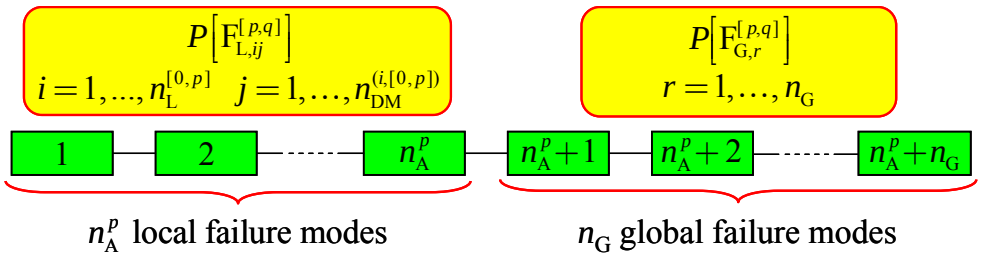

Figure 7.5: Series system abstraction of the real structure used to compute lower and upper uni-modal bounds to the probability of system failure $P\left[\mathrm{F}_{\mathrm{sys}}^{[p,q]}\right]$.

To conclude this section, the structural system is considered failed (conservatively) when the upper bound for $P\left[\mathrm{F}_{\mathrm{sys}}^{[p,q]}\right]$ reaches or exceeds a critical and pre-defined safety threshold ($\overline{p}_{\mathrm{F}}$). At that particular time, the structural system (or part thereof) needs to be replaced or repaired.

7.5.2. Derivation of lower and upper uni-modal bounds for the probability of system failure $P\left[\breve{\mathbf{F}}_{\mathbf{sys}}^{[p,q]}\right]$ assuming a single NDE inspection opportunity at time $t_p^q = t_p + q\Delta\tau$

Similarly to the derivations followed during the discussion concerning the local component reliability analysis (in Section 7.3.2), the failure event representative of the overall system failure can alternatively be defined as

$$\breve{\mathrm{F}}_{\mathrm{sys}}^{[p,q]} \triangleq \left\{\left[\bigcup_{i=1}^{n_{\mathrm{L}}^{[0,p]}}\left(\bigcup_{j=1}^{n_{\mathrm{DM}}^{(i,[0,p])}} \mathrm{F}_{\mathrm{L},ij}^{[p,q]}\right)\right] \cup \left(\bigcup_{r=1}^{n_{\mathrm{G}}} \mathrm{F}_{\mathrm{G},r}^{[p,q]}\right)\right\} \cap \left[\bigcap_{i=1}^{n_{\mathrm{L}}^{[0,p]}}\left(\bigcap_{j=1}^{n_{\mathrm{DM}}^{(i,[0,p])}} A_m^{(i,j,[p,q])} < a_c^{ij}\right)\right] \tag{7.36}$$

or, in a more compact form, as

$$\breve{\mathrm{F}}_{\mathrm{sys}}^{[p,q]} \triangleq \mathrm{F}_{\mathrm{sys}}^{[p,q]} \cap \left[\bigcap_{i=1}^{n_{\mathrm{L}}^{[0,p]}}\left(\bigcap_{j=1}^{n_{\mathrm{DM}}^{(i,[0,p])}} A_m^{(i,j,[p,q])} < a_c^{ij}\right)\right] \tag{7.37}$$

i.e., the event that at least one of the $n_{\mathrm{A}}^p + n_{\mathrm{G}}$ reliability components ($\mathrm{F}_{\mathrm{L},ij}^{[p,q]}$ and $\mathrm{F}_{\mathrm{G},r}^{[p,q]}$) has failed and, at the same time, each of the n_{A}^p NDE measurement outcomes, $A_m^{(i,j,[p,q])}$ (with $i = 1, \ldots, n_{\mathrm{L}}^{[0,p]}$ and $j = 1, \ldots, n_{\mathrm{DM}}^{(i,[0,p])}$), from the assumed single NDE inspection opportunity at time t_p^q is lower than a_c^{ij}. Uni-modal bounds for the probability of this

alternative failure event are more complicated than those derived for $P\left[\mathrm{F}_{\mathrm{sys}}^{[p,q]}\right]$ and can be expressed as (see Appendix C)

$$\max\left(P_{low}\left[\breve{\mathrm{F}}_{\mathrm{local}}^{[p,q]}\right], P_{low}\left[\breve{\mathrm{F}}_{\mathrm{global}}^{[p,q]}\right]\right) \le P\left[\breve{\mathrm{F}}_{\mathrm{sys}}^{[p,q]}\right] \le \min\left[1, \left(P_{up}\left[\breve{\mathrm{F}}_{\mathrm{local}}^{[p,q]}\right] + P_{up}\left[\breve{\mathrm{F}}_{\mathrm{global}}^{[p,q]}\right]\right)\right] \tag{7.38}$$

where $P_{low}\left[\breve{\mathrm{F}}_{\mathrm{local}}^{[p,q]}\right]$ is expressed as

$$P_{low}\left[\breve{\mathrm{F}}_{\mathrm{local}}^{[p,q]}\right] = \max_{i,j}\left[R_{\mathrm{L},ij}^{[p,q]} \cdot \max\left(0, P\left[\mathrm{F}_{\mathrm{L},ij}^{[p,q]}\right] + P_{ij}^{*} - n_{\mathrm{A}}^{p} + 1\right)\right] \tag{7.39}$$

in which $R_{\mathrm{L},ij}^{[p,q]} = P\left[\tilde{\mathrm{F}}_{\mathrm{L},ij}^{[p,q]}\right] \Big/ P\left[\mathrm{F}_{\mathrm{L},ij}^{[p,q]}\right]$ and the term P_{ij}^{*}, is defined as

$$P_{ij}^{*} = \sum_{l=1}^{n_{\mathrm{L}}^{[0,p]}} \sum_{m=1}^{n_{\mathrm{DM}}^{(l,[0,p])}} P\left[A_{m}^{(l,m,[p,q])} < a_{c}^{lm}\right]\left(1 - \delta_{il}\delta_{jm}\right) \tag{7.40}$$

with δ_{il} and δ_{jm} being the *Kronecker delta*, i.e.,

$$\delta_{il} = \begin{cases} 1 & \text{if } i = l \\ 0 & \text{if } i \neq l \end{cases} \quad \text{and} \quad \delta_{jm} = \begin{cases} 1 & \text{if } j = m \\ 0 & \text{if } j \neq m \end{cases} \tag{7.41}$$

The term $P_{up}\left[\breve{\mathrm{F}}_{\mathrm{local}}^{[p,q]}\right]$ is instead calculated using the following equation

$$P_{up}\left[\breve{\mathrm{F}}_{\mathrm{local}}^{[p,q]}\right] = \min\left(1, \sum_{i=1}^{n_{\mathrm{L}}^{[0,p]}} \sum_{j=1}^{n_{\mathrm{DM}}^{(i,[0,p])}} \left[R_{\mathrm{L},ij}^{[p,q]} \cdot \min\left(P\left[\mathrm{F}_{\mathrm{L},ij}^{[p,q]}\right], P_{ij}^{**}\right)\right]\right) \tag{7.42}$$

where the contribution P_{ij}^{**} is defined as

$$P_{ij}^{**} = \min_{l,m}\left(P\left[A_{m}^{(l,m,[p,q])} < a_{c}^{lm}\right]\right), \quad \forall (l,m) \neq (i,j) \tag{7.43}$$

Finally, the two remaining terms, $P_{low}\left[\breve{\mathrm{F}}_{\mathrm{global}}^{[p,q]}\right]$ and $P_{up}\left[\breve{\mathrm{F}}_{\mathrm{global}}^{[p,q]}\right]$, can be computed as

$$P_{low}\left[\breve{\mathrm{F}}_{\mathrm{global}}^{[p,q]}\right]=\max\left(0,\ \max_{r}\left(P\left[\mathrm{F}_{\mathrm{G},r}^{[p,q]}\right]\right)+\sum_{i=1}^{n_{\mathrm{L}}^{[0,p]}}\sum_{j=1}^{n_{\mathrm{DM}}^{(i,[0,p])}}P\left[A_m^{(i,j,[p,q])}<a_c^{ij}\right]-n_{\mathrm{A}}^{p}\right) \tag{7.44}$$

$$P_{up}\left[\breve{\mathrm{F}}_{\mathrm{global}}^{[p,q]}\right]=\min\left(1,\ \sum_{r=1}^{n_{\mathrm{G}}}P\left[\mathrm{F}_{\mathrm{G},r}^{[p,q]}\right],\ \min_{i,j}\left(P\left[A_m^{(i,j,[p,q])}<a_c^{ij}\right]\right)\right) \tag{7.45}$$

Also in this case, Equations (7.44) and (7.45) remain valid when the global component failure probabilities $P\left[\mathrm{F}_{\mathrm{G},r}^{[p,q]}\right]$ are replaced by $P\left[\tilde{\mathrm{F}}_{\mathrm{G},r}^{[p,q]}\right]$, as derived in Equation (7.32).

7.5.3. Proposed logical expression for the failure event $\widehat{\mathrm{F}}_{\mathrm{sys}}^{[p,q]}$ assuming multiple NDE inspection opportunities at time $t_p^q=t_p+q\Delta\tau$

When multiple NDE measurements — i.e., a total of $n_{\mathrm{MS}}^{(i,j,[p,q])}\geq 1$ — are assumed to be collected during the NDE inspection at time t_p^q for each (i,j) combination, the failure criterion introduced in Equation (7.36) can be modified as follows:

$$\widehat{\mathrm{F}}_{\mathrm{sys}}^{[p,q]}\triangleq\left\{\left[\bigcup_{i=1}^{n_{\mathrm{L}}^{[0,p]}}\left(\bigcup_{j=1}^{n_{\mathrm{DM}}^{(i,[0,p])}}\mathrm{F}_{\mathrm{L},ij}^{[p,q]}\right)\right]\cup\left(\bigcup_{r=1}^{n_{\mathrm{G}}}\mathrm{F}_{\mathrm{G},r}^{[p,q]}\right)\right\}\cap\left[\bigcap_{i=1}^{n_{\mathrm{L}}^{[0,p]}}\left(\bigcap_{j=1}^{n_{\mathrm{DM}}^{(i,[0,p])}}\overline{n}_{\mathrm{MS}}^{(i,j,[p,q])}\geq\overline{\overline{n}}_{\mathrm{MS}}^{(i,j,[p,q])}\right)\right] \tag{7.46}$$

or, in a more compact form, as

$$\widehat{\mathrm{F}}_{\mathrm{sys}}^{[p,q]}\triangleq\mathrm{F}_{\mathrm{sys}}^{[p,q]}\cap\left[\bigcap_{i=1}^{n_{\mathrm{L}}^{[0,p]}}\left(\bigcap_{j=1}^{n_{\mathrm{DM}}^{(i,[0,p])}}\overline{n}_{\mathrm{MS}}^{(i,j,[p,q])}\geq\overline{\overline{n}}_{\mathrm{MS}}^{(i,j,[p,q])}\right)\right] \tag{7.47}$$

Equations (7.46) and (7.47) can be interpreted as follows: at least one of the $n_{\mathrm{A}}^{p}+n_{\mathrm{G}}$ reliability components ($\mathrm{F}_{\mathrm{L},ij}^{[p,q]}$ and $\mathrm{F}_{\mathrm{G},r}^{[p,q]}$) has failed and, at the same time, at least

$\overline{\overline{n}}_{\mathrm{MS}}^{(i,j,[p,q])}$ out of the assumed $n_{\mathrm{MS}}^{(i,j,[p,q])}$ NDE measurements (performed at time t_p^q) are lower than the critical crack damage size (a_c^{ij}) for each (i,j) combination. Both Equations listed above remain valid when the global component failure probabilities $P\left[\mathrm{F}_{\mathrm{G},r}^{[p,q]}\right]$ are replaced by $P\left[\tilde{\mathrm{F}}_{\mathrm{G},r}^{[p,q]}\right]$. As a final remark, if $\overline{n}_{\mathrm{MS}}^{(i,j,[p,q])} = \overline{\overline{n}}_{\mathrm{MS}}^{(i,j,[p,q])} = 1$ for each (i,j) combination, then Equation (7.46) reduces to Equation (7.36).

7.5.4. Derivation of lower and upper uni-modal bounds for the probability of false-call at the global system level, $P\left[\breve{\mathcal{F}}_{\mathrm{sys}}^{[p,q]}\right]$, assuming a single NDE inspection opportunity at time $t_p^q = t_p + q\Delta\tau$

The false-call event for the entire system (i.e., the event of having a false alarm during an assumed single NDE inspection opportunity at time t_p^q), herein denoted $\breve{\mathcal{F}}_{\mathrm{sys}}^{[p,q]}$, is defined as

$$\breve{\mathcal{F}}_{\mathrm{sys}}^{[p,q]} \triangleq \left\{\left[\bigcap_{i=1}^{n_{\mathrm{L}}^{[0,p]}}\left(\bigcap_{j=1}^{n_{\mathrm{DM}}^{(i,[0,p])}} \overline{\mathrm{F}_{\mathrm{L},ij}^{[p,q]}}\right)\right] \cap \left(\bigcap_{r=1}^{n_{\mathrm{G}}} \overline{\mathrm{F}_{\mathrm{G},r}^{[p,q]}}\right)\right\} \cap \left[\bigcup_{i=1}^{n_{\mathrm{L}}^{[0,p]}}\left(\bigcup_{j=1}^{n_{\mathrm{DM}}^{(i,[0,p])}} A_m^{(i,j,[p,q])} \geq a_c^{ij}\right)\right] \qquad (7.48)$$

where $\overline{\mathrm{F}_{\mathrm{L},ij}^{[p,q]}}$ and $\overline{\mathrm{F}_{\mathrm{G},r}^{[p,q]}}$ denote the complement of the local and global component failure events $\mathrm{F}_{\mathrm{L},ij}^{[p,q]}$ and $\mathrm{F}_{\mathrm{G},r}^{[p,q]}$, respectively. Equation (7.48) represents the event that, at least for one (i,j) combination, the measured damage size $A_m^{(i,j,[p,q])}$, from the single NDE inspection opportunity at time t_p^q, is larger than or equal to a_c^{ij} and (at the same time) all local and global reliability components, associated with the local and global

failure events $\mathrm{F}_{\mathrm{L},ij}^{[p,q]}$ and $\mathrm{F}_{\mathrm{G},r}^{[p,q]}$, have not failed. Uni-modal bounds for $P\left[\breve{\mathscr{F}}_{\mathrm{sys}}^{[p,q]}\right]$ are specified in terms of (i) the modal false-call probabilities, $P\left[\breve{\mathscr{F}}_{\mathrm{sys}}^{[p,q]}\right]$ (with $i=1,\ldots,n_{\mathrm{L}}^{[0,p]}$ and $j=1,\ldots,n_{\mathrm{DM}}^{(i,[0,p])}$), provided in Equation (7.24), (ii) the complements of the local component failure probabilities — i.e., $P\left[\overline{\mathrm{F}_{\mathrm{L},ij}^{[p,q]}}\right]=1-P\left[\mathrm{F}_{\mathrm{L},ij}^{[p,q]}\right]=F_{A_a^{(i,j,[p,q])}}\left(a_c^{ij}\right)$ (with $i=1,\ldots,n_{\mathrm{L}}^{[0,p]}$ and $j=1,\ldots,n_{\mathrm{DM}}^{(i,[0,p])}$) — from Equation (7.3), and (iii) the complements of the global component failure probabilities $P\left[\overline{\mathrm{F}_{\mathrm{G},r}^{[p,q]}}\right]=1-P\left[\mathrm{F}_{\mathrm{G},r}^{[p,q]}\right]$ (with $r=1,\ldots,n_{\mathrm{G}}$). These lower and upper uni-modal bounds for $P\left[\breve{\mathscr{F}}_{\mathrm{sys}}^{[p,q]}\right]$ can be expressed as (see Appendix D)

$$P\left[\breve{\mathscr{F}}_{\mathrm{sys}}^{[p,q]}\right]\geq\max\left(0,P_{low}\left[\mathrm{FC}_{\mathrm{local}}^{[p,q]}\right]+\sum_{r=1}^{n_{\mathrm{G}}}\left(1-P\left[\mathrm{F}_{\mathrm{G},r}^{[p,q]}\right]\right)-n_{\mathrm{G}}\right) \tag{7.49}$$

$$P\left[\breve{\mathscr{F}}_{\mathrm{sys}}^{[p,q]}\right]\leq\min\left[P_{up}\left[\mathrm{FC}_{\mathrm{local}}^{[p,q]}\right],\min_{r}\left(1-P\left[\mathrm{F}_{\mathrm{G},r}^{[p,q]}\right]\right)\right] \tag{7.50}$$

where $P_{low}\left[\mathrm{FC}_{\mathrm{local}}^{[p,q]}\right]$ is equal to

$$P_{low}\left[\mathrm{FC}_{\mathrm{local}}^{[p,q]}\right]=\max_{i,j}\left(\frac{P\left[\tilde{\mathscr{F}}_{\mathrm{L},ij}^{[p,q]}\right]}{1-P\left[\mathrm{F}_{\mathrm{L},ij}^{[p,q]}\right]}\right)\times\max\left(0,\left[\sum_{i=1}^{n_{\mathrm{L}}^{[0,p]}}\sum_{j=1}^{n_{\mathrm{DM}}^{(i,[0,p])}}\left(1-P\left[\mathrm{F}_{\mathrm{L},ij}^{[p,q]}\right]\right)\right]-\left(n_{\mathrm{A}}^{p}-1\right)\right) \tag{7.51}$$

and $P_{up}\left[\mathrm{FC}_{\mathrm{local}}^{[p,q]}\right]$ is computed as

$$P_{up}\left[\mathrm{FC}_{\mathrm{local}}^{[p,q]}\right]=\min\left(1,\left[\sum_{i=1}^{n_{\mathrm{L}}^{[0,p]}}\sum_{j=1}^{n_{\mathrm{DM}}^{(i,[0,p])}}\frac{P\left[\tilde{\mathscr{F}}_{\mathrm{L},ij}^{[p,q]}\right]}{1-P\left[\mathrm{F}_{\mathrm{L},ij}^{[p,q]}\right]}\right]\right)\times\min_{i,j}\left[\left(1-P\left[\mathrm{F}_{\mathrm{L},ij}^{[p,q]}\right]\right)\right] \tag{7.52}$$

Additionally, Equations (7.49) and (7.50) remain valid when the global component failure probabilities $P\left[\mathrm{F}_{\mathrm{G},r}^{[p,q]}\right]$ are replaced by $P\left[\tilde{\mathrm{F}}_{\mathrm{G},r}^{[p,q]}\right]$.

7.5.5. Proposed logical expression for the probability of false-call at the global system level, $P\left[\widehat{\mathscr{F}}_{\mathrm{sys}}^{[p,q]}\right]$, assuming multiple NDE inspection opportunities at time $t_p^q = t_p + q\Delta\tau$

When multiple NDE measurements (i.e., $n_{\mathrm{MS}}^{(i,j,[p,q])}$) are assumed to be collected during the NDE inspection at time t_p^q for each (i,j) combination, the failure criterion introduced in Equation (7.48) can be modified as follows:

$$\widehat{\mathscr{F}}_{\mathrm{sys}}^{[p,q]} \triangleq \left\{\left[\bigcap_{i=1}^{n_{\mathrm{L}}^{[0,p]}}\left(\bigcap_{j=1}^{n_{\mathrm{DM}}^{(i,[0,p])}}\overline{\mathrm{F}_{\mathrm{L},ij}^{[p,q]}}\right)\right]\cap\left(\bigcap_{r=1}^{n_{\mathrm{G}}}\overline{\mathrm{F}_{\mathrm{G},r}^{[p,q]}}\right)\right\}\cap\left[\bigcup_{i=1}^{n_{\mathrm{L}}^{[0,p]}}\left(\bigcup_{j=1}^{n_{\mathrm{DM}}^{(i,[0,p])}}\overline{n}_{\mathrm{MS}}^{(i,j,[p,q])} < \overline{\overline{n}}_{\mathrm{MS}}^{(i,j,[p,q])}\right)\right] \quad (7.53)$$

Equation (7.53) can be interpreted as follows: all local and global reliability components, associated with the local and global failure events $\mathrm{F}_{\mathrm{L},ij}^{[p,q]}$ and $\mathrm{F}_{\mathrm{G},r}^{[p,q]}$, have not failed and, at the same time, at most $\left(\overline{\overline{n}}_{\mathrm{MS}}^{(i,j,[p,q])}-1\right)$ out of the $n_{\mathrm{MS}}^{(i,j,[p,q])}$ NDE measurements (assumed to be performed at time t_p^q) are lower than the critical damage size at least for one (i,j) combination. Furthermore, the equation listed above remains valid when the global component failure probabilities $P\left[\mathrm{F}_{\mathrm{G},r}^{[p,q]}\right]$ are replaced by $P\left[\tilde{\mathrm{F}}_{\mathrm{G},r}^{[p,q]}\right]$. It is worth noting that, if $\overline{n}_{\mathrm{MS}}^{(i,j,[p,q])} = \overline{\overline{n}}_{\mathrm{MS}}^{(i,j,[p,q])} = 1$ for each (i,j) combination, then Equation (7.53) reduces to Equation (7.48).

References

B.F. Backman, *Composite structures, design, safety and innovation*, Elsevier, 2005.

G. Boole, The laws of thought in which are founded the mathematical theories of logic and probabilities, American Reprint of 1854 edition, Dover, New York, 1958.

O. Ditlevsen, Narrow reliability bounds for structural systems, *Mechanics Based Design of Structures and Machines*, 7(4), 453-472, 1979.

M. Fréchet, Généralisations du théorème des probabilités totales, *Fundamenta Mathematicae*, 25, 379-387, 1935.

C. Huang, and K.Y. Lin, A method for reliability assessment of aircraft structures subject to accidental damage, Proc. 46th AIAA/ASME/ASCE/AHS/ASC Structures, Structural Dynamics, and Materials Conference, Austin, TX, April 2005.

K.Y. Lin, J. Du, and D. Rusk, Structural design methodology based on concepts of uncertainty, Report NASA/CR-2000-209847, NASA Langley Research Center, Hampton, VA, 2000.

A.V. Styuart, M. Mor, E. Livne, and K.Y. Lin, Aeroelastic failure risk assessment in damage tolerant composite airframe structures, Proc. 48th AIAA/ASME/ASCE/ AHS/ASC Structures, Structural Dynamics, and Materials Conference, Honolulu, Hi, April 23-26,2007.

P. Thoft-Christensen, and J.D. Sorensen, Reliability of structural systems with correlated elements, *Applied Mathematic Modelling*, 6(3),171-178, 1982.

Y.C. Zhang, Higher-order reliability bounds for series systems and applications to structural systems, *Computers & Structures*, 46(2), 381-386, 1993.

CHAPTER 8

VERIFICATION OF THE PROPOSED RELIABILITY-BASED DAMAGE PROGNOSIS FRAMEWORK VIA A POSTULATED (EXPONENTIAL) DAMAGE PROPAGATION PROCESS

8.1. Introduction

This Chapter is intended to provide a generalization and a partial verification and validation of the proposed reliability-based damage prognosis framework discussed thus far in this thesis. Sections 8.2 and 8.3 cover the theoretical aspects of the generalized version of the framework; Section 8.4 discusses the applicability of the

proposed methodology by analyzing the fatigue-driven damage evolution process along the adhesive interface in a simple benchmark structure; Section 8.5 provides additional insight into the proposed recursive Bayesian inference scheme through a series of parametric studies; finally, Sections 8.6 and 8.7 briefly investigate alternative expressions for computing lower and upper uni-modal bounds for the probabilities of failure and false-call $P\left[\breve{\mathrm{F}}_{\mathrm{sys}}^{[p,q]}\right]$ and $P\left[\breve{\mathcal{F}}_{\mathrm{sys}}^{[p,q]}\right]$, and compare the tightness of these (alternative) bounds with those obtained from the relationships provided in Sections 7.5.2 and 7.5.4 in Chapter 7.

8.2. Background on structural health monitoring and damage prognosis

Probabilistic design, risk assessment and combined structural health monitoring & damage prognosis (SHM-DP) methodologies (Inman *et al*., 2005; Guan *et al*., 2009) for civil infrastructures, mechanical systems, offshore platforms (Moan, 2005, 2007, 2008), and aerospace structures (Yang *et al*., 1974; Deodatis *et al*., 1996; Lin and Styuart, 2007) such as commercial, transport, and fighter aircrafts, have been under development by the research community for a considerable time. Furthermore, the increasing use of high-performance lightweight composite materials — well-known to be very sensitive to both fatigue- and impact-induced damage — is rendering these rigorous probabilistic design and analysis approaches essential. Various damage mechanisms can in fact initiate and develop, potentially invisibly, to catastrophic levels in the most damage-sensitive components of these structures. Among them, unmanned aerial vehicles (UAVs) are exemplary of how extensively composite materials can be used in aircraft structures; furthermore, the absence of a

pilot, the operational conditions, and the deployment in military zones of these vehicles lead to higher levels of damage tolerance in the airframe compared to commercial airplanes. In particular, as discussed in Chapter 1 and Chapter 2, the wing skin-to-spar adhesive joints are recognized by UAV manufacturers and operators as one of the most fatigue-sensitive subcomponents of a lightweight composite UAV, with the fatigue-driven debonding process progressively evolving from the wing-root and compromising both local component/sub-component strength and global aeroelastic performance (Bauchau and Loewy, 1997; Wang *et al*., 2005; Styuart *et al*., 2007).

The probabilistic framework for remaining fatigue life prediction overviewed in this chapter (in Section 8.3) represents a generalization of the SHM-DP methodology proposed and thoroughly analyzed in Chapters 2 through 7. According to this approach, data collected during non-destructive evaluation (NDE) inspections are used to assess the current state of damage of the monitored structure or structural component (i.e., damage location, damage mechanism, damage size/extent, and damage model evolution parameters). A recursive Bayesian inference scheme is used to update the joint probability distribution function (PDF) of the damage extents at the inspected damage locations as well as the joint PDF of the damage evolution model parameters used to characterize the fatigue-driven damage growth. The Bayesian inference outcome (i.e. the posterior knowledge about the current state of damage of the monitored system) is then used, in the predictive modeling block of the proposed framework, to provide recursive predictions of the reliability index of the structure at

future times (damage prognosis) as shown conceptually in Figure 2.1 in Chapter 2. This predictive modeling part of the framework uses a load hazard model for the probabilistic characterization of future service loads and a damage evolution model to stochastically propagate damage in time. Local (e.g., exceedance of a critical damage size at a certain damage location) and global (e.g., exceedance of the flutter instability boundary, and/or initiation of limit cycle oscillation behavior) failure criteria are finally used to compute the evolution in time of the probability of *system failure* and *false-call* using well-established component and system reliability analysis methods (Ditlevsen and Madsen, 1996).

The proposed methodology constitutes an advanced tool for performing SHM-DP of a composite structural system, or structural component/element, with potential multi-site fatigue-driven damage growth and monitored through periodic and/or continuous NDE inspections. This novel framework integrates (i) probabilistic treatment of NDE inspection results, (ii) recursive Bayesian inference, (iii) stochastic characterization and superposition of operational loads, (iv) mechanics-based damage evolution prediction, (v) state-of-the-art component and system reliability analyses, and (vi) decision making. The verification, practicability, and robustness of this framework are demonstrated through a numerical application, analyzing the fatigue-driven debonding propagation along a pre-defined adhesive interface in a simply supported laminated composite beam (Section 8.4). Although this particular application does not engage all the analytical steps of the proposed damage prognosis methodology, it demonstrates the efficiency and robustness of the proposed recursive

Bayesian updating scheme, which updates simultaneously the joint PDFs of both damage extents and damage evolution model parameters, and shows the use of the proposed component and system reliability analyses to predict the evolution in time of the probabilities of failure and false-alarm of the structure.

8.3. Overview of the generalized damage prognosis methodology

The flowchart shown in Figure 8.1 illustrates the process of uncertainty quantification and propagation needed to estimate the remaining fatigue life of a given monitored structural system once a new NDE inspection outcome, at current time t_p, becomes available. The *inspection outcome* is herein defined as the measured (through NDE sensor-based data processing) damage size vector, $\mathbf{a}_{\mathrm{m}}^{p}$, at the inspected locations at time t_p, and is viewed as a particular realization of the random vector $\mathbf{A}_{\mathrm{m}}^{p}$. This new

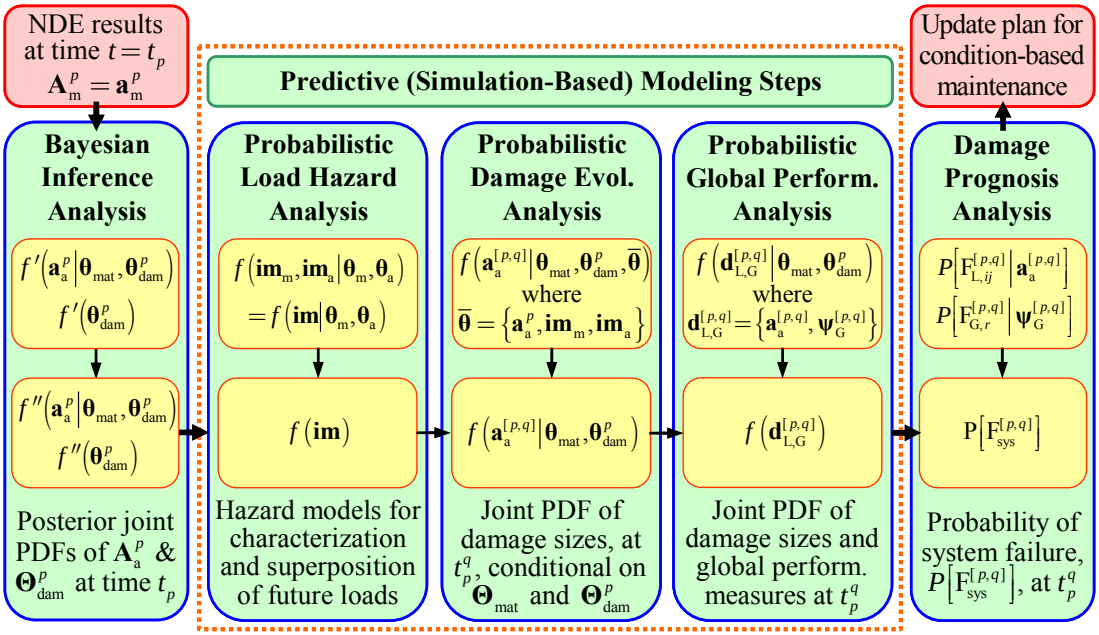

Figure 8.1: Extension of the proposed damage prognosis methodology to other monitored structural systems with multi-site fatigue-driven damage growth.

information is used in the *Bayesian inference* step to compute the posterior joint PDF of the actual damage size vector, $\mathbf{A}_{\mathrm{a}}^{p}$, conditional on the material ($\boldsymbol{\Theta}_{\mathrm{mat}}$) and damage model parameters ($\boldsymbol{\Theta}_{\mathrm{dam}}^{p}$), as well as on all NDE measurement outcomes up to time t_p, denoted by $\mathbf{a}_{\mathrm{m}}^{[0,p]}=\left\{\mathbf{a}_{\mathrm{m}}^{0},\mathbf{a}_{\mathrm{m}}^{1},...,\mathbf{a}_{\mathrm{m}}^{p}\right\}$ and not explicitly included in the notation of Figure 8.1. Henceforth, this conditional joint PDF is denoted as $f''_{\mathbf{A}_{\mathrm{a}}^{p}\left|\boldsymbol{\Theta}_{\mathrm{mat}},\boldsymbol{\Theta}_{\mathrm{dam}}^{p}\right.}\left(\mathbf{a}_{\mathrm{a}}^{p}\left|\boldsymbol{\theta}_{\mathrm{mat}},\boldsymbol{\theta}_{\mathrm{dam}}^{p}\right.\right)$. The dimension of the random vector $\mathbf{A}_{\mathrm{a}}^{p}$ is equal to $n_{\mathrm{A}}^{p}=\sum_{i=1}^{n_{\mathrm{L}}^{[0,p]}}n_{\mathrm{DM}}^{(i,[0,p])}$, where $n_{\mathrm{DM}}^{(i,[0,p])}$ represents the total number of detected damage mechanisms, at damage location *i* up to time t_p, and $n_{\mathrm{L}}^{[0,p]}$ denotes the total number of damage locations inspected up to time t_p. Simultaneously, the measured damage sizes collected in $\mathbf{a}_{\mathrm{m}}^{p}$ are also used to compute the posterior joint PDF of the damage evolution model parameters, $f''_{\boldsymbol{\Theta}_{\mathrm{dam}}^{p}}\left(\boldsymbol{\theta}_{\mathrm{dam}}^{p}\right)$.

As indicated by the notation introduced above, multiple damage locations and multiple damage mechanisms (developing simultaneously at a given damage location) can be readily accommodated by the proposed Bayesian updating scheme. In reality, both damage locations and damage mechanisms are uncertain due to the inherent imperfections of NDE techniques; however, as a simplifying assumption, they are considered deterministic and known in this study. The random parameter vector $\boldsymbol{\Theta}_{\mathrm{mat}}$ (of length n_{mat}) exclusively describes the uncertainty of the material properties used to model the parts of the structure which are assumed to be non-damageable while the

random vector $\boldsymbol{\Theta}_{\text{dam}}^{p}$ (of length n_{dam}) quantifies the uncertainty of those parameters that control the fatigue-driven material degradation in the pre-identified damageable sub-components (e.g., the adhesive joints/interfaces) and, as pointed out in Chapter 2, it does not characterize the bulk material properties of these identified damageable sub-components. Furthermore, Since $\boldsymbol{\Theta}_{\text{mat}}$ and $\boldsymbol{\Theta}_{\text{dam}}^{p}$ characterize the mechanical properties of different materials and/or sub-components, they are reasonably assumed to be statistically independent (s.i.) hereafter.

The second step of the methodology, *probabilistic load hazard analysis*, defines the joint PDF of a vector of intensity measures, $\mathbf{IM}$. This vector characterizes future operational/service loads, including extreme load events such as unexpected rough turbulence-induced loads impacting an aircraft during flight. In this study, the vector $\mathbf{IM}$ is defined as $\mathbf{IM}=\left\{\mathbf{IM}_{\text{m}},\mathbf{IM}_{\text{a}}\right\}$: $\mathbf{IM}_{\text{m}}$ provides the probabilistic characterization of the average (mean) load intensity acting on the structure, whereas $\mathbf{IM}_{\text{a}}$ defines the intensity/amplitude of the superimposed random load (or load fluctuations) about the mean load. This concept was already introduced and outlined in Chapter 2. For example, when considering an aircraft structure, $\mathbf{IM}_{\text{m}}$ could describe the intensity of maneuver-induced loads, while $\mathbf{IM}_{\text{a}}$ could characterize the randomness of the turbulence velocity fields encountered by the aircraft during flight; a detailed treatment of this specific case is provided in Chapter 4. The joint PDF of $\mathbf{IM}$ is herein denoted as $f_{\mathbf{IM}}\left(\mathbf{im}\right)$ and computed by unconditioning the conditional joint PDF $f_{\mathbf{IM}|\boldsymbol{\Theta}_{\text{m}},\boldsymbol{\Theta}_{\text{a}}}\left(\mathbf{im}\middle|\boldsymbol{\theta}_{\text{m}},\boldsymbol{\theta}_{\text{a}}\right)$ with respect to (w.r.t.) the distribution parameter

vectors $\boldsymbol{\Theta}_{\mathrm{m}}$ and $\boldsymbol{\Theta}_{\mathrm{a}}$ — i.e., those parameters characterizing the joint PDF of $\mathbf{IM}_{\mathrm{m}}$ and $\mathbf{IM}_{\mathrm{a}}$ as described in detail in Section 8.3.2.

In the third step of the proposed methodology, *probabilistic damage evolution analysis*, the conditional joint PDF of the system structural response — expressed in terms of the predicted damage size vector, $\mathbf{A}_{\mathrm{a}}^{[p,q]}$, at future time $t_p^q = t_p + q\Delta\tau$ with $q \in \{1, 2, ..., \overline{q}\}$ — is computed through extensive Monte Carlo (MC) simulations. Computationally efficient surrogate models (Myers and Montgomery, 1995) are used for this purpose; these models are fitted and calibrated upon an appropriate design of experiments involving the detailed mechanics-based finite element (FE) model of the structure. The joint PDF of $\mathbf{A}_{\mathrm{a}}^{[p,q]}$, conditional on $\boldsymbol{\Theta}_{\mathrm{mat}}$, $\boldsymbol{\Theta}_{\mathrm{dam}}^{p}$, and all the previous NDE outcomes $\mathbf{a}_{\mathrm{m}}^{[0,p]}$ (not explicitly included in the notation), is denoted as $f_{\mathbf{A}_{\mathrm{a}}^{[p,q]}\left|\boldsymbol{\Theta}_{\mathrm{mat}},\boldsymbol{\Theta}_{\mathrm{dam}}^{p}\right.}\left(\mathbf{a}_{\mathrm{a}}^{[p,q]} \mid \boldsymbol{\theta}_{\mathrm{mat}}, \boldsymbol{\theta}_{\mathrm{dam}}^{p}\right)$ and is computed by unconditioning the conditional joint PDF $f_{\mathbf{A}_{\mathrm{a}}^{[p,q]}\left|\boldsymbol{\Theta}_{\mathrm{mat}},\boldsymbol{\Theta}_{\mathrm{dam}}^{p},\mathbf{A}_{\mathrm{a}}^{p},\mathbf{IM}\right.}\left(\mathbf{a}_{\mathrm{a}}^{[p,q]} \mid \boldsymbol{\theta}_{\mathrm{mat}}, \boldsymbol{\theta}_{\mathrm{dam}}^{p}, \mathbf{a}_{\mathrm{a}}^{p}, \mathbf{im}\right)$ w.r.t. $\mathbf{A}_{\mathrm{a}}^{p}$ and $\mathbf{IM}$. The quantity $\mathbf{A}_{\mathrm{a}}^{[p,q]}$ provides a probabilistic characterization of the future state of damage at the local level. Furthermore, the quantity $\Delta\tau$ is a suitable fixed time interval related to the time-scale of the damage propagation process of interest as discussed in Chapter 5. To conclude this brief overview of the *probabilistic damage evolution analysis* step, it should be pointed out that in some cases (e.g., structures subjected to harmonic loads or any other cyclic loading conditions) it is more appropriate to express all the above considerations in terms of number of load cycles. Current time, t_p, is replaced by the

current number of cycles, N_p, and the time between two subsequent damage propagation evaluations, $\Delta\tau$, is substituted with the number of cycles, ΔN. As a direct consequence, the number of cycles at future time t_p^q, denoted as N_p^q, can then be expressed as $N_p^q = N_p + q\Delta N$ with $q \in \{1, 2, ..., \overline{q}\}$. This latter approach will be used in the application examples discussed in Section 8.4 and in Chapter 9.

The fourth step, *probabilistic global performance analysis*, estimates the joint PDF of the $\mathbf{A}_{\mathrm{a}}^{[p,q]}$ and n_{G} global performance metrics/measures (collected in $\boldsymbol{\Psi}_{\mathrm{g}}^{[p,q]}$) at the generic future time $t_p^q = t_p + q\Delta\tau$ — i.e., the joint PDF $f_{\mathbf{A}_{\mathrm{a}}^{[p,q]}, \boldsymbol{\Psi}_{\mathrm{g}}^{[p,q]}}\left(\mathbf{a}_{\mathrm{a}}^{[p,q]}, \boldsymbol{\psi}_{\mathrm{g}}^{[p,q]}\right)$. To provide some examples, the random vector $\boldsymbol{\Psi}_{\mathrm{g}}^{[p,q]}$ could collect a given set of natural frequencies of the monitored structure, the reduced (due to damage) flutter velocity of an aircraft wing, the reduced (due to damage) initial stiffness and/or peak resistance of a structure under a push-over load of a given spatial distribution, etc. The joint PDF $f_{\mathbf{A}_{\mathrm{a}}^{[p,q]}, \boldsymbol{\Psi}_{\mathrm{g}}^{[p,q]}}\left(\mathbf{a}_{\mathrm{a}}^{[p,q]}, \boldsymbol{\psi}_{\mathrm{g}}^{[p,q]}\right)$ thus contains both local (through $\mathbf{A}_{\mathrm{a}}^{[p,q]}$) and global (through $\boldsymbol{\Psi}_{\mathrm{g}}^{[p,q]}$) damage-related information, and is denoted $f_{\mathbf{D}_{\mathrm{L,G}}^{[p,q]}}\left(\mathbf{d}_{\mathrm{L,G}}^{[p,q]}\right)$, where $\mathbf{D}_{\mathrm{L,G}}^{[p,q]} = \left\{\mathbf{A}_{\mathrm{a}}^{[p,q]}, \boldsymbol{\Psi}_{\mathrm{g}}^{[p,q]}\right\}$. This PDF can be obtained through three sub-steps: (i) computation of the conditional joint PDF $f_{\boldsymbol{\Psi}_{\mathrm{g}}^{[p,q]} \left| \mathbf{A}_{\mathrm{a}}^{p}, \boldsymbol{\Theta}_{\mathrm{mat}}, \boldsymbol{\Theta}_{\mathrm{dam}}^{p}\right.}\left(\boldsymbol{\psi}_{\mathrm{g}}^{[p,q]} \left| \mathbf{a}_{\mathrm{a}}^{p}, \boldsymbol{\theta}_{\mathrm{mat}}, \boldsymbol{\theta}_{\mathrm{dam}}^{p}\right.\right)$ through a series of numerical simulations using surrogate models for the response quantities of interest collected in $\boldsymbol{\Psi}_{\mathrm{g}}^{[p,q]}$; (ii) derivation of the conditional joint PDF $f_{\boldsymbol{\Psi}_{\mathrm{g}}^{[p,q]} \left| \mathbf{A}_{\mathrm{a}}^{p}\right.}\left(\boldsymbol{\psi}_{\mathrm{g}}^{[p,q]} \left| \mathbf{a}_{\mathrm{a}}^{p}\right.\right)$ by unconditioning the previously computed quantity,

$f_{\boldsymbol{\Psi}_{\mathrm{g}}^{[p,q]}\left|\mathbf{A}_{\mathrm{a}}^{p},\boldsymbol{\Theta}_{\mathrm{mat}},\boldsymbol{\Theta}_{\mathrm{dam}}^{p}\right.}\left(\boldsymbol{\psi}_{\mathrm{g}}^{[p,q]}\left|\mathbf{a}_{\mathrm{a}}^{p},\boldsymbol{\theta}_{\mathrm{mat}},\boldsymbol{\theta}_{\mathrm{dam}}^{p}\right.\right)$, w.r.t. $\boldsymbol{\Theta}_{\mathrm{mat}}$ and $\boldsymbol{\Theta}_{\mathrm{dam}}^{p}$; (iii) estimation of $f_{\mathbf{A}_{\mathrm{a}}^{[p,q]},\boldsymbol{\Psi}_{\mathrm{g}}^{[p,q]}}\left(\mathbf{a}_{\mathrm{a}}^{[p,q]},\boldsymbol{\psi}_{\mathrm{g}}^{[p,q]}\right)$ by using the definition of a conditional PDF as

$$f_{\mathbf{D}_{\mathrm{L,G}}^{[p,q]}}\left(\mathbf{d}_{\mathrm{L,G}}^{[p,q]}\right)=f_{\mathbf{A}_{\mathrm{a}}^{[p,q]},\boldsymbol{\Psi}_{\mathrm{g}}^{[p,q]}}\left(\mathbf{a}_{\mathrm{a}}^{[p,q]},\boldsymbol{\psi}_{\mathrm{g}}^{[p,q]}\right)=f_{\boldsymbol{\Psi}_{\mathrm{g}}^{[p,q]}\left|\mathbf{A}_{\mathrm{a}}^{p}\right.}\left(\boldsymbol{\psi}_{\mathrm{g}}^{[p,q]}\left|\mathbf{a}_{\mathrm{a}}^{[p,q]}\right.\right)\cdot f_{\mathbf{A}_{\mathrm{a}}^{[p,q]}}\left(\mathbf{a}_{\mathrm{a}}^{[p,q]}\right) \tag{8.1}$$

where the marginal PDF $f_{\mathbf{A}_{\mathrm{a}}^{[p,q]}}\left(\mathbf{a}_{\mathrm{a}}^{[p,q]}\right)$ is computed as

$$f_{\mathbf{A}_{\mathrm{a}}^{[p,q]}}\left(\mathbf{a}_{\mathrm{a}}^{[p,q]}\right)=\int_{\boldsymbol{\Theta}_{\mathrm{mat}}}\int_{\boldsymbol{\Theta}_{\mathrm{dam}}^{p}}f_{\mathbf{A}_{\mathrm{a}}^{[p,q]}\left|\boldsymbol{\Theta}_{\mathrm{mat}},\boldsymbol{\Theta}_{\mathrm{dam}}^{p}\right.}\left(\mathbf{a}_{\mathrm{a}}^{[p,q]}\left|\boldsymbol{\theta}_{\mathrm{mat}},\boldsymbol{\theta}_{\mathrm{dam}}^{p}\right.\right)d\boldsymbol{\theta}_{\mathrm{mat}}\,d\boldsymbol{\theta}_{\mathrm{dam}}^{p} \tag{8.2}$$

Once the joint PDF $f_{\mathbf{D}_{\mathrm{L,G}}^{[p,q]}}\left(\mathbf{d}_{\mathrm{L,G}}^{[p,q]}\right)$ is determined, the probability of *system failure* at time t_p^q, $P\left[\mathrm{F}_{\mathrm{sys}}^{[p,q]}\right]$, can be estimated by performing component and system reliability analyses. These analyses are part of the fifth step of the framework, namely *damage prognosis analysis*, and are carried out through three sub-steps: (i) computation of the component (or modal) conditional failure probabilities, $P\left[\mathrm{F}_{\mathrm{L},ij}^{[p,q]}\left|\mathbf{A}_{\mathrm{a}}^{[p,q]}\right.\right]$ with $i=1,\ldots,n_{\mathrm{L}}^{[0,p]}$ and $j=1,\ldots,n_{\mathrm{DM}}^{(i,[0,p])}$, and $P\left[\mathrm{F}_{\mathrm{G},r}^{[p,q]}\left|\boldsymbol{\Psi}_{\mathrm{g}}^{[p,q]}\right.\right]$ with $r=1,\ldots,n_{\mathrm{G}}$, associated with each local and global failure mode/condition, respectively; (ii) computation of the unconditional modal failure probabilities; and (iii) computation of lower and upper bounds (e.g., uni-modal bounds) for $P\left[\mathrm{F}_{\mathrm{sys}}^{[p,q]}\right]$ by abstracting the real structure into a combination of series and parallel sub-systems. It is worth mentioning that the use of these bounds is no longer necessary when direct simulation techniques and a sample representation of the aforementioned PDFs is

adopted, exploiting for example transitional Markov Chain Monte Carlo methods, TMCMC (Ching and Chen, 2007).

The final stage of the proposed methodology consists of the *decision making* process. It essentially uses the damage prognosis results obtained in the previous step to optimize the maintenance and repair/retrofit program and consequently reduce their cost over the entire or remaining service life of the structure. The decisions made in this step, at current time t_p, can be revised later as new NDE data are collected at times t_{p+1}, t_{p+2}, … Scheduling of the next maintenance can be obtained by interpolating or extrapolating the predictions for $P\left[\mathrm{F}_{\mathrm{sys}}^{[p,q]}\right]$ (with $q = 1, 2, ..., \overline{q}$) in order to estimate the time at which this probability will exceed a specified safety threshold $\overline{p}_{\mathrm{F}}$.

8.3.1. Proposed Recursive Bayesian inference scheme

Information on the current state of damage of the structural system (or structural component/element) is assumed to be provided by continuous and/or periodic NDE inspections. The following three main assumptions are made herein about an NDE inspection: (i) an NDE inspection can detect and locate damage, identify the damage mechanisms developing concurrently at a specified damage location, and, in the best case scenario, quantify the extents of damage for each damage mechanism detected and identified; (ii) The overall uncertainty (i.e., including both systematic and random errors) associated with the measured extent of damage provided by a given NDE technique, is dependent on damage location, damage mechanism, and damage extent; (iii) for simplicity, it is assumed that both detection

and measurement of the extent of a certain damage mechanism, developing at a given damage location, depend only on the actual and unknown damage extent (or stage of formation) of this damage mechanism at the time of inspection.

As more thoroughly analyzed in Chapter 3, the detection capability of a given NDE technique is provided by the so-called *probability of detection* (*POD*) *curve* (Berens, 1989; Staat, 1993). Under the constraint $a_a^{(i,j,p)} > 0$, the *POD* for a particular combination of damage location (i), damage mechanism (j), and inspection time , t_p, i.e., a particular (i,j,p) combination, is defined as

$$POD\left(a_a^{(i,j,p)}\right) = P\left[A_m^{(i,j,p)} > 0 \middle| A_a^{(i,j,p)} = a_a^{(i,j,p)}\right] \tag{8.3}$$

On the other hand, the probability that the NDE outcome constitutes a false-call (or false-alarm) — i.e., damage detected ($A_m^{(i,j,p)} > 0$) even though in reality there is no actual damage ($a_a^{(i,j,p)} = 0$) — is referred to as *false-call probability (FCP)*, and it is defined as

$$FCP_{(i,j,p)} = P\left[A_m^{(i,j,p)} > 0 \,|\, A_a^{(i,j,p)} = 0\right] = POD\left(a_a^{(i,j,p)} = 0\right) \tag{8.4}$$

A particular example of the *POD* curve model proposed by Berens (1989), for a given set of model parameters, is shown in Figure 8.2. This specific *POD* curve will also be used in the application example proposed later in this Chapter, as well as in all the parametric studies provided in Sections 8.4 and 8.5.

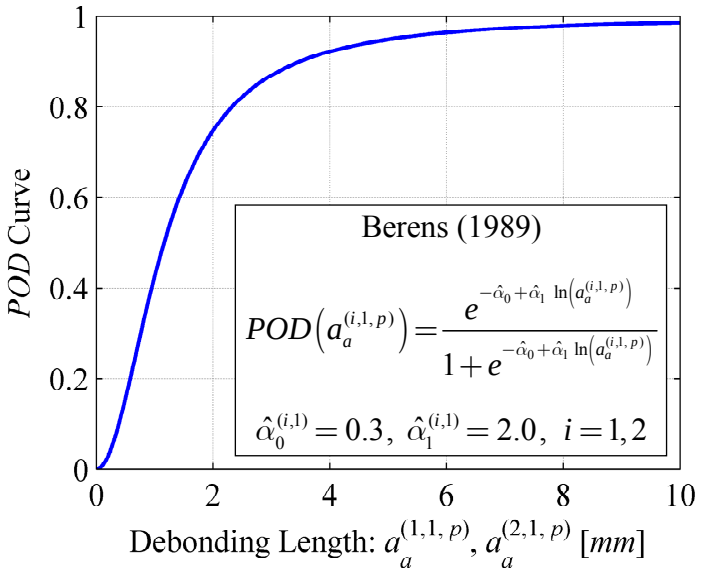

Figure 8.2: Example of *POD* curve model found in the literature (Berens, 1989) and used later in the application example and parametric studies in Sections 8.4 and 8.5.

Once, for a given (i, j, p) combination, damage is detected (D) and its extent measured, it is natural to question the accuracy of that NDE measurement conditional on the actual (but unknown) damage size. As already discussed in Chapter 3, this accuracy is herein modeled by using the following linear damage-size measurement model (see Figure 8.3):

$$A_m^{(i,j,p)}\left(A_a^{(i,j,p)} = a_a^{(i,j,p)}, D\right) = \beta_0^{(i,j)} + \beta_1^{(i,j)}\, a_a^{(i,j,p)} + \varepsilon_{ij} \tag{8.5}$$

where $A_a^{(i,j,p)}$ and $A_m^{(i,j,p)}$ are respectively the actual and measured damage size for damage location i, damage mechanism j, and inspection time t_p. The quantity $a_a^{(i,j,p)}$ denotes the value of the actual damage size for the particular (i, j, p) combination considered. The two terms $\beta_0^{(i,j)}$ and $\beta_1^{(i,j)}$ are the coefficients of the (assumed) linear

model in Equation (8.5) accounting for the systematic measurement errors. Finally, $\varepsilon_{ij} \sim N\left(0, \sigma_{\varepsilon_{ij}}\right)$ represents the random measurement error assumed to be Gaussian distributed with zero-mean and standard deviation $\sigma_{\varepsilon_{ij}}$ assumed, for the sake of simplicity, to be constant and independent of $a_a^{(i,j,p)}$ (Zhang and Mahadevan, 2001). The damage-size measurement model parameters $\beta_0^{(i,j)}$, $\beta_1^{(i,j)}$, and $\sigma_{\varepsilon_{ij}}$ are unknown and have to be estimated, for each (i,j) combination, through a linear regression analysis on a given set of known damage sizes (see Chapter 3). The estimated linear regression coefficients and standard deviation of the random measurement error are respectively denoted $\hat{\beta}_0^{(i,j)}$, $\hat{\beta}_1^{(i,j)}$, and $\hat{\sigma}_{\varepsilon_{ij}}$. With these estimates, it is then possible to derive the PDF of the measured damage size $A_m^{(i,j,p)}$, conditional on the actual damage size $A_a^{(i,j,p)} = a_a^{(i,j,p)}$ as (see Chapter 3)

$$f_{A_m^{(i,j,p)}\left|A_a^{(i,j,p)}\right.}\left(a_m^{(i,j,p)}\middle|a_a^{(i,j,p)}\right) = \varphi\left(a_m^{(i,j,p)}; \hat{\mu}_{A_m|A_a}^{(i,j,p)}, \hat{\sigma}_{\varepsilon_{ij}}\right) \tag{8.6}$$

where $\varphi\left(a_m^{(i,j,p)}; \hat{\mu}_{A_m|A_a}^{(i,j,p)}, \hat{\sigma}_{\varepsilon_{ij}}\right)$ is the conditional Normal PDF of $A_m^{(i,j,p)}$ with mean $\hat{\mu}_{A_m|A_a}^{(i,j,p)} = \hat{\beta}_0^{(i,j)} + \hat{\beta}_1^{(i,j)} a_a^{(i,j,p)}$ and standard deviation $\hat{\sigma}_{\varepsilon_{ij}}$. However, as shown in Figure 8.3, this conditional PDF is meaningful only in the range $A_m^{(i,j,p)} > 0$ and is therefore scaled as

$$\tilde{\varphi}\left(a_m^{(i,j,p)}; \hat{\mu}_{A_m|A_a}^{(i,j,p)}, \hat{\sigma}_{\varepsilon_{ij}}\right) = \varphi\left(a_m^{(i,j,p)}; \hat{\mu}_{A_m|A_a}^{(i,j,p)}, \hat{\sigma}_{\varepsilon_{ij}}\right)\left[\Phi\left(\frac{\hat{\beta}_0^{(i,j)} + \hat{\beta}_1^{(i,j)} a_a^{(i,j,p)}}{\hat{\sigma}_{\varepsilon_{ij}}}\right)\right]^{-1} \tag{8.7}$$

where $\Phi(\cdot)$ represents the Standard Normal cumulative distribution function (CDF).

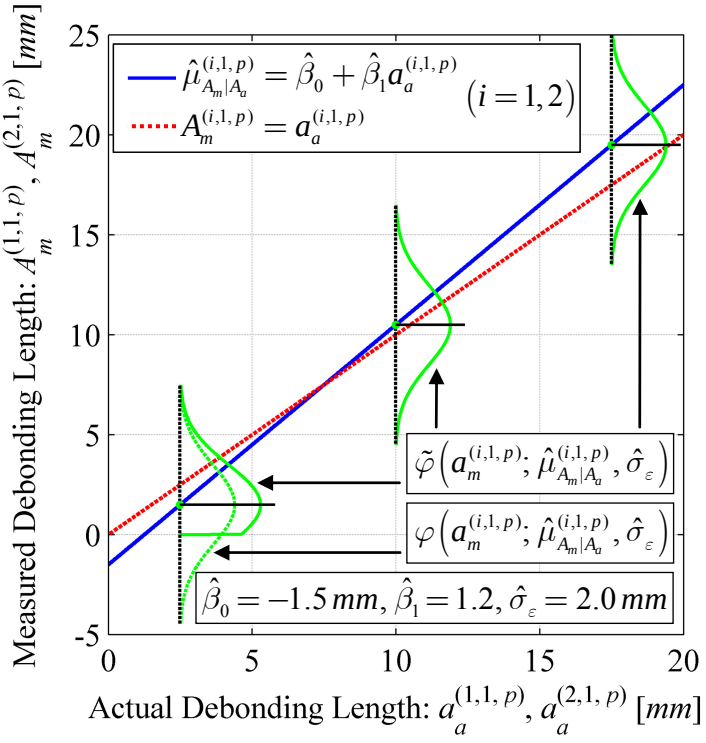

Figure 8.3: Linear sizing model characterized by a (truncated) Gaussian distributed measurement error and plotted for a given set of estimated model parameters $\hat{\beta}_0^{(1,1)} = \hat{\beta}_0^{(2,1)} = \hat{\beta}_0 = -1.5\,mm$, $\hat{\beta}_1^{(1,1)} = \hat{\beta}_1^{(2,1)} = \hat{\beta}_1 = 1.2$, and $\hat{\sigma}_{\varepsilon_{1,1}} = \hat{\sigma}_{\varepsilon_{2,1}} = \hat{\sigma}_\varepsilon = 2\,mm$.

POD curve and Equation (8.7) are used together to derive the likelihood function, $L\left(\mathbf{a}_{\mathrm{a}}^{p} \middle| \mathbf{a}_{\mathrm{m}}^{p}\right)$, needed to update the prior conditional joint PDF, $f'_{\mathbf{A}_{\mathrm{a}}^{p}|\boldsymbol{\Theta}_{\mathrm{mat}},\boldsymbol{\Theta}_{\mathrm{dam}}^{p}}\left(\mathbf{a}_{\mathrm{a}}^{p} \middle| \boldsymbol{\theta}_{\mathrm{mat}}, \boldsymbol{\theta}_{\mathrm{dam}}^{p}\right)$, into the posterior conditional joint PDF, $f''_{\mathbf{A}_{\mathrm{a}}^{p}|\boldsymbol{\Theta}_{\mathrm{mat}},\boldsymbol{\Theta}_{\mathrm{dam}}^{p}}\left(\mathbf{a}_{\mathrm{a}}^{p} \middle| \boldsymbol{\theta}_{\mathrm{mat}}, \boldsymbol{\theta}_{\mathrm{dam}}^{p}\right)$, as the new measurement results, $\mathbf{a}_{\mathrm{m}}^{p}$, become available at the inspection time t_p. Simultaneously, the NDE results obtained at time t_p are also used to compute the posterior joint PDF of the damage evolution model parameters,

$f''_{\boldsymbol{\Theta}^p_{\text{dam}}}\left(\boldsymbol{\theta}^p_{\text{dam}}\right)$. All the mathematical details and derivations together with an exhaustive discussion of this topic are provided in Chapter 3. The updating Equations derived in Chapter 3 are used later in the application example presented in Section 8.4.

8.3.2. Probabilistic load hazard analysis

In this second part of the thesis, aimed at providing a more general version of the proposed damage prognosis framework, a random dynamic load acting on the monitored structural system is conveniently decomposed into two components: its mean/average intensity, characterized probabilistically by the intensity measure vector $\mathbf{IM}_{\text{m}}$, and the superimposed random stochastic load (or load fluctuations) about the mean-load intensity, probabilistically described by the intensity measure vector $\mathbf{IM}_{\text{a}}$. A realization of such a stochastic load is conceptually illustrated in Figure 8.4 and a particularization of this load decomposition and superposition approach, when the load fluctuations are represented by a harmonic load of given/fixed frequency and random amplitude, is conceptually depicted in Figure 8.5. Additionally, to facilitate the description and discussion of the proposed probabilistic load hazard analysis step, it is assumed throughout this section that the external load acting on the structure is characterized by a given/fixed spatial distribution thereby reducing the problem to the probabilistic characterization of a single/scalar load quantity. However, the theory presented hereafter can be generalized to the case of multiple load spatial distributions as well as to a scenario involving multiple random concentrated loads with potential spatial cross-correlation (He *et al.*, 2008).

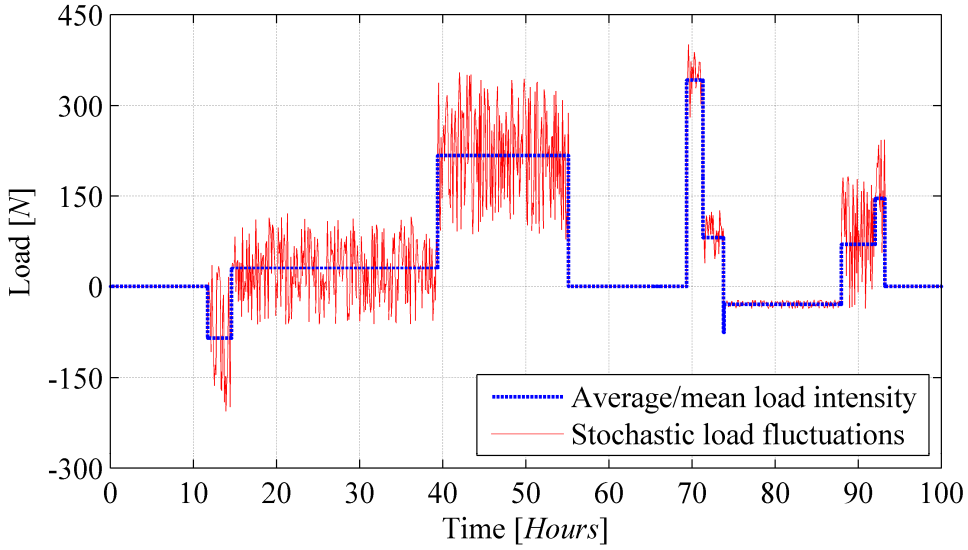

Figure 8.4: Illustrative example of load superposition for the case in which mean-load intensity and RMS value of the load fluctuations are considered to be statistically dependent. The RMS value of the load fluctuations is renewed at each mean-load pulse occurrence, remains constant for the entire duration of each mean-load pulse, and is equal to zero when the mean-load pulse intensity is equal to zero.

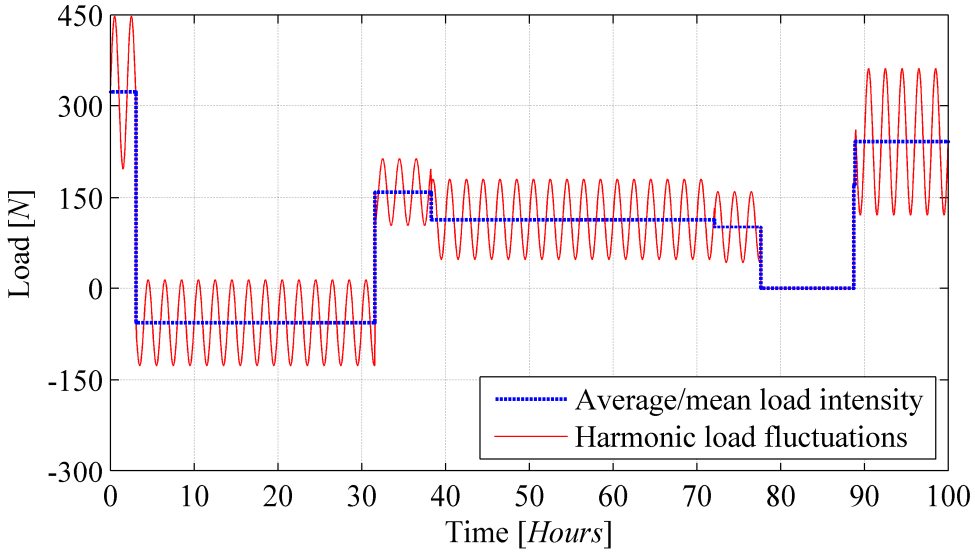

Figure 8.5: Illustrative example of load superposition for the case in which mean-load intensity and amplitude of the harmonic load fluctuations are considered to be statistically dependent. The amplitude value of the load fluctuations is renewed at each mean-load pulse occurrence, remains constant for the entire duration of each mean-load pulse, and is equal to zero when the mean-load pulse intensity is equal to zero.

The random sequence of the applied mean-load (e.g., blue line in Figure 8.4 and Figure 8.5) is modeled and simulated using a homogeneous Poisson rectangular pulse process (Wen, 1990) with mean rate of occurrence $\lambda_{\mathrm{m}} = 1/\mu_{\Delta T_{\mathrm{m}}}$ (where $\mu_{\Delta T_{\mathrm{m}}}$, collected in the random parameter vector $\boldsymbol{\Theta}_{\mathrm{m}}$, denotes the average duration of the mean-load pulses). Each arrival (in time) of a Poisson event raises a rectangular pulse of random intensity P_{m} — according to its conditional PDF $f_{P_{\mathrm{m}}|\boldsymbol{\Theta}_{\mathrm{m}}}\left(p_{\mathrm{m}}\,|\,\boldsymbol{\theta}_{\mathrm{m}}\right)$ — until the next arrival. Based on these considerations, the intensity measure vector $\mathbf{IM}_{\mathrm{m}}$ is defined as $\mathbf{IM}_{\mathrm{m}} = \left\{P_{\mathrm{m}}, \Delta T_{\mathrm{m}}\right\}$. Additionally, a generic realization of the random vector $\mathbf{IM}_{\mathrm{m}} = \mathbf{im}_{\mathrm{m}}$ in $\left[t_p, t_p^{\bar{q}}\right]$ is herein defined as $\mathbf{im}_{\mathrm{m}} \triangleq \left\{\mathbf{im}_{\mathrm{m}}^{(k)},\ k = 1, ..., n_{\mathrm{m}}\right\}$ with (i) $\mathbf{im}_{\mathrm{m}}^{(k)} = \left\{p_{\mathrm{m}}^{(k)}, \Delta t_{\mathrm{m}}^{(k)}\right\}$ specifying the intensity and duration of the k^{th} mean-load pulse and (ii) n_{m} representing the total number of pulses randomly generated during a generic realization of $\mathbf{IM}_{\mathrm{m}}$. The mean-load intensity, $p_{\mathrm{m}}^{(k)}$, is sampled according to the conditional PDF $f_{P_{\mathrm{m}}|\boldsymbol{\Theta}_{\mathrm{m}}}\left(p_{\mathrm{m}}\,|\,\boldsymbol{\theta}_{\mathrm{m}}\right)$ while the pulse duration, $\Delta t_{\mathrm{m}}^{(k)}$, is drawn from the exponential distribution of ΔT_{m} characterized by the mean value $\mu_{\Delta T_{\mathrm{m}}}$. From the discussion above, it is also deduced that the random parameter vector $\boldsymbol{\Theta}_{\mathrm{m}}$ collects all the distribution parameters necessary to probabilistically characterize the random variables P_{m} and ΔT_{m}. For example, if the conditional PDF $f_{P_{\mathrm{m}}|\boldsymbol{\Theta}_{\mathrm{m}}}\left(p_{\mathrm{m}}\,|\,\boldsymbol{\theta}_{\mathrm{m}}\right)$ is modeled using a uniform distribution, then the two boundaries of this distribution (i.e., the lower boundary $P_{\mathrm{m}}^{\min}$ and the upper boundary $P_{\mathrm{m}}^{\max}$) would be contained in $\boldsymbol{\Theta}_{\mathrm{m}}$ and could themselves be considered (in the most general case) as random variables.

Once the random sequence of mean/average load pulses, $\mathbf{IM}_{\mathrm{m}} = \mathbf{im}_{\mathrm{m}}$, is stochastically realized, according to the procedure outlined above, an additional random sequence of load pulses, $\mathbf{IM}_{\mathrm{a}} = \mathbf{im}_{\mathrm{a}}$, characterizing the intensity of the stochastic load fluctuations, is generated and superimposed to $\mathbf{im}_{\mathrm{m}}$. These stochastic load fluctuations are modeled as a zero-mean stationary (within each pulse) random process — completely characterized by its power spectral density (PSD) function — and they are considered to be the driving factor of the fatigue-induced damage growth throughout the pre-identified damageable sub-components of the structure (see Chapter 2). For the sake of simplicity and illustration purposes, the area (Σ_{a}) under the PSD function, defining the stochastic load fluctuations, is considered as the only random variable characterized by the conditional PDF $f_{\Sigma_{\mathrm{a}}|\boldsymbol{\Theta}_{\mathrm{a}}}\left(\sigma_{\mathrm{a}} \,|\, \boldsymbol{\theta}_{\mathrm{a}}\right)$. In other words, for given values of $\Sigma_{\mathrm{a}} = \sigma_{\mathrm{a}}$ and $\boldsymbol{\Theta}_{\mathrm{a}} = \boldsymbol{\theta}_{\mathrm{a}}$ the random process, used to model and simulate these load fluctuations, is completely defined and can be stochastically realized (e.g., by using spectral representation methods; Priestley, 1987). Furthermore, if $\mathbf{IM}_{\mathrm{a}}$ is considered to be s.i. of $\mathbf{IM}_{\mathrm{m}}$, the same reasoning as the one outlined above for $\mathbf{IM}_{\mathrm{m}}$ can be used. A homogeneous Poisson rectangular pulse process with mean rate of occurrence $\lambda_{\mathrm{a}} = 1/\mu_{\Delta T_{\mathrm{a}}}$ (where $\mu_{\Delta T_{\mathrm{a}}}$, collected in the random parameter vector $\boldsymbol{\Theta}_{\mathrm{a}}$, denotes the average duration of the load pulse) is also used to model and simulate the random sequence of the intensity (measured, as outlined above, through its root-mean-square value, Σ_{a}) of the stochastic dynamic load fluctuations about the mean-load intensity (P_{m}). Each arrival (in time) of a Poisson event raises a rectangular pulse of random

intensity Σ_a according to its conditional PDF $f_{\Sigma_a|\boldsymbol{\Theta}_a}(\sigma_a|\boldsymbol{\theta}_a)$. Additionally, a generic realization of the random vector $\mathbf{IM}_a = \mathbf{im}_a$ in $\left[t_p, t_p^{\bar{q}}\right]$ is defined as $\mathbf{im}_a \triangleq \left\{\mathbf{im}_a^{(k)},\ k = 1, ..., n_a\right\}$ with (i) $\mathbf{im}_a^{(k)} = \left\{\sigma_a^{(k)}, \Delta t_a^{(k)}\right\}$ specifying the intensity and duration of the k^{th} pulse and (ii) n_a representing the total number of pulses randomly generated during a generic realization of $\mathbf{IM}_a$. The quantity $\sigma_a^{(k)}$ is sampled according to the conditional PDF $f_{\Sigma_a|\boldsymbol{\Theta}_a}(\sigma_a|\boldsymbol{\theta}_a)$ while the pulse duration, $\Delta t_a^{(k)}$, is drawn from the exponential distribution of ΔT_a defined by the mean value $\mu_{\Delta T_a}$. However, in the most general case, $\mathbf{IM}_m$ and $\mathbf{IM}_a$ can or must be considered statistically dependent. For example, as depicted in Figure 8.4 and Figure 8.5, the physics behind the loading process being modeled or (sometimes) mathematical convenience could dictate that $\Delta t_a^{(k)} = \Delta t_m^{(k)}$ (for $k = 1, ..., n_m$) and/or $\sigma_a = 0$ when $p_m = 0$. In this second (and more complicated) scenario, once the vector $\mathbf{im}_m$ is randomly realized, then the other intensity measure vector, $\mathbf{im}_a$, must be sampled from the conditional PDF $f_{\mathbf{IM}_a|\mathbf{IM}_m,\boldsymbol{\Theta}_a}(\mathbf{im}_m|\mathbf{im}_m,\boldsymbol{\theta}_a)$.

8.3.3. Probabilistic damage evolution analysis

The third step of the proposed methodology (namely *probabilistic damage evolution analysis*) is the most computationally expensive analysis step; therefore, the use of metamodels and reasonably simplifying assumptions becomes essentials in order to maintain the computational feasibility of the overall framework. This analysis

step aims at computing the conditional joint PDF $f_{\mathbf{A}_{\mathrm{a}}^{[p,q]}\left|\boldsymbol{\Theta}_{\mathrm{mat}},\boldsymbol{\Theta}_{\mathrm{dam}}^{p}\right.}\left(\mathbf{a}_{\mathrm{a}}^{[p,q]}\left|\boldsymbol{\theta}_{\mathrm{mat}},\boldsymbol{\theta}_{\mathrm{dam}}^{p}\right.\right)$ at time $t_p^q = t_p + q\Delta\tau$ (with $q = 1, 2, ..., \overline{q}$) by unconditioning the conditional joint PDF $f_{\mathbf{A}_{\mathrm{a}}^{[p,q]}\left|\boldsymbol{\Theta}_{\mathrm{mat}},\boldsymbol{\Theta}_{\mathrm{dam}}^{p},\mathbf{A}_{\mathrm{a}}^{p},\mathbf{IM}\right.}\left(\mathbf{a}_{\mathrm{a}}^{[p,q]}\left|\boldsymbol{\theta}_{\mathrm{mat}},\boldsymbol{\theta}_{\mathrm{dam}}^{p},\mathbf{a}_{\mathrm{a}}^{p},\mathbf{im}\right.\right)$ — appearing at the beginning of the third analytical step in Figure 8.1 — w.r.t. $\mathbf{A}_{\mathrm{a}}^{p}$ and $\mathbf{IM}$ as shown below

$$
\begin{aligned}
&f_{\mathbf{A}_{\mathrm{a}}^{[p,q]}\left|\boldsymbol{\Theta}_{\mathrm{mat}},\boldsymbol{\Theta}_{\mathrm{dam}}^{p}\right.}\left(\mathbf{a}_{\mathrm{a}}^{[p,q]}\left|\boldsymbol{\theta}_{\mathrm{mat}},\boldsymbol{\theta}_{\mathrm{dam}}^{p}\right.\right)= \\
&\int_{\mathbf{A}_{\mathrm{a}}^{p}}\int_{\mathbf{IM}} f_{\mathbf{A}_{\mathrm{a}}^{[p,q]}\left|\boldsymbol{\Theta}_{\mathrm{mat}},\boldsymbol{\Theta}_{\mathrm{dam}}^{p},\mathbf{A}_{\mathrm{a}}^{p},\mathbf{IM}\right.}\left(\mathbf{a}_{\mathrm{a}}^{[p,q]}\left|\boldsymbol{\theta}_{\mathrm{mat}},\boldsymbol{\theta}_{\mathrm{dam}}^{p},\mathbf{a}_{\mathrm{a}}^{p},\mathbf{im}\right.\right) \\
&\qquad f''_{\mathbf{A}_{\mathrm{a}}^{p}\left|\boldsymbol{\Theta}_{\mathrm{mat}},\boldsymbol{\Theta}_{\mathrm{dam}}^{p}\right.}\left(\mathbf{a}_{\mathrm{a}}^{p}\left|\boldsymbol{\theta}_{\mathrm{mat}},\boldsymbol{\theta}_{\mathrm{dam}}^{p}\right.\right) f_{\mathbf{IM}}(\mathbf{im})\, d\mathbf{im}\, d\mathbf{a}_{\mathrm{a}}^{p}
\end{aligned}
\tag{8.8}
$$

Equation (8.8) is an application of the total probability theorem (TPT) and its final result is obtained through extensive Monte Carlo (MC) simulations during which the random vectors $\mathbf{A}_{\mathrm{a}}^{p}$ and $\mathbf{IM}$ are sampled according to their PDFs — i.e., $f''_{\mathbf{A}_{\mathrm{a}}^{p}\left|\boldsymbol{\Theta}_{\mathrm{mat}},\boldsymbol{\Theta}_{\mathrm{dam}}\right.}\left(\mathbf{a}_{\mathrm{a}}^{p}\left|\boldsymbol{\theta}_{\mathrm{mat}},\boldsymbol{\theta}_{\mathrm{dam}}\right.\right)$ and $f_{\mathbf{IM}}(\mathbf{im})$. It is worth noting that the uncertainty of $\mathbf{A}_{\mathrm{a}}^{[p,q]}$ for given/fixed values of $\boldsymbol{\Theta}_{\mathrm{mat}} = \boldsymbol{\theta}_{\mathrm{mat}}$, $\boldsymbol{\Theta}_{\mathrm{dam}}^{p} = \boldsymbol{\theta}_{\mathrm{dam}}^{p}$, $\mathbf{A}_{\mathrm{a}}^{p} = \mathbf{a}_{\mathrm{a}}^{p}$, and $\mathbf{IM} = \mathbf{im}$ — i.e., the uncertainty quantified by the joint conditional PDF $f_{\mathbf{A}_{\mathrm{a}}^{[p,q]}\left|\boldsymbol{\Theta}_{\mathrm{mat}},\boldsymbol{\Theta}_{\mathrm{dam}}^{p},\mathbf{A}_{\mathrm{a}}^{p},\mathbf{IM}\right.}\left(\mathbf{a}_{\mathrm{a}}^{[p,q]}\left|\boldsymbol{\theta}_{\mathrm{mat}},\boldsymbol{\theta}_{\mathrm{dam}}^{p},\mathbf{a}_{\mathrm{a}}^{p},\mathbf{im}\right.\right)$ inside the integral in Equation (8.8) — arises from the record-to-record variability of the structural response across the ensemble of load time histories realized for a given value of the load intensity $\mathbf{IM}_{\mathrm{a}} = \mathbf{im}_{\mathrm{a}}$ (e.g., for a given/fixed power spectral density representation of the load fluctuations about the mean-load intensity previously described in Section 8.3.2). This

variability of the structural response across the ensemble of load time history realizations represents an additional (nested) layer of uncertainty, expressed by the above PDF, within the third step of the proposed methodology. In light of these considerations and in order to reduce the computational cost of this third analysis step, the record-to-record variability of the quantity $\left(\mathbf{A}_{\mathrm{a}}^{[p,q]}\middle|\boldsymbol{\theta}_{\mathrm{mat}},\boldsymbol{\theta}_{\mathrm{dam}}^{p},\mathbf{a}_{\mathrm{a}}^{p},\mathbf{im}\right)$ is neglected in this study and, in the forthcoming discussion, the conditional joint PDF $f_{\mathbf{A}_{\mathrm{a}}^{[p,q]}\middle|\boldsymbol{\Theta}_{\mathrm{mat}},\boldsymbol{\Theta}_{\mathrm{dam}}^{p},\mathbf{A}_{\mathrm{a}}^{p},\mathbf{IM}}\left(\mathbf{a}_{\mathrm{a}}^{[p,q]}\middle|\boldsymbol{\theta}_{\mathrm{mat}},\boldsymbol{\theta}_{\mathrm{dam}}^{p},\mathbf{a}_{\mathrm{a}}^{p},\mathbf{im}\right)$ is replaced by the conditional mean value of the random variable $\left(\mathbf{A}_{\mathrm{a}}^{[p,q]}\middle|\boldsymbol{\theta}_{\mathrm{mat}},\boldsymbol{\theta}_{\mathrm{dam}}^{p},\mathbf{a}_{\mathrm{a}}^{p},\mathbf{im}\right)$. Under this perspective the conditional joint PDF, $f_{\mathbf{A}_{\mathrm{a}}^{[p,q]}\middle|\boldsymbol{\Theta}_{\mathrm{mat}},\boldsymbol{\Theta}_{\mathrm{dam}}^{p},\mathbf{A}_{\mathrm{a}}^{p},\mathbf{IM}}\left(\mathbf{a}_{\mathrm{a}}^{[p,q]}\middle|\boldsymbol{\theta}_{\mathrm{mat}},\boldsymbol{\theta}_{\mathrm{dam}}^{p},\mathbf{a}_{\mathrm{a}}^{p},\mathbf{im}\right)$, is conveniently rewritten as

$$f_{\mathbf{A}_{\mathrm{a}}^{[p,q]}\middle|\boldsymbol{\Theta}_{\mathrm{mat}},\boldsymbol{\Theta}_{\mathrm{dam}}^{p},\mathbf{A}_{\mathrm{a}}^{p},\mathbf{IM}}\left(\mathbf{a}_{\mathrm{a}}^{[p,q]}\middle|\boldsymbol{\theta}_{\mathrm{mat}},\boldsymbol{\theta}_{\mathrm{dam}}^{p},\mathbf{a}_{\mathrm{a}}^{p},\mathbf{im}\right)\cong\delta\left(\mathbf{a}_{\mathrm{a}}^{[p,q]}-\overline{\mathbf{a}}_{\mathrm{a}}^{[p,q]}\right) \tag{8.9}$$

where (i) the term $\delta(\cdot)$ denotes the *Dirac Delta* and (ii) the vector $\overline{\mathbf{a}}_{\mathrm{a}}^{[p,q]}$, introduced in the above equation for the sake of conciseness, is defined as $\overline{\mathbf{a}}_{\mathrm{a}}^{[p,q]}=\overline{\mathbf{a}}_{\mathrm{a}}^{[p,q]}\left(\boldsymbol{\theta}_{\mathrm{mat}},\boldsymbol{\theta}_{\mathrm{dam}}^{p},\mathbf{a}_{\mathrm{a}}^{p},\mathbf{im}\right)=E_{\mathrm{ens}}\left[\mathbf{A}_{\mathrm{a}}^{[p,q]}\middle|\boldsymbol{\theta}_{\mathrm{mat}},\boldsymbol{\theta}_{\mathrm{dam}}^{p},\mathbf{a}_{\mathrm{a}}^{p},\mathbf{im}\right]$ and represents the conditional expectation of $\mathbf{a}_{\mathrm{a}}^{[p,q]}$ (at time t_p^q) across the ensemble of the load time history realizations for fixed values of $\mathbf{IM}_{\mathrm{m}}=\mathbf{im}_{\mathrm{m}}$ and $\mathbf{IM}_{\mathrm{a}}=\mathbf{im}_{\mathrm{a}}$. Substituting Equation (8.9) into Equation (8.8) yields to

$$\begin{aligned}&f_{\mathbf{A}_{\mathrm{a}}^{[p,q]}\middle|\boldsymbol{\Theta}_{\mathrm{mat}},\boldsymbol{\Theta}_{\mathrm{dam}}^{p}}\left(\mathbf{a}_{\mathrm{a}}^{[p,q]}\middle|\boldsymbol{\theta}_{\mathrm{mat}},\boldsymbol{\theta}_{\mathrm{dam}}^{p}\right)=\\&\int_{\mathbf{A}_{\mathrm{a}}^{p}}\int_{\mathbf{IM}}\delta\left(\mathbf{a}_{\mathrm{a}}^{[p,q]}-\overline{\mathbf{a}}_{\mathrm{a}}^{[p,q]}\right)f''_{\mathbf{A}_{\mathrm{a}}^{p}\middle|\boldsymbol{\Theta}_{\mathrm{mat}},\boldsymbol{\Theta}_{\mathrm{dam}}^{p}}\left(\mathbf{a}_{\mathrm{a}}^{p}\middle|\boldsymbol{\theta}_{\mathrm{mat}},\boldsymbol{\theta}_{\mathrm{dam}}^{p}\right)f_{\mathbf{IM}}(\mathbf{im})\,d\mathbf{im}\,d\mathbf{a}_{\mathrm{a}}^{p}\end{aligned} \tag{8.10}$$

In order to compute the quantity $\overline{\mathbf{a}}_{\mathrm{a}}^{[p,q]}$ in a computationally efficient manner, the conditional expectation (across the ensemble of load time histories for given/fixed $\mathbf{IM}=\mathbf{im}$) of the rate of damage propagation at time $t \geq t_p$ — i.e., $E_{\mathrm{ens}}\left[d\left(\mathbf{A}_{\mathrm{a}}^{[p,t]} \middle| \boldsymbol{\theta}_{\mathrm{mat}}, \boldsymbol{\theta}_{\mathrm{dam}}^{p}, \mathbf{a}_{\mathrm{a}}^{p}, \mathbf{im}\right) \middle/ dt \right]$ — is fitted with a surrogate/polynomial model, $\mathbf{G}(\cdot)$. Following a dimensional analysis approach for the response quantity of interest (Navarro and De Los Rios, 1987; Sanford, 2003) this polynomial model is herein assumed to depend on (i) the conditional expectation of $\mathbf{a}_{\mathrm{a}}^{[p,t]}$ (at time $t \geq t_p$), denoted as $\overline{\mathbf{a}}_{\mathrm{a}}^{[p,t]}$ and defined as $\overline{\mathbf{a}}_{\mathrm{a}}^{[p,t]} = \overline{\mathbf{a}}_{\mathrm{a}}^{[p,t]}\left(\boldsymbol{\theta}_{\mathrm{mat}}, \boldsymbol{\theta}_{\mathrm{dam}}^{p}, \mathbf{a}_{\mathrm{a}}^{p}, \mathbf{im}\right) = E_{\mathrm{ens}}\left[\mathbf{A}_{\mathrm{a}}^{[p,t]} \middle| \boldsymbol{\theta}_{\mathrm{mat}}, \boldsymbol{\theta}_{\mathrm{dam}}^{p}, \mathbf{a}_{\mathrm{a}}^{p}, \mathbf{im}\right]$, (ii) the intensity measure vector $\mathbf{IM}=\mathbf{im}$ through the load intensity measures p_{m} and σ_{a} introduced and discussed in Section 8.3.2, (iii) the material parameter vector $\boldsymbol{\Theta}_{\mathrm{mat}} = \boldsymbol{\theta}_{\mathrm{mat}}$, and (iv) the vector of damage evolution model parameters $\boldsymbol{\Theta}_{\mathrm{dam}}^{p} = \boldsymbol{\theta}_{\mathrm{dam}}^{p}$. Under the aforementioned assumptions, this polynomial fitting yields to

$$E_{\mathrm{ens}}\left[\frac{d}{dt}\left(\mathbf{A}_{\mathrm{a}}^{[p,t]} \middle| \boldsymbol{\theta}_{\mathrm{mat}}, \boldsymbol{\theta}_{\mathrm{dam}}^{p}, \mathbf{a}_{\mathrm{a}}^{p}, \mathbf{im}\right) \right] = \mathbf{G}\left(\overline{\mathbf{a}}_{\mathrm{a}}^{[p,t]}, p_{\mathrm{m}}, \sigma_{\mathrm{a}}; \boldsymbol{\theta}_{\mathrm{mat}}, \boldsymbol{\theta}_{\mathrm{dam}}^{p}\right), \quad t \geq t_p \qquad (8.11)$$

where the quantity $d\left(\mathbf{A}_{\mathrm{a}}^{[p,t]} \middle| \boldsymbol{\theta}_{\mathrm{mat}}, \boldsymbol{\theta}_{\mathrm{dam}}^{p}, \mathbf{a}_{\mathrm{a}}^{p}, \mathbf{im}\right) \middle/ dt$ (with dt being a macro increment of time as discussed in Chapter 5) denotes the first-order time derivative of the random process $\left(\mathbf{A}_{\mathrm{a}}^{[p,q]} \middle| \boldsymbol{\theta}_{\mathrm{mat}}, \boldsymbol{\theta}_{\mathrm{dam}}^{p}, \mathbf{a}_{\mathrm{a}}^{p}, \mathbf{im}\right)$. The general nonlinear mapping $\mathbf{G}(\cdot): \mathbb{R}^{n_{\mathrm{inp}}} \rightarrow \mathbb{R}_{+}^{n_{\mathrm{A}}^{p}}$ (with $n_{\mathrm{inp}} = n_{\mathrm{A}}^{p} + 2 + n_{\mathrm{mat}} + n_{\mathrm{dam}}$), between the input and (positive) output real vector spaces, represents the metamodel fitted (through an appropriate and computationally

feasible *design of experiments*) over the desired design space for the input parameters using the simulation results from a (mechanics-based) nonlinear FE model of the structure obtained for each realization of the load time histories. Furthermore, if the condition for mean square differentiability of the random process $\left(\mathbf{A}_{\mathrm{a}}^{[p,t]}\middle|\boldsymbol{\theta}_{\mathrm{mat}},\boldsymbol{\theta}_{\mathrm{dam}}^{p},\mathbf{a}_{\mathrm{a}}^{p},\mathbf{im}\right)$ is satisfied, expectation and differentiation operators can permute, i.e.,

$$E_{\mathrm{ens}}\left[\frac{d}{dt}\left(\mathbf{A}_{\mathrm{a}}^{[p,t]}\middle|\boldsymbol{\theta}_{\mathrm{mat}},\boldsymbol{\theta}_{\mathrm{dam}}^{p},\mathbf{a}_{\mathrm{a}}^{p},\mathbf{im}\right)\right]=\frac{d}{dt}E_{\mathrm{ens}}\left[\left(\mathbf{A}_{\mathrm{a}}^{[p,t]}\middle|\boldsymbol{\theta}_{\mathrm{mat}},\boldsymbol{\theta}_{\mathrm{dam}}^{p},\mathbf{a}_{\mathrm{a}}^{p},\mathbf{im}\right)\right]=\frac{d\,\overline{\mathbf{a}}_{\mathrm{a}}^{[p,t]}}{dt} \quad (8.12)$$

Thus Equation (8.11), for $t\geq t_p$, can be rewritten as

$$\begin{cases}\dfrac{d}{dt}\overline{\mathbf{a}}_{\mathrm{a}}^{[p,t]}=\mathbf{G}\left(\overline{\mathbf{a}}_{\mathrm{a}}^{[p,t]},p_{\mathrm{m}},\sigma_{\mathrm{a}};\boldsymbol{\theta}_{\mathrm{mat}},\boldsymbol{\theta}_{\mathrm{dam}}^{p}\right)\\ \overline{\mathbf{a}}_{\mathrm{a}}^{p}=\mathbf{a}_{\mathrm{a}}^{p}\end{cases} \quad (8.13)$$

where $\overline{\mathbf{a}}_{\mathrm{a}}^{p}$ represents the value of the vector $\overline{\mathbf{a}}_{\mathrm{a}}^{[p,t]}$ at time $t=t_p$ (i.e., at current time, immediately after the last NDE inspection), and $\mathbf{a}_{\mathrm{a}}^{p}$ is a particular realization of $\mathbf{A}_{\mathrm{a}}^{p}$ according to the posterior joint PDF $f''_{\mathbf{A}_{\mathrm{a}}^{p}\left|\boldsymbol{\Theta}_{\mathrm{mat}},\boldsymbol{\Theta}_{\mathrm{dam}}^{p}\right.}\left(\mathbf{a}_{\mathrm{a}}^{p}\middle|\boldsymbol{\theta}_{\mathrm{mat}},\boldsymbol{\theta}_{\mathrm{dam}}^{p}\right)$ computed as outlined in Section 8.3.1. Hence, Equation (8.13) represents a system of $n_{\mathrm{A}}^{p}=\sum_{i=1}^{n_{\mathrm{L}}^{[0,p]}}n_{\mathrm{DM}}^{(i,[0,p])}$ generally coupled (see Appendix G) first-order ordinary differential equations that can now be numerically integrated (e.g., by using the 4$^{\mathrm{th}}$ order Runge-Kutta time marching scheme) between current time t_p and t_p^q to compute $\overline{\mathbf{a}}_{\mathrm{a}}^{[p,q]}$ (with $q=1,2,...,\overline{q}$).

As a final remark in this Section, for the particular and simpler case in which the load fluctuations about the mean-load intensity are represented by a harmonic load with random amplitude (AMP_{a}) and, potentially, also random frequency (Ω_{a}), the intensity measure vector $\mathbf{IM}_{\mathrm{a}}$ takes the form $\mathbf{IM}_{\mathrm{a}} = \left\{ AMP_{\mathrm{a}}, \Omega_{\mathrm{a}}, \Delta T_{\mathrm{a}} \right\}$. Furthermore, for a given/fixed value of $\mathbf{IM} = \mathbf{im}$, the record-to-record variability (across the ensemble of loading time histories) discussed earlier no longer exists. In other words, the random term $\left(\mathbf{A}_{\mathrm{a}}^{[p,q]} \middle| \boldsymbol{\theta}_{\mathrm{mat}}, \boldsymbol{\theta}_{\mathrm{dam}}^{p}, \mathbf{a}_{\mathrm{a}}^{p}, \mathbf{im} \right)$ becomes a deterministic quantity — i.e., $\overline{\mathbf{a}}_{\mathrm{a}}^{[p,q]} = \left(\mathbf{A}_{\mathrm{a}}^{[p,q]} \middle| \boldsymbol{\theta}_{\mathrm{mat}}, \boldsymbol{\theta}_{\mathrm{dam}}^{p}, \mathbf{a}_{\mathrm{a}}^{p}, \mathbf{im} \right) = \left(\mathbf{a}_{\mathrm{a}}^{[p,q]} \middle| \boldsymbol{\theta}_{\mathrm{mat}}, \boldsymbol{\theta}_{\mathrm{dam}}^{p}, \mathbf{a}_{\mathrm{a}}^{p}, \mathbf{im} \right)$ — and, similarly, the random process $\left(\mathbf{A}_{\mathrm{a}}^{[p,t]} \middle| \boldsymbol{\theta}_{\mathrm{mat}}, \boldsymbol{\theta}_{\mathrm{dam}}^{p}, \mathbf{a}_{\mathrm{a}}^{p}, \mathbf{im} \right)$ (with $t \geq t_p$) reduces to a deterministic (damage evolution) process — i.e., $\overline{\mathbf{a}}_{\mathrm{a}}^{[p,t]} = \left(\mathbf{A}_{\mathrm{a}}^{[p,t]} \middle| \boldsymbol{\theta}_{\mathrm{mat}}, \boldsymbol{\theta}_{\mathrm{dam}}^{p}, \mathbf{a}_{\mathrm{a}}^{p}, \mathbf{im} \right) = \left(\mathbf{a}_{\mathrm{a}}^{[p,t]} \middle| \boldsymbol{\theta}_{\mathrm{mat}}, \boldsymbol{\theta}_{\mathrm{dam}}^{p}, \mathbf{a}_{\mathrm{a}}^{p}, \mathbf{im} \right)$. Consequently, the conditional joint PDF of $\mathbf{A}_{\mathrm{a}}^{[p,q]}$, $f_{\mathbf{A}_{\mathrm{a}}^{[p,q]} \middle| \boldsymbol{\Theta}_{\mathrm{mat}}, \boldsymbol{\Theta}_{\mathrm{dam}}^{p}, \mathbf{A}_{\mathrm{a}}^{p}, \mathbf{IM}} \left(\mathbf{a}_{\mathrm{a}}^{[p,q]} \middle| \boldsymbol{\theta}_{\mathrm{mat}}, \boldsymbol{\theta}_{\mathrm{dam}}^{p}, \mathbf{a}_{\mathrm{a}}^{p}, \mathbf{im} \right)$, is now represented by a *Dirac Delta* located at $\overline{\mathbf{a}}_{\mathrm{a}}^{[p,q]} = \left(\mathbf{a}_{\mathrm{a}}^{[p,q]} \middle| \boldsymbol{\theta}_{\mathrm{mat}}, \boldsymbol{\theta}_{\mathrm{dam}}^{p}, \mathbf{a}_{\mathrm{a}}^{p}, \mathbf{im} \right)$ and the fitting of the metamodel $\mathbf{G}\left(\cdot \right) : \mathbb{R}^{n_{\mathrm{inp}}} \to \mathbb{R}_{+}^{n_{\mathrm{A}}^{p}}$ becomes easier and computationally less expensive since it does no longer involve the averaging across the ensemble of load time histories.

8.3.4. Probabilistic global performance analysis

Similarly to the original version of the proposed framework, as presented in Chapter 6, the fourth step of the generalized damage prognosis methodology discussed in this chapter uses the results obtained from the damage evolution prediction analysis

from time t_p to time t_p^q (with $q = 1, 2, ..., \overline{q}$), for estimating (at future time t_p^q) the joint PDF of (i) the damage size vector $\mathbf{A}_{\mathrm{a}}^{[p,q]}$ and (ii) the vector of global performance measures $\boldsymbol{\Psi}_{\mathrm{g}}^{[p,q]}$.

The (ideal) final outcome of this step is represented by the joint PDF, $f_{\mathbf{D}_{\mathrm{L,G}}^{[p,q]}}\left(\mathbf{d}_{\mathrm{L,G}}^{[p,q]}\right) = f_{\mathbf{A}_{\mathrm{a}}^{[p,q]},\boldsymbol{\Psi}_{\mathrm{g}}^{[p,q]}}\left(\mathbf{a}_{\mathrm{a}}^{[p,q]}, \boldsymbol{\psi}_{\mathrm{g}}^{[p,q]}\right)$, of the random vector $\mathbf{D}_{\mathrm{L,G}}^{[p,q]} = \left\{\mathbf{A}_{\mathrm{a}}^{[p,q]}, \boldsymbol{\Psi}_{\mathrm{g}}^{[p,q]}\right\}$. This joint PDF can be obtained through two sub-steps. In the first sub-step, the joint conditional PDF $f_{\boldsymbol{\Psi}_{\mathrm{g}}^{[p,q]}\left|\mathbf{A}_{\mathrm{a}}^{[p,q]},\boldsymbol{\Theta}_{\mathrm{mat}},\boldsymbol{\Theta}_{\mathrm{dam}}^{p}\right.}\left(\boldsymbol{\psi}_{\mathrm{g}}^{[p,q]}\left|\mathbf{a}_{\mathrm{a}}^{[p,q]}, \boldsymbol{\theta}_{\mathrm{mat}}, \boldsymbol{\theta}_{\mathrm{dam}}^{p}\right.\right)$ is numerically estimated through Monte Carlo (MC) simulations — each of them for a fixed realization of (i) the predicted (during the probabilistic structural response and damage evolution analysis) damage size vector $\mathbf{a}_{\mathrm{a}}^{[p,q]}$, and (ii) the vectors $\boldsymbol{\theta}_{\mathrm{mat}}$ and $\boldsymbol{\theta}_{\mathrm{dam}}^{p}$ sampled from their PDFs $f_{\boldsymbol{\Theta}_{\mathrm{mat}}}\left(\boldsymbol{\theta}_{\mathrm{mat}}\right)$ and $f_{\boldsymbol{\Theta}_{\mathrm{dam}}^{p}}\left(\boldsymbol{\theta}_{\mathrm{dam}}^{p}\right)$. In the second sub-step, the unconditional joint PDF of $\mathbf{D}_{\mathrm{L,G}}^{[p,q]}$ is computed as

$$f_{\mathbf{D}_{\mathrm{L,G}}^{[p,q]}}\left(\mathbf{d}_{\mathrm{L,G}}^{[p,q]}\right) = f_{\mathbf{A}_{\mathrm{a}}^{[p,q]},\boldsymbol{\Psi}_{\mathrm{g}}^{[p,q]}}\left(\mathbf{a}_{\mathrm{a}}^{[p,q]}, \boldsymbol{\psi}_{\mathrm{g}}^{[p,q]}\right) = f_{\boldsymbol{\Psi}_{\mathrm{g}}^{[p,q]}\left|\mathbf{A}_{\mathrm{a}}^{[p,q]}\right.}\left(\boldsymbol{\psi}_{\mathrm{g}}^{[p,q]}\left|\mathbf{a}_{\mathrm{a}}^{[p,q]}\right.\right) \cdot f_{\mathbf{A}_{\mathrm{a}}^{[p,q]}}\left(\mathbf{a}_{\mathrm{a}}^{[p,q]}\right) \quad (8.14)$$

where the conditional joint PDF, $f_{\boldsymbol{\Psi}_{\mathrm{g}}^{[p,q]}\left|\mathbf{A}_{\mathrm{a}}^{[p,q]}\right.}\left(\boldsymbol{\psi}_{\mathrm{g}}^{[p,q]}\left|\mathbf{a}_{\mathrm{a}}^{[p,q]}\right.\right)$, of the performance measure vector ($\boldsymbol{\Psi}_{\mathrm{g}}^{[p,q]}$) is obtained as

$$f_{\boldsymbol{\Psi}_{\mathrm{g}}^{[p,q]}\left|\mathbf{A}_{\mathrm{a}}^{[p,q]}\right.}\left(\boldsymbol{\psi}_{\mathrm{g}}^{[p,q]}\left|\mathbf{a}_{\mathrm{a}}^{[p,q]}\right.\right) = \int_{\boldsymbol{\Theta}_{\mathrm{mat}}}\int_{\boldsymbol{\Theta}_{\mathrm{dam}}^{p}} f_{\boldsymbol{\Psi}_{\mathrm{g}}^{[p,q]}\left|\mathbf{A}_{\mathrm{a}}^{[p,q]},\boldsymbol{\Theta}_{\mathrm{mat}},\boldsymbol{\Theta}_{\mathrm{dam}}^{p}\right.}\left(\boldsymbol{\psi}_{\mathrm{g}}^{[p,q]}\left|\mathbf{a}_{\mathrm{a}}^{[p,q]}, \boldsymbol{\theta}_{\mathrm{mat}}, \boldsymbol{\theta}_{\mathrm{dam}}^{p}\right.\right) f_{\boldsymbol{\Theta}_{\mathrm{mat}}}\left(\boldsymbol{\theta}_{\mathrm{mat}}\right) f_{\boldsymbol{\Theta}_{\mathrm{dam}}^{p}}\left(\boldsymbol{\theta}_{\mathrm{dam}}^{p}\right) d\boldsymbol{\theta}_{\mathrm{mat}}\, d\boldsymbol{\theta}_{\mathrm{dam}}^{p} \quad (8.15)$$

and the marginal joint PDF, $f_{\mathbf{A}_{\mathrm{a}}^{[p,q]}}\left(\mathbf{a}_{\mathrm{a}}^{[p,q]}\right)$, can be expressed as

$$f_{\mathbf{A}_{\mathrm{a}}^{[p,q]}}\left(\mathbf{a}_{\mathrm{a}}^{[p,q]}\right) = \int_{\boldsymbol{\Theta}_{\mathrm{mat}}}\int_{\boldsymbol{\Theta}_{\mathrm{dam}}^{p}} f_{\mathbf{A}_{\mathrm{a}}^{[p,q]}|\boldsymbol{\Theta}_{\mathrm{mat}},\boldsymbol{\Theta}_{\mathrm{dam}}}\left(\mathbf{a}_{\mathrm{a}}^{[p,q]}\middle|\boldsymbol{\theta}_{\mathrm{mat}},\boldsymbol{\theta}_{\mathrm{dam}}^{p}\right) f_{\boldsymbol{\Theta}_{\mathrm{mat}}}\left(\boldsymbol{\theta}_{\mathrm{mat}}\right) f_{\boldsymbol{\Theta}_{\mathrm{dam}}^{p}}\left(\boldsymbol{\theta}_{\mathrm{dam}}^{p}\right) d\boldsymbol{\theta}_{\mathrm{mat}}\, d\boldsymbol{\theta}_{\mathrm{dam}}^{p} \tag{8.16}$$

Also in this fourth step of the proposed methodology, the use of metamodels is extremely useful in order to reduce the computational cost of the MC numerical simulations involved. A Metamodel, $\mathbf{Q}(\cdot):\mathbb{R}^{n_{\mathrm{inp}}}\rightarrow\mathbb{R}_{+}^{n_{\mathrm{G}}}$ (with $n_{\mathrm{inp}}=n_{\mathrm{A}}^{p}+n_{\mathrm{mat}}+n_{\mathrm{dam}}$), is used to compute the conditional joint PDF of the vector of global performance measures, $f_{\boldsymbol{\Psi}_{\mathrm{g}}^{[p,q]}\left|\mathbf{A}_{\mathrm{a}}^{[p,q]},\boldsymbol{\Theta}_{\mathrm{mat}},\boldsymbol{\Theta}_{\mathrm{dam}}^{p}\right.}\left(\boldsymbol{\psi}_{\mathrm{g}}^{[p,q]}\middle|\mathbf{a}_{\mathrm{a}}^{[p,q]},\boldsymbol{\theta}_{\mathrm{mat}},\boldsymbol{\theta}_{\mathrm{dam}}^{p}\right)$, as

$$f_{\boldsymbol{\Psi}_{\mathrm{g}}^{[p,q]}\left|\mathbf{A}_{\mathrm{a}}^{[p,q]},\boldsymbol{\Theta}_{\mathrm{mat}},\boldsymbol{\Theta}_{\mathrm{dam}}^{p}\right.}\left(\boldsymbol{\psi}_{\mathrm{g}}^{[p,q]}\middle|\mathbf{a}_{\mathrm{a}}^{[p,q]},\boldsymbol{\theta}_{\mathrm{mat}},\boldsymbol{\theta}_{\mathrm{dam}}^{p}\right)=\delta\left(\boldsymbol{\psi}_{\mathrm{g}}^{[p,q]}-\bar{\boldsymbol{\psi}}_{\mathrm{g}}^{[p,q]}\right) \tag{8.17}$$

where the vector $\bar{\boldsymbol{\psi}}_{\mathrm{g}}^{[p,q]}$ is defined as

$$\bar{\boldsymbol{\psi}}_{\mathrm{g}}^{[p,q]}=\bar{\boldsymbol{\psi}}_{\mathrm{g}}^{[p,q]}\left(\boldsymbol{\Psi}_{\mathrm{g}}^{[p,q]}\middle|\mathbf{a}_{\mathrm{a}}^{[p,q]},\boldsymbol{\theta}_{\mathrm{mat}},\boldsymbol{\theta}_{\mathrm{dam}}^{p}\right)=\mathbf{Q}\left(\mathbf{a}_{\mathrm{a}}^{[p,q]};\boldsymbol{\theta}_{\mathrm{mat}},\boldsymbol{\theta}_{\mathrm{dam}}^{p}\right) \tag{8.18}$$

As a further result, Equation (8.15) can therefore be simplified as

$$f_{\boldsymbol{\Psi}_{\mathrm{g}}^{[p,q]}\left|\mathbf{A}_{\mathrm{a}}^{[p,q]}\right.}\left(\boldsymbol{\psi}_{\mathrm{g}}^{[p,q]}\middle|\mathbf{a}_{\mathrm{a}}^{[p,q]}\right) = \int_{\boldsymbol{\Theta}_{\mathrm{mat}}}\int_{\boldsymbol{\Theta}_{\mathrm{dam}}^{p}} \delta\left(\boldsymbol{\psi}_{\mathrm{g}}^{[p,q]}-\bar{\boldsymbol{\psi}}_{\mathrm{g}}^{[p,q]}\right) f_{\boldsymbol{\Theta}_{\mathrm{mat}}}\left(\boldsymbol{\theta}_{\mathrm{mat}}\right) f_{\boldsymbol{\Theta}_{\mathrm{dam}}^{p}}\left(\boldsymbol{\theta}_{\mathrm{dam}}^{p}\right) d\boldsymbol{\theta}_{\mathrm{mat}}\, d\boldsymbol{\theta}_{\mathrm{dam}}^{p} \tag{8.19}$$

and the marginal joint PDF of $\boldsymbol{\Psi}_{\mathrm{g}}^{[p,q]}$, used to compute upper and lower uni-modal bounds to the probabilities of failure and false-call, in the subsequent system reliability analysis, can be expressed as

$$f_{\boldsymbol{\Psi}_{\mathrm{g}}^{[p,q]}}\left(\boldsymbol{\psi}_{\mathrm{g}}^{[p,q]}\right)= \int\limits_{\mathbf{A}_{\mathrm{a}}^{[p,q]}}\int\limits_{\boldsymbol{\Theta}_{\mathrm{mat}}}\int\limits_{\boldsymbol{\Theta}_{\mathrm{dam}}^{p}} \delta\left(\boldsymbol{\psi}_{\mathrm{g}}^{[p,q]}-\overline{\boldsymbol{\psi}}_{\mathrm{g}}^{[p,q]}\right) f''_{\mathbf{A}_{\mathrm{a}}^{[p,q]}\left|\boldsymbol{\Theta}_{\mathrm{mat}},\boldsymbol{\Theta}_{\mathrm{dam}}^{p}\right.}\left(\mathbf{a}_{\mathrm{a}}^{[p,q]}\left|\boldsymbol{\theta}_{\mathrm{mat}},\boldsymbol{\theta}_{\mathrm{dam}}^{p}\right.\right) f_{\boldsymbol{\Theta}_{\mathrm{mat}}}\left(\boldsymbol{\theta}_{\mathrm{mat}}\right) f''_{\boldsymbol{\Theta}_{\mathrm{dam}}^{p}}\left(\boldsymbol{\theta}_{\mathrm{dam}}^{p}\right) d\mathbf{a}_{\mathrm{a}}^{[p,q]}\, d\boldsymbol{\theta}_{\mathrm{mat}}\, d\boldsymbol{\theta}_{\mathrm{dam}}^{p} \tag{8.20}$$

8.3.5. Damage prognosis analysis

The fifth step, *damage prognosis analysis*, represents the final computational step of the proposed methodology (before the decision making process) and it aims at providing an estimate of the probabilities of failure and false-call for the monitored structural system at future times (i.e., $t \geq t_p$) by performing component and system reliability analyses. Local and global failure criteria are therefore needed in order to compute the component (or modal) probabilities of failure and false-call which are then combined in the subsequent system reliability analysis. The simplest (and most logical) local failure event $\mathrm{F}_{\mathrm{L},ij}^{[p,q]}$ — i.e., the failure event (at time t_p^q) associated with the j^{th} detected damage mechanism, developing at the i^{th} monitored damage location — can be defined as $\mathrm{F}_{\mathrm{L},ij}^{[p,q]} \triangleq \left\{A_a^{(i,j,[p,q])} \geq a_c^{ij}\right\}$ and the corresponding modal failure probability is expressed as $P\left[\mathrm{F}_{\mathrm{L},ij}^{[p,q]}\right] = 1 - F_{A_a^{(i,j,[p,q])}}\left(a_c^{ij}\right)$.

As already stated in Chapter 7, alternative definitions for the local failure event can be adopted in the proposed framework. For instance, in previous research work by Lin *et al*. (2000), Huang and Lin (2005), and Backman (2005), the local failure event $\tilde{\mathrm{F}}_{\mathrm{L},ij}^{[p,q]}$ is defined as $\tilde{\mathrm{F}}_{\mathrm{L},ij}^{[p,q]} \triangleq \left\{\mathrm{F}_{\mathrm{L},ij}^{[p,q]} \cap \left(A_m^{(i,j,[p,q])} < a_c^{ij}\right)\right\}$, its graphical interpretation is shown in Figure 8.6, and the associated modal failure probability can be computed as

(see Chapter 7 and Appendix A for all the mathematical derivations)

$$P\left[\tilde{\mathrm{F}}_{\mathrm{L},ij}^{[p,q]}\right]=P\left[\mathrm{F}_{\mathrm{L},ij}^{[p,q]}\right]-\int_{a_c^{ij}}^{+\infty}\hat{\psi}\left(a_a^{(i,j,[p,q])}\right)POD\left(a_a^{(i,j,[p,q])}\right)f_{A_a^{(i,j,[p,q])}}\left(a_a^{(i,j,[p,q])}\right)da_a^{(i,j,[p,q])} \quad (8.21)$$

where the strictly positive function $\hat{\psi}\left(a_a^{(i,j,[p,q])}\right)$ is defined as (see Chapter 7 and Appendix A)

$$\hat{\psi}\left(a_a^{(i,j,[p,q])}\right)=\Phi\left(\frac{\hat{\beta}_0^{(i,j)}+\hat{\beta}_1^{(i,j)}a_a^{(i,j,[p,q])}-a_c^{ij}}{\hat{\sigma}_{\varepsilon_{ij}}}\right)\cdot\left[\Phi\left(\frac{\hat{\beta}_0^{(i,j)}+\hat{\beta}_1^{(i,j)}a_a^{(i,j,[p,q])}}{\hat{\sigma}_{\varepsilon_{ij}}}\right)\right]^{-1} \quad (8.22)$$

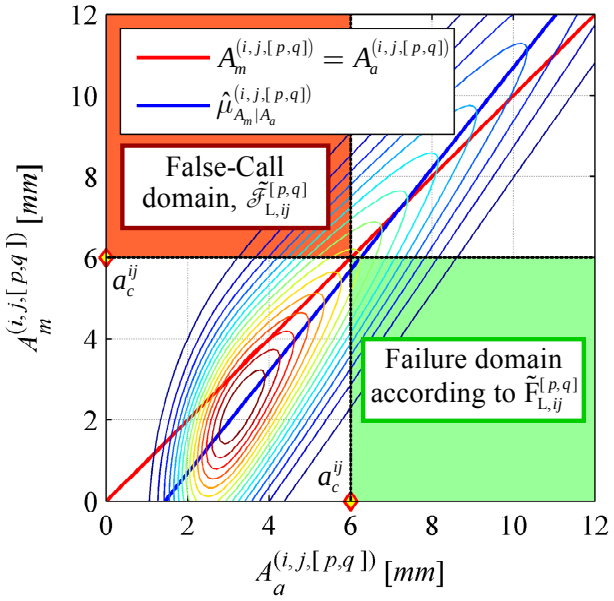

Figure 8.6: Conceptual illustration of the failure and false-call domains according to the failure and false-call events $\tilde{\mathrm{F}}_{\mathrm{L},ij}^{[p,q]}$ and $\tilde{\mathcal{F}}_{\mathrm{L},ij}^{[p,q]}$, respectively.

Besides the local failure event $\tilde{\mathrm{F}}_{\mathrm{L},ij}^{[p,q]}$, the local false-call event, $\tilde{\mathcal{F}}_{\mathrm{L},ij}^{[p,q]}$, is also of interest. This event is defined as $\tilde{\mathcal{F}}_{\mathrm{L},ij}^{[p,q]}\triangleq\left\{\left(A_a^{(i,j,[p,q])}<a_c^{ij}\right)\cap\left(A_m^{(i,j,[p,q])}\geq a_c^{ij}\right)\right\}$, its

graphical representation is shown in Figure 8.6, and the associated modal probability of false-call can be computed as (see Chapter 7 and Appendix B)

$$P\left[\tilde{\mathcal{F}}_{\mathrm{L},ij}^{[p,q]}\right] = P\left[\left(A_a^{(i,j,[p,q])} < a_c^{ij}\right) \cap \left(A_m^{(i,j,[p,q])} \geq a_c^{ij}\right)\right] = \int_0^{a_c^{ij}} \hat{\psi}\left(a_a^{(i,j,[p,q])}\right) POD\left(a_a^{(i,j,[p,q])}\right) f_{A_a^{(i,j,[p,q])}}\left(a_a^{(i,j,[p,q])}\right) da_a^{(i,j,[p,q])} \tag{8.23}$$

On the other hand, the global component failure events $\mathrm{F}_{\mathrm{G},r}^{[p,q]}$ (with $r = 1, \ldots, n_{\mathrm{G}}$) are defined on the basis of the global performance measures computed in the *probabilistic global performance analysis* step and collected in the random vector $\boldsymbol{\Psi}_{\mathrm{g}}^{[p,q]}$. For instance, if the global aeroelastic performance of the structure is of primary concern, one component (e.g., the r^{th} component) of the random vector $\boldsymbol{\Psi}_{\mathrm{g}}^{[p,q]}$ could be taken as the flutter velocity (V_{F}) and the corresponding failure event could be defined as $\mathrm{F}_{\mathrm{G},r}^{[p,q]} \triangleq \left\{V_{\mathrm{F}}^{[p,q]} \leq v_{\mathrm{F}}^{crit}\right\}$ where v_{F}^{crit} is the critical flutter velocity that can be expressed as a fraction of the nominal flutter velocity (v_{F}^{nom}) as $v_{\mathrm{F}}^{crit} = \alpha \times v_{\mathrm{F}}^{nom}$ (e.g., $v_{\mathrm{F}}^{crit} = 0.90 \times v_{\mathrm{F}}^{nom}$). Alternatively, it could be of interest to monitor the downtrend (due to damage propagation) of a given natural frequency (e.g., the j^{th} natural frequency, $\omega_j^{[p,q]}$) and the corresponding failure event could be defined as $\mathrm{F}_{\mathrm{G},r}^{[p,q]} \triangleq \left\{\omega_j^{[p,q]} \leq \omega_j^{crit}\right\}$ where ω_j^{crit} represents a critical frequency threshold that can be taken as a fraction of the nominal frequency (ω_j^{nom}) as $\omega_j^{crit} = \alpha \times \omega_j^{nom}$ (e.g., $\omega_j^{crit} = 0.90 \times \omega_j^{nom}$).

Finally, as shown in Equations (8.24) through (8.28), local and global failure ($\mathrm{F}_{\mathrm{L},ij}^{[p,q]}$, $\mathrm{F}_{\mathrm{G},r}^{[p,q]}$) events, their complements ($\overline{\mathrm{F}}_{\mathrm{L},ij}^{[p,q]}$, $\overline{\mathrm{F}}_{\mathrm{G},r}^{[p,q]}$), and false-call ($\tilde{\mathcal{F}}_{\mathrm{L},ij}^{[p,q]}$) events are combined together to define failure ($\mathrm{F}_{\mathrm{sys}}^{[p,q]}$, $\breve{\mathrm{F}}_{\mathrm{sys}}^{[p,q]}$, $\widehat{\mathrm{F}}_{\mathrm{sys}}^{[p,q]}$) and false-call ($\breve{\mathcal{F}}_{\mathrm{sys}}^{[p,q]}$, $\widehat{\mathcal{F}}_{\mathrm{sys}}^{[p,q]}$) events at the system level, by abstracting the real structure into a combination of series and parallel sub-systems. Upper and lower uni-modal bounds for each of these events can be computed as detailed in Section 7.5 in Chapter 7.

$$\mathrm{F}_{\mathrm{sys}}^{[p,q]} \triangleq \left\{ \left[\bigcup_{i=1}^{n_{\mathrm{L}}^{[0,p]}} \left(\bigcup_{j=1}^{n_{\mathrm{DM}}^{(i,[0,p])}} \mathrm{F}_{\mathrm{L},ij}^{[p,q]} \right) \right] \cup \left(\bigcup_{r=1}^{n_{\mathrm{G}}} \mathrm{F}_{\mathrm{G},r}^{[p,q]} \right) \right\} \tag{8.24}$$

$$\breve{\mathrm{F}}_{\mathrm{sys}}^{[p,q]} \triangleq \mathrm{F}_{\mathrm{sys}}^{[p,q]} \cap \left[\bigcap_{i=1}^{n_{\mathrm{L}}^{[0,p]}} \left(\bigcap_{j=1}^{n_{\mathrm{DM}}^{(i,[0,p])}} A_m^{(i,j,[p,q])} < a_c^{ij} \right) \right] \tag{8.25}$$

$$\widehat{\mathrm{F}}_{\mathrm{sys}}^{[p,q]} \triangleq \mathrm{F}_{\mathrm{sys}}^{[p,q]} \cap \left[\bigcap_{i=1}^{n_{\mathrm{L}}^{[0,p]}} \left(\bigcap_{j=1}^{n_{\mathrm{DM}}^{(i,[0,p])}} \overline{n}_{\mathrm{MS}}^{(i,j,[p,q])} \geq \overline{\overline{n}}_{\mathrm{MS}}^{(i,j,[p,q])} \right) \right] \tag{8.26}$$

$$\breve{\mathcal{F}}_{\mathrm{sys}}^{[p,q]} \triangleq \left\{ \left[\bigcap_{i=1}^{n_{\mathrm{L}}^{[0,p]}} \left(\bigcap_{j=1}^{n_{\mathrm{DM}}^{(i,[0,p])}} \overline{\mathrm{F}_{\mathrm{L},ij}^{[p,q]}} \right) \right] \cap \left(\bigcap_{r=1}^{n_{\mathrm{G}}} \overline{\mathrm{F}_{\mathrm{G},r}^{[p,q]}} \right) \right\} \cap \left[\bigcup_{i=1}^{n_{\mathrm{L}}^{[0,p]}} \left(\bigcup_{j=1}^{n_{\mathrm{DM}}^{(i,[0,p])}} A_m^{(i,j,[p,q])} \geq a_c^{ij} \right) \right] \tag{8.27}$$

$$\widehat{\mathcal{F}}_{\mathrm{sys}}^{[p,q]} \triangleq \left\{ \left[\bigcap_{i=1}^{n_{\mathrm{L}}^{[0,p]}} \left(\bigcap_{j=1}^{n_{\mathrm{DM}}^{(i,[0,p])}} \overline{\mathrm{F}_{\mathrm{L},ij}^{[p,q]}} \right) \right] \cap \left(\bigcap_{r=1}^{n_{\mathrm{G}}} \overline{\mathrm{F}_{\mathrm{G},r}^{[p,q]}} \right) \right\} \cap \left[\bigcup_{i=1}^{n_{\mathrm{L}}^{[0,p]}} \left(\bigcup_{j=1}^{n_{\mathrm{DM}}^{(i,[0,p])}} \overline{n}_{\mathrm{MS}}^{(i,j,[p,q])} < \overline{\overline{n}}_{\mathrm{MS}}^{(i,j,[p,q])} \right) \right] \tag{8.28}$$

In the Boolean equations above, $n_{\mathrm{DM}}^{(i,[0,p])}$ denotes the number of detected (up to time t_p) damage mechanisms developing at the i^{th} damage location and $n_{\mathrm{L}}^{[0,p]}$ the number of inspected damage locations up to time t_p. Therefore, the total number of local reliability components (n_{A}^{p}) at time t_p can be expressed as $n_{\mathrm{A}}^{p} = \sum_{i=1}^{n_{\mathrm{L}}^{[0,p]}} n_{\mathrm{DM}}^{(i,[0,p])}$.

8.4. Application example: Simply-supported laminated composite beam characterized by two debonding fronts

The numerical example presented below aims at (i) validating the proposed recursive Bayesian inference scheme used to update both damage extents and damage evolution model parameters, (ii) assessing the computational feasibility of the proposed failure criteria (both local and global), and (iii) quantifying the confidence level on the damage prognosis results obtained by making use of uni-modal bounds for the probabilities of system failure and false-call, as defined and computed in Chapter 7. The benchmark structure used in this application example is shown in Figure 8.7 and consists of a simply supported composite beam, of length $2L = 250.0\,mm$, made out of two identical unidirectional laminated composite adherends, with solid rectangular cross section, bonded through an idealized zero-thickness adhesive interface/layer. The width and depth of each unidirectional laminated composite adherend are $b = 25.0\,mm$ and $h = 3.0\,mm$, respectively.

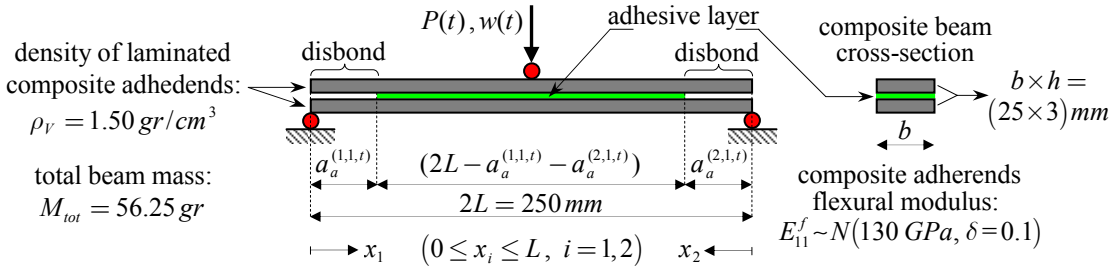

Figure 8.7: Simply-supported composite beam with two debonding fronts (evolving from the beam ends) subjected to a concentrated load, $P(t)$, applied at its midspan.

The only material parameter of interest is represented by the flexural modulus (Jones, 1976) of the lower and upper unidirectional composite adherends (i.e.,

$\boldsymbol{\Theta}_{\text{mat}} = \Theta_{\text{mat}} = E_{11}^{f}$) assumed to follow a Normal distribution with mean $\mu_{E_{11}^{f}} = 130.0\,GPa$ and a coefficient of variation of 10%. (see Figure 8.8 below)

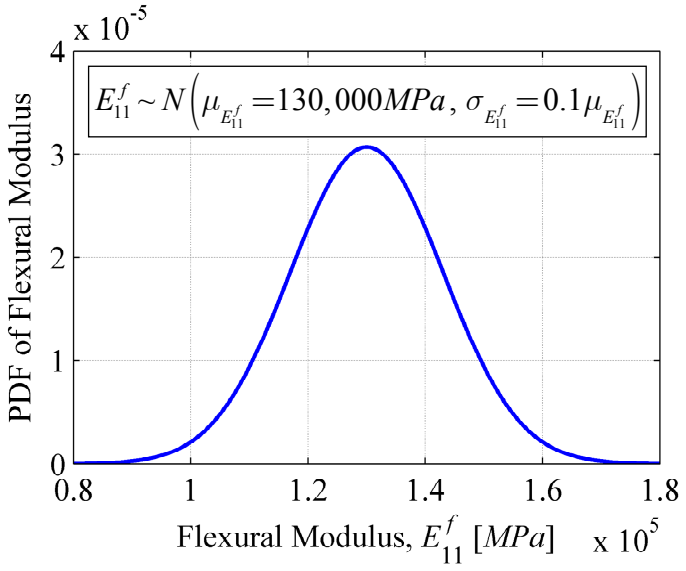

Figure 8.8: PDF of the composite adherends flexural modulus, E_{11}^{f}

The debonding, along the adhesive interface between the two composite adherends, is considered the only damage mechanism (i.e., $j = 1$ at all damage locations) evolving in time. More specifically, two debonding fronts, propagating from the two end supports (i.e., from the beam ends) towards the beam midspan, are considered in this example. The lengths of the two disbonds at generic time *t* are denoted as $a_a^{(1,1,t)}$ (i.e., $i = 1$ and $j = 1$) and $a_a^{(2,1,t)}$ (i.e., $i = 2$ and $j = 1$), respectively. Similarly, the two damage locations are hereafter referred to as *damage location 1* (i.e., $i = 1$) and *damage location 2* (i.e., $i = 2$), respectively. The beam is subjected to a dynamic concentrated load, applied at its midspan, constituting the driving factor of the debonding propagation process along the adhesive interface; however, for the narrow

scope of this application example, it is postulated herein that the debonding propagation process, at time $t \geq t_p$, is governed by the following system of uncoupled ordinary differential equations

$$\begin{cases} \dfrac{d}{dt}\overline{a}_a^{(1,1,[p,t])} = G\left(\gamma^{(1,1,p)}\right) \\ \dfrac{d}{dt}\overline{a}_a^{(2,1,[p,t])} = G\left(\gamma^{(2,1,p)}\right) \\ \overline{a}_a^{(1,1,p)} = a_a^{(1,1,p)} \\ \overline{a}_a^{(2,1,p)} = a_a^{(2,1,p)} \end{cases} \qquad \left(t \geq t_p,\ \ p = 0, 1, 2, ...\right) \tag{8.29}$$

Furthermore, it is assumed that $G\left(\gamma^{(1,1,p)}\right) = \exp\left(\gamma^{(1,1,p)}\right)$ and $G\left(\gamma^{(2,1,p)}\right) = \exp\left(\gamma^{(2,1,p)}\right)$, and therefore Equation (8.29) is rewritten as shown in Equations (8.30) and (8.31):

$$\begin{cases} \dfrac{d}{dt}\overline{a}_a^{(1,1,[p,t])} = \exp\left(\gamma^{(1,1,p)}\right) \\ \overline{a}_a^{(1,1,p)} = a_a^{(1,1,p)} \end{cases} \qquad \left(t \geq t_p,\ \ p = 0, 1, 2, ...\right) \tag{8.30}$$

$$\begin{cases} \dfrac{d}{dt}\overline{a}_a^{(2,1,[p,t])} = \exp\left(\gamma^{(2,1,p)}\right) \\ \overline{a}_a^{(2,1,p)} = a_a^{(2,1,p)} \end{cases} \qquad \left(t \geq t_p,\ \ p = 0, 1, 2, ...\right) \tag{8.31}$$

Finally, by performing the analytical integration between current time t_p and a generic future time $t \geq t_p$, the equations dictating the debonding propagation processes, at the two identified damage locations, are expressed as

$$\overline{a}_a^{(1,1,[p,t])} = a_a^{(1,1,p)} \cdot \exp\left[\gamma^{(1,1,p)}\left(t - t_p\right)\right] \qquad \left(t \geq t_p,\ \ p = 0, 1, 2, ...\right) \tag{8.32}$$

$$\overline{a}_a^{(2,1,[p,t])} = a_a^{(2,1,p)} \cdot \exp\left[\gamma^{(2,1,p)}\left(t - t_p\right)\right] \qquad \left(t \geq t_p,\ \ p = 0, 1, 2, ...\right) \tag{8.33}$$

where: (i) the two outputs, $\overline{a}_a^{(1,1,[p,t])}$ and $\overline{a}_a^{(2,1,[p,t])}$, are the predicted (from time t_p) debonding lengths at time $t \geq t_p$; (ii) $a_a^{(1,1,p)}$ and $a_a^{(2,1,p)}$ represent a particular realization of the actual and unknown debonding lengths ($A_a^{(1,1,p)}$ and $A_a^{(2,1,p)}$) at time t_p, distributed according to the posterior conditional joint PDF $f''_{\mathbf{A}_a^p|\boldsymbol{\Theta}_{\text{mat}},\boldsymbol{\Theta}_{\text{dam}}^p}\left(\mathbf{a}_a^p \middle| \boldsymbol{\theta}_{\text{mat}}, \boldsymbol{\theta}_{\text{dam}}^p\right) = f''_{\mathbf{A}_a^p|\boldsymbol{\Theta}_{\text{dam}}^p}\left(\mathbf{a}_a^p \middle| \boldsymbol{\theta}_{\text{dam}}^p\right)$, in which the damage size vector $\mathbf{A}_a^p$ is given by $\mathbf{A}_a^p = \left\{A_a^{(1,1,p)}, A_a^{(2,1,p)}\right\}$; and finally, (iii) $\gamma^{(1,1,p)}$ and $\gamma^{(2,1,p)}$ constitute a particular realization of the random damage evolution model parameters $\Gamma^{(1,1,p)}$ and $\Gamma^{(2,1,p)}$, distributed according to the posterior joint PDF $f''_{\boldsymbol{\Theta}_{\text{dam}}^p}\left(\boldsymbol{\theta}_{\text{dam}}^p\right)$, in which the damage evolution model parameter vector $\boldsymbol{\Theta}_{\text{dam}}^p$ is given by $\boldsymbol{\Theta}_{\text{dam}}^p = \left\{\Gamma^{(1,1,p)}, \Gamma^{(2,1,p)}\right\}$. At

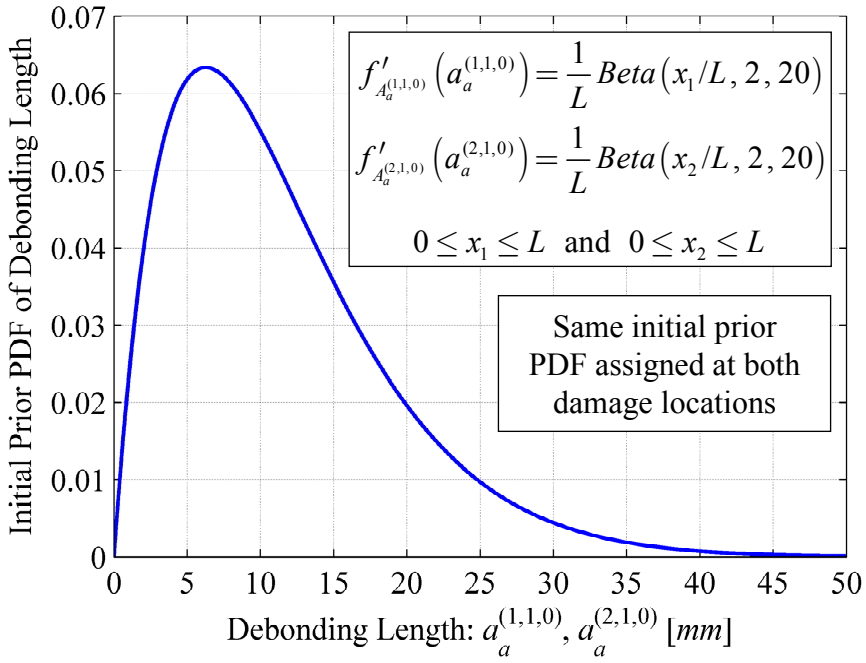

Figure 8.9: Initial prior PDF of debonding length at both damage locations

initial time $t_0 = 0$, the debonding lengths $A_a^{(1,1,0)}$ and $A_a^{(2,1,0)}$ are assumed to be s.i. and distributed according to the scaled Beta distribution shown in Figure 8.9. Similarly, the two damage evolution parameters $\Gamma^{(1,1,0)}$ and $\Gamma^{(2,1,0)}$ are also considered to be s.i. and uniformly distributed in $[1.0, 2.0]\times 10^{-5}$ (see Figure 8.10).

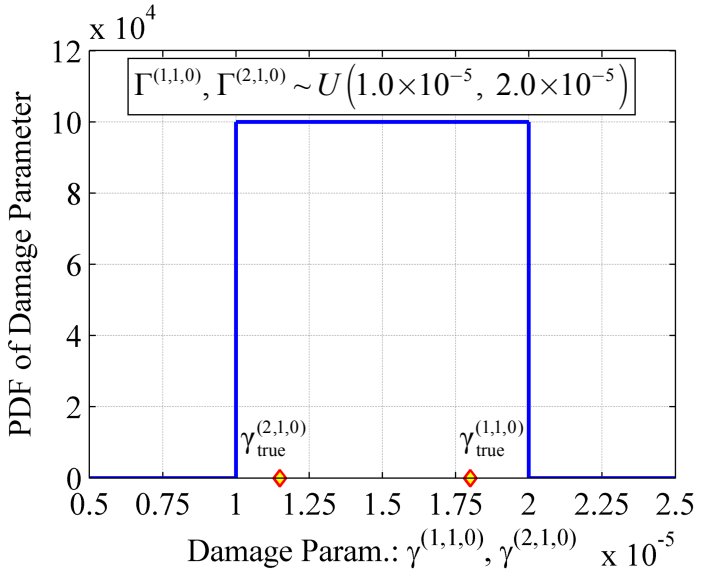

Figure 8.10: Initial prior PDF of damage evolution parameters $\Gamma^{(1,1,0)}$ and $\Gamma^{(2,1,0)}$.

The true (but in reality unknown) values of the damage evolution model parameter at *damage location 1* and *damage location 2* are taken as $\gamma_{\text{true}}^{(1,1)} = 1.80\times 10^{-5}$ and $\gamma_{\text{true}}^{(2,1)} = 1.15\times 10^{-5}$, respectively. These two values, together with the assumed initial true debonding lengths ($a_{a,\text{true}}^{(1,1,0)} = 1.0\, mm$ and $a_{a,\text{true}}^{(2,1,0)} = 2.0\, mm$), and Equations (8.32) and (8.33), provide the pair of true damage evolution paths shown in Figure 8.11. These two debonding evolution paths are used to simulate random NDE measurements at each inspection opportunity (and at each of the two damage locations) according to the *POD* curve model proposed by Berens (1989), depicted in Figure 8.2, and the

linear damage size measurement model (Zhang and Mahadevan, 2001) introduced earlier in Equation (8.5) and shown in Figure 8.3.

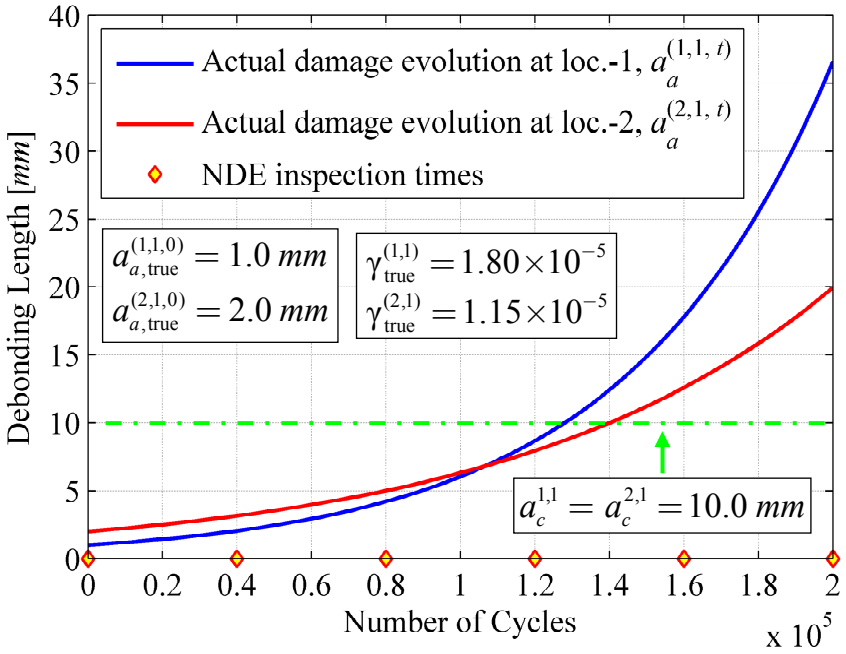

Figure 8.11: True damage evolution paths at each damage location together with the assumed six NDE inspection opportunities evenly spaced at 40,000 cycles.

For the specific benchmark structure analyzed in this chapter, the *POD* curve model proposed by Berens (1989) is expressed as

$$POD\left(a_a^{(i,j,p)}\right) = \frac{e^{-\alpha_0^{(i,j)}+\alpha_1^{(i,j)}\ln\left[a_a^{(i,j,p)}\right]}}{1+e^{-\alpha_0^{(i,j)}+\alpha_1^{(i,j)}\ln\left[a_a^{(i,j,p)}\right]}} \quad \left(i=1,2 \text{ and } j=1\right) \tag{8.34}$$

where the values for the model parameters, $\alpha_0^{(i,j)}$ and $\alpha_1^{(i,j)}$, are estimated through logistic regression analysis (Kutner, 2004). These estimates are denoted as $\hat{\alpha}_0^{(i,j)}$ and $\hat{\alpha}_1^{(i,j)}$, and for the particular application example presented in this chapter they are assigned the following values: $\hat{\alpha}_0^{(1,1)} = \hat{\alpha}_0^{(2,1)} = \hat{\alpha}_0 = 0.3$ and $\hat{\alpha}_1^{(1,1)} = \hat{\alpha}_1^{(2,1)} = \hat{\alpha}_1 = 2.0$.

Similarly, the estimates (obtained from linear regression analysis; Seber and Lee, 2003) for $\beta_0^{(i,j)}$, $\beta_1^{(i,j)}$, and $\sigma^{(i,j,p)}_{A_m|A_a} = \sigma_{\varepsilon_{ij}}$ in Equation (8.5) are denoted as $\hat{\beta}_0^{(i,j)}$, $\hat{\beta}_1^{(i,j)}$ and $\hat{\sigma}_{\varepsilon_{ij}}$, and are assumed to be equal to: $\hat{\beta}_0^{(1,1)} = \hat{\beta}_0^{(2,1)} = \hat{\beta}_0 = -1.5\,mm$, $\hat{\beta}_1^{(1,1)} = \hat{\beta}_1^{(2,1)} = \hat{\beta}_1 = 1.2$, and $\hat{\sigma}_{\varepsilon_{11}} = \hat{\sigma}_{\varepsilon_{21}} = \hat{\sigma}_{\varepsilon} = 2.0\,mm$.

8.4.1. Local and global failure modes

Two local failure criteria are defined (and then used in the component reliability analyses) for this specific application example. The first local failure criterion is based on the discussions presented in Section 8.3.5 and in Section 7.3.1 in Chapter 7, and, within the benchmark application discussed herein, is particularized as

$$\mathrm{F}_{\mathrm{L},i1}^{[p,q]} \triangleq \left\{ A_a^{(i,1,[p,q])} \geq a_c^{i,1} \right\}, \quad i = 1,2 \tag{8.35}$$

with the critical debonding length, a_{crit}, set to be equal to $a_{crit} = 10.0\,mm$ at both damage locations (i.e., $a_c^{1,1} = a_c^{2,1} = a_{crit}$) as already shown in Figure 8.11. Thus, the probability of local component failure, associated with the local failure event, $\mathrm{F}_{\mathrm{L},i1}^{[p,q]}$, in Equation (8.35), is computed as

$$P\left[\mathrm{F}_{\mathrm{L},i1}^{[p,q]}\right] = P\left[A_a^{(i,1,[p,q])} \geq a_c^{i,1}\right] = 1 - F_{A_a^{(i,1,[p,q])}}\left(a_c^{i,1}\right), \quad i = 1,2 \tag{8.36}$$

where $F_{A_a^{(i,1,[p,q])}}(\bullet)$ represents the marginal CDF of the actual debonding length $A_a^{(i,1,[p,q])}$, $i = 1,2$. The second local component failure criterion is instead based on the level-of-safety (LOS) formulation, with single NDE inspection opportunity,

introduced and discussed in Section 7.3.2 in Chapter 7. This alternative failure criterion, when applied to the specific application example presented herein, can be particularized as follows

$$\tilde{\mathrm{F}}_{\mathrm{L},i1}^{[p,q]} \triangleq \left\{ \mathrm{F}_{\mathrm{L},i1}^{[p,q]} \cap \left(A_m^{(i,1,[p,q])} < a_c^{i,1} \right) \right\}, \quad i = 1,2 \tag{8.37}$$

where $A_m^{(i,1,[p,q])}$ (with $i = 1,2$) represents the measurement outcome from the assumed single NDE inspection opportunity performed at *damage location* i at time t_p^q. Consequently, the probability of local component failure, associated with the local failure event in Equation (8.37), is computed as

$$\begin{aligned} & P\left[\tilde{\mathrm{F}}_{\mathrm{L},i1}^{[p,q]}\right] = \\ & P\left[\mathrm{F}_{\mathrm{L},i1}^{[p,q]} \cap \left(A_m^{(i,1,[p,q])} < a_c^{i,1} \right)\right] = \qquad i = 1,2 \\ & P\left[\mathrm{F}_{\mathrm{L},i1}^{[p,q]}\right] - \int_{a_c^{i,1}}^{+\infty} \hat{\psi}\left(a_a^{(i,1,[p,q])}\right) POD\left(a_a^{(i,1,[p,q])}\right) f_{A_a^{(i,1,[p,q])}}\left(a_a^{(i,1,[p,q])}\right) da_a^{(i,1,[p,q])} \end{aligned} \tag{8.38}$$

where the function $\hat{\psi}\left(a_a^{(i,1,[p,q])}\right)$ is expressed in Equation (8.22) and the probability of detection $POD\left(a_a^{(i,1,[p,q])}\right)$ is computed by using Equation (8.34). This alternative failure criterion, shown in Equation (8.37), introduces the following false-call event:

$$\tilde{\mathscr{F}}_{\mathrm{L},i1}^{[p,q]} \triangleq \left\{ \overline{\mathrm{F}_{\mathrm{L},i1}^{[p,q]}} \cap \left(A_m^{(i,1,[p,q])} \geq a_c^{i,1} \right) \right\}, \quad i = 1,2 \tag{8.39}$$

where $\overline{\mathrm{F}_{\mathrm{L},i1}^{[p,q]}}$ represents the complement of the local component failure event $\mathrm{F}_{\mathrm{L},i1}^{[p,q]}$. Hence, the probability, $P\left[\tilde{\mathscr{F}}_{\mathrm{L},i1}^{[p,q]}\right]$, associated with this local false-call event is computed as

$$P\left[\tilde{\mathcal{F}}_{\mathrm{L},ij}^{[p,q]}\right]=$$
$$P\left[\overline{\mathrm{F}_{\mathrm{L},i1}^{[p,q]}}\cap\left(A_m^{(i,1,[p,q])}\geq a_c^{i,1}\right)\right]= \qquad i=1,2 \qquad (8.40)$$
$$\int_0^{a_c^{i,1}}\hat{\psi}\left(a_a^{(i,1,[p,q])}\right)POD\left(a_a^{(i,1,[p,q])}\right)f_{A_a^{(i,1,[p,q])}}\left(a_a^{(i,1,[p,q])}\right)da_a^{(i,1,[p,q])}$$

and represents a particularization of Equation (7.22) derived in Section 7.3.4 in Chapter 7.

Similarly, two global failure criteria, $\mathrm{F}_{\mathrm{G},r}^{[p,q]}$ (with $r=1,2$), are also introduced (and then used in the component reliability analyses) in this benchmark application. The first global failure criterion is defined as

$$\mathrm{F}_{\mathrm{G},1}^{[p,q]}\triangleq\left\{\Omega_1^{[p,q]}\leq\omega_1^{crit}\right\} \qquad (8.41)$$

where the quantity $\Omega_1^{[p,q]}$ represents the reduced (due to damage) first bending frequency of the composite beam at time t_p^q, as predicted from current time t_p. ω_1^{crit} is a critical threshold for the bending frequency $\Omega_1^{[p,q]}$ and is herein chosen as a fraction of the nominal first bending frequency, ω_1^{nom}. In this specific example the assigned values are $\omega_1^{crit}=0.85\times\omega_1^{nom}$ and $\omega_1^{nom}=\omega_1\left(a_a^{(1,1)}=0,\ a_a^{(2,1)}=0,\ E_{11}^f=130.0\,GPa\right)$ — i.e., ω_1^{nom} represents the first bending frequency of the undamaged beam evaluated at the mean value of $E_{11}^f=\mu_{E_{11}^f}=130.0\,GPa$. The probability of local component failure, associated with the global failure event in Equation (8.41), is then computed as

$$P\left[\mathrm{F}_{\mathrm{G},1}^{[p,q]}\right]=P\left[\Omega_1^{[p,q]}\leq\omega_1^{crit}\right]=F_{\Omega_1^{[p,q]}}\left(\omega_1^{crit}\right) \qquad (8.42)$$

where $F_{\Omega_1^{[p,q]}}(\bullet)$ represents the marginal CDF of the first bending frequency, $\Omega_1^{[p,q]}$. The second global failure criterion is instead defined as

$$\mathrm{F}_{\mathrm{G},2}^{[p,q]} \triangleq \left\{ W_{st}^{[p,q]} \geq w_{st}^{crit} \right\} \tag{8.43}$$

where $W_{st}^{[p,q]}$ is the predicted midspan vertical displacement generated by a given static concentrated load ($P_{st}^{\max} = 1,500\,N$) acting at the beam midspan. Finally, $w_{st}^{crit} = L/10 = 12.5\,mm$ constitutes the assumed critical threshold for $W_{st}^{[p,q]}$. Due to the simple geometry and the simple damage scenario of the benchmark structure used in this application example, response surface (RS) models for the first bending frequency, $\overline{\omega}_1^{[p,t]} = \left(\Omega_1^{[p,q]} \middle| a_a^{(1,1,t)}, a_a^{(2,1,t)}, E_{11}^f \right)$, and the beam midspan displacement, $\overline{w}_{st}^{[p,t]} = \left(W_{st}^{[p,q]} \middle| a_a^{(1,1,t)}, a_a^{(2,1,t)}, E_{11}^f, P_{st}^{\max} \right)$, at time $t \geq t_p$, are derived analytically (i.e., by using exact or approximate analytical methods as opposed to a carefully designed set of FE model simulations). More specifically, the midspan displacement conditional on the debonding lengths, $A_a^{(1,1,t)} = a_a^{(1,1,t)}$ and $A_a^{(2,1,t)} = a_a^{(2,1,t)}$ at time $t \geq t_p$, the flexural modulus of the adherends E_{11}^f, and the maximum applied load $P_{st}^{\max}$, can be computed in closed-form as (see Appendix E)

$$\overline{w}_{st}^{[p,t]} = \left(W_{st}^{[p,q]} \middle| a_a^{(1,1,t)}, a_a^{(2,1,t)}, E_{11}^f, P_{st}^{\max} \right) = \frac{2L^3 + 3\left[\left(a_a^{(1,1,t)} \right)^3 + \left(a_a^{(2,1,t)} \right)^3 \right]}{8\, E_{11}^f\, b\, h^3} P_{st}^{\max} \tag{8.44}$$

Consequently, the compliance, $C\left(a_a^{(1,1,t)}, a_a^{(2,1,t)}, E_{11}^f \right)$, defined as the ratio between $\overline{w}_{st}^{[p,t]}$ and $P_{st}^{\max}$, can be expressed as

$$C\left(\, a_a^{(1,1,t)}, a_a^{(2,1,t)}, E_{11}^f\right) = \frac{\overline{w}_{st}^{[p,t]}}{P_{st}^{\max}} = \frac{2L^3 + 3\left[\left(a_a^{(1,1,t)}\right)^3 + \left(a_a^{(2,1,t)}\right)^3\right]}{8\, E_{11}^f\, b\, h^3} \tag{8.45}$$

On the other hand, any bending frequency (in the vertical plane) of the composite beam shown in Figure 8.7 can be computed by making use of the *Ritz method* as illustrated in the four points below:

(vi) Approximate the deflected shape of the beam, using a linear combination of n_ϕ harmonic terms, as

$$w(x) = C_m \phi_m(x) = \sum_{m=1}^{n_\phi} C_m \sin\left(m \frac{\pi x}{2L}\right) \qquad 0 \le x \le 2L \tag{8.46}$$

(vii) Compute the coefficients of the $\left(n_\phi \times n_\phi\right)$ stiffness matrix $\mathbf{K} = \left[K_{mn}\right]$ of the damaged composite beam (at generic time $t \ge t_p$) as

$$\begin{aligned} K_{mn} &= \int_0^{2L} E_{11}^f(x_1)\, I(x_1) \frac{d^2\phi_m(x_1)}{dx_1^2} \frac{d^2\phi_n(x_1)}{dx_1^2} dx_1 \\ &= E_{11}^f I_{(0)} \left[\int_0^{a_a^{(1,1,t)}} \frac{d^2\phi_m(x_1)}{dx_1^2} \frac{d^2\phi_n(x_1)}{dx_1^2} dx_1 + 4 \int_{a_a^{(1,1,t)}}^{2L-a_a^{(2,1,t)}} \frac{d^2\phi_m(x_1)}{dx_1^2} \frac{d^2\phi_n(x_1)}{dx_1^2} dx_1 + \right. \\ &\qquad \left. \int_{2L-a_a^{(2,1,t)}}^{2L} \frac{d^2\phi_m(x_1)}{dx_1^2} \frac{d^2\phi_n(x_1)}{dx_1^2} dx_1 \right] \end{aligned} \tag{8.47}$$

where: $I(x) = I_{(0)} = 2\left(bh^3/12\right)$ in the range $0 \le x \le a_a^{(1,1,t)}$ and $2L - a_a^{(2,1,t)} \le x \le 2L$; and $I(x) = I_{(\infty)} = 8\left(bh^3/12\right) = 4I_{(0)}$ in the range $a_a^{(1,1,t)} < x < 2L - a_a^{(2,1,t)}$; results that can also be expressed as a function of the moment of inertia of the single composite adherend, $I_a = bh^3/12$, as

$I_{(0)} = 2I_a$ and $I_{(\infty)} = 4I_{(0)} = 8I_a$, respectively. Carrying out the analytical integration of Equation (8.47) leads to the off-diagonal terms (i.e., $m \neq n$)

$$\begin{aligned} K_{mn} = \frac{3}{8}\frac{m^2 n^2 \pi^3 E_{11}^f I_{(0)}}{\left(m^2 - n^2\right)L^3}\Bigg\{ & m\sin\left(n\frac{a_a^{(1,1,t)}\pi}{2L}\right)\cos\left(m\frac{a_a^{(1,1,t)}\pi}{2L}\right) - \\ & n\sin\left(m\frac{a_a^{(1,1,t)}\pi}{2L}\right)\cos\left(n\frac{a_a^{(1,1,t)}\pi}{2L}\right) + \\ & n\sin\left[i\frac{\left(2L - a_a^{(2,1,t)}\right)\pi}{2L}\right]\cos\left[n\frac{\left(2L - a_a^{(2,1,t)}\right)\pi}{2L}\right] - \\ & m\sin\left[n\frac{\left(2L - a_a^{(2,1,t)}\right)\pi}{2L}\right]\cos\left[m\frac{\left(2L - a_a^{(2,1,t)}\right)\pi}{2L}\right]\Bigg\} \end{aligned} \tag{8.48}$$

and to the following diagonal terms (i.e., $m = n$)

$$\begin{aligned} K_{mm} = \frac{m^3 \pi^3 E_{11}^f I_{(0)}}{32L^4}\Bigg\{ & 3L\sin\left(m\frac{a_a^{(1,1,t)}\pi}{L}\right) - 3L\sin\left[m\frac{\left(2L - a_a^{(2,1,t)}\right)\pi}{L}\right] + \\ & m\left(8L - 3a_a^{(1,1,t)} - 3a_a^{(2,1,t)}\right)\Bigg\} \end{aligned} \tag{8.49}$$

(viii) Compute the coefficients of the $\left(n_\phi \times n_\phi\right)$ mass matrix $\mathbf{M} = \left[M_{mn}\right]$ of the composite beam as

$$M_{mn} = \int_0^{2L} \rho_L I(x)\phi_m(x)\phi_n(x)dx = \begin{cases} \rho_L L & \text{if } m = n \\ 0 & \text{if } m \neq n \end{cases} \tag{8.50}$$

where ρ_L represents the density per unit length of the composite beam and is computed as $\rho_L = 2\times\left(b\times h\right)\rho_V$, with $\left(b\times h\right)$ being the cross-section area of a single composite adherend and ρ_V representing the volumetric density

of the composite material (see Figure 8.7).

(ix) Compute the first n_ϕ natural bending frequencies of the composite beam by solving the eigenvalue problem in Equation (8.51)

$$\left|\mathbf{K}-\omega^2\mathbf{M}\right|=0 \tag{8.51}$$

A set of selected response surfaces, computed according to Equations (8.45) and (8.51), and conditional on the mean value of the flexural modulus of the composite laminated adherends (i.e., $\mu_{E_{11}^f}=130.0\,GPa$), are shown (for illustrative purposes) in Figures 8.12 through 8.15.

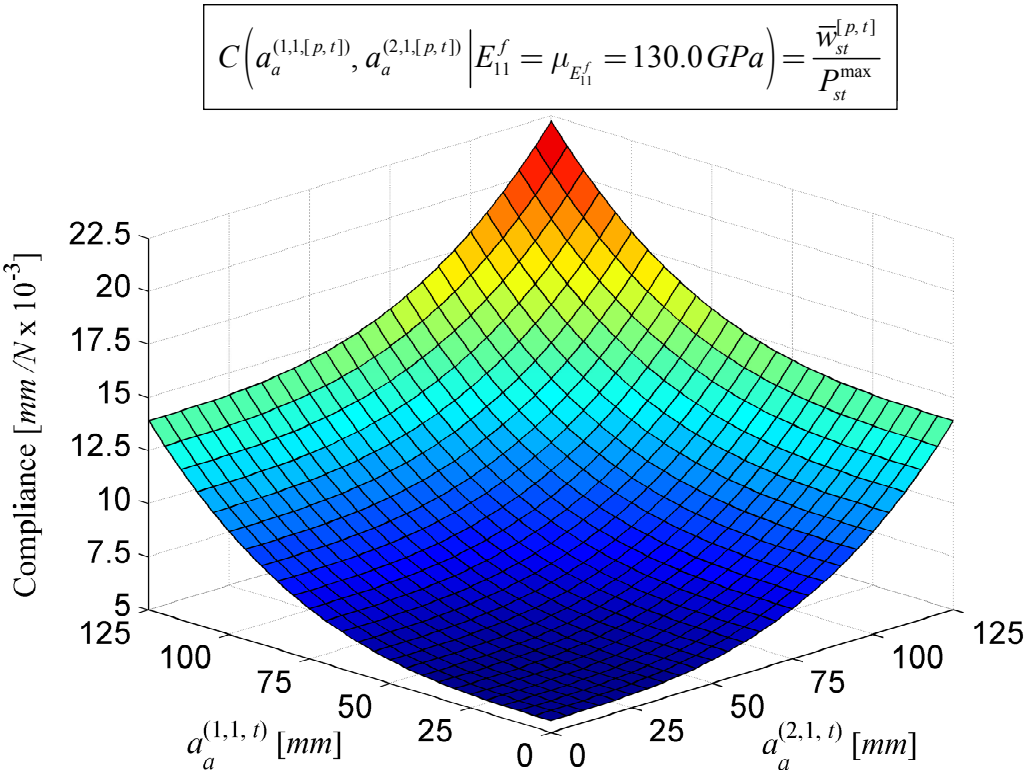

Figure 8.12: Response surface for the midspan compliance, defined in Equation (8.45) and conditional on $E_{11}^f=\mu_{E_{11}^f}=130.0\,GPa$, as a function of the level of damage.

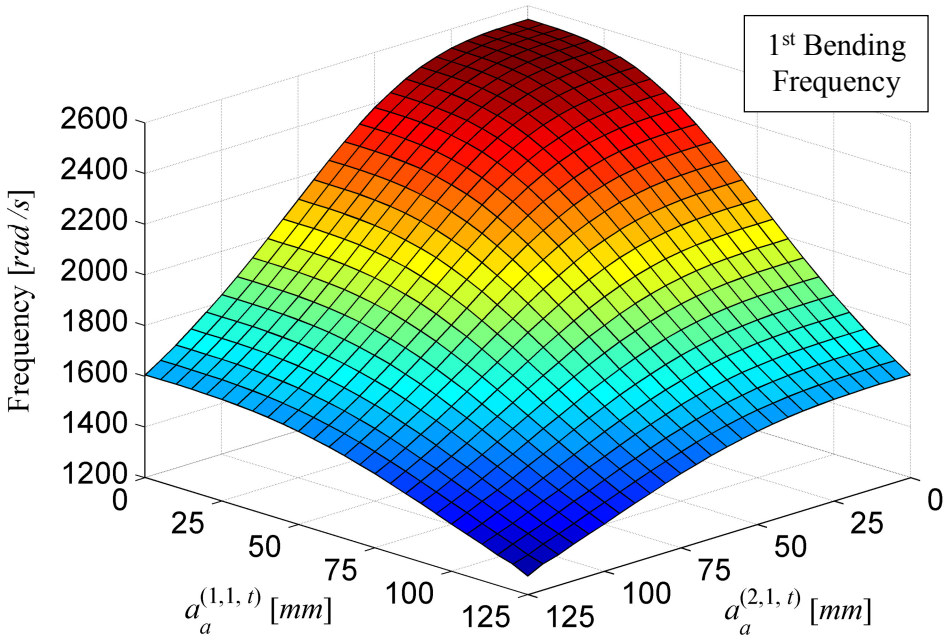

Figure 8.13: First bending frequency as a function of the level of damage ($n_\phi = 20$).

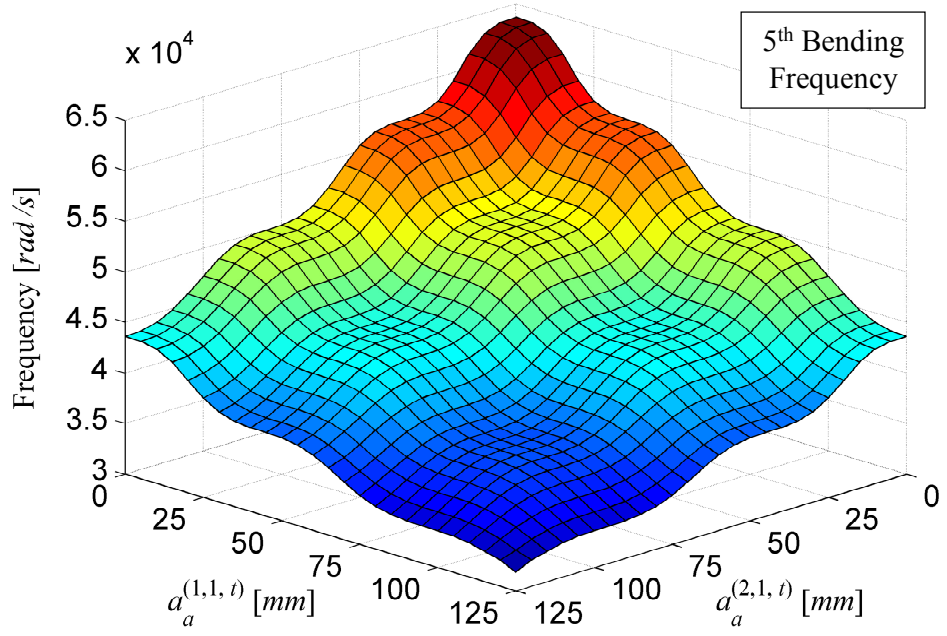

Figure 8.14: Fifth bending frequency as a function of the level of damage ($n_\phi = 20$).

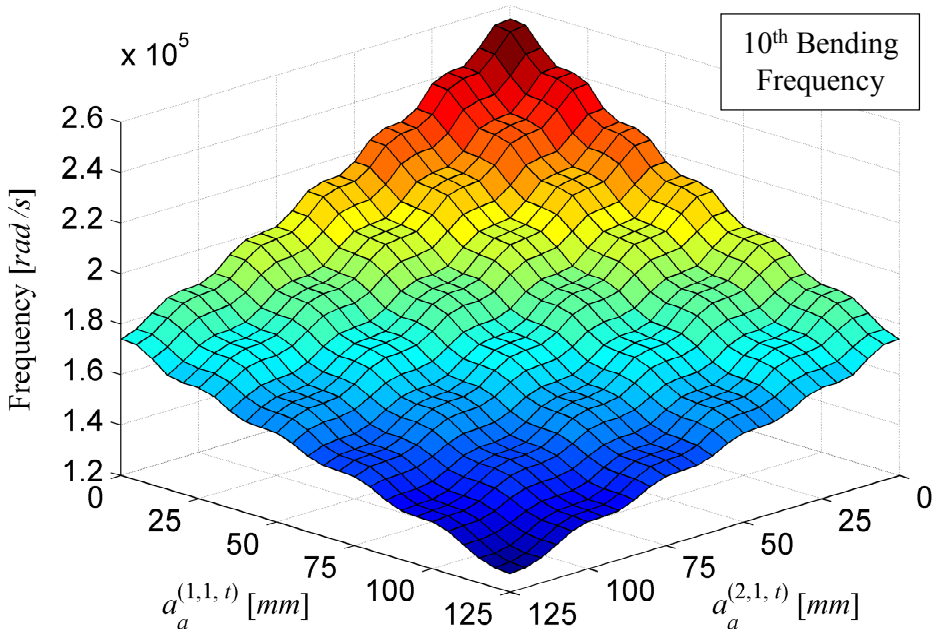

Figure 8.15: Tenth bending frequency as a function of the level of damage ($n_\phi = 20$).

8.4.2. Bayesian updating results

This section presents a selection of the Bayesian updating results obtained through the proposed recursive Bayesian inference scheme introduced in Chapter 3 and briefly reviewed in Section 8.3.1. Within this scheme, debonding extents, $A_a^{(1,1,p)}$ and $A_a^{(2,1,p)}$, and damage evolution model parameters, $\Gamma^{(1,1,p)}$ and $\Gamma^{(2,1,p)}$, are simultaneously updated after each NDE inspection. As shown in Figure 8.11, a total of six NDE inspections (evenly spaced every 40,000 load cycles) are considered in this application example and, at each NDE inspection opportunity, three different scenarios are envisioned. In the first scenario, five s.i. NDE measurements are taken and processed using the proposed Bayesian inference scheme. In the second scenario, ten

s.i. NDE measurements are considered. Lastly, in the third scenario, twenty s.i. NDE measurements are used to repeatedly compute the posterior PDFs of $\mathbf{A}_a^p$ and $\mathbf{\Theta}_{\text{dam}}^p$. Furthermore, the three sets of measurements are assumed to be mutually statistically independent. Figure 8.16 and Figure 8.17 report the posterior marginal PDFs (after each NDE inspection) of the debonding extents $A_a^{(1,1,p)}$ and $A_a^{(2,1,p)}$, respectively. Figure 8.18 and Figure 8.19 show the posterior marginal PDFs (after each NDE inspection) of the damage evolution model parameters $\Gamma^{(1,1,p)}$ and $\Gamma^{(2,1,p)}$, respectively. These four figures highlight the benefit, in terms of uncertainty reduction, provided by the larger number of NDE measurements collected at each NDE inspection opportunity. Figure 8.16 and Figure 8.17 also indicate that a larger set of NDE measurements allows for a better collocation/centering of the computed posterior marginal PDFs of $A_a^{(1,1,p)}$ and $A_a^{(2,1,p)}$ on the true debonding lengths. Focusing now on the Bayesian updating results for the damage model parameters ($\Gamma^{(1,1,p)}$ and $\Gamma^{(2,1,p)}$), it is observed (see Figure 8.18) that at *damage location 1*, three to four NDE inspections are needed in order to start having the posterior PDF of the damage model parameter converge towards the true value of the parameter, $\gamma_{\text{true}}^{(1,1)} = 1.80 \times 10^{-5}$. On the other hand, at *damage location 2*, the correct convergence trend, towards $\gamma_{\text{true}}^{(2,1)} = 1.15 \times 10^{-5}$, is already captured right after the second NDE inspection at time N_1 (see Figure 8.19). It is worth emphasizing that in this study, it is assumed that the damage propagation law is known and only the damage parameters (i.e., $\Gamma^{(1,1,p)}$ and $\Gamma^{(2,1,p)}$, in the specific application example presented herein) are considered unknown and modeled as random variables.

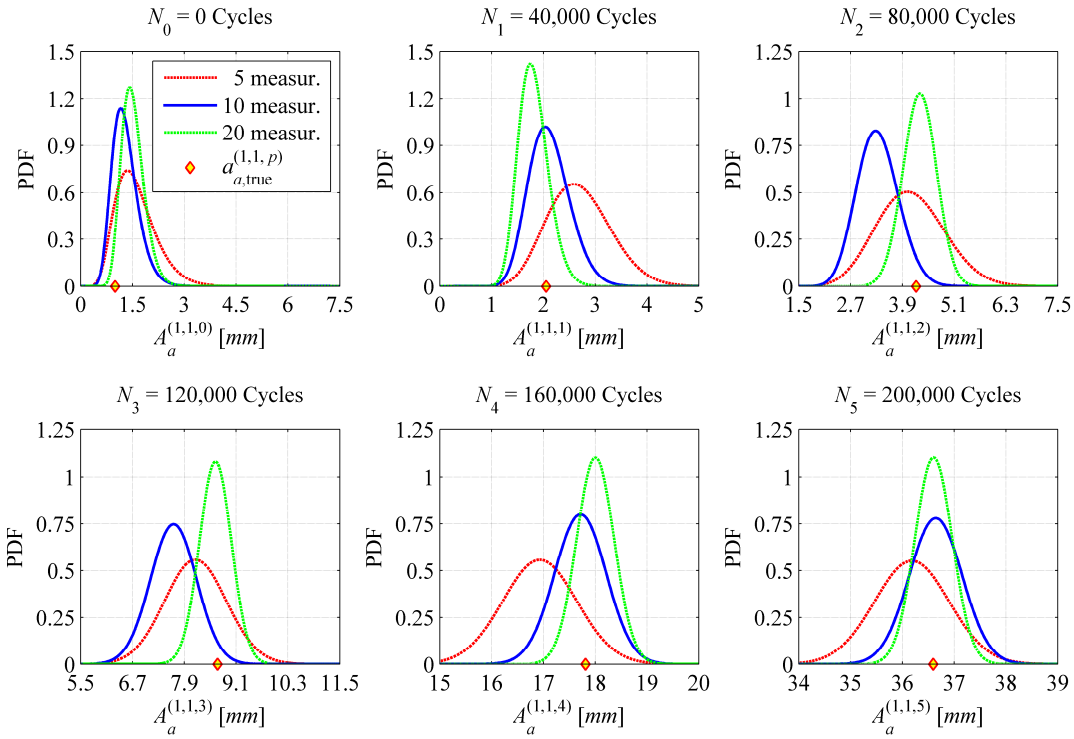

Figure 8.16: Posterior marginal PDF of debonding length at *damage location 1*.

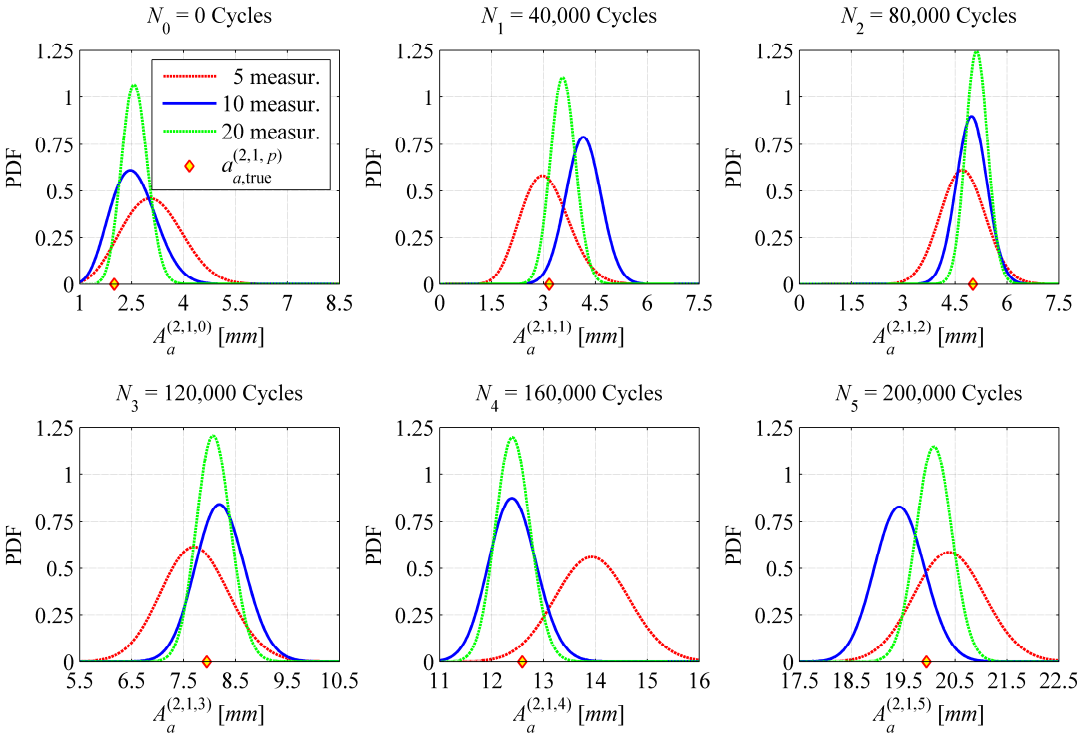

Figure 8.17: Posterior marginal PDF of debonding length at *damage location 2*.

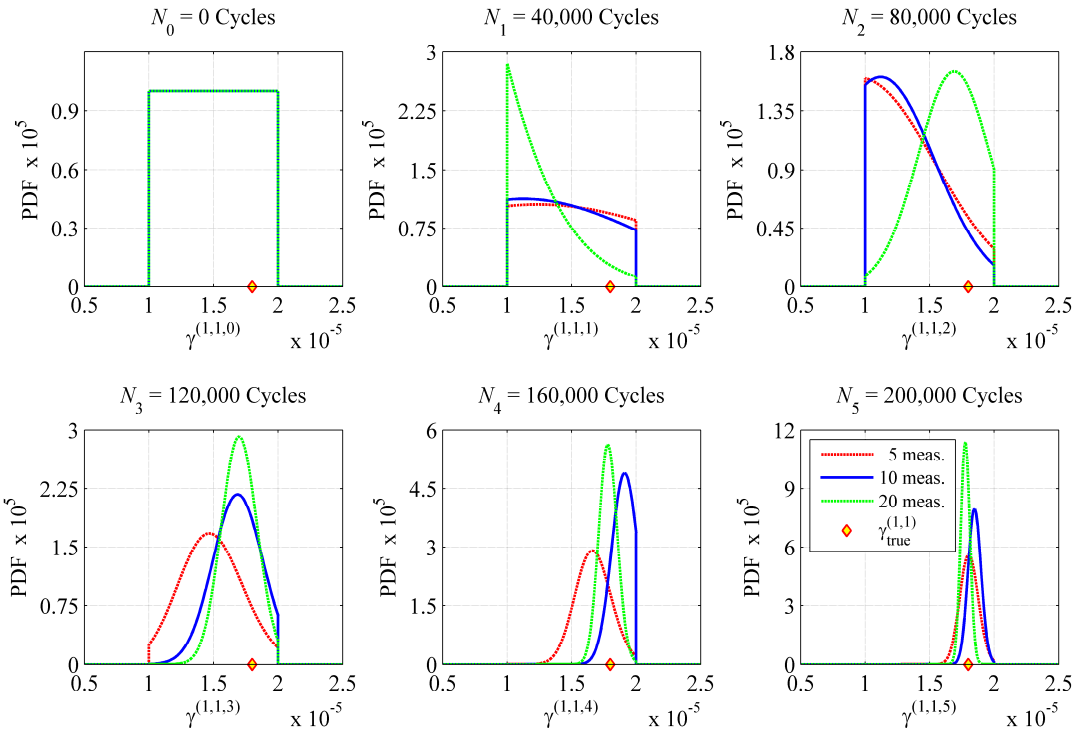

Figure 8.18: Posterior marginal PDF of $\Gamma^{(1,1,p)}$ after each NDE inspection.

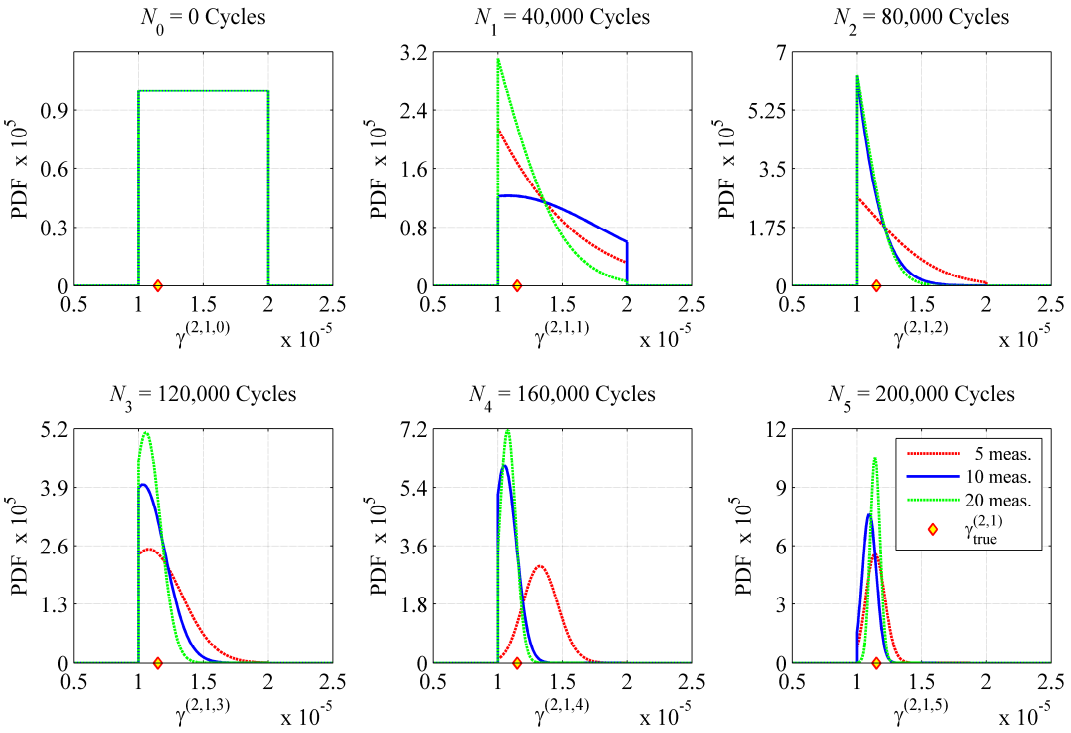

Figure 8.19: Posterior marginal PDF of $\Gamma^{(2,1,p)}$ after each NDE inspection.

8.4.3. Comparison between partial and full Bayesian updating schemes

The set of results presented in this Section shows the importance of performing a full Bayesian updating (i.e., when the PDFs of both, damage sizes and damage evolution model parameters, are simultaneously updated) versus a partial Bayesian updating (i.e., when only the PDF of the damage sizes is updated). To this end, Figure 8.20 and Figure 8.21 compare (after each NDE inspection) the posterior marginal PDFs of $A_a^{(1,1,p)}$ and $A_a^{(2,1,p)}$, obtained from the two Bayesian updating approaches mentioned above, when $n_{\mathrm{MS}}^{(i,1,p)} = 10$ ($i = 1,2$ and $p = 0,1,...,5$).

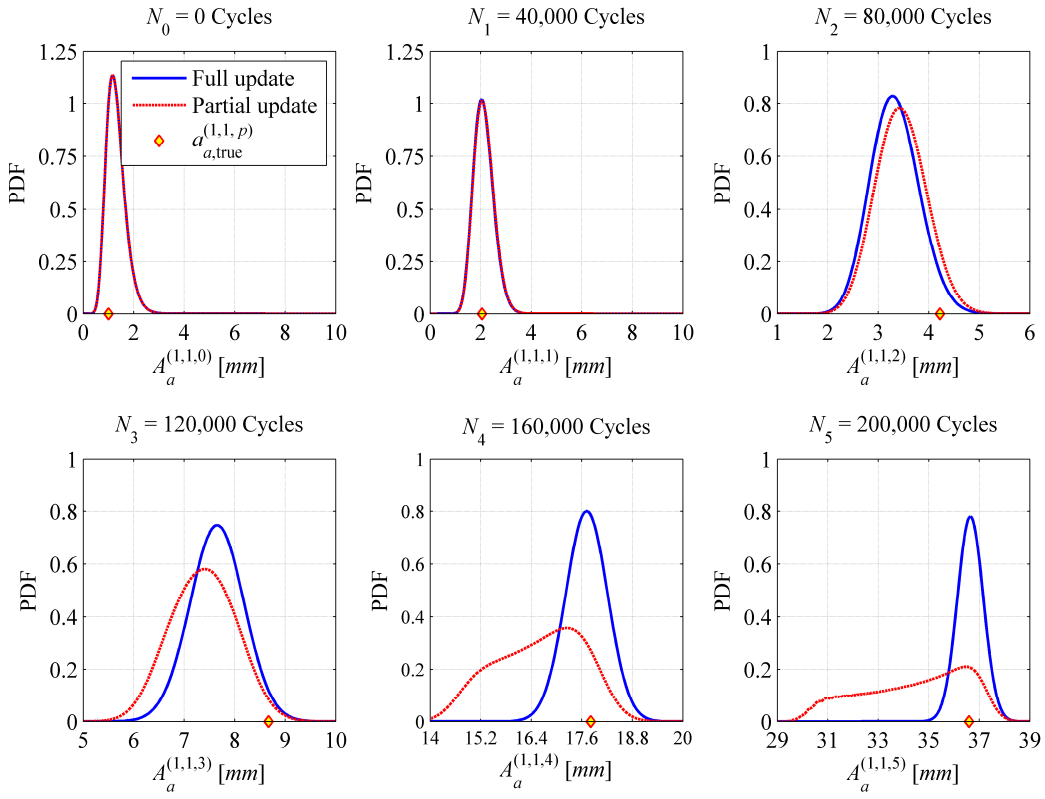

Figure 8.20: Comparison between the results obtained from the proposed full and partial updating schemes in terms of uncertainty reduction in the evaluation of the posterior marginal PDF of the debonding length, $A_a^{(1,1,p)}$, at *damage location 1*; $n_{\mathrm{MS}}^{(i,1,p)} = 10$ ($i = 1,2$ and $p = 0,1,...,5$).

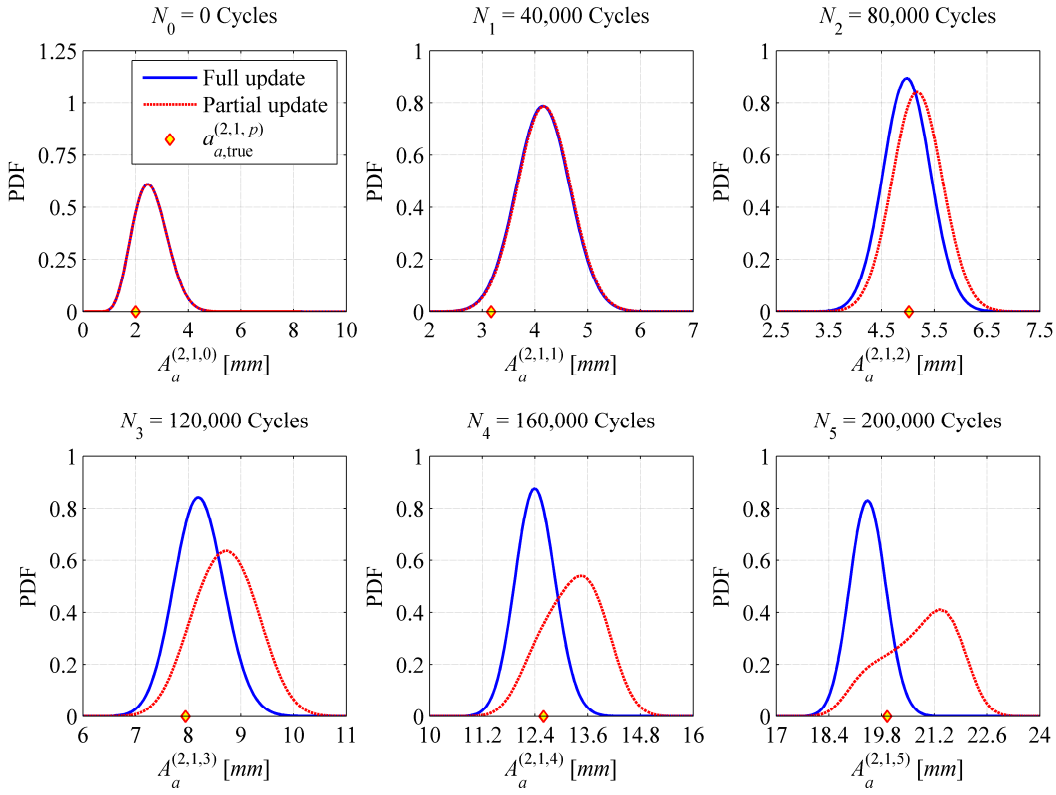

Figure 8.21: Comparison between the results obtained from the proposed full and partial updating schemes in terms of uncertainty reduction in the evaluation of the posterior marginal PDF of the debonding length, $A_a^{(2,1,p)}$, at *damage location 2*; $n_{\text{MS}}^{(i,1,p)} = 10$ ($i = 1,2$ and $p = 0,1,...,5$).

From the Bayesian updating results presented above, it is observed that the accuracy in computing the posterior marginal PDFs of $A_a^{(1,1,p)}$ and $A_a^{(2,1,p)}$ degrades considerably after the fourth NDE inspection (at $N_3 = 120,000$ cycles). Furthermore, the debonding length $A_a^{(1,1,p)}$ is consistently underestimated at $N_4 = 160,000$ cycles and $N_5 = 200,000$ cycles (see Figure 8.20) while $A_a^{(2,1,p)}$ becomes biased towards larger debonding extents (see Figure 8.21).

8.4.4. Global performance analysis results

A selected set of results from the fourth step of the proposed methodology (i.e., probabilistic global performance analysis) is shown in Figure 8.22 and Figure 8.23. As discussed earlier two global performance metrics/measures have been selected for this specific application example: midspan displacement, $W_{st}^{[p,q]}$, conditional on an assumed maximum operational (static) load $P_{st}^{\max} = 1,500\,N$, and first bending frequency, $\Omega_1^{[p,q]}$. The marginal PDFs of these two quantities, computed — semi-analytically through Equations (8.44) and (8.51), respectively — after each NDE inspection for the case in which $n_{\mathrm{MS}}^{(i,1,p)} = 10$ ($i = 1,2$ and $p = 0,1,...,5$) are shown in the figures below. Thus, six PDF curves are provided in each of the two plots and only at the 6$^{\text{th}}$ NDE inspection — i.e., when both local reliability components have already failed — an appreciable damage-induced change/shift of both PDFs can be observed. Recalling the true underlying debonding evolution paths shown in Figure 8.11, it can be seen that both debonding lengths exceed the critical threshold, $a_{crit} = 10.0\,mm$, between the forth (at $N_3 = 120,000$ cycles) and the fifth (at $N_4 = 160,000$ cycles) NDE inspection. More specifically, the debonding length at *damage location 1* exceeds $a_{crit} = 10.0\,mm$ at time $N_{crit}^{(1,1)} = N\left(a_{a,\mathrm{true}}^{(1,1,N)} = a_{crit}\right) = 127,900$ cycles, while the debonding length at *damage location 2* exceeds the critical threshold at time $N_{crit}^{(2,1)} = N\left(a_{a,\mathrm{true}}^{(2,1,N)} = a_{crit}\right) = 139,900$ cycles. Therefore, the two global failure criteria (arbitrarily) chosen for this specific application example are not able to detect the exceedance of the (selected) critical local damage thresholds (i.e., $a_{crit} = 10.0\,mm$) at

an early enough stage. In other words, the two global reliability components, selected in this application example, do not represent the dominant failure modes in the subsequent system reliability analyses discussed in Section 8.4.5. As a direct consequence, and for this specific application example, it can be equivalently stated that the predictions for the probability of *system failure* and *false-call* (discussed in the next Section) are dominated by the two local reliability components (i.e., the debonding lengths at *damage location 1*, $A_a^{(1,1,[p,q])}$, and at *damage location 2*, $A_a^{(2,1,[p,q])}$) and the corresponding local component failure criteria introduced earlier in Section 8.4.1. Furthermore, $A_a^{(1,1,[p,q])}$ represents the overall dominant failure mode since $N_{crit}^{(1,1)} < N_{crit}^{(2,1)}$. This fact is well captured by the proposed system reliability analyses part of the damage prognosis step of the methodology.

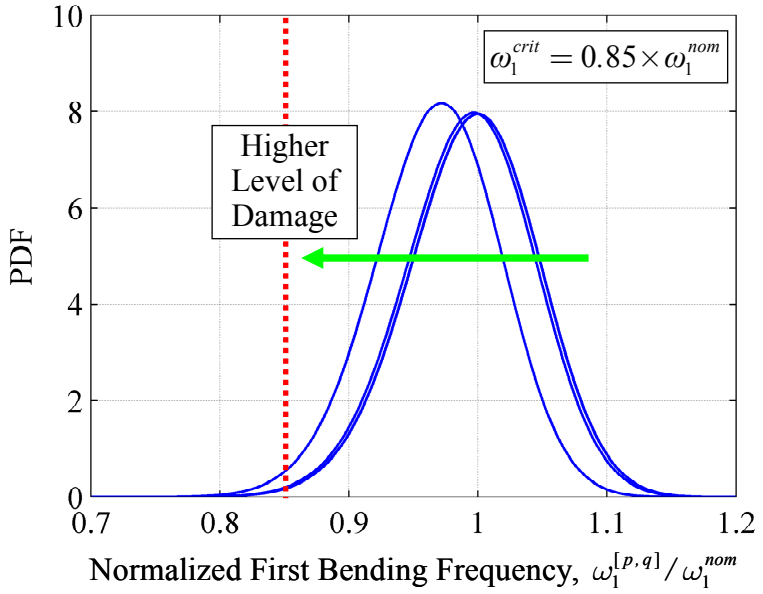

Figure 8.22: Marginal PDFs of first bending frequency, Ω_1^p, computed after each NDE inspection for the case in which $n_{\mathrm{MS}}^{(i,1,p)} = 10$ ($i = 1,2$ and $p = 0,1,...,5$).

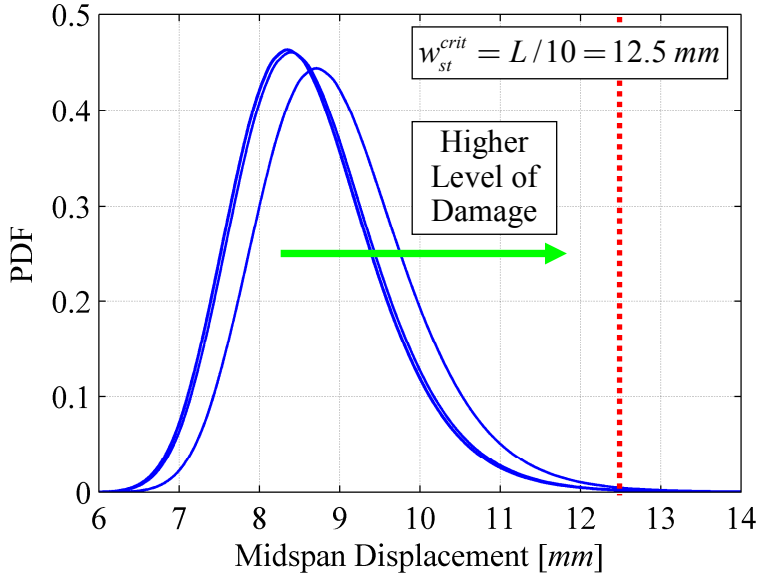

Figure 8.23: Marginal PDFs of beam midspan displacement, W_{st}^{p}, computed after each NDE inspection for the case in which $n_{\mathrm{MS}}^{(i,1,p)} = 10$ ($i = 1,2$ and $p = 0,1,...,5$).

8.4.5. Damage prognosis analysis results

In the first part of this section, a selected set of the damage prognosis results for $P\left[\mathrm{F}_{\mathrm{sys}}^{[p,q]}\right]$ — obtained by making use of (i) the outcomes of the previous analysis steps, (ii) the local failure criteria defined in Equation (8.35), and (iii) the global failure criteria provided in Equations (8.41) and (8.43) — is presented and discussed. Figures 8.24 through 8.26 show the predictions for the lower and upper uni-modal bounds to the probability of system failure, $P\left[\mathrm{F}_{\mathrm{sys}}^{[p,q]}\right]$, corresponding to three different NDE inspection scenarios, i.e., $n_{\mathrm{MS}}^{(i,1,p)} = 5, 10, 20$ (with $i = 1,2$ and $p = 0,1,...,4$). The results obtained from the damage prognosis analysis performed at initial time $N_0 = 0$ cycles make use only of the NDE inspection results collected at that time. On the other

hand, the results from the damage prognosis analysis performed at $N_1 = 40,000$, $N_2 = 80,000$, and $N_3 = 120,000$ cycles make use of the NDE inspection results collected up to that particular number of cycles. Furthermore, the number of cycles between two successive damage prognosis predictions was chosen as $\Delta N = 4,000$ cycles, and the prediction window was chosen to be equal to $N_p^{\bar{q}} - N_p = \bar{q}\Delta N = 120,000$ load cycles (where $\bar{q} = 30$).

Figures 8.24 through 8.26, indicate that the increasing number of NDE measurements collected at each inspection (from 5 to 20) significantly increases the tightness of the lower and upper bounds of the time-dependent probability of failure, $P\left[\mathrm{F}_{\mathrm{sys}}^{[p,q]}\right]$. Additionally, the results of the damage prognosis analysis performed at initial time t_0 significantly underestimate the time at which the true debonding length $a_{a,\mathrm{true}}^{(1,1,t)}$ reaches the critical threshold $a_{crit} = 10.0\,mm$. Note that, all these types of observations are possible because in this benchmark application — unlike in a real-world application of the damage prognosis framework presented herein — the instants of time (or the number of cycles) at which the true debonding lengths exceed 10.0 *mm* are known exactly as indicated by the blue and green vertical lines in Figures 8.24 through 8.26.

The results for the time-dependent upper uni-modal bound of the probability of system failure $P\left[\mathrm{F}_{\mathrm{sys}}^{[p,q]}\right]$ (obtained from the damage prognosis analyses performed at $N_0 = 0$, $N_1 = 40,000$, $N_2 = 80,000$, and $N_3 = 120,000$ cycles) are combined together in Figure 8.27. In this figure, the prediction for the upper uni-modal bound of

$P\left[\mathrm{F}_{\mathrm{sys}}^{[p,q]}\right]$ between time N_p and time N_{p+1} (with $p=0,1,2,3$) is obtained by making use of the NDE results up to N_p (i.e., $a_m^{(i,1,[0,p])}$, $i=1,2$). As it can be noticed from the figure, every time new NDE data are assimilated by the proposed framework, the estimate for the probability of failure of the system is updated and a new branch for the upper bound of $P\left[\mathrm{F}_{\mathrm{sys}}^{[p,q]}\right]$ is computed. Furthermore, Figure 8.27 also indicates that the results from the damage prognosis analysis performed at time $t_3=120,000$ hours (i.e., inspection time closest to the time at which the true failure of the system occurs, as identified by the vertical blue line at $N\left(a_{a,\mathrm{true}}^{(1,1,t)}\right)=127,900$ cycles) tend to capture the real underlying "*step-function*" behavior for $P\left[\mathrm{F}_{\mathrm{sys}}^{[p,q]}\right]$. Additionally, it is worth mentioning that the value for $P\left[\mathrm{F}_{\mathrm{sys}}^{[p,q]}\right]$, in the range $0\le N\le 120,000$ cycles, is dominated by the contribution of $P\left[\Omega_1^{[p,q]}\le\omega_1^{crit}\right]=0.436\%$ (constant over the entire range of load cycles due to the considerations discussed in Section 8.4.4 and the results shown in Figure 8.22). These results emphasize the strength and robustness of the proposed recursive updating and prediction scheme for damage prognosis aimed at providing more accurate damage prognosis predictions every time new NDE data are collected and processed (i.e., used to updated the PDFs of $\mathbf{A}_{\mathrm{a}}^{p}$ and $\boldsymbol{\Theta}_{\mathrm{dam}}^{p}$). They also show (see light-blue boxes and arrows in Figure 8.27) a gain of accuracy in the damage prognosis predictions obtained as the number of NDE measurements — collected at each NDE inspection opportunity — increases (i.e., from 5 to 20 for the specific case analyzed herein and shown in Figures 8.24 through 8.27).

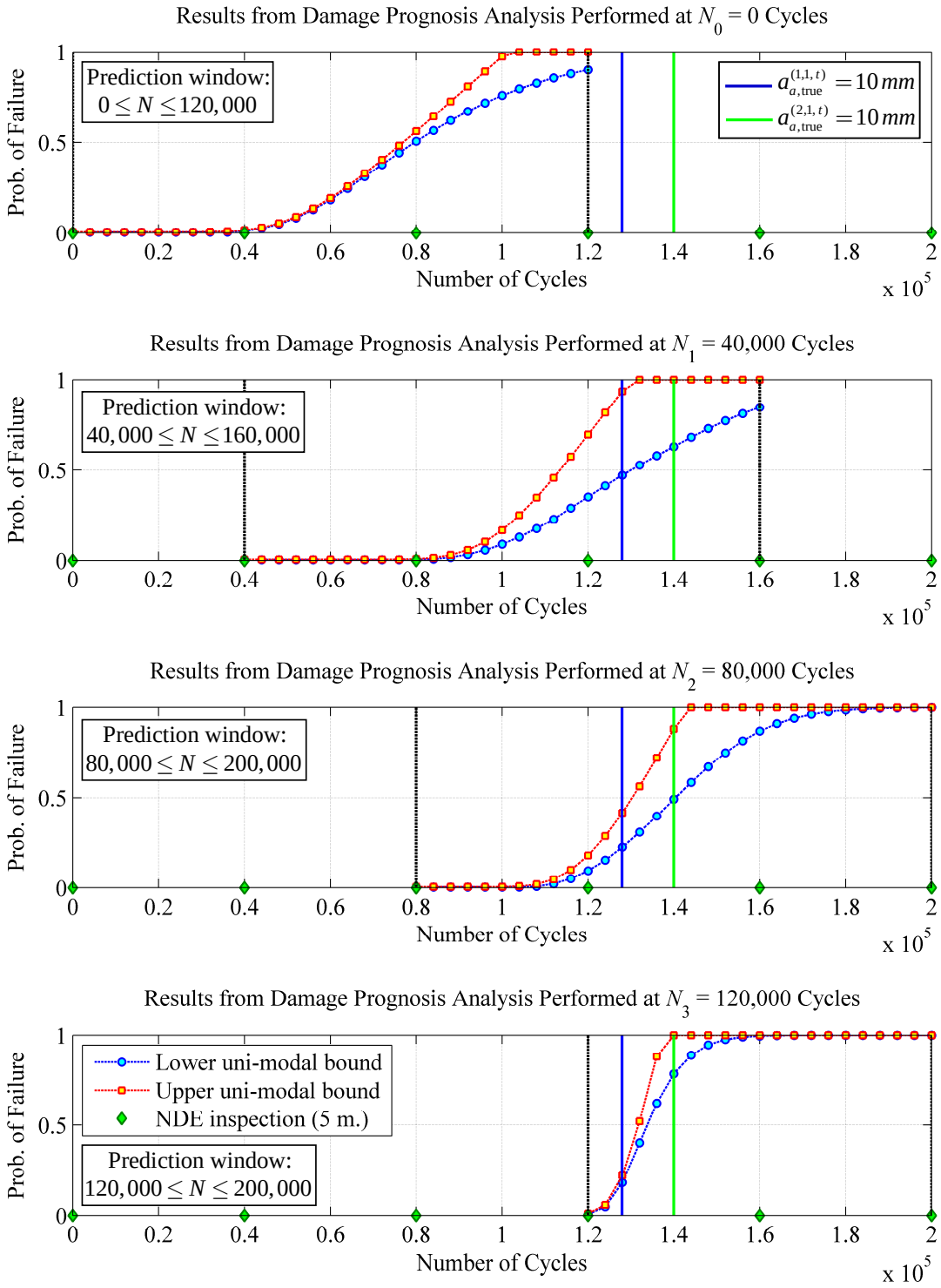

Figure 8.24: Time-dependent lower and upper uni-modal bounds for the probability of system failure, $P\left[\mathrm{F}_{\text{sys}}^{[p,q]}\right]$, as computed immediately after the first four NDE inspections using 5 NDE measurements (i.e., $n_{\text{MS}}^{(i,1,p)} = 5$ for $i = 1,2$ and $p = 0,1,...,4$).

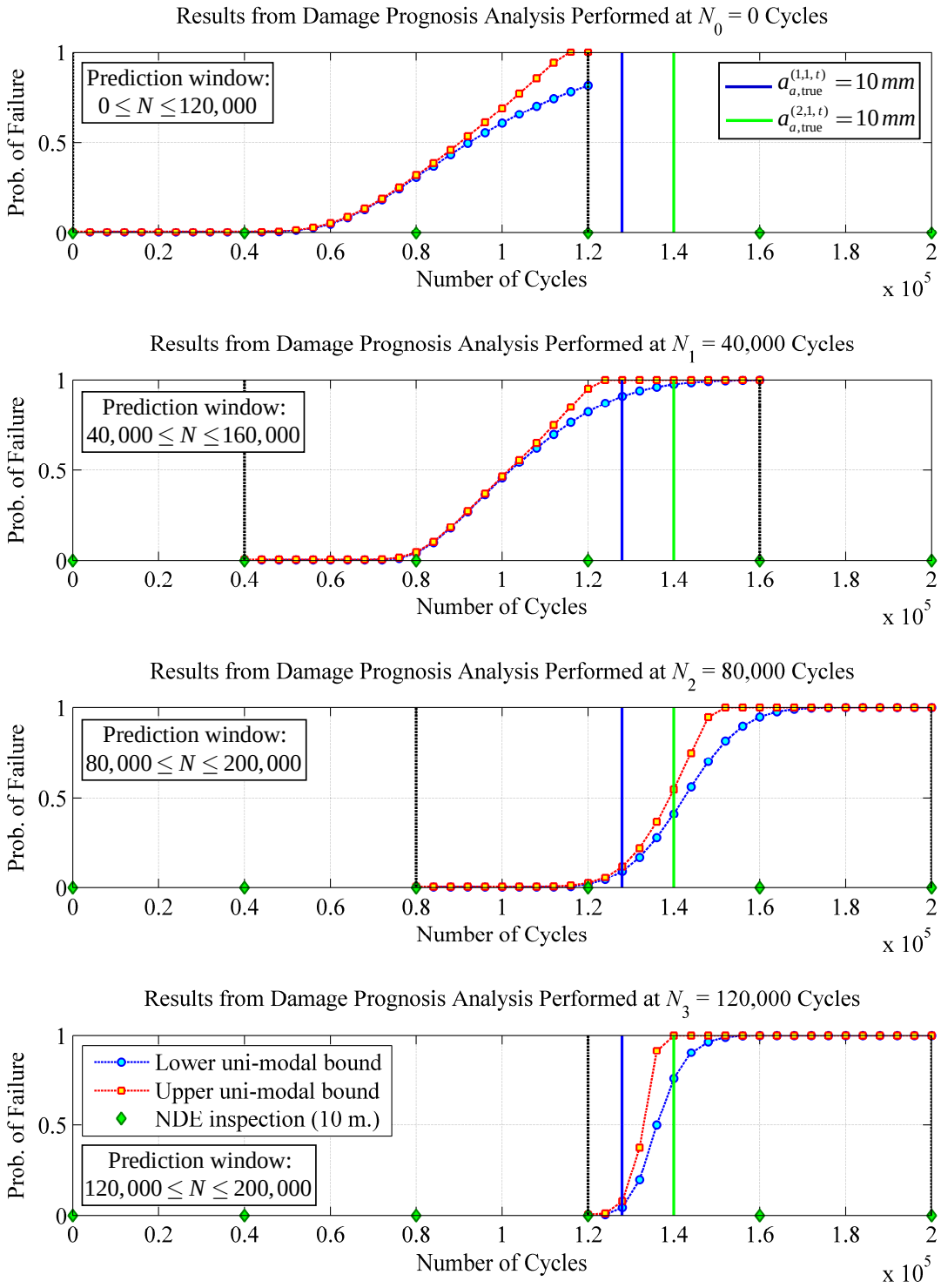

Figure 8.25: Time-dependent lower and upper uni-modal bounds for the probability of system failure, $P\left[\mathrm{F}_{\text{sys}}^{[p,q]}\right]$, as computed immediately after the first four NDE inspections using 10 NDE measurements (i.e., $n_{\text{MS}}^{(i,1,p)} = 10$ for $i = 1,2$ and $p = 0,1,...,4$).

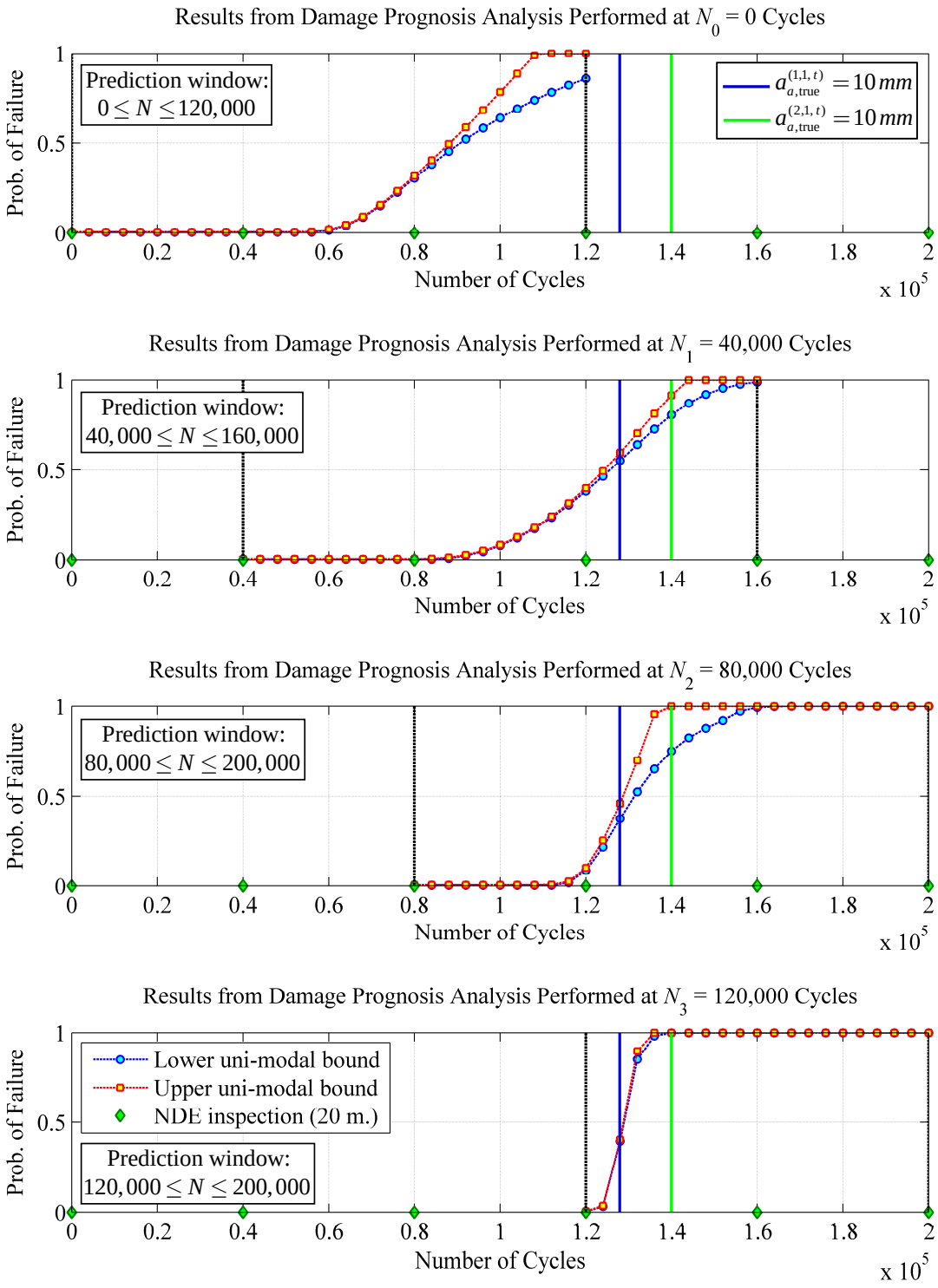

Figure 8.26: Time-dependent lower and upper uni-modal bounds for the probability of system failure, $P\left[\mathrm{F}_{\text{sys}}^{[p,q]}\right]$, as computed immediately after the first four NDE inspections using 20 NDE measurements (i.e., $n_{\text{MS}}^{(i,1,p)} = 20$ for $i = 1, 2$ and $p = 0, 1, \ldots, 4$).

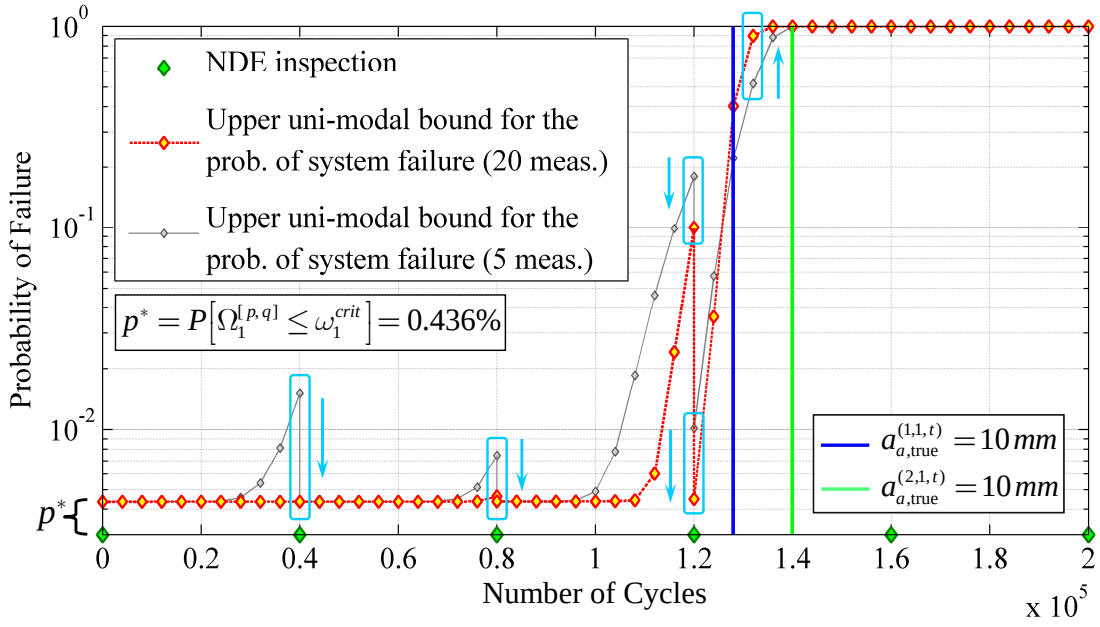

Figure 8.27: Comparison between two sets of recursive damage prognosis predictions for the upper uni-modal bound of the probability of system failure, $P\left[\mathrm{F}_{\text{sys}}^{[p,q]}\right]$, $n_{\text{MS}}^{(i,1,p)} = 5$ vs. $n_{\text{MS}}^{(i,1,p)} = 20$ (with $i = 1,2$ and $p = 0,1,2,3$).

Similar results, discussions, and conclusions can be provided for the recursive predictions of: (i) the probability of system failure, $P\left[\breve{\mathrm{F}}_{\text{sys}}^{[p,q]}\right]$, computed according to the failure event $\breve{\mathrm{F}}_{\text{sys}}^{[p,q]}$, as defined in Equation (8.25), and (ii) the probability of false-call, $P\left[\breve{\mathcal{F}}_{\text{sys}}^{[p,q]}\right]$, computed according to the false-call event, $\breve{\mathcal{F}}_{\text{sys}}^{[p,q]}$, as defined in Equation (8.27). Figures 8.28 through 8.30 show the predictions for the lower and upper uni-modal bounds to the probability of system failure, $P\left[\breve{\mathrm{F}}_{\text{sys}}^{[p,q]}\right]$, corresponding to three different NDE inspection scenarios already discussed earlier, i.e., $n_{\text{MS}}^{(i,1,p)} = 5, 10, 20$ $\left(\text{with } i = 1,2 \text{ and } p = 0,1,\ldots,4\right)$. Also in this case, the results obtained from the damage prognosis analysis performed at initial time $N_0 = 0$ cycles make use

only of the NDE inspection results collected at that time. On the other hand, the results from the damage prognosis analysis performed at $N_1 = 40,000$, $N_2 = 80,000$, and $N_3 = 120,000$ cycles make use of the NDE inspection results collected up to that particular number of cycles (i.e., up to the most recent NDE inspection). Furthermore, the number of cycles between two successive damage prognosis predictions was chosen again as $\Delta N = 4,000$ cycles and the prediction window, used in the damage prognosis analyses, was selected as $N_p^{\bar{q}} - N_p = \bar{q}\Delta N = 120,000$ cycles (where $\bar{q} = 30$).

From Figures 8.28 through 8.31, it is observed that the increase in the number of NDE measurements collected at each inspection (from 5 to 20) generally increases the tightness of the lower and upper bounds of the time-dependent probability of failure, $P\left[\breve{\mathrm{F}}_{\mathrm{sys}}^{[p,q]}\right]$. Also, as the number of NDE measurements increases and the prediction time moves closer to the time at which the true failure of the system occurs — i.e., the time identified by the vertical blue line at $N\left(a_{a,\mathrm{true}}^{(1,1,t)}\right) = 127,900$ cycles — the prediction for $P\left[\breve{\mathrm{F}}_{\mathrm{sys}}^{[p,q]}\right]$ tends to capture the ideal "*Dirac delta*" proportional behavior that can be mathematically expressed as

$$P\left[\breve{\mathrm{F}}_{\mathrm{sys}}^{[p,q]}\right] \propto \delta\left[N - N\left(a_{a,\mathrm{true}}^{(1,1,t)}\right)\right] \tag{8.52}$$

Analogously to Figure 8.27, the results for the time-dependent upper uni-modal bound of the probability of system failure $P\left[\breve{\mathrm{F}}_{\mathrm{sys}}^{[p,q]}\right]$ — obtained from the four damage prognosis analyses performed at $N_0 = 0$, $N_1 = 40,000$, $N_2 = 80,000$, and $N_3 = 120,000$ cycles, respectively — are combined together in the plot of Figure 8.31.

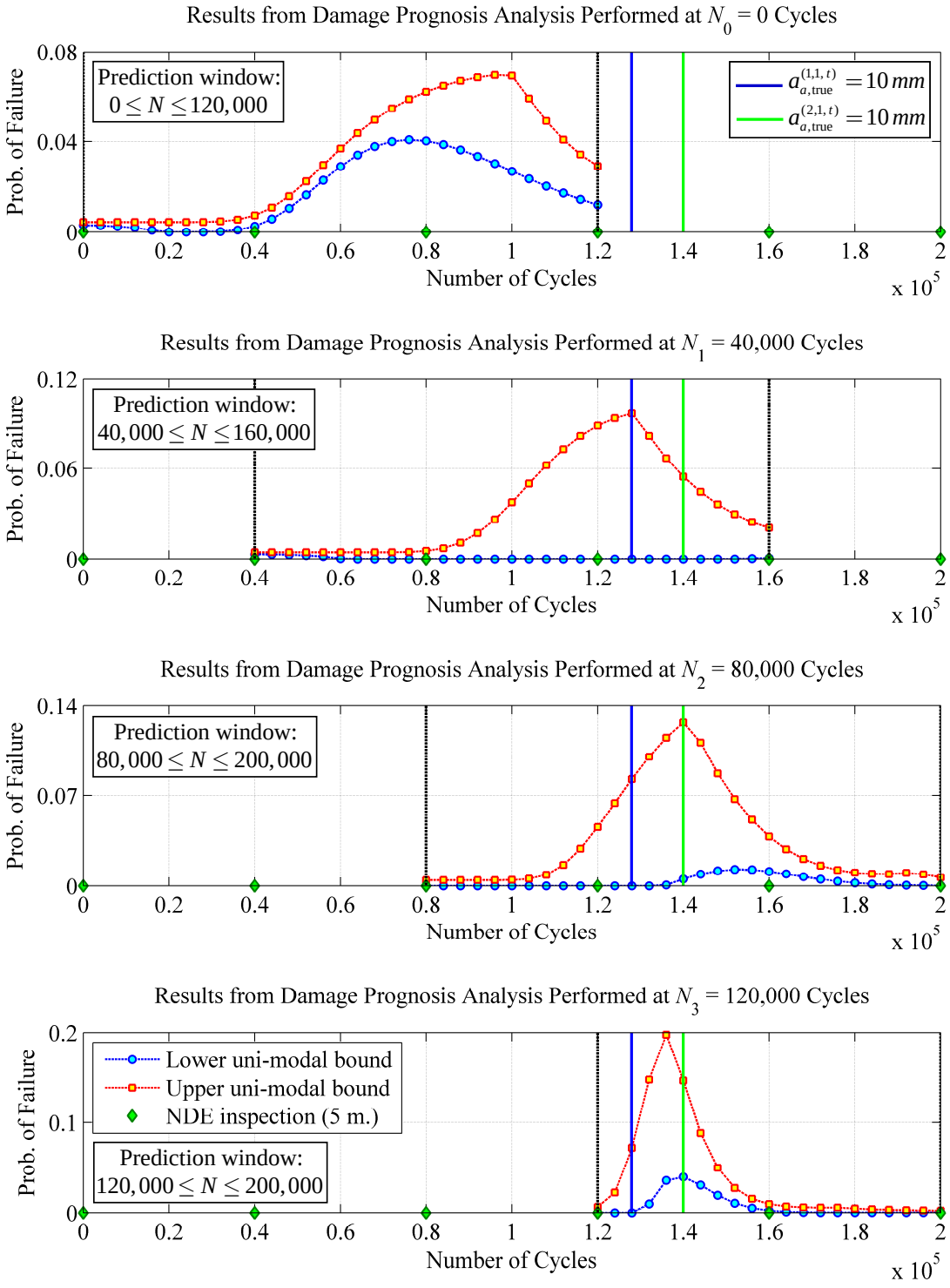

Figure 8.28: Time-dependent lower and upper uni-modal bounds for the probability of system failure, $P\left[\breve{F}_{\text{sys}}^{[p,q]}\right]$, as computed immediately after the first four NDE inspections using 5 NDE measurements (i.e., $n_{\text{MS}}^{(i,1,p)} = 5$ for $i = 1,2$ and $p = 0,1,...,4$).

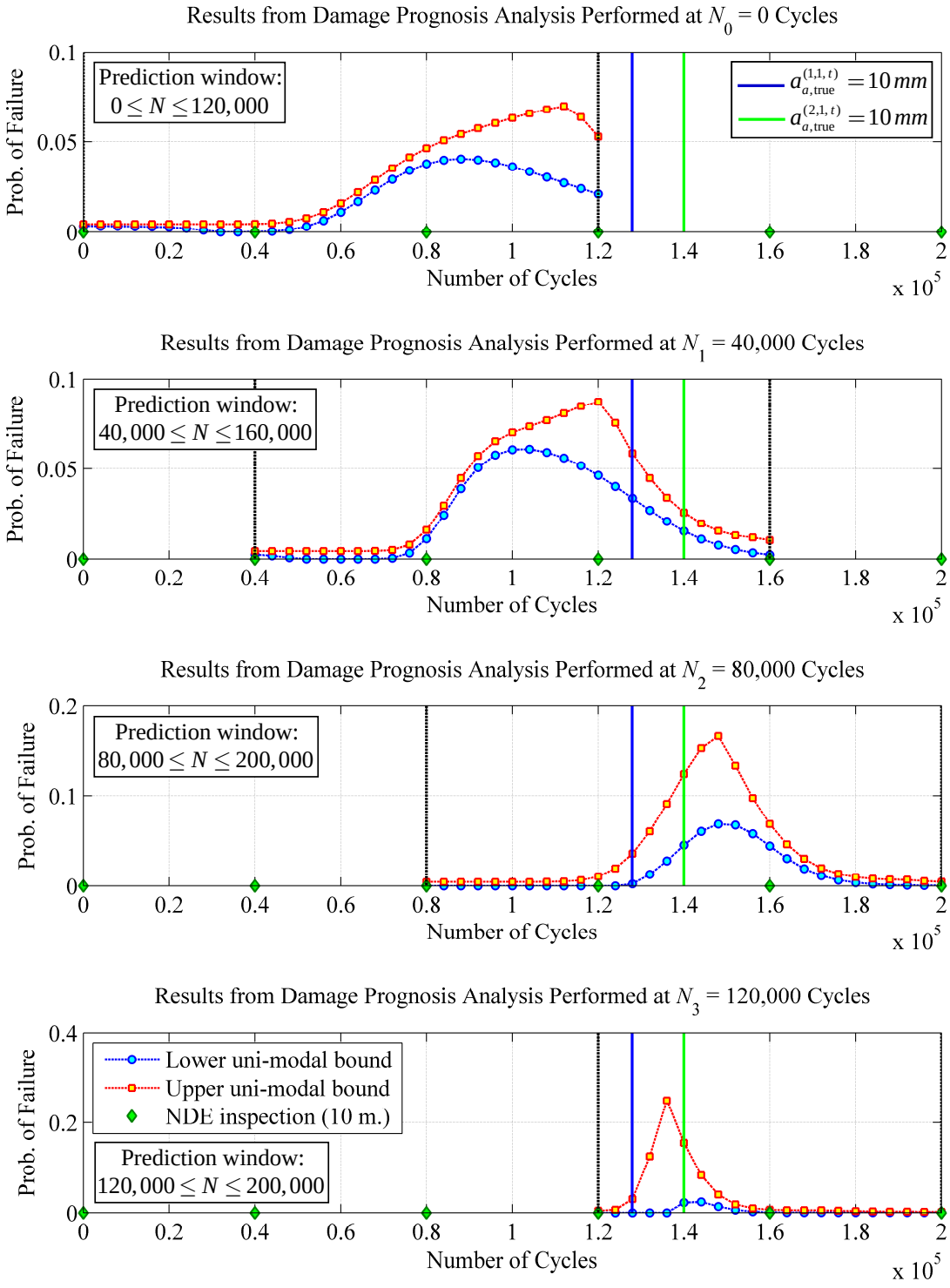

Figure 8.29: Time-dependent lower and upper uni-modal bounds for the probability of system failure, $P\left[\breve{F}_{\text{sys}}^{[p,q]}\right]$, as computed immediately after the first four NDE inspections using 10 NDE measurements (i.e., $n_{\text{MS}}^{(i,1,p)} = 10$ for $i = 1,2$ and $p = 0,1,...,4$).

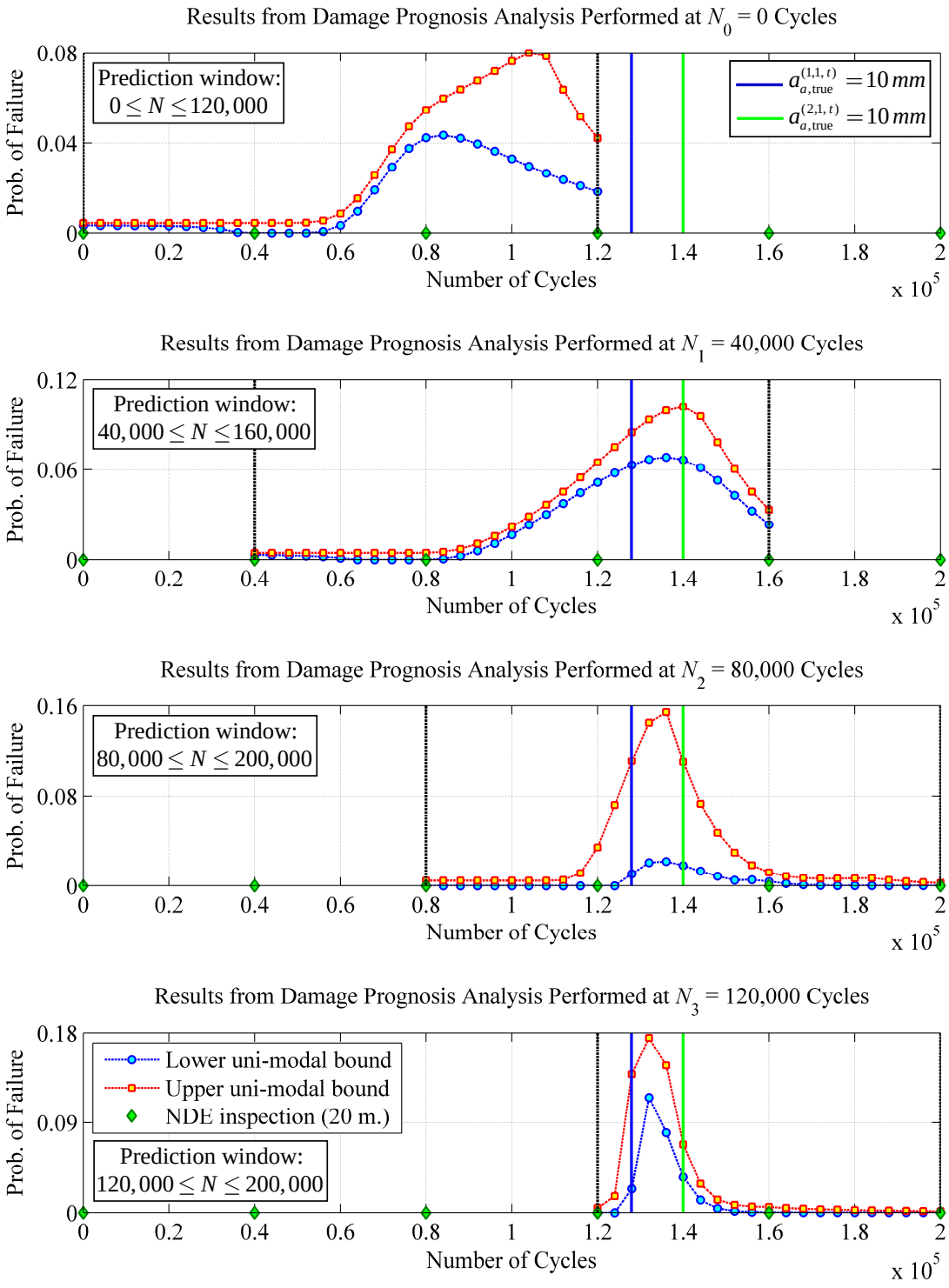

Figure 8.30: Time-dependent lower and upper uni-modal bounds for the probability of system failure, $P\left[\breve{F}_{\text{sys}}^{[p,q]}\right]$, as computed immediately after the first four NDE inspections using 20 NDE measurements (i.e., $n_{\text{MS}}^{(i,1,p)} = 20$ for $i = 1,2$ and $p = 0,1,...,4$).

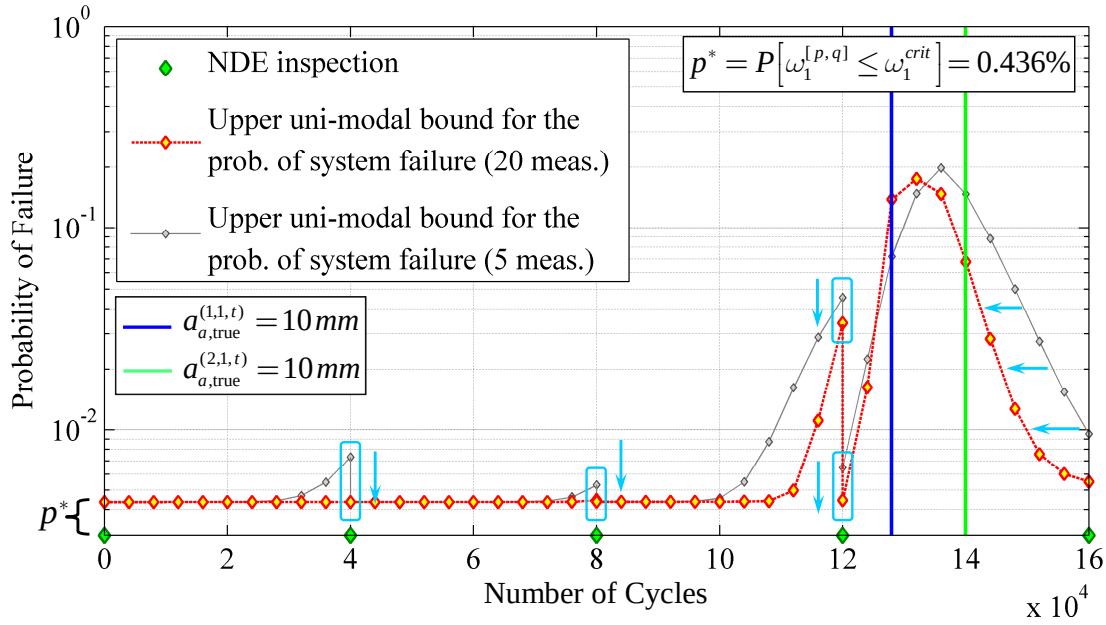

Figure 8.31: Comparison between two sets of recursive damage prognosis predictions for the upper uni-modal bound of the probability of system failure, $P\left[\breve{\mathrm{F}}_{\text{sys}}^{[p,q]}\right]$, $n_{\text{MS}}^{(i,1,p)} = 5$ vs. $n_{\text{MS}}^{(i,1,p)} = 20$ (with $i = 1,2$ and $p = 0,1,2,3$).

Also for this plot, the prediction for the upper uni-modal bound of $P\left[\breve{\mathrm{F}}_{\text{sys}}^{[p,q]}\right]$ between time N_p and time N_{p+1} (with $p = 0,1,2,3$) is obtained by making use of the NDE results up to N_p (i.e., $a_m^{(i,1,[0,p])}$, $i = 1,2$). The light-blue boxes and arrows in Figure 8.31 emphasize the benefits in the prediction results due to the larger number of NDE measurements. However, providing a larger number of NDE measurements does not help to reduce the value of $P\left[\breve{\mathrm{F}}_{\text{sys}}^{[p,q]}\right]$ in the range $0 \le N \le 120,000$ cycles, due to the fact that, in this range of load cycles, $P\left[\breve{\mathrm{F}}_{\text{sys}}^{[p,q]}\right]$ is essentially equal to the global component failure probability $P\left[\Omega_1^{[p,q]} \le \omega_1^{crit}\right] = 0.436\%$ (constant over the range $0 \le N \le 120,000$ cycles). It should be pointed out that the global component

probability of failure, $P\left[\Omega_1^{[p,q]} \leq \omega_1^{crit}\right]$, is dominated by the uncertainty of $\boldsymbol{\Theta}_{\text{mat}} = \Theta_{\text{mat}} = E_{11}^f$; an uncertainty quantified by the PDF shown in Figure 8.8 and never updated during this particular application of the proposed framework. This choice is dictated by the fact that the material parameter E_{11}^f is not involved in the postulated damage propagation law introduced in Equations (8.32) and (8.33), and therefore its PDF cannot be recursively updated through the proposed Bayesian inference scheme. If E_{11}^f was part of the damage propagation law, its PDF could be updated after each NDE inspection and, as a direct consequence, the uncertainty of $\Omega_1^{[p,q]}$ could be reduced and the prediction for $P\left[\Omega_1^{[p,q]} \leq \omega_1^{crit}\right]$ improved.

Finally, Figures 8.32 through 8.35 show the predictions for the lower and upper uni-modal bounds to the probability of false-call, $P\left[\breve{\mathcal{F}}_{\text{sys}}^{[p,q]}\right]$, corresponding to the three NDE inspection scenarios already discussed above. From Figures 8.32 through 8.34, it is observed that the increase in the number of NDE measurements collected at each inspection generally increases the tightness of the lower and upper bounds of the time-dependent probability of false-call, $P\left[\breve{\mathcal{F}}_{\text{sys}}^{[p,q]}\right]$. These results also indicate that as the number of NDE measurements increases and the prediction time moves closer to the time at which the true failure of the system occurs — i.e., the time identified by the vertical blue line at $N\left(a_{a,\text{true}}^{(1,1,t)}\right) = 127,900$ cycles — the prediction for $P\left[\breve{\mathcal{F}}_{\text{sys}}^{[p,q]}\right]$ tends to capture the ideal "*Dirac Delta*" proportional behavior that can be mathematically expressed as $P\left[\breve{\mathcal{F}}_{\text{sys}}^{[p,q]}\right] \propto \delta\left[N - N\left(a_{a,\text{true}}^{(1,1,t)}\right)\right]$.

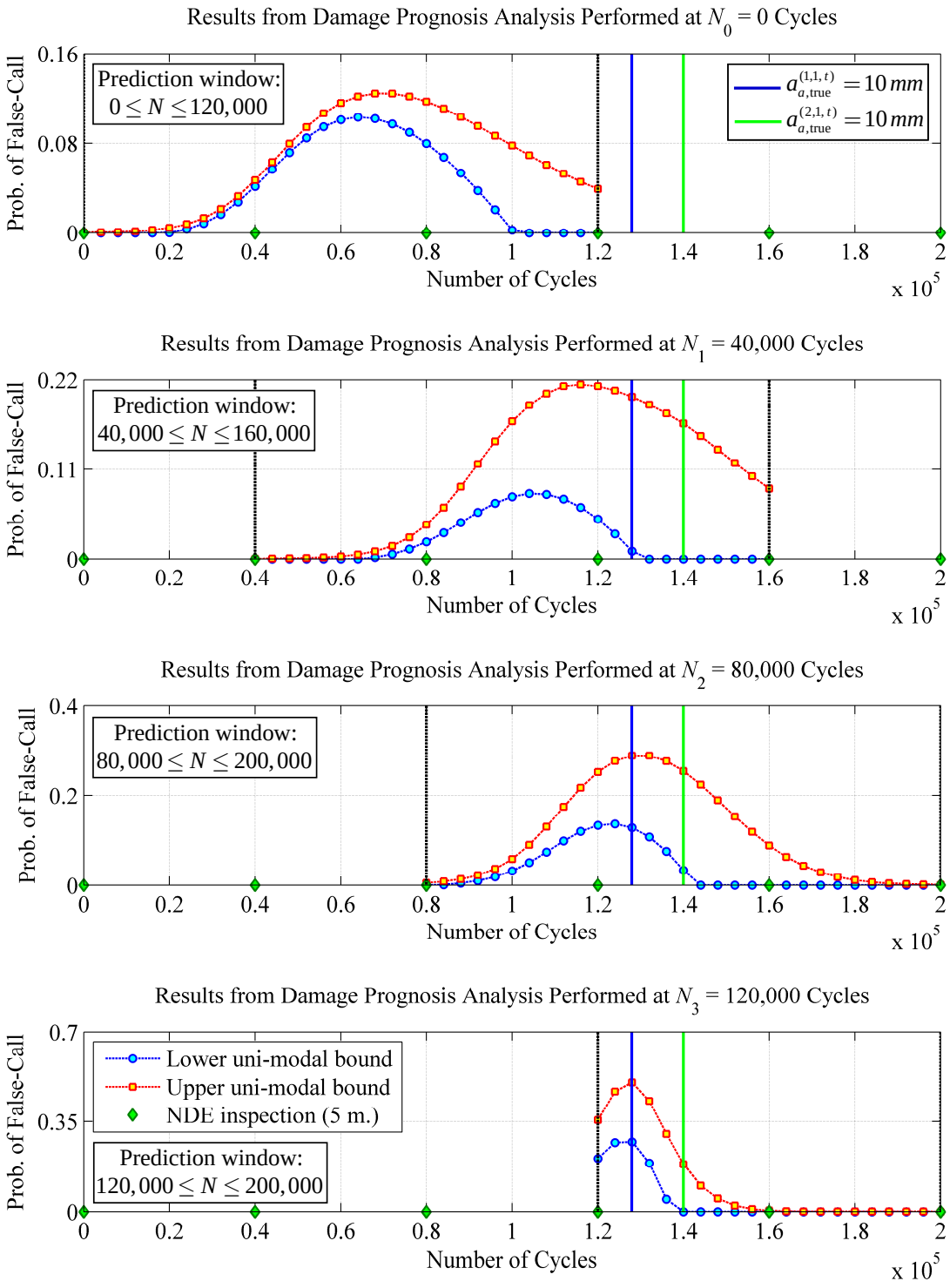

Figure 8.32: Time-dependent lower and upper uni-modal bounds for the probability of system failure, $P\left[\tilde{\mathcal{F}}_{\text{sys}}^{[p,q]}\right]$, as computed immediately after the first four NDE inspections using 5 NDE measurements (i.e., $n_{\text{MS}}^{(i,1,p)} = 5$ for $i = 1,2$ and $p = 0,1,...,4$).

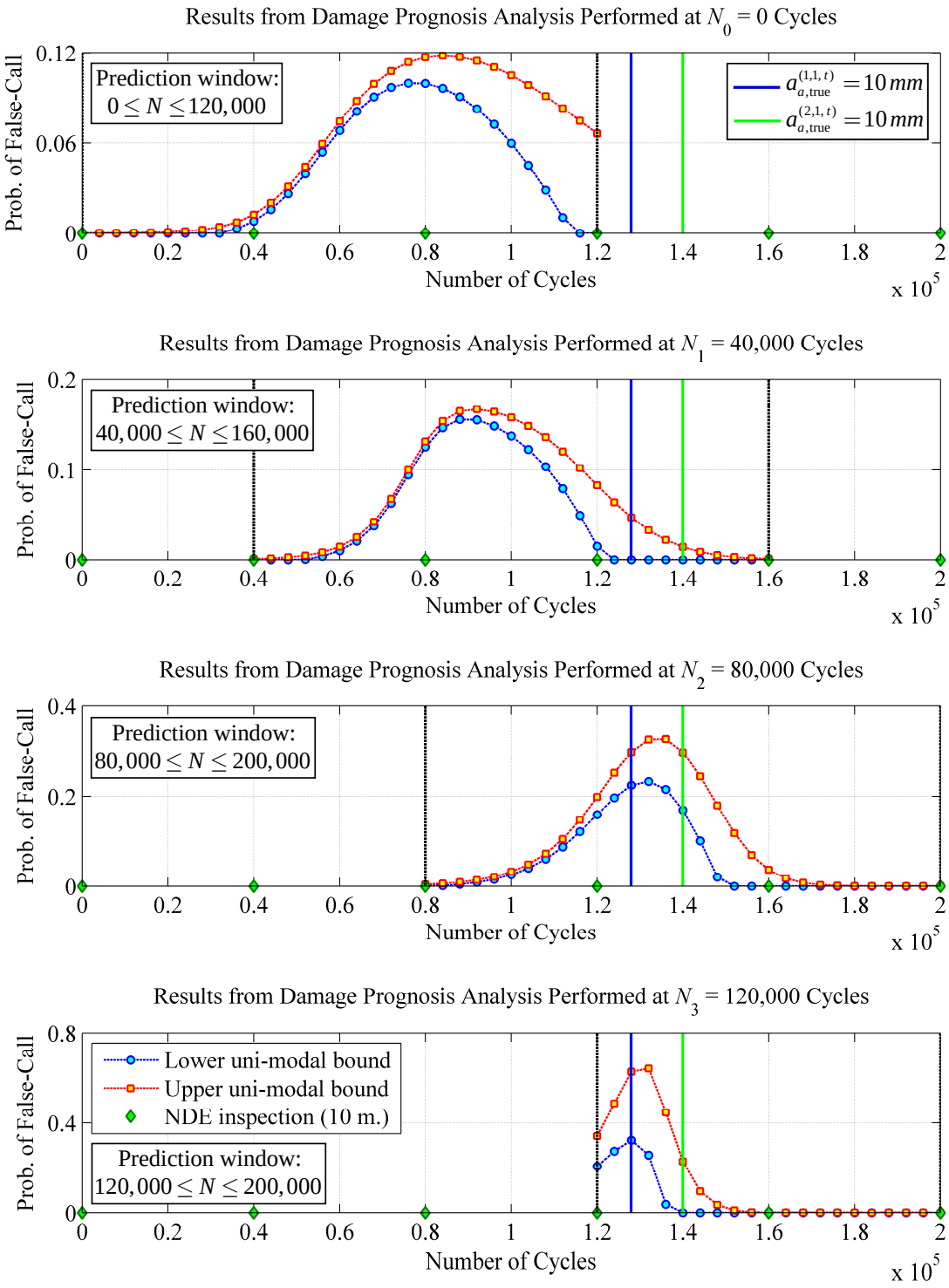

Figure 8.33: Time-dependent lower and upper uni-modal bounds for the probability of system failure, $P\left[\tilde{\mathcal{F}}_{\text{sys}}^{[p,q]}\right]$, as computed immediately after the first four NDE inspections using 10 NDE measurements (i.e., $n_{\text{MS}}^{(i,1,p)} = 10$ for $i = 1,2$ and $p = 0,1,...,4$).

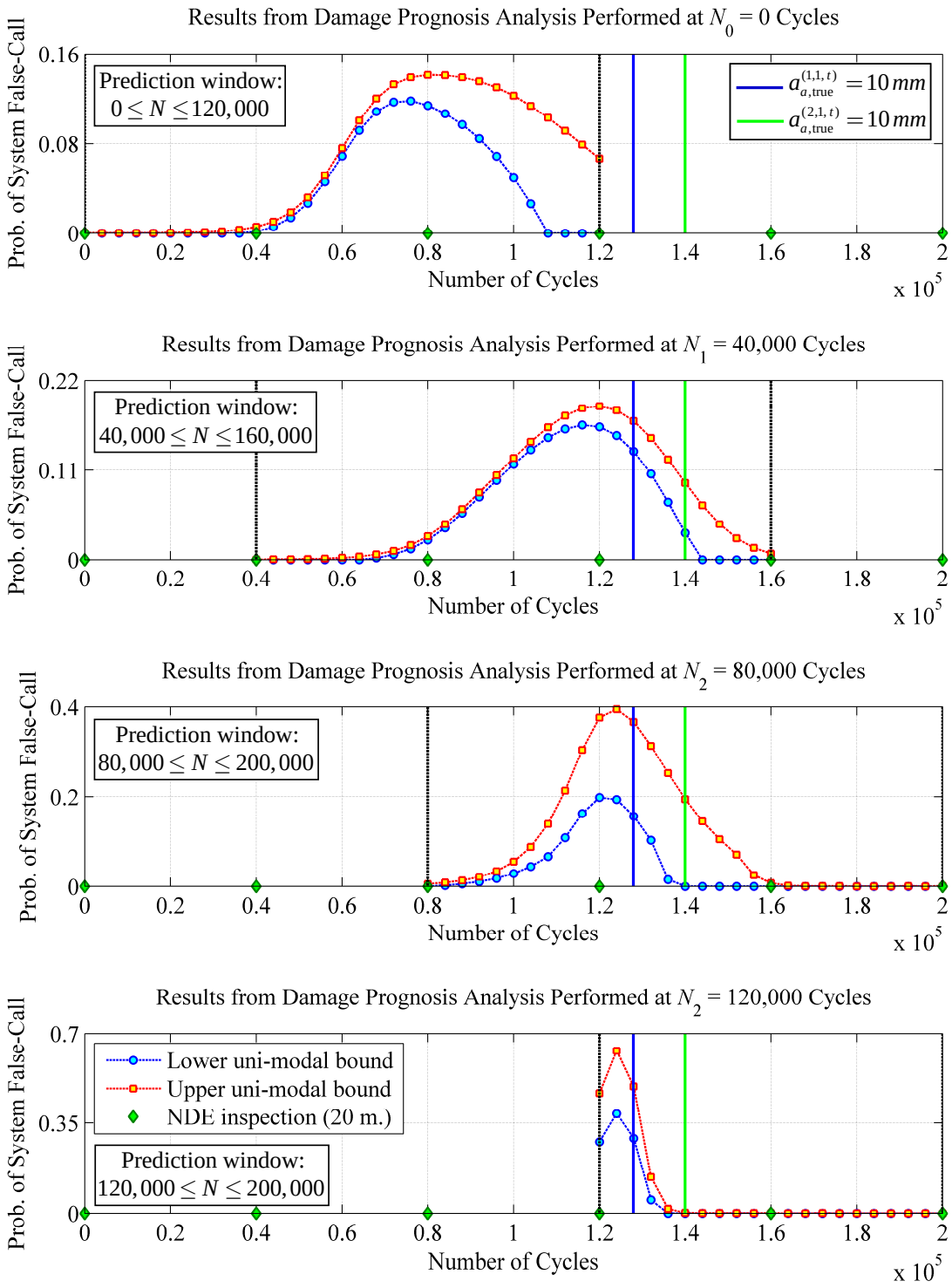

Figure 8.34: Time-dependent lower and upper uni-modal bounds for the probability of system failure, $P\left[\tilde{\mathcal{F}}_{\text{sys}}^{[p,q]}\right]$, as computed immediately after the first four NDE inspections using 20 NDE measurements (i.e., $n_{\text{MS}}^{(i,1,p)} = 20$ for $i = 1,2$ and $p = 0,1,...,4$).

Analogously to Figure 8.27 and Figure 8.31, the results for the time-dependent upper uni-modal bound of the probability of false-call $P\left[\breve{\mathcal{F}}_{\text{sys}}^{[p,q]}\right]$ (obtained from the damage prognosis analyses performed at $N_0 = 0$, $N_1 = 40,000$, $N_2 = 80,000$, and $N_3 = 120,000$ cycles) are combined together in the plot depicted in Figure 8.35. From the two cases shown in this figure (i.e., $n_{\text{MS}}^{(i,1,p)} = 5$ and $n_{\text{MS}}^{(i,1,p)} = 20$, for $i = 1,2$ and $p = 0,1,2,3$), the benefit provided by a larger number of NDE measurements is apparent (see light-blue boxes and arrows).

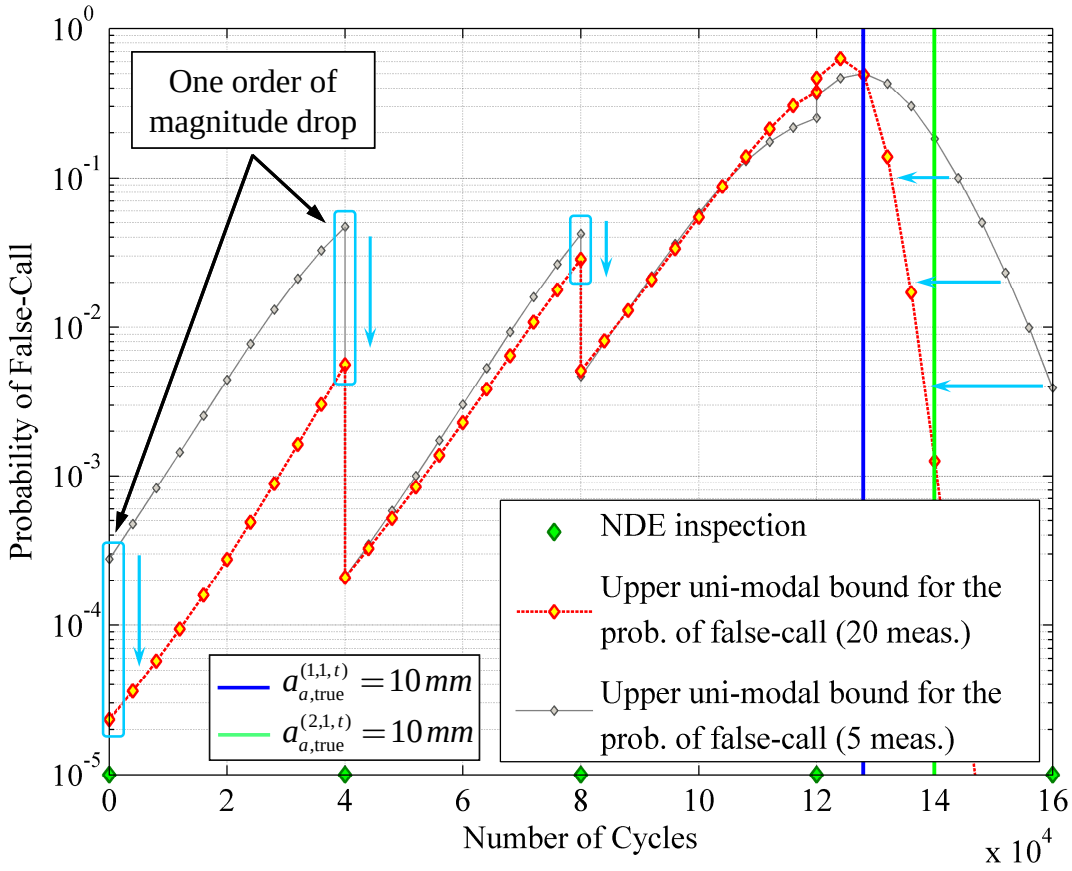

Figure 8.35: Comparison between two sets of recursive damage prognosis predictions for the upper uni-modal bound of the probability of false-call, $P\left[\breve{\mathcal{F}}_{\text{sys}}^{[p,q]}\right]$, $n_{\text{MS}}^{(i,1,p)} = 5$ vs. $n_{\text{MS}}^{(i,1,p)} = 20$ (with $i = 1,2$ and $p = 0,1,2,3$).

8.5. Additional considerations and parametric studies related to the proposed Bayesian inference scheme

In this section, the results from a selected set of comparative analyses and parametric studies is presented and discussed with the objective to demonstrate the versatility, consistency, and robustness of the proposed recursive Bayesian updating scheme. In more detail:

(i) Section 8.5.1 analyzes the influence of the NDE detection capability on the Bayesian updating results at $t_p \geq t_0$;

(ii) Section 8.5.2 discusses the influence of the initial prior distribution function assigned to $\mathbf{A}_{\mathbf{a}}^{0}$ on the Bayesian updating results at $t_p > t_0$;

(iii) Section 8.5.3 illustrates the influence of the number of NDE measurements, collected and processed at each NDE inspection opportunity, on the posterior PDF of $\mathbf{A}_{\mathbf{a}}^{p}$.

These comparative analyses and parametric studies use the benchmark structure and all the assumptions discussed in Section 8.4.

8.5.1. Influence of NDE detection and sizing capabilities on the Bayesian updating results obtained after each NDE inspection

In this first comparative analysis, two different NDE detection and sizing capability levels are considered: in the first case, the NDE technique is assumed to be capable of detecting and measuring a given damage extent (i.e., once damage is detected a measurement, quantifying the damage extent, is also provided); in the

second case, alternatively, it is assumed that the NDE technique is only capable of providing a binary outcome (i.e., either damage detected, *D*, or damage not detected, *ND*) without any additional measurement information (Kutner, 2004). The first case is representative of the so-called *continuous resolution NDE technique* (i.e., the best scenario), whereas the second case corresponds to the *least capable NDE technique*. Both cases have already been considered and discussed in Chapter 3 and Equations (3.22) and (3.23) show how the detection and measurement/sizing capabilities of a given NDE technique are affecting the mathematical form of the likelihood function to be used in the proposed recursive Bayesian updating scheme.

Figures 8.36 through 8.39 can be used to qualitatively analyze the effect of the NDE detection capability on the posterior PDFs of damage extents ($\mathbf{A}_{\mathrm{a}}^{p}$) and damage evolution model parameters ($\boldsymbol{\Theta}_{\mathrm{dam}}^{p}$), which are computed after each NDE inspection opportunity according to the proposed Bayesian updating scheme. The *POD* curve and the damage size measurement model used to perform this comparative study are shown in Figure 8.2 and Figure 8.3, respectively; the initial prior PDF (at $N_0 = 0$ cycles) is represented by the scaled Beta distribution reported in Figure 8.9; and the (assumed) underlying true damage evolution paths, at the two damage locations of the composite beam shown in Figure 8.7, are those paths reported in Figure 8.11. Furthermore, only the scenario in which $n_{\mathrm{MS}}^{(i,1,p)} = 10$ (with $i = 1,2$ and $p = 0,1,...,5$) is considered in this comparative study. Therefore, the results corresponding to the *continuous resolution NDE* (blue lines in Figures 8.36 through 8.39) are identical to those already derived in Section 8.4.2 (i.e., blue lines in Figures 8.16 through 8.19).

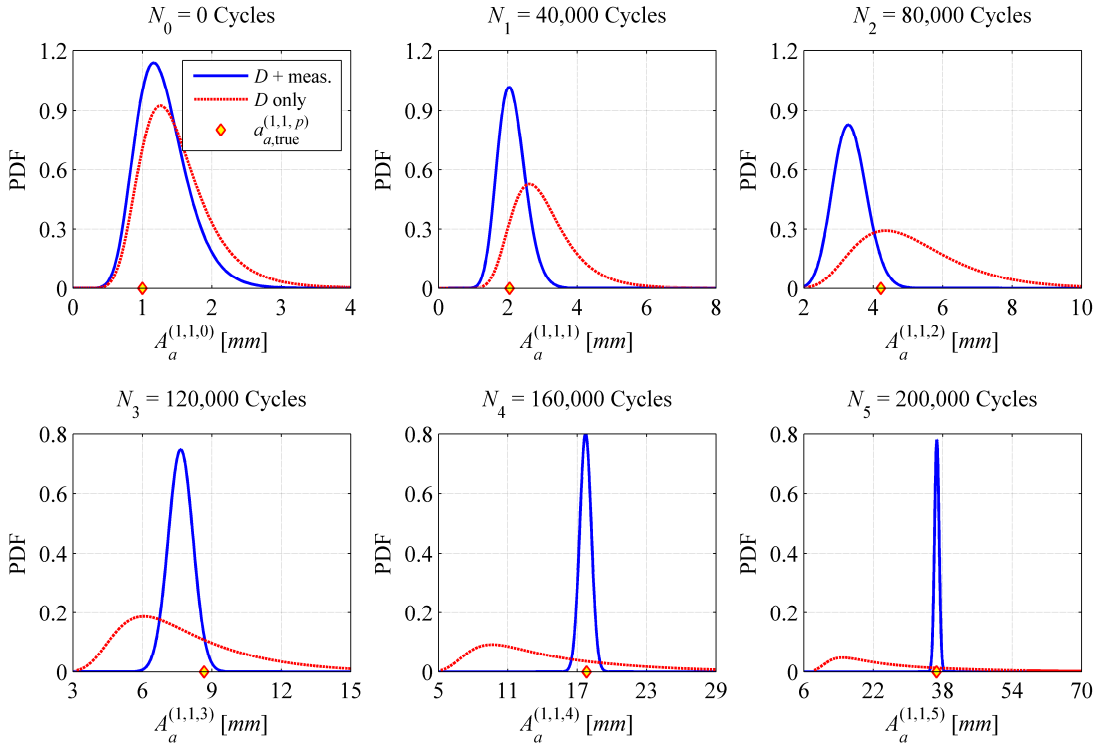

Figure 8.36: Posterior marginal PDF of debonding length $A_a^{(1,1,p)}$, at *damage location 1*, computed after each NDE inspection according to the proposed Bayesian inference scheme for the specific case in which $n_{\text{MS}}^{(i,1,p)} = 10$ (with $i = 1,2$ and $p = 0,1,...,5$). Blue lines: *continuous resolution NDE technique*. Red lines: *least capable NDE technique*

Figure 8.36 and Figure 8.37 show the posterior PDFs of $A_a^{(1,1,p)}$ and $A_a^{(2,1,p)}$ computed according to the two detection and sizing capability levels outlined earlier. Within the specific application example provided in this study, both figures represent a clear evidence of the benefits provided by the use of a *continuous resolution NDE technique*. The loss of accuracy in evaluating $f''_{A_a^{(1,1,p)}}\left(a_a^{(1,1,p)}\right)$ and $f''_{A_a^{(2,1,p)}}\left(a_a^{(2,1,p)}\right)$, associated with the use of the *least capable NDE technique*, becomes apparent already after the second NDE inspection opportunity, at $N_1 = 40,000$ load cycles.

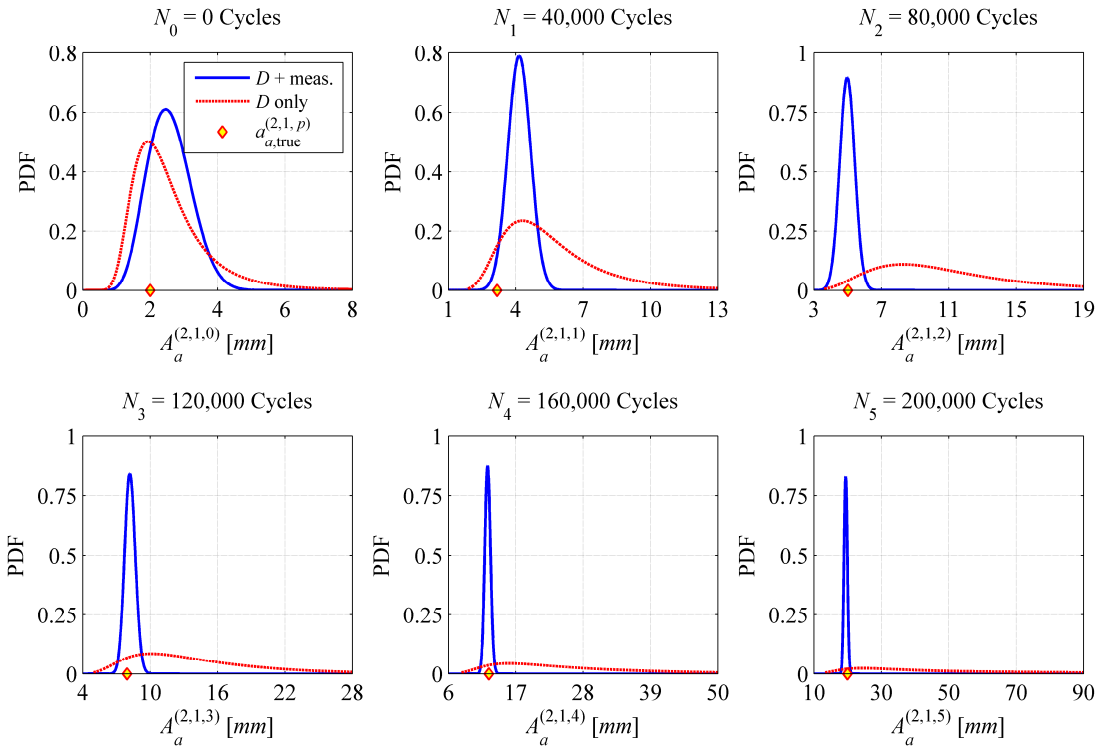

Figure 8.37: Posterior marginal PDF of debonding length $A_a^{(2,1,p)}$, at *damage location 2*, computed after each NDE inspection according to the proposed Bayesian inference scheme for the specific case in which $n_{\text{MS}}^{(i,1,p)} = 10$ (with $i = 1,2$ and $p = 0,1,...,5$). Blue lines: *continuous resolution NDE technique*. Red lines: *least capable NDE technique.*

On the other hand, Figure 8.38 and Figure 8.39 report the posterior marginal PDFs of $\Gamma^{(1,1,p)}$ and $\Gamma^{(2,1,p)}$ (at time t_p) computed according to the same two detection and sizing capability levels discussed above. By simple inspection of the results presented in these two figures, it is evident that the posterior PDFs $f''_{\Gamma^{(1,1,p)}}\left(\gamma_a^{(1,1,p)}\right)$ and $f''_{\Gamma^{(2,1,p)}}\left(\gamma_a^{(2,1,p)}\right)$, obtained by using the *least capable NDE technique*, are unable to converge towards the true (underlying) values of the postulated damage evolution parameters, $\gamma_{\text{true}}^{(1,1)} = 1.80\times10^{-5}$ and $\gamma_{\text{true}}^{(2,1)} = 1.15\times10^{-5}$, respectively.

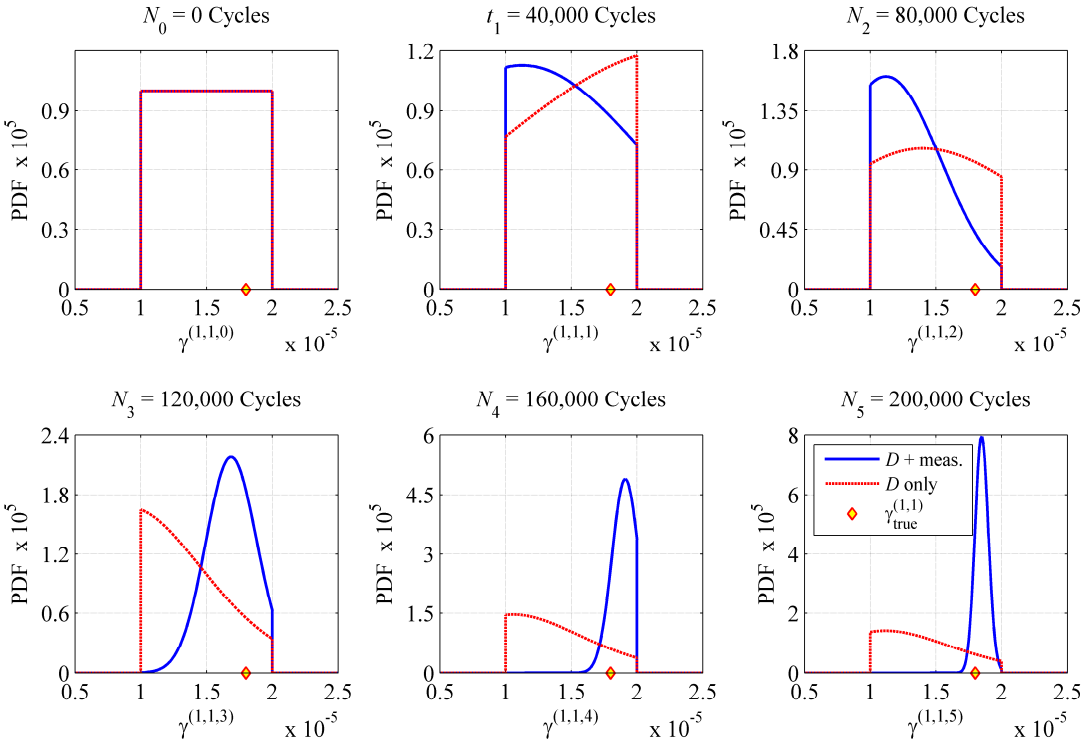

Figure 8.38: Posterior marginal PDF of postulated damage evolution parameter $\Gamma^{(1,1,p)}$, at *damage location 1*, computed after each NDE inspection according to the proposed Bayesian inference scheme when $n_{MS}^{(i,1,p)} = 10$ (with $i = 1,2$ and $p = 0,1,...,5$). Blue lines: *continuous resolution NDE technique*. Red lines: *least capable NDE technique*.

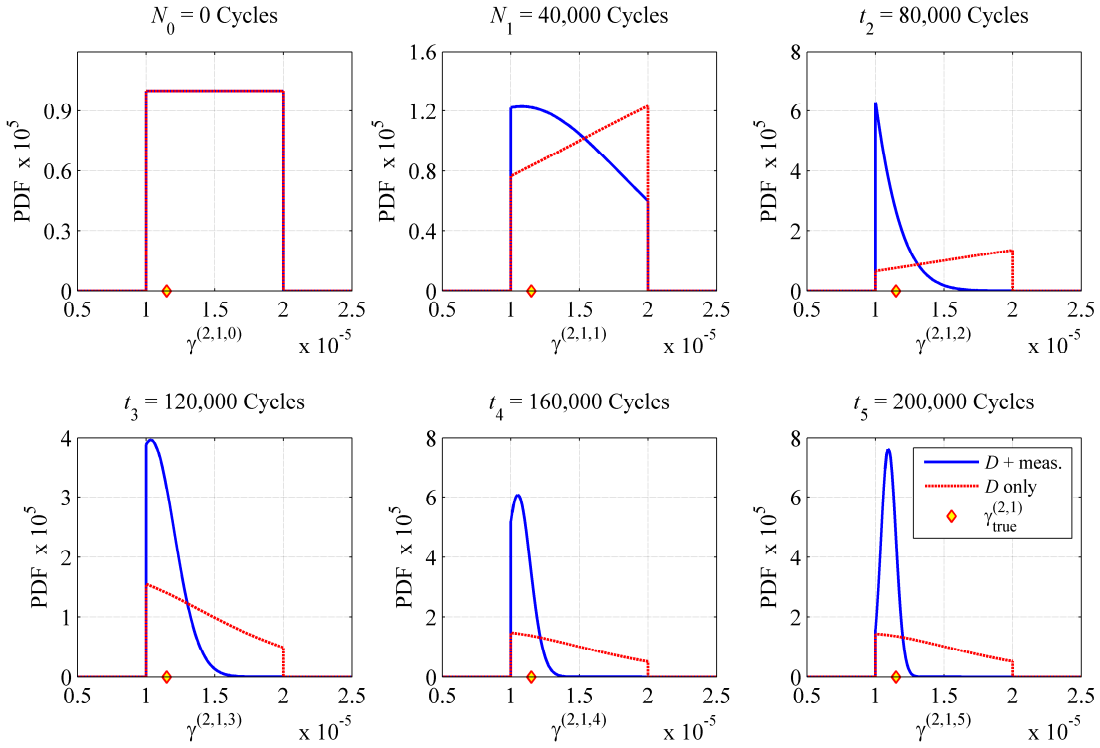

Figure 8.39: Posterior marginal PDF of postulated damage evolution parameter $\Gamma^{(2,1,p)}$, at *damage location 2*, computed after each NDE inspection according to the proposed Bayesian inference scheme when $n_{\text{MS}}^{(i,1,p)} = 10$ (with $i = 1,2$ and $p = 0,1,...,5$). Blue lines: *continuous resolution NDE technique*. Red lines: *least capable NDE technique*.

8.5.2. Influence of initial prior PDF assigned to $\mathbf{A}_{\mathbf{a}}^{\mathbf{0}}$ on the Bayesian updating results obtained after each NDE inspection

The proposed recursive Bayesian inference scheme, presented in Chapter 3 and briefly recalled in Section 8.3.1 in the present chapter, must be provided with an initial prior PDF for the damage size vector $\mathbf{A}_{\mathbf{a}}^{\mathbf{0}}$ at initial time t_0. This initial prior PDF, denoted as $f'_{\mathbf{A}_{\mathbf{a}}^{\mathbf{0}}}\left(\mathbf{a}_{\mathbf{a}}^{\mathbf{0}}\right)$ throughout this thesis, is normally chosen on the basis of engineering judgment (Lin *et al.*, 2000) and has a negligible influence on the posterior

joint conditional PDF of the damage size vector, $f''_{\mathbf{A}_a^p|\boldsymbol{\Theta}_{mat},\boldsymbol{\Theta}_{dam}^p}\left(\mathbf{a}_a^p\middle|\boldsymbol{\theta}_{mat},\boldsymbol{\theta}_{dam}^p\right)$, as well as on the posterior joint PDF of the damage evolution parameters, $f''_{\boldsymbol{\Theta}_{dam}^p}\left(\boldsymbol{\theta}_{dam}^p\right)$, when a large amount of NDE measurement data is available. Figures 8.40 through 8.43 intend to qualitatively demonstrate this statement by reanalyzing the same benchmark application discussed in Section 8.4. The *POD* curve and the damage size measurement model used to perform this comparative study are shown in Figure 8.2 and Figure 8.3, respectively; and the (assumed) underlying true damage evolution paths, at the two damage locations of the composite beam shown in Figure 8.7, are those reported in Figure 8.11. However, two different initial prior marginal PDFs of the s.i. debonding lengths $A_a^{(1,1,0)}$ and $A_a^{(2,1,0)}$ (at $N_0 = 0$ load cycles) are now assigned: the first one is represented by the scaled Beta distribution reported in Figure 8.9; the second one is given by a uniform distribution between $0\,mm$ and $50\,mm$ — i.e., $A_a^{(i,1,0)} \sim U(0,50)$, with $i = 1,2$. Furthermore, only the scenario in which $n_{MS}^{(i,1,p)} = 5$ (with $i = 1,2$ and $p = 0,1,...,5$) is considered in this second comparative study and therefore the results corresponding to the choice of a scaled Beta distribution as initial prior PDF for $A_a^{(1,1,0)}$ and $A_a^{(2,1,0)}$ (blue lines in Figures 8.36 through 8.39) are identical to those presented in Section 8.4.2 (i.e., red lines in Figures 8.16 through 8.19). If the influence of $f'_{\mathbf{A}_a^0}\left(\mathbf{a}_a^0\right)$ on $f''_{\mathbf{A}_a^p|\boldsymbol{\Theta}_{mat},\boldsymbol{\Theta}_{dam}^p}\left(\mathbf{a}_a^p\middle|\boldsymbol{\theta}_{mat},\boldsymbol{\theta}_{dam}^p\right)$ and $f''_{\boldsymbol{\Theta}_{dam}^p}\left(\boldsymbol{\theta}_{dam}^p\right)$ becomes negligible with $n_{MS}^{(i,1,p)} = 5$, it will be even more imperceptible when a larger number of NDE results (i.e., $n_{MS}^{(i,1,p)} = 10$ and $n_{MS}^{(i,1,p)} = 20$) is used.

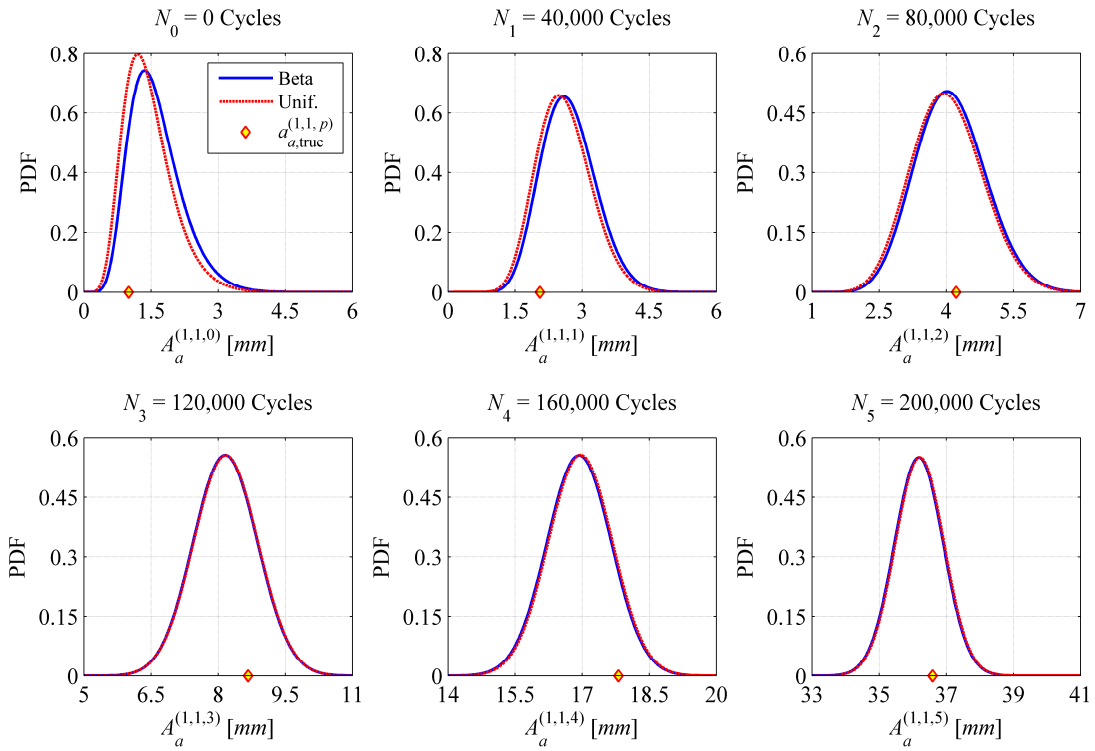

Figure 8.40: Posterior marginal PDF of debonding length $A_a^{(1,1,p)}$, at *damage location 1*, computed after each NDE inspection according to the proposed Bayesian inference scheme for the specific case in which $n_{\text{MS}}^{(i,1,p)} = 5$ (with $i = 1,2$ and $p = 0,1,...,5$). Blue lines: $f'_{\mathbf{A}_\mathbf{a}^\mathbf{0}}\left(\mathbf{a}_\mathbf{a}^\mathbf{0}\right)$ = Scaled Beta distribution. Red lines: $f'_{\mathbf{A}_\mathbf{a}^\mathbf{0}}\left(\mathbf{a}_\mathbf{a}^\mathbf{0}\right)$ = Uniform distribution.

For the particular case studied herein, the results presented in Figures 8.40 through 8.43 indicate that the effect of a different choice for $f'_{\mathbf{A}_\mathbf{a}^\mathbf{0}}\left(\mathbf{a}_\mathbf{a}^\mathbf{0}\right)$ becomes negligible — in the evaluation of both $f''_{\mathbf{A}_\mathbf{a}^p \mid \boldsymbol{\Theta}_{\text{mat}}, \boldsymbol{\Theta}_{\text{dam}}^p}\left(\mathbf{a}_\mathbf{a}^p \mid \boldsymbol{\theta}_{\text{mat}}, \boldsymbol{\theta}_{\text{dam}}^p\right)$ and $f''_{\boldsymbol{\Theta}_{\text{dam}}^p}\left(\boldsymbol{\theta}_{\text{dam}}^p\right)$ — immediately after the third (at $N_2 = 80,000$ load cycles) and fifth (at $N_4 = 160,000$ load cycles) NDE inspections, respectively. Similar results and conclusions can be drawn when different PDF models for $f'_{\boldsymbol{\Theta}_{\text{dam}}^0}\left(\boldsymbol{\theta}_{\text{dam}}^0\right)$ are assigned.

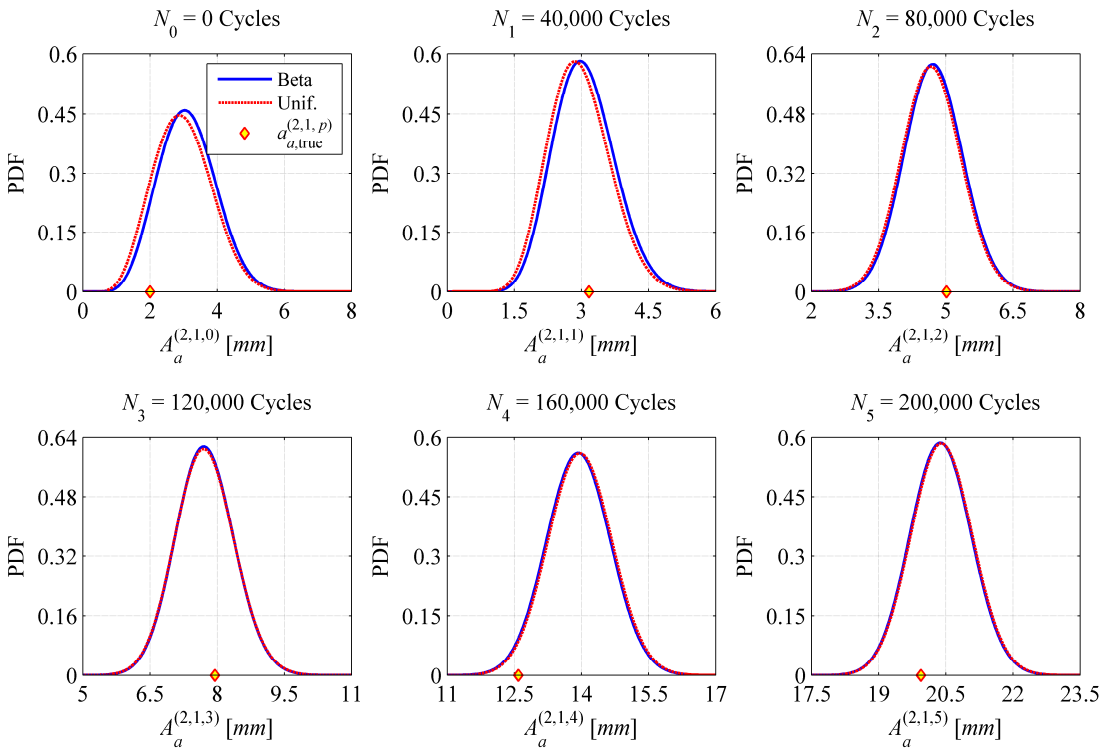

Figure 8.41: Posterior marginal PDF of debonding length $A_a^{(2,1,p)}$, at *damage location 2*, computed after each NDE inspection according to the proposed Bayesian inference scheme for the specific case in which $n_{\text{MS}}^{(i,1,p)} = 5$ (with $i = 1, 2$ and $p = 0, 1, ..., 5$). Blue lines: $f'_{\mathbf{A}_\mathbf{a}^0}\left(\mathbf{a}_\mathbf{a}^0\right)$ = Scaled Beta distribution. Red lines: $f'_{\mathbf{A}_\mathbf{a}^0}\left(\mathbf{a}_\mathbf{a}^0\right)$ = Uniform distribution.

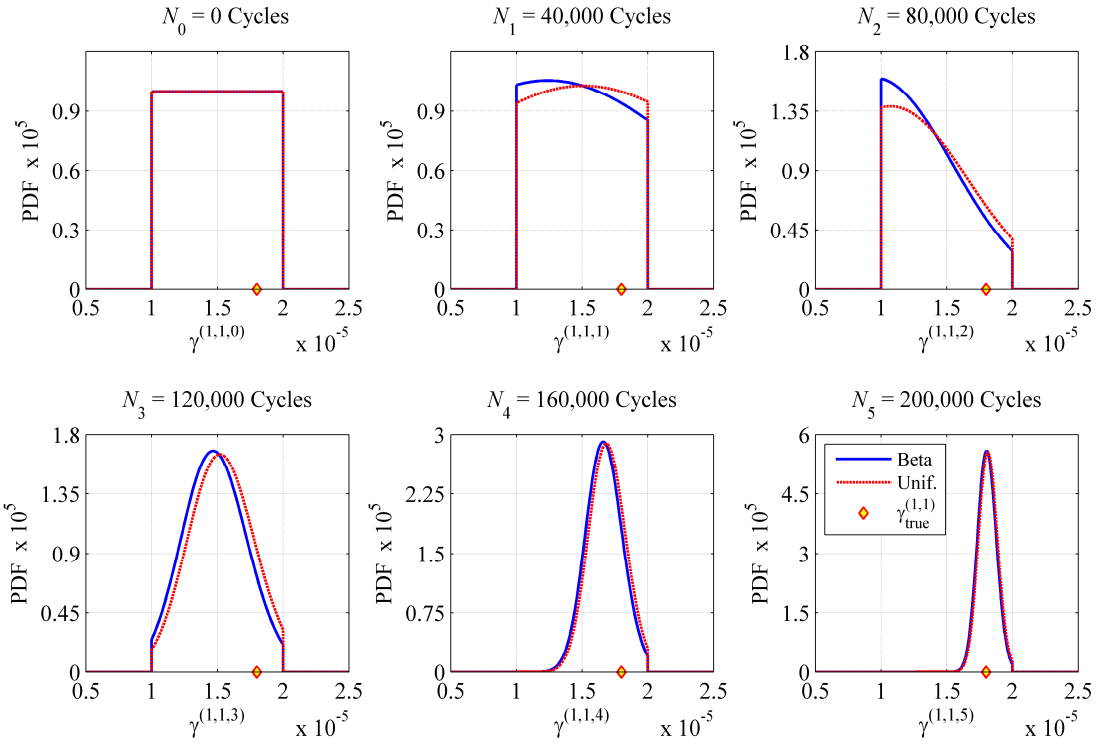

Figure 8.42: Posterior marginal PDF of postulated damage evolution parameter $\Gamma^{(1,1,p)}$, at *damage location 1*, computed after each NDE inspection according to the proposed Bayesian inference scheme when $n_{\text{MS}}^{(i,1,p)} = 5$ (with $i = 1,2$ and $p = 0,1,...,5$). Blue lines: $f'_{\mathbf{A}_\mathbf{a}^0}\left(\mathbf{a}_\mathbf{a}^0\right)$ = Scaled Beta distribution. Red lines: $f'_{\mathbf{A}_\mathbf{a}^0}\left(\mathbf{a}_\mathbf{a}^0\right)$ = Uniform distribution.

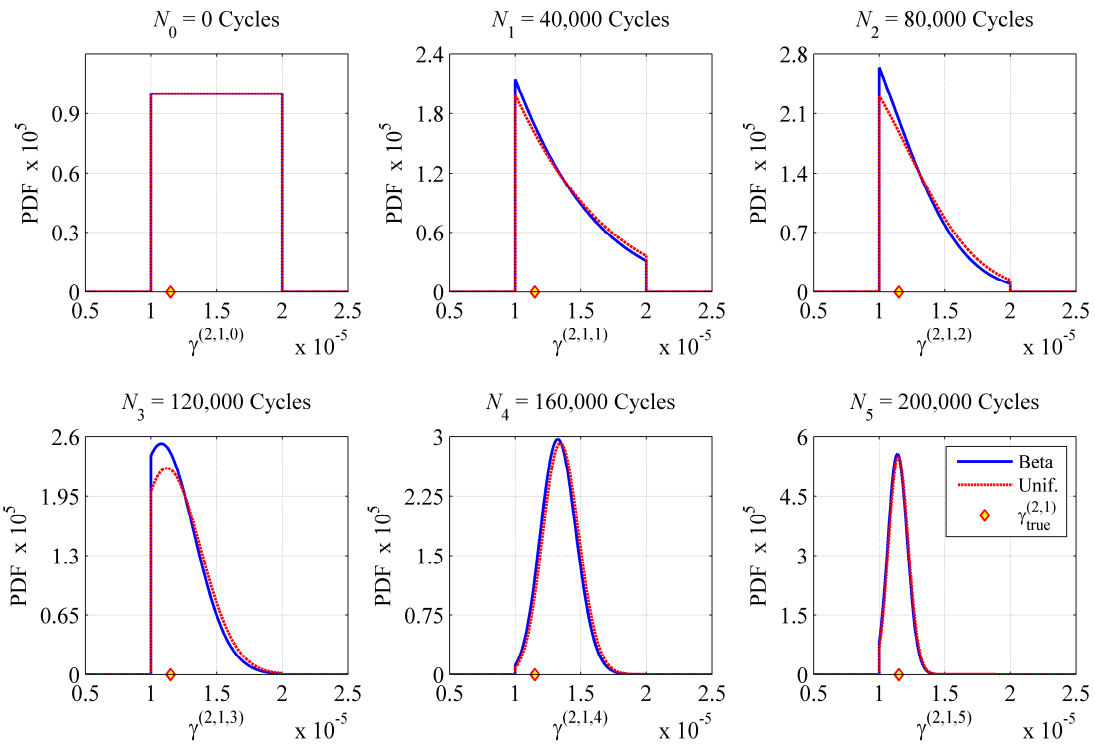

Figure 8.43: Posterior marginal PDF of postulated damage evolution parameter $\Gamma^{(2,1,p)}$, at *damage location 2*, computed after each NDE inspection according to the proposed Bayesian inference scheme when $n_{\text{MS}}^{(i,1,p)} = 5$ (with $i = 1,2$ and $p = 0,1,...,5$). Blue lines: $f'_{\mathbf{A}_\mathbf{a}^\mathbf{0}}\left(\mathbf{a}_\mathbf{a}^\mathbf{0}\right)$ = Scaled Beta distribution. Red lines: $f'_{\mathbf{A}_\mathbf{a}^\mathbf{0}}\left(\mathbf{a}_\mathbf{a}^\mathbf{0}\right)$ = Uniform distribution.

8.5.3. Influence of number of NDE measurements and random measurement error on the variance of the posterior PDF of $\mathbf{A}_\mathbf{a}^p$

This section presents the results of a parametric study conducted on the same benchmark application discussed in Section 8.4 and aims at qualitatively assessing the influence of both, (i) the number of NDE measurements and (ii) the standard deviation of the random measurement error, on the variance of the posterior PDFs of the debonding lengths at the two damage locations. The *POD* curve and the damage size

measurement model used to perform this parametric study are those shown in Figure 8.2 and Figure 8.3, respectively; the initial prior PDF (at $N_0 = 0$ cycles) is represented by the scaled Beta distribution reported in Figure 8.9; and the (assumed) underlying true damage evolution paths, at the two damage locations of the composite beam shown in Figure 8.7, are those reported in Figure 8.11. Two different series of NDE inspection opportunities are assumed herein: in the first case, a series of six NDE inspections, evenly spaced every 40,000 cycles, is considered (i.e., $p = 0,1,...,5$); in the second case, a series of eleven NDE inspections, evenly spaced every 20,000 cycles (i.e., $p = 0,1,...,10$), is used in the proposed recursive Bayesian updating scheme . In each of these two cases, three different scenarios for the number of NDE measurements collected at each NDE inspection opportunity are also considered: $n_{\mathrm{MS}}^{(i,1,p)} = 5, 10, 20$ (with $i = 1,2$ and $p = 0,1,...,5$) in the first case where six NDE inspections are involved, while $n_{\mathrm{MS}}^{(i,1,p)} = 5, 10, 20$ (with $i = 1,2$ and $p = 0,1,...,10$) in the second one. Furthermore, within each of these three scenarios, three different values for the standard deviation of the random measurement error $\varepsilon_{ij} \sim N\left(0, \sigma_{\varepsilon_{ij}}\right)$, introduced in Equation (8.5), are taken into account: $\sigma_{\varepsilon_{ij}} = \sigma_{\varepsilon} = 2.0, 4.0,$ and $8.0\, mm$).

In the specific benchmark application discussed in Section 8.4, the actual debonding lengths, $A_a^{(1,1,p)}$ and $A_a^{(2,1,p)}$ ($p = 0,1,...$), are independent random variables; a direct consequence of (i) the assumed statistically independent prior PDFs for $A_a^{(1,1,0)}$ and $A_a^{(2,1,0)}$ at initial time t_0 depicted in Figure 8.9, and (ii) the uncoupled postulated damage propagation laws, shown in Equations (8.32) and (8.33), governing

the debonding propagation at the two damage locations. These considerations allow for rewriting the Bayesian updating equation for $A_a^{(1,1,p)}$ and $A_a^{(2,1,p)}$ as follows:

$$f''_{A_a^{(i,1,p)}\left|\Gamma^{(i,1,p)}\right.}\left(a_a^{(i,1,p)}\left|\gamma^{(i,1,p)}\right.\right) \propto \left[\prod_{k=1}^{n_{\mathrm{MS}}^{(i,1,p)}} L\left(a_a^{(i,1,p)}\left|a_{m_k}^{(i,1,p)}\right.\right)\right] f'_{A_a^{(i,1,p)}\left|\Gamma^{(i,1,p)}\right.}\left(a_a^{(i,1,p)}\left|\gamma^{(i,1,p)}\right.\right) \qquad \left(i=1,2\right) \tag{8.53}$$

where $f'_{A_a^{(i,1,p)}\left|\Gamma^{(i,1,p)}\right.}\left(a_a^{(i,1,p)}\left|\gamma^{(i,1,p)}\right.\right)$ and $f''_{A_a^{(i,1,p)}\left|\Gamma^{(i,1,p)}\right.}\left(a_a^{(i,1,p)}\left|\gamma^{(i,1,p)}\right.\right)$ represent the prior and posterior conditional PDFs of $A_a^{(i,1,p)}$ (with $i=1,2$), respectively; and $L\left(a_a^{(i,1,p)}\left|a_{m_k}^{(i,1,p)}\right.\right)$ denotes the likelihood function of $a_a^{(i,1,p)}$ given $A_{m_k}^{(i,1,p)}=a_{m_k}^{(i,1,p)}$, whose mathematical expression is shown in Equation (3.22) in Chapter 3. It is thus of interest to evaluate the effect of (i) the number of NDE measurements, $n_{\mathrm{MS}}^{(i,1,p)}$, used in the likelihood function of Equation (8.53), and (ii) the standard deviation, $\sigma_{\varepsilon_{ij}}=\sigma_\varepsilon$, of the random measurement error introduced in Equation (8.5), on the standard deviation of the posterior PDF $f''_{A_a^{(i,1,p)}\left|\Gamma^{(i,1,p)}\right.}\left(a_a^{(i,1,p)}\left|\gamma^{(i,1,p)}\right.\right)$, herein denoted as $\sigma_{post}\left(A_a^{(i,j,p)}, n_{\mathrm{MS}}^{(i,1,p)}, \sigma_\varepsilon\right)$. This effect is analyzed by computing the std ratios, $\sigma_{ratio}^{10,5}\left(\sigma_\varepsilon\right)$ and $\sigma_{ratio}^{20,5}\left(\sigma_\varepsilon\right)$, expressed in Equations (8.54) and (8.55) below, after each NDE inspection.

$$\sigma_{ratio}^{10,5}\left(\sigma_\varepsilon\right)=\frac{\sigma_{post}\left(A_a^{(i,1,p)}, n_{\mathrm{MS}}^{(i,1,p)}=10, \sigma_\varepsilon\right)}{\sigma_{post}\left(A_a^{(i,1,p)}, n_{\mathrm{MS}}^{(i,1,p)}=5, \sigma_\varepsilon\right)} \qquad \left(\sigma_\varepsilon=2.0, 4.0, 8.0\ mm\right) \tag{8.54}$$

$$\sigma_{ratio}^{20,5}\left(\sigma_\varepsilon\right)=\frac{\sigma_{post}\left(A_a^{(i,1,p)}, n_{\mathrm{MS}}^{(i,1,p)}=20, \sigma_\varepsilon\right)}{\sigma_{post}\left(A_a^{(i,1,p)}, n_{\mathrm{MS}}^{(i,1,p)}=5, \sigma_\varepsilon\right)} \qquad \left(\sigma_\varepsilon=2.0, 4.0, 8.0\ mm\right) \tag{8.55}$$

The results obtained through the application of these two equations are reported in Figure 8.44 (for the case of six NDE inspections, i.e., $p = 0,1,...,5$) and Figure 8.45 (for the case of eleven NDE inspections, i.e., $p = 0,1,...,10$). Both figures show that the quantity $\sigma_{ratio}^{10,5}(\sigma_\varepsilon)$ tends to converge to $1/\sqrt{2}$ while the ration $\sigma_{ratio}^{20,5}(\sigma_\varepsilon)$ approaches $1/2$. Furthermore, the convergence towards these constant values is faster for the smallest σ_ε considered (i.e., $\sigma_\varepsilon = 2.0$). This behavior can be explained by recalling the closed-form solution for the variance of the posterior PDF in the classical conjugate Gaussian univariate case (Duda *et al.*, 2001). Adapting this closed-form solution to this specific case study, when the prior PDF of $A_a^{(i,1,p)}$ (with $i = 1,2$) is represented by a Gaussian distribution, with variance denoted by $\sigma_{prior}^2\left(A_a^{(i,1,p)}\right)$, and the likelihood function, $L\left(a_a^{(i,1,p)} \middle| a_{m_k}^{(i,1,p)}\right)$ in Equation (8.53), is also provided by a Gaussian distribution, then, it can be shown (Duda *et al.*, 2001) that the posterior PDF of $A_a^{(i,1,p)}$ is Gaussian and its variance can be expressed as

$$\sigma_{post}^2\left(A_a^{(i,1,p)}, n_{\mathrm{MS}}^{(i,1,p)}, \sigma_\varepsilon\right) = \frac{\sigma_{prior}^2\left(A_a^{(i,1,p)}\right)\cdot\sigma_\varepsilon^2}{n_{\mathrm{MS}}^{(i,1,p)}\sigma_{prior}^2\left(A_a^{(i,1,p)}\right)+\sigma_\varepsilon^2} \tag{8.56}$$

For a large number of NDE measurements (i.e., a large value for $n_{\mathrm{MS}}^{(i,1,p)}$), the above equation can be approximated as

$$\sigma_{post}^2\left(A_a^{(i,1,p)}, n_{\mathrm{MS}}^{(i,1,p)}, \sigma_\varepsilon\right) \approx \frac{\sigma_{prior}^2\left(A_a^{(i,1,p)}\right)\cdot\sigma_\varepsilon^2}{n_{\mathrm{MS}}^{(i,1,p)}\sigma_{prior}^2\left(A_a^{(i,1,p)}\right)} = \frac{\sigma_\varepsilon^2}{n_{\mathrm{MS}}^{(i,1,p)}} \tag{8.57}$$

and, as a direct consequence, the following relationships for $\sigma_{ratio}^{10,5}(\sigma_\varepsilon)$ and $\sigma_{ratio}^{20,5}(\sigma_\varepsilon)$ can be derived:

$$\frac{\sigma_{post}^2\left(A_a^{(i,1,p)}, n_{\mathrm{MS}}^{(i,1,p)}=10\right)}{\sigma_{post}^2\left(A_a^{(i,1,p)}, n_{\mathrm{MS}}^{(i,1,p)}=5\right)}=\frac{1}{2} \quad \Rightarrow \quad \sigma_{ratio}^{10,5}(\sigma_\varepsilon)=\frac{\sigma_{post}\left(A_a^{(i,1,p)}, n_{\mathrm{MS}}^{(i,1,p)}=10\right)}{\sigma_{post}\left(A_a^{(i,1,p)}, n_{\mathrm{MS}}^{(i,1,p)}=5\right)}=\frac{1}{\sqrt{2}} \tag{8.58}$$

$$\frac{\sigma_{post}^2\left(A_a^{(i,1,p)}, n_{\mathrm{MS}}^{(i,1,p)}=20\right)}{\sigma_{post}^2\left(A_a^{(i,1,p)}, n_{\mathrm{MS}}^{(i,1,p)}=5\right)}=\frac{1}{4} \quad \Rightarrow \quad \sigma_{ratio}^{20,5}(\sigma_\varepsilon)=\frac{\sigma_{post}\left(A_a^{(i,1,p)}, n_{\mathrm{MS}}^{(i,1,p)}=20\right)}{\sigma_{post}\left(A_a^{(i,1,p)}, n_{\mathrm{MS}}^{(i,1,p)}=5\right)}=\frac{1}{2} \tag{8.59}$$

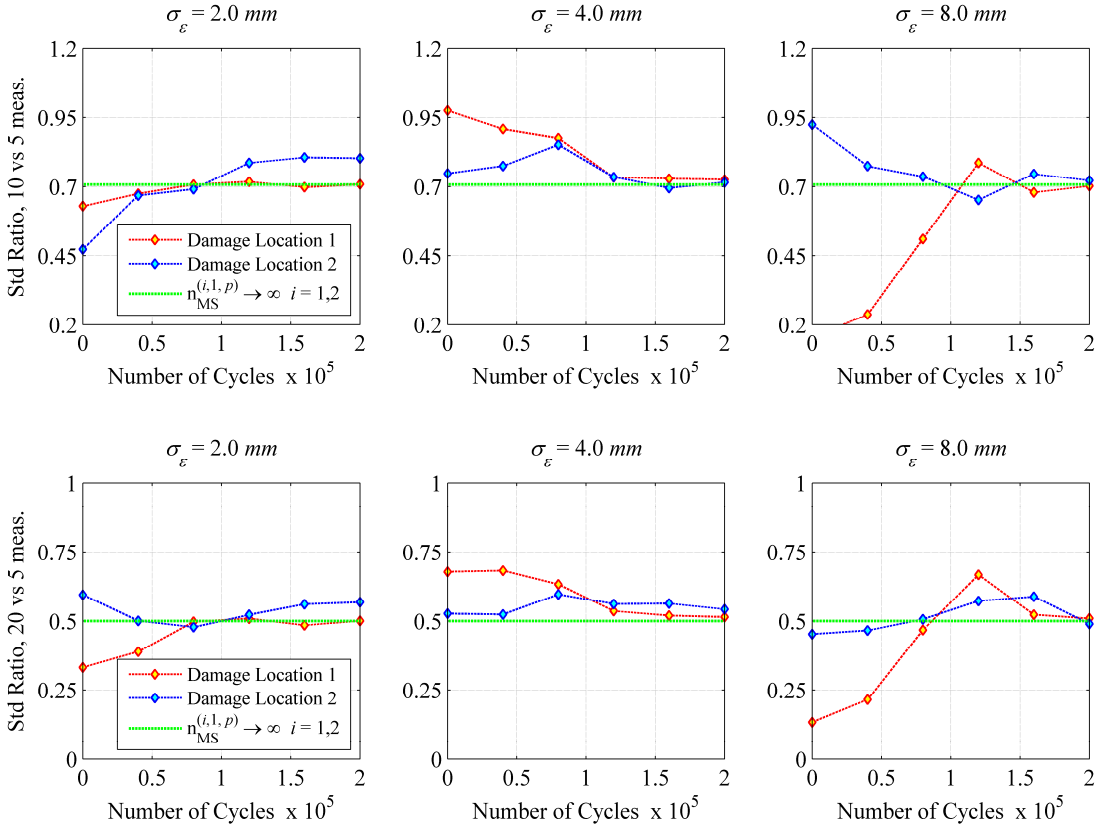

Figure 8.44: Ratio between the standard deviation of the posterior marginal PDFs of $A_a^{(i,j,p)}$ and $A_a^{(i,j,p)}$, as defined in Equations (8.58) and (8.59), evaluated after each of the (assumed) six NDE inspections for three different values of the standard deviation of the random measurement error (i.e., $\sigma_\varepsilon = 2.0, 4.0,$ and $8.0\ mm$).

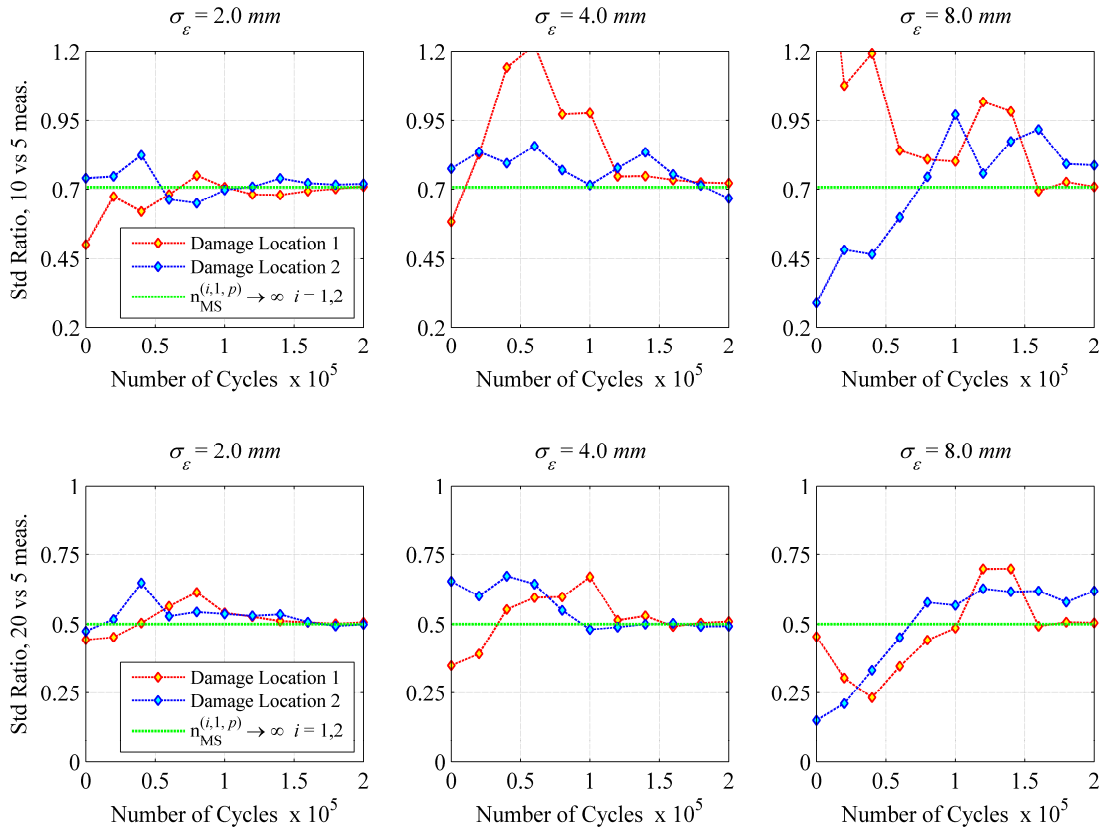

Figure 8.45: Ratio between the standard deviation of the posterior marginal PDFs of $A_a^{(i,j,p)}$ and $A_a^{(i,j,p)}$, as defined in Equations (8.58) and (8.59), evaluated after each of the (assumed) eleven NDE inspections for three different values of the standard deviation of the random measurement error (i.e., $\sigma_\varepsilon = 2.0, 4.0,$ and $8.0\ mm$).

8.6. Additional insight on the derivation of lower and upper uni-modal bounds for the probability of system failure, $P\left[\breve{F}_{sys}^{[p,q]}\right]$

In Section 7.5.2 in Chapter 7 and in Section 8.3.5 of this chapter, the alternative failure event, $\breve{F}_{sys}^{[p,q]}$, used to characterize the overall system failure at time $t_p^q = t_p + q\Delta\tau$, was defined as

$$\breve{\mathrm{F}}_{\mathrm{sys}}^{[p,q]} \triangleq \mathrm{F}_{\mathrm{sys}}^{[p,q]} \cap \left[\bigcap_{i=1}^{n_{\mathrm{L}}^{[0,p]}} \left(\bigcap_{j=1}^{n_{\mathrm{DM}}^{(i,[0,p])}} A_m^{(i,j,[p,q])} < a_c^{ij} \right) \right] \tag{8.60}$$

and an expression for lower and upper uni-modal bounds of the probability associated with this failure event, $P\left[\breve{\mathrm{F}}_{\mathrm{sys}}^{[p,q]}\right]$, was provided in Equation (7.38) in Chapter 7. However, by combining the reliability components of Equation (8.60) in different ways, different expressions for lower and upper uni-modal bounds of $P\left[\breve{\mathrm{F}}_{\mathrm{sys}}^{[p,q]}\right]$ are obtained. For instance, lower and upper uni-modal bounds for the probability associated with the first failure event in Equation (8.60), $\mathrm{F}_{\mathrm{sys}}^{[p,q]}$, were derived in Equation (7.34) in Chapter 7. These bounds can be expressed as

$$P_{low}\left[\mathrm{F}_{\mathrm{sys}}^{[p,q]}\right] \leq P\left[\mathrm{F}_{\mathrm{sys}}^{[p,q]}\right] \leq P_{up}\left[\mathrm{F}_{\mathrm{sys}}^{[p,q]}\right] \tag{8.61}$$

where $P_{low}\left[\mathrm{F}_{\mathrm{sys}}^{[p,q]}\right]$ and $P_{up}\left[\mathrm{F}_{\mathrm{sys}}^{[p,q]}\right]$ are mathematically written as shown below:

$$P_{low}\left[\mathrm{F}_{\mathrm{sys}}^{[p,q]}\right] = \max_{i,j,r}\left(P\left[\mathrm{F}_{\mathrm{L},ij}^{[p,q]}\right], P\left[\mathrm{F}_{\mathrm{G},r}^{[p,q]}\right]\right) \tag{8.62}$$

$$P_{up}\left[\mathrm{F}_{\mathrm{sys}}^{[p,q]}\right] = \min\left(1, \left[\sum_{i=1}^{n_{\mathrm{L}}^{[0,p]}} \sum_{j=1}^{n_{\mathrm{DM}}^{(i,[0,p])}} P\left[\mathrm{F}_{\mathrm{L},ij}^{[p,q]}\right] + \sum_{r=1}^{n_{\mathrm{G}}} P\left[\mathrm{F}_{\mathrm{G},r}^{[p,q]}\right]\right]\right) \tag{8.63}$$

Hence, Equation (8.60) can now be viewed as a parallel system with $n_{\mathrm{A}}^{p}+1$ reliability components, and n_{A}^{p} defined as $n_{\mathrm{A}}^{p} = \sum_{i=1}^{n_{\mathrm{L}}^{[0,p]}} n_{\mathrm{DM}}^{(i,[0,p])}$. Lower and upper uni-modal bounds of the probability associated with the failure event, $\breve{\mathrm{F}}_{\mathrm{sys}}^{[p,q]}$, of this parallel system can then be specified as (Fréchet, 1935)

$$P\left[\breve{\mathrm{F}}_{\mathrm{sys}}^{[p,q]}\right] \geq \max\left(0\,,\; P_{low}\left[\mathrm{F}_{\mathrm{sys}}^{[p,q]}\right] + \sum_{i=1}^{n_{\mathrm{L}}^{[0,p]}} \sum_{j=1}^{n_{\mathrm{DM}}^{(i,[0,p])}} P\left[A_m^{(i,j,[p,q])} < a_c^{ij}\right] - n_{\mathrm{A}}^{p}\right) \tag{8.64}$$

$$P\left[\breve{\mathrm{F}}_{\mathrm{sys}}^{[p,q]}\right] \leq \min\left[P_{up}\left[\mathrm{F}_{\mathrm{sys}}^{[p,q]}\right],\; \min_{i,j}\left(P\left[A_m^{(i,j,[p,q])} < a_c^{ij}\right]\right)\right] \tag{8.65}$$

These bounds are much simpler than those derived in Equation (7.38) in Chapter 7; however, the tightness of these simpler bounds is considerably compromised as shown in Figure 8.46. To the author's knowledge, Equation (7.38) in chapter 7 provides the tightest lower and upper uni-modal bounds for $P\left[\breve{\mathrm{F}}_{\mathrm{sys}}^{[p,q]}\right]$.

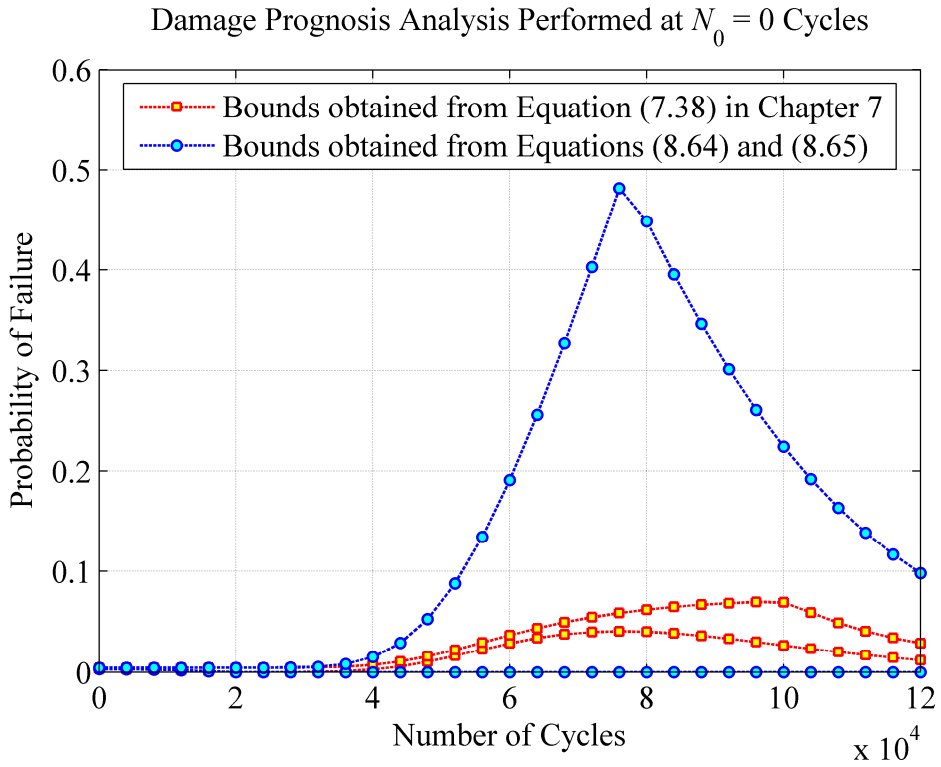

Figure 8.46: Time-dependent lower and upper uni-modal bounds of the probability of system failure, $P\left[\breve{\mathrm{F}}_{\mathrm{sys}}^{[p,q]}\right]$, for the benchmark application discussed in Section 8.4. Bounds computed immediately after the first NDE inspection (at $N_0 = 0$ cycles) using 5 NDE measurements at each damage location (i.e., $n_{\mathrm{MS}}^{(i,1,0)} = 5$ with $i = 1,2$).

8.7. Additional insight on the derivation of lower and upper uni-modal bounds for the probability of false-call, $P\left[\breve{\mathcal{F}}_{\text{sys}}^{[p,q]}\right]$

In Section 7.5.4 in Chapter 7 and in Section 8.3.5 in this chapter, the false-call event, $\breve{\mathcal{F}}_{\text{sys}}^{[p,q]}$, used to characterize the false-call event at the overall system level at time $t_p^q = t_p + q\Delta\tau$, was defined as

$$\begin{aligned}\breve{\mathcal{F}}_{\text{sys}}^{[p,q]} &\triangleq \left\{\left[\bigcap_{i=1}^{n_{\text{L}}^{[0,p]}}\left(\bigcap_{j=1}^{n_{\text{DM}}^{(i,[0,p])}}\overline{\text{F}_{\text{L},ij}^{[p,q]}}\right)\right]\cap\left(\bigcap_{r=1}^{n_{\text{G}}}\overline{\text{F}_{\text{G},r}^{[p,q]}}\right)\right\}\cap\left[\bigcup_{i=1}^{n_{\text{L}}^{[0,p]}}\left(\bigcup_{j=1}^{n_{\text{DM}}^{(i,[0,p])}}A_m^{(i,j,[p,q])}\geq a_c^{ij}\right)\right] \\ &\triangleq \left[\bigcap_{i=1}^{n_{\text{L}}^{[0,p]}}\left(\bigcap_{j=1}^{n_{\text{DM}}^{(i,[0,p])}}\overline{\text{F}_{\text{L},ij}^{[p,q]}}\right)\right]\cap\left(\bigcap_{r=1}^{n_{\text{G}}}\overline{\text{F}_{\text{G},r}^{[p,q]}}\right)\cap E_4\end{aligned} \tag{8.66}$$

where the event E_4, introduced for the sake of clarity, represents a series system and therefore lower and upper uni-modal bounds for the associated probability, $P\left[E_4\right]$, can be expressed as $P_{low}\left[E_4\right]\leq P\left[E_4\right]\leq P_{up}\left[E_4\right]$, with $P_{low}\left[E_4\right]$ and $P_{up}\left[E_4\right]$ defined as

$$P_{low}\left[E_4\right] = \max_{i,j}\left(P\left[A_m^{(i,j,[p,q])}\geq a_c^{ij}\right]\right) \tag{8.67}$$

$$P_{up}\left[E_4\right] = \min\left(1,\left[\sum_{i=1}^{n_{\text{L}}^{[0,p]}}\sum_{j=1}^{n_{\text{DM}}^{(i,[0,p])}}P\left[A_m^{(i,j,[p,q])}\geq a_c^{ij}\right]\right]\right) \tag{8.68}$$

Additionally, Equation (8.66) can be viewed as a parallel system with $n_{\text{A}}^p + n_{\text{G}} + 1$ reliability components; therefore, lower and upper uni-modal bounds of the probability associated with the false-call event, $\breve{\mathcal{F}}_{\text{sys}}^{[p,q]}$, of this parallel system can be specified as (Fréchet, 1935)

$$P\left[\breve{\mathcal{F}}_{\text{sys}}^{[p,q]}\right] \geq \max\left(0, \left[\sum_{i=1}^{n_{\text{L}}^{[0,p]}} \sum_{j=1}^{n_{\text{DM}}^{(i,[0,p])}} P\left[\overline{\text{F}_{\text{L},ij}^{[p,q]}}\right]\right] + \left[\sum_{r=1}^{n_{\text{G}}} P\left[\overline{\text{F}_{\text{G},r}^{[p,q]}}\right]\right] + P_{low}\left[E_4\right] - \left(n_{\text{A}}^{p} + n_{\text{G}}\right)\right) \quad (8.69)$$

$$P\left[\breve{\mathcal{F}}_{\text{sys}}^{[p,q]}\right] \leq \min\left[\min_{i,j,r}\left(P\left[\overline{\text{F}_{\text{L},ij}^{[p,q]}}\right], P\left[\overline{\text{F}_{\text{G},r}^{[p,q]}}\right]\right), P_{up}\left[E_4\right]\right] \quad (8.70)$$

These bounds are much simpler than those derived in Equations (7.49) and (7.50) in Chapter 7; however, as pointed out also in the previous section, the tightness of these simpler bounds is considerably compromise and an example to validate this statement is provided in Figure 8.47.

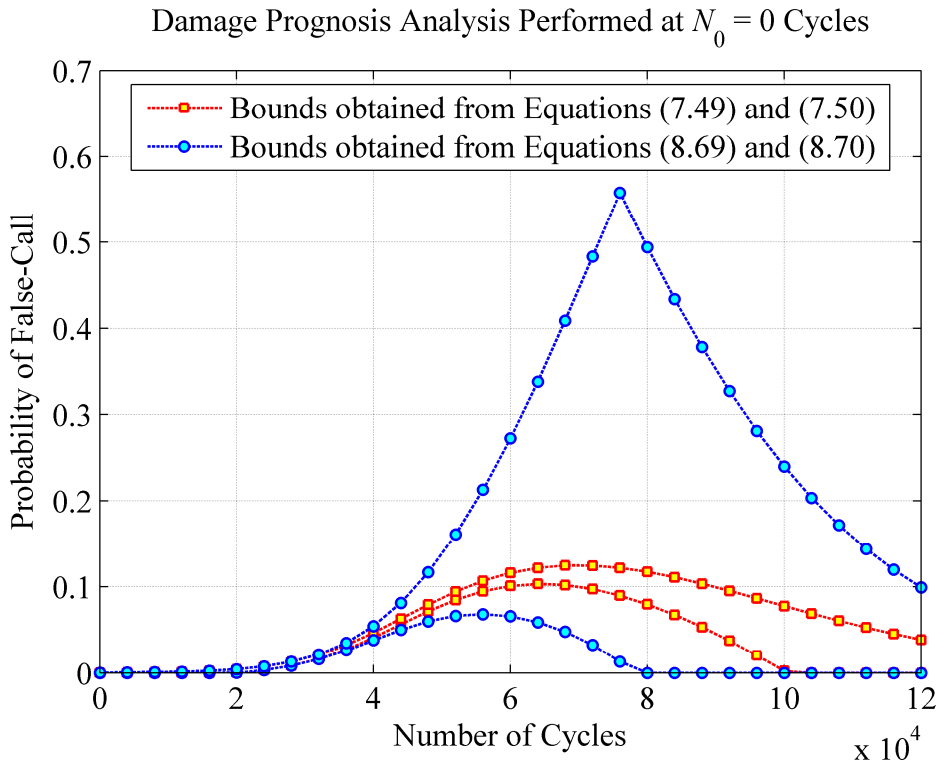

Figure 8.47: Time-dependent lower and upper uni-modal bounds of the probability of system failure, $P\left[\breve{\mathcal{F}}_{\text{sys}}^{[p,q]}\right]$, for the benchmark application discussed in Section 8.4. Bounds computed immediately after the first NDE inspection (at $N_0 = 0$ cycles) using 5 NDE measurements at each damage location (i.e., $n_{\text{MS}}^{(i,1,0)} = 5$ with $i = 1,2$).

To the author's knowledge, Equations (7.49) and (7.50) constitute the tightest uni-modal bounds for $P\left[\tilde{\mathcal{F}}_{\text{sys}}^{[p,q]}\right]$.

References

B.F. Backman, *Composite structures, design, safety and innovation*, Elsevier, 2005.

O.A. Bauchau, and R.G. Loewy, *Nonlinear aeroelastic effects in damaged composite aerospace structures*, Technical Report, School of Aerospace Engineering, Georgia Institute of Technology, Atlanta, GA, 1997.

A.P. Berens, NDE reliability analysis, *Metals Handbook*, Vol. 17. 9th ed. ASM International, 689-701, 1989.

J. Ching and Y.-C. Chen, Transitional Markov Chain Monte Carlo method for Bayesian model updating, model class selection, and model averaging, Journal of Engineering Mechanics, 133(7), 816-832, 2007.

G. Deodatis, H. Asada, and S. Ito, Reliability of aircraft structures under non-periodic inspection: a Bayesian approach, *Engineering Fracture Mechanics*, 53(5), 789-805, 1996.

O. Ditlevsen and H.O. Madsen, *Structural reliability methods*, Wiley, West Sussex, England, 1996.

R. O. Duda, P. E. Hart, and D. G. Stork, Pattern classification, second edition, Wiley-Interscience, 2001.

M. Fréchet, Généralisations du théorème des probabilités totales, *Fundamenta Mathematicae*., 25, 379-387, 1935.

X. Guan, R. Jha, and Y. Liu, Probabilistic fatigue damage prognosis using maximum entropy approach, *Journal of intelligent manufacturing*, 2009.

X. He, B. Moaveni, J.P. Conte, A. Elgamal, and S.F. Masri, Modal identification of Vincent Thomas Bridge using simulated wind response data, *Journal of Computer Aided Civil and Infrastructure Engineering*, 23(5), 373-388, 2008.

C. Huang, and K.Y. Lin, A Method for reliability assessment of aircraft structures subject to accidental damage, *Proc. 46th AIAA/ASME/ASCE/AHS/ASC Structures, Structural Dynamics, & Materials Conference*, Austin, TX, April 2005.

D.J. Inman, C.R. Farrar, V. Lopez Jr., V. Steffen Jr., *Damage prognosis for aerospace, civil and mechanical systems*, Wiley, 2005.

R.M. Jones, Apparent flexural modulus and strength of multimodulus materials, *Journal of Composite Materials*, 10, 342-354, 1976.

S.S. Kulkarni, and J.D. Achenbach, Structural health monitoring and damage prognosis in fatigue, *Structural Health Monitoring*, 7(1), 37-49, 2008.

M. Kutner, C. Nachtsheim, J. Neter, and W. Li, *Applied linear statistical models*, 5th edition, McGraw-Hill, 2004.

K.Y. Lin, J. Du, and D. Rusk, *Structural design methodology based on concepts of uncertainty*, Report NASA/CR-2000-209847, NASA Langley Research Center, Hampton, VA, 2000.

K.Y. Lin, and A.V. Styuart, Probabilistic approach to damage tolerance design of aircraft composite structures, *Journal of Aircraft*, 44(4), 1309-1317, 2007.

T. Moan, Reliability-based management of inspection, maintenance and repair of offshore structures, *Structure and Infrastructure Engineering*, 1(1), 33-62, 2005.

T. Moan, Design of offshore structures and ships for damage tolerance, Systems & Ocean Technology, *Journal of SOBENA*, 3(1), 51-65, 2007.

T. Moan, *Reliability of aged offshore structures*, Chapter 11, In Paik, J.K. & Melchers, R.E. Condition Assessment of Aged Structures, CRC Press, Boca Raton, 2008.

R.H. Myers, and D.C. Montgomery, *Response Surface Methodology*, John Wiley and Sons, Inc., New York, NY, 1995.

A. Navarro and E.R De Los Rios, On dimensional analysis of fatigue crack growth rate and geometrical similitude of cracks, *Fatigue & Fracture of Engineering Materials and Structures*, 9(5), 373-378, 1987.

M.B. Priestley, *Spectral analysis and time series, volume 1: Univariate series, volume 2: Multivariate series, prediction and control*, Academic Press, London (UK) (1987) Fifth printing.

R.J. Sanford, *Principles of fracture mechanics*, Prentice Hall, 2003.

G.A.F. Seber, and A.J. Lee, *Linear regression analysis*, second edition, Wiley Series in Probability and Statistics, John Wiley & Sons Inc., NJ, 2003.

M. Staat, Sensitivity of and influences on the reliability of an HTR-module primary circuit pressure boundary, *Proc. 12th International Conference on Structural Mechanics in Reactor Technology (SMiRT)*, Amsterdam, The Netherlands, August 1993.

A.V. Styuart, M. Mor, E. Livne, and K.Y. Lin., Aeroelastic failure risk assessment in damage tolerant composite airframe structures, *Proc. 48th AIAA/ASME/ASCE/ AHS/ASC Structures, Structural Dynamics, and Materials Conference*, Honolulu, Hi, April 23-26,2007.

K. Wang, D.J. Inman, and C.R. Farrar, Crack-induced changes in divergence and flutter of cantilevered composite panels, *Structural Health Monitoring*, 4(4), 377-392, 2005.

Y.-K. Wen, *Structural load modeling and combination for performance and safety evaluation*, Elsevier, 1990.

J.N. Yang, and W.J. Trapp, Reliability analysis of aircraft structures under random loading and periodic inspection, *AIAA Journal*, 12(12), 1623-1630, 1974.

R. Zhang, and S. Mahadevan, Fatigue reliability analysis using non-destructive inspection, Journal of Structural Engineering, ASCE, 127(8), 957-965, 2001.

R. Zheng, and B.R. Ellingwood, Role of non-destructive evaluation in time-dependent reliability analysis, *Structural Safety*, 20(4), 325-339, 1998.

CHAPTER 9

VERIFICATION AND VALIDATION OF THE PROPOSED RELIABILITY-BASED DAMAGE PROGNOSIS FRAMEWORK VIA DAMAGE PROPAGATION LAWS BASED ON LINEAR ELASTIC FRACTURE MECHANICS

9.1. Introduction

This chapter presents two additional numerical applications of the proposed damage prognosis framework, used for code verification and experimental validation purposes. The first numerical application, described in Section 9.2, uses the same benchmark structure introduced in Chapter 8 to study the fatigue-driven debonding

propagation along the idealized zero-thickness adhesive interface in a simply supported composite beam. However, conversely to the approach followed in Chapter 8, the debonding propagation process is herein simulated by using a damage propagation law based on linear elastic fracture mechanics (LEFM) and experimental observations, namely the Forman's model (Forman, 1972). This analysis approach allows for a complete engagement of all probabilistic analysis steps of the proposed methodology shown in Figure 9.1 (i.e., even the probabilistic load hazard analysis step which was bypassed in the numerical application presented in the previous chapter). In the second part of this chapter, in Section 9.3, a set of experimental fatigue test data found in the literature (Virkler *et al.*, 1979) is used to provide a first experimental validation of the proposed framework, with special emphasis towards the recursive Bayesian inference scheme and the probabilistic damage evolution analysis step.

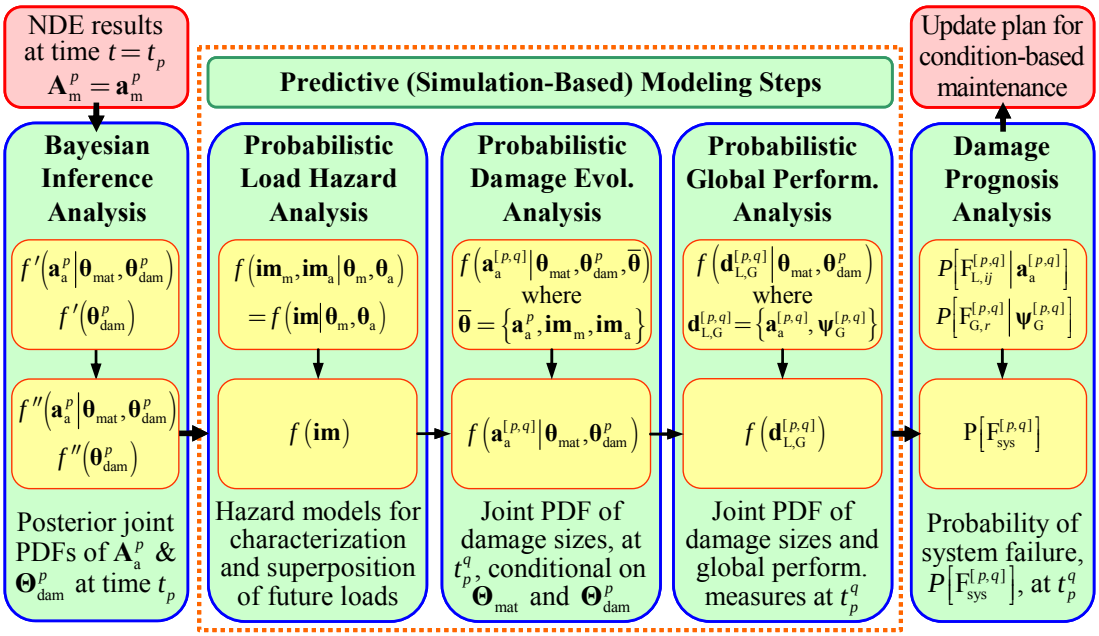

Figure 9.1: Flowchart of the proposed reliability-based damage prognosis.

9.2. Benchmark application: fatigue-driven debonding propagation analysis in a simply supported composite beam

The numerical example presented in this section aims at (i) engaging all five probabilistic analysis step of the proposed damage prognosis methodology; (ii) further validating the proposed recursive Bayesian inference scheme by applying it to a more complicated scenario; (iii) illustrating the practical use of the proposed stochastic load simulation and superposition via censored Poisson processes (see Chapter 4 and Section 8.3.2 in Chapter 8); (iv) assessing the computational feasibility of the proposed framework when the stochasticity of the applied load is explicitly taken into account; (v) demonstrating that well-known damage propagation models — such as Paris law (Paris and Erdogan, 1963), Forman's model (Forman, 1972), and many others (Degrieck and Paepegem, 2001; Blanco *et al*., 2004) available in the literature — can be readily used within the proposed framework; and (vi) proposing reasonable simplifying assumptions within the probabilistic damage evolution analysis step in order to gain computational feasibility without excessively compromising the effectiveness of the other steps of the methodology.

The benchmark structure used in this application example is the same one already introduced in Section 8.4 of Chapter 8 and, for the sake of clarity, is shown again here in Figure 9.2. It consists of a simply supported composite beam, of length $2L = 250.0\,mm$, made out of two identical unidirectional laminated composite adherends, with solid rectangular cross section, bonded through an idealized zero-thickness adhesive interface/layer. The width and depth of each unidirectional

laminated composite adherend are $b = 25.0\,mm$ and $h = 3.0\,mm$, respectively. The only material parameter of interest is represented by the flexural modulus (Jones, 1976) of the lower and upper unidirectional composite adherends (i.e., $\boldsymbol{\Theta}_{\text{mat}} = \Theta_{\text{mat}} = E_{11}^{f}$) assumed to follow a Normal distribution with mean $\mu_{E_{11}^{f}} = 130.0\,GPa$ and a coefficient of variation of 5%. The debonding, along the adhesive interface between the two composite adherends, is considered the only damage mechanism (i.e., $j = 1$ at all damage locations) evolving in time. More specifically, two debonding fronts, propagating from the two end supports (i.e., from the beam ends) towards the beam midspan, are considered in this example. The lengths of the two disbonds at generic time t are denoted as $a_a^{(1,1,t)}$ (i.e., $i = 1$ and $j = 1$) and $a_a^{(2,1,t)}$ (i.e., $i = 2$ and $j = 1$), respectively. Similarly, the two damage locations are hereafter referred to as *damage location 1* (i.e., $i = 1$) and *damage location 2* (i.e., $i = 2$), respectively. Finally, the beam is subjected to a harmonic concentrated load, applied at its midspan, constituting the driving factor of the debonding propagation process along the adhesive interface.

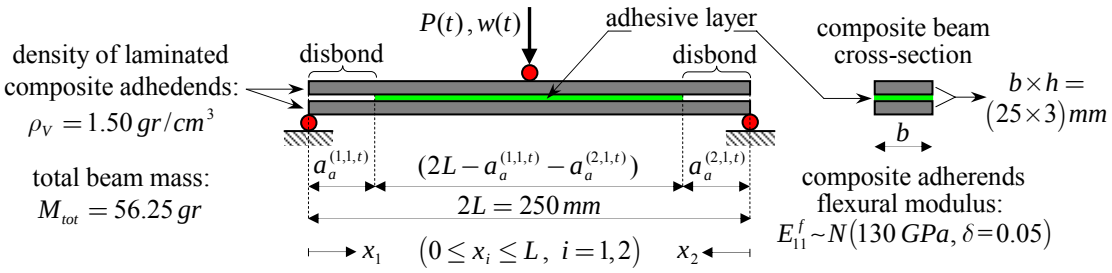

Figure 9.2: Simply-supported composite beam with two debonding fronts (evolving from the beam ends) subjected to a concentrated load, *P*(*t*), applied at its midspan.

9.2.1. Probabilistic characterization of loading conditions

As already discussed in Section 8.3.2 of Chapter 8, a random harmonic load acting on the monitored structural system is herein conveniently decomposed into two components: its mean/average intensity, characterized probabilistically by the intensity measure vector $\mathbf{IM}_{\mathrm{m}} = \{P_{\mathrm{m}}, \Delta T_{\mathrm{m}}\}$, and the superimposed harmonic load fluctuations about the mean-load intensity, probabilistically described by the intensity measure vector $\mathbf{IM}_{\mathrm{a}} = \{AMP, \Delta T_{\mathrm{a}}\}$; a realization of such a stochastic load, emphasizing the superposition of mean-load and amplitude-load rectangular pulses, is illustrated in Figure 9.3. The random variable P_{m} represents the intensity of the applied mean-load pulse, ΔT_{m} denotes the duration (herein expressed in number of cycles) of the mean-

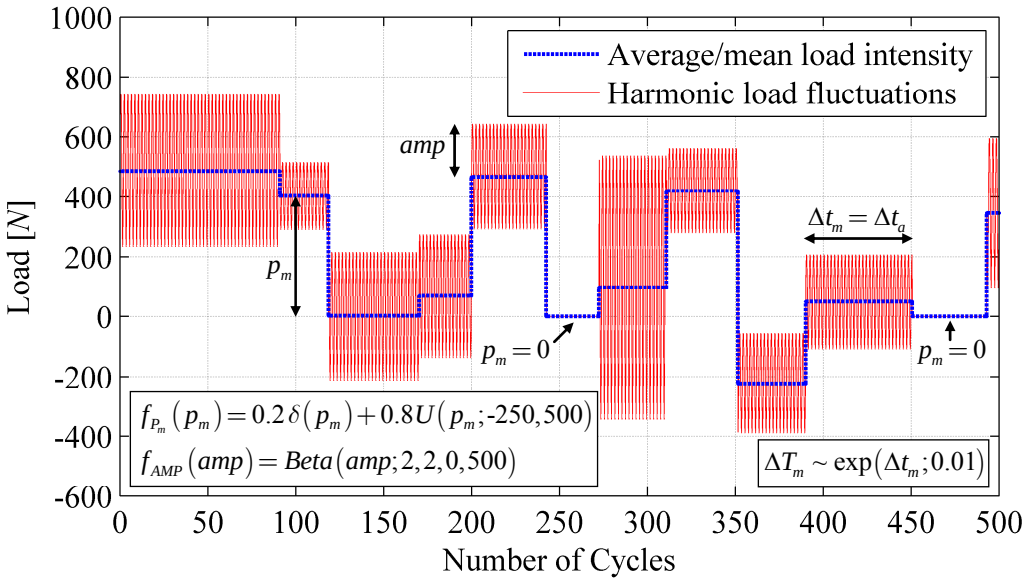

Figure 9.3: Example of load superposition for the case in which mean-load intensity and amplitude of the harmonic load fluctuations are considered to be statistically dependent. The amplitude value of the harmonic load fluctuations is renewed at each mean-load pulse occurrence, remains constant for the entire duration of each mean-load pulse, and is equal to zero when the mean-load pulse intensity is equal to zero.

load pulse, AMP_a indicate the amplitude of the harmonic load fluctuations about the mean-load intensity P_m, and ΔT_a symbolizes the duration (herein expressed in number of cycles) of the harmonic load pulse of intensity/amplitude AMP_a.

The random sequence of the applied mean-load (e.g., blue line in Figure 9.3) is modeled and simulated using a homogeneous Poisson rectangular pulse process (Wen, 1990) with mean rate of occurrence $\lambda_m = 1/\mu_{\Delta T_m}$ (where $\mu_{\Delta T_m}$, collected in the random parameter vector $\boldsymbol{\Theta}_m$, denotes the average duration of the mean-load pulses). Each arrival (in time) of a Poisson event raises a rectangular pulse of random intensity P_m — according to its conditional PDF $f_{P_m|\boldsymbol{\Theta}_m}(p_m|\boldsymbol{\theta}_m)$ — until the next arrival. Additionally, a generic realization of the random vector $\mathbf{IM}_m = \mathbf{im}_m$ in $\left[t_p, t_p^{\bar{q}}\right]$ is herein defined as $\mathbf{im}_m \triangleq \left\{\mathbf{im}_m^{(k)},\ k = 1, ..., n_m\right\}$ with (i) $\mathbf{im}_m^{(k)} = \left\{p_m^{(k)}, \Delta t_m^{(k)}\right\}$ specifying the intensity and duration of the k^{th} mean-load pulse and (ii) n_m representing the total number of pulses randomly generated during a generic realization of $\mathbf{IM}_m$. The mean-load intensity, $p_m^{(k)}$, is sampled according to the conditional PDF $f_{P_m|\boldsymbol{\Theta}_m}(p_m|\boldsymbol{\theta}_m)$ while the pulse duration, $\Delta t_m^{(k)}$, is drawn from the exponential distribution of ΔT_m characterized by the mean value $\mu_{\Delta T_m}$. Based on these considerations, it is deduced that the random parameter vector $\boldsymbol{\Theta}_m$ collects all the distribution parameters necessary to probabilistically characterize the random variables P_m and ΔT_m. For example, if the conditional PDF $f_{P_m|\boldsymbol{\Theta}_m}(p_m|\boldsymbol{\theta}_m)$ is modeled using a uniform distribution, then the two

boundaries of this distribution (i.e., the lower boundary $P_{\mathrm{m}}^{\min}$ and the upper boundary $P_{\mathrm{m}}^{\max}$) would be contained in $\boldsymbol{\Theta}_{\mathrm{m}}$ and could themselves be considered (in the most general case) as random variables.

Once the random sequence of mean/average load pulses, $\mathbf{IM}_{\mathrm{m}} = \mathbf{im}_{\mathrm{m}}$, is stochastically realized, according to the procedure outlined above, an additional random sequence of load pulses, $\mathbf{IM}_{\mathrm{a}} = \mathbf{im}_{\mathrm{a}}$, characterizing the intensity of the harmonic load fluctuations, is generated and superimposed to $\mathbf{im}_{\mathrm{m}}$. These harmonic load fluctuations are assumed to be characterized by a fixed frequency and random amplitude (*AMP*), with the latter distributed according to the conditional PDF $f_{AMP|\boldsymbol{\Theta}_{\mathrm{a}}}\left(amp|\boldsymbol{\theta}_{\mathrm{a}}\right)$ and renewed at each load pulse occurrence. In other words, for given values of $AMP = amp$ and $\boldsymbol{\Theta}_{\mathrm{a}} = \boldsymbol{\theta}_{\mathrm{a}}$ the harmonic load intensity to be superimposed to $\mathbf{IM}_{\mathrm{m}} = \mathbf{im}_{\mathrm{m}}$ is completely defined. Furthermore, if $\mathbf{IM}_{\mathrm{a}}$ is considered to be statistically independent of $\mathbf{IM}_{\mathrm{m}}$, the same reasoning as the one outlined above for $\mathbf{IM}_{\mathrm{m}}$ can be used. A homogeneous Poisson rectangular pulse process with mean rate of occurrence $\lambda_{\mathrm{a}} = 1/\mu_{\Delta T_{\mathrm{a}}}$ (where $\mu_{\Delta T_{\mathrm{a}}}$, collected in the random parameter vector $\boldsymbol{\Theta}_{\mathrm{a}}$, denotes the average duration of the load pulse) is also used to model and simulate the random sequence of the intensity of the harmonic load fluctuations about the mean-load intensity (P_{m}). Each arrival (in time) of a Poisson event raises a rectangular pulse of random intensity/amplitude AMP, distributed according to its conditional PDF $f_{AMP|\boldsymbol{\Theta}_{\mathrm{a}}}\left(amp|\boldsymbol{\theta}_{\mathrm{a}}\right)$, until the next arrival. Additionally, a generic realization of the

random vector $\mathbf{IM}_{\mathrm{a}} = \mathbf{im}_{\mathrm{a}}$ in $\left[t_p, t_p^{\bar{q}}\right]$ is defined as $\mathbf{im}_{\mathrm{a}} \triangleq \left\{\mathbf{im}_{\mathrm{a}}^{(k)},\ k = 1, ..., n_{\mathrm{a}}\right\}$ with (i) $\mathbf{im}_{\mathrm{a}}^{(k)} = \left\{amp^{(k)}, \Delta t_{\mathrm{a}}^{(k)}\right\}$ specifying the intensity and duration of the k^{th} pulse and (ii) n_{a} representing the total number of pulses randomly generated during a generic realization of $\mathbf{IM}_{\mathrm{a}}$. The quantity $amp^{(k)}$ is sampled according to the conditional PDF $f_{AMP|\boldsymbol{\Theta}_{\mathrm{a}}}\left(amp|\,\boldsymbol{\theta}_{\mathrm{a}}\right)$ while the pulse duration, $\Delta t_{\mathrm{a}}^{(k)}$, is drawn from the exponential distribution of ΔT_{a} defined by the mean value $\mu_{\Delta T_{\mathrm{a}}}$. However, in the most general case, $\mathbf{IM}_{\mathrm{m}}$ and $\mathbf{IM}_{\mathrm{a}}$ can or must be considered statistically dependent. For example, as depicted in Figure 9.3, the constraints $\Delta t_{\mathrm{a}}^{(k)} = \Delta t_{\mathrm{m}}^{(k)}$ (for $k = 1, ..., n_{\mathrm{m}}$) and/or $f_{AMP|P_{\mathrm{m}}}\left(amp|\ p_{\mathrm{m}} = 0\right) = \delta\left(amp\right)$ can be imposed. In this alternative scenario, once the vector $\mathbf{im}_{\mathrm{m}}$ is randomly realized, then the other intensity measure vector, $\mathbf{im}_{\mathrm{a}}$, must be sampled from the conditional PDF $f_{\mathbf{IM}_{\mathrm{a}}|\mathbf{IM}_{\mathrm{m}},\boldsymbol{\Theta}_{\mathrm{a}}}\left(\mathbf{im}_{\mathrm{m}}|\,\mathbf{im}_{\mathrm{m}}, \boldsymbol{\theta}_{\mathrm{a}}\right)$. This alternative load modeling approach is used in the proposed numerical application.

In this specific application example the average duration of the applied mean-load pulses, $\mu_{\Delta T_{\mathrm{m}}}$, is set to be equal to 100 cycles. Therefore, the mean rate of occurrence of these mean-load pulses (blue dashed line in Figure 9.3) becomes $\lambda_{\mathrm{m}} = 1/\mu_{\Delta T_{\mathrm{m}}} = 0.01$ and the exponential PDF of ΔT_m can be written as

$$\Delta T_m \sim \exp\left(\Delta t_m; \lambda_{\mathrm{m}} = 0.01\right) \quad \Rightarrow \quad f_{\Delta T_m}\left(\Delta t_m\right) = \lambda_{\mathrm{m}} \exp\left(-\lambda_{\mathrm{m}} \cdot \Delta t_m\right), \quad \Delta t_m \geq 0 \qquad (9.1)$$

At each random occurrence in time, the intensity/magnitude of the mean-load pulse is then assumed to follow the mixed PDF shown below

$$\begin{aligned} f_{P_m}(p_m) &= \left(1-p_m^{sel}\right)\cdot\delta(p_m)+p_m^{sel}\cdot U\left(p_m;P_{\mathrm{m}}^{\min},P_{\mathrm{m}}^{\max}\right) \\ &= (1-0.8)\cdot\delta(p_m)+0.8\cdot U(p_m;-250,+500) \end{aligned} \tag{9.2}$$

where $p_m^{sel}=0.8$ represents the probability of selection (see Chapter 4) of the censored Poisson pulse process (Wen, 1990), $\delta(\bullet)$ denotes the *Dirac Delta*, and $U\left(p_m;P_{\mathrm{m}}^{\min},P_{\mathrm{m}}^{\max}\right)$ indicates the Uniform PDF for the random load intensity P_m between $P_{\mathrm{m}}^{\min}=-250.0\,N$ and $P_{\mathrm{m}}^{\max}=+500.0\,N$. Finally, within each mean-load pulse, the random amplitude (*AMP*) of the superimposed harmonic load fluctuations is distributed according to the following PDF:

$$f_{AMP}(amp)=\begin{cases}0 & \text{if } P_m=0\\ Beta(amp;\,2.0,\,2.0,\,0,\,500) & \text{otherwise}\end{cases} \tag{9.3}$$

where $Beta(amp;\,\alpha,\,\beta,\,amp_{\min},\,amp_{\max})=Beta(amp;\,2.0,\,2.0,\,0,\,500)$ represents the four-parameter Beta distribution with $\alpha=\beta=2.0$ defined over the domain $[amp_{\min},\,amp_{\max}]=[0,\,500]N$. The mathematical expression of such PDF is expressed as (Kleiber and Kotz, 2003)

$$\begin{aligned} f_{AMP}(amp) &= \frac{1}{B(\alpha,\beta)}\frac{(amp-amp_{\min})^{\alpha-1}(amp_{\max}-amp)^{\beta-1}}{(amp_{\max}-amp_{\min})^{\alpha+\beta-1}} \\ &= \frac{1}{B(2,2)}\frac{amp(500-amp)}{500^3} \quad (0\le amp\le 500) \end{aligned} \qquad 0\le amp\le 500 \tag{9.4}$$

where the normalizing constant $B(\alpha,\beta)$ is the *Beta function* (sometimes also referred to as the Euler integral of the first kind) defined as

$$B(\alpha,\beta)=\int_0^1 t^{\alpha-1}(1-t)^{\beta-1}\,dt \tag{9.5}$$

9.2.2. Damage evolution model

The debonding propagation process, along the adhesive interface between the two composite adherends, is modeled and simulated by using a damage evolution model based on LEFM principles and experimental observation, namely the Forman's model (Forman, 1972). This model essentially represents an improved version of the Paris law (Paris and Erdogan, 1963) by including — as it will be shown later — load ratio effects and capturing the unstable damage propagation behavior within the so-called *Stage III growth* (Sanford, 2003). Under these assumptions and for the specific case studied herein, the debonding propagation process, at load cycle $N \geq N_p$, is governed by the following system of uncoupled ordinary differential equations:

$$\begin{cases} \dfrac{d}{dN}\overline{a}_a^{(1,1,[p,N])} = \dfrac{C^{(1,1,p)}}{1-Q}\,\dfrac{\left(\Delta G^{(1,N)}\right)^{n^{(1,1,p)}}}{G_C^{(1,1,p)}-\tilde{G}_{\max}^{(1,N)}} \\ \dfrac{d}{dN}\overline{a}_a^{(2,1,[p,N])} = \dfrac{C^{(2,1,p)}}{1-Q}\,\dfrac{\left(\Delta G^{(2,N)}\right)^{n^{(2,1,p)}}}{G_C^{(2,1,p)}-\tilde{G}_{\max}^{(2,N)}} \qquad \left(N \geq N_p,\ \ p=0,1,2,\ldots\right) \\ \overline{a}_a^{(1,1,p)} = a_a^{(1,1,p)} \\ \overline{a}_a^{(2,1,p)} = a_a^{(2,1,p)} \end{cases} \tag{9.6}$$

where $C^{(i,1,p)}$, $n^{(i,1,p)}$, and $G_C^{(i,1,p)}$ $\left(\text{with } i=1,2\right)$ are the three damage evolution model parameters involved in the damage propagation process at each of the two damage locations considered in this benchmark application. Each of these two triplets of damage evolution parameters is collected in the sub-vector $\boldsymbol{\Theta}_{\text{dam}}^{(i,p)}$, defined as

$\boldsymbol{\Theta}_{\text{dam}}^{(i,p)} = \left\{ C^{(i,1,p)}, n^{(i,1,p)}, G_C^{(i,1,p)} \right\}$, and these two sub-vectors are then grouped together as $\boldsymbol{\Theta}_{\text{dam}}^{p} = \left\{ \boldsymbol{\Theta}_{\text{dam}}^{(1,p)}, \boldsymbol{\Theta}_{\text{dam}}^{(2,p)} \right\}$. The quantities $C^{(i,1,p)}$ and $n^{(i,1,p)}$ $\left(\text{with } i = 1,2\right)$ are material-dependent empirical parameters determined through the analysis and curve fitting of fatigue test data, while $G_C^{(i,1,p)}$ $\left(\text{with } i = 1,2\right)$ denotes the critical fracture energy of the adhesive interface, at either *damage location 1* or *damage location 2*, and can be experimentally evaluated through standardized static tests according to the ASTM standards (ASTM Standard D6671-04). The coefficient Q accounts for both load ratio and shear reversal (Degrieck and Paepegem, 2001) effects and is defined as

$$Q = \begin{cases} R_P & \text{if } -1 \le R_P \le +1 \\ \dfrac{1}{R_P} & \text{if } \left|R_P\right| > 1 \end{cases} \tag{9.7}$$

where R_P represents the load ratio and is computed as the ratio between the minimum (P_{min}) and maximum (P_{max}) applied load within the N^{th} load cycle, i.e.,

$$R_P = \frac{P_{\text{min}}}{P_{\text{max}}} = \frac{P_{\text{m}} - AMP}{P_{\text{m}} + AMP} \tag{9.8}$$

The quantity $\Delta G^{(i,N)}$ $\left(\text{with } i = 1,2\right)$, in Equation (9.6), constitutes the range of applied strain energy release rate (SERR), at either *damage location 1* ($i = 1$) or *damage location 2* ($i = 2$), during the N^{th} load cycle and is defined as

$$\Delta G^{(i,N)} = \begin{cases} G_{\text{max}}^{(i,N)} - G_{\text{min}}^{(i,N)} & \text{if } Q \ge 0 \\ G_{\text{max}}^{(i,N)} + G_{\text{min}}^{(i,N)} & \text{if } Q < 0 \end{cases} \qquad \left(i = 1,2\right) \tag{9.9}$$

in which $G_{\text{max}}^{(i,N)}$ and $G_{\text{min}}^{(i,N)}$ $\left(\text{with } i = 1,2\right)$ can be expressed as (see Appendix F)

$$G_{\max}^{(i,N)} = \frac{9}{16}\frac{\left(P_m^{\max}\right)^2\left(\overline{a}_a^{(i,1,[p,N])}\right)^2}{E_{11}^f b^2 h^3} \qquad (i=1,2) \tag{9.10}$$

$$G_{\min}^{(i,N)} = \frac{9}{16}\frac{\left(P_m^{\min}\right)^2\left(\overline{a}_a^{(i,1,[p,N])}\right)^2}{E_{11}^f b^2 h^3} \qquad (i=1,2) \tag{9.11}$$

Finally, $\tilde{G}_{\max}^{(i,N)}$ characterizes the maximum (in absolute value sense) applied SERR during the N^{th} load cycle and is mathematically computed as

$$\tilde{G}_{\max}^{(i,N)} = \max\left(\left|G_{\min}^{(i,N)}\right|, \left|G_{\max}^{(i,N)}\right|\right) \qquad (i=1,2) \tag{9.12}$$

Maintaining the focus on Equation (9.6), $\overline{a}_a^{(1,1,[p,N])}$ and $\overline{a}_a^{(2,1,[p,N])}$ are the predicted (from current load cycle N_p) debonding lengths at load cycle $N \geq N_p$; $d\overline{a}_a^{(1,1,[p,N])}/dN$ and $d\overline{a}_a^{(2,1,[p,N])}/dN$ represent the rate of debonding propagation, expressed in increment of debonding length per load cycle; lastly, $a_a^{(1,1,p)}$ and $a_a^{(2,1,p)}$ represent a particular realization of the actual debonding lengths ($A_a^{(1,1,p)}$ and $A_a^{(2,1,p)}$) at current load cycle N_p, distributed according to the posterior conditional joint PDF $f''_{\mathbf{A}_a^p|\boldsymbol{\Theta}_{\text{mat}},\boldsymbol{\Theta}_{\text{dam}}^p}\left(\mathbf{a}_a^p \middle| \boldsymbol{\theta}_{\text{mat}}, \boldsymbol{\theta}_{\text{dam}}^p\right)$, in which the damage size vector $\mathbf{A}_a^p$ is given by $\mathbf{A}_a^p = \left\{A_a^{(1,1,p)}, A_a^{(2,1,p)}\right\}$.

Equation (9.6) is integrated numerically between current load cycle N_p and (future) load cycle $N_p^q = N_p + q\Delta N$ (with $q = 1, 2, ..., \overline{q}$) to provide the conditional joint PDF $f_{\mathbf{A}_a^{[p,q]}|\boldsymbol{\Theta}_{\text{mat}},\boldsymbol{\Theta}_{\text{dam}}^p,\mathbf{A}_a^p,\mathbf{IM}}\left(\mathbf{a}_a^{[p,q]} \middle| \boldsymbol{\theta}_{\text{mat}}, \boldsymbol{\theta}_{\text{dam}}^p, \mathbf{a}_a^p, \mathbf{im}\right)$ appearing at the beginning of the

third analytical step of the proposed damage prognosis methodology, namely probabilistic damage evolution analysis (see Figure 9.1). Under the assumptions discussed thus far, this conditional joint PDF can be expressed as

$$f_{\mathbf{A}_{\mathrm{a}}^{[p,\,q]}\left|\boldsymbol{\Theta}_{\mathrm{mat}},\,\boldsymbol{\Theta}_{\mathrm{dam}}^{p},\,\mathbf{A}_{\mathrm{a}}^{p},\,\mathbf{IM}\right.}\left(\mathbf{a}_{\mathrm{a}}^{[p,\,q]}\left|\boldsymbol{\theta}_{\mathrm{mat}},\,\boldsymbol{\theta}_{\mathrm{dam}}^{p},\,\mathbf{a}_{\mathrm{a}}^{p},\mathbf{im}\right.\right)=\delta\left(\mathbf{a}_{\mathrm{a}}^{[p,\,q]}-\overline{\mathbf{a}}_{\mathrm{a}}^{[p,\,q]}\right) \tag{9.13}$$

where $\overline{\mathbf{a}}_{\mathrm{a}}^{[p,\,q]}$ represents the outcome from the numerical integration of Equation (9.6), between current load cycle N_p and (future) load cycle $N_p^q=N_p+q\Delta N$, for a given realization of $\boldsymbol{\Theta}_{\mathrm{mat}}=\boldsymbol{\theta}_{\mathrm{mat}}$, $\boldsymbol{\Theta}_{\mathrm{dam}}^{p}=\boldsymbol{\theta}_{\mathrm{dam}}^{p}$, $\mathbf{A}_{\mathrm{a}}^{p}=\mathbf{a}_{\mathrm{a}}^{p}$, and $\mathbf{IM}=\mathbf{im}=\left\{\mathbf{im}_{\mathrm{m}},\mathbf{im}_{\mathrm{a}}\right\}$, i.e., $\overline{\mathbf{a}}_{\mathrm{a}}^{[p,\,q]}=\overline{\mathbf{a}}_{\mathrm{a}}^{[p,\,q]}\left(\boldsymbol{\theta}_{\mathrm{mat}},\,\boldsymbol{\theta}_{\mathrm{dam}}^{p},\,\mathbf{a}_{\mathrm{a}}^{p},\mathbf{im}\right)=\left(\mathbf{A}_{\mathrm{a}}^{[p,\,q]}\left|\boldsymbol{\theta}_{\mathrm{mat}},\,\boldsymbol{\theta}_{\mathrm{dam}}^{p},\,\mathbf{a}_{\mathrm{a}}^{p},\mathbf{im}\right.\right)$. The conditional joint PDF in Equation (9.13) is then used to compute the conditional joint PDF $f_{\mathbf{A}_{\mathrm{a}}^{[p,\,q]}\left|\boldsymbol{\Theta}_{\mathrm{mat}},\,\boldsymbol{\Theta}_{\mathrm{dam}}^{p},\,\mathbf{A}_{\mathrm{a}}^{p}\right.}\left(\mathbf{a}_{\mathrm{a}}^{[p,\,q]}\left|\boldsymbol{\theta}_{\mathrm{mat}},\,\boldsymbol{\theta}_{\mathrm{dam}}^{p},\,\mathbf{a}_{\mathrm{a}}^{p}\right.\right)$ through the total probability theorem as

$$\begin{aligned}
&f_{\mathbf{A}_{\mathrm{a}}^{[p,\,q]}\left|\boldsymbol{\Theta}_{\mathrm{mat}},\,\boldsymbol{\Theta}_{\mathrm{dam}}^{p},\,\mathbf{A}_{\mathrm{a}}^{p}\right.}\left(\mathbf{a}_{\mathrm{a}}^{[p,\,q]}\left|\boldsymbol{\theta}_{\mathrm{mat}},\,\boldsymbol{\theta}_{\mathrm{dam}}^{p},\,\mathbf{a}_{\mathrm{a}}^{p}\right.\right)=\\
&\int_{\mathbf{IM}} f_{\mathbf{A}_{\mathrm{a}}^{[p,\,q]}\left|\boldsymbol{\Theta}_{\mathrm{mat}},\,\boldsymbol{\Theta}_{\mathrm{dam}}^{p},\,\mathbf{A}_{\mathrm{a}}^{p},\,\mathbf{IM}\right.}\left(\mathbf{a}_{\mathrm{a}}^{[p,\,q]}\left|\boldsymbol{\theta}_{\mathrm{mat}},\,\boldsymbol{\theta}_{\mathrm{dam}}^{p},\,\mathbf{a}_{\mathrm{a}}^{p},\mathbf{im}\right.\right) f_{\mathbf{IM}}\left(\mathbf{im}\right)d\mathbf{im}=\\
&\int_{\mathbf{IM}} \delta\left(\mathbf{a}_{\mathrm{a}}^{[p,\,q]}-\overline{\mathbf{a}}_{\mathrm{a}}^{[p,\,q]}\right) f_{\mathbf{IM}}\left(\mathbf{im}\right)d\mathbf{im}
\end{aligned} \tag{9.14}$$

and the result from Equation (9.14) is subsequently exploited to estimate the conditional joint PDF $f_{\mathbf{A}_{\mathrm{a}}^{[p,\,q]}\left|\boldsymbol{\Theta}_{\mathrm{mat}},\,\boldsymbol{\Theta}_{\mathrm{dam}}^{p}\right.}\left(\mathbf{a}_{\mathrm{a}}^{[p,\,q]}\left|\boldsymbol{\theta}_{\mathrm{mat}},\,\boldsymbol{\theta}_{\mathrm{dam}}^{p}\right.\right)$ as

$$\begin{aligned}
&f_{\mathbf{A}_{\mathrm{a}}^{[p,\,q]}\left|\boldsymbol{\Theta}_{\mathrm{mat}},\,\boldsymbol{\Theta}_{\mathrm{dam}}^{p}\right.}\left(\mathbf{a}_{\mathrm{a}}^{[p,\,q]}\left|\boldsymbol{\theta}_{\mathrm{mat}},\,\boldsymbol{\theta}_{\mathrm{dam}}^{p}\right.\right)=\\
&\int_{\mathbf{A}_{\mathrm{a}}^{[p,\,q]}} f_{\mathbf{A}_{\mathrm{a}}^{[p,q]}\left|\boldsymbol{\Theta}_{\mathrm{mat}},\,\boldsymbol{\Theta}_{\mathrm{dam}}^{p},\,\mathbf{A}_{\mathrm{a}}^{p}\right.}\left(\mathbf{a}_{\mathrm{a}}^{[p,q]}\left|\boldsymbol{\theta}_{\mathrm{mat}},\,\boldsymbol{\theta}_{\mathrm{dam}}^{p},\,\mathbf{a}_{\mathrm{a}}^{p}\right.\right) f_{\mathbf{A}_{\mathrm{a}}^{p}\left|\boldsymbol{\Theta}_{\mathrm{mat}},\,\boldsymbol{\Theta}_{\mathrm{dam}}^{p}\right.}\left(\mathbf{a}_{\mathrm{a}}^{p}\left|\boldsymbol{\theta}_{\mathrm{mat}},\,\boldsymbol{\theta}_{\mathrm{dam}}^{p}\right.\right)d\mathbf{a}_{\mathrm{a}}^{p}
\end{aligned} \tag{9.15}$$

This result represents the final outcome of the third analytical step of the proposed damage prognosis framework.

In order to gain computational feasibility within the probabilistic damage evolution analysis step, the conditional joint PDF of $\mathbf{A}_{\mathrm{a}}^{[p,q]}$ obtained from Equation (9.14) — i.e., $f_{\mathbf{A}_{\mathrm{a}}^{[p,q]}\left|\boldsymbol{\Theta}_{\mathrm{mat}},\boldsymbol{\Theta}_{\mathrm{dam}}^{p},\mathbf{A}_{\mathrm{a}}^{p}\right.}\left(\mathbf{a}_{\mathrm{a}}^{[p,q]}\left|\boldsymbol{\theta}_{\mathrm{mat}},\boldsymbol{\theta}_{\mathrm{dam}}^{p},\mathbf{a}_{\mathrm{a}}^{p}\right.\right)$ — can be approximated by its (conditional) expectation $E_{\mathbf{A}_{\mathrm{a}}^{[p,q]}}\left[\mathbf{a}_{\mathrm{a}}^{[p,q]}\left|\boldsymbol{\theta}_{\mathrm{mat}},\boldsymbol{\theta}_{\mathrm{dam}}^{p},\mathbf{a}_{\mathrm{a}}^{p}\right.\right]$, defined as

$$E_{\mathbf{A}_{\mathrm{a}}^{[p,q]}}\left[\mathbf{a}_{\mathrm{a}}^{[p,q]}\left|\boldsymbol{\theta}_{\mathrm{mat}},\boldsymbol{\theta}_{\mathrm{dam}}^{p},\mathbf{a}_{\mathrm{a}}^{p}\right.\right]= \int_{\mathbf{A}_{\mathrm{a}}^{[p,q]}}\mathbf{a}_{\mathrm{a}}^{[p,q]}\, f_{\mathbf{A}_{\mathrm{a}}^{[p,q]}\left|\boldsymbol{\Theta}_{\mathrm{mat}},\boldsymbol{\Theta}_{\mathrm{dam}}^{p},\mathbf{A}_{\mathrm{a}}^{p}\right.}\left(\mathbf{a}_{\mathrm{a}}^{[p,q]}\left|\boldsymbol{\theta}_{\mathrm{mat}},\boldsymbol{\theta}_{\mathrm{dam}}^{p},\mathbf{a}_{\mathrm{a}}^{p}\right.\right)d\mathbf{a}_{\mathrm{a}}^{[p,q]} \tag{9.16}$$

Equation (9.16) can be further expanded as

$$\begin{aligned} &E_{\mathbf{A}_{\mathrm{a}}^{[p,q]}}\left[\mathbf{a}_{\mathrm{a}}^{[p,q]}\left|\boldsymbol{\theta}_{\mathrm{mat}},\boldsymbol{\theta}_{\mathrm{dam}}^{p},\mathbf{a}_{\mathrm{a}}^{p}\right.\right]= \\ &\int_{\mathbf{A}_{\mathrm{a}}^{[p,q]}}\mathbf{a}_{\mathrm{a}}^{[p,q]}\, f_{\mathbf{A}_{\mathrm{a}}^{[p,q]}\left|\boldsymbol{\Theta}_{\mathrm{mat}},\boldsymbol{\Theta}_{\mathrm{dam}}^{p},\mathbf{A}_{\mathrm{a}}^{p}\right.}\left(\mathbf{a}_{\mathrm{a}}^{[p,q]}\left|\boldsymbol{\theta}_{\mathrm{mat}},\boldsymbol{\theta}_{\mathrm{dam}}^{p},\mathbf{a}_{\mathrm{a}}^{p}\right.\right)d\mathbf{a}_{\mathrm{a}}^{[p,q]}= \\ &\int_{\mathbf{A}_{\mathrm{a}}^{[p,q]}}\mathbf{a}_{\mathrm{a}}^{[p,q]}\left[\int_{\mathbf{IM}} f_{\mathbf{A}_{\mathrm{a}}^{[p,q]}\left|\boldsymbol{\Theta}_{\mathrm{mat}},\boldsymbol{\Theta}_{\mathrm{dam}}^{p},\mathbf{A}_{\mathrm{a}}^{p},\mathbf{IM}\right.}\left(\mathbf{a}_{\mathrm{a}}^{[p,q]}\left|\boldsymbol{\theta}_{\mathrm{mat}},\boldsymbol{\theta}_{\mathrm{dam}}^{p},\mathbf{a}_{\mathrm{a}}^{p},\mathbf{im}\right.\right) f_{\mathbf{IM}}\left(\mathbf{im}\right)d\mathbf{im}\right]d\mathbf{a}_{\mathrm{a}}^{[p,q]} \end{aligned} \tag{9.17}$$

and, by swapping the order of integration and making use of the result obtained in Equation (9.13), it is possible to rewrite the above equation as

$$\begin{aligned} E_{\mathbf{A}_{\mathrm{a}}^{[p,q]}}\left[\mathbf{a}_{\mathrm{a}}^{[p,q]}\left|\boldsymbol{\theta}_{\mathrm{mat}},\boldsymbol{\theta}_{\mathrm{dam}}^{p},\mathbf{a}_{\mathrm{a}}^{p}\right.\right] &= \int_{\mathbf{IM}}\left[\int_{\mathbf{A}_{\mathrm{a}}^{[p,q]}}\mathbf{a}_{\mathrm{a}}^{[p,q]}\,\delta\left(\mathbf{a}_{\mathrm{a}}^{[p,q]}-\overline{\mathbf{a}}_{\mathrm{a}}^{[p,q]}\right)d\mathbf{a}_{\mathrm{a}}^{[p,q]}\right] f_{\mathbf{IM}}\left(\mathbf{im}\right)d\mathbf{im} \\ &= \int_{\mathbf{IM}}\overline{\mathbf{a}}_{\mathrm{a}}^{[p,q]}\, f_{\mathbf{IM}}\left(\mathbf{im}\right)d\mathbf{im} \\ &= E_{\mathbf{IM}}\left[\overline{\mathbf{a}}_{\mathrm{a}}^{[p,q]}\right] \end{aligned} \tag{9.18}$$

In other words, the conditional expectation of $\left(\mathbf{A}_{\mathrm{a}}^{[p,q]}\middle|\boldsymbol{\theta}_{\mathrm{mat}},\boldsymbol{\theta}_{\mathrm{dam}}^{p},\mathbf{a}_{\mathrm{a}}^{p}\right)$, defined in Equation (9.16) is equal to the average, with respect to **IM**, of the output $\bar{\mathbf{a}}_{\mathrm{a}}^{[p,q]}$ obtained from the numerical integration of Equation (9.6), between current load cycle N_p and (future) load cycle $N_p^q = N_p + q\Delta N$. This result is conceptually shown in Figure 9.4 below. Each of the light-blue debonding propagation trajectories, shown in the figure, was obtained by numerically integrating Equation (9.6) for a given set of material and damage evolution model parameters and a given initial debonding length equal to 6.0 *mm*. The dashed red line represents instead the expected trajectory of debonding

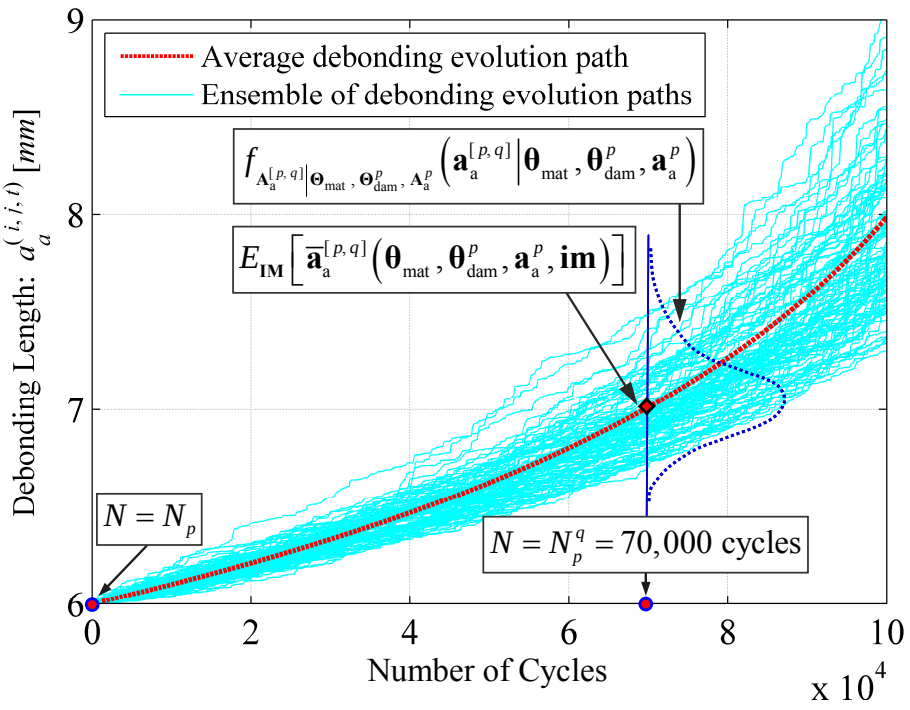

Figure 9.4: Illustrative example of an ensemble of debonding propagation trajectories obtained by integrating Equation (9.6) for a given/fixed set of material and damage evolution model parameters and a given initial debonding length. The dashed red line indicates the average debonding propagation trajectory computed numerically from the numerical time integration of the ODE in Equation (9.19)

propagation, computed by solving numerically the following system of ordinary differential equations (ODEs), with the same set/realization of material and damage evolution parameters:

$$\begin{cases} \dfrac{d}{dN} E_{\mathbf{IM}}\left[\overline{a}_a^{(1,1,[p,N])}\right] = E_{\mathbf{IM}}\left[\dfrac{C^{(i,1,p)}}{1-Q}\,\dfrac{\left(\Delta G^{(i,N)}\right)^{n^{(i,1,p)}}}{G_C^{(i,1,p)} - \tilde{G}_{\max}^{(i,N)}}\right] \\ \overline{a}_a^{(i,1,p)} = a_a^{(i,1,p)} = 6.0\ mm \end{cases} \qquad \left(N \geq 0 \text{ and } i = 1,2\right) \quad (9.19)$$

This approximation is reasonable and does not compromise the efficiency and accuracy of the other analysis steps of the proposed damage prognosis framework only for closely spaced NDE inspections (i.e., only when a continuous monitoring system is envisioned). In this case, the variability of $\left(\mathbf{A}_{\mathrm{a}}^{[p,q]} \middle| \boldsymbol{\theta}_{\mathrm{mat}}, \boldsymbol{\theta}_{\mathrm{dam}}^{p}, \mathbf{a}_{\mathrm{a}}^{p}\right)$, induced by the loading uncertainty, is kept within reasonable bounds and does not overcome the other sources of uncertainties involved in the prognosis process (e.g., damage evolution model parameters uncertainty, NDE measurement uncertainty, etc.).

9.2.3. Probability distribution functions assigned to the damage evolution model parameters $\boldsymbol{\Theta}_{\mathrm{dam}}^{0}$

As anticipated in Section 9.2.2, at each of the two damage locations shown in Figure 9.2, there are three damage evolution model parameters involved in the propagation process governed by the system of ODEs introduced in Equation (9.6). Parameters $C^{(1,1,p)}$, $n^{(1,1,p)}$, and $G_C^{(1,1,p)}$ at *damage location 1* and parameters $C^{(2,1,p)}$, $n^{(2,1,p)}$, and $G_C^{(2,1,p)}$ at *damage location 2*. The first triplet of damage evolution model

parameters is collected in $\boldsymbol{\Theta}_{\text{dam}}^{(1,p)}$ as $\boldsymbol{\Theta}_{\text{dam}}^{(1,p)} = \left\{ C^{(1,1,p)}, n^{(1,1,p)}, G_C^{(1,1,p)} \right\}$, while the second triplet is grouped in $\boldsymbol{\Theta}_{\text{dam}}^{(2,p)}$ as $\boldsymbol{\Theta}_{\text{dam}}^{(2,p)} = \left\{ C^{(2,1,p)}, n^{(2,1,p)}, G_C^{(2,1,p)} \right\}$. The vectors $\boldsymbol{\Theta}_{\text{dam}}^{(1,p)}$ and $\boldsymbol{\Theta}_{\text{dam}}^{(2,p)}$ are assumed to be statistically independent; a reasonable assumption already discussed and explained in Chapter 3. Additionally, for the sake of simplicity, the three damage evolution parameters collected in $\boldsymbol{\Theta}_{\text{dam}}^{(1,0)}$ and $\boldsymbol{\Theta}_{\text{dam}}^{(2,0)}$ (at initial time $N_0 = 0$ cycles) are considered mutually statistically independent. In reality, as shown later on in Section 9.3, $C^{(i,1,p)}$ and $n^{(i,1,p)}$ $\left(\text{with } i = 1,2 \text{ and } p \geq 0\right)$ are generally statistically correlated; however, within the limited scope of this particular application example presented in this section, considering $C^{(i,1,0)}$, $n^{(i,1,0)}$, and $G_C^{(i,1,0)}$ $\left(\text{with } i = 1,2\right)$ to be statistically independent does not represent a crucial assumption towards the verification and validation of the proposed recursive Bayesian updating scheme and probabilistic damage evolution analysis step.

Parameter $C^{(i,1,0)}$ $\left(\text{with } i = 1,2\right)$ is assumed to follow a Normal distribution with mean equal to $E\left[C^{(i,1,0)} \right] = \mu_{C^{(i,1,0)}} = 0.04$ and a coefficient of variation of 10%. Parameter $n^{(i,1,0)}$ $\left(\text{with } i = 1,2\right)$ is considered to be uniformly distributed between a lower bound of 2.7 and an upper bound of 3.1 — i.e., $n^{(i,1,0)} \sim U\left(2.7, 3.1\right)$. Finally, the critical fracture energy $G_C^{(i,1,0)}$ $\left(\text{with } i = 1,2\right)$ is modeled as a random variable normally distributed with mean equal to $E\left[G_C^{(i,1,0)} \right] = \mu_{G_C^{(i,1,0)}} = 1.50\ N/mm$ and a coefficient of variation of 10%.

9.2.4. Effect screening of material and damage evolution model parameters

The material parameter $P_1 = E_{11}^f$, introduced at the beginning of Section 9.2, and the three damage evolution model parameters $P_2 = n^{(i,1,p)}$, $P_3 = G_C^{(i,1,p)}$, and $P_4 = C^{(i,1,p)}$, introduced in Equation (9.6) and briefly discussed in Section 9.2.3, do not equally contribute to the total variability of the rate of debonding propagation denoted by $d\overline{a}_a^{(i,1,[p,N])}/dN$ (with $N \geq N_p$). The relative contribution of each of these four parameters (P_k, $k = 1, 2, 3, 4$) to the total variability of the response quantity of interest, at time $N \geq N_p$, can be measured through the so-called correlation ratio (Kenney and Keeping, 1951) herein denoted as $\eta^2_{[p,N]}(P_k)$ and based on the posterior PDFs of the damage evolution parameter computed at time $N = N_p$. Based on these considerations, it is evident that the relative contribution of each parameter can vary in time and therefore, in a real-world scenario, this process of effect screening should be performed multiple times during the monitoring process in order to account for the effects induced by the changes in the posterior PDFs of the damage evolution parameters (which are recursively updated every time new NDE data become available). At initial time, $N_0 = 0$ cycles, the correlation ratio $\eta^2_{[p=0,N=0]}(P_k)$ is expressed as

$$\eta^2_{[0,0]}(P_k) = \frac{Var\left(E\left[\frac{d\overline{a}_a^{(i,1,0)}}{dN} \middle| P_k \right] \right)}{Var\left(\frac{d\overline{a}_a^{(i,1,0)}}{dN} \right)}, \quad k = 1, 2, 3, 4 \tag{9.20}$$

and is numerically computed by using the initial prior PDFs of material and damage evolution model parameters presented at the beginning of Section 9.2 and in Section 9.2.3. The numerator of the right-hand-side (RHS) of Equation (9.20) denotes the so-called *explained variance* of the rate of debonding propagation at time $N_0 = 0$ cycles, while the denominator represents the total variance of the rate of debonding propagation at time $N_0 = 0$ cycles. A large value of $\eta^2_{[p=0,N=0]}(P_k)$, relative to the other values obtained, indicates that the corresponding parameter P_k is significant to control how the response quantity of interest varies (i.e., the rate of debonding propagation in this specific case). Figure 9.5 shows the relative contribution of each of the three damage evolution parameters ($C^{(i,1,0)}$, $n^{(i,1,0)}$, and $G_C^{(i,1,0)}$) and of the material model

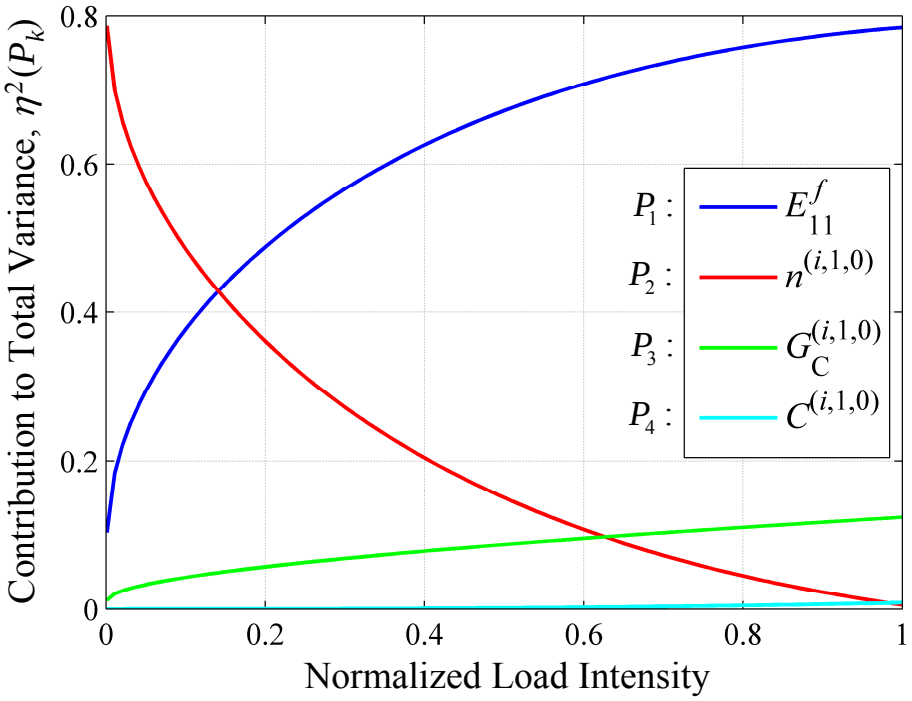

Figure 9.5: Marginal contribution (at $N_0 = 0$) of each random parameter to the total variability of the rate of debonding propagation as a function of the load intensity.

parameter (E_{11}^{f}) to the total variability of $d\bar{a}_a^{(i,1,[0,0])}/dN$. These contributions are plotted as a function of the applied load, normalized with respect to the maximum load that the composite beam can take before the disbond front starts propagating unstably (see Appendix F). Figure 9.5 indicates that the contribution of $C^{(i,1,0)}$ to the total variability of $d\bar{a}_a^{(i,1,[0,0])}/dN$ is negligible and therefore can be replaced by its mean value $E\left[C^{(i,1,0)}\right]=\mu_{C^{(i,1,0)}}=0.04$ during the subsequent analyses. Similarly, $G_C^{(i,1,0)}$ contributes less than 10% to the total variance of $d\bar{a}_a^{(i,1,[0,0])}/dN$ within the load range of interest in fatigue-driven damage growth analyses (i.e., for load levels not exceeding 50% of the critical/maximum load). Due to this fact, it will be challenging to update the PDF of $G_C^{(i,1,0)}$ through the proposed recursive Bayesian updating scheme. Furthermore, Figure 9.5 also suggests that the contributions of E_{11}^{f} and $n^{(i,1,0)}$ are directly and inversely proportional to the load level intensity, respectively; an expected result since the higher the load intensity the higher the tendency to have a sudden and unstable propagation of the debonding front. (i.e., a mode of propagation which is not controlled by the fatigue damage parameters $C^{(i,1,0)}$, $n^{(i,1,0)}$, and $G_C^{(i,1,0)}$).

9.2.5. NDE technique detection capability and measurement accuracy

The detection capability of a given NDE technique is probabilistically characterized through its probability of detection (*POD*) curve, while the measurement accuracy is quantified by using a sizing model. An exhaustive discussion of these two important aspects of a given NDE technique is provided in Chapter 3 and in Section

8.3.1 of Chapter 8, where the *POD* curve model proposed by Berens (1989) and the damage size measurement model used by Zhang and Mahadevan (2001) are presented and discussed. The *POD* curve model proposed by Berens is expressed as

$$POD\left(a_a^{(i,j,p)}\right)=\frac{e^{-\alpha_0^{(i,j)}+\alpha_1^{(i,j)}\ln\left[a_a^{(i,j,p)}\right]}}{1+e^{-\alpha_0^{(i,j)}+\alpha_1^{(i,j)}\ln\left[a_a^{(i,j,p)}\right]}} \quad \left(i=1,2 \text{ and } j=1\right) \tag{9.21}$$

where the values of the model parameters, $\alpha_0^{(i,j)}$ and $\alpha_1^{(i,j)}$, are estimated through logistic regression analysis (Kutner, 2004). These estimates are denoted as $\hat{\alpha}_0^{(i,j)}$ and $\hat{\alpha}_1^{(i,j)}$, and, for the particular application example presented in this section, they are assigned the following values: $\hat{\alpha}_0^{(1,1)}=\hat{\alpha}_0^{(2,1)}=\hat{\alpha}_0=0.3$ and $\hat{\alpha}_1^{(1,1)}=\hat{\alpha}_1^{(2,1)}=\hat{\alpha}_1=2.0$. The substitution of these two estimates into Equation (9.21) generates the *POD* curve shown in Figure 9.6 .

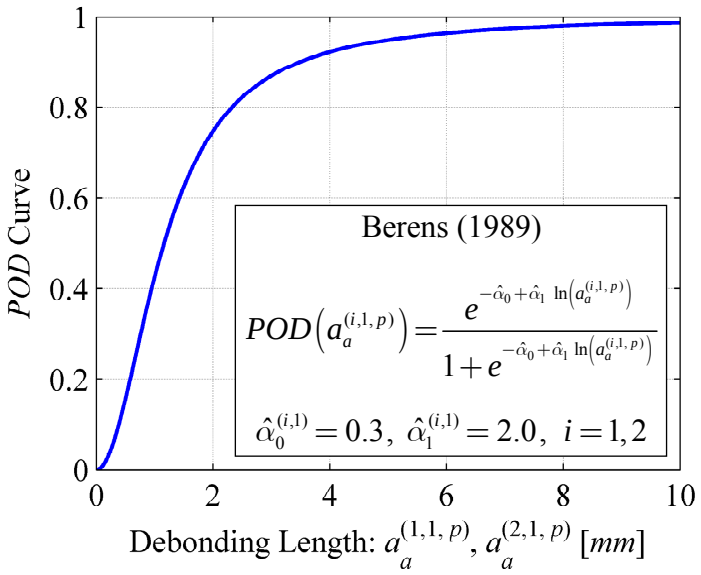

Figure 9.6: *POD* curve model found in the literature (Berens, 1989) and used in the application examples presented in Section 9.2 and Section 9.3.

Once damage is detected (D) and its extent measured, it is natural to question the accuracy of that NDE measurement conditional on the actual (but unknown) damage size. This accuracy is herein quantified through the linear damage-size measurement model reported in Figure 9.7 and expressed as

$$A_m^{(i,j,p)}\left(A_a^{(i,j,p)}=a_a^{(i,j,p)},D\right)=\beta_0^{(i,j)}+\beta_1^{(i,j)}\,a_a^{(i,j,p)}+\varepsilon_{ij} \quad \left(i=1,2 \text{ and } j=1\right) \qquad (9.22)$$

where $A_a^{(i,j,p)}$ and $A_m^{(i,j,p)}$ are respectively the actual and measured damage sizes for damage location i, damage mechanism j, and inspection time t_p. The quantity $a_a^{(i,j,p)}$ denotes the value of the actual damage size for the particular (i,j,p) combination considered. The two terms $\beta_0^{(i,j)}$ and $\beta_1^{(i,j)}$ are the coefficients of the (assumed) linear

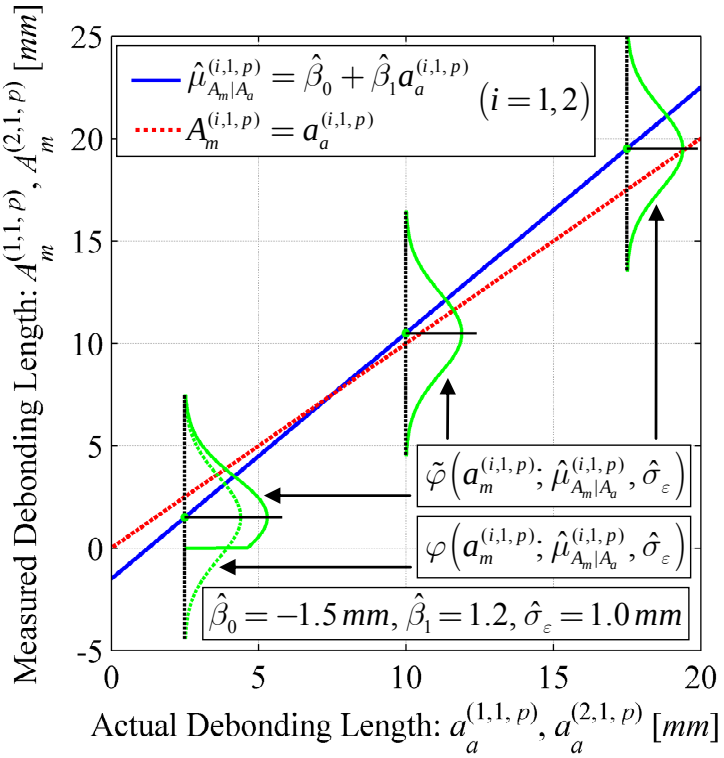

Figure 9.7: Damage size measurement model (Zhang and Mahadevan, 2001).

model accounting for the systematic measurement errors. Finally, $\varepsilon_{ij} \sim N\left(0, \sigma_{\varepsilon_{ij}}\right)$ represents the random measurement error Gaussian distributed with zero-mean and standard deviation $\sigma_{\varepsilon_{ij}}$, herein assumed — for the sake of simplicity — to be constant and independent of $a_a^{(i,j,p)}$ (Zhang and Mahadevan, 2001). The estimates (obtained from linear regression analysis; Seber and Lee, 2003) for $\beta_0^{(i,j)}$, $\beta_1^{(i,j)}$, and $\sigma_{A_m|A_a}^{(i,j,p)} = \sigma_{\varepsilon_{ij}}$ are denoted as $\hat{\beta}_0^{(i,j)}$, $\hat{\beta}_1^{(i,j)}$ and $\hat{\sigma}_{\varepsilon_{ij}}$, and — for the particular application example discussed here — are assumed to be equal to: $\hat{\beta}_0^{(1,1)} = \hat{\beta}_0^{(2,1)} = \hat{\beta}_0 = -1.5\,mm$, $\hat{\beta}_1^{(1,1)} = \hat{\beta}_1^{(2,1)} = \hat{\beta}_1 = 1.2$, and $\hat{\sigma}_{\varepsilon_{11}} = \hat{\sigma}_{\varepsilon_{21}} = \hat{\sigma}_{\varepsilon} = 1.0\,mm$.

9.2.6. Underlying (true) debonding evolution trajectories, assumed NDE inspection opportunities, and random NDE measurement generation

In order to be able to apply the proposed prognosis framework to the benchmark structure shown in Figure 9.2, two underlying (true) debonding propagation trajectories (i.e., one at each damage location) must be generated. These two trajectories are generated by numerically integrating the system of ODEs introduced earlier in Equation (9.6) with a given pair of initial debonding lengths ($a_{a,\text{true}}^{(1,1,0)} = 6.0\,mm$, $a_{a,\text{true}}^{(2,1,0)} = 7.0\,mm$), a given set of true material and damage evolution parameters (as listed above), and a randomly generated loading time history according to the procedure discussed in Section 9.2.1. The pair of underlying (true) propagation trajectories, together with the initial debonding lengths and the (assumed) true values of material and damage evolution model parameters, is shown in Figure 9.8.

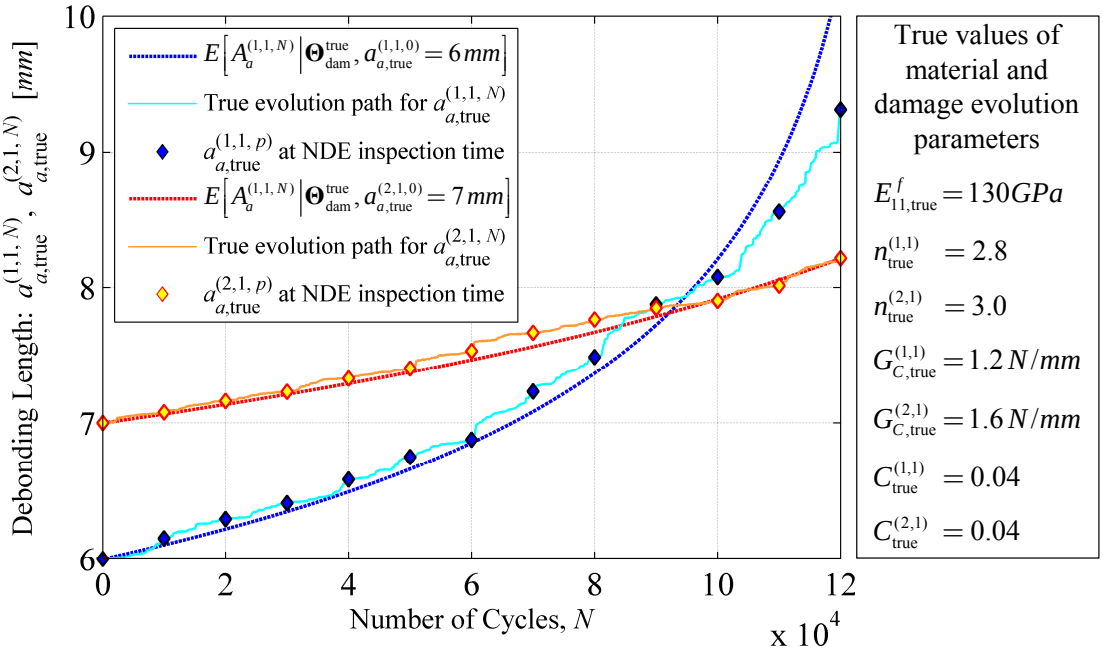

Figure 9.8: Underlying (true) debonding propagation trajectories at *damage location 1* and *damage location 2*, generated by numerically integrating Equation (9.6) with a given pair of initial debonding lengths ($a_{a,\text{true}}^{(1,1,0)} = 6.0\,mm$, $a_{a,\text{true}}^{(2,1,0)} = 7.0\,mm$) and a given set of true material and damage evolution parameters (as listed above).

The two debonding propagation trajectories, $a_{a,\text{true}}^{(1,1,N)}$ and $a_{a,\text{true}}^{(2,1,N)}$ (with $0 \le N \le 120{,}000$ cycles), depicted in Figure 9.8 are then used to randomly generate NDE measurements, $\mathbf{A}_{\text{m}}^{(1,1,p)}$ and $\mathbf{A}_{\text{m}}^{(2,1,p)}$, at evenly spaced intervals. In this specific application example, a total of forty-eight NDE inspections (evenly spaced every $\Delta N = 2{,}500$ load cycles) are considered and, at each NDE inspection opportunity, two different scenarios are envisioned. In the first scenario, five statistically independent NDE measurements are taken and processed using the proposed Bayesian inference scheme. In the second scenario, ten statistically independent NDE measurements are considered and used to repeatedly compute the posterior PDFs of

$\mathbf{A}_a^p$ and $\mathbf{\Theta}_{\text{dam}}^p$. Furthermore, the two sets of (randomly generated) measurements are mutually statistically independent. The procedure to generate a single NDE measurement corresponding to damage location *i*, damage mechanism *j*, at time N_p (i.e., the inspection time at which the true underlying damage size is denoted by $a_{a,\text{true}}^{(i,j,p)}$) can be summarized as follows:

1) Generate a random number, u_1, from a uniform distribution between 0 and 1 — i.e., $u_1 \sim U(0,1)$;

2) If $u \geq POD\left(a_{a,\text{true}}^{(i,j,p)}\right)$ then set $a_m^{(i,j,p)_{a,\text{true}}} = 0$ (i.e., damage not detected);

3) If $u < POD\left(a_{a,\text{true}}^{(i,j,p)}\right)$ (i.e., damage detected) generate another random number, u_2, from a Normal distribution with mean $\mu_{u_2} = \hat{\beta}_0^{(i,j)} + \hat{\beta}_1^{(i,j)} a_{a,\text{true}}^{(i,j,p)}$ and standard deviation $\sigma_{u_2} = \sigma_{\varepsilon_{ij}}$ — i.e., $u_2 \sim N\left(\hat{\beta}_0^{(i,j)} + \hat{\beta}_1^{(i,j)} a_{a,\text{true}}^{(i,j,p)}, \sigma_{\varepsilon_{ij}}\right)$. Then set $a_m^{(i,j,p)_{a,\text{true}}} = u_2$.

The same procedure is repeated to generate a whole series of statistically independent NDE measurements for any (i, j, p) combination.

9.2.7. Bayesian updating results

This section presents a selection of the Bayesian updating results obtained through the proposed recursive Bayesian inference scheme presented in Chapter 3. Within this scheme, the debonding extents, $A_a^{(1,1,p)}$ and $A_a^{(2,1,p)}$, and the damage evolution model parameters, $n^{(i,1,p)}$ and $G_C^{(i,1,p)}$ $\left(\text{with } i = 1,2\right)$, are simultaneously

updated after each NDE inspection. The Bayesian updating results presented herein cover the time window $0 \leq N \leq 85{,}000$ load cycles and therefore, since the time between two subsequent NDE inspections is set to be equal to $\Delta N = 2{,}500$ cycles, a total of thirty-five NDE inspections are involved in this specific numerical example.

Figure 9.9 reports the posterior marginal PDFs of the debonding extents $A_a^{(1,1,p)}$ (top row) and $A_a^{(2,1,p)}$ (bottom row) computed after the NDE inspections at times $N_0 = 0$ cycles, $N_{14} = 35{,}000$ cycles, and $N_{34} = 85{,}000$ cycles — i.e., immediately

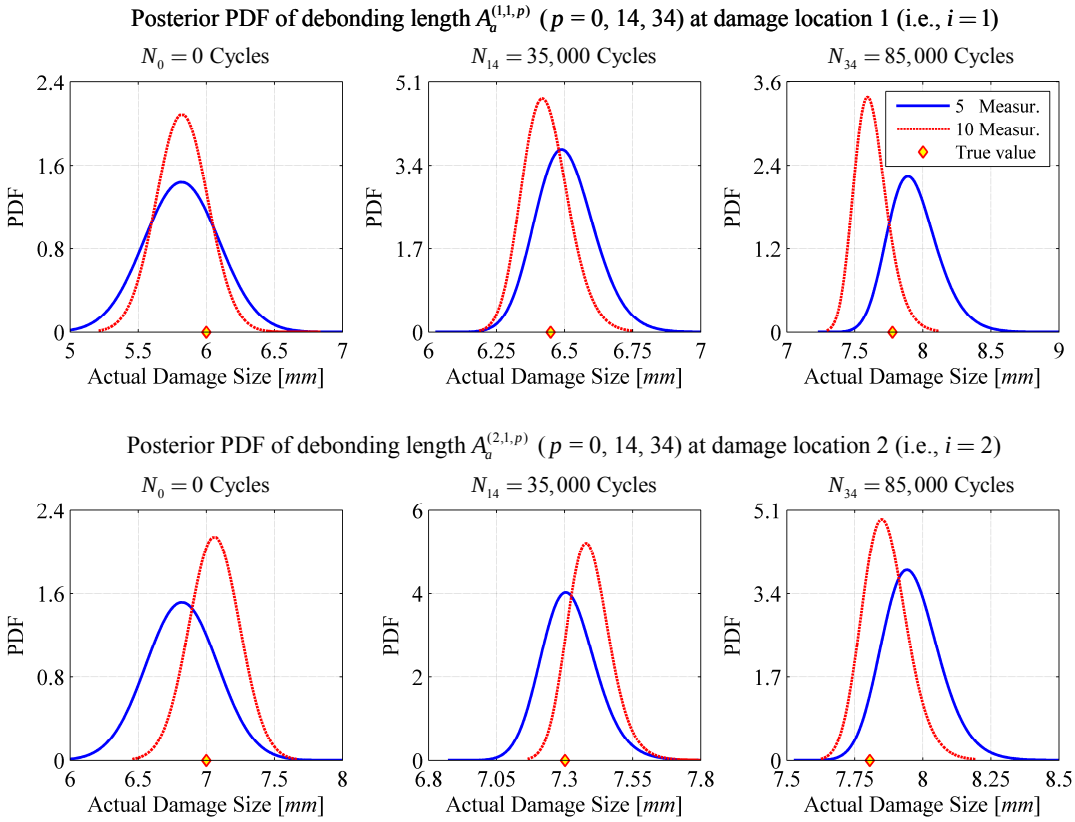

Figure 9.9: Posterior marginal PDFs of debonding lengths at *damage location 1* and *damage location 2* after three (selected) NDE inspections at times $N_0 = 0$ cycles, $N_{14} = 35{,}000$ cycles, and $N_{34} = 85{,}000$ cycles.

after the first, fifteenth, and thirty-fifth inspections. These results were obtained by assigning to $A_a^{(1,1,0)}$ and $A_a^{(2,1,0)}$ the same initial prior PDF used in Chapter 8, namely the scaled Beta distribution shown in Figure 8.9. Similarly to the results obtained in Chapter 8, Figure 9.9 also indicates that a larger set of NDE measurements allows for a better collocation/centering of the computed posterior marginal PDFs of $A_a^{(1,1,p)}$ and $A_a^{(2,1,p)}$ on the true debonding lengths $a_{a,\text{true}}^{(1,1,p)}$ and $a_{a,\text{true}}^{(2,1,p)}$, respectively.

With focus on the Bayesian updating results for the two pairs of damage evolution model parameters, $n^{(i,1,p)}$ and $G_C^{(i,1,p)}$ $\left(\text{with } i=1,2\right)$, it is observed (see

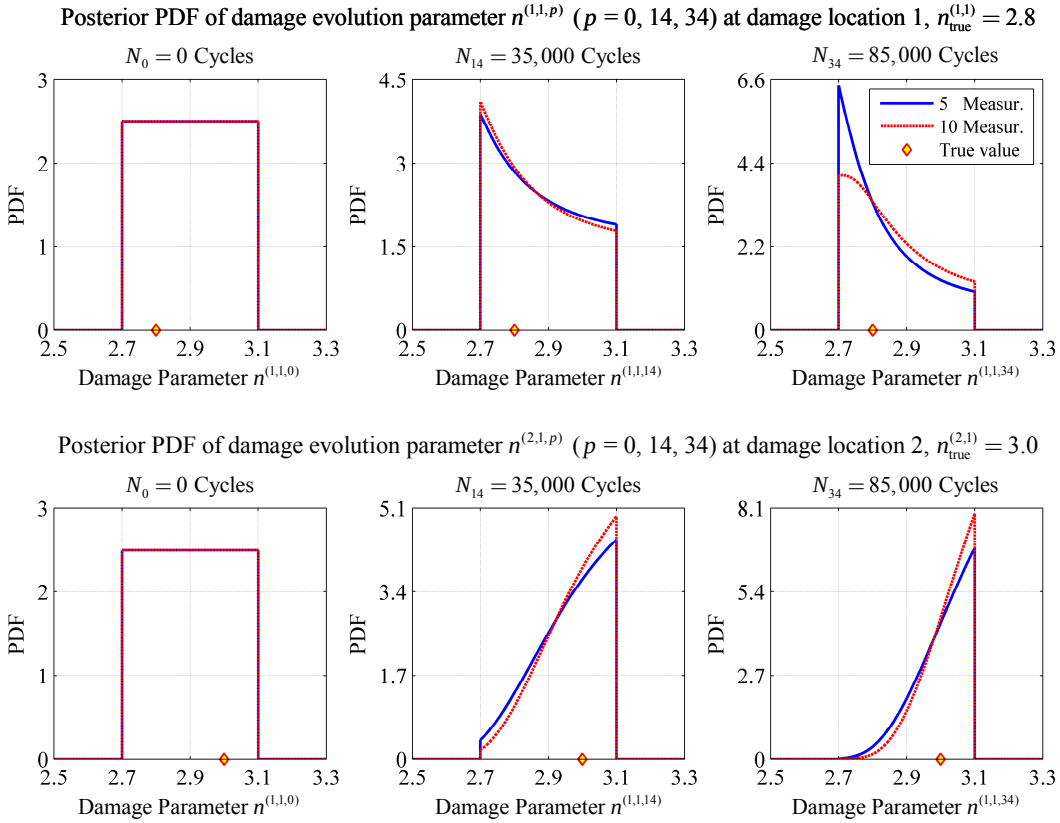

Figure 9.10: Posterior marginal PDFs of damage parameter $n^{(i,1,p)}$ at *damage location 1* ($i=1$) and *damage location 2* ($i=2$) after three (selected) NDE inspections at times $N_0 = 0$ cycles, $N_{14} = 35{,}000$ cycles, and $N_{34} = 85{,}000$ cycles.

Figure 9.10) that the posterior marginal PDFs of $n^{(i,1,p)}$ $\left(\text{with } p=0,14,34\right)$ correctly converge towards the true values of the parameters, $n_{\text{true}}^{(1,1)}=2.8$ and $n_{\text{true}}^{(1,1)}=3.0$, at both damage locations. However, the rate of convergence is sensibly slower than the one observed in the previous application example in Chapter 8; a fact which can be explained by the explicit consideration of loading uncertainty and by the lager number of damage evolution parameters involved in the debonding propagation phase. On the other hand, the proposed recursive Bayesian updating scheme is not able to reduce the uncertainty associated with the other damage model evolution parameter, the critical

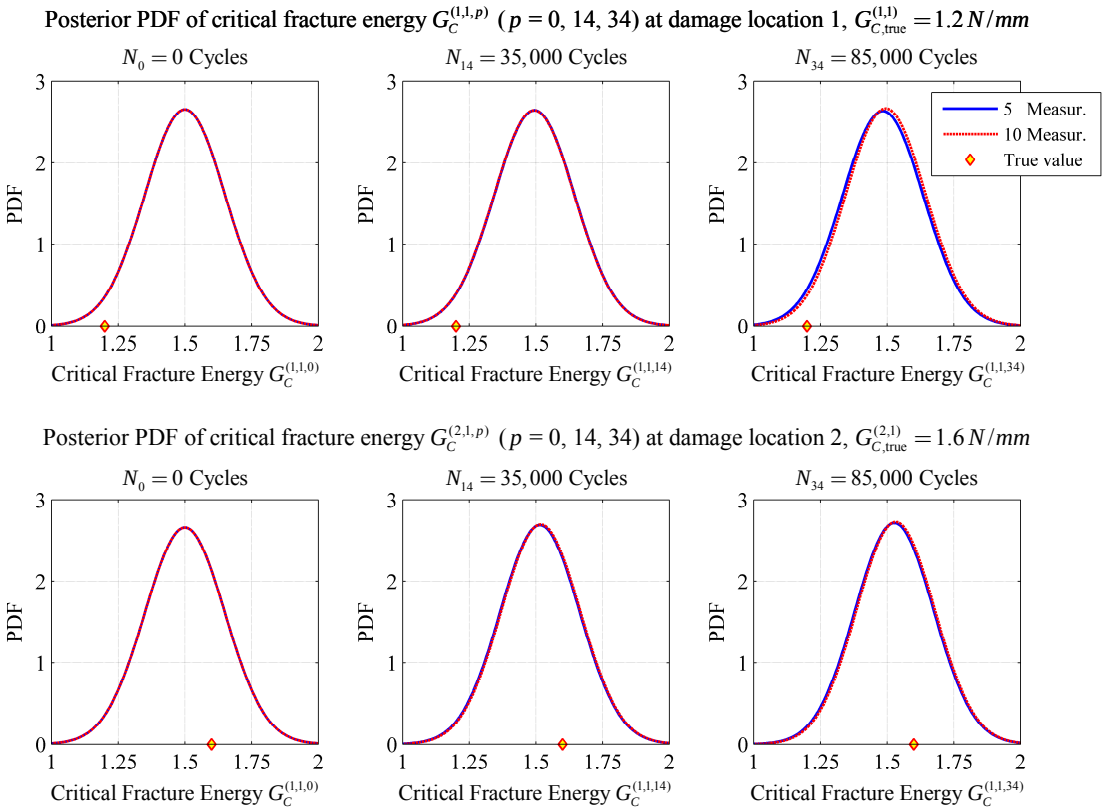

Figure 9.11: Posterior marginal PDFs of critical fracture energy, $G_C^{(i,1,p)}$, at *damage location 1* ($i=1$) and *damage location 2* ($i=2$) after three (selected) NDE inspections at times $N_0=0$ cycles, $N_{14}=35{,}000$ cycles, and $N_{34}=85{,}000$ cycles.

fracture energy of the adhesive interface $G_C^{(i,1,p)}$ $\left(\text{with } i=1,2\right)$; a direct consequence of the results discussed earlier in Section 9.2.4 and shown in Figure 9.5. Finally, it is worth emphasizing that, also in this second case study presented in the thesis, the damage propagation law is considered in a deterministic fashion and only the damage evolution parameters are treated as random variables. A more general analysis approach would also consider uncertain the damage propagation model; a case that could be handled using *Bayesian model class selection* (Ching and Chen, 2007).

9.3. Validation of proposed recursive Bayesian inference and probabilistic damage evolution analysis steps using experimental fatigue test data

In this section a set of experimental fatigue test data available in the literature (Virkler *et al.*, 1979) is used to provide a first experimental validation of the proposed damage prognosis framework, with special emphasis on the recursive Bayesian inference scheme and the probabilistic damage evolution analysis step. The dataset used consists of 68 crack propagation trajectories, each of them containing 164 measurement points, obtained from fatigue tests performed on center-cracked 2024-T3 aluminum plates. All the specimens tested had the same geometry: length $L=558.80\,mm$, width $w=152.40\,mm$, thickness $t=2.54\,mm$, and a center crack of initial length $2a_a^0=18.00\,mm$. The tests were performed at room temperature and under load control using a sinusoidal input at $20\,Hz$ producing a constant stress range of $\Delta\sigma=48.28\,MPa$ with a stress ratio equal to $R_\sigma=\sigma_{\min}/\sigma_{\max}=0.2$. The 68 crack propagation trajectories, together with a simple scheme of the test specimen geometry,

are provided in Figure 9.12. Among these 68 trajectories, two sample trajectories are selected and are conveniently highlighted in Figure 9.12: *Sample trajectory #1* (already selected by Ostergaard and Hillberry, 1983) and *Sample trajectory #2*. These 2 trajectories, similarly to the approach followed in Section 8.4 of Chapter 8 and in Section 9.2.6 of the current chapter, will later be used as true underlying crack propagation paths in the application of the proposed damage prognosis framework.

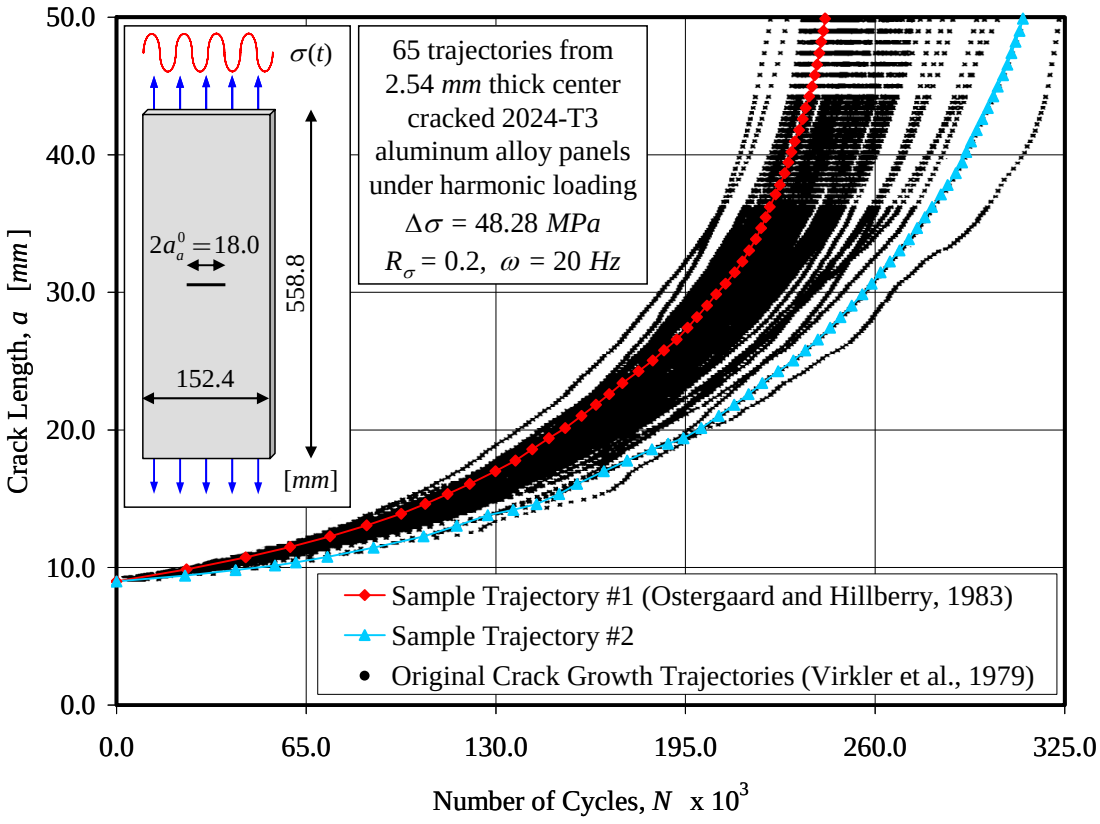

Figure 9.12: Crack propagation trajectories obtained from fatigue tests performed on center-cracked aluminum plates (Virkler *et al.*, 1979).

Kotulski (1998) curve fitted each of the 68 crack propagation trajectories obtained by Virkler with the well-known Paris law (Paris and Erdogan, 1963):

$$\frac{da}{dN} = C\left(\Delta K\right)^{m} \tag{9.23}$$

where da/dN, expressed in $mm/cycle$, represents the rate of crack propagation; C and m are the material constants to be determined by curve fitting each of the experimental trajectory with Equation (9.23); the quantity ΔK, expressed in $MN \cdot mm^{3/2}$, denotes the range of the stress intensity factor at the crack-tip within a given load cycle and can be mathematically expressed as

$$\Delta K = \sqrt{\pi a}\, \Delta\sigma\, F\left(\frac{a}{w}\right) \tag{9.24}$$

where the geometric correction factor $F\left(a/w\right)$ takes the form

$$F\left(\frac{a}{w}\right) = \frac{1}{\sqrt{\cos\left(\pi \frac{a}{w}\right)}}, \qquad \frac{a}{w} \leq 0.85 \tag{9.25}$$

and, according to Sanford (2003), this secant approximation for $F\left(a/w\right)$, proposed by Fedderson (1966), well matches the more exact result for $F\left(a/w\right)$, proposed by Brown and Srawley (1966) and based on previous research by Isida (1966). The curve fitting of each of the 68 trajectories in Figure 9.12 can be performed through linear regression analysis by conveniently recasting Equation (9.23) in the following form:

$$\ln\left(\frac{da}{dN}\right) = \ln\left(C\right) + m \cdot \ln\left(\Delta K\right) \tag{9.26}$$

The results obtained by fitting (through simple linear regression analysis; Seber and Lee, 2003) the two sample trajectories highlighted in Figure 9.12 with Equation (9.26)

are shown in Figure 9.13 and Figure 9.14. The estimated Paris law parameters (C and m), obtained from these two independent linear regressions, will later be used as true values of the damage evolution model parameter to verify and validate the proposed recursive Bayesian inference scheme and assess its robustness and effectiveness. The straight-line regression of the *sample trajectory #1* (Ostergaard and Hillberry, 1983), shown in Figure 9.13, yielded to $\ln C_{\text{true}}^{\#1} = -26.7949$ and $m_{\text{true}}^{\#1} = 2.9855$. On the other hand, the linear regression analysis on the experimental data point belonging to the *sample trajectory #2*, shown in Figure 9.14, led to $\ln C_{\text{true}}^{\#2} = -26.7528$ and $m_{\text{true}}^{\#2} = 2.9358$.

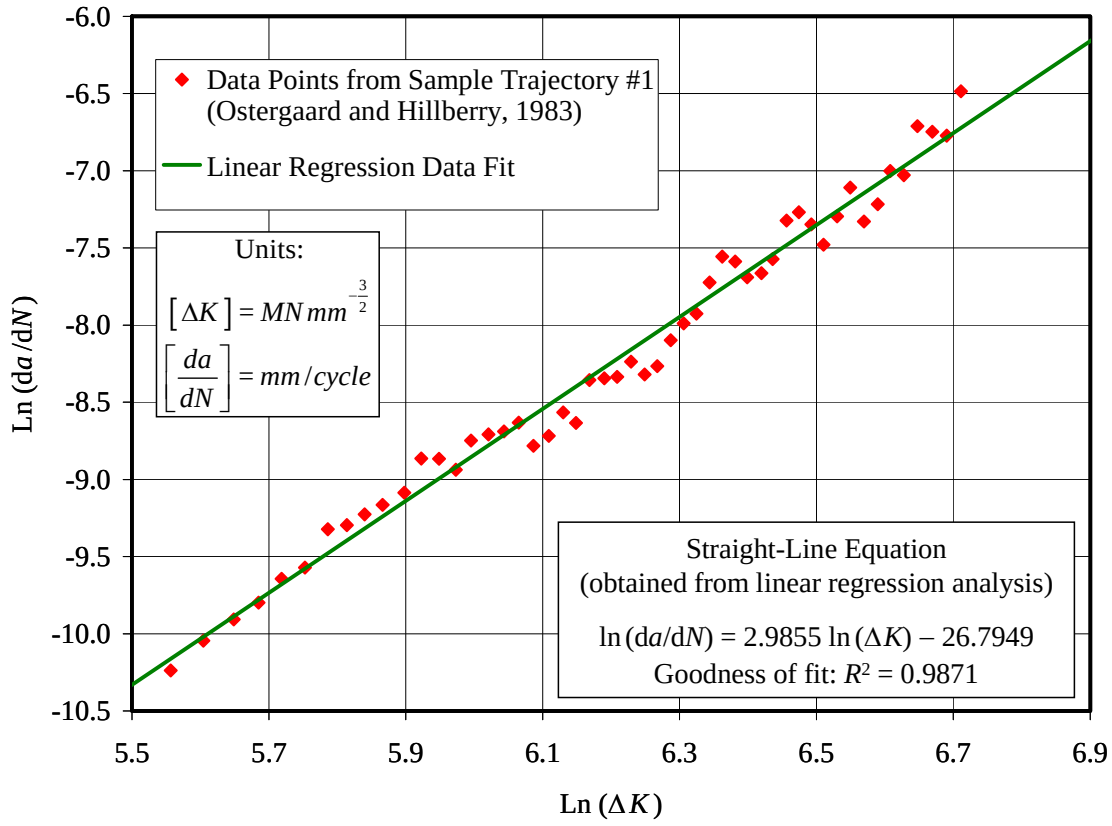

Figure 9.13: Linear regression on data points from experimental sample trajectory #1.

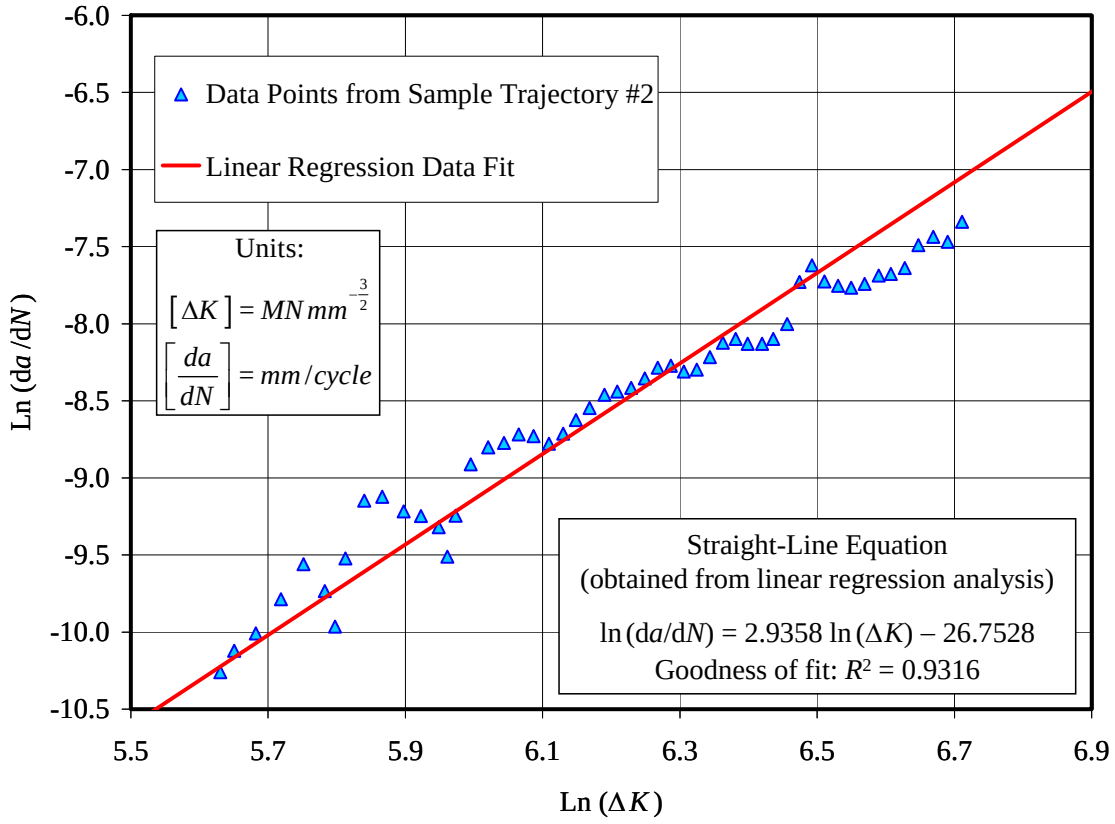

Figure 9.14: Linear regression on data points from experimental sample trajectory #2.

9.3.1. Initial prior PDFs of crack length, a_a^0, and damage evolution model parameters, $\boldsymbol{\Theta}_{\mathbf{dam}}^{\mathbf{0}}$, at time $N_0 = 0$ cycles

The whole recursive Bayesian inference scheme proposed in this thesis, as any other Bayesian inference procedure, needs to be provided with the initial prior distributions of the crack length, a_a^0, and the damage evolution model parameters, $\boldsymbol{\Theta}_{\text{dam}}^0$, at time $N_0 = 0$ cycles. These two initial prior PDFs are denoted as $f'_{A_a^0}\left(a_a^0\right)$ and, $f'_{\boldsymbol{\Theta}_{\text{dam}}^0}\left(\boldsymbol{\theta}_{\text{dam}}^0\right)$ respectively; furthermore, a_a^0 and $\boldsymbol{\Theta}_{\text{dam}}^0$ are reasonably considered to be

statistically independent at time $N_0 = 0$ cycles (see Chapters 2 and 3). The initial crack length, a_a^0, is assumed to be distributed according to the scaled Beta distribution defined as

$$f'_{A_a^0}\left(a_a^0\right) = \frac{1}{w} Beta\left(\frac{a_a^0}{w}, \alpha, \beta\right), \quad 0 \le \frac{a_a^0}{w} \le w \tag{9.27}$$

in which $w = 152.4\,mm$ denotes the width of the center-cracked aluminum plate, while $Beta\left(\left(a_a^0/w\right), \alpha, \beta\right)$ indicates the Beta PDF expressed as

$$Beta\left(\frac{a_a^0}{w}, \alpha, \beta\right) = \frac{1}{B(\alpha,\beta)}\left(\frac{a_a^0}{w}\right)^{\alpha-1}\left[1-\left(\frac{a_a^0}{w}\right)\right]^{\beta-1}, \quad 0 \le \frac{a_a^0}{w} \le 1 \tag{9.28}$$

with the term $B(\alpha,\beta)$ representing the Beta function defined earlier in Equation (9.5).

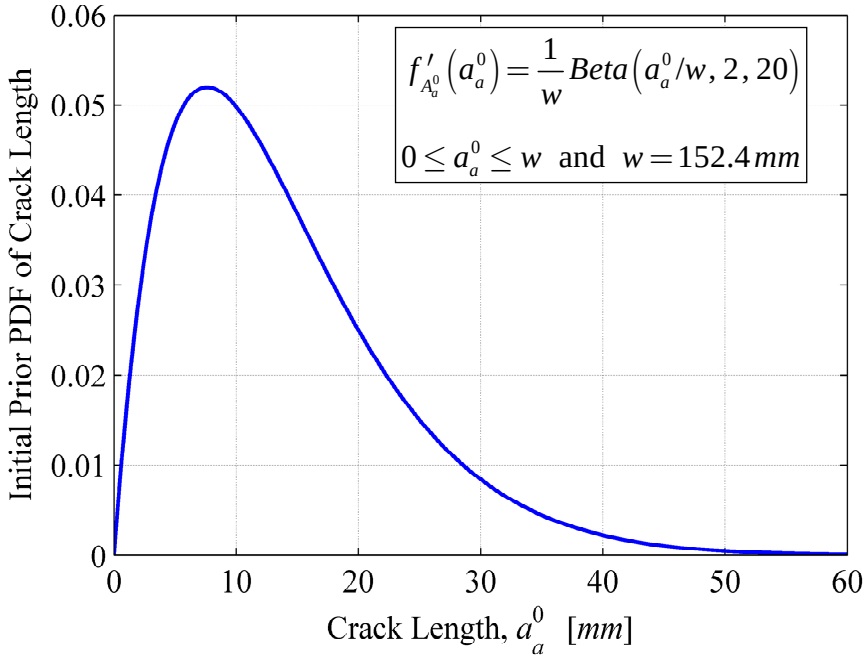

Figure 9.15: Initial prior PDF of crack length at time $N_0 = 0$ cycles.

On the other hand, the damage evolution model parameter vector, immediately after the NDE inspection at time N_p, is herein defined as $\boldsymbol{\Theta}_{\text{dam}}^{p} = \left\{\ln C^{p}, m^{p}\right\}^{\text{T}}$. Consequently, the corresponding prior and posterior joint PDFs, at time N_p, are denoted by $f'_{\boldsymbol{\Theta}_{\text{dam}}^{p}}\left(\boldsymbol{\theta}_{\text{dam}}^{p}\right) = f'_{\ln C^{p},\, m^{p}}\left(\ln C^{p}, m^{p}\right)$ and $f''_{\boldsymbol{\Theta}_{\text{dam}}^{p}}\left(\boldsymbol{\theta}_{\text{dam}}^{p}\right) = f''_{\ln C^{p},\, m^{p}}\left(\ln C^{p}, m^{p}\right)$, respectively. Furthermore, at time $N_0 = 0$ cycles, these two joint PDFs are logically rewritten as $f'_{\boldsymbol{\Theta}_{\text{dam}}^{0}}\left(\boldsymbol{\theta}_{\text{dam}}^{0}\right) = f'_{\ln C^{0},\, m^{0}}\left(\ln C^{0}, m^{0}\right)$ and $f''_{\boldsymbol{\Theta}_{\text{dam}}^{0}}\left(\boldsymbol{\theta}_{\text{dam}}^{0}\right) = f''_{\ln C^{0},\, m^{0}}\left(\ln C^{0}, m^{0}\right)$, respectively. Based on Kotulski's work (1998), the random variable $\ln C^{0}$ is considered to be normally distributed with mean $E\left[\ln C^{0}\right] = \mu_{\ln C^{0}} = -26.155$ and variance $Var\left[\ln C^{0}\right] = \sigma^{2}_{\ln C^{0}} = 0.939$; similarly, also the variable m^{0} was found to follow a Normal distribution with mean $E\left[m^{0}\right] = \mu_{m^{0}} = 2.874$ and variance $Var\left[m^{0}\right] = \sigma^{2}_{m^{0}} = 0.0274$. Herein, $\ln C^{0}$ and m^{0} are assumed to be jointly Normal with mean vector defined as $E\left[\boldsymbol{\Theta}_{\text{dam}}^{0}\right] = \mu_{\boldsymbol{\Theta}_{\text{dam}}^{0}} = \left\{E\left[\text{Ln}\left(C^{0}\right)\right], E\left[m^{0}\right]\right\}^{\text{T}} = \left\{-26.155, 2.874\right\}^{\text{T}}$ and covariance matrix given by

$$\begin{aligned}
\boldsymbol{\Sigma}_{\boldsymbol{\Theta}_{\text{dam}}^{0}} = \boldsymbol{\Sigma}_{\ln C^{0}, m^{0}} &= \begin{bmatrix} \sigma^{2}_{\ln C^{0}} & \rho_{\ln C^{0}, m^{0}} \cdot \sigma_{\ln C^{0}} \cdot \sigma_{m^{0}} \\ \rho_{\ln C^{0}, m^{0}} \cdot \sigma_{\ln C^{0}} \cdot \sigma_{m^{0}} & \sigma^{2}_{m^{0}} \end{bmatrix} \\
&= \begin{bmatrix} 0.939 & -0.8\sqrt{0.939 \cdot 0.0274} \\ -0.8\sqrt{0.939 \cdot 0.0274} & 0.0274 \end{bmatrix} \\
&= \begin{bmatrix} 0.939 & -0.1282 \\ -0.1282 & 0.0274 \end{bmatrix}
\end{aligned} \tag{9.29}$$

where $\rho_{\ln C^{0}, m^{0}} = -0.8$ represents the assumed correlation coefficient between $\ln C^{0}$

and m^0. Furthermore, within this specific application of the proposed damage prognosis framework, the damage evolution model parameter vector, $\boldsymbol{\Theta}_{\text{dam}}^0$, is transformed as $\mathbf{Z}^0 = \boldsymbol{\Phi}\left(\boldsymbol{\Theta}_{\text{dam}}^0 - \mu_{\boldsymbol{\Theta}_{\text{dam}}^0}\right)$

$$\mathbf{Z}^0 = \boldsymbol{\Phi}\left(\boldsymbol{\Theta}_{\text{dam}}^0 - \mu_{\boldsymbol{\Theta}_{\text{dam}}^0}\right) \tag{9.30}$$

where the random vector $\mathbf{Z}^0 = \left\{ Z_1 \; Z_2 \right\}^{\text{T}}$ denotes the transformed damage evolution model parameter vector, used in the analyses, and where the 2×2 matrix $\boldsymbol{\Phi}$ is defined as

$$\boldsymbol{\Phi} = \left[\boldsymbol{\Phi}_1 \; \boldsymbol{\Phi}_2 \right] = \begin{bmatrix} 0.1212 & 0.8788 \\ 0.8788 & -0.1212 \end{bmatrix} \tag{9.31}$$

with $\boldsymbol{\Phi}_1$ and $\boldsymbol{\Phi}_2$ representing the eigenvectors of the covariance matrix $\boldsymbol{\Sigma}_{\boldsymbol{\Theta}_{\text{dam}}^0}$. Equation (9.30) is a linear transformation of the random vector $\boldsymbol{\Theta}_{\text{dam}}^0$ and therefore the two random variables Z_1^0 and Z_2^0 are also jointly Normal with zero mean (i.e., $\mu_{\mathbf{Z}^0} = \mathbf{0}$) and covariance matrix, $\boldsymbol{\Sigma}_{\mathbf{Z}^0}$, equal to

$$\boldsymbol{\Sigma}_{\mathbf{Z}^0} = \boldsymbol{\Phi}\, \boldsymbol{\Sigma}_{\boldsymbol{\Theta}_{\text{dam}}^0} \boldsymbol{\Phi}^{\text{T}} = \begin{bmatrix} Var\left[Z_1^0\right] & 0 \\ 0 & Var\left[Z_2^0\right] \end{bmatrix} = \begin{bmatrix} 0.0076 & 0 \\ 0 & 0.7528 \end{bmatrix} \tag{9.32}$$

The prior joint PDF of $\mathbf{Z}^0$ is herein denoted by $f'_{\mathbf{Z}^0}\left(\mathbf{z}^0\right)$ and is shown in Figure 9.16 and Figure 9.17. Furthermore, the forward and backward transformations, after the NDE inspection at time $N_p \geq N_0$, can be written as $\mathbf{Z}^p = \boldsymbol{\Phi}\left(\boldsymbol{\Theta}_{\text{dam}}^p - \mu_{\boldsymbol{\Theta}_{\text{dam}}^0}\right)$ and

$\boldsymbol{\Theta}_{\text{dam}}^{p} = \boldsymbol{\Phi}^{-1}\mathbf{Z}^{p} + \mu_{\boldsymbol{\Theta}_{\text{dam}}^{0}}$, respectively. Applying Equation (9.30) to the true damage evolution model parameters, $\ln C_{\text{true}}^{\#1} = -26.7949$ and $m_{\text{true}}^{\#1} = 2.9855$ (reported in Figure 9.13 and obtained from the linear regression analysis on the experimental data points of the *sample trajectory #1* depicted in Figure 9.12), lead to the following pair of transformed values, collected in $\mathbf{z}_{\text{true}}^{\#1}$ and shown in Figure 9.16:

$$\mathbf{z}_{\text{true}}^{\#1} = \begin{Bmatrix} z_{1,\text{true}}^{\#1} \\ z_{2,\text{true}}^{\#1} \end{Bmatrix} = \boldsymbol{\Phi}\left[\begin{pmatrix} \ln C_{\text{true}}^{\#1} \\ m_{\text{true}}^{\#1} \end{pmatrix} - \mu_{\boldsymbol{\Theta}_{\text{dam}}^{0}}\right] = \begin{Bmatrix} 0.02039 \\ -0.57583 \end{Bmatrix} \tag{9.33}$$

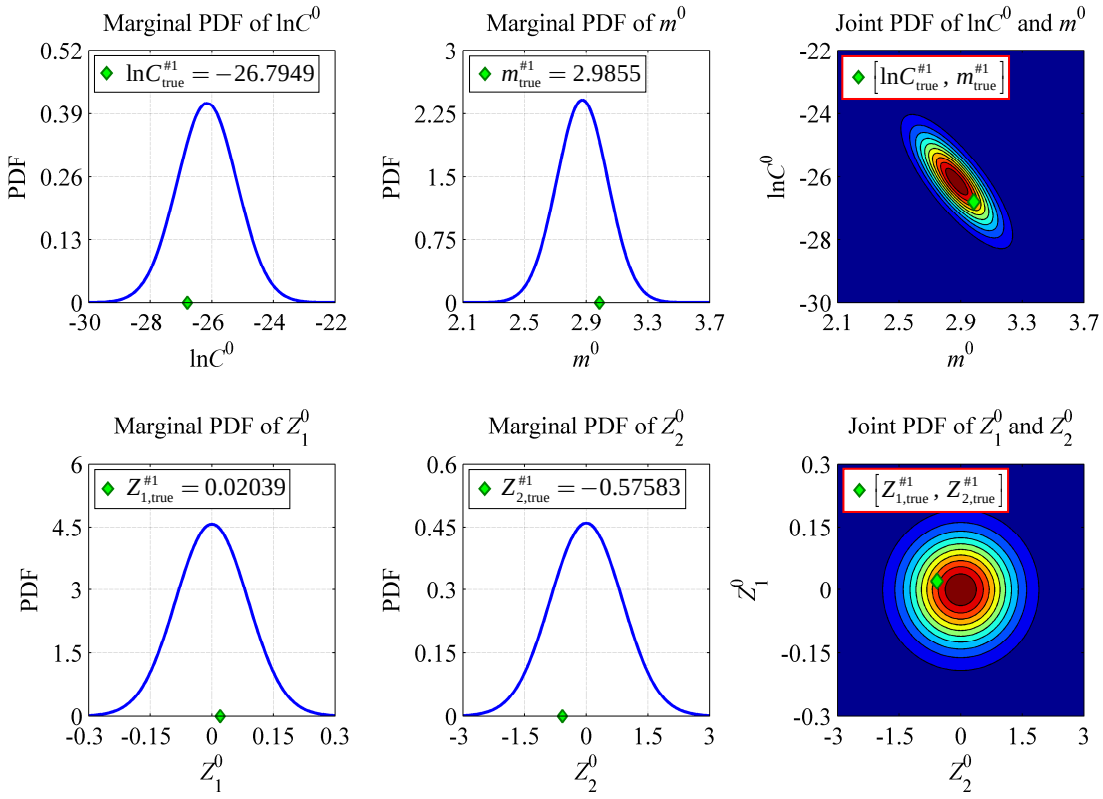

Figure 9.16: Initial prior PDFs of $\boldsymbol{\Theta}_{\text{dam}}^{0}$ and $\mathbf{Z}^{0}$, together with the true values of the damage evolution model parameters, $\boldsymbol{\Theta}_{\text{dam}}^{true} = \left\{\ln C_{\text{true}}^{\#1}, m_{\text{true}}^{\#1}\right\}$ and $\mathbf{Z}_{\text{true}}^{\#1} = \left\{Z_{1,\text{true}}^{\#1}, Z_{2,\text{true}}^{\#1}\right\}$, obtained from linear regression analysis on the data points of the *sample trajectory #1* (see Figure 9.12 and Figure 9.13).

Similarly, if Equation (9.30) is used to transform the other pair of true damage evolution model parameters, $\ln C_{\text{true}}^{\#2} = -26.7528$ and $m_{\text{true}}^{\#2} = 2.9358$ (obtained from the linear regression analysis on the experimental data points of the *sample trajectory #2*), the following result for $\mathbf{Z}_{\text{true}}^{\#2}$, shown in Equation (9.34) below as well as in Figure 9.17, is obtained:

$$\mathbf{Z}_{\text{true}}^{\#2} = \begin{Bmatrix} Z_{1,\text{true}}^{\#2} \\ Z_{2,\text{true}}^{\#2} \end{Bmatrix} = \mathbf{\Phi}\left[\begin{pmatrix} \ln C_{\text{true}}^{\#2} \\ m_{\text{true}}^{\#2} \end{pmatrix} - \mu_{\mathbf{\Theta}_{\text{dam}}^{0}} \right] = \begin{Bmatrix} -0.01817 \\ -0.53281 \end{Bmatrix} \tag{9.34}$$

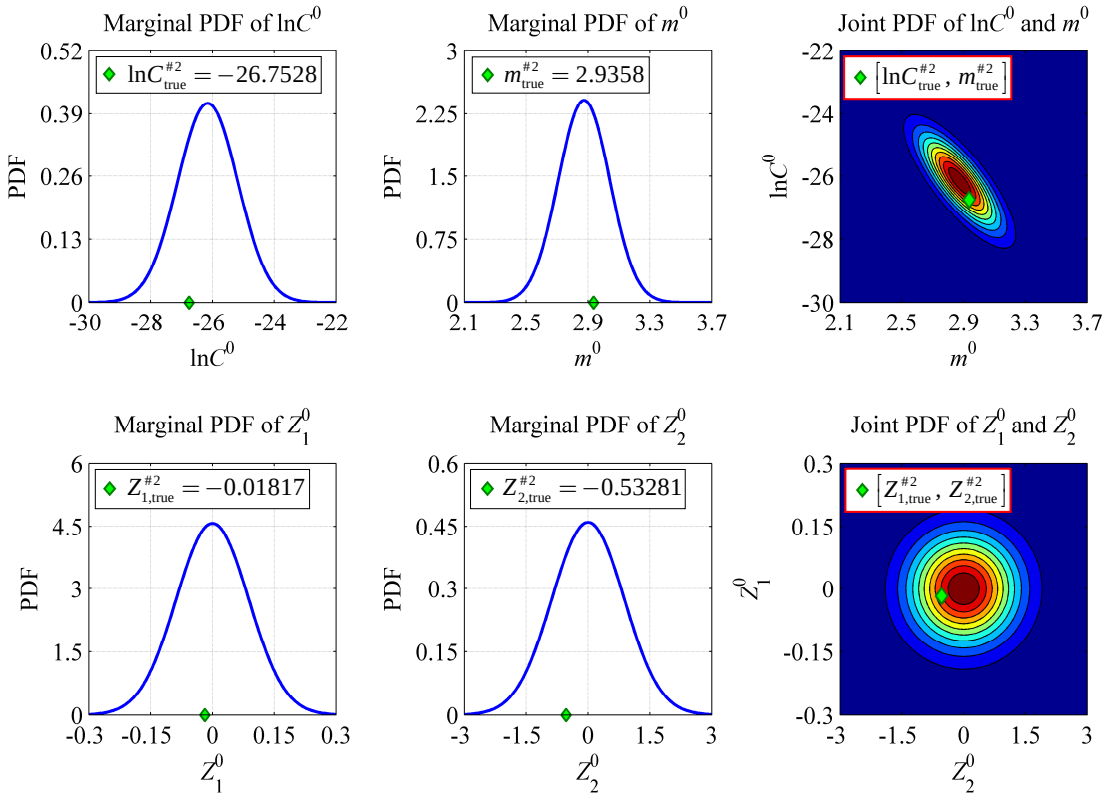

Figure 9.17: Initial prior PDFs of $\mathbf{\Theta}_{\text{dam}}^{0}$ and $\mathbf{Z}^{0}$, together with the true values of the damage evolution model parameters, $\mathbf{\Theta}_{\text{dam}}^{true} = \left\{ \ln C_{\text{true}}^{\#2}, m_{\text{true}}^{\#2} \right\}$ and $\mathbf{Z}_{\text{true}}^{\#2} = \left\{ Z_{1,\text{true}}^{\#2}, Z_{2,\text{true}}^{\#2} \right\}$, obtained from linear regression analysis on the data points of the *sample trajectory #2* (see Figure 9.12 and Figure 9.14).

9.3.2. NDE technique detection capability and measurement accuracy

In this third application example, the detection capability of a given NDE technique is probabilistically characterized through the *POD* curve model proposed by Berens (1989) and reported in Equation (9.21). The values of the *POD* model parameters used in this specific application example are: $\hat{\alpha}_0^{(1,1)} = \hat{\alpha}_0^{(2,1)} = \hat{\alpha}_0 = 0.3$ and $\hat{\alpha}_1^{(1,1)} = \hat{\alpha}_1^{(2,1)} = \hat{\alpha}_1 = 2.0$. The use of these parameters in Equation (9.21) generates the *POD* curve shown in Figure 9.6. On the other hand, the measurement accuracy of the NDE technique envisioned for this third case study is provided by the linear sizing model (Zhang and Mahadevan, 2001) shown in Figure 8.3 of Chapter 8. The values of the sizing model parameters used subsequently are: $\hat{\beta}_0^{(1,1)} = \hat{\beta}_0^{(2,1)} = \hat{\beta}_0 = -1.5\,mm$, $\hat{\beta}_1^{(1,1)} = \hat{\beta}_1^{(2,1)} = \hat{\beta}_1 = 1.2$, and $\hat{\sigma}_{\varepsilon_{11}} = \hat{\sigma}_{\varepsilon_{21}} = \hat{\sigma}_{\varepsilon} = 2.0\,mm$.

9.3.3. Underlying (true) crack propagation trajectories, assumed NDE inspection opportunities, and random NDE measurements generation

As already anticipated at the beginning of Section 9.3, among the 65 crack propagation trajectories provided by Virkler *et al.* (1979), two sample paths are selected and used as underlying (true) crack propagation processes in order to verify and validate the proposed prognosis framework. These two sample trajectories and their corresponding damage evolution model parameters (obtained from curve fitting the Paris law equation to the experimental data points) are provided in Figures 9.12, 9.13, and 9.14. These two trajectories, are then used to randomly generate NDE measurements, $\mathbf{A}_{\mathrm{m}}^{p}$, at evenly spaced intervals. In this specific application example, a

total of forty-one NDE inspections — evenly spaced every $\Delta N = 5{,}000$ load cycles and covering the loading window $[0\ 200{,}000]$ load cycles — are used to monitor the crack propagation process identified by the sample trajectory #1, while fifty-one NDE inspections — evenly spaced every $\Delta N = 5{,}000$ load cycles and covering the loading window $[0\ 250{,}000]$ load cycles — are employed to track the crack propagation process associated with the sample trajectory #2.

At each NDE inspection opportunity, three different scenarios are envisioned. In the first scenario, five statistically independent NDE measurements are taken and processed using the proposed Bayesian inference scheme; an example is shown in Figure 9.18. In the second scenario, ten statistically independent NDE measurements

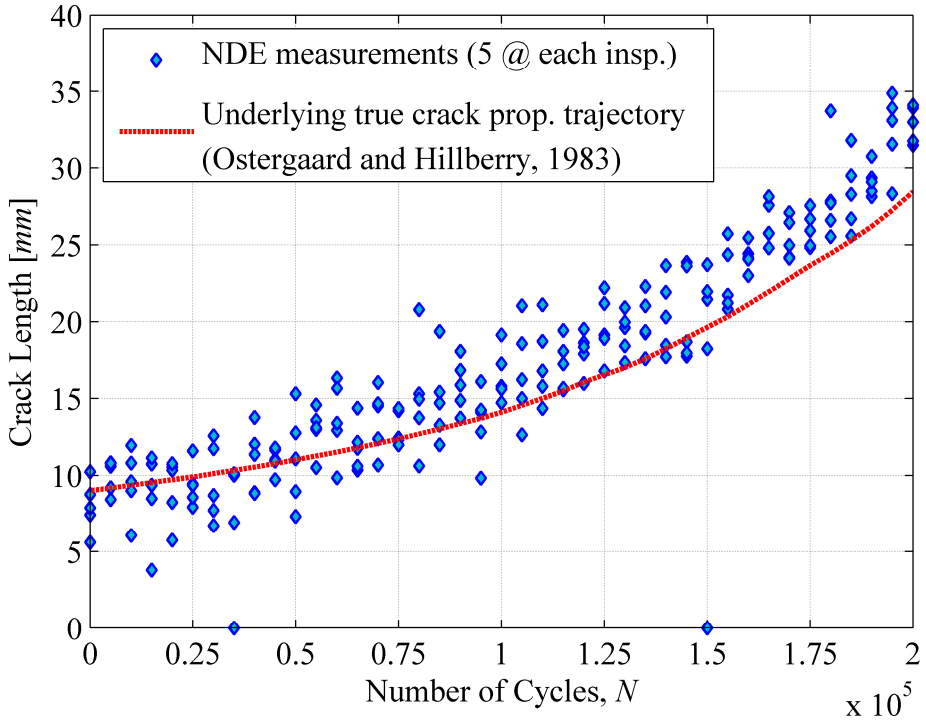

Figure 9.18: Random realization of NDE measurements associated with the sample trajectory #1; 5 NDE measurements at each of the forty-one inspection opportunities.

are considered. Lastly, in the third scenario, twenty statistically independent NDE measurements are considered and used to repeatedly compute the posterior PDFs of A_a^p and $\boldsymbol{\Theta}_{\text{dam}}^p$. Furthermore, the three sets of measurements (randomly generated according to the procedure discussed in Section 9.2.6) are mutually statistically independent.

9.3.4. Probabilistic crack propagation analysis

The NDE measurements collected are used to provide the posterior conditional PDF of the crack length, A_a^p, as well as the joint posterior PDF of the damage evolution parameters, $\boldsymbol{\Theta}_{\text{dam}}^p$ or (equivalently) $\mathbf{Z}^p = \boldsymbol{\Phi}\left(\boldsymbol{\Theta}_{\text{dam}}^p - \mu_{\boldsymbol{\Theta}_{\text{dam}}^0}\right)$. These two posterior PDFs are herein denoted as $f''_{A_a^p \mid \boldsymbol{\Theta}_{\text{dam}}^p}\left(a_a^p \,\middle|\, \boldsymbol{\theta}_{\text{dam}}^p\right)$ and $f''_{\boldsymbol{\Theta}_{\text{dam}}^p}\left(\boldsymbol{\theta}_{\text{dam}}^p\right) = f''_{\ln C^p,\, m^p}\left(\ln C^p, m^p\right)$, respectively. After each NDE inspection at time N_p (with $p = 0, 1, 2, \ldots$), the crack propagation process is modeled and simulated using the Paris law equation already introduced at the beginning of Section 9.3. This ordinary differential equation can now be conveniently rewritten as

$$\begin{cases} \dfrac{d}{dN}\overline{a}_a^{[p,N]} = C^p\left(\Delta K_{[p,N]}\right)^{m^p} \\ \overline{a}_a^p = a_a^p \end{cases} \qquad \left(N \geq N_p,\ p = 0, 1, 2, \ldots\right) \tag{9.35}$$

where $\overline{a}_a^{[p,N]}$ denotes the predicted crack length at time $N \geq N_p$; $d\overline{a}_a^{[p,N]}/dN$, expressed in $mm/cycle$, represents the rate of crack propagation at time $N \geq N_p$; $\overline{a}_a^p$ indicates the value of $\overline{a}_a^{[p,N]}$ at $N = N_p$ (i.e., the value for the crack length at current

time, immediately after the last NDE inspection); a_{a}^{p} is a particular realization of A_{a}^{p} according to the posterior PDF $f''_{A_a^p}\left(a_a^p\right)$; C^p and m^p are the two damage evolution parameters sampled from $f''_{\boldsymbol{\Theta}_{\mathrm{dam}}^p}\left(\boldsymbol{\theta}_{\mathrm{dam}}^p\right) = f''_{\ln C^p,\, m^p}\left(\ln C^p, m^p\right)$; finally, the quantity $\Delta K_{[p,\,N]}$, expressed in $MN\cdot mm^{3/2}$, denotes the range of the stress intensity factor at the crack-tip within a given load cycle and can be mathematically expressed as

$$\Delta K_{[p,\,N]} = \sqrt{\pi\, \bar{a}_a^{[p,\,N]}}\, \Delta\sigma F\left(\frac{\bar{a}_a^{[p,\,N]}}{w}\right) \tag{9.36}$$

where $\Delta\sigma = 48.28\, MPa$ is the constant stress range used during the fatigue tests performed by Virkler *et al.* (1979) and $F\left(\bar{a}_a^{[p,\,N]}/w\right)$ characterizes the geometric correction factor that takes the following form:

$$F\left(\frac{\bar{a}_a^{[p,\,N]}}{w}\right) = \frac{1}{\sqrt{\cos\left(\pi\,\dfrac{\bar{a}_a^{[p,\,N]}}{w}\right)}}, \qquad \frac{\bar{a}_a^{[p,\,N]}}{w} \le 0.85 \tag{9.37}$$

Equation (9.35) is integrated numerically between current load cycle N_p and (future) load cycle $N_p^q = N_p + q\Delta N$ (with $q = 1, 2, ..., \bar{q}$) to provide the conditional joint PDF $f_{\mathbf{A}_{\mathrm{a}}^{[p,\,q]}\left|\boldsymbol{\Theta}_{\mathrm{mat}},\,\boldsymbol{\Theta}_{\mathrm{dam}}^p,\,\mathbf{A}_{\mathrm{a}}^p,\,\mathbf{IM}\right.}\left(\mathbf{a}_{\mathrm{a}}^{[p,\,q]}\left|\boldsymbol{\theta}_{\mathrm{mat}}, \boldsymbol{\theta}_{\mathrm{dam}}^p, \mathbf{a}_{\mathrm{a}}^p, \mathbf{im}\right.\right) = f_{A_{\mathrm{a}}^{[p,\,q]}\left|\boldsymbol{\Theta}_{\mathrm{dam}}^p,\,A_{\mathrm{a}}^p\right.}\left(a_{\mathrm{a}}^{[p,\,q]}\left|\boldsymbol{\theta}_{\mathrm{dam}}^p, a_{\mathrm{a}}^p\right.\right)$ appearing at the beginning of the third analytical step of the proposed damage prognosis methodology, namely probabilistic damage evolution analysis (see Figure 9.1). It is worth mentioning that, within this particular application example, the random vector $\boldsymbol{\Theta}_{\mathrm{mat}}$ is not defined and therefore is never involved in the computations. Even more

importantly, since the quantities $\Delta\sigma = 48.28\,MPa$ and $R_\sigma = \sigma_{\min}/\sigma_{\max} = 0.2$ are assumed to be known and fixed/constant, no load uncertainty is considered in the crack propagation process. In light of these considerations, the conditional joint PDF $f_{A_{\mathrm{a}}^{[p,q]}\left|\boldsymbol{\Theta}_{\mathrm{dam}}^{p},A_{\mathrm{a}}^{p}\right.}\left(a_{\mathrm{a}}^{[p,q]}\left|\boldsymbol{\theta}_{\mathrm{dam}}^{p},a_{\mathrm{a}}^{p}\right.\right)$ can be expressed as

$$f_{A_{\mathrm{a}}^{[p,q]}\left|\boldsymbol{\Theta}_{\mathrm{dam}}^{p},A_{\mathrm{a}}^{p}\right.}\left(a_{\mathrm{a}}^{[p,q]}\left|\boldsymbol{\theta}_{\mathrm{dam}}^{p},a_{\mathrm{a}}^{p}\right.\right)=\delta\left(\mathbf{a}_{\mathrm{a}}^{[p,q]}-\overline{a}_{a}^{[p,q]}\right) \tag{9.38}$$

where $\delta(\bullet)$ is the *Dirac Delta* and the term $\overline{a}_{a}^{[p,q]}$ represents the outcome from the numerical integration of Equation (9.35), between current load cycle N_p and (future) load cycle $N_p^q = N_p + q\Delta N$, for a given realization of $\boldsymbol{\Theta}_{\mathrm{dam}}^{p} = \boldsymbol{\theta}_{\mathrm{dam}}^{p}$ and $A_{\mathrm{a}}^{p} = a_{\mathrm{a}}^{p}$, i.e., $\overline{a}_{a}^{[p,q]} = \overline{a}_{a}^{[p,q]}\left(\boldsymbol{\theta}_{\mathrm{dam}}^{p},a_{\mathrm{a}}^{p}\right) = \left(A_{\mathrm{a}}^{[p,q]}\left|\boldsymbol{\theta}_{\mathrm{dam}}^{p},a_{\mathrm{a}}^{p}\right.\right)$. The result obtained in Equation (9.38) is then used to compute the conditional PDF $f_{A_{\mathrm{a}}^{[p,q]}\left|\boldsymbol{\Theta}_{\mathrm{dam}}^{p}\right.}\left(a_{\mathrm{a}}^{[p,q]}\left|\boldsymbol{\theta}_{\mathrm{dam}}^{p}\right.\right)$ through the total probability theorem as

$$f_{A_{\mathrm{a}}^{[p,q]}\left|\boldsymbol{\Theta}_{\mathrm{dam}}^{p}\right.}\left(a_{\mathrm{a}}^{[p,q]}\left|\boldsymbol{\theta}_{\mathrm{dam}}^{p}\right.\right)=\int_{A_{\mathrm{a}}^{[p,q]}}\delta\left(a_{\mathrm{a}}^{[p,q]}-\overline{a}_{a}^{[p,q]}\right)f''_{A_{\mathrm{a}}^{p}\left|\boldsymbol{\Theta}_{\mathrm{dam}}^{p}\right.}\left(a_{\mathrm{a}}^{p}\left|\boldsymbol{\theta}_{\mathrm{dam}}^{p}\right.\right)da_{\mathrm{a}}^{p} \tag{9.39}$$

9.3.5. Bayesian updating results associated with sample trajectory #1

This section presents a selected set of the Bayesian updating results obtained by applying the proposed damage prognosis framework (and in particular the proposed Bayesian inference scheme and probabilistic damage evolution analysis step) to the assumed underlying crack propagation path identified by the sample trajectory #1 (see Figure 9.12 at the beginning of Section 9.3). Figure 9.19 and Figure 9.20 report the

posterior marginal PDFs of the damage evolution model parameters, Z_1^p and Z_2^p, respectively. Additionally, Figure 9.21 reports the posterior joint probabilistic characterization of the aforementioned quantities — i.e., the posterior joint PDF of the damage evolution model parameter vector, $\mathbf{Z}^p$, defined as $\mathbf{Z}^p = \left\{ Z_1^p \;\; Z_2^p \right\}^{\mathrm{T}}$.

The selected crack propagation trajectory is monitored from initial time $N_0 = 0$ cycles up to final time $N_{40} = 200{,}000$ cycles through a series of 41 NDE inspections, evenly spaced every $\Delta N = 5{,}000$ cycles. After each of these 41 NDE

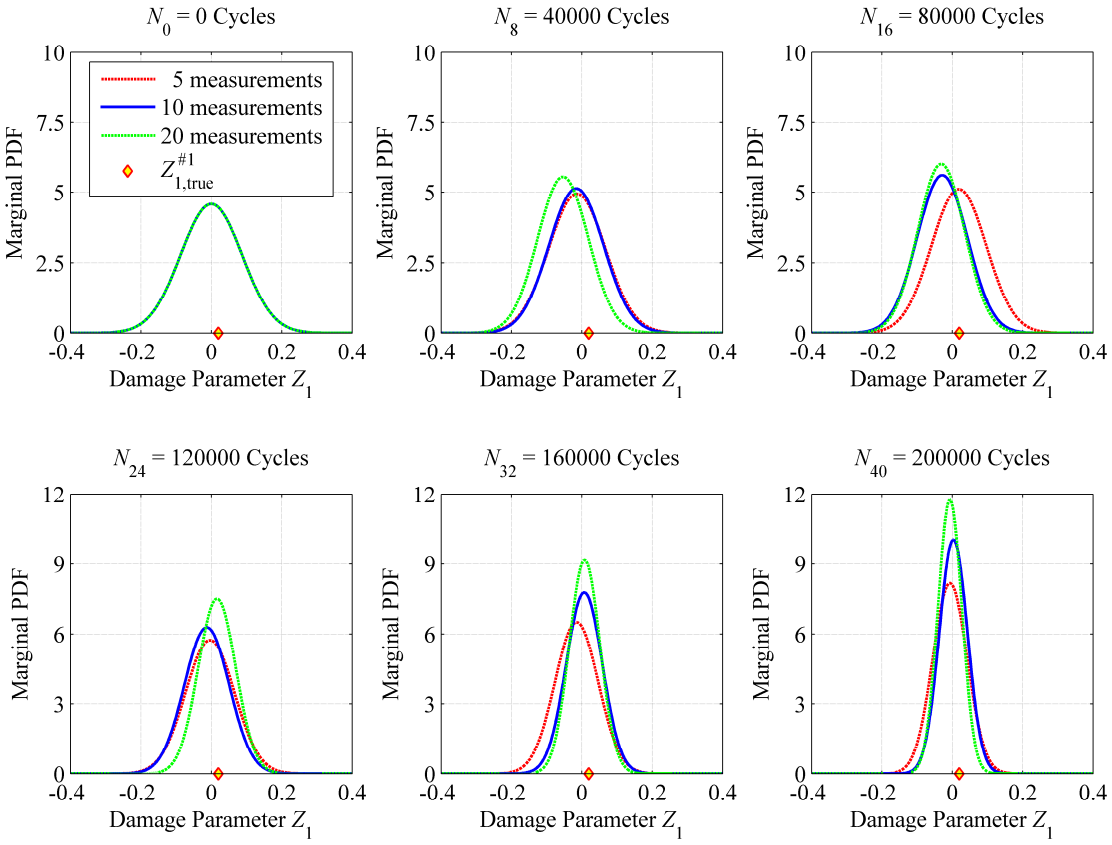

Figure 9.19: Posterior marginal PDF of damage parameter Z_1^p after six (selected) NDE inspections, evenly spaced every $\Delta N = 40{,}000$ cycles; results obtained from the application of the proposed damage prognosis framework to the *sample trajectory #1*.

inspections, the posterior PDFs of crack length (A_a^p) and damage evolution model parameters (Z_1^p and Z_2^p) are recursively computed through the proposed recursive Bayesian inference scheme. Six, out of these 41 inspection times, are selected and the corresponding posterior PDFs (computed at each of these six inspection times) are reported in the figures below. Focusing on the Bayesian updating results for the two damage evolution model parameters involved in this particular application example, it is observed that only the uncertainty associated with Z_1^p is progressively reduced. On

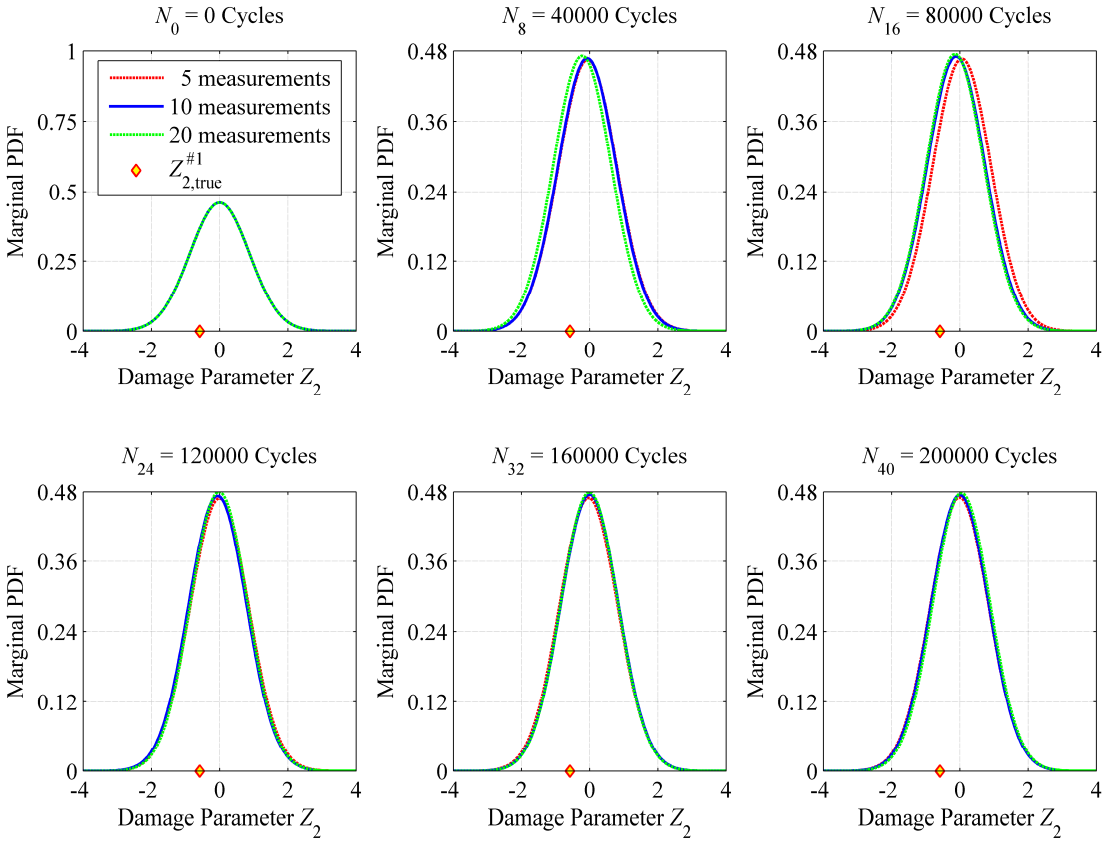

Figure 9.20: Posterior marginal PDF of damage parameter Z_2^p after six (selected) NDE inspections, evenly spaced every $\Delta N = 40{,}000$ cycles; results obtained from the application of the proposed damage prognosis framework to the *sample trajectory #1*.

the other hand, the posterior marginal PDF of Z_2^p never changes substantially during the 41 Bayesian updating operations performed between $N_0 = 0$ cycles and $N_{40} = 200,000$ cycles. This fact can be explained by analyzing Equations (9.30) and (9.31) in Section 9.3.1. These equations indicate that Z_1^p preserves almost 90% of the uncertainty related to m^p, while Z_2^p retains almost 90% of the uncertainty associated with $\ln C^p$. As a direct consequence, stating that the marginal PDF of Z_2^p

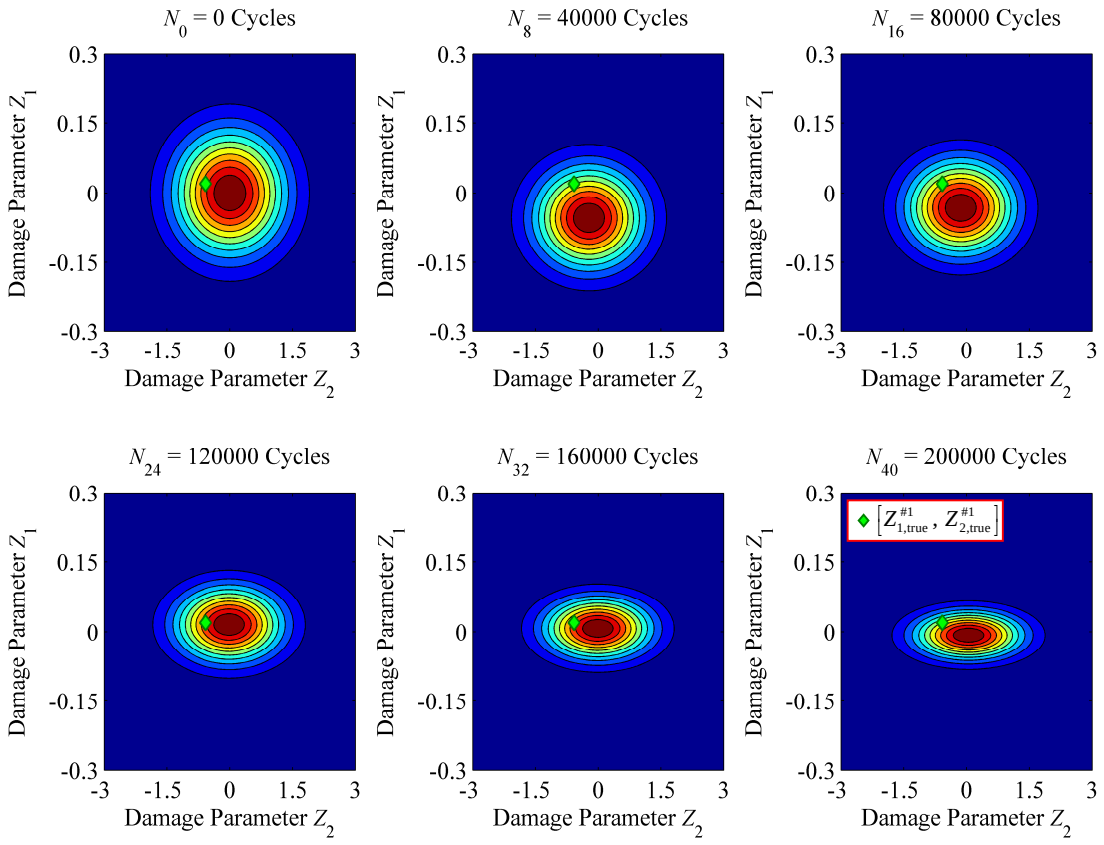

Figure 9.21: Posterior joint PDF of damage parameters Z_1^p and Z_2^p after six (selected) NDE inspections, evenly spaced every $\Delta N = 40,000$ cycles; results obtained from the application of the proposed damage prognosis framework to the *sample trajectory #1* with 20 NDE measurements collected at each NDE inspection opportunity.

cannot be updated (through the proposed Bayesian updating scheme) is essentially equivalent to affirm that the damage evolution model parameter $\ln C^p$ does not contribute significantly to the variability of the crack propagation process and therefore its PDF is not sensitive to the Bayesian updating procedure. This is the exact same result already encountered in Section 9.2.4 where the effect screening performed on the Forman's model parameters (see Figure 9.5) indicated that the contribution of the damage parameter C could have been neglected during the whole damage prognosis process. In more detail, Equations (9.40) and (9.41) quantify, in terms of variance reduction and for the specific case in which $n_{\mathrm{MS}}^p = 20$ ($p = 1, 2, ..., 41$), the benefit provided by the proposed recursive Bayesian updating scheme. Equation (9.40) indicates that the variance of Z_1^{40}, at time $N_{40} = 200{,}000$ cycles, is about 16% of its initial variance at time $N_0 = 0$ cycles — i.e., the variance reported earlier in Equation (9.32). On the other hand, Equation (9.41) shows that the variance of Z_2^{40} is reduced by less than 10%.

$$\frac{Var\left[Z_1\left(N_{40} = 200{,}000 \text{ cycles}, n_{\mathrm{MS}}^p = 20\right)\right]}{Var\left[Z_1\left(N_0 = 0 \text{ cycles}\right)\right]} = \frac{Var\left[Z_1^{40}\left(n_{\mathrm{MS}}^p = 20\right)\right]}{Var\left[Z_1^0\right]} \cong 0.16 \qquad (9.40)$$

$$\frac{Var\left[Z_2\left(N_{40} = 200{,}000 \text{ cycles}, n_{\mathrm{MS}}^p = 20\right)\right]}{Var\left[Z_2\left(N_0 = 0 \text{ cycles}\right)\right]} = \frac{Var\left[Z_2^{40}\left(n_{\mathrm{MS}}^p = 20\right)\right]}{Var\left[Z_2^0\right]} \cong 0.93 \qquad (9.41)$$

Finally, Figure 9.22 reports the posterior marginal PDF of the crack length, A_a^p, computed immediately after the NDE inspections at $N_0 = 0$, $N_8 = 40{,}000$,

$N_{16}=80,000$, $N_{24}=120,000$, $N_{32}=160,000$, and $N_{40}=200,000$ cycles. Similarly to Figure 9.19 and Figure 9.20, also in this case, three different NDE inspection scenarios are considered and reported in Figure 9.22, namely $n_{\mathrm{MS}}^{p}=5$, $n_{\mathrm{MS}}^{p}=10$, and $n_{\mathrm{MS}}^{p}=20$ (with $p=1,2,...,41$). The benefit, in terms of uncertainty reduction, provided by the larger number of NDE measurements collected at each NDE inspection opportunity is evident; furthermore, a larger set of NDE measurements allows for a better collocation/centering of the computed posterior marginal PDF at any given time.

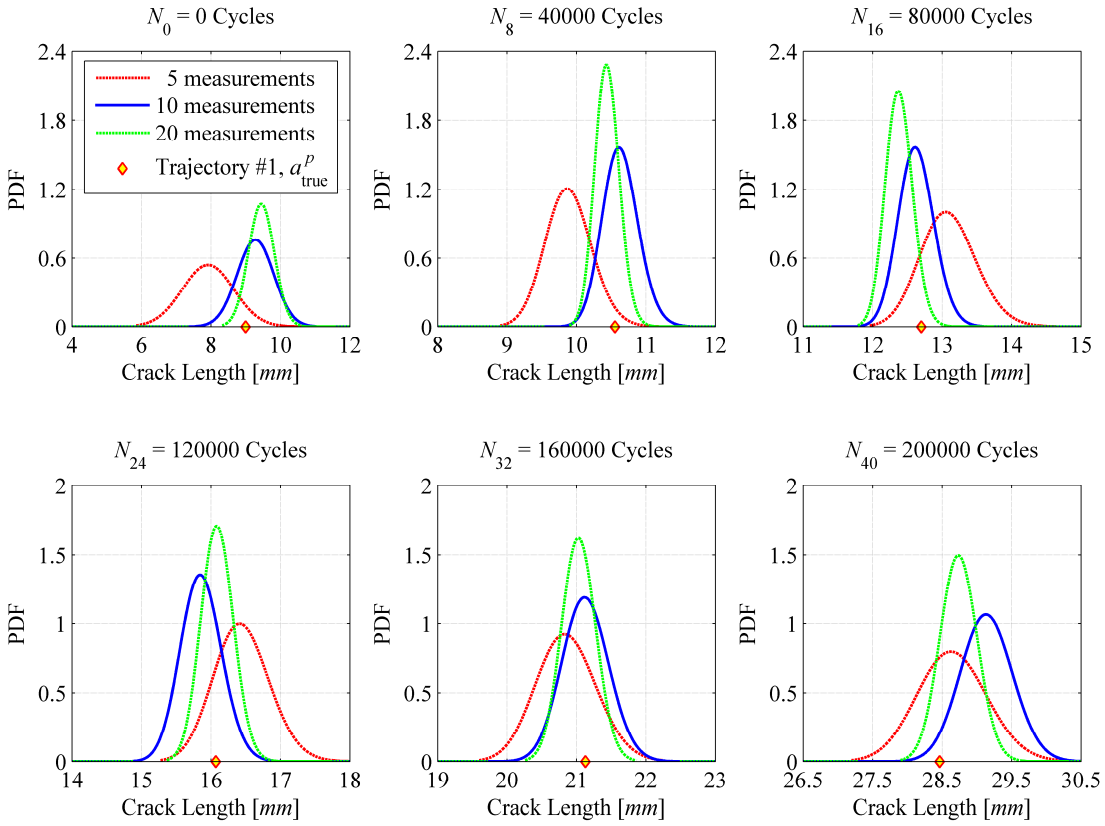

Figure 9.22: Posterior marginal PDF of crack length A_a^p after six (selected) NDE inspections, evenly spaced every $\Delta N=40,000$ cycles; results obtained from the application of the proposed damage prognosis framework to the *sample trajectory #1*.

9.3.6. Bayesian updating results associated with sample trajectory #2

Similarly to Section 9.3.5, a selected set of the Bayesian updating results obtained by applying the proposed damage prognosis framework to the assumed underlying crack propagation path identified by the sample trajectory #2 (see Figure 9.12 at the beginning of Section) is hereafter presented and discussed. This second sample trajectory represents a more challenging scenario for the proposed damage prognosis methodology since the values of the associated underlying (true) damage evolution model parameters, $\ln C_{\text{true}}^{\#2} = -26.7528$ and $m_{\text{true}}^{\#2} = 2.9358$, fall in the tail of the assigned initial prior joint PDF $f'_{\boldsymbol{\Theta}_{\text{dam}}^0}\left(\boldsymbol{\theta}_{\text{dam}}^0\right) = f'_{\ln C^0,\, m^0}\left(\ln C^0, m^0\right)$ (see Figure 9.17). This second crack propagation trajectory is monitored from initial time $N_0 = 0$ cycles up to final time $N_{50} = 250,000$ cycles through a series of 51 NDE inspections, evenly spaced every $\Delta N = 5,000$ cycles. After each of these 51 NDE inspections, the posterior PDFs of crack length (A_a^p) and damage evolution model parameters (Z_1^p and Z_2^p) are recursively computed through the proposed recursive Bayesian inference scheme. Six, out of these 51 inspection times, are selected and the corresponding posterior PDFs (computed at each of these six inspection times) are reported in the following figures. Figure 9.23 and Figure 9.24 report the posterior marginal PDFs of the damage evolution model parameters, Z_1^p and Z_2^p, respectively. Figure 9.25 shows the posterior marginal PDF of the crack length, A_a^p, computed immediately after the NDE inspections at $N_0 = 0$, $N_{10} = 50,000$, $N_{20} = 100,000$, $N_{30} = 150,000$,

$N_{40} = 200,000$, and $N_{50} = 250,000$ cycles., As already discussed in Section 9.3.5, also in this case three different NDE inspection scenarios are considered, namely $n_{\mathrm{MS}}^{p}=5$, $n_{\mathrm{MS}}^{p}=10$, and $n_{\mathrm{MS}}^{p}=20$ (with $p=1,2,...,51$). The benefit, in terms of uncertainty reduction, provided by the larger number of NDE measurements collected at each NDE inspection opportunity is also evident in this second case; furthermore, a larger set of NDE measurements allows for a better collocation/centering of the computed posterior marginal PDF of A_a^p at any given inspection time.

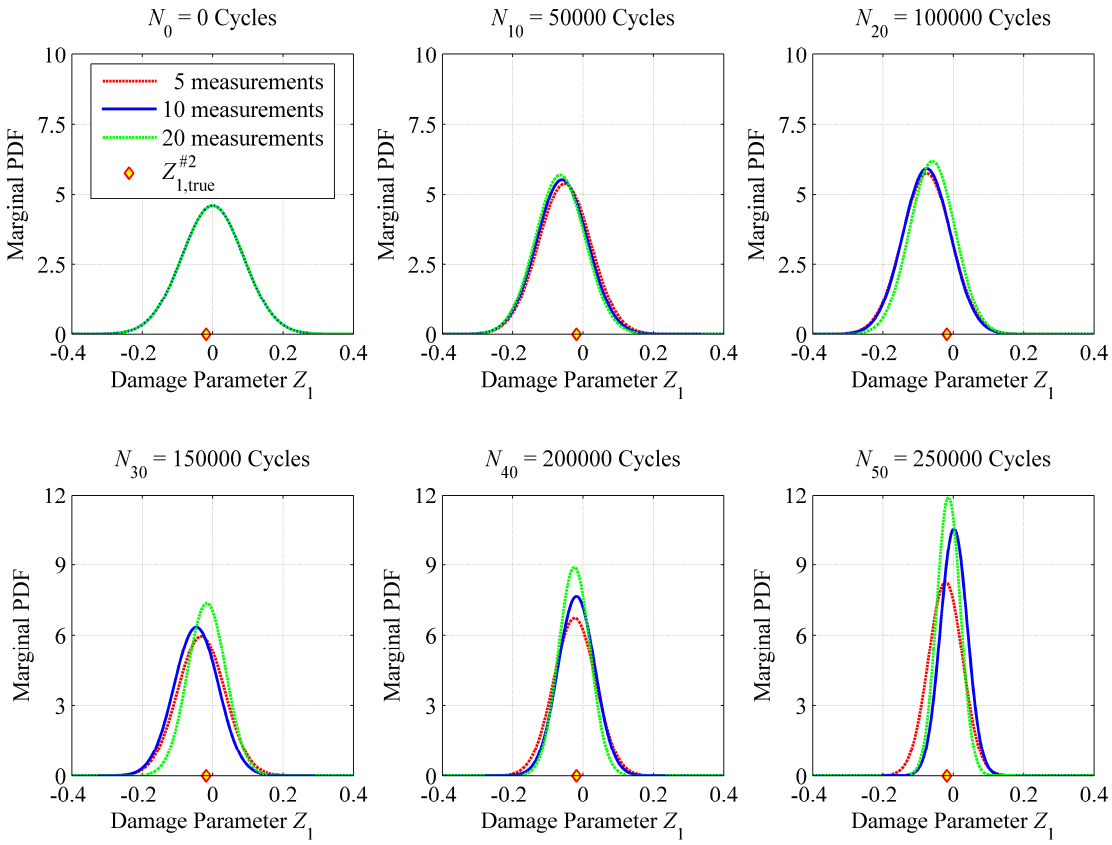

Figure 9.23: Posterior marginal PDF of damage parameter Z_1^p after six (selected) NDE inspections, evenly spaced every $\Delta N = 50,000$ cycles ; results obtained from the application of the proposed damage prognosis framework to the *sample trajectory #2*.

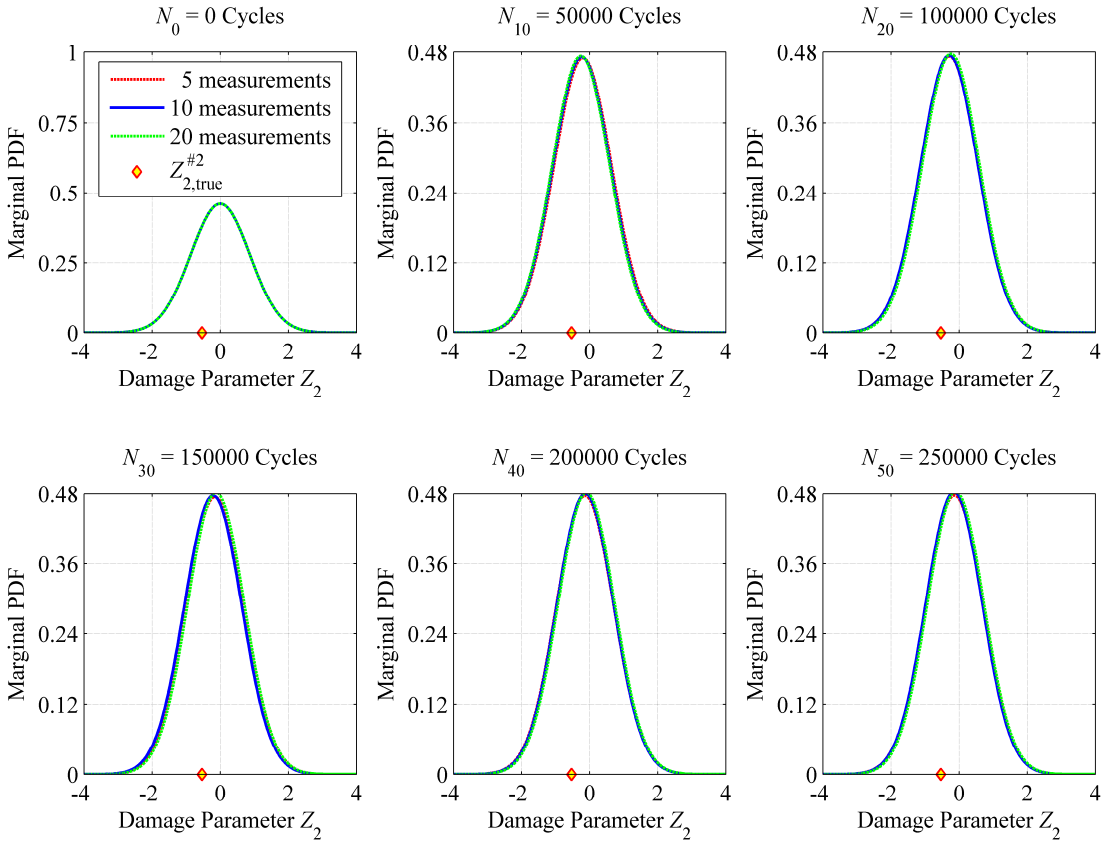

Figure 9.24: Posterior marginal PDF of damage parameter Z_2^p after six (selected) NDE inspections, evenly spaced every $\Delta N = 50,000$ cycles; results obtained from the application of the proposed damage prognosis framework to the *sample trajectory #2*.

It is worth mentioning that all the Bayesian updating results provided in Sections 9.3.5 and 9.3.6 are obtained by processing a single realization of the NDE measurements at each inspection opportunity. Therefore, it would be of great interest studying the statistical variability of the Bayesian inference results by considering a whole ensemble of NDE inspection results at each inspection opportunity. This consideration applies also to the subsequent sections where the most probable crack propagation trajectories and their prediction bands are derived and discussed.

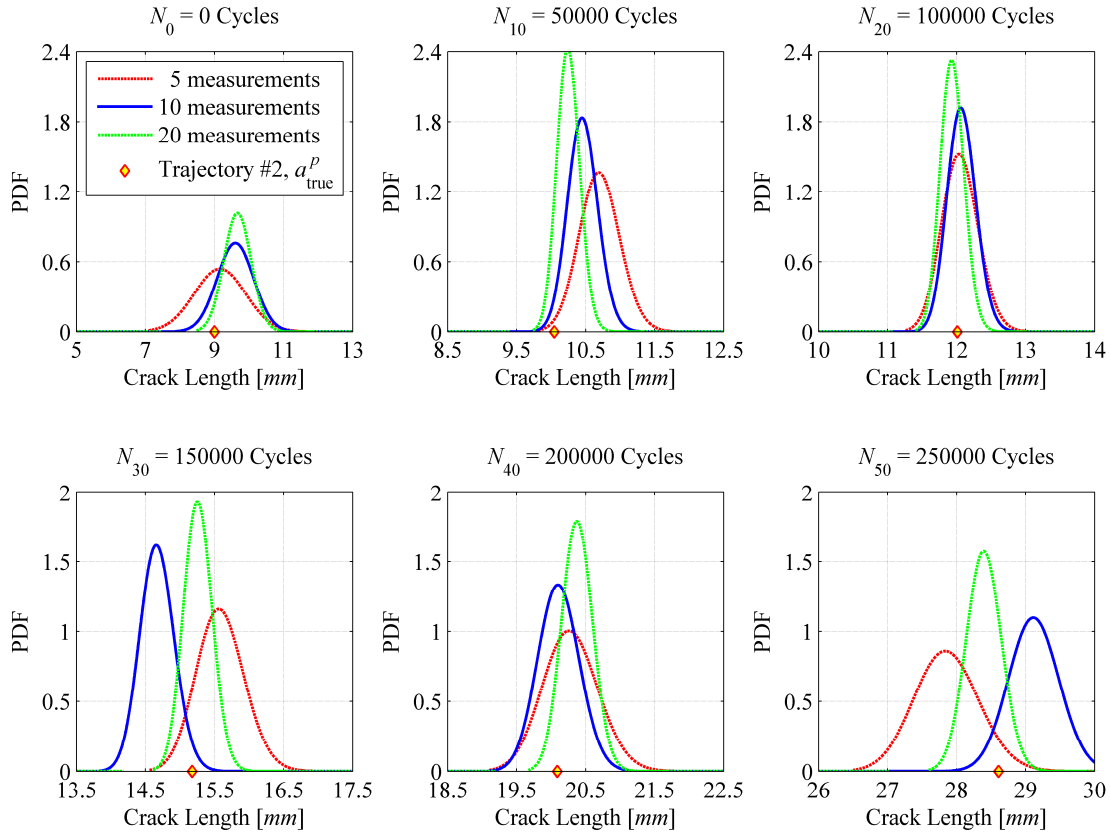

Figure 9.25: Posterior marginal PDF of crack length A_a^p after six (selected) NDE inspections, evenly spaced every $\Delta N = 50,000$ cycles; results obtained from the application of the proposed damage prognosis framework to the *sample trajectory #2*.

9.3.7. Prediction intervals associated with the continuous monitoring of the sample damage evolution trajectory #1

After each of the 41 NDE inspections (evenly spaced every $\Delta N = 5,000$ cycles) envisioned for the continuous monitoring of the selected *sample trajectory #1*, the posterior PDF of the crack length A_a^p, denoted as $f''_{A_a^p}\left(a_a^p\right)$, and the posterior joint PDF of the damage evolution model parameter vector $\mathbf{Z}^p = \left\{Z_1^p, Z_2^p\right\}$, symbolized by

$f''_{\mathbf{Z}^p}\left(\mathbf{z}^p\right)$, are recursively updated through the proposed Bayesian inference scheme which uses the NDE measurements collected during the inspection opportunity. The posterior (unconditional) PDF $f''_{A_a^p}\left(a_a^p\right)$ is computed by using the total probability theorem as

$$\begin{aligned} f''_{A_{\mathrm{a}}^p}\left(a_{\mathrm{a}}^p\right) &= \int_{\boldsymbol{\Theta}_{\mathrm{dam}}^p} f''_{A_{\mathrm{a}}^p\left|\mathbf{Z}^p\right.}\left(a_{\mathrm{a}}^p\left|\mathbf{z}^p\right.\right) f''_{\mathbf{Z}^p}\left(\mathbf{z}^p\right) d\mathbf{z}^p \\ &= \int_{Z_1^p}\int_{Z_2^p} f''_{A_{\mathrm{a}}^p\left|Z_1^p,\, Z_2^p\right.}\left(a_{\mathrm{a}}^p\left|z_1^p, z_2^p\right.\right) f''_{Z_1^p,\, Z_2^p}\left(z_1^p, z_2^p\right) dz_1^p dz_2^p \end{aligned} \tag{9.42}$$

or equivalently, according to the notation used throughout this section, as

$$\begin{aligned} f''_{A_{\mathrm{a}}^p}\left(a_{\mathrm{a}}^p\right) &= \int_{\boldsymbol{\Theta}_{\mathrm{dam}}^p} f''_{A_{\mathrm{a}}^p\left|\boldsymbol{\Theta}_{\mathrm{dam}}^p\right.}\left(a_{\mathrm{a}}^p\left|\boldsymbol{\theta}_{\mathrm{dam}}^p\right.\right) f''_{\boldsymbol{\Theta}_{\mathrm{dam}}^p}\left(\boldsymbol{\theta}_{\mathrm{dam}}^p\right) d\boldsymbol{\theta}_{\mathrm{dam}}^p \\ &= \int_{\ln C^p}\int_{m^p} f''_{A_{\mathrm{a}}^p\left|\ln C^p,\, m^p\right.}\left(a_{\mathrm{a}}^p\left|\ln C^p, m^p\right.\right) f''_{\ln C^p,\, m^p}\left(\ln C^p, m^p\right) d\ln C^p\, dm^p \end{aligned} \tag{9.43}$$

where the joint PDF $f''_{\boldsymbol{\Theta}_{\mathrm{dam}}^p}\left(\boldsymbol{\theta}_{\mathrm{dam}}^p\right)$ is defined as $f''_{\boldsymbol{\Theta}_{\mathrm{dam}}^p}\left(\boldsymbol{\theta}_{\mathrm{dam}}^p\right) = f''_{\ln C^p,\, m^p}\left(\ln C^p, m^p\right)$ and, during the practical application of the proposed prognosis framework to this specific application example, is computed by mapping $f''_{\mathbf{Z}^p}\left(\mathbf{z}^p\right)$ into the physical parameter space $\boldsymbol{\Theta}_{\mathrm{dam}}^p$ through the linear transformation $\boldsymbol{\Theta}_{\mathrm{dam}}^p = \boldsymbol{\Phi}^{-1}\mathbf{Z}^p + \mu_{\boldsymbol{\Theta}_{\mathrm{dam}}^0}$ presented earlier.

The crack propagation analysis at time N_p thus depends on the three random variables A_a^p, Z_1^p, and Z_2^p; or, in an equivalent way, on A_a^p, $\ln C^p$, and m^p. The most probable crack propagation trajectory can therefore be computed by solving Equation (9.35) for the corresponding modal values of the three random variables involved. This approach is herein referred to as Maximum a posteriori probability

(MAP) criterion and uses the modal values of A_a^p, Z_1^p, and Z_2^p based on their corresponding posterior marginal PDFs computed at time N_p: $f''_{A_a^p}\left(a_a^p\right)$, $f''_{Z_1^p}\left(z_1^p\right)$, and $f''_{Z_2^p}\left(z_2^p\right)$. Alternatively, the expected values of A_a^p, Z_1^p, and Z_2^p could be used in place of the modal values. The result obtained from the numerical integration of Equation (9.35) according to this alternative approach would provide the expected (i.e., average) crack propagation trajectory. For the case in which the posterior PDFs of A_a^p, Z_1^p, and Z_2^p are unimodal and symmetric with respect to their modal values, the two approaches aforementioned would lead to the same result — i.e., the MAP crack propagation trajectory would coincide with the expected propagation path.

Together with the MAP and/or the expected crack propagation trajectory, it is also possible to provide prediction intervals (or prediction bands) of $(1-\alpha)\%$ confidence level for the crack propagation predictions. This result is achieved by defining $(1-\alpha/3)\%$ probability intervals for each of the three random variables involved in the propagation process as shown in the two Equations below:

$$\left(z_{i,\min}^p, z_{i,\max}^p\right): P\left[z_{i,\min}^p \le Z_i^p \le z_{i,\max}^p\right] = P\left[E_i\right] = 1-\frac{\alpha}{3}, \quad i=1,2 \tag{9.44}$$

$$\left(a_{a,\min}^p, a_{a,\max}^p\right): P\left[a_{a,\min}^p \le A_a^p \le a_{a,\max}^p\right] = P\left[E_3\right] = 1-\frac{\alpha}{3} \tag{9.45}$$

According to this procedure, the three pairs of values $\left(z_{1,\min}^p, z_{1,\max}^p\right)$, $\left(z_{2,\min}^p, z_{2,\max}^p\right)$, and $\left(a_{a,\min}^p, a_{a,\max}^p\right)$, satisfy the two conditions shown below:

$$\int_{z_{i,\min}^{p}}^{z_{i,\max}^{p}} f''_{Z_i^p}\left(z_i^p\right) dz_i^p = P\left[E_i\right] = 1 - \frac{\alpha}{3}, \quad i = 1,2 \tag{9.46}$$

$$\int_{a_{a,\min}^{p}}^{a_{a,\max}^{p}} f''_{A_a^p}\left(a_a^p\right) da_a^p = P\left[E_3\right] = 1 - \frac{\alpha}{3} \tag{9.47}$$

Furthermore, by making use of Bonferroni inequality (Seber and Lee, 2003), the confidence level for the simultaneous event defined by $E \triangleq \left\{E_1 \cap E_2 \cap E_3\right\}$ can be expressed as

$$P\left[E_1 \cap E_2 \cap E_3\right] \geq 1 - 3\left(\frac{\alpha}{3}\right) = \left(1 - \alpha\right) \tag{9.48}$$

In this specific numerical application, the value of α is set as $\alpha = 0.1$ and therefore the simultaneous prediction interval exhibits a confidence level of at least 90%. The least and most critical combinations, in terms of rate of crack propagation, of the values $\left(z_{1,\min}^{p}, z_{1,\max}^{p}\right)$, $\left(z_{2,\min}^{p}, z_{2,\max}^{p}\right)$, and $\left(a_{a,\min}^{p}, a_{a,\max}^{p}\right)$ are then used in the damage propagation law reported in Equation (9.35) to provide the prediction bands, with 90% level of confidence, shown in figures 9.26 through 9.29.

Figure 9.26 shows the MAP crack propagation predictions (dashed red line) and the corresponding 90% prediction bands (light-yellow patches) computed using 5 NDE measurements at each inspection opportunity (i.e., $n_{\mathrm{MS}}^{p} = 5,\ p = 0, 1, ..., 40$). MAP predictions and their corresponding prediction bands are updated after each NDE inspection (i.e., every $\Delta N = 5{,}000$ cycles in this specific application example); however, for illustration and demonstration purposes and to facilitate the interpretation

of figures 9.26 through 9.29, these predictions are recursively updated every 20,000 cycles (i.e., every four NDE inspections). The MAP crack propagation prediction and its corresponding prediction band between $N_0 = 0$ cycles and $N_4 = 20,000$ cycles are computed by making use of the posterior PDF of A_a^0, $f''_{A_a^0}\left(a_a^0\right)$, and the initial prior joint PDF of $\mathbf{Z}^0$, $f''_{\mathbf{Z}^0}\left(\mathbf{z}^0\right)$. The predictions, between $N_4 = 20,000$ cycles and $N_8 = 40,000$ cycles, are instead based on the posterior PDF of A_a^4, $f''_{A_a^4}\left(a_a^4\right)$, and the posterior joint PDF of $\mathbf{Z}^4$, $f''_{\mathbf{Z}^4}\left(\mathbf{z}^4\right)$. This process is repeated up to $N_{40} = 200,000$ cycles.

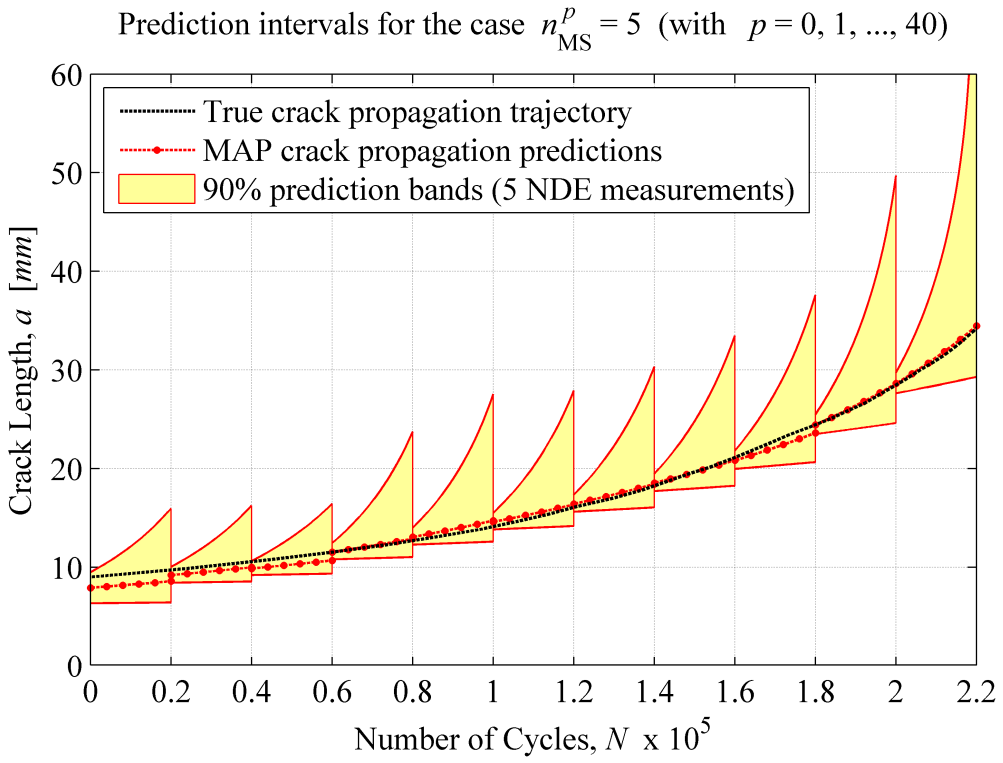

Figure 9.26: MAP crack propagation predictions and corresponding 90% prediction intervals for *sample trajectory #1*, obtained by using 5 NDE measurements at each NDE inspection opportunity. Predictions recursively updated every 20,000 cycles.

Figure 9.27 and Figure 9.28 present the same type of results, associated to the pseudo-continuous NDE monitoring of the *sample trajectory #1* and computed for the case in which $n_{MS}^{p} = 10$ and $n_{MS}^{p} = 20$ (with $p = 0, 1, ..., 40$), respectively. These two additional sets of results indicate that a larger number of NDE measurements substantially improves the MAP crack propagation predictions and, at the same time, helps to provide tighter prediction bands.

Finally, Figure 9.29 compares the two sets of results corresponding to $n_{MS}^{p} = 5$ and $n_{MS}^{p} = 20$ (with $p = 0, 1, ..., 40$). This comparison emphasizes, one more time, the clear benefit provided by a larger set of NDE measurements. It is indeed straightforward

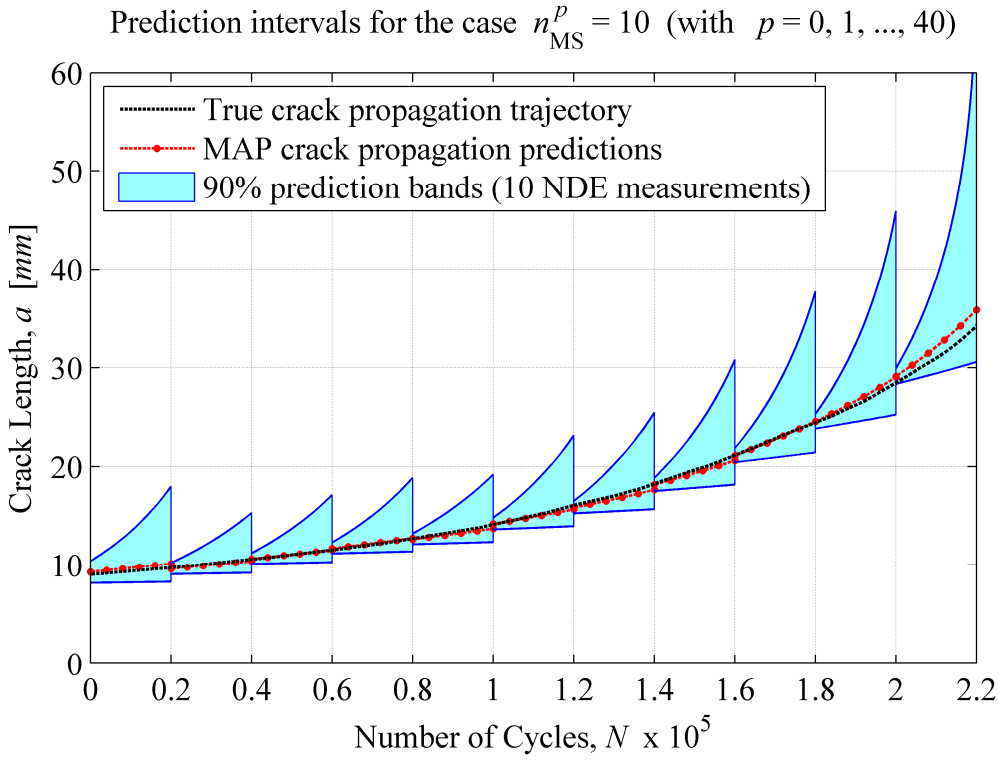

Figure 9.27: MAP crack propagation predictions and corresponding 90% prediction intervals for *sample trajectory #1*, obtained by using 10 NDE measurements at each NDE inspection opportunity. Predictions recursively updated every 20,000 cycles.

to observe from Figure 9.29 how the prediction bands corresponding to the case $n_{\text{MS}}^{p} = 20$ (with $p = 0, 1, ..., 40$) are always tighter than their counterparts (i.e., the prediction intervals computed using 5 NDE measurements at each inspection opportunity). More specifically for this particular example, at the eleven instants of time $\left(N_p + 20{,}000\right)$ cycles — with $N_p = \left(5{,}000 \times p\right)$ cycles and $p = 0, 4, 8, ..., 40$ — the prediction bands obtained by making use of 5 NDE measurements at each inspection opportunity are on average ~1.70 times wider than those derived for the case in which 20 NDE measurements are collected and processed at each inspection opportunity, i.e., $n_{\text{MS}}^{p} = 20$ (with $p = 0, 1, ..., 40$). Furthermore, the maximum gain is determined as

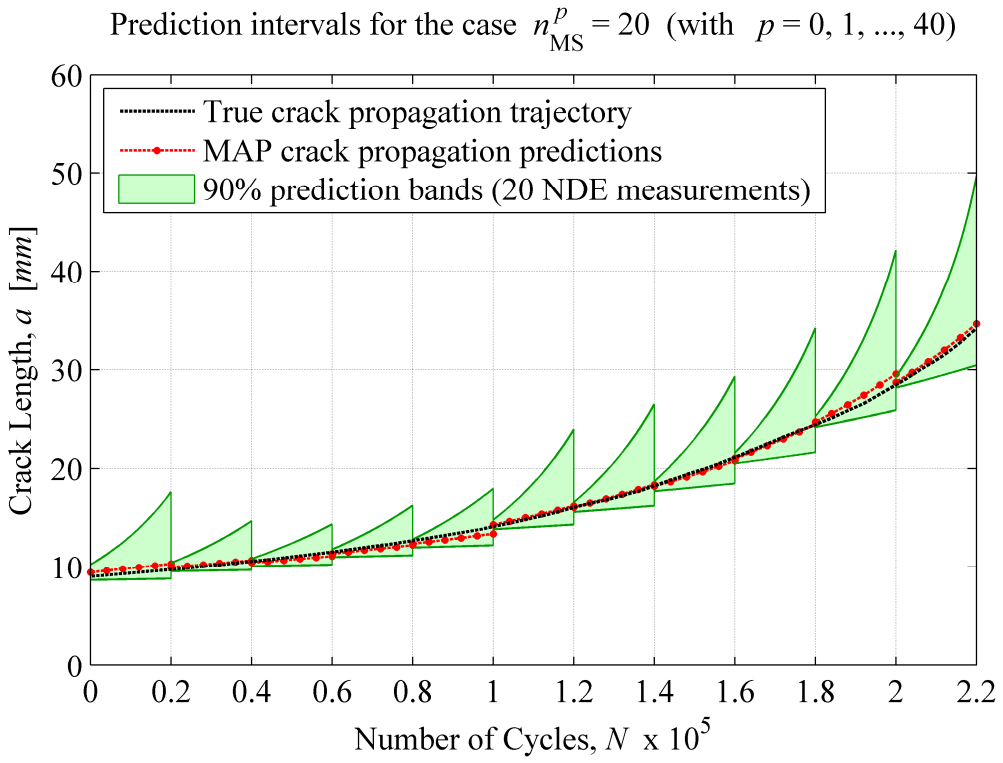

Figure 9.28: MAP crack propagation predictions and corresponding 90% prediction intervals for *sample trajectory #1*, obtained by using 20 NDE measurements at each NDE inspection opportunity. Predictions recursively updated every 20,000 cycles.

$$\max_{p}\left(\frac{a_{a,upper}^{[p,4]}\left(n_{\mathrm{MS}}^{p}=5\right)-a_{a,lower}^{[p,4]}\left(n_{\mathrm{MS}}^{p}=5\right)}{a_{a,upper}^{[p,4]}\left(n_{\mathrm{MS}}^{p}=20\right)-a_{a,lower}^{[p,4]}\left(n_{\mathrm{MS}}^{p}=20\right)}\right)\cong 2.60,\quad p=0,4,8,...,40 \tag{9.49}$$

where $a_{a,upper}^{[p,4]}(\bullet)$ and $a_{a,lower}^{[p,4]}(\bullet)$ are the upper and lower bounds (at time $N_p^q = N_p + q\Delta N = N_p + 4\times 5{,}000$ cycles) for the 90% prediction intervals computed at time N_p. The two terms at the numerator correspond to the case $n_{\mathrm{MS}}^{p}=5$ (with $p=0,1,...,40$), while the other two terms at the denominator refer to $n_{\mathrm{MS}}^{p}=20$ (with $p=0,1,...,40$). As can also be inferred from Figure 9.29, this maximum gain (in terms

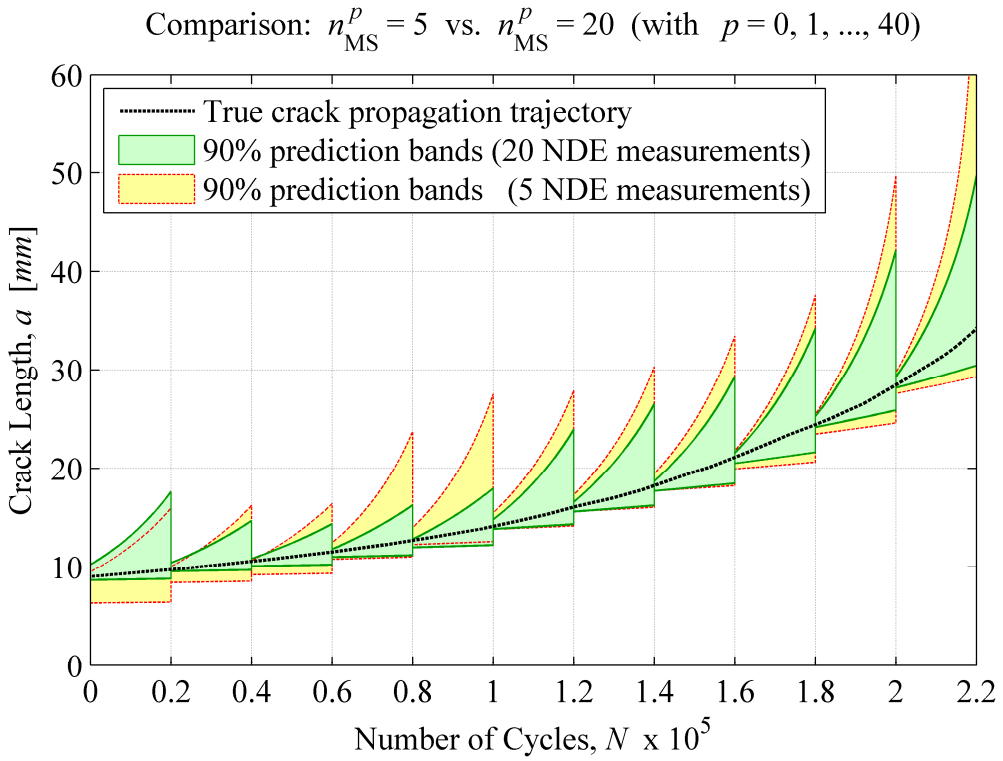

Figure 9.29: Comparison between two sets of 90% prediction intervals for *sample trajectory #1*. Yellow patches: prediction bands obtained by using 5 NDE measurements at each inspection opportunity. Green patches: prediction bands obtained by using 20 NDE measurements at each inspection opportunity. Predictions recursively updated every 20,000 cycles for illustration purposes.

of bandwidth reduction of the prediction intervals) is obtained at time $N_{16}+20,000=$ $(5,000\times16)+20,000=100,000$ cycles. At that instant of time the prediction band obtained by making use of 5 NDE measurements at each inspection opportunity is about 2.60 times wider than the corresponding counterpart, derived for the case in which 20 NDE measurements are collected and processed at each inspection opportunity

9.3.8. Prediction intervals associated with the continuous monitoring of the sample damage evolution trajectory #2

The selected *sample trajectory #2*, is monitored through 51 NDE inspections (evenly spaced every $\Delta N=5,000$ cycles) between time $N_0=0$ cycles and time $N_{50}=250,000$ cycles. After each of these 51 NDE inspections, the posterior PDF of the crack length A_a^p, denoted as $f''_{A_a^p}\left(a_a^p\right)$, and the posterior joint PDF of the damage evolution model parameter vector $\mathbf{Z}^p=\left\{Z_1^p,Z_2^p\right\}$, symbolized by $f''_{\mathbf{Z}^p}\left(\mathbf{z}^p\right)$, are recursively updated through the proposed Bayesian inference scheme. This recursive updating process uses the NDE measurements collected at each inspection opportunity and therefore, for the specific case presented herein, it uses either 5, 10, or 20 NDE measurements at each of the 51 inspection opportunities envisioned. The posterior (unconditional) PDF $f''_{A_a^p}\left(a_a^p\right)$, computed by taking advantage of the total probability theorem as already shown in Equations (9.42) and (9.43), is then used together with $f''_{\mathbf{Z}^p}\left(\mathbf{z}^p\right)$ to provide the MAP crack propagation predictions and their corresponding prediction intervals (or prediction bands). These intervals, with a confidence level of

$(1-\alpha)\%$, are computed according to the procedure outlined in Section 9.3.7. The results obtained by applying this procedure to the NDE monitoring of the *sample trajectory #2* are summarized in figures 9.30 through 9.33. The predictions, between $N_p = 5{,}000 \cdot (p-1)$ cycles and $N_{p+1} = N_p + 20{,}000$ cycles (with $p = 0, 1, ..., 50$), are based on the posterior PDF of A_a^p, denoted as $f''_{A_a^p}(a_a^p)$, and the posterior joint PDF of $\mathbf{Z}^p$, represented by $f''_{\mathbf{Z}^p}(\mathbf{z}^p)$. Furthermore, as it was done in Section 9.3.7, even though MAP crack propagation predictions and their corresponding prediction bands are updated after each NDE inspection (i.e., every 5,000 cycles in this specific

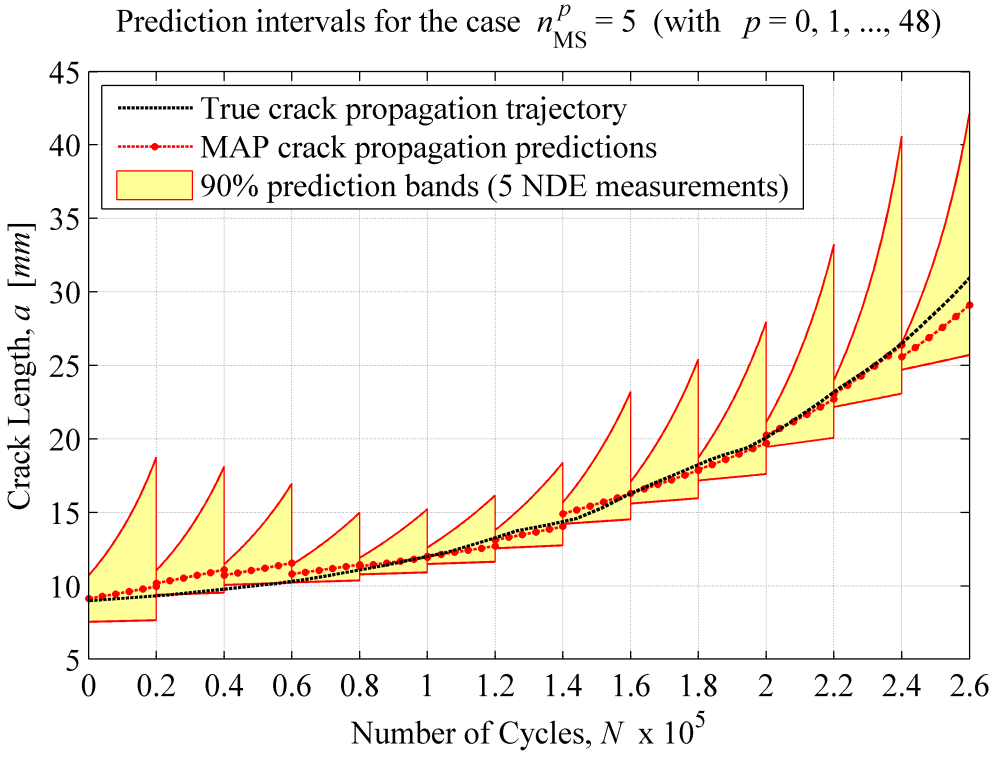

Figure 9.30: MAP crack propagation predictions and corresponding 90% prediction intervals for *sample trajectory #2*, obtained by using 5 NDE measurements at each NDE inspection opportunity. Predictions recursively updated every 20,000 cycles.

application example), they are recursively updated only every 20,000 cycles (i.e., every four NDE inspections) in the subsequent figures. Again, this choice is exclusively intended for illustration and demonstration purposes and it also facilitates the interpretation of figures 9.30 through 9.33. More specifically for this particular example, at the eleven instants of time $\left(N_p + 20{,}000\right)$ cycles — with $N_p = \left(5{,}000 \times p\right)$ cycles and $p = 0, 4, 8, ..., 40$ — the prediction bands obtained by making use of 5 NDE measurements at each inspection opportunity are on average ~1.60 times wider than those derived for the case in which 20 NDE measurements are collected and processed at each inspection opportunity, i.e., $n_{\text{MS}}^{p} = 20$ (with $p = 0, 1, ..., 40$). Furthermore,

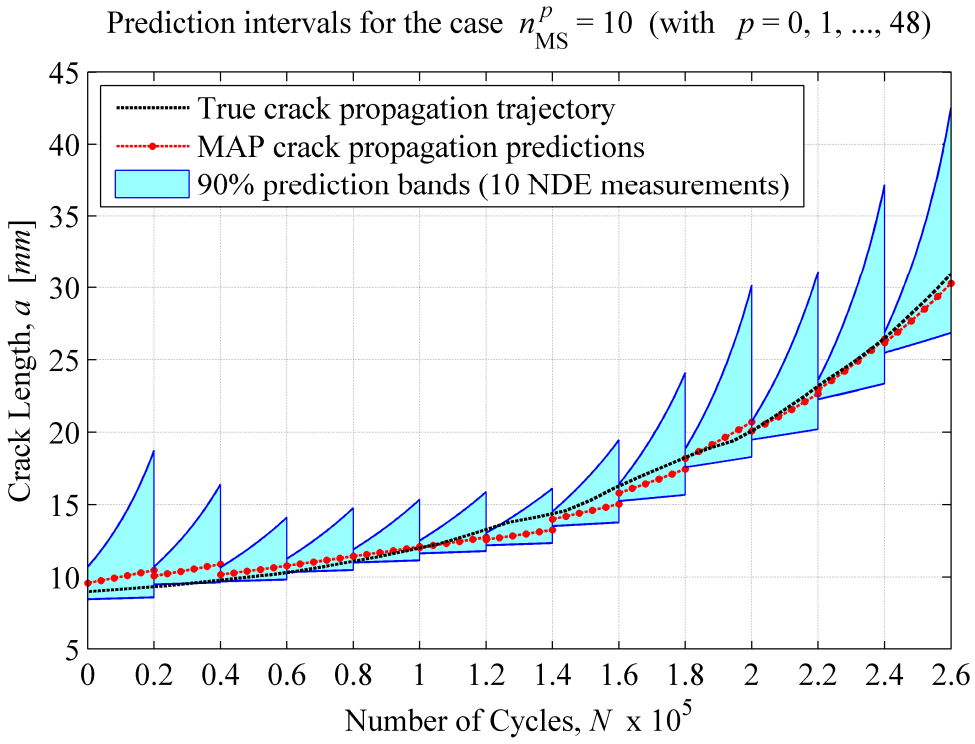

Figure 9.31: MAP crack propagation predictions and corresponding 90% prediction intervals for *sample trajectory #2*, obtained by using 10 NDE measurements at each NDE inspection opportunity. Predictions recursively updated every 20,000 cycles.

using the same notation introduced in Section 9.3.7, the maximum gain (provided by the larger number of NDE measurements) is determined as

$$\max_{p}\left(\frac{a_{a,upper}^{[p,p+4]}\left(n_{\mathrm{MS}}^{[0,p]}=5\right)-a_{a,lower}^{[p,p+4]}\left(n_{\mathrm{MS}}^{[0,p]}=5\right)}{a_{a,upper}^{[p,p+4]}\left(n_{\mathrm{MS}}^{[0,p]}=20\right)-a_{a,lower}^{[p,p+4]}\left(n_{\mathrm{MS}}^{[0,p]}=20\right)}\right)\cong 1.75,\quad p=0,4,8,...,40 \qquad (9.50)$$

and it is obtained at time $N_{44}+20{,}000=\left(5{,}000\times 44\right)+20{,}000=240{,}000$ cycles. At that instant of time the prediction band obtained by making use of 5 NDE measurements at each inspection opportunity is about 1.75 times wider than the corresponding counterpart, derived for the case in which 20 NDE measurements are collected and processed at each inspection opportunity.

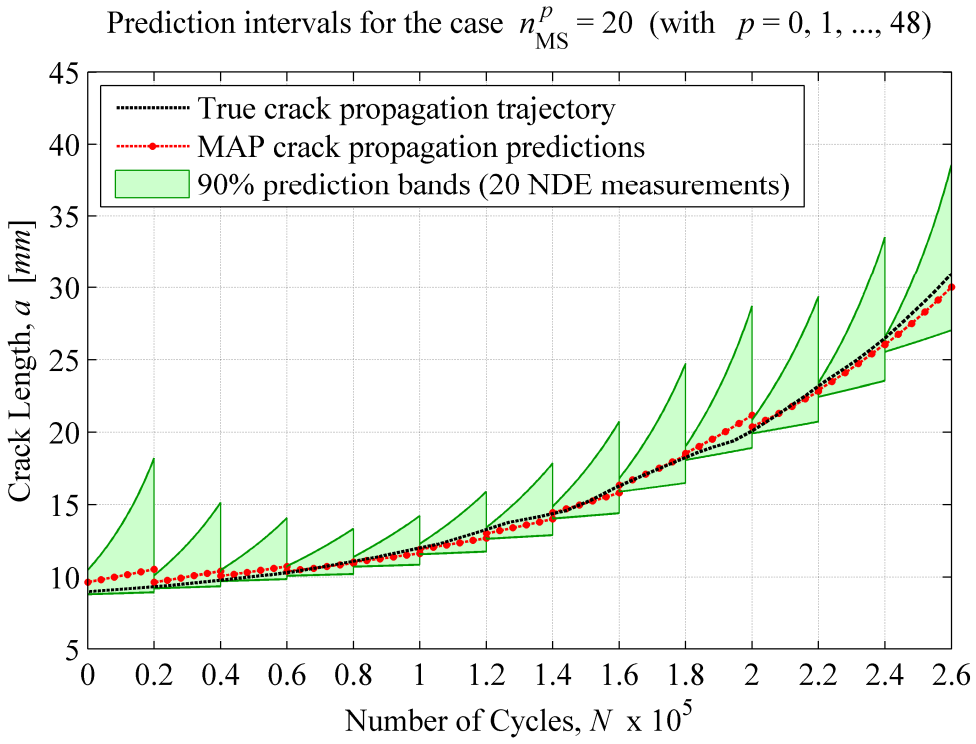

Figure 9.32: MAP crack propagation predictions and corresponding 90% prediction intervals for *sample trajectory #2*, obtained by using 20 NDE measurements at each NDE inspection opportunity. Predictions recursively updated every 20,000 cycles.

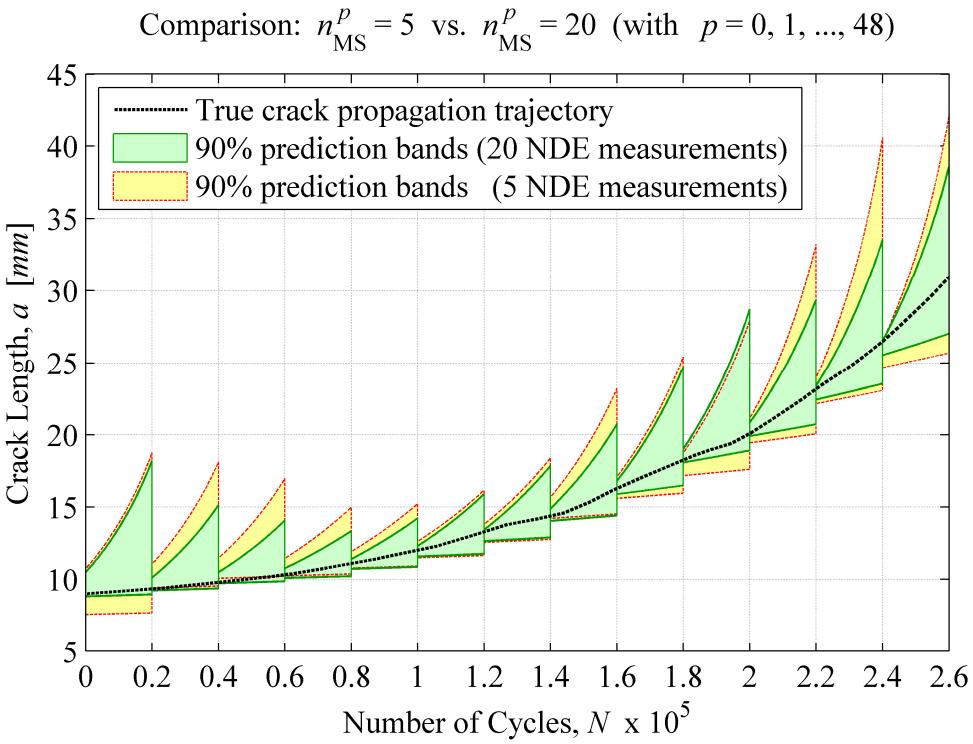

Figure 9.33: Comparison between two sets of 90% prediction intervals for *sample trajectory #2*. Yellow patches: prediction bands obtained by using 5 NDE measurements at each inspection opportunity. Green patches: prediction bands obtained by using 20 NDE measurements at each inspection opportunity. Predictions recursively updated every 20,000 cycles for illustration purposes.

References

ASTM Standard D6671-04, Standard test method for mixed mode I - mode II interlaminar fracture toughness of unidirectional fiber reinforced polymer matrix composites, 2004.

A.P. Berens, NDE reliability analysis, *Metals Handbook*, Vol. 17. 9th ed. ASM International, 689-701, 1989.

N. Blanco, E.K. Gamstedt, L.E. Asp, and J. Costa, Mixed-mode delamination growth in carbon-fiber composite laminates under cyclic loading, *International Journal of Solids and Structures*, 41(15), 4219-4235, 2004.

W.F. Brown and J.E. Srawley, Plane strain crack toughness testing of high strength metallic materials, STP 410, ASTM, Philadelphia, 1-65, 1966.

J. Ching and Y.-C. Chen, Transitional Markov Chain Monte Carlo method for Bayesian model updating, model class selection, and model averaging, *Journal of Engineering Mechanics*, 133(7), 816-832, 2007.

J. Degrieck and W.V. Paepegem, Fatigue damage modeling of fibre-reinforced composite materials: Review, *Applied Mechanics Reviews*, 54(4), 2001.

C.E. Fedderson, Plain strain crack toughness testing of high strength metallic materials, STP 410, ASTM, Philadelphia, 77-79, 1966.

R.G. Forman, Study of fatigue crack initiation from flaws using fracture mechanics theory. *Engineering Fracture Mechanics*, 4(2), 333-345, 1972.

X. Guan, R. Jha, and Y. Liu, Probabilistic fatigue damage prognosis using maximum entropy approach, *Journal of Intelligent Manufacturing*, 20(6), 2009.

N. Isida, Stress-intensity factors for the tension of an eccentrically cracked strip, *Journal of Applied Mechanics*, 33, 674-675, 1966.

R.M. Jones, Apparent flexural modulus and strength of multimodulus materials, *Journal of Composite Materials*, 10, 342-354, 1976.

J.F. Kenney and E.S. Keeping, *Mathematics of Statistics, Pt. 2, 2nd ed.*, Princeton, NJ: Van Nostrand, 1951.

C. Kleiber and S. Kotz, *Statistical Size Distributions in Economics and Actuarial Sciences*, John Wiley & Sons Inc., NJ, 2003.

Z.A. Kotulski, On efficiency of identification of a stochastic crack propagation model based on Virkler experimental data, *Archives of Mechanics*, 50(5), 829-847, 1998.

M. Kutner, C. Nachtsheim, J. Neter, and W. Li, *Applied linear statistical models*, 5th edition, McGraw-Hill, 2004.

D.F. Ostergaard and B.M. Hillberry, Characterization of the variability in fatigue crack propagation data, *Probabilistic Fracture Mechanics and Fatigue Methods: Applications for Structural Design and Maintenance, ASTM STP 798, J.M. Bloom and J.C. Ekvall (Eds.)*, 97-115, 1983.

G.A.F. Seber, and A.J. Lee, *Linear regression analysis*, second edition, Wiley Series in Probability and Statistics, John Wiley & Sons Inc., NJ, 2003.

R.J. Sanford, *Principles of fracture mechanics*, Prentice Hall, 2003.

D.A. Virkler, B.M. Hillberry, and P.K. Goel, The statistical nature of fatigue crack propagation, *Transactions of ASME - Journal of Engineering Materials and Technology*, 101, 148-153, 1979.

Y.-K. Wen, *Structural load modeling and combination for performance and safety evaluation*, Elsevier, 1990.

R. Zhang, and S. Mahadevan, Fatigue reliability analysis using non-destructive inspection, Journal of Structural Engineering, ASCE, 127(8), 957-965, 2001.

CHAPTER 10

CONCLUSIONS AND FUTURE WORK

10.1. Summary of the research work performed

The research work presented in this thesis is focused on the development of a novel and comprehensive reliability-based damage prognosis framework for time-dependent reliability assessment and remaining fatigue life prediction of bonded composite structures used in the aerospace field. Among these structures, unmanned aerial vehicles (UAVs) represent a typical example of how extensively light-weight composite materials can be used in aircrafts and aerospace systems in general. Various damage mechanisms (e.g., debonding, inter-ply delamination, fiber breakage, and matrix cracking) can initiate and invisibly propagate to catastrophic levels in the most damage-sensitive UAV primary structural components, such as the wings, the tail stabilizers, and the fuselage. Furthermore, the absence of an onboard pilot on this type of vehicles and their operating environments (e.g., military zones) lead to higher levels

of damage tolerance in the airframe. Therefore, as a direct consequence, there is the need of providing an effective structural monitoring through continuous (online) and periodic (on ground) non destructive evaluation (NDE) inspections.

As a result of the considerations outlined above, the first seven chapters of this thesis address the applicability of the proposed damage prognosis framework to a composite UAV wing whose skin-to-spar adhesive joints are recognized as one of the most critical and fatigue-sensitive sub-components of the entire aircraft. The proposed framework repeatedly uses processed NDE results (i.e., results after NDE sensor data processing) to recursively provide an updated probabilistic characterization of the current structural integrity. This updated information is then used as starting point to perform all the subsequent analysis steps, part of the methodology, and predict the time-dependent reliability index of the structural system as fatigue-driven damage progresses. The final results, obtained from the application of the proposed damage prognosis framework, can be used as a rational and objective basis for updating the remaining service life of the monitored structural system as well as the maintenance program, thereby optimizing the overall life-cycle cost of the structure. This last objective represents the ultimate goal of an integrated structural health monitoring and damage prognosis (SHM-DP) methodology. The target results aforementioned are herein achieved through five analytical steps: (1) Bayesian inference analysis, (2) probabilistic load hazard analysis, (3) probabilistic structural response analysis, (4) probabilistic flutter & limit cycle oscillation (LCO) analyses, and (5) damage prognosis analysis. The major sources of uncertainty in each of these five analytical

steps of the proposed framework have been explicitly and rigorously accounted for throughout this thesis. Furthermore, all these steps are carefully integrated into the framework by making use of the total probability theorem — i.e., the probabilistic tool allowing for the uncertainty propagation process through the various analysis steps mentioned above.

In Chapters 8 and 9 the proposed damage prognosis framework is generalized to other structural systems and is exercised, verified, and validated through three numerical applications, with increasing levels of complexity. Additionally, in Chapter 8, the effectiveness and robustness of the framework is assessed through a series of comparative and parametric studies. In these two chapters, the five analytical steps presented in Chapters 3 through 7 are generalized and re-designated as: (1) Bayesian inference analysis, (2) probabilistic load hazard analysis, (3) probabilistic damage evolution analysis, (4) probabilistic global performance analysis, and (5) damage prognosis analysis. *Step 1* (i.e., Bayesian inference) and *Step 5* (i.e., damage prognosis) are identical to the corresponding steps discussed and analyzed in Chapter 3 and Chapter 7, respectively. On the other hand, in this generalized version of the proposed framework, *Step 2* (i.e., probabilistic load hazard analysis) accommodates the probabilistic characterization of different loading scenarios (i.e., not only maneuver-induced and turbulence-induced loads as undertaken in Chapter 4). *Step 3*, namely probabilistic damage evolution analysis, is nearly identical to its counterpart described in Chapter 5, but it now uses different loading information (due to the changes in *Step 2*). Finally, *Step 4* (i.e., probabilistic global performance analysis)

allows for the consideration of a broader spectrum of global performance measures/metrics (i.e., not only flutter and limit cycle oscillation velocities as originally presented in Chapter 6).

The numerical application presented in Chapter 8 and the first one of Chapter 9, use a simple benchmark structure consisting of a simply supported composite beam made out of two identical unidirectional laminated composite adherends with solid rectangular cross section. These two adherends are bonded together through an idealized (but imperfect) zero-thickness adhesive interface/layer that is recognized as the unique damageable sub-component of the composite beam. The debonding process along the adhesive interface is considered as the only damage mechanism evolving in time and is assumed to be driven by a dynamic concentrated load applied at the beam midspan. Furthermore, two debonding fronts, propagating from the two end supports (i.e., from the beam ends) towards the beam midspan, are considered in the application examples provided. In Chapter 8, the damage propagation process along the adhesive interface is postulated to follow an exponential law, while in Chapter 9, a damage propagation model (*Forman's model*) based on linear elastic fracture mechanics (LEFM) principles is successfully used within the proposed framework. In the third numerical application, a set of experimental fatigue test data, obtained from the literature, is used to provide a first experimental validation of the proposed damage prognosis framework, with special emphasis on the recursive Bayesian inference scheme and the probabilistic damage evolution analysis step. The dataset used consists

of 68 crack propagation trajectories obtained from a series of fatigue tests performed on center-cracked 2024-T3 aluminum plates.

The three benchmark applications provided in chapters 8 and 9 of the thesis, and briefly recalled above, allowed for:

(i) Verifying and validating the proposed recursive Bayesian inference scheme used to update both damage extents and damage evolution model parameters, with the measured damage sizes representing an indicator of the stage of formation of a particular failure mechanism;

(ii) Illustrating the use of the proposed probabilistic load characterization and superposition analysis, thoroughly discussed in Chapter 4 and in Section 8.3.2 in Chapter 8;

(iii) Evaluating the computational cost of the probabilistic damage propagation analysis step and the approximations introduced by the proposed simplifying assumptions introduced in the numerical implementation of the proposed damage prognosis framework (see Chapter 9);

(iv) Assessing the correctness and effectiveness of the proposed local and global component failure criteria, used in the component reliability analyses and thoroughly analyzed in Chapter 7 and Chapter 8;

(v) Quantifying the precision and confidence levels of the damage prognosis results obtained by making use of the enhanced state-of-the-art expressions for the uni-modal bounds of the probabilities of system failure and false-call, defined and derived in Chapter 7 and Chapter 8.

(vi) Validating the proposed recursive Bayesian inference scheme and the probabilistic damage evolution analysis step with a large dataset of experimental fatigue test data obtained from the literature.

The success of combined SHM-DP methodologies, aimed at providing an optimal structural health management over the entire service life of a given structural, mechanical, aerospace, or automotive system, can be quantified through different measures such as (i) total cost reduction to the owner, (ii) reduction in the number of maintenance-hours per operational hour, (iii) reduction in system downtime, (iv) extension of system service life, and (v) enhancement of system reliability. Under this perspective, the damage prognosis framework proposed in this research work constitutes an essential tool to accomplish these objectives through a condition-based and cost-efficient maintenance that uses real-time NDE data, collected during the regular operation of the system, to prioritize and optimize maintenance resources, i.e., to perform maintenance only upon the evidence of need.

10.2. Summary of major findings and novel contributions

The field of SHM-DP for civil, mechanical, and aerospace structures and infrastructures is a complex and multidisciplinary emerging research field. Technical expertise and advanced knowledge from different engineering fields must be synergically combined together in order to be able to successfully deploy an efficient and robust SHM-DP system. Under this perspective, the proposed reliability-based damage prognosis methodology developed and analyzed in this thesis, represents an advanced and flexible analysis tool rigorously integrating in a meaningful and

powerful manner (i) probabilistic treatment of (local) NDE inspection results, (ii) recursive Bayesian inference, (iii) damage evolution prediction, (iv) state-of-the-art component and system reliability analyses, and (v) decision making for optimal life-cycle cost management.

The principal contributions and the major findings of this research work are summarized below:

(i) The proposed framework is formulated to allow direct consideration of the uncertainties related to: NDE detection and measurement capabilities, material model parameters, damage evolution model parameters, and future operational loads. Modeling uncertainties could also be included in the framework; however, this topic is not included in this thesis.

(ii) The proposed recursive Bayesian inference scheme is capable of repeatedly updating the joint probability distribution functions (PDFs) of damage sizes and damage evolution model parameters. This updating operation is performed in a simultaneous fashion every time new NDE results become available and are incorporated into the framework. This research work shows the consistent benefits provided by a *full* recursive updating scheme (i.e., when the PDFs of both, damage sizes and damage evolution model parameters, are simultaneously updated) as opposed to a *partial* recursive Bayesian updating scheme (i.e., an updating scheme in which only the joint PDF of the damage sizes is updated). These benefits can be quantified in terms of uncertainty reduction in the posterior PDFs of damage sizes and damage evolution model

parameters, computed through the proposed updating scheme presented in Chapter 3. Additionally, the discrepancy between the predicted (based on the posterior PDFs) and the true values of the variables/parameters of interest can also be used to qualitatively evaluate the advantages offered by a *full* updating scheme. This proposed Bayesian updating approach permits to remain in touch with reality by exploiting the data collected from an envisioned continuous NDE monitoring system. Using this Bayesian framework, an initial probability model of a given set of engineering quantities (i.e., damage sizes and/or damage evolution model parameters) can be tuned into reality by processing observational information.

(iii) The proposed recursive Bayesian inference scheme can incorporate various NDE detection and sizing capabilities, from the *least capable* to *continuous resolution* NDE techniques. The least capable NDE technique provides only binary outputs (i.e., either *damage detected* or *damage not detected*) whereas a continuous resolution NDE technique, once damage is detected, can also quantify its extent. This quantification is affected by systematic and random measurement errors that need to be accounted for by using a so-called damage size measurement model (sometimes referred to as sizing model). A linear damage size measurement model, available in the literature, was used throughout this thesis; however, as discussed in Chapter 3, other damage size measurement models can be used and easily incorporated within the proposed Bayesian updating scheme. The observations made in this paragraph

demonstrate the versatility and the flexibility of the proposed recursive Bayesian inference scheme.

(iv) When a large amount of NDE results becomes available, the posterior PDFs of damage sizes and damage evolution model parameters, obtained from the proposed Bayesian updating scheme, are no longer influenced by the particular choice of the initial prior PDFs of damage sizes and damage evolution model parameters (i.e., those PDFs assigned at the beginning of the damage prognosis analyses on the basis of engineering judgment). A brief comparison study validating this statement is provided in Section 8.5.2 in Chapter 8.

(v) The influence of the number of NDE measurements and their precision (quantified through the standard deviation of the random measurement error) on the variance of the posterior PDF of the damage sizes is investigated in Section 8.5.3 in Chapter 8. As more and more data are collected, the variance of the posterior marginal PDFs of the damage sizes tend to become proportional to the inverse of the number of measurements.

(vi) Within the proposed component reliability analyses, introduced and thoroughly discussed in Chapter 7, various failure and false-call criteria are proposed by considering both, local and global, component level failures. Among them, the local component failure criterion, based on the level-of-safety (LOS) formulation with single NDE inspection opportunity, was recalled in Chapter 7 and, together with its dual counterpart (i.e., the false call event at the local component level based on the LOS formulation with single NDE inspection

opportunity), was efficiently incorporated in the proposed damage prognosis framework. This fact shows that results and theoretical developments from previous research work can be embedded into the proposed analysis framework.

(vii) The criteria for local component failure and false-call, based on the LOS formulation with single NDE inspection opportunity, are extended to the more general case in which multiple NDE inspection opportunities can be envisioned. Expressions for the probability of failure and false-call, associated with this failure and false-call criteria/events, are provided in Chapter 7.

(viii) Three distinct criteria for the probability of failure and two distinct criteria for the probability of false-call (at the overall system level) are provided in the discussion of the proposed system reliability analyses (see Section 7.5 in Chapter 7). Brief comparison studies analyzing the tightness of the proposed lower and upper uni-modal bounds are provided in Chapter 8.

(ix) The proposed failure criteria mentioned in parts (vii) and (viii) provide mathematical expressions for the limit state functions (at both component and system level) to be used when sample representations of the PDFs involved in the analyses are used. This is a very crucial point because it essentially states that the proposed framework can be readily adopted when Markov Chain Monte Carlo (MCMC) methods are used.

10.3. Recommendations for future research work

Based on the research work performed and presented in this thesis, several research topics and potential new research outlets in need of future work have been identified and hereafter summarized:

(i) The benchmark applications presented in this thesis, although enclosing the essential ingredients to mathematically engage all the five analytical steps of the proposed damage prognosis framework, do not involve any aerodynamic load modeling or fluid-structure interaction (FSI) response analysis. In the near future this research task must be undertaken to further verify and validate the proposed damage prognosis framework.

(ii) The results obtained from the application examples presented in Chapter 8 and Chapter 9 use a single realization of the NDE measurements at each inspection opportunity. Therefore, it is of interest studying the statistical variability of Bayesian inference, damage evolution, global performance, and component and system reliability analysis results. This objective is accomplished by generating an ensemble of NDE inspection results at each inspection opportunity, applying the proposed framework for each of these realizations (as described in Chapter 8 and Chapter 9), and evaluating the statistics of the response quantities of interest, such as lower and upper bounds of the probabilities of failure and false-call, across the ensemble of NDE measurements.

(iii) The overall computational feasibility, consistency, and robustness of the proposed damage prognosis framework need to be verified within the use of advanced MCMC methods. These methods use sample representations of all the random quantities involved in the uncertainty quantification and propagation process throughout the proposed framework. Their use is strongly recommended when dealing with a high-dimensional parameter space which, for the specific topic discussed in this thesis, translates into a large number of damage locations, damage mechanisms, as well as multiple material model and damage evolution model parameters.

(iv) The third analysis step of the proposed framework, namely *damage evolution analysis*, must be further verified by analyzing a fully coupled multi-site fatigue damage growth process. An example of a benchmark structure that could be used to verify and validate the third step of the proposed methodology under these more general and complicated constraints is provided in Appendix G.

(v) The use of mechanics-based damage models, calibrated and validated through experimental fatigue test data, can also be considered in future research work. The potential use of cohesive zone models (CZMs) to simulate fatigue-driven damage evolution processes along the adhesive joints of composite bonded structures was briefly discussed in Chapter 2 and Chapter 5. These types of models are embedded in the full finite

element model of the structure which is then used to derive more computationally efficient surrogate models.

(vi) Including impact-induced damage in the proposed framework represents another step to be considered in future research. This addition can be readily included within the proposed recursive Bayesian updating scheme; however, more research is needed in order to have an overall efficient embedment of this new feature. The damage evolution and global performance analysis steps represent a crucial part of the framework to be thoroughly investigated when impact-induced damage is considered. Including impact-induced damage as additional source of damage initiation will lead to consider adaptive response surface methods within the proposed probabilistic damage evolution and probabilistic global performance analysis steps. These methods are intended to provide computationally efficient surrogate models that can be adapted as new damage locations and/or damage mechanisms randomly form during the structure service life.

(vii) Integrating local NDE and global SHM data into the recursive Bayesian inference scheme will render the proposed damage prognosis framework even more robust and suitable for a broader range of applications (especially critical civil structures and infrastructures).

(viii) Finally, in the near future, the proposed framework can be extended, verified, and validated through its application to more realistic and

complex structural systems such as a realistic composite UAV wing, offshore platforms, and composite wind turbine blades. Furthermore, operational loads and extreme load events — such as earthquakes, tsunamis, and hurricanes — should be simultaneously considered (in a multi-hazard analysis fashion) in future work.

APPENDIX A

DERIVATION OF THE PROBABILITY OF LOCAL COMPONENT FAILURE, $P\left[\tilde{\mathrm{F}}_{\mathrm{L},ij}^{[p,q]}\right]$, ACCORDING TO THE LEVEL-OF-SAFETY FORMULATION WITH SINGLE NDE INSPECTION OPPORTUNITY

According to the local component failure event, $\tilde{\mathrm{F}}_{\mathrm{L},ij}^{[p,q]}$, based on the level-of-safety (LOS) formulation with single NDE inspection opportunity at time t_p^q (as introduced and discussed in Chapter 7), for a given/fixed value of the actual damage size $A_a^{(i,j,[p,q])} = a_a^{(i,j,[p,q])}$, and under the constraint $a_a^{(i,j,[p,q])} \geq a_c^{ij}$, the conditional modal probability of local component failure, $P\left[\tilde{\mathrm{F}}_{\mathrm{L},ij}^{[p,q]} \middle| a_a^{(i,j,[p,q])}\right]$, can be written as

$$\begin{aligned} P\left[\tilde{\mathrm{F}}_{\mathrm{L},ij}^{[p,q]} \middle| a_a^{(i,j,[p,q])}\right] &= P\left[\left\{\left(A_a^{(i,j,[p,q])} \geq a_c^{ij}\right) \cap \left(A_m^{(i,j,[p,q])} < a_c^{ij}\right)\right\} \middle| a_a^{(i,j,[p,q])}\right] \\ &= P\left[A_m^{(i,j,[p,q])} < a_c^{ij} \middle| a_a^{(i,j,[p,q])}\right] \end{aligned} \tag{A1}$$

Using now the total probability theorem (TPT) and the definitions of probability of detection (*POD*) and probability of non detection (*PND*) provided in Equations (3.1) and (3.3) in Chapter 3, Equation (A1) can be rewritten as

$$P\left[\tilde{\mathrm{F}}_{\mathrm{L},ij}^{[p,q]}\left|a_a^{(i,j,[p,q])}\right.\right]=P\left[A_m^{(i,j,[p,q])}<a_c^{ij}\left|a_a^{(i,j,[p,q])},D\right.\right]POD\left(a_a^{(i,j,[p,q])}\right)+ P\left[A_m^{(i,j,[p,q])}<a_c^{ij}\left|a_a^{(i,j,[p,q])},ND\right.\right]\left[1-POD\left(a_a^{(i,j,[p,q])}\right)\right] \quad \text{(A2)}$$

where *D* represents the detection event defined as $D\triangleq\left\{a_m^{(i,j,[p,q])}>0\right\}$ and *ND* denotes its complement (i.e., non-detection event) defined as $ND\triangleq\left\{a_m^{(i,j,[p,q])}=0\right\}$. Additionally, by noticing that $P\left[A_m^{(i,j,[p,q])}<a_c^{ij}\left|a_a^{(i,j,[p,q])},ND\right.\right]=1$, Equation (A2) can be simplified to

$$P\left[\tilde{\mathrm{F}}_{\mathrm{L},ij}^{[p,q]}\left|a_a^{(i,j,[p,q])}\right.\right]=1-\left\{1-P\left[A_m^{(i,j,[p,q])}<a_c^{ij}\left|a_a^{(i,j,[p,q])},D\right.\right]\right\}POD\left(a_a^{(i,j,[p,q])}\right) \quad \text{(A3)}$$

By recalling Equations (3.8) and (3.9) to express the conditional probability $P\left[A_m^{(i,j,[p,q])}<a_c^{ij}\left|a_a^{(i,j,[p,q])},D\right.\right]$, the above equation used to compute $P\left[\tilde{\mathrm{F}}_{\mathrm{L},ij}^{[p,q]}\left|a_a^{(i,j,[p,q])}\right.\right]$ can be further simplified to

$$P\left[\tilde{\mathrm{F}}_{\mathrm{L},ij}^{[p,q]}\left|a_a^{(i,j,[p,q])}\right.\right]=1-\left[1-\left(\int_{0^+}^{a_c^{ij}}\tilde{\varphi}\left(a_m^{(i,j,[p,q])},\hat{\mu}_{\mathrm{A_m|A_a}}^{(\mathrm{i,j,[p,q])}},\hat{\sigma}_{\varepsilon_{ij}}\right)da_m^{(i,j,[p,q])}\right)\right]POD\left(a_a^{(i,j,[p,q])}\right) \quad \text{(A4)}$$

where, by making use again of Equation (3.9) from Chapter 3, the integral between 0^+ and a_c^{ij} of the function $\tilde{\varphi}\left(a_m^{(i,j,[p,q])},\hat{\mu}_{\mathrm{A_m|A_a}}^{(i,j,[p,q])},\hat{\sigma}_{\varepsilon_{ij}}\right)$ can be expressed as

$$\int_{0^+}^{a_c^{ij}} \tilde{\varphi}\left(a_m^{(i,j,[p,q])}, \hat{\mu}_{A_m|A_a}^{(i,j,[p,q])}, \hat{\sigma}_{\varepsilon_{ij}}\right) da_m^{(i,j,[p,q])} =$$

$$\frac{\Phi\left(\dfrac{a_c^{ij} - \hat{\mu}_{A_m|A_a}^{(i,j,[p,q])}}{\hat{\sigma}_{\varepsilon_{ij}}}\right) - \Phi\left(-\dfrac{\hat{\mu}_{A_m|A_a}^{(i,j,[p,q])}}{\hat{\sigma}_{\varepsilon_{ij}}}\right)}{\Phi\left(\dfrac{\hat{\mu}_{A_m|A_a}^{(i,j,[p,q])}}{\hat{\sigma}_{\varepsilon_{ij}}}\right)} = 1 - \frac{\Phi\left(\dfrac{\hat{\mu}_{A_m|A_a}^{(i,j,[p,q])} - a_c^{ij}}{\hat{\sigma}_{\varepsilon_{ij}}}\right)}{\Phi\left(\dfrac{\hat{\mu}_{A_m|A_a}^{(i,j,[p,q])}}{\hat{\sigma}_{\varepsilon_{ij}}}\right)} \tag{A5}$$

By noticing that the conditional mean $\hat{\mu}_{A_m|A_a}^{(i,j,[p,q])}$ can be expressed as $\hat{\mu}_{A_m|A_a}^{(i,j,[p,q])} = \hat{\beta}_0^{(i,j)} + \hat{\beta}_1^{(i,j)} a_a^{(i,j,[p,q])}$, the above equation is rewritten as

$$\int_{0^+}^{a_c^{ij}} \tilde{\varphi}\left(a_m^{(i,j,[p,q])}, \hat{\mu}_{A_m|A_a}^{(i,j,[p,q])}, \hat{\sigma}_{\varepsilon_{ij}}\right) da_m^{(i,j,[p,q])} =$$

$$1 - \frac{\Phi\left(\dfrac{\hat{\beta}_0^{(i,j)} + \hat{\beta}_1^{(i,j)} a_a^{(i,j,[p,q])} - a_c^{ij}}{\hat{\sigma}_{\varepsilon_{ij}}}\right)}{\Phi\left(\dfrac{\hat{\beta}_0^{(i,j)} + \hat{\beta}_1^{(i,j)} a_a^{(i,j,[p,q])}}{\hat{\sigma}_{\varepsilon_{ij}}}\right)} = 1 - \hat{\psi}\left(a_a^{(i,j,[p,q])}; \hat{\beta}_0^{(i,j)}, \hat{\beta}_1^{(i,j)}, \hat{\sigma}_{\varepsilon_{ij}}\right) \tag{A6}$$

Finally, by substituting the result from Equation (A6) in Equation (A4), the conditional modal probability of failure, $P\left[\mathrm{F}_{\mathrm{L},ij}^{[p,q]} \middle| a_a^{(i,j,[p,q])}\right]$ (with $a_a^{(i,j,[p,q])} \geq a_c^{ij}$), can be expressed as

$$P\left[\tilde{\mathrm{F}}_{\mathrm{L},ij}^{[p,q]} \middle| a_a^{(i,j,[p,q])}\right] = 1 - \hat{\psi}\left(a_a^{(i,j,[p,q])}; \hat{\beta}_0^{(i,j)}, \hat{\beta}_1^{(i,j)}, \hat{\sigma}_{\varepsilon_{ij}}\right) POD\left(a_a^{(i,j,[p,q])}\right) \tag{A7}$$

And, by taking advantage of the TPT, the unconditional modal failure probability is then computed as shown in Equation (A8) below:

$$
\begin{aligned}
&P\left[\tilde{\mathrm{F}}_{\mathrm{L},ij}^{[p,q]}\right]= \\
&\int_{0}^{+\infty} P\left[\tilde{\mathrm{F}}_{\mathrm{L},ij}^{[p,q]}\,\middle|\,a_a^{(i,j,[p,q])}\right] f_{A_a^{(i,j,[p,q])}}\left(a_a^{(i,j,[p,q])}\right) da_a^{(i,j,[p,q])} = \\
&\left[1-F_{A_a^{(i,j,[p,q])}}\left(a_c^{ij}\right)\right]-\int_{a_c^{ij}}^{+\infty}\hat{\psi}\left(a_a^{(i,j,[p,q])}\right) POD\left(a_a^{(i,j,[p,q])}\right) f_{A_a^{(i,j,[p,q])}}\left(a_a^{(i,j,[p,q])}\right) da_a^{(i,j,[p,q])} = \\
&P\left[\mathrm{F}_{\mathrm{L},ij}^{[p,q]}\right]-\int_{a_c^{ij}}^{+\infty}\hat{\psi}\left(a_a^{(i,j,[p,q])}\right) POD\left(a_a^{(i,j,[p,q])}\right) f_{A_a^{(i,j,[p,q])}}\left(a_a^{(i,j,[p,q])}\right) da_a^{(i,j,[p,q])}
\end{aligned}
\tag{A8}
$$

APPENDIX B

DERIVATION OF THE PROBABILITY OF LOCAL COMPONENT FALSE-CALL, $P\left[\tilde{\mathscr{F}}_{\mathrm{L},ij}^{[p,q]}\right]$, ACCORDING TO THE LEVEL-OF-SAFETY FORMULATION WITH SINGLE NDE INSPECTION OPPORTUNITY

According to the local component false-call event, $\tilde{\mathscr{F}}_{\mathrm{L},ij}^{[p,q]}$, based on the level-of-safety (LOS) formulation with single NDE inspection opportunity at time t_p^q (as introduced and discussed in Chapter 7) for a given value of the actual damage size $A_a^{(i,j,[p,q])} = a_a^{(i,j,[p,q])}$, and under the condition $a_a^{(i,j,[p,q])} < a_c^{ij}$, the conditional probability of having a false-call (or false-alarm), $P\left[\tilde{\mathscr{F}}_{\mathrm{L},ij}^{[p,q]} \middle| a_a^{(i,j,[p,q])}\right]$, can be written as

$$\begin{aligned} P\left[\tilde{\mathscr{F}}_{\mathrm{L},ij}^{[p,q]} \middle| a_a^{(i,j,[p,q])}\right] &= P\left[\left\{\left(A_a^{(i,j,[p,q])} < a_c^{ij}\right) \cap \left(A_m^{(i,j,[p,q])} \geq a_c^{ij}\right)\right\} \middle| a_a^{(i,j,[p,q])}\right] \\ &= P\left[A_m^{(i,j,[p,q])} \geq a_c^{ij} \middle| a_a^{(i,j,[p,q])}\right] \end{aligned} \tag{B1}$$

Using the TPT and the definitions of *POD* and *PND* given in Equations (3.1) and (3.3) in Chapter 3, Equation (B1) can be rewritten as

$$\begin{aligned} P\left[\tilde{\mathcal{F}}_{\mathrm{L},ij}^{[p,q]} \middle| a_a^{(i,j,[p,q])}\right] &= P\left[A_m^{(i,j,[p,q])} \geq a_c^{ij} \middle| a_a^{(i,j,[p,q])}, D\right] POD\left(a_a^{(i,j,[p,q])}\right) + \\ &\quad P\left[A_m^{(i,j,[p,q])} \geq a_c^{ij} \middle| a_a^{(i,j,[p,q])}, ND\right]\left[1 - POD\left(a_a^{(i,j,[p,q])}\right)\right] \\ &= P\left[A_m^{(i,j,[p,q])} \geq a_c^{ij} \middle| a_a^{(i,j,[p,q])}, D\right] POD\left(a_a^{(i,j,[p,q])}\right) \end{aligned} \tag{B2}$$

where D represents the detection event defined as $D \triangleq \left\{a_m^{(i,j,[p,q])} > 0\right\}$ and *ND* denotes its complement (i.e., non-detection event) defined as $ND \triangleq \left\{a_m^{(i,j,[p,q])} = 0\right\}$. Employing Equations (3.8) and (3.9) to express the probability $P\left[A_m^{(i,j,[p,q])} \geq a_c^{ij} \middle| a_a^{(i,j,[p,q])}, D\right]$, the above equation further simplifies to

$$P\left[\tilde{\mathcal{F}}_{\mathrm{L},ij}^{[p,q]} \middle| a_a^{(i,j,[p,q])}\right] = \left(\int_{a_c^{ij}}^{+\infty} \tilde{\varphi}\left(a_m^{(i,j,[p,q])}, \hat{\mu}_{\mathrm{A_m|A_a}}^{(\mathrm{i,j,[p,q])}}, \hat{\sigma}_{\varepsilon_{ij}}\right) da_m^{(i,j,[p,q])}\right) POD\left(a_a^{(i,j,[p,q])}\right) \tag{B3}$$

where, by recalling again Equation (3.9) from Chapter 3, the integral between a_c^{ij} and $+\infty$ of the function $\tilde{\varphi}\left(a_m^{(i,j,[p,q])}, \hat{\mu}_{\mathrm{A_m|A_a}}^{(i,j,[p,q])}, \hat{\sigma}_{\varepsilon_{ij}}\right)$ can be expressed as

$$\begin{aligned} &\int_{a_c^{ij}}^{+\infty} \tilde{\varphi}\left(a_m^{(i,j,[p,q])}, \hat{\mu}_{\mathrm{A_m|A_a}}^{(i,j,[p,q])}, \hat{\sigma}_{\varepsilon_{ij}}\right) da_m^{(i,j,[p,q])} = \\ &\frac{1 - \Phi\left(\dfrac{a_c^{ij} - \hat{\mu}_{A_m|A_a}^{(i,j,[p,q])}}{\hat{\sigma}_{\varepsilon_{ij}}}\right)}{\Phi\left(\dfrac{\hat{\mu}_{A_m|A_a}^{(i,j,[p,q])}}{\hat{\sigma}_{\varepsilon_{ij}}}\right)} = \frac{\Phi\left(\dfrac{\hat{\mu}_{A_m|A_a}^{(i,j,[p,q])} - a_c^{ij}}{\hat{\sigma}_{\varepsilon_{ij}}}\right)}{\Phi\left(\dfrac{\hat{\mu}_{A_m|A_a}^{(i,j,[p,q])}}{\hat{\sigma}_{\varepsilon_{ij}}}\right)} = \\ &\hat{\psi}\left(a_a^{(i,j,[p,q])}; \hat{\beta}_0^{(i,j)}, \hat{\beta}_1^{(i,j)}, \hat{\sigma}_{\varepsilon_{ij}}\right) \end{aligned} \tag{B4}$$

Lastly, by substituting the final result of Equation (B4) into Equation (B3), the conditional modal probability of false-call, $P\left[\tilde{\mathscr{F}}_{\mathrm{L},ij}^{[p,q]} \middle| a_a^{(i,j,[p,q])}\right]$ (with $a_a^{(i,j,[p,q])} < a_c^{ij}$), can be expressed as

$$P\left[\tilde{\mathscr{F}}_{\mathrm{L},ij}^{[p,q]} \middle| a_a^{(i,j,[p,q])}\right] = \hat{\psi}\left(a_a^{(i,j,[p,q])}; \hat{\beta}_0^{(i,j)}, \hat{\beta}_1^{(i,j)}, \hat{\sigma}_{\varepsilon_{ij}}\right) POD\left(a_a^{(i,j,[p,q])}\right) \tag{B5}$$

and the unconditional modal probability of false-call is then computed, by taking advantage of the TPT, as shown in Equation (B6) below:

$$\begin{aligned} P\left[\tilde{\mathscr{F}}_{\mathrm{L},ij}^{[p,q]}\right] &= \int_0^{+\infty} P\left[\tilde{\mathscr{F}}_{\mathrm{L},ij}^{[p,q]} \middle| a_a^{(i,j,[p,q])}\right] f_{A_a^{(i,j,[p,q])}}\left(a_a^{(i,j,[p,q])}\right) da_a^{(i,j,[p,q])} \\ &= \int_0^{a_c^{ij}} \left[1 - \overline{\psi}\left(a_a^{(i,j,[p,q])}\right)\right] f_{A_a^{(i,j,[p,q])}}\left(a_a^{(i,j,[p,q])}\right) da_a^{(i,j,[p,q])} \\ &= \int_0^{a_c^{ij}} \hat{\psi}\left(a_a^{(i,j,[p,q])}\right) POD\left(a_a^{(i,j,[p,q])}\right) f_{A_a^{(i,j,[p,q])}}\left(a_a^{(i,j,[p,q])}\right) da_a^{(i,j,[p,q])} \end{aligned} \tag{B6}$$

APPENDIX C

DERIVATION OF LOWER AND UPPER UNI-MODAL BOUNDS TO THE PROBABILITY OF SYSTEM FAILURE, $P\left[\breve{F}_{sys}^{[p,q]}\right]$, ACCORDING TO THE LEVEL-OF-SAFETY FORMULATION WITH AN ASSUMED SINGLE NDE INSPECTION OPPORTUNITY

The expression for the failure event $\breve{F}_{sys}^{[p,q]}$, provided in Equations (7.36) and (7.37) in Chapter 7, can be rewritten (using set theory language) as

$$\breve{F}_{sys}^{[p,q]} \triangleq \breve{F}_{local}^{[p,q]} \cup \breve{F}_{global}^{[p,q]} \tag{C1}$$

where the two sub-events, $\breve{F}_{local}^{[p,q]}$ and $\breve{F}_{global}^{[p,q]}$, in Equation (C1) are introduced for the sake of conciseness and are defined as

$$\breve{\mathrm{F}}_{\mathrm{local}}^{[p,q]} \triangleq \left\{ \left[\bigcup_{i=1}^{n_{\mathrm{L}}^{[0,p]}} \left(\bigcup_{j=1}^{n_{\mathrm{DM}}^{(i,[0,p])}} \mathrm{F}_{\mathrm{L},ij}^{[p,q]} \right) \right] \cap \left[\bigcap_{i=1}^{n_{\mathrm{L}}^{[0,p]}} \left(\bigcap_{j=1}^{n_{\mathrm{DM}}^{(i,[0,p])}} A_m^{(i,j,[p,q])} < a_c^{ij} \right) \right] \right\} \tag{C2}$$

$$\begin{aligned} \breve{\mathrm{F}}_{\mathrm{global}}^{[p,q]} &\triangleq \left\{ \left(\bigcup_{r=1}^{n_{\mathrm{G}}} \mathrm{F}_{\mathrm{G},r}^{[p,q]} \right) \cap \left[\bigcap_{i=1}^{n_{\mathrm{L}}^{[0,p]}} \left(\bigcap_{j=1}^{n_{\mathrm{DM}}^{(i,[0,p])}} A_m^{(i,j,[p,q])} < a_c^{ij} \right) \right] \right\} \\ &\triangleq \left\{ E_1 \cap \left[\bigcap_{i=1}^{n_{\mathrm{L}}^{[0,p]}} \left(\bigcap_{j=1}^{n_{\mathrm{DM}}^{(i,[0,p])}} A_m^{(i,j,[p,q])} < a_c^{ij} \right) \right] \right\} \end{aligned} \tag{C3}$$

The probability of the failure event $\breve{\mathrm{F}}_{\mathrm{sys}}^{[p,q]}$ can therefore be computed by (i) viewing $\breve{\mathrm{F}}_{\mathrm{sys}}^{[p,q]}$ as a series system with two reliability components ($\breve{\mathrm{F}}_{\mathrm{local}}^{[p,q]}$ and $\breve{\mathrm{F}}_{\mathrm{global}}^{[p,q]}$) and (ii) combining lower bounds with lower bounds (i.e., $P_{low}\left[\breve{\mathrm{F}}_{\mathrm{local}}^{[p,q]}\right]$ and $P_{low}\left[\breve{\mathrm{F}}_{\mathrm{global}}^{[p,q]}\right]$) and upper bounds with upper bounds (i.e., $P_{up}\left[\breve{\mathrm{F}}_{\mathrm{local}}^{[p,q]}\right]$ and $P_{up}\left[\breve{\mathrm{F}}_{\mathrm{global}}^{[p,q]}\right]$) of the probabilities associated with the two sub-events $\breve{\mathrm{F}}_{\mathrm{local}}^{[p,q]}$ and $\breve{\mathrm{F}}_{\mathrm{global}}^{[p,q]}$ defined above. Following this approach, Equation (7.38) in Chapter 7 can be retrieved:

$$\max\left(P_{low}\left[\breve{\mathrm{F}}_{\mathrm{local}}^{[p,q]}\right], P_{low}\left[\breve{\mathrm{F}}_{\mathrm{global}}^{[p,q]}\right]\right) \leq P\left[\breve{\mathrm{F}}_{\mathrm{sys}}^{[p,q]}\right] \leq \min\left[1, \left(P_{up}\left[\breve{\mathrm{F}}_{\mathrm{local}}^{[p,q]}\right] + P_{up}\left[\breve{\mathrm{F}}_{\mathrm{global}}^{[p,q]}\right]\right)\right] \tag{C4}$$

Thus, in light of these considerations, this appendix shows the step-by-step derivations to obtain lower and upper uni-modal bounds for the two sub-events $\breve{\mathrm{F}}_{\mathrm{local}}^{[p,q]}$ and $\breve{\mathrm{F}}_{\mathrm{global}}^{[p,q]}$.

As a first step, in order to compute lower and upper uni-modal bounds for $P\left[\breve{\mathrm{F}}_{\mathrm{local}}^{[p,q]}\right]$, the sub-events $\mathrm{F}_{\mathrm{L},ij}^{[p,q]}$ and $A_m^{(i,j,[p,q])} < a_c^{ij}$, in Equation (C2), are reordered in the following (equivalent) way

$$\bigcup_{i=1}^{n_{\mathrm{L}}^{[0,p]}} \left\{ \bigcup_{j=1}^{n_{\mathrm{DM}}^{(i,[0,p])}} \left[\mathrm{F}_{\mathrm{L},ij}^{[p,q]} \cap E_2 \right] \right\} \tag{C5}$$

where the event E_2 is introduced for the sake of clarity and is defined as

$$E_2 \triangleq \bigcap_{i=1}^{n_{\mathrm{L}}^{[0,p]}} \left(\bigcap_{j=1}^{n_{\mathrm{DM}}^{(i,[0,p])}} A_m^{(i,j,[p,q])} < a_c^{ij} \right) \tag{C6}$$

Equation (C5) thus represents a series system formed by the union of n_{A}^{p} parallel sub-systems, $\left[\mathrm{F}_{\mathrm{L},ij}^{[p,q]} \cap E_2 \right]$, with n_{A}^{p} defined as $n_{\mathrm{A}}^{p} = \sum_{i=1}^{n_{\mathrm{L}}^{[0,p]}} n_{\mathrm{DM}}^{(i,[0,p])}$. The probabilities associated with each of the n_{A}^{p} events $\left[\mathrm{F}_{\mathrm{L},ij}^{[p,q]} \cap E_2 \right]$ can be expressed as

$$\begin{aligned}
P\left[\mathrm{F}_{\mathrm{L},ij}^{[p,q]} \cap E_2 \right] &= P\left[A_m^{(i,j,[p,q])} < a_c^{ij} \,\middle|\, \left(A_a^{(i,j,[p,q])} \geq a_c^{ij} \cap E_3^{ij} \right) \right] \cdot P\left[A_a^{(i,j,[p,q])} \geq a_c^{ij} \cap E_3^{ij} \right] \\
&= P\left[A_m^{(i,j,[p,q])} < a_c^{ij} \,\middle|\, A_a^{(i,j,[p,q])} \geq a_c^{ij} \right] \cdot P\left[A_a^{(i,j,[p,q])} \geq a_c^{ij} \cap E_3^{ij} \right] \\
&= \frac{P\left[\left(A_m^{(i,j,[p,q])} < a_c^{ij} \right) \cap \left(A_a^{(i,j,[p,q])} \geq a_c^{ij} \right) \right]}{P\left[A_a^{(i,j,[p,q])} \geq a_c^{ij} \right]} \cdot P\left[A_a^{(i,j,[p,q])} \geq a_c^{ij} \cap E_3^{ij} \right] \\
&= \frac{P\left[\tilde{\mathrm{F}}_{\mathrm{L},ij}^{[p,q]} \right]}{P\left[\mathrm{F}_{\mathrm{L},ij}^{[p,q]} \right]} \cdot P\left[\mathrm{F}_{\mathrm{L},ij}^{[p,q]} \cap E_3^{ij} \right]
\end{aligned} \tag{C7}$$

where the event E_3^{ij} is defined as

$$E_3^{ij} \triangleq \left[\bigcap_{l=1}^{n_{\mathrm{L}}^{[0,p]}} \left(\bigcap_{m=1}^{n_{\mathrm{DM}}^{(l,[0,p])}} A_m^{(l,m,[p,q])} < a_c^{lm} \right) \right], \quad \forall (l,m) \neq (i,j) \tag{C8}$$

Using Equation (C7) and the results reported by Fréchet (1935), it is now possible to provide a mathematical expression for lower and upper uni-modal bounds to the probability $P\left[\mathrm{F}_{\mathrm{L},ij}^{[p,q]} \cap E_2 \right]$ as

$$P\left[\mathrm{F}_{\mathrm{L},ij}^{[p,q]} \cap E_2\right] \geq \frac{P\left[\tilde{\mathrm{F}}_{\mathrm{L},ij}^{[p,q]}\right]}{P\left[\mathrm{F}_{\mathrm{L},ij}^{[p,q]}\right]} \cdot \max\left(0, P\left[\mathrm{F}_{\mathrm{L},ij}^{[p,q]}\right] + P_{ij}^{*} - n_{\mathrm{A}}^{p} + 1\right) \tag{C9}$$

$$P\left[\mathrm{F}_{\mathrm{L},ij}^{[p,q]} \cap E_2\right] \leq \frac{P\left[\tilde{\mathrm{F}}_{\mathrm{L},ij}^{[p,q]}\right]}{P\left[\mathrm{F}_{\mathrm{L},ij}^{[p,q]}\right]} \cdot \min\left(P\left[\mathrm{F}_{\mathrm{L},ij}^{[p,q]}\right], P_{ij}^{**}\right) \tag{C10}$$

where the mathematical relations for the two probabilities P_{ij}^{*} and P_{ij}^{**} are shown below in Equations (C11) and (C12), respectively.

$$P_{ij}^{*} = \sum_{l=1}^{n_{\mathrm{L}}^{[0,p]}} \sum_{m=1}^{n_{\mathrm{DM}}^{(l,[0,p])}} P\left[A_m^{(l,m,[p,q])} < a_c^{lm}\right]\left(1 - \delta_{il}\delta_{jm}\right) \tag{C11}$$

$$P_{ij}^{**} = \min_{l,m}\left(P\left[A_m^{(l,m,[p,q])} < a_c^{lm}\right]\right), \quad \forall (l,m) \neq (i,j) \tag{C12}$$

with δ_{il} and δ_{jm}, in Equation (C11), being the *Kronecker delta*, i.e.,

$$\delta_{il} = \begin{cases} 1 & \text{if } i = l \\ 0 & \text{if } i \neq l \end{cases} \quad \text{and} \quad \delta_{jm} = \begin{cases} 1 & \text{if } j = m \\ 0 & \text{if } j \neq m \end{cases} \tag{C13}$$

Finally, lower and upper uni-modal bounds for the probability $P\left[\breve{\mathrm{F}}_{\mathrm{local}}^{[p,q]}\right]$, with the event $\breve{\mathrm{F}}_{\mathrm{local}}^{[p,q]}$ defined earlier in Equation (C2), can be easily obtained by combining the results from Equations (C9) and (C10) with the well-known uni-modal bounds of a series system. These lower and upper uni-modal bounds are denoted as $P_{low}\left[\breve{\mathrm{F}}_{\mathrm{local}}^{[p,q]}\right]$ and $P_{up}\left[\breve{\mathrm{F}}_{\mathrm{local}}^{[p,q]}\right]$, respectively, and their mathematical expressions are provided in Equations (C14) and (C15).

$$P_{low}\left[\breve{\mathrm{F}}_{\mathrm{local}}^{[p,q]}\right]=\max_{i,j}\left[R_{\mathrm{L},ij}^{[p,q]}\cdot\max\left(0,P\left[\mathrm{F}_{\mathrm{L},ij}^{[p,q]}\right]+P_{ij}^{*}-n_{\mathrm{A}}^{p}+1\right)\right] \tag{C14}$$

$$P_{up}\left[\breve{\mathrm{F}}_{\mathrm{local}}^{[p,q]}\right]=\min\left(1,\sum_{i=1}^{n_{\mathrm{L}}^{[0,p]}}\sum_{j=1}^{n_{\mathrm{DM}}^{(i,[0,p])}}\left[R_{\mathrm{L},ij}^{[p,q]}\cdot\min\left(P\left[\mathrm{F}_{\mathrm{L},ij}^{[p,q]}\right],P_{ij}^{**}\right)\right]\right) \tag{C15}$$

On the other hand, the event $\breve{\mathrm{F}}_{\mathrm{global}}^{[p,q]}$ can be viewed as a parallel system composed of $n_{\mathrm{A}}^{p}+1$ sub-components, with n_{A}^{p} defined as $n_{\mathrm{A}}^{p}=\sum_{i=1}^{n_{\mathrm{L}}^{[0,p]}}n_{\mathrm{DM}}^{(i,[0,p])}$. Its first sub-component, identified by the event E_1 in Equation (C3), can be viewed as a series system and lower and upper uni-modal bounds for the probability associated with this event can be expressed as

$$\max_{r}\left(P\left[\mathrm{F}_{\mathrm{G},r}^{[p,q]}\right]\right)\le P\left[E_1\right]\le\min\left(1,\sum_{r=1}^{n_{\mathrm{G}}}P\left[\mathrm{F}_{\mathrm{G},r}^{[p,q]}\right]\right) \tag{C16}$$

A result that can now be used to provide lower and upper uni-modal bounds (i.e., $P_{low}\left[\breve{\mathrm{F}}_{\mathrm{global}}^{[p,q]}\right]$ and $P_{up}\left[\breve{\mathrm{F}}_{\mathrm{global}}^{[p,q]}\right]$) for the probability of the event $\breve{\mathrm{F}}_{\mathrm{global}}^{[p,q]}$. The mathematical expressions for these bounds are provided by Fréchet (1935) and their particularization, for the specific problem studied herein, is provided in Equations (C17) and (C18).

$$P_{low}\left[\breve{\mathrm{F}}_{\mathrm{global}}^{[p,q]}\right]=\max\left(0,\max_{r}\left(P\left[\mathrm{F}_{\mathrm{G},r}^{[p,q]}\right]\right)+\sum_{i=1}^{n_{\mathrm{L}}^{[0,p]}}\sum_{j=1}^{n_{\mathrm{DM}}^{(i,[0,p])}}P\left[A_m^{(i,j,[p,q])}<a_c^{ij}\right]-n_{\mathrm{A}}^{p}\right) \tag{C17}$$

$$P_{up}\left[\breve{\mathrm{F}}_{\mathrm{global}}^{[p,q]}\right]=\min\left(1,\sum_{r=1}^{n_{\mathrm{G}}}P\left[\mathrm{F}_{\mathrm{G},r}^{[p,q]}\right],\min_{i,j}\left(P\left[A_m^{(i,j,[p,q])}<a_c^{ij}\right]\right)\right) \tag{C18}$$

It is worth noting that, Equations (C17) and (C18) remain valid when the global component failure probabilities $P\left[\mathrm{F}_{\mathrm{G},r}^{[p,q]}\right]$ are replaced by $P\left[\tilde{\mathrm{F}}_{\mathrm{G},r}^{[p,q]}\right]$.

References

M. Fréchet, Généralisations du théorème des probabilités totales, *Fundamenta Mathematicae*., 25, 379-387, 1935.

APPENDIX D

DERIVATION OF LOWER AND UPPER UNI-MODAL BOUNDS TO THE PROBABILITY OF FALSE-CALL, $P\left[\breve{\mathscr{F}}_{\text{sys}}^{[p,q]}\right]$, ACCORDING TO THE LEVEL-OF-SAFETY FORMULATION WITH AN ASSUMED SINGLE NDE INSPECTION OPPORTUNITY

The expression for the false-call event $\breve{\mathscr{F}}_{\text{sys}}^{[p,q]}$, provided in Equation (7.48) in Chapter 7, clearly represents a combination of series and parallel systems and can be rearranged (using set theory language) as

$$\begin{aligned}\breve{\mathscr{F}}_{\text{sys}}^{[p,q]} &\triangleq \left\{\left[\bigcup_{i=1}^{n_{\text{L}}^{[0,p]}}\left(\bigcup_{j=1}^{n_{\text{DM}}^{(i,[0,p])}} A_m^{(i,j,[p,q])} \geq a_c^{ij}\right)\right] \cap \left[\bigcap_{i=1}^{n_{\text{L}}^{[0,p]}}\left(\bigcap_{j=1}^{n_{\text{DM}}^{(i,[0,p])}} \overline{\text{F}_{\text{L},ij}^{[p,q]}}\right)\right]\right\} \cap \left(\bigcap_{r=1}^{n_{\text{G}}} \overline{\text{F}_{\text{G},r}^{[p,q]}}\right) \\ &\triangleq \text{FC}_{\text{local}}^{[p,q]} \cap \left(\bigcap_{r=1}^{n_{\text{G}}} \overline{\text{F}_{\text{G},r}^{[p,q]}}\right)\end{aligned} \tag{D1}$$

where the events $\overline{\mathrm{F}_{\mathrm{L},ij}^{[p,q]}}$ (with $i=1,\ldots,n_{\mathrm{L}}^{[0,p]}$ and $j=1,\ldots,n_{\mathrm{DM}}^{(i,[0,p])}$) and $\overline{\mathrm{F}_{\mathrm{G},r}^{[p,q]}}$ (with $r=1,\ldots,n_{\mathrm{G}}$) represent the complement of the failure events $\mathrm{F}_{\mathrm{L},ij}^{[p,q]}$ and $\mathrm{F}_{\mathrm{G},r}^{[p,q]}$, respectively. The event $\mathrm{FC}_{\mathrm{local}}^{[p,q]}$, in Equation (D1), would represent the false-call event (at the overall system level) when only the local reliability components (or local failure modes) are considered. The probability of this event, herein denoted as $P\left[\mathrm{FC}_{\mathrm{local}}^{[p,q]}\right]$, can be computed as

$$\begin{aligned} P\left[\mathrm{FC}_{\mathrm{local}}^{[p,q]}\right] &= P\left[\left\{\bigcup_{i=1}^{n_{\mathrm{L}}^{[0,p]}}\left(\bigcup_{j=1}^{n_{\mathrm{DM}}^{(i,[0,p])}} A_m^{(i,j,[p,q])} \geq a_c^{ij}\right)\right\} \,\middle|\, \left\{\bigcap_{i=1}^{n_{\mathrm{L}}^{[0,p]}}\left(\bigcap_{j=1}^{n_{\mathrm{DM}}^{(i,[0,p])}} A_a^{(i,j,[p,q])} < a_c^{ij}\right)\right\}\right] \times \\ & \qquad P\left[\left\{\bigcap_{i=1}^{n_{\mathrm{L}}^{[0,p]}}\left(\bigcap_{j=1}^{n_{\mathrm{DM}}^{(i,[0,p])}} A_a^{(i,j,[p,q])} < a_c^{ij}\right)\right\}\right] \\ &= P\left[E_4 \,\middle|\, E_5\right] \times P\left[E_5\right] \end{aligned} \tag{D2}$$

where the two events E_4 and E_5 are introduced for the sake of conciseness, and event E_4 in Equation (D2) can be viewed as the failure event of a series system with $n_{\mathrm{A}}^{p} = \sum_{i=1}^{n_{\mathrm{L}}^{[0,p]}} n_{\mathrm{DM}}^{(i,[0,p])}$ components. Thus, similarly to Equation (7.34) in Chapter 7, lower and upper uni-modal bounds for $P\left[E_4 \,\middle|\, E_5\right]$ can be obtained by employing assumption (iii) about the damage size measurement model used in this work (see Chapter 3) together with the definition of the false-call event $\tilde{\mathcal{F}}_{\mathrm{L},ij}^{[p,q]} \triangleq \left\{\left(A_a^{(i,j,[p,q])} < a_c^{ij}\right) \cap \left(A_m^{(i,j,[p,q])} \geq a_c^{ij}\right)\right\}$. The results, obtained according to this approach, are shown in Equations (D3) and (D4) below:

$$
\begin{aligned}
P\left[E_4 \middle| E_5\right] &\geq \max_{i,j}\left(P\left[A_m^{(i,j,[p,q])} \geq a_c^{ij} \middle| E_2\right]\right) \\
&\geq \max_{i,j}\left(P\left[A_m^{(i,j,[p,q])} \geq a_c^{ij} \middle| A_a^{(i,j,[p,q])} < a_c^{ij}\right]\right) \\
&\geq \max_{i,j}\left(\frac{P\left[\tilde{\mathscr{F}}_{\mathrm{L},ij}^{[p,q]}\right]}{F_{A_a^{(i,j,[p,q])}}\left(a_c^{ij}\right)}\right) \\
&\geq \max_{i,j}\left(\frac{P\left[\tilde{\mathscr{F}}_{\mathrm{L},ij}^{[p,q]}\right]}{1-P\left[\mathrm{F}_{\mathrm{L},ij}^{[p,q]}\right]}\right)
\end{aligned}
\tag{D3}
$$

$$
\begin{aligned}
P\left[E_4 \middle| E_5\right] &\leq \min\left(1, \left[\sum_{i=1}^{n_{\mathrm{L}}^{[0,p]}} \sum_{j=1}^{n_{\mathrm{DM}}^{(i,[0,p])}} P\left[A_m^{(i,j,[p,q])} \geq a_c^{ij} \middle| E_2\right]\right]\right) \\
&\leq \min\left(1, \left[\sum_{i=1}^{n_{\mathrm{L}}^{[0,p]}} \sum_{j=1}^{n_{\mathrm{DM}}^{(i,[0,p])}} P\left[A_m^{(i,j,[p,q])} \geq a_c^{ij} \middle| A_a^{(i,j,[p,q])} < a_c^{ij}\right]\right]\right) \\
&\leq \min\left(1, \left[\sum_{i=1}^{n_{\mathrm{L}}^{[0,p]}} \sum_{j=1}^{n_{\mathrm{DM}}^{(i,[0,p])}} \frac{P\left[\tilde{\mathscr{F}}_{\mathrm{L},ij}^{[p,q]}\right]}{F_{A_a^{(i,j,[p,q])}}\left(a_c^{ij}\right)}\right]\right) \\
&\leq \min\left(1, \left[\sum_{i=1}^{n_{\mathrm{L}}^{[0,p]}} \sum_{j=1}^{n_{\mathrm{DM}}^{(i,[0,p])}} \frac{P\left[\tilde{\mathscr{F}}_{\mathrm{L},ij}^{[p,q]}\right]}{1-P\left[\mathrm{F}_{\mathrm{L},ij}^{[p,q]}\right]}\right]\right)
\end{aligned}
\tag{D4}
$$

The second term on the right-hand-side of Equation (D2) — i.e., $P\left[E_5\right]$ — can be viewed as a parallel system for which the narrowest lower and upper uni-modal bounds (Fréchet, 1935) are expressed as

$$
\max\left(0, \left[\sum_{i=1}^{n_{\mathrm{L}}^{[0,p]}} \sum_{j=1}^{n_{\mathrm{DM}}^{(i,[0,p])}} F_{A_a^{(i,j,[p,q])}}\left(a_c^{ij}\right)\right] - \left(n_{\mathrm{A}}^{p} - 1\right)\right) \leq P\left[E_5\right] \leq \min_{i,j}\left(F_{A_a^{(i,j,[p,q])}}\left(a_c^{ij}\right)\right) \tag{D5}
$$

or, by making use of the equivalence $F_{A_a^{(i,j,[p,q])}}\left(a_c^{ij}\right) = 1 - P\left[\mathrm{F}_{\mathrm{L},ij}^{[p,q]}\right]$, as

$$\max\left(0,\left[\sum_{i=1}^{n_{\mathrm{L}}^{[0,p]}}\sum_{j=1}^{n_{\mathrm{DM}}^{(i,[0,p])}}\left(1-P\left[\mathrm{F}_{\mathrm{L},ij}^{[p,q]}\right]\right)\right]-\left(n_{\mathrm{A}}^{p}-1\right)\right)\le P\left[E_5\right]\le\min_{i,j}\left[\left(1-P\left[\mathrm{F}_{\mathrm{L},ij}^{[p,q]}\right]\right)\right] \quad \text{(D6)}$$

where n_{A}^{p} denotes the dimension of the damage size vector (see Chapter 3), which can vary (increase) in time. Substituting the results of Equations (D3), (D4) and (D6) into Equation (D2) (multiplying lower bound with lower bound and upper bound with upper bound) yields to the lower and upper uni-modal bounds of $P\left[\mathrm{FC}_{\mathrm{local}}^{[p,q]}\right]$ provided in Equations (D7) and (D8).

$$P_{low}\left[\mathrm{FC}_{\mathrm{local}}^{[p,q]}\right]=\max_{i,j}\left(\frac{P\left[\tilde{\mathscr{F}}_{\mathrm{L},ij}^{[p,q]}\right]}{1-P\left[\mathrm{F}_{\mathrm{L},ij}^{[p,q]}\right]}\right)\times\max\left(0,\left[\sum_{i=1}^{n_{\mathrm{L}}^{[0,p]}}\sum_{j=1}^{n_{\mathrm{DM}}^{(i,[0,p])}}\left(1-P\left[\mathrm{F}_{\mathrm{L},ij}^{[p,q]}\right]\right)\right]-\left(n_{\mathrm{A}}^{p}-1\right)\right) \quad \text{(D7)}$$

$$P_{up}\left[\mathrm{FC}_{\mathrm{local}}^{[p,q]}\right]=\min\left(1,\left[\sum_{i=1}^{n_{\mathrm{L}}^{[0,p]}}\sum_{j=1}^{n_{\mathrm{DM}}^{(i,[0,p])}}\frac{P\left[\tilde{\mathscr{F}}_{\mathrm{L},ij}^{[p,q]}\right]}{1-P\left[\mathrm{F}_{\mathrm{L},ij}^{[p,q]}\right]}\right]\right)\times\min_{i,j}\left[\left(1-P\left[\mathrm{F}_{\mathrm{L},ij}^{[p,q]}\right]\right)\right] \quad \text{(D8)}$$

Finally, lower and upper uni-modal bounds for the parallel system in Equation (D1) defined as $\tilde{\mathscr{F}}_{\mathrm{sys}}^{[p,q]}\triangleq\mathrm{FC}_{\mathrm{local}}^{[p,q]}\cap\left(\bigcap_{r=1}^{n_{\mathrm{G}}}\overline{\mathrm{F}_{\mathrm{G},r}^{[p,q]}}\right)$ are computed, according to Fréchet (1935), using the results provided above in Equations (D7) , and (D8). This approach leads to the final results shown in Equations (D9) and (D10) below.

$$P\left[\tilde{\mathscr{F}}_{\mathrm{sys}}^{[p,q]}\right]\ge\max\left(0,P_{low}\left[\mathrm{FC}_{\mathrm{local}}^{[p,q]}\right]+\sum_{r=1}^{n_{\mathrm{G}}}\left(1-P\left[\mathrm{F}_{\mathrm{G},r}^{[p,q]}\right]\right)-n_{\mathrm{G}}\right) \quad \text{(D9)}$$

$$P\left[\tilde{\mathscr{F}}_{\mathrm{sys}}^{[p,q]}\right]\le\min\left[P_{up}\left[\mathrm{FC}_{\mathrm{local}}^{[p,q]}\right],\min_{r}\left(1-P\left[\mathrm{F}_{\mathrm{G},r}^{[p,q]}\right]\right)\right] \quad \text{(D10)}$$

References

M. Fréchet, Généralisations du théorème des probabilités totales, *Fundamenta Mathematicae*., 25, 379-387, 1935.

APPENDIX E

CLOSED-FORM SOLUTION FOR THE MIDSPAN COMPLIANCE OF A SIMPLY SUPPORTED COMPOSITE BEAM WITH TWO DEBONDING FRONTS AND A STATIC CONCENTRATED LOAD APPLIED AT MIDSPAN

Consider the simply-supported composite beam shown in Figure E.1. The beam is composed of two unidirectional laminated composite adherends, of equal rectangular cross section ($b \times h$), bonded together by an idealized (and imperfect) zero-thickness adhesive layer. This layer is characterized by two disbonds (starting from the two beam ends) of length a_1 and a_2, respectively. As a direct consequence, the moment of inertia of the whole beam cross section (i.e., considering both adherends) can be expressed as follows:

$$I_{(0)} = 2\frac{b\,h^3}{12} = \frac{b\,h^3}{6} \qquad 0 \le x_1 \le a_1 \text{ and } 0 \le x_2 \le a_2 \tag{E1}$$

$$I_{(\infty)} = \frac{b(2h)^3}{12} = 4\frac{b\,h^3}{6} = 4I_{(0)} \qquad a_1 \le x_1 \le L \text{ and } a_2 \le x_2 \le L \tag{E2}$$

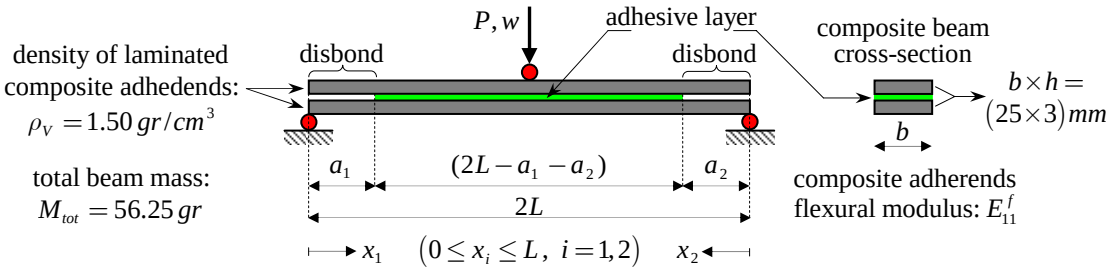

Figure E.1: Simply-supported composite beam with two debonding fronts and subjected to a static concentrated static load (*P*) applied at its midspan.

.

The beam is subjected to a concentrated static load (*P*) applied at its midspan and the corresponding midspan deflection (function of the load intensity as well as of the two debonding lengths a_1 and a_2) is denoted as *w*. By using the *principle of virtual work*, it is possible to find an expression for *w* as a function of *P*, a_1, a_2, and the other beam properties (i.e., beam cross section, beam span, 2*L*, and elastic flexural modulus of the adherends, E_{11}^f).

According to the principle of virtual work, a dummy load (*Q*) is applied at the point where the deflection needs to be evaluated. Although the dummy load *Q* can have any value/magnitude, typically a unit load is used; therefore, as a direct consequence, the equivalence between external and internal virtual work can be expressed as

$$Q \cdot w = 1 \cdot w = \int_0^L M_Q(x_1) \frac{M_P(x_1)}{E_{11}^f I(x_1)} dx_1 + \int_0^L M_Q(x_2) \frac{M_P(x_2)}{E_{11}^f I(x_2)} dx_2 \tag{E3}$$

where $M_Q(x_1)$ and $M_Q(x_2)$ are the bending moments generated by the unit dummy load *Q*, while $M_P(x_1)$ and $M_P(x_2)$ are the bending moments produced by the real load *P*. From simple equilibrium equations, it is easy to verify how (for the beam structure shown in Figure E.1) the bending moments M_Q and M_P have the following relationships:

$$\begin{aligned} M_Q(x_1) &= \frac{x_1}{2} \qquad 0 \le x_1 \le L \\ M_Q(x_2) &= \frac{x_2}{2} \qquad 0 \le x_2 \le L \end{aligned} \tag{E4}$$

$$\begin{aligned} M_P(x_1) &= \frac{P x_1}{2} \qquad 0 \le x_1 \le L \\ M_P(x_2) &= \frac{P x_2}{2} \qquad 0 \le x_2 \le L \end{aligned} \tag{E5}$$

Taking into account these two Equations, together with Equations (E1) and (E2), it is possible to rewrite Equation (E3) as

$$\begin{aligned} w = &\int_0^{a_1} \frac{x_1}{2} \frac{P x_1}{2} \frac{1}{E_{11}^f I_{(0)}} dx_1 + \int_{a_1}^{L} \frac{x_1}{2} \frac{P x_1}{2} \frac{1}{E_{11}^f I_{(\infty)}} dx_1 + \\ &\int_0^{a_2} \frac{x_2}{2} \frac{P x_2}{2} \frac{1}{E_{11}^f I_{(0)}} dx_2 + \int_{a_2}^{L} \frac{x_2}{2} \frac{P x_2}{2} \frac{1}{E_{11}^f I_{(\infty)}} dx_2 \end{aligned} \tag{E6}$$

and then obtain the following result:

$$
\begin{aligned}
w &= \frac{P a_1^3}{12\, E_{11}^f\, I_{(0)}} + \frac{P}{12\, E_{11}^f\, I_{(\infty)}}\left(L^3 - a_1^3\right) + \frac{P a_2^3}{12\, E_{11}^f\, I_{(0)}} + \frac{P}{12\, E_{11}^f\, I_{(\infty)}}\left(L^3 - a_2^3\right) \\
&= \frac{P}{12\, E_{11}^f\, I_{(0)}}\left(a_1^3 + a_2^3 + \frac{L^3 - a_1^3}{4} + \frac{L^3 - a_2^3}{4}\right) \\
&= \frac{2L^3 + 3\left(a_1^3 + a_2^3\right)}{8\, E_{11}^f\, b\, h^3} P
\end{aligned}
\tag{E7}
$$

Finally, the beam compliance (defined in this specific case as the ratio between the midspan displacement and the applied load) can be expressed as

$$
C\left(a_1, a_2\right) = \frac{w}{P} = \frac{2L^3 + 3\left(a_1^3 + a_2^3\right)}{8\, E_{11}^f\, b\, h^3} \tag{E8}
$$

As a final check, by setting $a_1 = a_2 = 0$, the well-known results for a simply supported Euler-Bernoulli beam are recovered:

$$
w = \frac{2PL^3}{8\, E_{11}^f\, b\, h^3} = \frac{1}{48}\frac{P\left(2L\right)^3}{E_{11}^f\, I_{(\infty)}} \tag{E9}
$$

$$
C\left(a_1 = 0, a_2 = 0\right) = \frac{2L^3}{8\, E_{11}^f\, b\, h^3} = \frac{P\left(2L\right)^3}{48\, E_{11}^f\, I_{(\infty)}} \tag{E10}
$$

APPENDIX F

AN OVERVIEW OF THE ENERGY FORMULATION IN LINEAR ELASTIC FRACTURE MECHANICS

This appendix is intended to provide a brief overview of the energy formulation in Linear Elastic Fracture Mechanics (LEFM) and apply some of the fundamental results to study the debonding propagation along the adhesive interface of a simply supported composite beam with two debonding fronts subjected to a concentrated load applied at its midspan (i.e., the same benchmark structure used in Appendix E). The results obtained in this Appendix will then be generalized in Appendix G to study a more complicated structure: a two-span composite beam characterized by four debonding fronts and subjected to two concentrated loads applied at each of the two midspan locations (see Figure G.1 in Appendix G).

In LEFM, the total potential energy, $\pi(\mathbf{A})$, of an arbitrary cracked/damaged body (characterized by a linear elastic material) under a given state of deformation (induced by the external loads) can be expressed as (Sanford, 2003)

$$\pi(\mathbf{A}) = U(\mathbf{A}) - W_{ext}(\mathbf{A}) + S(\mathbf{A}) \tag{F1}$$

where, $U(\mathbf{A})$ represents the internal elastic strain energy, $W_{ext}(\mathbf{A})$ the work done by the external forces, and $S(\mathbf{A})$ the surface energy dissipated to create the cracks (or in a more general way the current state of damage). The vector $\mathbf{A} = \{A_i, i = 1,\ldots,n_A\}^T$ denotes the (new) area, inside the elastic body, created by each of the n_A cracks. Figure F.1 is an illustration of this concept for the case of a linear elastic body with a single crack.

In order for the cracked body to be in equilibrium (either stable or unstable), the first variation of the total potential energy must be equal to zero, i.e.

$$\delta[\pi(\mathbf{A})] = \delta[U(\mathbf{A})] - \delta[W_{ext}(\mathbf{A})] + \delta[S(\mathbf{A})] = \nabla_{\mathbf{A}}[\pi(\mathbf{A})]\delta\mathbf{A} = 0 \tag{F2}$$

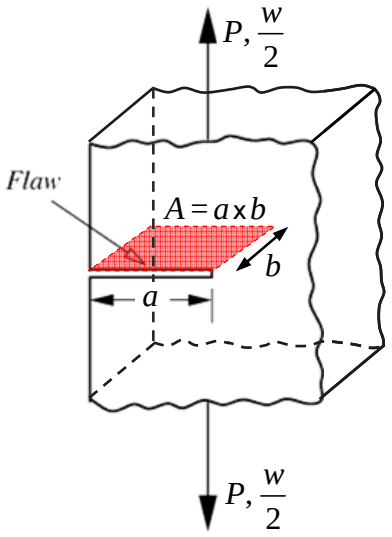

Figure F.1: Illustration of a 3-D linear elastic body with a single edge crack generating a new surface (internal to the body) of area equal to $A = a \times b$.

where the gradient operator, $\nabla_{\mathbf{A}}$, is defined as $\nabla_{\mathbf{A}} \triangleq \left\{ \frac{\partial}{\partial A_1}, \frac{\partial}{\partial A_2}, \ldots, \frac{\partial}{\partial A_{n_A}} \right\}$. Since Equation (F2) must be satisfied for any possible variation $\delta\mathbf{A}$ (with the obvious constraint that $\delta A_i \geq 0,\ i = 1, \ldots, n_A$), it is straightforward to rewrite the equilibrium condition as

$$\nabla_{\mathbf{A}} \left[\pi(\mathbf{A}) \right] = \nabla_{\mathbf{A}} \left[U(\mathbf{A}) - W_{ext}(\mathbf{A}) + S(\mathbf{A}) \right] = 0 \tag{F3}$$

By defining the n_A-dimensional row vector $\mathbf{G}(\mathbf{A})$ as $\mathbf{G}(\mathbf{A}) \triangleq \nabla_{\mathbf{A}} \left[S(\mathbf{A}) \right]$, from Equation (F3) it is then possible to obtain the following relationship:

$$\mathbf{G}(\mathbf{A}) = \nabla_{\mathbf{A}} \left[W_{ext}(\mathbf{A}) - U(\mathbf{A}) \right] \tag{F4}$$

where the i^{th} component of i^{th} — i.e., $G_i(\mathbf{A})$ — represents the strain energy release rated (SERR) at the tip of the i^{th} crack. Consequently, as a logical extension, the vector $\mathbf{G}(\mathbf{A})$ is hereafter referred to as the *SERR vector*. Under a gradually increasing external loading, the first component of the SERR vector $\mathbf{G}(\mathbf{A})$ (e.g., the j^{th} component) reaching the condition $G_j(\mathbf{A}) \geq G_j^{crit}$ — with G_j^{crit} being the critical fracture energy of the material at the j^{th} damage location and for that particular mode of fracture induced by the external loading — would imply the propagation (either stable or unstable) of the j^{th} crack. Furthermore, for a linear elastic continuum under a constant load, it is known that $\nabla_{\mathbf{A}} \left[W_{ext}(\mathbf{A}) \right] = 2\nabla_{\mathbf{A}} \left[U(\mathbf{A}) \right]$ and therefore Equation (F4) can be rewritten as

$$\mathbf{G}(\mathbf{A}) = \nabla_{\mathbf{A}}\left[W_{ext}(\mathbf{A}) - U(\mathbf{A})\right] = \nabla_{\mathbf{A}}\left[U(\mathbf{A})\right] \tag{F5}$$

On the other hand, for a system under constant displacement (normally referred to as *fixed grip* in LEFM applications) the work done by the external forces is zero (i.e., $\nabla_{\mathbf{A}}\left[W_{ext}(\mathbf{A})\right] = 0$) and therefore, Equation (F4) can be simplified as

$$\mathbf{G}(\mathbf{A}) = -\nabla_{\mathbf{A}}\left[U(\mathbf{A})\right] \tag{F6}$$

The vector Equations (F5) and (F6) can be rewritten for each crack location as shown below in Equations (F7) and (F8), respectively:

$$G_i(\mathbf{A}) = \frac{\partial}{\partial A_i} W_{ext}(\mathbf{A}) - \frac{\partial}{\partial A_i} U(\mathbf{A}) = \frac{\partial}{\partial A_i} U(\mathbf{A}) \qquad i = 1,\ldots,n_A \tag{F7}$$

$$G_i(\mathbf{A}) = -\frac{\partial}{\partial A_i} U(\mathbf{A}) \qquad i = 1,\ldots,n_A \tag{F8}$$

For simple systems subjected to a unique external load, such as the elastic body shown in Figure F.1 or the simply supported composite beam with two debonding fronts shown in Figure F.2, it is possible to express the SERR vector as a function of (i) the applied external load, $P(\mathbf{A})$, and (ii) the compliance, $C(\mathbf{A})$, of the structure; with the compliance defined as the ratio between the displacement $w(\mathbf{A})$, at the location where the load is applied, and the magnitude of the applied load itself, $P(\mathbf{A})$:

$$C(\mathbf{A}) = \frac{w(\mathbf{A})}{P(\mathbf{A})} \tag{F9}$$

Under constant/fixed load conditions, Equation (F5) can, in fact, be rewritten as

$$\begin{aligned} G(\mathbf{A}) &= \nabla_{\mathbf{A}}\left[U(\mathbf{A})\right] = \nabla_{\mathbf{A}}\left[\frac{1}{2}P(\mathbf{A})w(\mathbf{A})\right] \\ &= \nabla_{\mathbf{A}}\left[\frac{1}{2}P(\mathbf{A})^2 C(\mathbf{A})\right] = \frac{1}{2}P(\mathbf{A})^2 \nabla_{\mathbf{A}}\left[C(\mathbf{A})\right] \end{aligned} \tag{F10}$$

whereas under fixed displacement/grip conditions (during which the applied load is clearly a function of the vector $\mathbf{A}$), Equation (F6) can be recast as

$$\begin{aligned} G(\mathbf{A}) &= -\nabla_{\mathbf{A}}\left[U(\mathbf{A})\right] = -\nabla_{\mathbf{A}}\left[\frac{1}{2}P(\mathbf{A})w(\mathbf{A})\right] \\ &= -\nabla_{\mathbf{A}}\left[\frac{1}{2}\frac{w(\mathbf{A})^2}{C(\mathbf{A})}\right] = \frac{1}{2}w(\mathbf{A})^2\frac{\nabla_{\mathbf{A}}\left[C(\mathbf{A})\right]}{C(\mathbf{A})^2} = \frac{1}{2}P(\mathbf{A})^2\nabla_{\mathbf{A}}\left[C(\mathbf{A})\right] \end{aligned} \tag{F11}$$

which is identical to the result obtained in Equation (F10). In other words, the equilibrium equation — and, as a direct consequence, also the critical load at which the onset of crack propagation will occur — is invariant with respect to the loading conditions (i.e., either *fixed load* or *fixed grip*). However, these two different loading conditions have an important influence on the stability of the crack propagation process (Sanford, 2003) — an argument beyond the scope of this Appendix and therefore not discussed herein.

As an illustrative example, consider the simply supported composite beam shown in Figure F.2. The beam is made out of two identical unidirectional composite laminates (adherends) bonded together. In this case, it is possible to express the (new) area created by each of the two disbonds as a function of the disbond lengths as

$$\mathbf{A} = \left\{A_1, A_2\right\}^{\mathrm{T}} = b\left\{a_1, a_2\right\}^{\mathrm{T}} \tag{F12}$$

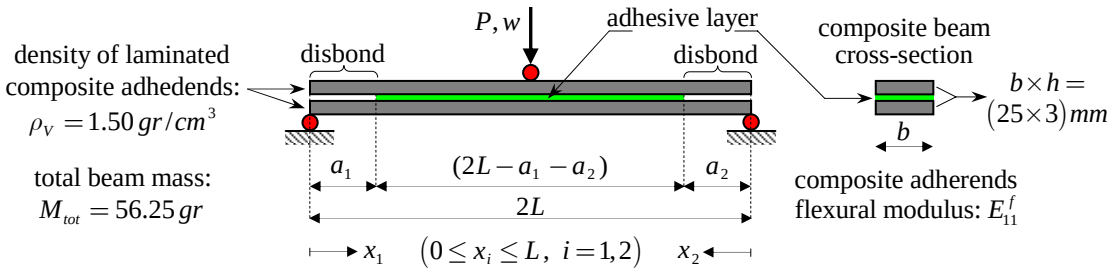

Figure F.2: Simply-supported composite beam with two debonding fronts and subjected to a static concentrated static load (*P*) applied at its midspan.

where *b* denotes the width of the beam (assumed to be constant along the entire span of the beam). By taking advantage of the chain rule of differentiation, the result for the SERR from either Equations (F10) or (F11), can therefore be rewritten as

$$G(\mathbf{a}) = \frac{1}{2}\frac{P(\mathbf{a})^2}{b}\nabla_{\mathbf{a}}\left[C(\mathbf{a})\right] \tag{F13}$$

By recalling the expression for the beam midspan compliance (see Appendix E), defined as the ratio between the midspan transversal displacement (*w*) and the applied load (*P*), and expressed as

$$C(\mathbf{A}) = C(a_1, a_2) = \frac{2L^3 + 3\left(a_1^3 + a_2^3\right)}{8\,E_{11}^f\,b\,h^3} \tag{F14}$$

it is possible to compute the SERR vector, $G(\mathbf{A})$,as

$$G(\mathbf{a}) = \frac{1}{2}\frac{P(\mathbf{a})^2}{b}\nabla_{\mathbf{a}}\left[C(\mathbf{a})\right] = \left\{\frac{9}{16}\frac{P^2 a_1^2}{E_{11}^f b^2 h^3},\ \frac{9}{16}\frac{P^2 a_2^2}{E_{11}^f b^2 h^3}\right\} = \left\{G_1(a_1),\ G_2(a_2)\right\} \tag{F15}$$

It is worth noting that for this simple case the relationship for the SERR at a given damage location only involves the disbond length at that particular location — i.e.,

$G_1(a_1, a_2) = G_1(a_1)$ and $G_2(a_1, a_2) = G_2(a_2)$. This type of result can be explained by noticing that the beam structure considered in this simple illustrative example is statically determined and therefore the value of bending moment at any cross-section of the beam — i.e., the only internal action needed to compute the elastic strain energy $U(\mathbf{A})$ — is independent of the two disbond lengths a_1 and a_2.

To provide more engineering insight into the formulation and results presented thus far, consider a simple linear elastic structural system characterized by a single initial crack (of area A) and a single external driving force (P); for instance, the simply supported composite beam shown in Figure F.2, now characterized by a single/unique debonding front (i.e., at either the left- or right-end of the beam, but not at both). For such a simple system more insight on the crack propagation process (and the energy dissipated during this process) can be gained by considering two hypothetical experiments. In the first experiment, suppose that the external concentrate load — applied at the beam midspan — is kept constant (i.e., *fixed load*) and that, under this constant load of intensity P_1, the disbond propagates from A to $A+\Delta A$ and the midspan deflection increases (due to the higher beam compliance) from w_1 to $w_2 = w_1 + \Delta w$. Instead, in the second experiment, suppose that the midspand deflection is kept constant (i.e., *fixed grip*) and that, under this constant deflection, w_1, the disbond propagates from A to $A+\Delta A$ whereas the applied load at the beam midspan decreases from P_1 to $P_2 = P_1 + \Delta P$ (with ΔP being a negative value). Both

experiments are schematically represented in Figure F.3-a and Figure F.3-b, respectively.

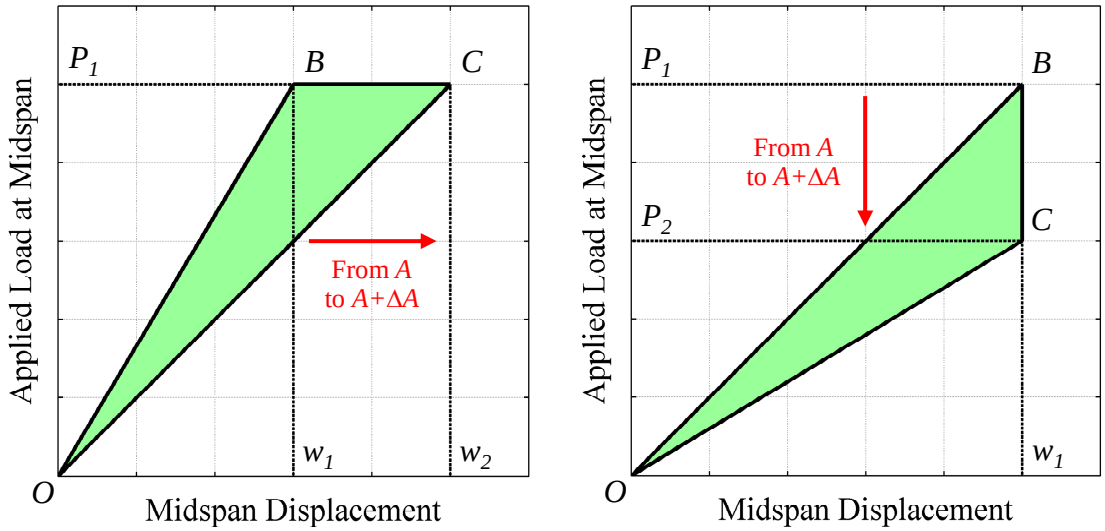

(a) (b)

Figure F.3: Illustrative force-displacement diagrams to conceptually explain the energy dissipation (identified by the green triangles in the plots) during the crack propagation process in an idealized single-degree-of-freedom structure with a unique crack and a unique external action. (a) Fixed load, (b) Fixed displacement.

Referring to the constant load experiment shown in Figure F.3-a, it is possible to rewrite the equilibrium condition expressed in Equation (F2) as

$$\Delta\left[U\left(\mathbf{A}\right)\right]-\Delta\left[W_{ext}\left(\mathbf{A}\right)\right]+\Delta\left[S\left(\mathbf{A}\right)\right]=\Delta\left[U\left(A\right)\right]-\Delta\left[W_{ext}\left(A\right)\right]+\Delta\left[S\left(A\right)\right]=0 \quad \text{(F16)}$$

where the finite variation of the internal strain energy, $\Delta\left[U\left(A\right)\right]$, can be expressed as

$$\begin{aligned}\Delta\left[U\left(A\right)\right] &= U\left(A+\Delta A\right)-U\left(A\right)\\ &= Area\left(O\,w_2\,C\right)-Area\left(O\,w_1\,B\right)\\ &= \frac{1}{2}P_1\left(w_2-w_1\right)=\frac{1}{2}P_1\,\Delta w\end{aligned} \quad \text{(F17)}$$

while the work done by the constant external load is equal to

$$\Delta\left[W_{ext}\left(A\right)\right] = Area\left(w_1 w_2 CB\right) = P_1 \Delta w = 2\Delta\left[U\left(A\right)\right] \tag{F18}$$

Therefore, the finite variation of the surface energy, $\Delta\left[S\left(A\right)\right]$, can be written as

$$\Delta\left[S\left(A\right)\right] = \Delta\left[W_{ext}\left(A\right)\right] - \Delta\left[U\left(A\right)\right] = \Delta\left[U\left(A\right)\right] = \frac{1}{2} P_1 \Delta w = Area\left(OCB\right) \tag{F19}$$

In other words, half of the work done by the external force is used to increase the internal strain energy, while the other half is dissipated through the propagation of the crack. Finally, as a last step, the SERR can be expressed as a function of the finite variation in the beam compliance as

$$G\left(A\right) = \frac{\Delta\left[U\left(A\right)\right]}{\Delta A} = \frac{1}{2} P_1 \frac{w_2 - w_1}{\Delta A} = \frac{1}{2} P_1^2 \frac{C_2 - C_1}{\Delta A} = \frac{1}{2} P_1^2 \frac{\Delta C}{\Delta A} \tag{F20}$$

and, by taking the limit as $\Delta A \to 0$, Equation (F10) can be retrieved.

Focusing on the constant displacement/deflection (i.e., *fixed grip*) experiment shown in Figure F.3-b, and noticing that $\Delta\left[W_{ext}\left(A\right)\right] = 0$, it is possible to rewrite the equilibrium condition expressed in Equation as

$$\Delta\left[U\left(\mathbf{A}\right)\right] - \Delta\left[W_{ext}\left(\mathbf{A}\right)\right] + \Delta\left[S\left(\mathbf{A}\right)\right] = \Delta\left[U\left(A\right)\right] + \Delta\left[S\left(A\right)\right] = 0 \tag{F21}$$

where the finite variation of the internal strain energy, $\Delta\left[U\left(A\right)\right]$, can be expressed as

$$\begin{aligned} \Delta\left[U\left(A\right)\right] &= U\left(A + \Delta A\right) - U\left(A\right) \\ &= Area\left(O\, w_1 C\right) - Area\left(O\, w_1 B\right) = \frac{1}{2}\left(P_2 - P_1\right) w_1 \end{aligned} \tag{F22}$$

and therefore, the variation in the surface energy can be written explicitly as

$$\Delta\left[S\left(A\right)\right]=-\Delta\left[U\left(A\right)\right]=\frac{1}{2}\left(P_2-P_1\right)w_1=Area\left(OCB\right) \tag{F23}$$

In other words, the quantity $\Delta\left[U\left(A\right)\right]$ is dissipated through the propagation of the crack. Finally, as done previously, the SERR can be expressed as a function of the finite variation in the beam compliance as

$$G=-\frac{\Delta\left[U\left(A\right)\right]}{\Delta A}=-\frac{1}{2}\frac{P_2-P_1}{\Delta A}w_1=-\frac{w_1^2}{2\Delta A}\frac{C_1-C_2}{C_1C_2}=\frac{1}{2}\frac{w_1^2}{C_1C_2}\frac{\Delta C}{\Delta A} \tag{F24}$$

By noticing that $C_1C_2=C_1\left(C_1+\Delta C\right)\cong C_1^2$, Equation (F24) can be approximated with the following relationship

$$G\cong\frac{1}{2}\frac{w_1^2}{C_1^2}\frac{\Delta C}{\Delta A}=\frac{1}{2}P_1^2\frac{\Delta C}{\Delta A} \tag{F25}$$

and, by taking the limit as $\Delta A\to 0$, Equation (F11) can be retrieved.

References

R.J. Sanford, *Principles of fracture mechanics*, Prentice Hall, 2003.

APPENDIX G

DERIVATION OF THE STRAIN ENERGY RELEASE RATE VECTOR FOR A TWO-SPAN COMPOSITE BEAM WITH MULTIPLE DEBONDING FRONTS

Consider the continuous two-span composite beam shown in Figure G.1. The beam is composed of two unidirectional laminated composite adherends, of equal rectangular cross section ($b \times h$), bonded together by an idealized (and imperfect) zero-thickness adhesive layer characterized by four disbonds of lengths a_1, a_2, a_3 and a_4, respectively. Furthermore, for the sake of simplicity, the bondline condition is herein treated as a binary state: it is considered either fully damaged (i.e., with complete loss of adhesive strength and tangential stiffness) or undamaged (i.e., in pristine condition with infinite tangential stiffness). In the first case, the two composite adherends (each of them with rectangular cross section $b \times h$) can freely slip without friction, whereas in the second one, it is possible to consider a monolithic beam cross

section of dimensions $b \times 2h$. As a direct consequence, the moment of inertia of the whole beam cross section with a fully damaged adhesive interface can be expressed as

$$I_{(0)} = 2\frac{b h^3}{12} = \frac{b h^3}{6} \quad \begin{cases} 0 \le x_1 \le a_1\,,\ 2L - a_3 \le x_1 \le 2L \\ 0 \le x_2 \le a_2\,,\ 2L - a_4 \le x_2 \le 2L \end{cases} \tag{G1}$$

while, in the case of a pristine adhesive interface, the cross sectional moment of inertia can be written as

$$I_{(\infty)} = \frac{b(2h)^3}{12} = 4\frac{b h^3}{6} = 4I_1 \quad \begin{cases} a_1 \le x_1 \le 2L - a_3 \\ a_2 \le x_2 \le 2L - a_4 \end{cases} \tag{G2}$$

These results can also be expressed as a function of the moment of inertia of the single composite adherend, $I_a = bh^3/12$, as $I_{(0)} = 2I_a$ and $I_{(\infty)} = 4I_{(0)} = 8I_a$, respectively.

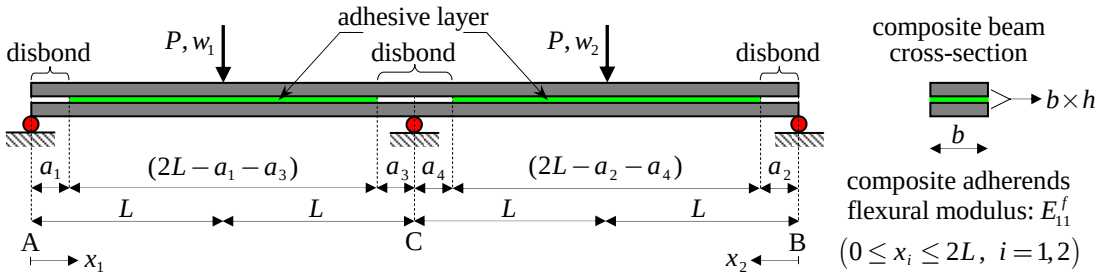

Figure G.1: Two-span composite beam characterized by four debonding fronts and subjected to two concentrated static loads applied at each of the two midspan points.

The beam is subjected to two concentrated static loads of identical intensity (*P*) applied at the midspan points of each of the two spans of the beam. Under these loading conditions and using Euler-Bernoulli beam theory, the scope of this appendix is computing the SERR vector already introduced in Appendix F and defined as

$$\mathbf{G}(\mathbf{A}) = \nabla_{\mathbf{A}}\left[W_{ext}(\mathbf{A}) - U(\mathbf{A})\right] = \nabla_{\mathbf{A}}\left[U(\mathbf{A})\right] \tag{G3}$$

where, for the specific case discussed herein, the damage size vector, **A**, is defined as $\mathbf{A} = \{A_1, A_2, A_3, A_4\}^{\mathrm{T}} = b\{a_1, a_2, a_3, a_4\}^{\mathrm{T}} = b\mathbf{a}$. Consequently, Equation (E3) can be rewritten as

$$\mathbf{G}(\mathbf{a}) = \frac{1}{b}\nabla_{\mathbf{a}}\left[U(\mathbf{a})\right] \tag{G4}$$

where the SERR vector, $\mathbf{G}(\mathbf{a})$, can be computed through the following three substeps: (i) Computation of the vertical reactions at supports A, B, and C (R_{A}, R_{B}, and R_{C}), (ii) Computation of the bending moment (M) produced by the two external loads, and (iii) Computation of the (damage dependent) elastic strain energy $U(\mathbf{a})$.

Computation of the vertical reactions at supports A, B, and C

The vertical reaction at support C is easily computed by recalling the *principle of virtual work* (already introduced and used in Appendix E) and by applying it twice to the auxiliary beams shown in Figures G.2 and G.3.

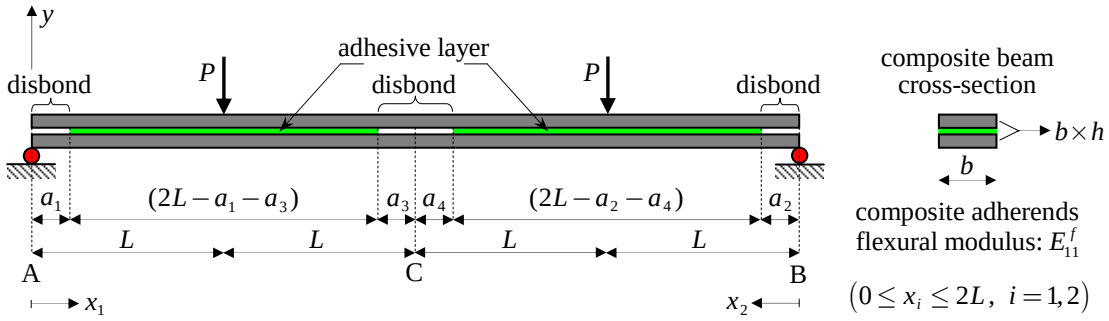

Figure G.2: Auxiliary simply-supported composite beam used to compute the vertical displacement at midspan (i.e., at point C) due to the real external concentrated loads.

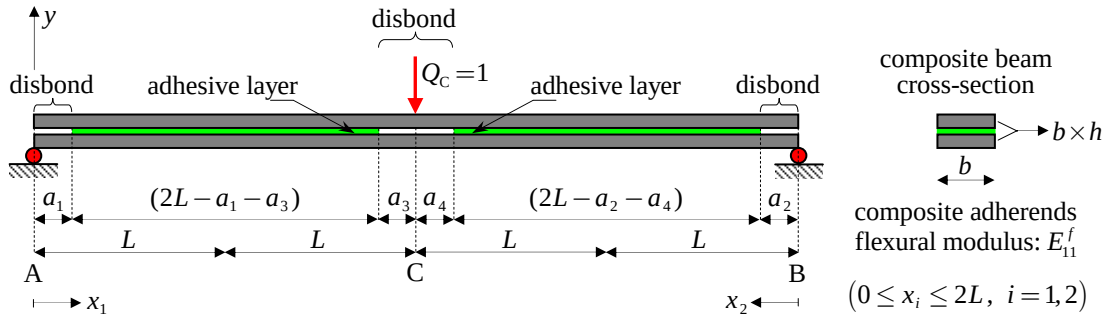

Figure G.3: Auxiliary simply-supported composite beam used to compute the vertical displacement at midspan (i.e., at point C) due to a unit dummy load Q applied at C.

With reference to Figure G.2, the vertical (i.e., along the y-direction) displacement at point C, due to the applied (real) concentrated loads, can be computed as follows:

$$w_C^{(P)} = -\left[\int_0^{a_1} \frac{Px^2}{4E_{11}^f I_a}dx_1 + \int_{a_1}^{L} \frac{Px^2}{16E_{11}^f I_a}dx_1 + \int_{L}^{2L-a_3} \frac{PLx}{16E_{11}^f I_a}dx_1 + \int_{2L-a_3}^{2L} \frac{PLx}{4E_{11}^f I_a}dx_1 + \right.$$
$$\left. \int_0^{a_2} \frac{Px^2}{4E_{11}^f I_a}dx_2 + \int_{a_2}^{L} \frac{Px^2}{16E_{11}^f I_a}dx_2 + \int_{L}^{2L-a_4} \frac{PLx}{16E_{11}^f I_a}dx_2 + \int_{2L-a_4}^{2L} \frac{PLx}{4E_{11}^f I_a}dx_2 \right] \quad \text{(G5)}$$
$$= -\frac{6\left(a_1^3 + a_2^3\right) - 9L\left(a_3^2 + a_4^2\right) + 36L^2\left(a_3 + a_4\right) + 22L^3}{96E_{11}^f I_a}P$$

whereas, with reference to Figure G.3, the vertical (i.e., along the y-direction) displacement at point C, due to the applied dummy unit load Q_C, is equal to

$$w_C^{(1)} = -\left[\int_0^{a_1} \frac{x^2}{8E_{11}^f I_a}dx_1 + \int_{a_1}^{2L-a_3} \frac{x^2}{32E_{11}^f I_a}dx_1 + \int_{2L-a_3}^{2L} \frac{x^2}{8E_{11}^f I_a}dx_1 + \right.$$
$$\left. \int_0^{a_2} \frac{x^2}{8E_{11}^f I_a}dx_2 + \int_{a_2}^{2L-a_4} \frac{x^2}{32E_{11}^f I_a}dx_2 + \int_{2L-a_4}^{2L} \frac{x^2}{8E_{11}^f I_a}dx_2 \right] \quad \text{(G6)}$$
$$= -\frac{3\left(a_1^3 + a_2^3 + a_3^3 + a_4^3\right) - 18L\left(a_3^2 + a_4^2\right) + 36L^2\left(a_3 + a_4\right) + 16L^3}{96E_{11}^f I_a}$$

To ensure zero-displacement at support C, as it is dictated by the beam configuration shown in Figure G.1, the condition $w_{\mathrm{C}}^{(P)} + R_{\mathrm{C}} w_{\mathrm{C}}^{(1)} = 0$ must be satisfied. This leads to the following expression for the vertical reaction at support C:

$$R_{\mathrm{C}} = \frac{6\left(a_1^3 + a_2^3\right) - 9L\left(a_3^2 + a_4^2\right) + 36L^2\left(a_3 + a_4\right) + 22L^3}{3\left(a_1^3 + a_2^3 + a_3^3 + a_4^3\right) - 18L\left(a_3^2 + a_4^2\right) + 36L^2\left(a_3 + a_4\right) + 16L^3} P \tag{G7}$$

If $a_3 = a_4 = 0$, Equation (G7) simplifies to

$$R_{\mathrm{C}} = \frac{6\left(a_1^3 + a_2^3\right) + 22L^3}{3\left(a_1^3 + a_2^3\right) + 16L^3} P \tag{G8}$$

and, by also setting $a_1 = a_2 = 0$, the well-known result for the middle-support reaction (support C according to the notation used in this Appendix) of a symmetric continuous two-span Euler-Bernoulli beam is retrieved:

$$R_{\mathrm{C}} = \frac{11}{8} P \tag{G9}$$

The reactions at supports A and B (R_{A} and R_{B}) can be computed through simple equilibrium equations and are equal to

$$R_{\mathrm{A}} = R_{\mathrm{B}} = \frac{6\left(a_3^3 + a_4^3\right) - 27L\left(a_3^2 + a_4^2\right) + 36L^2\left(a_3 + a_4\right) + 10L^3}{6\left(a_1^3 + a_2^3 + a_3^3 + a_4^3\right) - 36L\left(a_3^2 + a_4^2\right) + 72L^2\left(a_3 + a_4\right) + 32L^3} P \tag{G10}$$

If $a_3 = a_4 = 0$, Equation (G10) simplifies to

$$R_{\mathrm{A}} = R_{\mathrm{B}} = \frac{5L^3}{3\left(a_1^3 + a_2^3\right) + 16L^3} P \tag{G11}$$

and, by also setting $a_1 = a_2 = 0$, the well-known result for the end-support reactions of a symmetric continuous two-span Euler-Bernoulli beam is retrieved:

$$R_{\mathrm{A}} = R_{\mathrm{B}} = \frac{5}{16} P \tag{G12}$$

Computation of the bending moment produced by the external loads

Using the results obtained thus far, expressions for the bending moment produced by the external loads applied to the system shown in Figure G.1 can be easily derived through simple equilibrium considerations. The bending moment along the left span (i.e., between supports A and C) can be expressed as

$$M_{\text{A-C}}(x_1) = \begin{cases} R_{\mathrm{A}} x_1 = P - \dfrac{R_{\mathrm{C}}}{2} x_1 & 0 \le x_1 \le L \\ R_{\mathrm{A}} x_1 - P(x_1 - L) = PL - \dfrac{R_{\mathrm{C}}}{2} x_1 & L \le x_1 \le 2L \end{cases} \tag{G13}$$

whereas the bending moment acting along the right span of the beam (i.e., between supports B and C) takes the following (symmetric) form:

$$M_{\text{B-C}}(x_2) = \begin{cases} R_{\mathrm{B}} x_2 = P - \dfrac{R_{\mathrm{C}}}{2} x_2 & 0 \le x_2 \le L \\ R_{\mathrm{B}} x_2 - P(x_2 - L) = PL - \dfrac{R_{\mathrm{C}}}{2} x_2 & L \le x_2 \le 2L \end{cases} \tag{G14}$$

Both $M_{\text{A-C}}(x_1)$ and $M_{\text{B-C}}(x_2)$ are therefore functions of the level of damage quantified by the vector $\mathbf{a} = \{a_1, a_2, a_3, a_4\}^{\mathrm{T}}$.

Computation of the elastic strain energy $U(\mathbf{a})$

$$U(\mathbf{a}) = \int_0^{a_1} \frac{M_{\text{A-C}}^2}{4E_{11}^f I_a} dx_1 + \int_{a_1}^{L} \frac{M_{\text{A-C}}^2}{16E_{11}^f I_a} dx_1 + \int_{L}^{2L-a_3} \frac{M_{\text{A-C}}^2}{16E_{11}^f I_a} dx_1 + \int_{2L-a_3}^{2L} \frac{M_{\text{A-C}}^2}{4E_{11}^f I_a} dx_1 + \int_0^{a_2} \frac{M_{\text{B-C}}^2}{4E_{11}^f I_a} dx_2 + \int_{a_2}^{L} \frac{M_{\text{B-C}}^2}{16E_{11}^f I_a} dx_2 + \int_{L}^{2L-a_4} \frac{M_{\text{B-C}}^2}{16E_{11}^f I_a} dx_2 + \int_{2L-a_4}^{2L} \frac{M_{\text{B-C}}^2}{4E_{11}^f I_a} dx_2 \tag{G15}$$

The integration of Equation (G15), performed using Mathematica®, leads to the following result:

$$\begin{aligned} U(\mathbf{a}) = \frac{P^2}{\psi_U(\mathbf{a}) E_{11}^f I_a} \Big\{ & 36\left(a_1^3 + a_2^3\right)\left(a_3^3 + a_4^3\right) - 108L\left(a_1^3 + a_2^3\right)\left(a_3^2 + a_4^2\right) + \\ & 27L^2\left[\left(a_3 + a_4\right)\left(4a_1^3 + 4a_2^3 + a_3^3 + a_4^3\right) + 3a_3\, a_4\left(a_3 - a_4\right)^2\right] + \\ & 24L^3\left(a_1^3 + a_2^3 + 4a_3^3 + 4a_4^3\right) - 180L^4\left(a_3^2 + a_4^2\right) \\ & + 144L^5\left(a_3 + a_4\right) + 28L^6 \Big\} \end{aligned} \tag{G16}$$

where

$$\psi_U(\mathbf{a}) = 192\left[3\left(a_1^3 + a_2^3 + a_3^3 + a_4^3\right) - 18L\left(a_3^2 + a_4^2\right) + 36L^2\left(a_3 + a_4\right) + 16L^3\right] \tag{G17}$$

If $a_3 = a_4 = 0$, then $\mathbf{a} = \{a_1, a_2\}^{\mathrm{T}}$ and Equation (G16) simplifies to

$$\begin{aligned} U(a_1, a_2) = & \int_0^{a_1} \frac{M_{\text{A-C}}^2}{4E_{11}^f I_a} dx_1 + \int_{a_1}^{L} \frac{M_{\text{A-C}}^2}{16E_{11}^f I_a} dx_1 + \int_{L}^{2L} \frac{M_{\text{A-C}}^2}{16E_{11}^f I_a} dx_1 + \\ & \int_0^{a_2} \frac{M_{\text{B-C}}^2}{4E_{11}^f I_a} dx_2 + \int_{a_2}^{L} \frac{M_{\text{B-C}}^2}{16E_{11}^f I_a} dx_2 + \int_{L}^{2L} \frac{M_{\text{B-C}}^2}{16E_{11}^f I_a} dx_2 \\ = & \frac{P^2 L^3}{48E_{11}^f I_a} \frac{6\left(a_1^3 + a_2^3\right) + 7L^3}{3\left(a_1^3 + a_2^3\right) + 16L^3} \end{aligned} \tag{G18}$$

Computation of the strain energy release rate (SERR) vector $\mathbf{G}(\mathbf{a})$

The SERR vector $\mathbf{G}(\mathbf{a}) = \{G_1(\mathbf{a}) \;\; G_2(\mathbf{a}) \;\; G_3(\mathbf{a}) \;\; G_4(\mathbf{a})\} = \nabla_{\mathbf{A}}[U(\mathbf{a})]/b$ can now be derived by taking the four partial derivatives of $U(\mathbf{a})$ — derived previously in Equation (G16) — with respect to a_1, a_2, a_3, and a_4:

$$\mathbf{G}(\mathbf{a}) = \frac{1}{b}\left\{\frac{\partial U(\mathbf{a})}{\partial a_1} \;\; \frac{\partial U(\mathbf{a})}{\partial a_2} \;\; \frac{\partial U(\mathbf{a})}{\partial a_3} \;\; \frac{\partial U(\mathbf{a})}{\partial a_4}\right\} \tag{G19}$$

The expressions for the four components of $\mathbf{G}(\mathbf{a})$ are listed below:

$$G_1(\mathbf{a}) = \frac{1}{b}\frac{\partial U(\mathbf{a})}{\partial a_1} = \frac{9a_1^2P^2}{E_{11}^f b I_a}\left[\frac{\phi_U^{(1)}(\mathbf{a})}{\psi_U(\mathbf{a})}\right]^2 \tag{G20}$$

$$G_2(\mathbf{a}) = \frac{1}{b}\frac{\partial U(\mathbf{a})}{\partial a_2} = \frac{9a_2^2P^2}{E_{11}^f b I_a}\left[\frac{\phi_U^{(2)}(\mathbf{a})}{\psi_U(\mathbf{a})}\right]^2 \tag{G21}$$

$$G_3(\mathbf{a}) = \frac{1}{b}\frac{\partial U(\mathbf{a})}{\partial a_3} = \frac{9P^2}{E_{11}^f b I_a}\left[\frac{\phi_U^{(3)}(\mathbf{a})}{\psi_U(\mathbf{a})}\right]^2 \tag{G22}$$

$$G_4(\mathbf{a}) = \frac{1}{b}\frac{\partial U(\mathbf{a})}{\partial a_4} = \frac{9P^2}{E_{11}^f b I_a}\left[\frac{\phi_U^{(4)}(\mathbf{a})}{\psi_U(\mathbf{a})}\right]^2 \tag{G23}$$

where

$$\phi_U^{(1)}(\mathbf{a}) = \phi_U^{(2)}(\mathbf{a}) = 6\left(a_3^3 + a_4^3\right) - 27L\left(a_3^2 + a_4^2\right) + 36L^2\left(a_3 + a_4\right) + 10L^3 \tag{G24}$$

$$\begin{aligned}\phi_U^{(3)}(\mathbf{a}) = {} & 6a_3\left(a_1^3 + a_2^3\right) - 3L\left[2\left(a_1^3 + a_2^3 - a_4^3\right) + a_3\left(a_3^2 + 3a_4^2\right)\right] + \\ & 18L^2\left(a_3^2 + 2a_3a_4 - a_4^2\right) + 22a_3L^3 - 12L^4\end{aligned} \tag{G25}$$

$$\phi_U^{(4)}(\mathbf{a}) = 6a_4\left(a_1^3 + a_2^3\right) - 3L\left[2\left(a_1^3 + a_2^3 - a_3^3\right) + a_4\left(3a_3^2 + a_4^2\right)\right] + 18L^2\left(a_3^2 + 2a_3a_4 - a_4^2\right) + 22a_3L^3 - 12L^4 \tag{G26}$$

If $a_3 = a_4 = 0$, then the SERR vector, $\mathbf{G}(\mathbf{a})$, reduces to

$$\mathbf{G}(\mathbf{a}) = \mathbf{G}(a_1, a_2) = \left\{G_1(a_1, a_2) \;\; G_2(a_1, a_2)\right\} = \frac{1}{b}\left\{\frac{\partial U(\mathbf{a})}{\partial a_1} \;\; \frac{\partial U(\mathbf{a})}{\partial a_2}\right\} \tag{G27}$$

And, after some simple algebraic simplifications, each of its two components — i.e., $G_1(a_1, a_2)$ and $G_2(a_1, a_2)$ — can be expressed as

$$G_1(\mathbf{a}) = G_1(a_1, a_2) = \frac{1}{b}\frac{\partial U(a_1, a_2)}{\partial a_1} = \frac{75P^2L^6}{16E_{11}^f b I_a}\frac{a_1^2}{\left[3\left(a_1^3 + a_2^3\right) + 16L^3\right]^2} \tag{G28}$$

$$G_2(\mathbf{a}) = G_2(a_1, a_2) = \frac{1}{b}\frac{\partial U(a_1, a_2)}{\partial a_2} = \frac{75P^2L^6}{16E_{11}^f b I_a}\frac{a_2^2}{\left[3\left(a_1^3 + a_2^3\right) + 16L^3\right]^2} \tag{G29}$$

Equations (G20) through (G23), or Equations (G28) and (G29) for the simpler case in which $a_3 = a_4 = 0$, essentially state that the applied SERR at a given debonding front is a function of all the components of the damage size vector **a** and not only of the damage extent associated with that particular debonding front. As a direct consequence of this result, the fatigue-driven debonding propagation is a fully coupled process. For example, if the structural system shown in Figure G.1 is considered and Paris law (Paris and Erdogan, 1963) is used to simulate the debonding propagation process induced by the loading cycles, the system of (four) first-order ordinary differential governing this process can be written as

$$\begin{cases} \dfrac{da_1^{[p,t]}}{dt} = C_1 \cdot \left[\Delta G_1\left(a_1^{[p,t]}, a_2^{[p,t]}, a_3^{[p,t]}, a_4^{[p,t]}\right)\right]^{m_1} \\ \dfrac{da_2^{[p,t]}}{dt} = C_2 \cdot \left[\Delta G_2\left(a_1^{[p,t]}, a_2^{[p,t]}, a_3^{[p,t]}, a_4^{[p,t]}\right)\right]^{m_2} \\ \dfrac{da_3^{[p,t]}}{dt} = C_3 \cdot \left[\Delta G_3\left(a_1^{[p,t]}, a_2^{[p,t]}, a_3^{[p,t]}, a_4^{[p,t]}\right)\right]^{m_3} \\ \dfrac{da_4^{[p,t]}}{dt} = C_4 \cdot \left[\Delta G_4\left(a_1^{[p,t]}, a_2^{[p,t]}, a_3^{[p,t]}, a_4^{[p,t]}\right)\right]^{m_4} \\ a_1\left(t = t_p\right) = a_1^p \\ a_2\left(t = t_p\right) = a_2^p \\ a_3\left(t = t_p\right) = a_3^p \\ a_4\left(t = t_p\right) = a_4^p \end{cases} \tag{G30}$$

where C_i and m_i (with $i = 1,2,...4$) are the Paris law constants, $a_i^{[p,t]}$ (with $t \geq t_p$ $i = 1,2,...4$) represent the predicted debonding lengths at time $t \geq t_p$, and a_i^p (with $i = 1,2,...4$) constitute the initial debonding lengths at initial time t_p (e.g., current time immediately after the last NDE inspection, as described in Chapters 5 and 8).

References

P.C. Paris and F.A. Erdogan, Critical analysis of crack propagation laws, *Journal of Basic Engineering*, TRANS ASME, 85(Series D), 528-534, 1963.